The Meso-NH Atmospheric Simulation System:

Scientific Documentation

Part III: Physics

Acknowledgments

This volume contains contributions from P. Bechtold, S. Belair, Ph. Bougeault, J.M. Carrière, J. Cuxart, V. Ducrocq, C. Fischer, M. Georgelin, P. Héreil, J.-P. Lafore, C. Liousse, C. Mari, I. Mallet, P. J. Mascart, V. Masson, J.-P. Pinty, E. Richard, K. Suhre, J. Stein, P. Tulet, and J. Vilà-Guerau de Arellano. As editors, we would like to express our deep appreciation for the dedicated work of all contributors. The Meso-NH project is the achievement of a much larger team. Our thanks extend to all those who are not cited here, but have given their best to create this unique tool.

Philippe Bougeault and Patrick Mascart

Since the 2002 edition, in addition to the contributors cited above, thanks have to be extended to C. Augros, F. Auguste, D. Barbary, C. Barthe, S. Berthet, Y. Bouteloup, C. Bovalo, O. Caumont, J.-P. Chaboureau, M. Chong, A. Costes, F. Couvreux, T. Dauhut, G. Delautier, J. Escobar, O. Geoffroy, P.A. Joulin, C. Lac, P. Le Moigne, M. Leriche, Q. Libois, T. Lunet, M. Mandement, T. Marić, G. Molinié, T. Nagel, J., O. Nuissier, Pergaud, D. Ricard, Q. Rodier, R. Schoetter, F. Solmon, O. Thouron, M. Tomasini, B. Tsenova, B. Vié and F. Visentin.

Jean-Pierre Chaboureau

Chapter 1

The radiation parameterizations

Contents

1.1 Introduction to the radiation codes

1.1.1 Purpose

This chapter summarizes the salient features concerning the two radiation packages available in Meso-NH:

- the ’orignal’ radiation scheme running at ECMWF on March 2002 (CY23r4);
- the ecRad radiation scheme running at ECMWF on 2016.

The radiation packages calculate the radiative fluxes taking into account absorption-emission of longwave radiation and reflection, scattering and absorption of solar radiation by the earth’s atmosphere and surfaces. Notice that although the radiation parameterization can deliver a great deal of fluxes (up/down LW/SW in several bands), the package and its interface with Meso-NH only provides the surface shortwave and longwave fluxes with slope angle corrections and the 3D net radiative tendency of the thermodynamical variable θ to the regular user. In addition, some specific configurations of the scheme are available to save computation ressources when a great accuracy of the radiative effects is superfluous. This includes the possibility of calling the package at a different rate of the model timestep, with the ”clear sky” approximation, for the ”cloud only” air columns or for a larger step of the horizontal sweep out of the air columns. All the details of the parameterization and calling interface will be exposed in this section.

The aim of the routine RADIATIONS is to produce the net total radiative heat flux F used to evaluate the potential temperature tendency term:

$$\frac{\partial \theta}{\partial t} = \frac{g}{C_{ph}} \Pi \frac{\partial F}{\partial p},$$

where F is a net flux: i.e. $F = F^{\uparrow} + F^{\downarrow}$ sum of the upward $F^{\uparrow}$ and downward $F^{\downarrow}$ fluxes, and a total flux: i.e. $F = F_{LW} + F_{SW}$ sum of the solar or shortwave F_{SW} and atmospheric or longwave F_{LW} fluxes. Also in order to drive the surface process scheme, the routine RADIATIONS provides the total downward surface flux in the shortwave and longwave part of the spectrum. All these fluxes are expressed in W m^{-2} unit. The downward SW surface flux is partitioned into direct and diffuse contributions. Note that the radiation output fluxes are defined on a flat surface. A topographic correction is then applied (routine SURF_RAD_MODIF) to get the effective surface fluxes entering in the ISBA scheme (see the specific documentation). A number of other fields are available running the DIAG program as for example the LW and SW flux profiles, the specific LW and SW radiative tendencies, the cloud optical properties, etc (see the DIAG documentation).

1.1.2 The original ECMWF radiation code and its Meso-NH interface

The code treats successively the longwave and shortwave radiative transfers for independent air columns. The routine named ECMWF_RADIATION_VERS2 is the interface between the physical variables available in Meso-NH through routine RADIATIONS and the ECMWF LW and SW codes. This routine is used also to initialise cloud radiative properties that do not directly belong to the radiation scheme. It calls the subroutine LW (SW) which handles the infrared (solar) part, respectively.

1.1.3 The ecRad radiation code

The latest radiation code of ECMWF, ecRad (Hogan and Bozzo 2016) is available in Meso-NH since version 5.4. While a detailed scientific documentation for this code will be provided in a future version of this scientific documentation, here the main changes with regards to the original radiative code and the new options are outlined. the ecRad code is a very modular code that offers the possiblity to handle the various components of atmospheric radiative transfer separately, as detailed below.

The LW radiation is computed in 16 bands (140 g-points) corresponding to the correlated-k distribution of the Rapid Radiation Transfer Model (RRTM, Mlawer et al. 1997). In the SW, the ECMWF version of RRTM (Morcrette et al. 2008) with 14 bands and 112 g-points is used. Gas optical properties are all computed from the RRTM database, and the broadband solar irradiance at top of atmosphere has been updated to its present best estimate. See the RRTM section for more detail.

Liquid and ice cloud optical properties can be computed according to a variety of parameterizations. Liquid cloud optical radius is generally computed from liquid water content (LWC), including an updated version of the parameterization of Martin et al. (1994). Likewise, ice cloud optical radius can be computed from ice water content following Sun and Rikus (1999) and Sun (2001). Cloud optical properties (optical depth, single scattering albedo and asymmetry parameter) are then computed as a function of particle effective radius and liquid/ice water content. Notably, the SOCRATES parameterization (Manners 2015), in use at the Met Office, is now available. Ice water optical properties can be computed according to Ebert and Curry (1993), Smith and Shi (1992) or the recent database of Baran et al. (2014).

The main changes with regards to the original radiation code concern the treatment of unresolved clouds. First, the McICA scheme (Pincus et al. 2003) is used by default and allows a proper treatment of cloud fraction and subgrid water content heterogeneities. Two original solvers are also available : the TripleClouds method (Shonk and Hogan 2008) that efficiently deals with cloud horizontal hétérogeneities, and the SPARTACUS solver (Schäfer et al. 2016; Hogan et al. 2016) that represents lateral photon transport through cloud sides (Hogan and Shonk 2013) in a 1-D formalism. In addition, the cloud overlap assumption can now be prescribed. In particular, the Exponetial-Random and Exponential-Exponential options are available (Hogan and Illingworth 2000).

All these updates can result in significantly different radiative fluxes and heating rates, in particular in the SW for cloudy skies.

1.2 Longwave radiation

Two different LW schemes can be activated in Meso-NH (namelist CLW).

- The first one (CLW='MORC') corresponds to the LW scheme operationnal at ECMWF from may 1989 to June 2000 (Morcrette 1991; Gregory et al. 2000). The main characteristics of the scheme are given below (Table 1.1). Physical basis of this model are described in the ECMWF radiation documentation (Chapter 2.2.1 to 2.2.4) and are reproduced below.
- The second one (CLW='RRTM') corresponds to the Rapid Radiation Transfer Model which is currently operational at ECMWF. The main characteristics of RRTM are recalled below (Table 1.1). More details as well as bibliographic references are given in the ECMWF radiation documentation (Chapter 2.2.5) and are reproduced below.

Table 1.1: Main characteristics of LW schemes

	RRTM	MORC
Solution of radiative transfer equation	Two-stream method	Spectral emissivity method
Number of spectral intervals	16	6
Absorbers	H_2O, CO_2, $O3$, CH_4, N_2O, $CFC11$, $CFC12$, aerosols	H_2O, CO_2, $O3$, CH_4, N_2O, $CFC11$, $CFC12$, aerosols
Spectroscopic data base	HITRAN 1996	HITRAN 1992
Absorption coefficient	From LBLRTM line-by-line model	Fits on statistical model of transmission
Cloud handling	True cloud fraction	Effective cloud fraction (CF * emissivity)
Cloud optical properties: method	16-band spectral emissivity	Whole spectrum emissivity
Cloud overlap assumption	Maximum random	Maximum random (maximum and random also possible)
References	¢(Mlawer et al. 1997)	(Morcrette et al. 1986; Morcrette 1991; Gregory et al. 2000)

1.2.1 The Morcrette longwave radiation

1.2.2 First glance

The rate of net atmospheric cooling by emission-absorption of longwave radiation (`PDTLOG` is given in Kelvin/hour in the code) is:

$$\frac{\partial T}{\partial t} = \frac{g}{C_{ph}} \frac{\partial F}{\partial p}, \tag{1.1}$$

where $F = F_{LW}$ is the net total longwave flux.

Assuming a non-scattering atmosphere in local thermodynamic equilibrium, $F \equiv F^{\uparrow\downarrow}$ is given by:

$$F^{\uparrow\downarrow} = \int_{-1}^{+1} \mu \, d\mu \int_0^{\infty} \left[L_\nu(p_s, \mu) \, t_\nu(p_s, p, \mu) + \int_{p_s}^{0} L_\nu(p', \mu) \, dt_\nu \right] d\nu \tag{1.2}$$

where $L_\nu(p_s, \mu)$ is the monochromatic radiance of wavenumber ν at level p propagating in a direction such as $\mu \cos \vartheta$ is the cosine of the angle ϑ that this direction makes with the vertical and $t_\nu(p, p', \mu)$ is the monochromatic transmission through a layer whose limits are at p and p', seen under the same angle.

After separating the upward and downward components and integrating by parts, we obtain the radiation transfer equation as it is actually estimated in the radiation code

$$\begin{aligned} F_\nu^{\uparrow}(p) &= \left[B_\nu(T_s) - B_\nu(T_{0+}) \right] t_\nu(p_s, p; r) + B_\nu(T_p) + \int_{p_s}^{p} t_\nu(p, p'; r) \, dB_\nu, \\ F_\nu^{\downarrow}(p) &= \left[B_\nu(T_t) - B_\nu(T_\infty) \right] t_\nu(p, 0; r) - B_\nu(T_p) - \int_{p}^{0} t_\nu(p', p; r) \, dB_\nu. \end{aligned} \tag{1.3}$$

Taking benefit of the isotropic nature of the longwave radiations, the radiance L_ν of (1.2) is replaced by the Planck function $B_\nu(T)$ in unit of flux W m^{-2} (subroutine LWB) (hereafter B_ν always includes the π factor). Notice that T_s is the surface temperature (in fact a radiative surface temperature `PTSRAD` issuing from a surface process scheme such as ISBA) and that T_{0+} is the temperature of the air just above the surface. T_p is the air temperature (PT) at the Meso-NH mandatoy levels where the atmospherique pressure p needs also to be calculated. T_t is the temperature at the top of the atmosphere (standard atmosphere extension above the last atmospheric level) and $B_\nu(T_\infty$ is set to zero. The transmission t_ν is evaluated as the radiance transmission in a direction ϑ to the vertical such that $r = \sec \vartheta$ is the diffusivity factor (Elsasser 1942). Such an approximation for the integration over the angle is usual in radiative transfer calculations and tests on the validity of this approximation have been presented by Rodgers and Walshaw (1966) among others. The use of the diffusivity factor gives cooling rates within 2% of those obtained with a 4-point Gaussian quadrature.

1.2.3 Vertical integration

Integrals in (1.3) are evaluated numerically, after discretization over the vertical grid, considering the atmosphere as a pile of homogeneous layers (subroutine LWV). As the cooling rate is strongly dependent on local conditions of temperature and pressure and energy is mainly exchanged with the layers adjacent to the level where fluxes are calculated, the contribution of the distant layers is simply computed using a trapezoidal rule integration (subroutine LWVD), but the contribution of the adjacent layers is evaluated with a 2-point Gaussian quadrature (subroutine LWVN; see common YOMLW), thus

$$\int_{p_s}^{p_i} t_\nu(p, p'; r) = \sum_{l=1}^{2} w_l \, t_\nu(p_i, p_l; r) \, dB_\nu(l) + \frac{1}{2} \sum_{j=1}^{i-2} \left[t_\nu(p_i, p_j; r) + t_\nu(p_i, p_{j-1}; r) \right] dB_\nu(j) \tag{1.4}$$

where p_l and w_l are the pressure corresponding to the Gaussian root and the Gaussian weight, respectively. $dB_\nu(j)$ (PDBDT) and $dB_\nu(l)$ (PDBSL) are the Planck function gradients calculated between two interfaces and between mid-layer and interface, respectively.

1.2.4 Spectral integration

The integration over wavenumber ν is performed using a band emissivity method, as first discussed by Rodgers (1967). The longwave spectrum is divided into six spectral regions:

1	0 - 350 cm^{-1}	+	1450 - 1880 cm^{-1}
2	500 - 800 cm^{-1}		
3	800 - 970 cm^{-1}	+	1110 - 1250 cm^{-1}
4	970 - 1110 cm^{-1}		
5	350 - 500 cm^{-1}		
6	1250 - 1450 cm^{-1}	+	1880 - 2820 cm^{-1}

corresponding to the centers of the rotation and vibration-rotation bands of H_2O, the 15-μm band of CO_2, the atmospheric window, the 9.6-μm band of O_3, the 25-μm "window" region and the wings of the vibration-rotation band of H_2O, respectively. Over these spectral regions, band fluxes are evaluated with the help of band transmissivities precalculated from the narrow-band model of Morcrette and Fouquart (1985) – See Appendix of Morcrette et al. (1986) for details.

Integration of (1.3) over wavenumber ν within the wide k^{th} spectral region gives the upward and downward fluxes as

$$\begin{aligned}
F_k^{\uparrow}(p) &= \left[B_k(T_s) - B_k(T_{0^+})\right] t_{B_k}(ru(p_s,p), T_u(p_s,p)) \\
&\quad + B_k(T_p) + \int_{p_s}^{p} t_{dB_k}(ru(p,p'), T_u(p,p'))\, dB_k, \\
F_k^{\downarrow}(p) &= \left[B_k(T_0) - B_k(T_\infty)\right] t_{B_k}(ru(p,0), T_u(p,0)) \\
&\quad - B_k(T_p) - \int_{p}^{0} t_{dB_k}(ru(p',p), T_u(p',p))\, dB_k. \qquad (1.5)
\end{aligned}$$

The formulation accounts for the different temperature dependences involved in atmospheric flux calculations, namely that on T_p, the temperature at the level where fluxes are calculated and that on T_u, the temperature that governs the transmission through the temperature dependence of the intensities and half-widths of the lines absorbing in the concerned spectral region. The band transmissivities are non-isothermal accounting for the temperature dependence that arises from the wavenumber integration of the product of the monochromatic absorption and the Planck function. Two normalized band transmissivities are used for each absorber in a given spectral region (subroutine SWTT1): the first one $t_B(\overline{up}, T_p, T_u)$ for calculating the first r.h.s. term in (1.3) involving the boundaries; it corresponds to the weighted average of the transmission function by the Planck function

$$t_B(\overline{up}, T_p, T_u) = \frac{\int_{\nu_1}^{\nu_2} B_\nu(T_p)\, t_\nu(\overline{up}, T_u)\, d\nu}{\int_{\nu_1}^{\nu_2} B_\nu(T_p)\, d\nu} \qquad (1.6)$$

and the second one $t_{dB}(\overline{up}, T_p, T_u)$ for calculating the integral terms in (1.3) is the weighted average of the transmission function by the derivative of the Planck function

$$t_{dB}(\overline{up}, T_p, T_u) = \frac{\int_{\nu_1}^{\nu_2} dB_\nu(T_p)/dT \; t_\nu(\overline{up}, T_u)\, d\nu}{\int_{\nu_1}^{\nu_2} dB_\nu(T_p)/dT \; d\nu} \tag{1.7}$$

where $\overline{up}$ is the pressure weighted amount of absorber (computed in SWU).
In the scheme, the actual dependence on T_p is carried out explicity in the Planck functions integrated over the spectral regions. Although normalized relative to $B(T_p)$ (or $dB(T_p)/dT$), the transmissivities still depend on T_u both through Wien's displacement of the maximum of the Planck function with temperature and through the temperature dependence of the absorption coefficients. O_3 transmissivity is obtained using the Malkmus band model and CH_4, N_2O, $CFC-11$ and $CFC-12$ transmissivities with a statistical model. For computational efficiency, H_2O and CO_2 transmissivities have been developed into Padé approximants

$$t(\overline{up}, T_u) = \frac{\sum_{i=0}^{2} C_i \, u_{eff}^{i/2}}{\sum_{j=0}^{2} D_j \, u_{eff}^{j/2}}, \tag{1.8}$$

where $u_{eff} = r\,\overline{up}\, f(T_u, \overline{up})$ is an effective amount of absorber which incorporates the diffusivity factor r, the weighting of the absorber amount by pressure, $\overline{up}$ and the temperature dependence of the absorption coefficients f, with

$$f(T_u, \overline{up}) = \exp[a(\overline{up})\,(T_u - 250) + b(\overline{up})\,(T_u - 250)^2]. \tag{1.9}$$

The temperature dependence due to Wien's law is incorporated although there is no explicit variation of the coefficients C_i and D_j with temperature. These coefficients have been computed for temperatures between 187.5 and 312.5 K with a 12.5 K step and transmissivities corresponding to the reference temperature the closest to the pressure weighted temperature T_u are actually used in the scheme.

1.2.5 Incorporation of the effects of clouds

The incorporation of the effects of clouds on the longwave fluxes follows the treatment discussed by Washington and Williamson (1977). Whatever the state of cloudiness of the atmosphere, the scheme starts by calculating the clear-sky fluxes and stores the terms representing exchanges of energy between the levels (integrals in (1.3).
Let $F_0^{\uparrow}(i)$ and $F_0^{\downarrow}(i)$ be the upward and downward clear-sky fluxes (PFUP and PFDN in LWC). For any cloud layer actually present in the atmosphere, the scheme then evaluates the fluxes assuming a unique overcast cloud of unity emissivity. Let $F_n^{\uparrow}(i)$ and $F_n^{\downarrow}(i)$ the upward and downward fluxes when such a cloud is present in the n^{th} layer of the atmosphere. Downward fluxes above the cloud and upward fluxes below it have kept their clear-sky values that is:

$$\begin{aligned} F_n^{\uparrow}(i) &= F_0^{\uparrow}(i) \qquad for \qquad i \leq n, \\ F_n^{\downarrow}(i) &= F_0^{\downarrow}(i) \qquad for \qquad i > n. \end{aligned} \tag{1.10}$$

Upward fluxes above the cloud ($F_n^{\uparrow}(k)$ for $k \geq n+1$) and downward fluxes below it ($F_n^{\downarrow}(k)$ for $k < n$) can be expressed with expressions similar to (1.3) provided the boundary terms are now replaced by terms corresponding to possible temperature discontinuities between the cloud and the surrounding air

$$\begin{aligned} F_n^{\uparrow}(k) &= \left[F_{cld}^{\uparrow} - B(n+1)\right] t(p_k, p_{n+1}; r) + B(k) + \int_{p_{n+1}}^{p_k} t(p_k, p'; r)\, dB, \\ F_n^{\downarrow}(k) &= \left[F_{cld}^{\downarrow} - B(n)\right] t(p_k, p_n; r) + B(k) + \int_{p_k}^{p_n} t(p', p_k; r)\, dB. \end{aligned} \tag{1.11}$$

where $B(i)$ is now the total Planck function (integrated over the whole longwave spectrum) at level i and $F_{cld}^{\uparrow}$ and $F_{cld}^{\downarrow}$ are the fluxes at the upper and lower boundaries of the cloud. Terms under the integrals correspond to exchange of energy between layers in the clear-sky atmosphere and have already been computed in the first step of the calculations. This step is repeated for all cloudy layers. The fluxes for the actual atmosphere (with semi-transparent, fractional and/or multi-layered clouds) are derived from a linear combination of the fluxes calculated in previous steps with some cloud overlap assumption in the case of clouds present in several layers. Let N be the index of the layer containing the highest cloud. C_i the fractional cloud cover in layer i, with $C_0 = 1$ for the upward flux at the surface and with $C_{N+1} = 1$ and $F_{N+1}^{\downarrow} = F_0^{\downarrow}$ to have the right boundary condition for downward fluxes above the highest cloud. The cloudy upward ($F^{\uparrow}$) and downward ($F^{\downarrow}$) fluxes are obtained, with the hypothesis of a random covering of clouds, as:

$$\begin{gathered} F^{\uparrow}(i) = F_0^{\uparrow}(i) \qquad for\, i = 1 \\ F^{\uparrow}(i) = C_{i-1} F_{i-1}^{\uparrow}(i) + \sum_{n=0}^{i-2} C_n F_n^{\uparrow}(i) \prod_{l=n+1}^{i-1} (1 - C_l) \qquad for\, 2 \leq i \leq N+1 \\ F^{\uparrow}(i) = C_N F_N^{\uparrow}(i) + \sum_{n=0}^{N-1} C_n F_n^{\uparrow}(i) \prod_{l=n+1}^{N} (1 - C_l) \qquad for\, i \geq N+2 \end{gathered} \tag{1.12}$$

In case of semi-transparent clouds, the fractional cloudiness entering the calculations is an effective cloud cover equal to the product of the emissivity by the horizontal coverage of the cloud layer, with the emissivity related to the condensed water amount by:

$$\epsilon_i = 1 - \exp(-K_{abs}^{L}\, u_{LWP} - K_{abs}^{I}\, u_{IWP}) \tag{1.13}$$

where K_{abs}^{L} is the condensed water mass absorption coefficient (in m^2 kg^{-1}) and K_{abs}^{I}, the corresponding one for ice phase. Different parameterisations are avalaible (see subsection 1.4.5).

1.2.6 The Rapid Radiation Transfer Model (RRTM)

As stated in Mlawer et al. (1997), the objective in the development of RRTM has been to obtain an accuracy in the calculation of fluxes and heating rates consistent with the best line-by-line models. It utilizes the correlated-k methode and shows its filiation to the Atmospheric and Environmental Research, Inc. (AER) line-by-line model (LBLRTM; Clough et al. 1989, 1992; Clough and Iacono 1995) through its use of absorption coefficients for the relevant k-distributions derived from LBLRTM. Therefore the k-coefficients in RRTM include the effect of the CKD2.2 water vapour continuum (Clough et al. 1989).

The main point in the correlated-k method (Lacis and Oinas 1991; Fu and Liou 1992) is the mapping of the absorption coefficient $k(\nu)$ from the spectral space (where it varies irregularly with wavenumber ν) to the g-space (where $g(k)$ is the probability distribution function, i.e. the fraction of the absorption coefficients in the set smaller than k). The effect of this reordering is a rearrangement of the sequence of terms in the integral over wavenumber in the radiative transfer equation (RTE), which makes it equivalent to what would be done for monochromatic radiation.

In the ECMWF (hence, Meso-NH) model, no provision is presently taken for scattering in the longwave. Therefore, in order to get the downward radiance, the integration over the vertical dimension is simply done starting from the top of the atmosphere, going downward layer by layer. At the surface, the boundary condition (in terms of spectral emissivity, and potential reflection of downward radiance) is computed, then, in order to get the upward radiance, the integration over the vertical dimension is repeated, this from the surface upward.

The spectrally averaged radiance (between ν_1 and ν_2) emerging from an atmospheric layer is

$$\overline{R} = \frac{1}{(\nu_1 - \nu_2)} \int_{\nu_2}^{\nu_1} d\nu \left\{ R_0(\nu) + \int_{t_\nu}^{1} \left[B(\nu, T(t'_\nu))\, R_0(\nu) \right] dt' \right\} \tag{1.14}$$

where R_0 is the incoming radiance to the layer, $B(\nu, T)$ is the Planck function at wavenumber ν and temperature T, t_ν is the transmittance for the layer optical path, and t'_ν is the transmittance at a point along the optical path in the layer. Under the mapping $\nu \rightarrow g$, this becomes

$$\overline{R} - \int_0^1 dg \left\{ B_{\text{eff}}(g, T_g) + \left[R_0(g) - B_{\text{eff}}(g, T_g) \right] \exp \left[-k(g, P, T) \frac{\rho \delta z}{\cos \phi} \right] \right\} \tag{1.15}$$

where $B_{\text{eff}}(g, T)$ is an effective Planck function for the layer that varies with the layer's transmittance such as to ensure continuity of flux across layer boundaries for opaque conditions. The dependence of the transmittance is now written in terms of the absorption coefficient $k(g, P, T)$ at layer pressure P and temperature T, the absorber density ρ, the vertical thickness of the layer δz, and the angle ϕ of the optical path.

For a given spectral interval, the domain of the variable g is partitioned into subintervals (see Table 1.2, number of g-points), each corresponding to a limited range of $k(g)$ values and for which a characteristic value κ_j of the absorption coefficient is chosen. These κ_j are then used to compute the outgoing radiance

$$\overline{R} = \Sigma_j W_f \left[B_{\text{eff}_j} + (R_0(g) - B_{\text{eff}_j}) \exp \left(\kappa_j \frac{\rho \delta z}{\cos \phi} \right) \right] \tag{1.16}$$

where W_j is the size of the sub-intervals ($\Sigma W_f = 1$).

The accuracy of these absorption coefficients has been established by numerous and continuing high-resolution validations of LBLRTM with spectroscopic measurements, in particular those from the Atmospheric Radiation Measurement program (ARM). Compared to the original RRTM (Mlawer et al. 1997), the version used at ECMWF (hence, Meso-NH) has been slightly modified to account for cloud optical properties and surface emissivity defined for each of the 16 bands over which spectral fluxes are computed. For efficiency reason, the original number of g-points ($256 = 16 \times 16$) has been reduced to 140 (see Table 1.2). Other changes are the use of a diffusivity approximation (instead of the three-angle integration over the zenith angle used in the original scheme) to derive upward and downward fluxes from the radiances, and the modification of the original cloud random overlapping assumption to include (to the same degree of approximation as used in the operational SW scheme) a maximum-random overlapping of cloud layers. Given the monochromatic form of the RTE, the vertical integration is simply carried out one layer at a time from the top-of-the-atmosphere to the surface to get the downward fluxes. The downward fluxes at the surface are then used with the spectral surface emissivities and the surface temperature to get the upward longwave fluxes in each of the 140 subintervals. Then the upward fluxes are obtained in a similar fashion from the surface to the ToA.

Table 1.2: Spectral distribution of the absorption by atmospheric gases in RRTM

Spectral intervals cm^{-1}	Number of g-points	Gases included Troposphere	 Stratosphere
10-250	8	H2O	H2O
250-500	14	H2O	H2O
500-630	16	H2O, CO2	H2O, CO2
630-700	14	H2O, CO2	O3, CO2
700-820	16	H2O, CO2, CCl4	O3, CO2, CCl4
820-980	8	H2O, CFC11, CFC12	CFC11, CFC12
980-1080	12	H2O, O3	O3
1080-1180	8	H2O, CFC12, CFC22	O3, CFC12, CFC22
1180-1390	12	H2O, CH4	CH4

1.3 Shortwave radiation

The ECMWF operational SW scheme results from successive developments from the initial Morcrette et al. version. In Meso-NH, the SW scheme corresponds to the version which was operational at ECMWF until March 2002. Main characteristics are sumarised below. The physical content of this scheme is described in the ECMWF radiation documentation (Chapter 2.3 to 2.4).

- The scheme is based upon a two-stream formulation employed together with photon path distribution method (Fouquart and Bonnel 1980) in 6 spectral intervals (0.185-0.25-0.44-0.69-1.19-2.38-4.00 μm).[1]

- Rayleigh scattering (parametric expression of the Rayleigh optical thickness)

---

[1] The first three intervals are further referenced as the VISible domain while the others are the Near Infra-Red domain for the surface albedo nomenclature.

- Aerosol scattering and absorption (Mie parameters for 6 types of aerosols based on climatological models, see further for details on aerosol distributions)
- H_2O (two intervals)
- Uniformly mixed gases (one interval)
- O_3 (two intervals)
- Droplet absorption and scattering (employs a Delta-Eddington method with τ, ω and g determined from the liquid water path u_{LWP} and a parameterization of the effective radius r_e). See the further part for details on cloud optical properties.
- Gas absorption (included separately through the photon path distribution method)

1.3.1 First glance

The rate of atmospheric warming by absorption and scattering of shortwave radiation is:

$$\frac{\partial T}{\partial t} = \frac{g}{C_{ph}} \frac{\partial F}{\partial p} \tag{1.17}$$

where $F = F_{SW}$ is the net total shortwave flux, expressed in W m^{-2} and positive when downward:

$$F = \int_0^{\infty} d\nu \int_0^{\pi} d\phi \int_{-1}^{+1} \mu \, L_\nu(\delta, \mu, \phi) \, d\mu \, d\phi \tag{1.18}$$

L_ν is the diffuse radiance at wavenumber ν, in a direction given by ϕ, the azimuth angle and ϑ the zenith angle such as $\mu = \cos\vartheta$. Notice that ϕ (`PAZIMSOL`) and μ (`PMU0`) are computed in routine SUNPOS described in the last subsection. In (1.18), we assume a plane parallel atmosphere with the optical depth δ, as a convenient vertical coordinate when the energy source is outside the medium

$$\delta(p) = \int_p^0 \beta_\nu(p) \, dp \tag{1.19}$$

where $\beta_\nu^{ext}(p)$ is the extinction coefficient equal to the sum of the scattering coefficient β_ν^{sca} of the aerosol and cloud particle absorption coefficient β_ν^{abs} and of the purely molecular absorption coefficient k_ν. The diffuse radiance L_ν is governed by the radiation transfer equation

$$\begin{aligned} \mu \frac{dL_\nu(\delta, \mu, \phi)}{d\delta} &= L_\nu(\delta, \mu, \phi) - \frac{\overline{\omega}_\nu(\delta)}{4} P_\nu(\delta, \mu, \phi, \mu_0, \phi_0) \, E_\nu^0 e^{-\frac{\delta}{\mu_0}} \\ &- \frac{\overline{\omega}_\nu(\delta)}{4} \int_0^{2\pi} \int_{-1}^{+1} P_\nu(\delta, \mu, \phi, \mu', \phi') \, L_\nu(\delta, \mu', \phi') \, d\mu' \, d\phi'. \end{aligned} \tag{1.20}$$

E_ν^0 is the incident solar irradiance in the direction $\mu_0 = cos\vartheta_0$, $\overline{\omega}_\nu$ is the single scattering albedo $(= \beta_\nu^{sca}/k_\nu)$ and $P_\nu(\delta, \mu, \phi, \mu', \phi')$ is the scattering phase function which defines the probability that radiation coming from direction (μ', ϕ') is scattered in direction (μ, ϕ). The shortwave part of the scheme, originally developed by Fouquart and Bonnel (1980) solves the radiation transfer equation and integrates the fluxes over the whole shortwave spectrum between 0.2 and 4 μm. Upward and downward fluxes are obtained from the reflectances and transmittances of the layers, and the photon path distribution method allows to separate the parametrization of the scattering processes from that of the molecular absorption.

1.3.2 Spectral integration

Solar radiation is attenuated by absorbing gases, mainly water vapor, uniformly mixed gases (oxygen, carbon dioxide, methane, nitrous oxide) and ozone, and scattered by molecules (Rayleigh scattering), aerosols and cloud particles. Since scattering and molecular absorption occur simultaneously, the exact amount of absorber along the photon path length is unknown, and band models of the transmission function cannot be used directly as in the shortwave radiation transfer (see subsection 1.2.3). The approach of the photon path distribution method is to calculate the probability $p(U)\,dU$ that a photon contributing to the flux F_c in the conservative case (i.e. no absorption, $\overline{\omega}_\nu = 1, k_\nu = 0$) has encountered an absorber amount between U and $U + dU$. With this distribution, the radiative flux at wavenumber ν is related to F_c by

$$F_\nu = F_c \int_0^\infty p(U)\,\exp(-k_\nu U)\,dU \tag{1.21}$$

and the flux averaged over the spectral interval $\Delta\nu$ can then be calculated with the help of any band model of the transmission function $t_{\Delta\nu}$

$$F = \frac{1}{\Delta\nu}\int_{\Delta\nu} F_\nu\,d\nu = F_c \int_0^\infty p(U)\,t_{\Delta\nu}(U)\,d\nu. \tag{1.22}$$

To find the distribution function $p(U)$, the scattering problem is solved first, by any method, for a set of arbitrarily fixed absorption coefficients k_l, thus giving a set of simulated fluxes F_{k_l}. An inverse Laplace transform is then performed on (1.21) to get $p(U)$ (Fouquart 1974). The main advantage of the method is that the actual distribution $p(U)$ is smooth enough that (1.21) gives accurate results even if $p(U)$ itself is not known accurately. In fact, $p(U)(U)$ needs not be calculated explicitly as the spectrally integrated fluxes are, in the two limiting cases of weak and strong absorption:

$$\begin{aligned} F &= F_c\,t_{\Delta\nu}(<U>) &\quad \text{where} \quad & <U> = \int_0^\infty p(U)\,U\,dU \\ F &= F_c\,t_{\Delta\nu}(<U^{\frac{1}{2}}>) &\quad \text{where} \quad & <U^{\frac{1}{2}}> = \int_0^\infty p(U)\,U^{\frac{1}{2}}\,dU \end{aligned} \tag{1.23}$$

respectively. The atmospheric absorption in the water vapor bands is generally strong and the scheme determines an effective absorber amount U_e between $<U>$ and $<U^{\frac{1}{2}}>$ derived from

$$U_e = \frac{1}{k_e}\,\ln\left(\frac{F_{k_e}}{F_c}\right) \tag{1.24}$$

where k_e is an absorption coefficient chosen to approximate the spectrally averaged transmission of the clear-sky atmosphere:

$$k_e = (\frac{U_{tot}}{\mu_0})^{-1} \ln(t_{\Delta\nu}\frac{U_{tot}}{\mu_0}) \tag{1.25}$$

with U_{tot} the total amount of absorber in a vertical column and $\mu_0 = \cos\vartheta_0$ (PMU0 computed in routine SUNPOS). Once the effective absorber amounts of H_2O and uniformly mixed gases are found, the transmission functions are computed using Padé approximants:

$$t_{\Delta\nu}(U) = \frac{\sum\limits_{i=0}^{N} a_i U^{i-1}}{\sum\limits_{j=0}^{N} b_j U^{j-1}}. \tag{1.26}$$

Absorption by ozone is also taken into account, but since ozone is located at low pressure levels for which molecular scattering is small and Mie scattering is negligible, interactions between scattering processes and ozone absorption are neglected. Transmission through ozone is computed using (1.26) where the amount of ozone U_{O_3} is (POZON is the concentration in ozone (Pa/Pa) taken from a standard atmosphere):

$$U^d_{O_3} = M \int_p^0 dU_{O_3}$$

for the downward transmission of the direct solar beam, and:

$$U^u_{O_3} = r \int_{p_s}^p dU_{O_3} + U^d_{O_3}(p_s)$$

for the upward transmission of the diffuse radiation with $r = 1.66$ the diffusivity factor and M (PSEC in SWU), the magnification factor (Rodgers 1967) used instead of μ_0 to account for the sphericity of the atmosphere at very small solar elevations:

$$M = \frac{35}{\sqrt{1224\,\mu_0^2 + 1}}. \tag{1.27}$$

To perform the spectral integration, it is convenient to discretize the solar spectral interval into subintervals in which the surface reflectance can be considered as constant. Since the main cause of the important spectral variation of the surface albedo is the sharp increase in the reflectivity of the vegetation in the near infrared and since water vapor does not absorb below 0.68 μm, the shortwave scheme considers two spectral intervals, one for the visible (0.2 - 0.68 μm, subroutine SW1S) containing a fraction of 0.441676 the incoming solar energy and second one for the near infrared (0.68 - 4.0 μm, subroutine SW2S) for the 0.558324 remaining part of the solar spectrum. This cutoff at 0.68 μm also makes the scheme more computationally efficient, in as much as the interactions between gaseous absorption (by water vapor and uniformly mixed gases) and scattering processes are accounted for only in the near-infrared interval.

1.3.3 Vertical integration

Considering an atmosphere where a fraction C_{tot} (as seen from the surface or the top of the atmosphere) is covered by clouds (the fraction C_{tot} depends on which cloud overlap assumption is assumed for the calculations), the final fluxes are given as

$$F^{\downarrow} = C_{tot}\, F^{\downarrow}_{cloudy} \,+\, (1 - C_{tot})\, F^{\downarrow}_{clear} \tag{1.28}$$

with a similar expression holding for the upward flux. Contrarily to the scheme of Geleyn and Hollingsworth (1979), the fluxes are not obtained through the solution of a system of linear equations in a matrix form. Rather, assuming an atmosphere divided into N homogeneous layers, the upward and downward fluxes at a given interface j are given by:

$$\begin{aligned} F^{\downarrow}(j) &= F_0 \prod_{k=j}^{N} T_b(k), \\ F^{\uparrow}(j) &= F^{\downarrow}(j)\, R_t(j-1), \end{aligned} \tag{1.29}$$

where $R_t(j)$ and $T_b(j)$ are the reflectance at the top and the transmittance at the bottom of the j^{th} layer. Computations of R_t's start at the surface and work upward, whereas those of T_b's start at the top of the atmosphere and work downward. R_t and T_b account for the presence of cloud in the layer:

$$\begin{aligned} R_t &= C_j\, R_{cdy} + (1 - C_j)\, R_{clr}, \\ T_b &= C_j\, T_{cdy} + (1 - C_j)\, T_{clr}. \end{aligned} \tag{1.30}$$

The subscripts $_{clr}$ and $_{cdy}$ respectively refer to the clear-sky and cloudy fractions of the layer with C_j the cloud fraction of the layer j.

Cloudy fraction of the layers

$R_{t_{cdy}}$ and $T_{b_{cdy}}$ are the reflectance at the top and transmittance at the bottom of the cloudy fraction of the layer calculated with the Delta-Eddington approximation. Given δ_c (PTAU) and δ_a (PAER), the optical thicknesses for the cloud and the aerosol, g_c (PCG) and g_a (CGA) the cloud and aerosol asymmetry factors, $R_{t_{cdy}}$ and $T_{b_{cdy}}$ are calculated as functions of:

- the total optical thickness of the layer δ^*:

$$\delta^* = \delta_c + \delta_a$$

- the total single scattering albedo:

$$\omega^* = \frac{\omega_c\,\delta_c + \omega_a\,\delta_a}{\delta_c + \delta_a} \tag{1.31}$$

- the total asymmetry factor:

$$g^* = \frac{\omega_c\,\delta_c\,g_c + \omega_a\,\delta_a\,g_a}{\omega_c\,\delta_c + \omega_a\,\delta_a}$$

of the reflectance R_{-} of the underlying medium (surface or layers below the j^{th} interface) and of the effective solar zenith angle $\mu_e(j)$ which accounts for the decrease of the direct solar beam and the corresponding increase of the diffuse part of the downward radiation by the upper scattering layers (see further).
The scheme follows the Eddington approximation, first proposed by Shettle and Weinman (1970), then modified by Joseph et al. (1976) to account more accurately for the large fraction of radiation directly transmitted in the forward scattering peak in case of highly asymmetric phase functions. Eddington's approximation assumes that, in a scattering medium of optical thickness δ^*, of single scattering albedo ω, and of asymmetry factor g, the radiance L entering (1.20) can be written as:

$$L(\delta, \mu) = L_0(\delta) + \mu\,L_1(\delta). \tag{1.32}$$

In that case, when the phase function is expanded as a series of associated Legendre functions, all terms of order greater than one vanish when (1.20) is integrated over μ and ϕ. The phase function is therefore given by

$$P(\theta) = 1 + \beta_1(\theta)\,\cos\theta,$$

where θ is the angle between incident and scattered radiances. The integral in (1.20) thus becomes

$$\int_0^{2\pi}\int_{-1}^{+1} P(\mu,\phi,\mu',\phi')\,L(\mu',\phi')\,d\mu'\,d\phi' = 4\pi\,(L_0 + \pi L_1) \tag{1.33}$$

where g, the asymmetry factor identifies as

$$g = \frac{\beta}{3} = \frac{1}{2}\int_{-1}^{+1} P(\theta)\,\cos\theta\,d(\cos\theta).$$

Using (1.33) in (1.20) after integrating over μ and dividing by 2π, we get

$$\mu\,\frac{d(L_0 + \mu L_1)}{d\delta} = -(L_0 + \mu L_1) + \omega\,(L_0 + g\mu L_1) + \frac{1}{4}\omega\,F_0\,\exp(\frac{-\delta}{\mu_0})\,(1 + 3g\mu_0\,\mu). \tag{1.34}$$

We obtain a pair of equations for L_0 and L_1 by integrating (1.34) over μ:

$$\frac{d(L_0)}{d\delta} = -3(1-\omega)\,L_0 + \frac{3}{4}\omega\,F_0\,\exp(\frac{-\delta}{\mu_0}), \tag{1.35}$$

$$\frac{d(L_1)}{d\delta} = -(1-\omega g)\,L_1 + \frac{3}{4}\omega\,g\,\mu_0\,F_0\,\exp(\frac{-\delta}{\mu_0}). \tag{1.36}$$

For the cloudy layer assumed non-conservative ($\omega < 1$), the solutions to (1.35) and (1.36) are, in the range $0 \leq \delta \leq \delta^*$:

$$\begin{aligned} L_0(\delta) &= C_1\,\exp(-k\delta) + C_2\,\exp(+k\delta) - \alpha\,\exp(\frac{-\delta}{\mu_0}), \\ L_1(\delta) &= p(C_1\,\exp(-k\delta) - C_2\,\exp(+k\delta)) - \beta\,\exp(\frac{-\delta}{\mu_0}), \end{aligned} \tag{1.37}$$

where

$$\begin{aligned} k &= \left[3\,(1-\omega)\,(1-\omega g)\right]^{\frac{1}{2}} \\ p &= \left[3\,(1-\omega)/(1-\omega g)\right]^{\frac{1}{2}} \\ \alpha &= 3\,\omega\,F_0\,\mu_0^2\,\frac{\left[1+g\,(1-\omega)\right]}{4\,(1-k^2\mu_0^2)} \\ \beta &= 3\,\omega\,F_0\,\mu_0\,\frac{\left[1+3\,g\,(1-\omega)\,\mu_0^2\right]}{4\,(1-k^2\mu_0^2)}. \end{aligned}$$

The two boundary conditions allow to solve the system for C_1 and C_2. First, the downward directed diffuse flux at the top of the layer is zero

$$F^{\downarrow}(0) = \left[L_0(0) + \frac{2}{3}L_1(0)\right] = 0,$$

which translates into

$$(1+\frac{2p}{3})\,C_1 + (1-\frac{2p}{3})\,C_2 = \alpha + \frac{2\beta}{3}. \tag{1.38}$$

For the second condition, one assumes that the upward directed flux at the bottom of the layer is equal to the product of the downward directed diffuse and direct fluxes by the corresponding diffuse and direct reflectances (R_d and R_-, respectively) of the underlying medium

$$F^{\uparrow}(\delta^*) = \left[L_0(\delta^*) - \frac{2}{3}\,L_1(\delta^*)\right] = R_-\left[L_0(\delta^*) + \frac{2}{3}\,L_1(\delta^*)\right] + R_d\,\mu_0\,F_0\,\exp(\frac{-\delta^*}{\mu_0}),$$

which translates into

$$\begin{aligned}(1-R_- - \frac{2p}{3}\,(1+R_-))\,C_1\ \exp(-k\,\delta^*) + (1-R_- + \frac{2p}{3}\,(1+R_-))\,C_2 \quad \exp(+k\,\delta^*)\\ = ((1-R_-)\alpha - \frac{2}{3}\,(1+R_-)\beta + R_d\,\mu_0\,F_0) \quad \exp(\tfrac{-\delta^*}{\mu_0}) \qquad (1.39)\end{aligned}$$

In the Delta-Eddington approximation, the phase function is approximated by a Dirac delta function (forward scatter peak) and a two-term expansion of the phase function

$$P(\theta) = 2f\,(1-\cos\theta) + (1-f)\,(1+3g'\,\cos\theta),$$

where f is the fractional scattering into the forward peak and g' the asymmetry factor of the truncated phase function. As shown by Joseph et al. (1976), these parameters are:

$$\begin{aligned} f &= \frac{\omega_c\,\delta_c\,g_c^2 + \omega_a\,\delta_a\,g_a^2}{\omega_c\,\delta_c + \omega_a\,\delta_a} \\ g' &= \frac{g}{1+g}. \end{aligned} \qquad (1.40)$$

The solution of the Eddington's equations remains the same provided that the total optical thickness, single scattering albedo and asymmetry factor entering (1.34)-(1.39) take their transformed values:

$$\begin{aligned} \delta' &= (1-\omega f)\,\delta^*, \\ \omega' &= \frac{(1-f)\,\omega}{1-\omega f}. \end{aligned} \qquad (1.41)$$

Practically, the optical thickness, single scattering albedo, asymmetry factor, and solar zenith angle entering (1.38)-(1.41) are δ^*, ω^*, g^* and u_e defined in (1.31) and (1.47).
The effective solar zenith angle $\mu_e(j)$ is equal to:

$$\mu_e(j) = \left[\frac{(1-C^{al}(j))}{\mu} + r\,C^{al}(j)\right]^{-1}, \qquad (1.42)$$

with r is the diffusivity factor and is prescribed at 1.66, that corresponds to a zenith angle of 52.95°. The accuracy of this approximation in fact depends on the actual solar zenith angle, which implies that the fluxes cannot be determined at all the incoming solar zenith angles with the same accuracy. $C^{al}(j)$ is the cumulated scattering efficiency from the top of the atmosphere to the layer j:

$$C^{al}(j) = 1 - \prod_{i=j+1}^{N} (1 - CC(j))$$

with $CC(j)$ is the direct solar light scattering efficiency defined in each layer of the cloud column as:

$$CC(j) = C_j'\,(1-\exp\left[-\frac{\delta_c^{*'}(j)}{\mu}\right]) + (1-C_j')\,(1-\exp\left[-\frac{\delta_a^{*'}(j)}{\mu}\right]) \qquad (1.43)$$

with C_j' the cloud sub-fraction of the layer j defined with respect to the column fraction C_{tot} as:

$$C_j' = C_j / C_{tot} \qquad (1.44)$$

Clear-sky fraction of the layers

In the clear-sky fraction of the layers, the shortwave scheme accounts for scattering and absorption by molecules and aerosols. As optical thickness for both Rayleigh and aerosol scattering is small, $R_{clr}(j-1)$ and $T_{clr}(j)$ the reflectance at the top and transmittance at the bottom of the j^{th} layer can be calculated using respectively a first and a second-order expansion of the analytical solutions of the two-stream equations similar to that of Coakley and Chylek (1975). For Rayleigh scattering (subroutine SW1S), the optical thickness, single scattering albedo and asymmetry factor are respectively δ_R, $\omega_R = 1$ and $g_R = 0$, so that

$$\begin{aligned} R_R &= \frac{\delta_R}{2\,\mu + \delta_R}, \\ T_R &= \frac{2\mu}{2\,\mu + \delta_R}. \end{aligned} \tag{1.45}$$

The optical thickness δ_R of an atmospheric layer is simply:

$$\delta_R = \delta_R^* \frac{(p(j) - p(j-1))}{p_{surf}},$$

where δ_R^* is the Rayleigh optical thickness of the whole atmosphere parameterized as a function of solar zenith angle (Deschamps et al. 1983):

$$\delta_R^* = \sum_{i=0}^{5} a_i\, \mu_0^{i-1}.$$

For aerosol scattering and absorption, the optical thickness, single scattering albedo and asymmetry factor are respectively δ_a, ω_a (with $1 - \omega_a \ll 1$) and g_a so that:

$$\begin{aligned} den &= 1 + (1 - \omega_a + back(\mu_e)\,\omega_a)\,\frac{\delta_a}{\mu_e} + (1 - \omega_a)\,(1 - \omega_a + 2\,back(\mu_e)\,\omega_a)\,\frac{{\delta_a}^2}{{\mu_e}^2} \\ R(\mu_e) &= \frac{back(\mu_e)\,\omega_a\,\delta_a/\mu_e}{den} \\ T(\mu_e) &= \frac{1}{den} \end{aligned} \tag{1.46}$$

where $back(\mu_e) = (2 - 3\mu_e g_a)/4$ is the backscattering factor and $\mu_e(j)$ is the effective solar zenith angle:

$$\mu_e(j) = \left[\frac{(1 - C^{al}(j))}{\mu} + r\, C^{al}(j)\right]^{-1}, \tag{1.47}$$

with r is the diffusivity factor and is prescribed at 1.66, that corresponds to a zenith angle of 52.95°. The accuracy of this approximation in fact depends on the actual solar zenith angle, which implies that the fluxes cannot be determined at all the incoming solar zenith angles with the same accuracy. $C^{al}(j)$ is the cumulated scattering efficiency from the top of the atmosphere to the layer j:

$$C^{al}(j) = 1 - \prod_{i=j+1}^{N} (1 - CC(j))$$

with $CC(j)$ is the direct solar light scattering efficiency defined in each layer of the cloud column as:

$$CC(j) = 1 - \exp\left[-\frac{\delta_a^{*'}(j)}{\mu}\right] \tag{1.48}$$

Practically, R_{clr} and T_{clr} are computed using (1.46) and the combined effect of aerosol and Rayleigh scattering comes from using modified parameters corresponding to the addition of the two scatters with provision for the highly asymmetric aerosol phase function through a Delta-Eddington approximation of the forward scattering peak (as in (1.40)-(1.41)):

$$\begin{aligned}
f &= \frac{\delta_R + \omega_a\,\delta_a\,g_a^2}{\delta_R + \omega_a\,\delta_a} \\
g^{'} &= \frac{g}{1+g}. \\
\delta^{'} &= (1-\omega f)\,\delta, \\
\omega^{'} &= \frac{(1-f)\,\omega}{1-\omega f}.
\end{aligned} \tag{1.49}$$

with:

$$\begin{aligned}
\delta &= \delta_R + \delta_a \\
g &= \frac{\delta_R + \omega_a\,\delta_a\,g_a}{\delta_R + \omega_a\,\delta_a} \\
\omega &= \frac{\delta_R + \omega_a\,\delta_a}{\delta_R + \delta_a}
\end{aligned} \tag{1.50}$$

As for their cloudy counterparts, R_{clr} and T_{clr} must account for the multiple reflections due to the layers underneath:

$$\begin{aligned}
R_{clr} &= R(\mu_e) + \frac{T(\mu_e)}{1 - R^*\,R_-}\,R_-, \\
T_{clr} &= \frac{T(\mu_e)}{1 - R^*\,R_-},
\end{aligned} \tag{1.51}$$

with $R^* = R(1/r)$, $T^* = T(1/r)$, $R_- = R_t(j-1)$ is the reflectance of the underlying medium and r is the diffusivity factor.

Since interactions between molecular absorption and Rayleigh and aerosol scattering are negligible, the radiative fluxes in a clear-sky atmosphere are simply those calculated from (1.29) and

(1.51) attenuated by the gaseous transmissions (1.26) (subroutine SW2S).

These calculations are practically done twice, the first time for the clear-sky fraction $(1 - C_{tot})$ of the atmospheric column with μ_e computed using (1.48), simply modified for the effect of Rayleigh and aerosol scattering (subroutine SWCLR), the second time for the clear-sky fraction $(1 - C'_j)$ of each individual layer within the fraction C_{tot} of the atmospheric column with μ_e computed using (1.43) (subroutine SWR).

1.3.4 Multiple reflections between layers

To deal properly with the multiple reflections between the surface and the cloud layers, it should be necessary to separate the contribution of each individual reflecting surface to the layer reflectances and transmittances inasmuch as each such surface gives rise to a particular distribution of absorber amount. In case of an atmosphere including N cloud layers, the reflected light above the highest cloud consists of photons directly reflected by the highest cloud without interaction with the underlying atmosphere and of photons that have passed through this cloud layer and undergone at least one reflection on the underlying atmosphere. In fact, (1.22) should be written

$$F = \sum_{l=0}^{N} F_{cl} \int_0^{\infty} p_l(U)\, t_{\Delta\nu}(U)\, d\nu, \tag{1.52}$$

where F_{cl} and $p_l(U)$ are the conservative fluxes and the distributions of absorber amount corresponding to the different reflecting surfaces.

Fouquart and Bonnel (1980) have shown that a very good approximation to this problem is obtained by evaluating the reflectance and transmittance of each layer (using (1.39) and (1.51)), assuming successively a non-reflecting underlying medium ($R_{-} = 0$), then a reflecting underlying medium ($R_{-} \neq 0$). First calculations provide the contribution to reflectance and transmittance of those photons interacting only with the layer into consideration, whereas the second ones give the contribution of the photons with interactions also outside the layer itself.

From these two sets of layer reflectances and transmittances (R_{t_0}, T_{t_0}) and $(R_{t_{\neq}}, T_{t_{\neq}})$ respectively, effective absorber amounts to be applied to computing the transmission functions for upward and downward fluxes are then derived using (1.24) and starting from the surface and working the formulas upward:

$$\begin{aligned}
U^{\downarrow}_{e_0} &= \frac{1}{k_e} \ln\left(\frac{T_{b_0}}{T_{b_c}}\right), \\
U^{\downarrow}_{e_{\neq}} &= \frac{1}{k_e} \ln\left(\frac{T_{b_{\neq}}}{T_{b_c}}\right), \\
\\
U^{\uparrow}_{e_0} &= \frac{1}{k_e} \ln\left(\frac{R_{t_0}}{R_{t_c}}\right), \\
U^{\uparrow}_{e_{\neq}} &= \frac{1}{k_e} \ln\left(\frac{R_{t_{\neq}}}{R_{t_c}}\right),
\end{aligned} \tag{1.53}$$

where R_{t_c} and T_{b_c} are the layer reflectance and transmittance corresponding to a conservative scattering medium. Finally the upward and downward fluxes are obtained as:

$$F^{\uparrow}(j) = F_0 \left[R_{t_0}\, t_{\Delta\nu}(U^{\uparrow}_{e_0}) + (R_{t_{\neq}} - R_{t_0})\, t_{\Delta\nu} U^{\uparrow}_{e_{\neq}}) \right] \tag{1.54}$$

$$F^{\downarrow}(j) = F_0 \left[T_{b_0}\, t_{\Delta\nu}(U^{\downarrow}_{e_0}) + (T_{b_{\neq}} - T_{b_0})\, t_{\Delta\nu} U^{\downarrow}_{e_{\neq}}) \right] \tag{1.55}$$

1.3.5 Cloud shortwave optical properties

As seen in section (1.3.3), the cloud radiative properties depend on three different parameters: the optical thickness δ_c, the asymmetry factor g_c and the single scattering albedo ω_c. Presently the cloud optical properties are derived from Fouquart (1987) for the cloud water droplets and from Ebert and Curry (1992) for the cloud ice crystals. Alternate sets of cloud optical properties are also available, see subsection 1.4.5. In case of mixed phase cloud, one has to consider the combination formula:

$$\begin{aligned} \delta_c &= \delta_L + \delta_I \\ \omega_c &= (\omega_L\, \delta_L + \omega_I\, \delta_I)/\delta_c \\ g_c &= (\omega_L\, \delta_L\, g_L + \omega_I\, \delta_I\, g_I)/(\omega_L\, \delta_L + \omega_I\, \delta_I) \end{aligned} \tag{1.56}$$

Warm cloud case

By default, the option **Fouquart** is used for the computation of the warm cloud optical properties. In that case, the optical thickness δ_L depends on the cloud liquid water path u_{LWP} and on the mean effective radius of the cloud droplets size distribution r_e (Fouquart 1987):

$$\delta_L = (a + b/r_e) u_{LWP}$$

The liquid water path u_{LWP} is defined by $\int_{\Delta z} \rho r_c dz = \int_{\Delta p} r_c/g dp$. r_e can be computed either through the parameterization of Martin et al. (1994) (for the one-moment cloud schemes) or directly as the ratio of the 3$^{\text{rd}}$ and the 2$^{\text{nd}}$ moments of the cloud droplets distribution (for the two-moment cloud schemes).

The cloud single scattering albedo is computed in each of the six shortwave bands as a function of the cloud droplet chemical composition and diameter. In a first approximation, the cloud droplet composition can be retrived assuming that the cloud droplets form from the aerosols given by the global climatologies (Tegen et al. (1997) or Tanré et al. (1984)).

The global climatologies supply the extinction coefficient for 6 aerosol classes (Continental, Maritime, Desert, Urban, Volcanic and Stratospherical background). Each of these classes can be decomposed in five elementary aerosol types: dust, water soluble compounds, soot, sea-salt, sulphates (d'Almeida et al. 1991). Using the percentage of elementary aerosol types entering in one class and their normalized extinction coefficients (for 1 particle/cm^3) (Table 4.3 of

?)dAlmeida1991, one can deduce the normalized extinction coefficients of the 6 aforementioned classes. The number concentration in each class and the total number concentration (cm^{-3}) of the elementary types can be retrieved from the total number of aerosols entering in one class (derived as the ratio between the total extinction and the normalised extinction for 1 particle for that class). The volume fraction of one aerosol type into the cloud droplet is then computed as the ratio of the volume of all the particles of that type corresponding to one droplet and the droplet's volume: $v_f^i = (N_i/N_c) \cdot (R_i/R_e)^3$. N_i and R_i are the number concentration and a typical value of the mean radius of the aerosol of type i, N_c and R_e are the number concentration and the effective radius of the cloud droplets.

Table 1.3: Percentage of the aerosol types in the ECMWF classes (d'Almeida et al. 1991)

ECMWF classes	dust	water soluble	soot	sea salts	sulfates
marine	-	-	-	65 %	35 %
continental	$2.27 \cdot 10^{-4}$ %	93.877 %	6.123 %	-	-
urban	$1.67 \cdot 10^{-5}$ %	59.45 %	40.55 %	-	-
desert	100 %	-	-	-	-
volcanic	40 %	-	40 %	-	20 %
stratospherical background	100 %	-	-	-	-

Ice cloud case

For the optical properties of ice clouds, we have

$$\begin{aligned} \delta_I &= \mathrm{IWP}\,(a_I + b_I/r_e) \\ \omega_I &= c_I + d_I\, r_e \\ g_I &= c_I + f_I\, r_e \end{aligned} \tag{1.57}$$

By default, the coefficients have been derived from Ebert and Curry (1992), and r_e is parameterized (see subsection 1.4.5). Alternate sets of cloud optical properties are also available.

1.4 Input to the radiation scheme

1.4.1 Pressure, temperature, humidity, cloud water and ice fields

They are directly provided by the corresponding prognostic variables of Meso-NH. In order to allow for better fluxes in the stratosphere and above, the vertical profiles of temperature and humidity are completed aloft by using reference atmospheres (Mc Clatchey et al. 1972). One among the five different standard atmospheres:

- tropical

- mid-latitude in summer and winter
- polar in summer and winter

is selected to extend the relevant fields up to 50 km high.

The TSRAD radiative surface temperature calculated from surface scheme is used for lower boundary conditions. Presently, no radiative effects of rain water, graupel and snow are considered.

1.4.2 Ground albedo and emissivity

The SW radiation scheme requires albedo for each spectral band (6 bands in the most recent version, 0.185-0.25-0.44-0.69-1.19-2.38-4.00 μm). In Meso-NH, only visible and near infra-red bands are differentiated: the albedo components entering effectively in the SW scheme are then defined according to these two main bands. The SW radiation code requires also a distinction between ”direct” albedo (i.e. for direct radiation) and diffuse albedo. Such a distinction does not exist in Meso-NH so a single albedo value is used for diffuse and direct fluxes. The LW surface emissivity directly corresponds to the value calculated in Meso-NH.

1.4.3 Aerosols

Climatological aerosols

Aerosol effects on SW and LW radiations are taken into account provided that CAER is set to a value different of ’NONE’. Presently, six classes of aerosols are considered in the radiation scheme: The continental class including organic and sulfate-type aerosols, the sea class (i.e. sea-salt aerosols), the urban class (mainly black-carbon type aerosols), the desert class (soil dust type aerosols), the volcanic class and a stratospheric background class. Each one of these class are characterized by specific optical properties (optical depth, single scattering albedo, asymmetry factor, ...). The optical depth is directly linked to the effective concentration of aerosol and therefore must be spatially and temporally specified. Presently the spatial and temporal distributions of optical thickness are defined in the model initialisation step (subroutine INI_RADIATIONS).

- The ’TANR’ option directly refers to Tanré et al. (1984) climatological distributions. Total optical thickness (ground to top of the atmosphere TOA) associated to the land, sea, desert, and continental class are horizontally distributed on a T5 grid. This spectral distribution has been redefined on a regular ”lat-lon” grid by the Arpege-climat team and imported in Meso-NH. The horizontal fields are interpolated on the Meso-NH domain (INI_HOR_AERCLIM routine). Then the total optical thickness are associated to typical vertical distribution (based on pressure levels) depending on the aerosol class, this leading to the 3D aerosol fields. Note that the resulting fields are very smooth, and no temporal evolution is considered here.
- The ’TEGE’ option refers to the Tegen et al. (1997) climatological distribution. The total optical thickness fields are monthly provided at a ($4^\circ \times 5^\circ$) resolution. Time and spatial interpolation on the Meso-NH domain are made in the INI_HOR_AERCLIM routine. The same vertical profiles as in TANR case are considered.
- The ’SURF’ option provides an alternative method compared to climatical distributions. In this case the total optical thickness is directly linked to the nature and the percent of ground

covers in the grid cell (sea, desert, urban, continental). This option allows to better represent localized sources like urban area at fine resolution. The considered vertical distribution are the same than in TANR and TEGE cases. Note that the user can easily modify the maximum total optical thickness associated to the aerosol classes in the INI_RADIATIONS routine.

Remark: The stratospheric background represents a horizontally homogenous field defined by default in all cases.

The optical depth associated to the volcanic class are forced to an ”epsilon” value in INI_RADIATIONS step but, this can be modified easily if necessary. A historical climatology for volcanic aerosol is also available in the routines called by the TEGE option. This option is not activated.

It is always possible to define the aerosol fields from user’s own data base at the INI_RADIATIONS step.

Prognostic aerosols

When using prognostic aerosols, radiative properties of aerosols can be taken into account with either ? or ?.

This method aims to compute the optical properties online as a function of a given complex refractive index deduced from the aerosol chemical composition and the size parameters corresponding to the particles. The optical properties computed by the module according to the Mie theory (Mie 1908), and then are inputs for the radiative model are: the extinction coefficient ($\beta^{ext}_{\nu,a}(p)$), the single scattering albedo (ω_a), and the asymmetry parameter for the aerosol population (g_a, obtained by integrating the asymmetry parameter over the radius). They depend on the outputs of the aerosol module ORILAM which computes for each considered aerosol mode the chemical composition as well as the size distribution parameter.

In order to define a refractive index corresponding to an aerosol particle composed of different chemical components, the Maxwell-Garnett equation (Maxwell-Garnett 1904) as defined in Tombette et al. (2008) allows us to link the chemical composition of the aerosol to a refractive index and then to take the particle size distribution into account. This approach considers the aerosol as being made up of an inclusion and an extrusion. The inclusion is composed of the primary and solid parts of the aerosol, whereas the extrusion is composed of the secondary and liquid parts of the aerosol.

An analytical solution was used, employing a look-up table of aerosol optical properties and a mathematical analytical function approximating the Mie computation. In order to minimize the number of stored terms, the construction of the look-up tables was adjusted. The aerosol optical properties depending on four parameters (real and imaginary part of the refractive index, the median radius and the standard deviation for the lognormal law describing the considered mode), the look-up tables have four degrees of freedom.

Considering the median radius as a stored input parameter would be consistent for no more than a hundred cases as pointed out by Grini et al. (2006). To avoid this constraint, the computation and storage of the fifth degree dual-polynomial coefficients that best fitted the optical parameters evolving according to the median radius was taken. In this way, the input terms of the look-up tables are the complex refractive index and the geometric standard deviation. More details can be found on Aouizerats et al. (2010).

1.4.4 Radiatively active compounds

The concentrations of trace gases other than ozone are supposed to be constant spatially and temporally with the following characteristic values:

- CO_2: 360 ppm
- CH_4: 1.72 ppm
- N_2O: 0.31 ppm
- $CFC11$: 280 ppt
- $CFC12$: 484 ppt
- $O3$: The ozone field is defined from the Fortuin and Langematz (1994) climatology. The concentration depends on height, latitude and month. The 3-D climatology is loaded and interpolated on the Meso-NH domain in the INI_RADIATIONS step. The ozone field can be visualised running DIAG (see DIAG documentation).

1.4.5 Cloud optical properties

For the SW radiation, the cloud radiative properties depend on three different parameters: the optical thickness, the asymmetry factor and the single scattering albedo of particles. For LW the cloud properties (linked to emissivity and spectral optical thickness) depends of the scheme used (MORC or RRTM). All these properties are defined for water and ice particles in the ecmwf_radiation_vers2 routine. They depend on liquid (or ice) water path or on the effective radius of the particles. This characteristic parameter can be calculated by different ways according to CEFRADL and CEFRADI (ice particles) keywords:

Cloud liquid particles

- CEFRADL='PRES': the cloud water effective radius is calculated as a function of pressure (old parameterisation).
- CEFRADL='OCLN': the cloud effective radius is equal to 10 μm over land and equal to 13 μm over the ocean.
- CEFRADL='MART': parameterisation based on Martin et al. (1994).
- CEFRADL='C2R2': the effective radius of cloud particle is calculated from the 2-moment microphysical scheme C2R2 when explicitly called (see the microphyical scheme section for the nomenclature).

$$r_e = 0.5\frac{\int_0^{+\infty} D^3 n(D)dD}{\int_0^{+\infty} D^2 n(D)dD} 0.5\frac{\Gamma(\nu+3/\alpha)^{2/3}}{\Gamma(\nu+2/\alpha)}\left(\frac{\Gamma(\nu)}{\pi/6\rho_w}\frac{\rho\, r_c}{N_c}\right)^{1/3}$$

Cloud ice particles

- CEFRADI='FX40': the ice particle effective radius is fixed at 40 μm. The user can eventually change this value by modifying the ecmwf_radiation_vers2 routine.
- CEFRADI='LIOU': ice particle effective radius calculated as f(T) from Liou and Ou (1994).
- CEFRADI='SURI': Ice effective radius calculated as a function of temperature and ice content from Sun and Rikus (1999).
- CEFRADI='C3R5': the effective radius of ice particle is calculated from C3R5 prognostic particle concentrations. Of course it works only when C3R5 microphysical scheme is activated (not yet available).

Several options are also possible to define the optical properties from the primary parameters:

SW radiation

Cloud water optical properties depend on COPWSW:

- COPWSW ='SLIN', refers to Slingo (1989).
- COPWSW ='FOUQ', refers to Fouquart (1987).
- COPWSW ='MALA', refers to Malavelle (2007): Optical thickness of Savijarvi and Raisanen (1997), asymmetry factor of Fouquart (1991) and single scaterring albedo of Slingo (1989). Good compromise for the C2R2 and KHKO scheme in regard on the size distribution hypothesis

Ice water optical properties depend on COPISW:

- COPISW =' FULI', refers to Fu and Liou (1993).
- COPISW =' EBCU', refers to Ebert and Curry (1992).
- COPISW =' FU96', refers to **?**.

MORC LW radiation

Cloud water optical properties depend on COPWLW:

- COPWLW='SMSH', refers to Smith and Shi (1992).
- COPWLW='SAVI', refers to Savijarvi and Raisanen (1997).
- COPWLW='MALA', refers to Malavelle (2008): parameterization of the optical thickness of the cloud droplets and rain drops adapted to the size distribution hypothesis used in the C2R2 and KHKO scheme.

Ice water optical properties depend on COPILW:

- COPILW='EBCU', refers to Ebert and Curry (1992).
- COPILW='SMSH', refers to Smith and Shi (1992).

- COPILW='FULI', refers to Fu and Liou (1993).
- COPILW='FU98', refers to Fu et al. (1998).

RRTM LW radiation

Cloud water optical properties depend on COPWLW:

- COPWLW='SMSH', refers to Smith and Shi (1992).
- COPWLW='SAVI', refers to Savijarvi and Raisanen (1997).
- COPWLW='LILI', refers to Lindner and Li (2000).

Ice water optical properties depend on COPILW

- COPILW='EBCU', refers to Ebert and Curry (1992).
- COPILW='FULI', refers to Fu and Liou (1993).
- COPILW='FU98', refers to Fu et al. (1998).

Note: The resulting cloud optical properties as well as effective radius, liquid and ice water path can be visualized, running DIAG program (see DIAG documentation).

1.4.6 Cloud inhomogenity factor and cloud overlap assumption

In the initial ECMWF radiation code, an empirical cloud factor XFUDG is introduced to account for cloud subgrid inhomogenity in large cells following Tiedtke (1996). This factor weights the above defined optical properties and is initially set to 0.7. But it has been resized to 1 by default for Meso-NH applications, assuming that grid cell are smaller than in ECMWF model. However, as Meso-NH can be used on a wide range of resolution the value of XFUDG can be fixed by namelist.

The cloud overlap assumption is used for the determination of C_{tot} (see the SW documentation) and is important for the determination of radiation in cloudy columns when the subgrid condensation scheme is actived. It is determined by the NOVLP variable: NOVLP=5 means ”random overlap”, NOVLP=6 means ”maximum-random overlap ” and NOVLP=7 means ”maximum overlap”. By default NOVLP is set to 6 in the INI_RADCONF routine except if the Morcrette longwave radiation scheme is used. In this case, NOVLP is set to 5.

1.4.7 Solar astronomy

To run the shortwave radiative computations it is necessary to feed the code with the time varying solar zenithal and azimuthal angles and the daily solar constant, all derived by analytical formulae of astronomy (Paltridge and Platt 1976). For instance, the daily solar constant S_{sun}, the solar declination angle δ_{sun}, the cosine of the solar zenithal angle μ and the azimuthal solar angle β are given by:

$$S_{sun} = S_0(1.000110 + 0.034221\cos(d_r) + 0.001280\sin(d_r)$$

$$
\begin{aligned}
& \quad + 0.000719\cos(2d_r) + 0.000077\sin(2d_r)), && (1.58)\\
\delta_{sun} &= 0.006918 - 0.399912\cos(d_r) + 0.070257\sin(d_r) && \\
& \quad - 0.006758\cos(2d_r) + 0.000907\sin(2d_r) && \\
& \quad - 0.002697\cos(3d_r) + 0.001480\sin(3d_r), && (1.59)\\
\mu &= \cos(\phi)\cos(\delta_{sun})\cos(h_r) + \sin(\phi)\sin(\delta_{sun}), && (1.60)\\
\beta &= \sin^{-1}\left(\frac{\cos(\delta_{sun})\sin(h_r)}{\sin(arcos(\mu))}\right), && (1.61)
\end{aligned}
$$

respectively where $S_0 = 1370$ W/m^2, ϕ is the latitude, $d_r = 2\pi n_{day}/365$ (n_{day} is the day number) and $h_r = 2\pi hour/24$ with $hour$, the true hour of the day at the time t and at the longitude λ, defined by:

$$hour = \mod (24 + \mod (t/3600, 24), 24) + \lambda(12/\pi) - t^{cor}_{sideral}, \qquad (1.62)$$

with mod, the modulo arithmetic function and the sideral time correction $t^{cor}_{sideral}$ given by:

$$
\begin{aligned}
t^{cor}_{sideral} &= (7.67825\sin(1.00554 * n_{day} - 6.28306) + \\
& \quad 10.09176\sin(1.93946 * n_{day} + 23.35089))/60. && (1.63)
\end{aligned}
$$

All these calculations are performed in routine SUNPOS prior calling the radiation code.

1.5 Intermittent radiation call

Due to its relatively high cost, the radiation code can be unreasonably expensive if called at each model time step. Furthermore as the radiative time scales are significantly larger than the time step involved in the integration of a mesoscale model, it is recommended to refresh the radiative thermal tendency and downward surface fluxes at an adapted rate. To run even faster, some approximations of the radiative computations have been made available. The basic time step to call the radiation computation is `XDTRAD`. Il must be a multiple of the model time step `XTSTEP` and a default value is set to 900 s. Note that the radiative code operates on instantaneous fields but the angular position of the sun is calculated at the current time plus `XDTRAD`/2. Actually, three parameters can be set to enable partial radiative computations:

- LCLEAR_SKY when .TRUE. means that radiative computations over clear sky columns are made for the ensemble mean column only. This option is meaningful if the terrain is flat.
- XDTRAD_CLONLY is the time step of refreshment of the radiative fluxes and tendency for the cloudy columns and the ”new” clear columns i.e. where the cloud have just disappeared. Choosing XDTRAD_CLONLY as a divider of XDTRAD allows a faster update of the radiative transfer through cloudy columns as they are known to be the most perturbating ones for the radiations.

1.6 References

Aouizerats, B., O. Thouron, P. Tulet, M. Mallet, L. Gomes, and J. S. Henzing, 2010: Development of an online radiative module for the computation of aerosol optical properties in 3-D atmospheric models: validation during the EUCAARI campaign. *Geosci. Model Dev.*, **3**, 553–564, doi:10.5194/gmd-3-553-2010.

Baran, A. J., P. Hill, K. Furtado, P. Field, and J. Manners, 2014: A coupled cloud physics–radiation parameterization of the bulk optical properties of cirrus and its impact on the Met Office Unified Model Global Atmosphere 5.0 configuration. *J. Climate*, **27 (20)**, 7725–7752, doi: 10.1175/JCLI-D-13-00700.1.

Clough, S. A. and M. I. Iacono, 1995: Line-by-line calculation of atmospheric fluxes and cooling rates, 2. Application to carbon dioxide, ozone, methane, nitrous oxide and the halocarbons. *J. Geophys. Res.*, **100 (D8)**, 16 519–16 536, doi:10.1029/95JD01386.

Clough, S. A., M. J. Iacono, and J.-L. Moncet, 1992: Line-by-line calculations of atmospheric fluxes and cooling rates: Application to water vapor. *J. Geophys. Res.*, **97 (D14)**, 15 761–15 786, doi:10.1029/92JD01419.

Clough, S. A., F. X. Kneizys, and R. W. Davies, 1989: Line shape and the water vapor continuum. *Atmos. Res.*, **23**, 229–241, doi:10.1016/0169-8095(89)90020-3.

Coakley, J. A. J. and P. Chylek, 1975: The two-stream approximation in radiation transfer: Including the angle of the incident radiation. *J. Atmos. Sci.*, **32**, 409–418, doi:10.1175/1520-0469(1975)032%3C0409:TTSAIR%3E2.0.CO;2.

d'Almeida, G. A., P. Koepke, and E. P. Shettle, 1991: *Atmospheric aerosols: Global climatology and Radiative characteristics*. A. Deepak, Hampton, VA.

Deschamps, P.-Y., M. Herman, and D. D. Tanré, 1983: Modélisation du rayonnement solaire réfléchi par l'atmosphère et la Terre, entre 0,35 et 4 microns. Tech. rep., Rapport ESA 4393/80/F/DD(SC), 156 pp.

Ebert, E. E. and J. A. Curry, 1992: A parameterization of ice cloud optical properties for use in climate models. *J. Geophys. Res.*, **97 (D4)**, 3831–3836, doi:10.1029/91JD02472.

Ebert, E. E. and J. A. Curry, 1993: An intermediate one-dimensional thermodynamic sea ice model for investigating ice-atmosphere interactions. *J. Geophys. Res.*, **98 (C6)**, 10 085–10 109, doi: 10.1029/93JC00656.

Elsasser, W. M., 1942: *Heat Transfer by infrared Radiation in the Atmosphere*. Harvard University Press, 43 pp.

Fortuin, J. P. F. and U. Langematz, 1994: An update on the global ozone climatology and on concurrent ozone and temperature trends. *Proceedings SPIE, Atmos. Sensing and Modeling*, **2311**, 207–216.

Fouquart, Y., 1974: Utilisation des approximants de Padé pour l'étude des largeurs équivalentes des raies formées en atmosphère diffusante. *Beitr. Phys. Atmos.*, **14**, 497–506.

Fouquart, Y., 1987: Radiative transfer in climate modeling. *NATO Advanced Study Institute on Physically-Based Modeling and Simulation of Climate and Climatic Changes*, Erice, Sicily, 11-23 May 1986. M.E. Schlesinger, Ed., 223–283.

Fouquart, Y. and B. Bonnel, 1980: Computations of solar heating of the Earth's atmosphere: A new parametrization. *Beitr. Phys. Atmos.*, **53**, 35–62.

Fu, Q. and K. N. Liou, 1992: On the correlated k-distribution method for radiative transfer in nonhomogeneous atmosphere. *J. Atmos. Sci.*, **49**, 2139–2156, doi:10.1175/1520-0469(1992)049%3C2139:OTCDMF%3E2.0.CO;2.

Fu, Q., P. Yang, and W. B. Sun, 1998: An accurate parametrization of the infrared radiative properties of cirrus clouds of climate models. *J. Climate*, **11**, 2223–2237, doi:10.1175/1520-0442(1998)011%3C2223:AAPOTI%3E2.0.CO;2.

Geleyn, J.-F. and A. Hollingsworth, 1979: An economical analytical method for the computation of the interaction between scattering and line absorption of radiation. *Beitr. Phys. Atmos.*, **52**, 1–16.

Gregory, D., J.-J. Morcrette, C. Jakob, A. M. Beljaars, and T. Stockdale, 2000: Revision of convection, radiation and cloud schemes in the ECMWF model. *Quart. J. Roy. Meteor. Soc.*, **126**, 1685–1710, doi:10.1002/qj.49712656607.

Grini, A., P. Tulet, and L. Gomes, 2006: Dusty weather forecasts using the MesoNH mesoscale atmospheric model. *J. Geophys. Res.*, **111 (D19205)**, doi:10.1029/2005JD007007.

Hogan, R. J. and A. Bozzo, 2016: ECRAD: A new radiation scheme for the IFS. Tech. Rep. 787, ECMWF Technical Memorandum.

Hogan, R. J. and A. J. Illingworth, 2000: Deriving cloud overlap statistics from radar. *Quart. J. Roy. Meteor. Soc.*, **126 (569)**, 2903–2909, doi:10.1002/qj.49712656914.

Hogan, R. J., S. A. K. Schäfer, C. Klinger, J. C. Chiu, and B. Mayer, 2016: Representing 3-D cloud radiation effects in two-stream schemes: 2. Matrix formulation and broadband evaluation. *J. Geophys. Res.*, **121 (14)**, 8583–8599, doi:10.1002/2016JD024876.

Hogan, R. J. and J. K. P. Shonk, 2013: Incorporating the effects of 3D radiative transfer in the presence of clouds into two-stream radiation schemes. *J. Atmos. Sci.*, **70**, 708—724, doi:10.1175/JAS-D-12-041.1.

Joseph, J. H., W. J. Wiscombe, and J. A. Weinman, 1976: The Delta-Eddington approximation for radiative flux transfer. *J. Atmos. Sci.*, **33**, 2452–2459, doi:10.1175/1520-0469(1976)033%3C2452:TDEAFR%3E2.0.CO;2.

Lacis, A. A. and V. Oinas, 1991: A description of the correlated k distribution method for modeling nongray gaseous absorption, thermal emission, and multiple scattering in vertically inhomogeneous atmospheres. *J. Geophys. Res.*, **96 (D5)**, 9027–9063, doi:10.1029/90JD01945.

Lindner, T. H. and J. Li, 2000: Parameterization of the optical properties for water clouds in the infrared. *J. Climate*, **13**, 1797–1805, doi:10.1175/1520-0442(2000)013%3C1797:POTOPF%3E2.0.CO;2.

Manners, J., 2015: Socrates technical guide suite of community radiative transfer codes based on Edwards and Slingo. Tech. rep., Met Office, FitzRoy Rd, Exeter EX1 3PB.

Martin, G. M., D. W. Johnson, and A. Spice, 1994: The measurement and parameterization of effective radius of droplets in warm stratocumulus. *J. Atmos. Sci.*, **51**, 1823–1842, doi:10.1175/1520-0469(1994)051⟨1823:TMAPOE⟩2.0.CO;2.

Maxwell-Garnett, J., 1904: Colours in metal glasses and in metallic films. *Philos. T. Roy. Soc. A*, **203**, 385–420.

Mie, G., 1908: Beiträge zur Optik trüber Medien, speziell kolloidaler Metallösungen. *Ann. Phys.-Leipzig*, **330**, 377–445.

Mlawer, E. J., S. J. Taubman, P. D. Brown, M. J. Iacono, and S. A. Clough, 1997: Radiative transfer for inhomogeneous atmospheres: RRTM, a validated correlated-k model for the longwave. *J. Geophys. Res.*, **102 (D14)**, 16 663–16 682, doi:10.1029/97JD00237.

Morcrette, J.-J., 1991: Radiation and cloud radiative properties in the European Centre for Medium Range Weather Forecasts forecasting system. *J. Geophys. Res.*, **96**, 9121–9132, doi:10.1029/89JD01597.

Morcrette, J. J., H. W. Barker, J. N. S. Cole, M. J. Iacono, and R. Pincus, 2008: Impact of a new radiation package, McRad, in the ECMWF Integrated Forecasting System. *Mon. Weather Rev.*, **136 (12)**, 4773–4798, doi:10.1175/2008MWR2363.1.

Morcrette, J.-J. and Y. Fouquart, 1985: On systematic errors in parametrized calculations of longwave radiation transfer. *Quart. J. Roy. Meteor. Soc.*, **111**, 691–708, doi:10.1002/qj.49711146903.

Morcrette, J.-J., L. Smith, and Y. Fouquart, 1986: Pressure and temperature dependence of the absorption in longwave radiation parametrizations. *Beitr. Phys. Atmos.*, **59**, 455–469.

Paltridge, G. W. and C. M. R. Platt, 1976: *Radiative Processes in Meteorology and Climatology*. Elsevier.

Pincus, R., H. W. Barker, and J. J. Morcrette, 2003: A fast, flexible, approximate technique for computing radiative transfer in inhomogeneous cloud fields. *J. Geophys. Res.*, **108 (D13)**, 7725–7752, doi:10.1029/2002JD003322.

Rodgers, C. D., 1967: The radiative Heat Budget of the troposphere and lower stratosphere. Tech. Rep. 12, A2, Planetary Circulation Project, Dept. of Meteorology, Mass. Instit. Technology, Cambridge, Mass., 99 pp.

Rodgers, C. D. and C. D. Walshaw, 1966: The computation of infrared cooling rate in planetary atmospheres. *Quart. J. Roy. Meteor. Soc.*, **92**, 67–92, doi:10.1002/qj.49709239107.

Savijarvi, H. and P. Raisanen, 1997: Long-wave optical properties of water clouds and rain. *Tellus*, **50 (1)**, 1–11, doi:10.1034/j.1600-0870.1998.00001.x.

Schäfer, S. A. K., R. J. Hogan, C. Klinger, J. C. Chiu, and B. Mayer, 2016: Representing 3-D cloud radiation effects in two-stream schemes: 1. Longwave considerations and effective cloud edge length. *J. Geophys. Res.*, **121 (14)**, 8567–8582, doi:10.1002/2016JD024876.

Shettle, E. P. and J. A. Weinman, 1970: The transfer of solar irradiance through inhomogeneous turbid atmospheres evaluated by Eddington's approximation. *J. Atmos. Sci.*, **27**, 1048–1055, doi:10.1175/1520-0469(1970)027%3C1048:TTOSIT%3E2.0.CO;2.

Shonk, J. K. P. and R. J. Hogan, 2008: Tripleclouds: An Efficient Method for Representing Horizontal Cloud Inhomogeneity in 1D Radiation Schemes by Using Three Regions at Each Height. *J. Climate*, **21**, 2352–2370, doi:10.1175/2007JCLI1940.1.

Slingo, A., 1989: A GCM parameterization for the shortwave radiative properties of water clouds. *J. Atmos. Sci.*, **46**, 1419–1427, doi:10.1175/1520-0469(1989)046%3C1419:AGPFTS%3E2.0.CO;2.

Smith, E. A. and L. Shi, 1992: Surface forcing of the infrared cooling profile over the Tibetan plateau. Part I: influence of relative longwave radiative heating at high altitude. *J. Atmos. Sci.*, **49**, 805–822, doi:10.1175/1520-0469(1992)049%3C0805:SFOTIC%3E2.0.CO;2.

Sun, Z., 2001: Reply to comments by Greg M. McFarquhar on 'Parametrization of effective sizes of cirrus-cloud particles and its verification against observations'.(October B, 1999, 125, 3037–3055). *Quart. J. Roy. Meteor. Soc.*, **127 (571)**, 267–271, doi:10.1002/qj.49712757116.

Sun, Z. and L. Rikus, 1999: Parametrization of effective sizes of cirrus-cloud particles and its verification against observations. *Quart. J. Roy. Meteor. Soc.*, **125 (560)**, 3037–3055, doi:10.1002/qj.49712556012.

Tanré, D., J.-F. Geleyn, and J. Slingo, 1984: First results of the introduction of an advanced aerosol-radiation interaction in the ECMWF low resolution global model. *Aerosols and their Climatic Effects*, H. E. Gerber and A. Deepak, Eds., A. Deepak Publishing, Hampton, VA, 133–177.

Tegen, I., P. Hoorig, M. Chin, I. Fung, D. Jacob, and J. Penner, 1997: Contribution of different aerosol species to the global aerosol extinction optical thickness: Estimates from model results. *J. Geophys. Res.*, **102 (D20)**, 23 895–23 915, doi:10.1029/97JD01864.

Tiedtke, M., 1996: An Extension of Cloud-Radiation Parameterization in the ECMWF Model: The Representation of Subgrid-Scale Variations of Optical Depth). *Mon. Weather Rev.*, **124**, 745–750, doi:10.1175/1520-0493(1996)124%3C0745:AEOCRP%3E2.0.CO;2.

Tombette, M., P. Chazette, B. Sportisse, and Y. Roustan, 2008: Simulation of aerosol optical properties over Europe with a 3-D size resolved aerosol model: comparisons with AERONET data. *Atmos. Chem. Phys.*, **8**, 7115–7132, doi:10.5194/acp-8-7115-2008.

Washington, W. M. and D. L. Williamson, 1977: A description of the NCAR GCMs. *General Circulation Models of the Atmosphere*, J. Chang, Ed., Methods in Computational Physics, vol. 17, Academic Press, 111–172.

Chapter 2

Turbulence Scheme

Contents

2.1 Introduction

The Meso-NH model intends to emulate the capacities of various models, such as mesoscale meteorological models, cloud resolving models (CRM), and even Large Eddy Simulation (LES) models. One of the main differences between these models is the treatment of turbulence. In mesoscale hydrostatic models, the turbulence scheme is usually quasi-1D (on the vertical), since the horizontal resolution cannot resolve large gradients. In CRM and LES, this is not the case anymore, and 3D schemes, able to see turbulence sources by shear in all three spatial dimensions, are to be used.

The current turbulence scheme of Meso-NH is therefore a first step towards a unified approach. It takes its roots in the two schemes which were used in the Meso-NH group, namely the quasi 1D turbulence scheme of Bougeault and Lacarrère (1989) (BL89 in the following), which was used in Peridot and Salsa models, and the 3D scheme of Redelsperger et Sommeria (1981), (RS81 in the following), which was used in the CNRM cloud model.

The approach followed is very close to the RS81 derivation of the parameterization of the three-dimensional turbulent fluxes. The second-order moments equations are separated into isotropic and anisotropic parts, and the equations for the anisotropic parts are stationnarized. This leads to diagnostic expressions for the fluxes. On the other hand, the isotropic part reverts to a prognostic equation for the turbulence kinetic energy (TKE). In this derivation, the Coriolis effects, and the Earth curvature are neglected, as well as the third order moments in the anisotropic equations. A detailed derivation of the scheme and a discussion of present limitations is given by Cuxart (1997).

Note that a parameterization of third order moments of heat fluxes for the dry convective boundary layer was recently implemented into Meso-NH. The reader is referred to Tomas and Masson (2006).

The scheme offers a choice of three closure methods (currently only two are implemented). These may be selected by the parameter HTURBLEN (see sections 4 and 5). It may be run in either of two ”modes”: 1DIM and 3DIM. In ”1DIM” mode, the horizontal gradients are not considered. This is appropriate where the horizontal resolution is coarse, and saves computer resources. In ”3DIM” mode, the full computations are performed.

2.2 Turbulent fluxes in a Cartesian frame

We will first present the formulation of the scheme in a Cartesian frame of reference (x, y, z). The above mentioned treatment of the anisotropic part of the second-order moment equations leads to the following diagnostic equations:

$$
\begin{aligned}
\overline{u'_i\theta'} &= -\frac{2}{3}\frac{L}{C_s}e^{\frac{1}{2}}\frac{\partial\overline{\theta}}{\partial x_i}\phi_i, && (2.1)\\
\overline{u'_i r'_v} &= -\frac{2}{3}\frac{L}{C_h}e^{\frac{1}{2}}\frac{\partial\overline{r_v}}{\partial x_i}\psi_i, && (2.2)\\
\overline{u'_i\,u'_j} &= \frac{2}{3}\delta_{ij}\,e - \frac{4}{15}\frac{L}{C_m}e^{\frac{1}{2}}(\frac{\partial\overline{u_i}}{\partial x_j} + \frac{\partial\overline{u_j}}{\partial x_i} - \frac{2}{3}\delta_{ij}\frac{\partial\overline{u_m}}{\partial x_m}), && (2.3)\\
\overline{\theta' r'_v} &= C_2 L^2(\frac{\partial\overline{\theta}}{\partial x_m}\frac{\partial\overline{r_v}}{\partial x_m})(\phi_m + \psi_m), && (2.4)\\
\overline{\theta'^2} &= C_1 L^2(\frac{\partial\overline{\theta}}{\partial x_m}\frac{\partial\overline{\theta}}{\partial x_m})\phi_m, && (2.5)\\
\overline{r'^2_v} &= C_1 L^2(\frac{\partial\overline{r_v}}{\partial x_m}\frac{\partial\overline{r_v}}{\partial x_m})\psi_m. && (2.6)
\end{aligned}
$$

Note that the Einstein summation convention applies above to all m subscripts, even in the last three equations.

The quantity L is the eddy length scale. Its specification is discussed below. The quantity e is the kinetic energy of the turbulence.

Whenever necessary, the flux of potential virtual temperature may be retrieved from the fluxes of temperature and moisture using the two coefficients $E_\theta = \frac{\overline{\theta_v}}{\overline{\theta}}$, and $E_{moist} = 0.61\overline{\theta}$:

$$\overline{u'_i\theta'_v} = E_\theta\overline{u'_i\theta'} + E_{moist}\overline{u'_i r'_v} \tag{2.7}$$

These factors have different expressions in presence of clouds (see Chapter on the subgrid condensation schemes).

The numerical coefficients appearing in the above equations arise from the closures, and take the following values (after RS81):

$$
\begin{aligned}
C_s &= 4. && (2.8)\\
C_h &= 4. && (2.9)\\
C_m &= 4. && (2.10)\\
C_1 &= \frac{2}{3}\frac{1}{C_s\,C_\theta} && (2.11)\\
C_2 &= \frac{2}{3}\frac{1}{C_s\,C_{q\theta}} && (2.12)\\
C_\theta &= 1.2 && (2.13)\\
C_{q\theta} &= 2.4 && (2.14)
\end{aligned}
$$

Finally, the above equations use stability functions ϕ_i and ψ_i, to describe the enhancement or inhibition of turbulent transfers by stability effects. These functions have been defined by RS81 as:

$$\phi_i = \begin{cases} 1 & \text{for i=1,2} \\ 1 - \frac{(1+C_1R_{r1})(2C_2R^2_{\theta r3}+C_1R^2_{\theta 3})\frac{1}{R_{\theta 1}}+C_1C_2(R^2_{\theta 3}-R^2_{r3})}{1+(C_1+C_2)(R_{\theta 1}+R_{r1})+C_1(C_2(R^2_{\theta 1}+R^2_{r1})+C_1R_{\theta 1}R_{r1})} & \text{for i=3} \end{cases} \tag{2.15}$$

$$\psi_i = \begin{cases} 1 & \text{for i=1,2} \\ 1 - \frac{(1+C_1R_{\theta 1})(2C_2R^2_{\theta r3}+C_1R^2_{r3})\frac{1}{R_{r1}}+C_1C_2(R^2_{r3}-R^2_{\theta 3})}{1+(C_1+C_2)(R_{\theta 1}+R_{r1})+C_1(C_2(R^2_{\theta 1}+R^2_{r1})+C_1R_{\theta 1}R_{r1})} & \text{for i=3} \end{cases} \tag{2.16}$$

This uses the so-called Redelsperger (or Richardson) numbers

$$
\begin{aligned}
R_{\theta 1} &= \frac{g}{\theta_{v\,ref}}\frac{L^2}{e}E_\theta\frac{\partial\overline{\theta}}{\partial x_3}, && (2.17)\\
R_{\theta 3} &= \frac{g}{\theta_{v\,ref}}\frac{L^2}{e}E_\theta\Big(\frac{\partial\overline{\theta}}{\partial x_m}\frac{\partial\overline{\theta}}{\partial x_m}\Big)^{\frac{1}{2}}, && (2.18)\\
R_{r1} &= \frac{g}{\theta_{v\,ref}}\frac{L^2}{e}E_{moist}\frac{\partial\overline{r_v}}{\partial x_3}, && (2.19)\\
R_{r3} &= \frac{g}{\theta_{v\,ref}}\frac{L^2}{e}E_{moist}\Big(\frac{\partial\overline{r_v}}{\partial x_m}\frac{\partial\overline{r_v}}{\partial x_m}\Big)^{\frac{1}{2}}, && (2.20)\\
R^2_{\theta r3} &= \Big(\frac{g}{\theta_{v\,ref}}\frac{L^2}{e}\Big)^2E_\theta\frac{\partial\overline{\theta}}{\partial x_m}E_{moist}\frac{\partial\overline{r_v}}{\partial x_m}. && (2.21)
\end{aligned}
$$

2.3 Turbulence kinetic energy equation

We use the well known prognostic equation for the turbulence kinetic energy (TKE), expressed as

$$
\begin{aligned}
\frac{\partial e}{\partial t} = {}& -\frac{1}{\rho_{dref}}\frac{\partial}{\partial x_j}(\rho_{dref}e\overline{u_j}) - \overline{u'_iu'_j}\frac{\partial\overline{u_i}}{\partial x_j} + \frac{g}{\theta_{v\,ref}}\overline{u'_3\theta'_v}\\
& +\frac{1}{\rho_{dref}}\frac{\partial}{\partial x_j}\Big(C_{2m}\rho_{dref}Le^{\frac{1}{2}}\frac{\partial e}{\partial x_j}\Big) - C_\epsilon\frac{e^{\frac{3}{2}}}{L} && (2.22)
\end{aligned}
$$

The source terms appearing in (2.22) are respectively the advection of TKE, the shear production, the buoyancy production, the diffusion, and the dissipation. Note that the shear and buoyancy productions may contain a contribution from the shallow convection scheme.
The additional numerical constants take the values (RS81)

$$
\begin{aligned}
C_{2m} &= 0.2, && (2.23)\\
C_\epsilon &= 0.85. && (2.24)
\end{aligned}
$$

2.4 Closure by mixing length

There are currently two choices of mixing length formulations.

2.4.1 The grid-size

The grid size of the model is commonly used as the characteristic length scale of the sub-grid eddies. This is justified when the grid size falls into the inertial subrange of the turbulent flow. In Meso-NH, the formulation must take into account the possible anisotropy of the grid. For the standard 3D version of the model,

$$L = (d_{xx}.d_{yy}.d_{zz})^{1/3}. \tag{2.25}$$

For the 2D version,

$$L = (d_{xx}.d_{zz})^{1/2}, \tag{2.26}$$

and for the 1D, column version,

$$L = d_{zz}. \tag{2.27}$$

L is further limited in all cases to be smaller than kz, k being the Karman constant 0.4.
To activate this option, the parameter HTURBLEN has to be given the value 'DELT'. This is recommended when the model has high resolution and when the grid is nearly isotropic. Even in this case however, the assumption that the grid size falls within the inertial subrange may be in error, due for instance to the effects of stable stratification. This is to some extent mitigated by the use of the stability functions ϕ_i and ψ_i.

2.4.2 Bougeault-Lacarrère mixing length

BL89 postulate that the mixing length at any level in the atmosphere can be related to the distance a parcel of air having the initial kinetic energy of the level, can travel upwards (l_{up}) and downwards (l_{down}) before being stopped by buoyancy effects. These distances are defined by

$$\begin{aligned}
\int_{z}^{z+l_{up}} \frac{g}{\theta_{v\,ref}}(\theta(z)-\theta(z'))dz' &= -\,e(z), \\
\int_{z-l_{down}}^{z} \frac{g}{\theta_{v\,ref}}(\theta(z')-\theta(z))dz' &= -\,e(z), \qquad (2.28)\\
l_{down} &\leq z, \\
L &= \left[\frac{(l_{up})^{-2/3}+(l_{down})^{-2/3}}{2}\right]^{-3/2} \qquad (2.29)
\end{aligned}$$

where $e(z)$ is the turbulent kinetic energy at level z and. The coefficient 2/3=α of the previous equation can be generalized by

$$\alpha = \frac{log(16)}{4log(\kappa)+log(C_\epsilon)-3log(C_m)} \tag{2.30}$$

from Lemarié et al. 2021. This method allows the length scale at any level to be influenced not only by the stability at this level, but by the effect of remote stable zones, or the presence of the ground.
This formulation is recommended when the model is used in "meso-scale mode", with highly anisotropic grids. It assumes that all of turbulence is parameterized, and will for instance lead to underestimation of dissipation if used in the LES mode. To activate this option, set HTURBLEN='BL89'.
The code is based on a second order accuracy algorithm that provides better resolution in the stable layers. We will shortly describe the difference between the first and the second order approaches. In the computation of the BL length, when the residual TKE is not large enough to reach the next level of the model, an estimation of how far this particle can travel between the two levels must be given. This is very important for stably stratified layers. First of all, we will see how this length should behave analytically, and then compare to the first and second order approximations.

Value for stably stratified layers In that case, assuming the gradient of θ constant between two adjacent layers ($\alpha \equiv \frac{\partial\theta}{\partial z} = ct$),

$$\begin{aligned} \theta(z) - \theta(z') &= \alpha(z - z') && (2.31)\\ \int_{z_n}^{z_n+L} \beta\alpha(z - z')dz' &= -e(z) && (2.32) \end{aligned}$$

where $\beta = \frac{g}{\theta_0}$, z is the departing layer and z' the heights that the particle travels throughout. The integration gives

$$\begin{aligned} \left[zz' - \frac{z'^2}{2}\right]_z^{z+L} &= \frac{-e(z)}{\alpha\beta} && (2.33)\\ L &= \sqrt{\frac{2e(z)}{\alpha\beta}} && (2.34) \end{aligned}$$

First order development In a first order approach, the length (the proportion of the layer that the particle can travel) is estimated as

$$\begin{aligned} e &= \int_{z_n}^{z_n+L} \beta\Delta\theta\delta z && (2.35)\\ \Delta\theta &= \theta(z_{n+1}) - \theta(z_n) && (2.36) \end{aligned}$$

and from here the following expression can be derived

$$L = \frac{e}{\beta\Delta\theta} \qquad (2.37)$$

which do not fit the analytical expression.

Second order development For a second order approach, the following relation is taken

$$\theta(z') = \theta(z_n) + \frac{\partial\theta}{\partial z}(z' - z_n) \qquad (2.38)$$

Then, for the jump from the last reached level (with $E_p(z, z_n)$ energy wasted, and $e(z) - E_p(z, z_n)$ as energy available to rise the particle against negative buoyancy)

$$\begin{aligned} e(z) - E_p(z, z_n) &= \int_{z_n}^{z_n+L} \beta(\theta(z') - \theta(z))dz'\\ &\approx \int_{z_n}^{z_n+L} \beta\left[\theta(z_n) + \frac{\theta(z_{n+1}) - \theta(z_n)}{z_{n+1} - z_n}(z' - z_n) - \theta(z)\right]dz'\\ &= [\beta\theta(z_n)z']_{z_n}^{z_n+L} + \left[\beta\frac{\theta(z_{n+1}) - \theta(z_n)}{z_{n+1} - z_n}(\frac{z'^2}{2} - z_n z')\right]_{z_n}^{z_n+L}\\ &\quad - [\beta\theta(z)z']_{z_n}^{z_n+L} && (2.39) \end{aligned}$$

and a quadratic equation for L is obtained:

$$\frac{\beta}{2}\left[\frac{\theta(z_{n+1}) - \theta(z_n)}{z_{n+1} - z_n}\right]L^2 + \beta\left[\theta(z_n) - \theta(z)\right]L - (e(z) - E_p(z, z_n)) = 0. \qquad (2.40)$$

In stably stratified layers, for $L = \frac{-b \pm \sqrt{b^2-4ac}}{2a}$, for a single layer elevation,

$$a = \frac{\beta}{2}\left[\frac{\theta(z_{n+1}) - \theta(z_n)}{z_{n+1} - z_n}\right] \tag{2.41}$$

$$b = \beta\left[\theta(z_n) - \theta(z)\right] = 0. \tag{2.42}$$

$$c = -(e(z) - E_p(z, z_n)) = -e(z) \tag{2.43}$$

so, $L = +\frac{\sqrt{-4ac}}{2a}$, with a $+$ sign since $a > 0$ and $c < 0$, and the expression for L is

$$L = \sqrt{\frac{2e}{\beta\left[\frac{\theta(z_{n+1})-\theta(z_n)}{z_{n+1}-z_n}\right]}} \tag{2.44}$$

which fits the analytical expression.

2.4.3 Rodier and Masson mixing length

In a strictly neutral boundary layer, physical mixing is not captured by BL89 because the terms of the left-hand side of Equation 2.28 are zero. l_{up} and l_{down} extend to the numerical boundaries of the model in a neutral boundary layer (Figure 2.1). In stable boundary layers, BL89 overestimates the turbulent mixing (Rodier 2017).

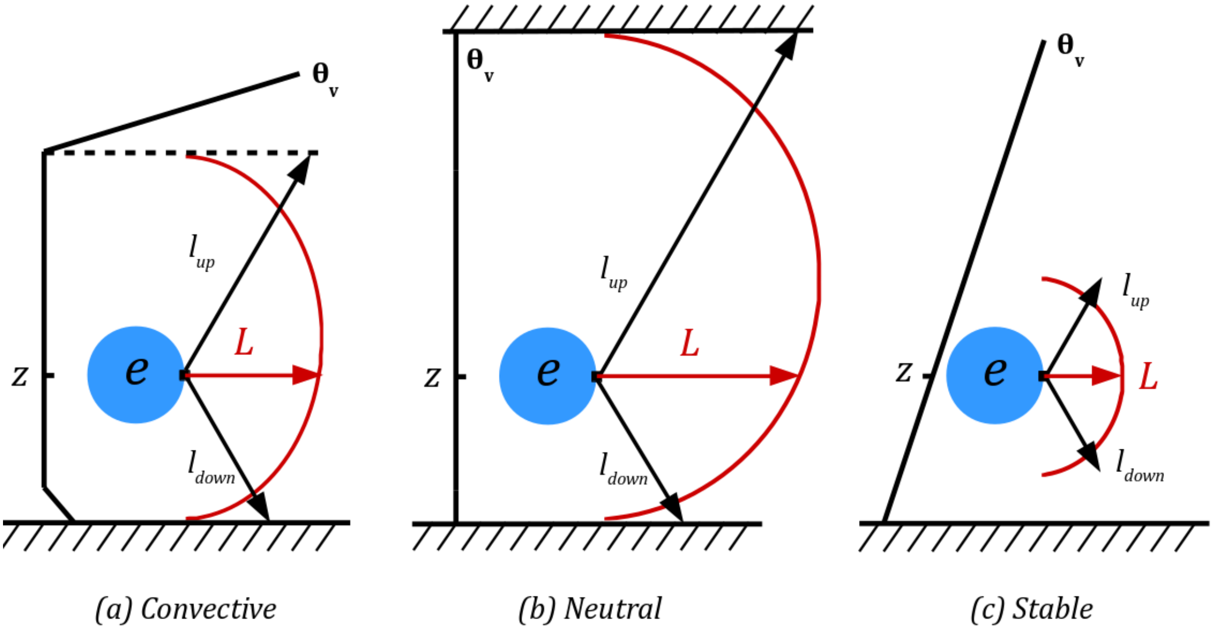

(a) Convective (b) Neutral (c) Stable

Figure 2.1: BL89 mixing length vertical profile (red) in convective, neutral and stable boundary layers.

To improve the representation of turbulent mixing in neutral and stable boundary layers, RM17 (Rodier and Masson, 2017) adds a local vertical wind shear term to the buoyancy-based BL89 formulation :

$$\begin{aligned}
\int_z^{z+l_{up}} \left[\frac{g}{\theta_{vref}}(\theta_v(z) - \theta_v(z')) + C_0\sqrt{e}S(z')\right] dz' = -e(z), \\
\int_{z-l_{down}}^{z} \left[\frac{g}{\theta_{vref}}(\theta_v(z') - \theta_v(z)) + C_0\sqrt{e}S(z')\right] dz' = -e(z),
\end{aligned} \tag{2.45}$$

where C_0 is a constant and $S(z')$ the local vertical wind shear:

$$S = \sqrt{\left(\frac{\partial \overline{u}}{\partial z}\right)^2 + \left(\frac{\partial \overline{v}}{\partial z}\right)^2} \tag{2.46}$$

The shear term corresponds to the slowdown effect produced by the vertical decoupling of turbulent structures when the local shear is strong (Figure 2.2). This effect also depends on the average eddy size with larger eddies more decoupled.

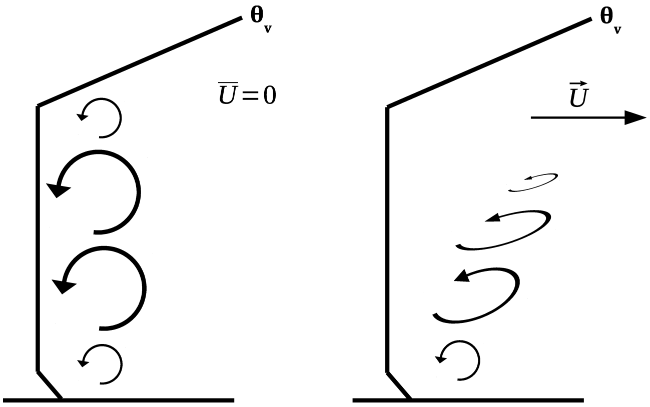

Figure 2.2: Schematic view of the effect of stratification and vertical wind shear on the reduction of the vertical mixing efficiency. Without wind shear (left), the turbulent structures are constrained by the distance to the surface and by the stratification. The presence of a wind shear (right) results in the stretching and vertical decoupling of the turbulent structures.

2.4.4 Mixing length for the grey zone of turbulence

This mixing length is adapted to the constraints of the hectometric-scale grey zone of turbulence for neutral and convective boundary layers. It combines a mixing length for mesoscale simulations L_{RM17} (see above), where the turbulence is fully subgrid and a mixing length for Large-Eddy Simulations, where the coarsest turbulent eddies are explicitly resolved.

$$L_{\triangle} = (\Delta x \Delta y)^{1/2}, \tag{2.47}$$

The mixing length $\mathfrak{L}$ is built for isotropic turbulence schemes, as well as schemes using the horizontal homogeneity assumption. $\mathfrak{L}$ is the minimum mixing length between the horizontal grid cell $L_{\triangle}$ and L_{RM17}:

$$\mathfrak{L} = min(\alpha L_{\triangle}, L_{RM17}), \tag{2.48}$$

where α is a tuning parameter set to 0.5, according to the numerical experiments detailed in Honnert et al. (2021).
With this new mixing length, the turbulence scheme produces the right proportion between subgrid and resolved turbulent exchanges in Large Eddy Simulations, in the grey zone of turbulence, as well as at the mesoscale. This opens the way of using a single mixing length whatever the grid mesh of the atmospheric model, the evolution stage or the depth of the boundary layer.

2.4.5 Qualitative behavior of the 1D dry system with BL length

Critical Richardson number Let us write the 1D TKE evolution equation introducing into it the expressions for the fluxes, and neglecting the turbulent transport for this particular case:

$$\frac{\partial e}{\partial t} = \frac{4L}{15C_m} e^{\frac{1}{2}} (\frac{\partial U}{\partial z})^2 - \frac{g}{\theta_{v0}} \frac{2L}{3C_s} e^{\frac{1}{2}} \frac{\partial \theta}{\partial z} \left(1 + C_1 \frac{L^2}{e} \frac{g}{\theta_{v0}} \frac{\partial \theta}{\partial z} \right)^{-1} - C_\epsilon \frac{e^{\frac{3}{2}}}{L} \tag{2.49}$$

where the term $(\ \ )^{-1}$ is the developed expression for ϕ_3 in 1D dry mode. Introducing the value for BL in stable layers ($L = \sqrt{\frac{2e(z)}{\alpha\beta}}$) and defining the buoyancy as $B = \beta\alpha$,

$$\frac{\partial e}{\partial t} = e \left[\frac{4\sqrt{2}}{15C_m} (\frac{\partial U}{\partial z})^2 \frac{1}{\sqrt{B}} - \sqrt{B}\sqrt{2} \frac{2}{3C_s} (\frac{1}{1+2C_1}) - \frac{C_\epsilon}{\sqrt{2}} \sqrt{B} \right] \tag{2.50}$$

The critical Richardson number is the one that nullifies the previous equation,

$$Ri_c = \frac{B}{(\frac{\partial U}{\partial z})^2} = \frac{\frac{4\sqrt{2}}{15C_m}}{\frac{2\sqrt{2}}{3C_s}(\frac{1}{1+2C_1}) + \frac{C_\epsilon}{\sqrt{2}}} \tag{2.51}$$

and entering the values of the constants (RS81), $C_m = C_s = 4, C_1 = 0.139, C_\epsilon = 0.7$, the critical Richardson of the 1D proposed scheme is $Ri_c = 0.139$.

2.4.6 Mixing length in clouds

From the masdev46 version a namelist `NAM_TURB_CLOUD` allows us to differentiate the mixing length inside and outside a cloud, for the chosen model `NMODEL_CLOUD`. Indeed, in a convective atmosphere, the cloud interface (but also inside the cloud) undergoes a small scale instabilities of a few meters which enhances the mixing (Squire 1958; Klaassen and Clark 1985; Emanuel 1994). The clear sky mixing length cannot be sufficient to take into account this turbulence enhancement when the physical gradients are not resolved. The proposed simple solution consists in chosen a specific cloud mixing length (`CTURBLEN_CLOUD`) which can be increased in the 3D turbulence scheme following an instability criterion. At each time step and in each horizontal direction, if a grid point satisfies all the following conditions:

- itself or its adjacent points are cloudy ($r_c + r_i > 0.001$ g/kg);
- G, the horizontal gradient of the non precipitating total water ($r_v + r_c + r_i$) is strong enough ($|G| \leq 0.1$ g/kg/km);
- G amplifies itself with time by advection, that is to say the frontogenetic type term $Q = dG/dt$ is of the same sign as G.

The mixing length at this point which appears in the diffusion coefficient $K = L\sqrt{e}$ of the horizontal fluxes is multiplied by the coefficient α, a linear function of Q (averaged in both horizontal directions) between two limits to be prescribed in the namelist (Q_{min} and Q_{max}), with a maximum α_{max} also to choose (Fig. 2.3). This local enhancement of the mixing length in clouds has been tested at resolutions of 2-3 km in a thunderstorm with extreme vertical velocities. With the following values, taken by default in the namelist, the vertical velocities and fluxes are reasonable compared to the high resolution simulation (400 m): $\alpha_{\text{max}} = 5$, $Q_{\text{min}} = 0.001$ g/kg/km/s, $Q_{\text{max}} = 0.01$ g/kg/km/s.

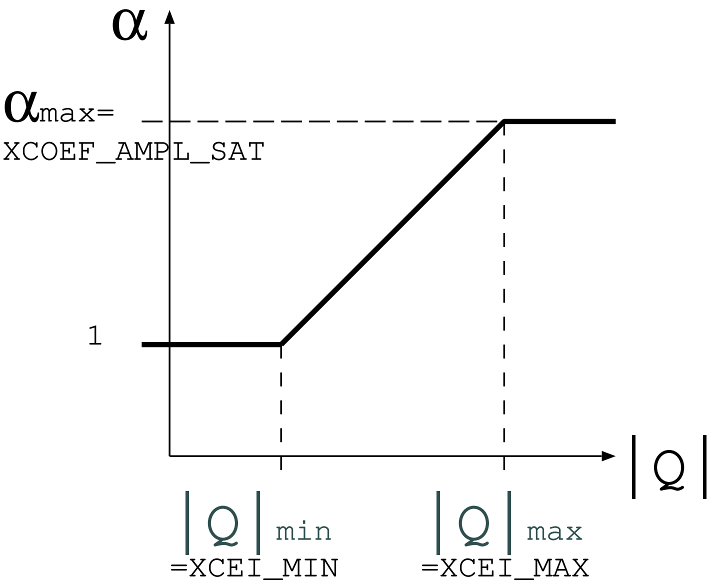

Figure 2.3: Coefficient α of in-cloud mixing length enhancement as function of the instability criterion Q.

2.5 Closure by dissipation equation

This is an alternative way to close the system (Hanjalic and Launder 1972), obtaining a value for L from an additional prognostic equation. The most popular method is the so-called $k-\epsilon$ approach, in the engineering vocabulary, where k stands for the TKE and ϵ for its dissipation.
The prognostic equation for ϵ reads

$$\frac{D\epsilon}{Dt} = P(\epsilon) - D(\epsilon) + T(\epsilon), \tag{2.52}$$

where the source terms are defined as

$$P(\epsilon) = -C_{\epsilon 1}\frac{\epsilon}{e}\overline{u_i'u_k'}\frac{\partial U_i}{\partial x_k} = C_{\epsilon 1}\frac{\epsilon}{e}P(e), \tag{2.53}$$

$$D(\epsilon) = C_{\epsilon 2}\frac{\epsilon^2}{e}, \tag{2.54}$$

$$T(\epsilon) = -\frac{\partial}{\partial x_j}(-c_\epsilon\frac{e}{\epsilon}\overline{u_j'u_k'}\frac{\partial \epsilon}{\partial x_k}) = -\frac{\partial\overline{w'\epsilon'}}{\partial z} \tag{2.55}$$

However, in the presence of stratification Duynkerke (1988) showed that it is necessary to use

$$P(\epsilon) = S + \max(0, B) + \max(0, T(e)) \tag{2.56}$$

where S, B and T stand for the shear production, buoyancy production and turbulent transport in the TKE evolution equation.

Knowing ϵ, the mixing length is recovered by inverting the Kolmogorov relation

$$\epsilon = C_\epsilon\frac{e^{\frac{3}{2}}}{L}. \tag{2.57}$$

Although it has been coded, this formulation is not yet giving satisfactory results, and is not currently available.

2.6 Conservation of the energy in Meso-NH

The examination of the energy conservation in a model of atmosphere is a very difficult task. In numerical models, this question is even untractable. However, a recent study of Blister and Emanuel (1998) pointed out that a thermodynamic energy arising from dissipative heating is always neglected in mesoscale models. Indeed this should not be the case when simulating hurricanes or very turbulent flows as omitting this term may lead to an appreciable underestimation of the intensity of tropical cyclones.
It is well known that the frictional dissipation of kinetic energy occurs at molecular scales where it is ultimately converted into thermal energy or heat. As numerical models perform a time integration of the ”mean” (grid-averaged) momentum equations, an additional equation is used to parameterize the sub-grid scale motions and their up-scaling fluxes.
The momentum conservation equation is rewritten here for convenience:

$$\begin{aligned}\frac{\partial}{\partial t}(\rho_{deff}U_i) + \frac{\partial}{\partial x_j}(\rho_{deff}U_i \cdot U_j) + \rho_{deff}\mathcal{F}_\Pi + \rho_{deff}\delta_{i3}g\frac{\theta_v - \theta_{vref}}{\theta_{vref}} + \rho_{deff}f\epsilon_{ij3}U_j = \\ +\nu\frac{\partial^2}{\partial x_j^2}(\rho_{deff}U_i) + \rho_{deff}\mathcal{F}, \qquad (2.58)\end{aligned}$$

where $\rho_{deff}\boldsymbol{\mathcal{F}_\Pi}$ is the pressure gradient force, which takes different forms in the three anelastic systems:

$$\rho_{deff}\boldsymbol{\mathcal{F}_\Pi} = \begin{cases} \rho_{deff}\boldsymbol{\nabla}(C_{pd}\theta_{vref}\Pi'), & \text{(Lipps-Hemler)} \qquad (2.59) \\ \rho_{deff}C_{pd}\theta_{vref}\boldsymbol{\nabla}\Pi', & \text{(Mod. Anelastic Eq.)} \qquad (2.60) \\ \rho_{deff}C_{pd}\theta_v\boldsymbol{\nabla}\Pi'. & \text{(Durran)} \qquad (2.61) \end{cases}$$

Expansion of the mean and turbulent parts ($U_i = \overline{U_i} + u'_i$) and applying Reynolds averaging rules on the momentum equation leads to

$$\begin{aligned}\frac{\partial}{\partial t}(\rho_{deff}\overline{U_i}) + \frac{\partial}{\partial x_j}(\rho_{deff}\overline{U_i} \cdot \overline{U_j}) + \rho_{deff}\overline{\mathcal{F}}_\Pi + \rho_{deff}\delta_{i3}g\frac{\overline{\theta_v} - \theta_{vref}}{\theta_{vref}} + \rho_{deff}f\epsilon_{ij3}\overline{U_j} = \\ +\nu\frac{\partial^2}{\partial x_j^2}(\rho_{deff}\overline{U_i}) - \frac{\partial}{\partial x_j}(\rho_{deff}\overline{u'_i u'_j}) + \rho_{deff}\overline{\mathcal{F}}, \qquad (2.62)\end{aligned}$$

where $\rho_{deff}\overline{u'_i u'_j}$ is the turbulent mean flux. The conservation equation of the turbulent part is obtained by subtracting equation (2.62) to (2.58)

$$\begin{aligned}\frac{\partial}{\partial t}(\rho_{deff}u'_i) + \frac{\partial}{\partial x_j}(\rho_{deff}u'_i \cdot \overline{U_j}) + \rho_{deff}(\mathcal{F}_\Pi)' + \rho_{deff}\delta_{i3}g\frac{\theta'_v}{\theta_{vref}} + \rho_{deff}f\epsilon_{ij3}u'_j = \\ -\frac{\partial}{\partial x_j}(\rho_{deff}u'_i u'_j) - \frac{\partial}{\partial x_j}(\rho_{deff}\overline{U_i} \cdot u'_j) \\ +\nu\frac{\partial^2}{\partial x_j^2}(\rho_{deff}u'_i) + \frac{\partial}{\partial x_j}(\rho_{deff}\overline{u'_i u'_j}) + \rho_{deff}(\mathcal{F})', \qquad (2.63)\end{aligned}$$

Multiplying equation (2.62) by $\overline{U_i}$ leads to the mean kinetic energy equation with $K = \rho_{deff}(\overline{U_i} \cdot \overline{U_i}/2)$ and using the anelastic continuity equation $\partial/\partial x_i(\rho_{deff}\overline{U_i}) = 0$ of the mean flow

$$\begin{aligned}\frac{\partial}{\partial t}K + \frac{\partial}{\partial x_j}(K \cdot \overline{U_j}) + \left[\rho_{deff}\overline{\mathcal{F}}_{\Pi} + \rho_{deff}\delta_{i3}g\frac{\overline{\theta_v} - \theta_{v\,ref}}{\theta_{v\,ref}} + \rho_{deff}f\epsilon_{ij3}\overline{U_j}\right] \cdot \overline{U_i} = \\ + \left[\nu\frac{\partial^2}{\partial x_j^2}(\rho_{deff}\overline{U_i}) - \frac{\partial}{\partial x_j}(\rho_{deff}\overline{u_i'u_j'}) + \rho_{deff}\overline{\mathcal{F}}\right] \cdot \overline{U_i},\end{aligned} \tag{2.64}$$

while multiplying equation (2.63) by u_i' and averaging after rearrangement leads to the turbulent kinetic energy equation with $TKE = \rho_{deff}(\overline{u_i'u_i'}/2)$ (the anelastic continuity equation $\partial/\partial x_i(\rho_{deff}u_i') = 0$ of the turbulent flow is used)

$$\begin{aligned}\frac{\partial}{\partial t}TKE + \frac{\partial}{\partial x_j}(TKE \cdot \overline{U_j}) + \rho_{deff}\overline{(\mathcal{F}_{\Pi})'u_i'} + \rho_{deff}\delta_{i3}g\frac{\overline{\theta_v'u_i'}}{\theta_{v\,ref}} + \rho_{deff}f\epsilon_{ij3}\overline{u_i'u_j'} = \\ \overline{-u_i'\frac{\partial}{\partial x_j}(\rho_{deff}u_i'u_j')} - \overline{u_i'\frac{\partial}{\partial x_j}(\rho_{deff}\overline{U_i} \cdot u_j')} + \overline{\nu u_i'\frac{\partial^2}{\partial x_j^2}(\rho_{deff}u_i')} + \rho_{deff}\overline{(\mathcal{F})'u_i'},\end{aligned} \tag{2.65}$$

which is equivalent to:

$$\begin{aligned}\frac{\partial}{\partial t}TKE + \frac{\partial}{\partial x_j}(TKE \cdot \overline{U_j}) + \rho_{deff}\overline{(\mathcal{F}_{\Pi})'u_i'} + \rho_{deff}\delta_{i3}g\frac{\overline{\theta_v'u_i'}}{\theta_{v\,ref}} + \rho_{deff}f\epsilon_{ij3}\overline{u_i'u_j'} = \\ -\frac{\partial}{\partial x_j}\overline{TKE'u_j'} - (\rho_{deff}\overline{u_i'u_j'})\frac{\partial}{\partial x_j}\overline{U_i} \\ + \frac{\nu}{\rho_{deff}}\left[\frac{\partial}{\partial x_j}\rho_{deff}\left[\frac{\partial}{\partial x_j}TKE\right]\right] - \frac{\nu}{\rho_{deff}}\overline{\left[\frac{\partial}{\partial x_j}\left(\rho_{deff}u_i'\right)\right]^2} + \rho_{deff}\overline{(\mathcal{F})'u_i'},\end{aligned} \tag{2.66}$$

where the flux-like notation $\overline{TKE'u_j'}$ stands for $\rho_{deff}\overline{(u_i'u_i'/2)u_j'}$. In the rhs of equation (2.66), the TKE-diffusion term, proportional to the molecular viscosity ν, is split in two terms. The "Laplacian" term is a redistribution term which is often neglected. The second term is much larger and is always negative (minus a squared quantity). This term corresponds to the viscous dissipation rate ε

$$\varepsilon_{TKE} = \frac{\nu}{\rho_{deff}}\overline{\left[\frac{\partial}{\partial x_j}\left(\rho_{deff}u_i'\right)\right]^2}, \tag{2.67}$$

Adding equations (2.64) and (2.66) gives the evolution of the total kinetic energy equation ($K + TKE$) which explicitly contains the momentum dissipation term ε. By virtue of the total energy conservation, a counterpart dissipative energy must be added to the thermodynamic equation. This can be simply done by the introduction of a dissipative heating term of the form

$$\frac{\partial}{\partial t}(\rho_{deff}\theta) + \boldsymbol{\nabla} \cdot (\rho_{deff}\theta\,\boldsymbol{U}) = \cdots + \frac{\rho_{deff}\varepsilon_e}{\Pi_{ref}C_{ph}}. \tag{2.68}$$

The turbulence scheme in Meso-NH is based on a turbulent kinetic equation of e defined as $e = TKE/\rho_{deff}$. Most of the second order terms in equation (2.66) including $\varepsilon_{TKE} = \varepsilon_e \times \rho_{deff}$ are parameterized according to Cuxart et al. (2000).

2.7 Terrain-following coordinate system

In Meso-NH, the coordinate system is not Cartesian, in order to account for steep terrain, and the sphericity of the earth. As explained in Part I, Chapters 3 and 4 on coordinate systems and discretization, respectively, we use a $(\overline{x}, \overline{y}, \overline{z})$ coordinate system, and the contravariant components of the velocity. By inserting these various elements in the basic equations, the form of the turbulent terms is readily obtained. For instance, the turbulent terms in the equation for the mean x momentum component read

$$
\begin{aligned}
\frac{\partial \tilde{\rho}\overline{u}}{\partial t} = \cdots \quad - & \left[\frac{\partial}{\partial \overline{x}}(\tilde{\rho}\frac{\overline{u'u'}}{d_{xx}}) + \frac{\partial}{\partial \overline{y}}(\tilde{\rho}\frac{\overline{u'v'}}{d_{yy}}) + \frac{\partial}{\partial \overline{z}}(\tilde{\rho}\frac{\overline{w'u'}}{d_{zz}} - \tilde{\rho}\overline{u'u'}\frac{d_{zx}}{d_{xx}d_{zz}} - \tilde{\rho}\overline{v'u'}\frac{d_{zy}}{d_{yy}d_{zz}}) \right] \\
+ & \quad \overline{u'v'}\frac{\tilde{\rho}cos\gamma}{rcos\varphi}(sin\varphi - K) + \overline{v'v'}\frac{\tilde{\rho}sin\gamma}{rcos\varphi}(sin\varphi - K) - \tilde{\rho}\frac{\overline{u'w'}}{r}. \qquad (2.69)
\end{aligned}
$$

The last line of this expression arises from the curvature terms generated by the sphericity of the Earth. In the following, we will assume that these sphericity terms have negligible contributions on the turbulence, and therefore ignore them.

On the other hand, we should stress that the (u, v, w) used in the equations are still the Cartesian components of the velocity. So, the terms that the turbulence scheme will supply to Meso-NH are

$$
\begin{aligned}
\frac{\partial}{\partial t}(\tilde{\rho}u) &= \cdots \quad - \left[\frac{\partial}{\partial \overline{x}}(\tilde{\rho}\frac{\overline{u'u'}}{d_{xx}}) + \frac{\partial}{\partial \overline{y}}(\tilde{\rho}\frac{\overline{u'v'}}{d_{yy}}) + \frac{\partial}{\partial \overline{z}}(\tilde{\rho}\frac{\overline{w'u'}}{d_{zz}} - \tilde{\rho}\overline{u'u'}\frac{d_{zx}}{d_{xx}d_{zz}} - \tilde{\rho}\overline{v'u'}\frac{d_{zy}}{d_{yy}d_{zz}}) \right], \\
\frac{\partial}{\partial t}(\tilde{\rho}v) &= \cdots \quad - \left[\frac{\partial}{\partial \overline{x}}(\tilde{\rho}\frac{\overline{u'v'}}{d_{xx}}) + \frac{\partial}{\partial \overline{y}}(\tilde{\rho}\frac{\overline{v'v'}}{d_{yy}}) + \frac{\partial}{\partial \overline{z}}(\tilde{\rho}\frac{\overline{v'w'}}{d_{zz}} - \tilde{\rho}\overline{u'v'}\frac{d_{zx}}{d_{xx}d_{zz}} - \tilde{\rho}\overline{v'v'}\frac{d_{zy}}{d_{yy}d_{zz}}) \right], \\
\frac{\partial}{\partial t}(\tilde{\rho}w) &= \cdots \quad - \left[\frac{\partial}{\partial \overline{x}}(\tilde{\rho}\frac{\overline{w'u'}}{d_{xx}}) + \frac{\partial}{\partial \overline{y}}(\tilde{\rho}\frac{\overline{w'v'}}{d_{yy}}) + \frac{\partial}{\partial \overline{z}}(\tilde{\rho}\frac{\overline{w'w'}}{d_{zz}} - \tilde{\rho}\overline{u'w'}\frac{d_{zx}}{d_{xx}d_{zz}} - \tilde{\rho}\overline{v'w'}\frac{d_{zy}}{d_{yy}d_{zz}}) \right], \\
\frac{\partial}{\partial t}(\tilde{\rho}s) &= \cdots \quad - \left[\frac{\partial}{\partial \overline{x}}(\tilde{\rho}\frac{\overline{s'u'}}{d_{xx}}) + \frac{\partial}{\partial \overline{y}}(\tilde{\rho}\frac{\overline{s'v'}}{d_{yy}}) + \frac{\partial}{\partial \overline{z}}(\tilde{\rho}\frac{\overline{w's'}}{d_{zz}} - \tilde{\rho}\overline{u's'}\frac{d_{zx}}{d_{xx}d_{zz}} - \tilde{\rho}\overline{v's'}\frac{d_{zy}}{d_{yy}d_{zz}}) \right],
\end{aligned}
$$

where s is any scalar.

In addition, all the gradients appearing in the flux formulation and in the TKE prognostic equation must be evaluated in the model coordinate system by the chain rule (see below).

2.8 Spatial discretization

The location of the different variables on the computation grid is shown in Fig. 2.4. All the variables shown share the same index values i,j,k. In the following, we will use the Schuman discretization operators, as defined in Part I, Chapter 4 on discretization (section 4.3).

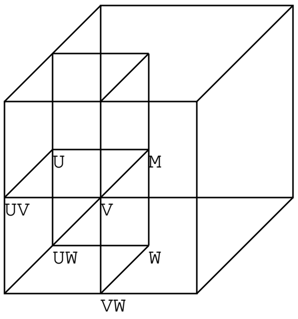

	Meso-NH	Turbulence
M	θ,ρ,λ,φ,π r,J,m,f	u'2,v'2,w'2 e,L
V	V,dyy	H2,Q2,v'S'
U	U,dxx	H1,Q1,u'S'
W	W,dzz	H3,Q3,w'S', φ3
UW	dzx	u'w'
VW	dzy	v'w'
UV	---	u'v'

Figure 2.4: Location of variables on the grid for turbulence computation.

The discretized form of the turbulence terms in the main equations reads

$$
\begin{aligned}
\delta_t\left[\overline{(\overline{\tilde\rho}^{x} u)}^{t}\right] = \cdots \quad - \quad & \delta_x(\tilde\rho\frac{\overline{u'u'}}{\overline{d_{xx}}^{x}}) - \delta_y(\overline{\tilde\rho}^{x,y}\frac{\overline{u'v'}}{\overline{d_{yy}}^{x}}) \\
- \quad & \delta_z(\overline{\tilde\rho}^{z,x}\frac{\overline{w'u'}}{\overline{d_{zz}}^{x}} - \overline{\tilde\rho}^{z,x}\overline{\overline{u'u'}}^{z,x}\frac{d_{zx}}{\overline{d_{xx}}^{z}\,\overline{d_{zz}}^{x}} - \overline{\tilde\rho}^{z,x}\overline{\overline{v'u'}}^{z,y}\frac{\overline{d_{zy}}^{x,y}}{\overline{d_{yy}}^{x,y,z}\,\overline{d_{zz}}^{x}}) \\
\delta_t\left[\overline{(\overline{\tilde\rho}^{y} v)}^{t}\right] = \cdots \quad - \quad & \delta_x(\overline{\tilde\rho}^{x,y}\frac{\overline{u'v'}}{\overline{d_{xx}}^{y}}) - \delta_y(\tilde\rho\frac{\overline{v'v'}}{\overline{d_{yy}}^{y}}) \\
- \quad & \delta_z(\overline{\tilde\rho}^{z,y}\frac{\overline{w'v'}}{\overline{d_{zz}}^{y}} - \overline{\tilde\rho}^{z,y}\overline{\overline{u'v'}}^{z,x}\frac{\overline{d_{zx}}^{y,x}}{\overline{d_{xx}}^{xyz}\,\overline{d_{zz}}^{y}} - \overline{\tilde\rho}^{z,y}\overline{\overline{v'v'}}^{z,y}\frac{d_{zy}}{\overline{d_{yy}}^{z}\,\overline{d_{zz}}^{y}}) \\
\delta_t\left[\overline{(\overline{\tilde\rho}^{z} w)}^{t}\right] = \cdots \quad - \quad & \delta_x(\overline{\tilde\rho}^{z,x}\frac{\overline{u'w'}}{\overline{d_{xx}}^{z}}) - \delta_y(\overline{\tilde\rho}^{z,y}\frac{\overline{v'w'}}{\overline{d_{yy}}^{z}}) \\
- \quad & \delta_z(\tilde\rho\frac{\overline{w'w'}}{\overline{d_{zz}}^{z}} - \tilde\rho\overline{\overline{u'w'}}^{z,x}\frac{\overline{d_{zx}}^{x,z}}{\overline{d_{xx}}^{x}\,\overline{d_{zz}}^{z}} - \tilde\rho\overline{\overline{v'w'}}^{y,z}\frac{\overline{d_{zy}}^{y,z}}{\overline{d_{yy}}^{x}\,\overline{d_{zz}}^{z}}) \\
\delta_t\left[\overline{(\tilde\rho s)}^{t}\right] = \cdots \quad - \quad & \delta_x(\overline{\tilde\rho}^{x}\frac{\overline{u's'}}{d_{xx}}) - \delta_y(\overline{\tilde\rho}^{y}\frac{\overline{v's'}}{d_{yy}}) \\
- \quad & \delta_z(\overline{\tilde\rho}^{z}\frac{\overline{w's'}}{d_{zz}} - \overline{\tilde\rho}^{z}\overline{\overline{u's'}}^{z,x}\frac{\overline{d^{x}_{zx}}}{\overline{d_{xx}}^{z,x}d_{zz}} - \overline{\tilde\rho}^{z}\overline{\overline{v's'}}^{z,y}\frac{\overline{d_{zy}}^{y}}{\overline{d_{yy}}^{z,y}d_{zz}})
\end{aligned}
\tag{2.70}
$$

Here, we have assumed that the time discretization is fully explicit, and all the terms on the right hand side are taken at time $t - \Delta t$. As explained in the final section however, we allow for some degree of implicitness in the time discretization of the purely vertical diffusion terms, in order to allow for longer time steps when the model is used in meso-scale mode.

In (2.70), we still use the expression of the turbulent fluxes in the Cartesian frame. Those must be expressed as a function of the gradients of the mean variables in the Cartesian frame. To ease this formulation, we have developed 15 different "Cartesian gradient operators", depending of the direction in which the gradient is taken, and the precise locations on the grid where the information is available. The generic notation for these operators is $GX_i\_A\_B$: X_i refers to the

(Cartesian) direction where the gradient is taken, A to the variable location, and B to the location where the gradients must be known. The detailed expression of these operators is the following.

1) Gradients at mass points for variables located at mass points:

$$
\begin{aligned}
\frac{\partial\bullet}{\partial x} &= \frac{1}{\overline{d_{xx}}^{x}}\left[\delta_x\overline{\bullet}^{x} - \overline{\left(\frac{\overline{d_{zx}}^{x}\delta_z\bullet}{d_{zz}}\right)}^{z}\right] && \equiv GX\_M\_M \\
\frac{\partial\bullet}{\partial y} &= \frac{1}{\overline{d_{yy}}^{y}}\left[\delta_y\overline{\bullet}^{y} - \overline{\left(\frac{\overline{d_{zy}}^{y}\delta_z\bullet}{d_{zz}}\right)}^{z}\right] && \equiv GY\_M\_M \\
\frac{\partial\bullet}{\partial z} &= \overline{\left(\frac{\delta_z\bullet}{d_{zz}}\right)}^{z} && \equiv GZ\_M\_M
\end{aligned}
\tag{2.71}
$$

2) Gradients at wind points for variables located at mass points: $(\overline{u_i'\theta'} \Longleftrightarrow \frac{\partial\theta}{\partial x_i})$

$$
\begin{aligned}
\frac{\partial\bullet}{\partial x} &= \frac{1}{d_{xx}}\left[\delta_x\bullet - \overline{\left(\frac{d_{zx}\overline{\delta_z\bullet}^{x}}{d_{zz}}\right)}^{z}\right] && \equiv GX\_M\_U \\
\frac{\partial\bullet}{\partial y} &= \frac{1}{d_{yy}}\left[\delta_y\bullet - \overline{\left(\frac{d_{zy}\overline{\delta_z\bullet}^{y}}{d_{zz}}\right)}^{z}\right] && \equiv GY\_M\_V \\
\frac{\partial\bullet}{\partial z} &= \frac{1}{d_{zz}}\delta_z\bullet && \equiv GZ\_M\_W
\end{aligned}
\tag{2.72}
$$

3) Gradients at mass points of variables located at wind points: $(\overline{u_i'^2} \Longleftrightarrow \frac{\partial u_i}{\partial x_i}$ unsummed)

$$
\begin{aligned}
\frac{\partial\bullet}{\partial x} &= \frac{1}{\overline{d_{xx}}^{x}}\left[\delta_x\bullet - \overline{\left(\frac{\overline{d_{zx}\delta_z\bullet}^{x}}{d_{zz}}\right)}^{z}\right] && \equiv GX\_U\_M \\
\frac{\partial\bullet}{\partial y} &= \frac{1}{\overline{d_{yy}}^{y}}\left[\delta_y\bullet - \overline{\left(\frac{\overline{d_{zy}\delta_z\bullet}^{y}}{d_{zz}}\right)}^{z}\right] && \equiv GY\_V\_M \\
\frac{\partial\bullet}{\partial z} &= \frac{1}{\overline{d_{zz}}^{z}}\delta_z\bullet && \equiv GZ\_W\_M
\end{aligned}
\tag{2.73}
$$

4) Gradients at vorticity points for variables located at wind points: $(\overline{u_i'u_j'} \Longleftrightarrow \frac{\partial u_i}{\partial x_j}, \frac{\partial u_j}{\partial x_i})$
For gradients localized at point UV:

$$
\begin{aligned}
\frac{\partial\bullet}{\partial x} &= \frac{1}{\overline{d_{xx}}^{y}}\left[\delta_x\bullet - \overline{\overline{\left(\frac{\delta_z\bullet}{\overline{d_{zz}}^{y}}\right)}^{x}\overline{d_{zx}}^{y}}^{z}\right] && \equiv GX\_V\_UV \\
\frac{\partial\bullet}{\partial y} &= \frac{1}{\overline{d_{yy}}^{x}}\left[\delta_y\bullet - \overline{\overline{\left(\frac{\delta_z\bullet}{\overline{d_{zz}}^{x}}\right)}^{y}\overline{d_{zy}}^{x}}^{z}\right] && \equiv GY\_U\_UV
\end{aligned}
\tag{2.74}
$$

For gradients localized at point UW:

$$
\begin{aligned}
\frac{\partial\bullet}{\partial x} &= \frac{1}{\overline{d_{xx}}^{z}}\left[\delta_x\bullet - \overline{\left(\frac{\overline{\delta_z\bullet}^{z}}{d_{zz}}\right)}^{x}d_{zx}\right] && \equiv GX\_W\_UW \\
\frac{\partial\bullet}{\partial z} &= \frac{\delta_z\bullet}{\overline{d_{zz}}^{x}} && \equiv GZ\_U\_UW
\end{aligned}
\tag{2.75}
$$

For gradients localized at point VW:

$$
\begin{aligned}
\frac{\partial\bullet}{\partial y} &= \frac{1}{\overline{d_{yy}}^{z}}\left[\delta_y\bullet - \overline{\left(\frac{\overline{\delta_z\bullet}^{z}}{d_{zz}}\right)}^{y}d_{zy}\right] && \equiv GY\_W\_VW \\
\frac{\partial\bullet}{\partial z} &= \frac{\delta_z\bullet}{\overline{d_{zz}}^{y}} && \equiv GZ\_V\_VW
\end{aligned}
\tag{2.76}
$$

Making use of these operators, the discretized form of the turbulent fluxes in the Cartesian frame reads as follows:

$$
\begin{aligned}
\overline{u'_i\,u'_j} &= \frac{2}{3}\delta_{ij}\,\overline{e}^{x_i,x_j} - \frac{4}{15}\frac{\overline{L}^{x_i,x_j}}{C_m}\overline{e^{\frac{1}{2}}}^{x_i,x_j}[GX_j\_U_i\_U_iU_j(u_i) + GX_i\_U_j\_U_iU_j(u_j) \\
&- \frac{2}{3}\delta_{ij}\sum_{m=1}^{3} GX_m\_U_m\_U_iU_j(u_m)] && (2.77) \\
\overline{u'_i\theta'} &= -\frac{2}{3}\frac{\overline{L}^{x_i}}{C_s}\overline{e^{\frac{1}{2}}}^{x_i}GX_i\_M\_U\_i(\theta)\phi_i && (2.78) \\
\overline{u'_i r'_v} &= -\frac{2}{3}\frac{\overline{L}^{x_i}}{C_s}\overline{e^{\frac{1}{2}}}^{x_i}GX_i\_M\_U\_i(r_v)\psi_i && (2.79) \\
\overline{\theta' r'_v} &= C_2L^2\sum_{m=1}^{3} GX_m\_M\_M(\theta)GX_m\_M\_M(r_v)(\overline{\phi_m}^{z} + \overline{\psi_m}^{z}) && (2.80) \\
\overline{\theta'^2} &= C_1L^2\sum_{m=1}^{3}(GX_m\_M\_M(\theta))^2)\overline{\phi_m}^{z} && (2.81) \\
\overline{r'^2_v} &= C_1L^2\sum_{m=1}^{3}(GX_m\_M\_M(r_v))^2)\overline{\psi_m}^{z} && (2.82) \\
\overline{u'_i\theta'_v} &= E_\theta\,\overline{u'_i\theta'}^{x_i} + E_{moist}\,\overline{u'_i r'_v}^{x_i} && (2.83)
\end{aligned}
$$

The ϕ_i and ψ_i stability functions are computed at W points. Their expression follows readily from (2.15, 2.16), using the discretized formulation of the Redelsperger numbers at W points:

$$
\begin{aligned}
R_{\theta 1} &= \overline{\frac{g}{\theta_{v\,ref}}\frac{L^2}{e}}^{z}\,\overline{E_\theta}^{z}\cdot GZ\_M\_W(\theta) && (2.84) \\
R^2_{\theta 3} &= R^2_{\theta 1} + (\overline{\frac{g}{\theta_{v\,ref}}\frac{L^2}{e}}^{z}\,\overline{E_\theta}^{z})^2\overline{[\sum_{m=2}^{3} GX_m\_M\_M(\theta)\cdot GX_m\_M\_M(\theta)]}^{z} && (2.85) \\
R_{r1} &= \overline{\frac{g}{\theta_{v\,ref}}\frac{L^2}{e}}^{z}\,\overline{E_{moist}}^{z}\cdot GZ\_M\_W(r_v) && (2.86) \\
R^2_{r3} &= R^2_{r1} + (\overline{\frac{g}{\theta_{v\,ref}}\frac{L^2}{e}}^{2}\,\overline{E_{moist}}^{z})^2\overline{[\sum_{m=2}^{3} GX_m\_M\_M(r_v)\cdot GX_m\_M\_M(r_v)]}^{z} && (2.87) \\
R^2_{\theta r3} &= R_{\theta 1}R_{r1} + (\overline{\frac{g}{\theta_{v\,ref}}\frac{L^2}{e}}^{z})^2\overline{E_\theta}^{z}\overline{E_{moist}}^{z}\overline{[\sum_{m=2}^{3} GX_m\_M\_M(\theta)\cdot GX_m\_M\_M(r_v)]}^{z} && (2.88)
\end{aligned}
$$

Let us now describe the TKE equation discretization. The generic form of this equation is

$$
\frac{\partial}{\partial t}(\tilde{\rho}e) = ADV(e) + \tilde{\rho}P^t - \frac{\partial}{\partial x}(\overline{\tilde{\rho}}^{x}\,\overline{u'e'}) - \frac{\partial}{\partial y}(\overline{\tilde{\rho}}^{y}\,\overline{v'e'}) - \frac{\partial}{\partial z}(\overline{\tilde{\rho}}^{z}\,\overline{w'e'}). \qquad (2.89)
$$

The advections term $ADV(e)$ is not treated in the turbulence scheme, but in the routine taking care of the general advection of scalar quantities (see Part I, Chapter 4 on discretization). P^t contains all the source terms, some of which are expressed at $t-1$, and others at t. This reads

$$\begin{aligned}
P^t &= -\overline{u'^2}\frac{\partial u}{\partial x} - \overline{\overline{u'v'}}^{x,y}\frac{\partial}{\partial y}(\overline{u}^{y,x}) - \overline{\overline{u'w'}}^{x,z}\frac{\partial}{\partial z}(\overline{u}^{z,x}) - \overline{\overline{v'u'}}^{x,y}\frac{\partial}{\partial x}(\overline{v}^{x,y}) \\
&- \overline{v'^2}\frac{\partial v}{\partial y} - \overline{\overline{v'w'}}^{y,z}\frac{\partial}{\partial z}(\overline{v}^{z,y}) - \overline{\overline{w'u'}}^{x,z}\frac{\partial}{\partial x}(\overline{w}^{x,z}) - \overline{\overline{w'v'}}^{y,z}\frac{\partial}{\partial y}(\overline{w}^{y,z}) - \overline{w'^2}\frac{\partial w}{\partial z} \\
&+ \frac{g}{\theta_{v\,ref}}\overline{\overline{w'\theta_v'}}^{z} - C_\epsilon\frac{e^{3/2}}{L}. \qquad (2.90)
\end{aligned}$$

Using the Cartesian gradient operators and leaving the advection term aside, this become therefore

$$\begin{aligned}
\delta_t\left[\overline{(\tilde{\rho}e)}^t\right] &= \tilde{\rho}[-\overline{u'^2}(GX\_U\_M(u)) - \overline{\overline{u'v'}}^{x,y}(GY\_V\_M(\overline{u}^{y,x})) - \overline{\overline{u'w'}}^{x,z}(GZ\_W\_M(\overline{u}^{z,x})) \\
&- \overline{\overline{v'u'}}^{x,y}(GX\_U\_M(\overline{v}^{x,y})) - \overline{v'^2}(GY\_V\_M(v)) - \overline{\overline{v'w'}}^{y,z}(GZ\_W\_M(\overline{v}^{z,y})) \\
&- \overline{\overline{w'u'}}^{x,z}(GX\_U\_M(\overline{w}^{x,z})) - \overline{\overline{w'v'}}^{y,z}(GY\_V\_M(\overline{w}^{y,z})) - \overline{w'^2}(GZ\_W\_M(w)) \\
&+ \frac{g}{\theta_{v\,ref}}\overline{\overline{w'\theta_v'}}^{z} - C_\epsilon\frac{e^{3/2}}{L}] \\
&- (GX\_U\_M(\overline{\tilde{\rho}}^x\overline{u'e'})) - (GY\_V\_M(\overline{\tilde{\rho}}^y\overline{v'e'})) - (GZ\_W\_M(\overline{\tilde{\rho}}^z\overline{w'e'})). \qquad (2.91)
\end{aligned}$$

This uses the turbulent fluxes of TKE, expressed at u_i points as

$$\overline{u_i'e'} = -C_{2m}\overline{Le^{\frac{1}{2}}}^{x_i}GX_i\_M\_U_i(e). \qquad (2.92)$$

2.9 Boundary conditions

2.9.1 Lateral boundary conditions

An important point for lateral boundary conditions is to realize that the computation of the source term for any prognostic variable at (i, j) will involve only quantities of the same nature at (i-1, i+1, j-1, j+1), as shown in Fig. 2.5. As a consequence, a clean treatment of lateral boundary conditions is obtained with only one extra grid point on each side. Referring to the terminology of Chapter 5 (in Part I), HEXT=1 is sufficient for the turbulence scheme. The two basic options for lateral boundary conditions are therefore supported.

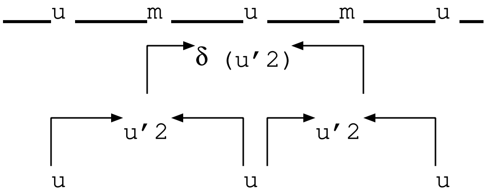

Figure 2.5: Discretization of second order terms.

Periodic LBC

In this case, the computation of all source terms in the turbulence routines is performed from I=1 to IMAX, and from J=1 to JMAX. It uses values of the mean variables at I=0 and IMAX+1, J=0 and

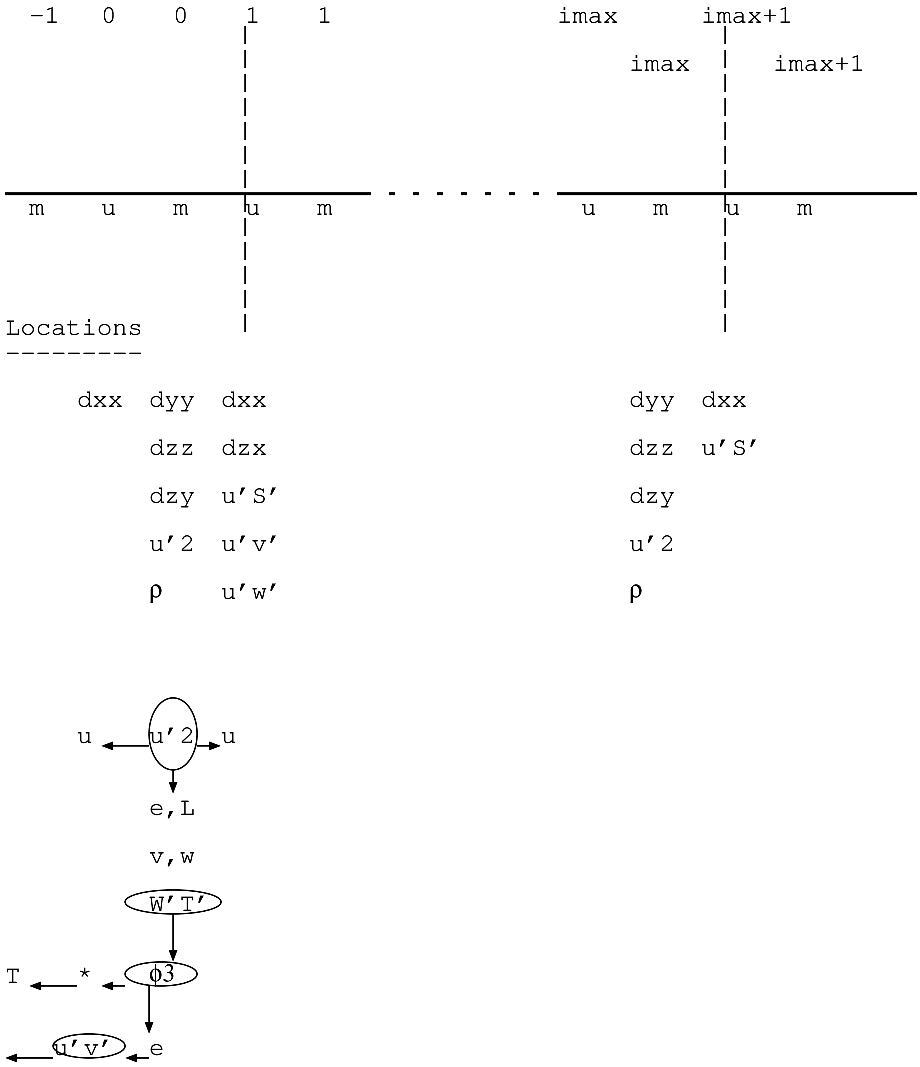

Figure 2.6: Cyclic lateral boundary conditions.

JMAX+1 (Fig. 2.6). These values are supplied by the routine BOUNDARY, as part of the general treatment of lateral boundaries. Note that the additional prognostic variables (the turbulence kinetic energy e and eventually the dissipation rate ϵ) are also made periodic by BOUNDARY.

Open LBC

In this case, the computation of the turbulent source terms is performed from I=1 to IMAX for scalars and non-normal velocity components, and from I=2 to IMAX for the normal velocity component. This is illustrated in Fig. 2.7. Indeed, there is no need to write an equation for the quantity u at I=1, since this value is to be prescribed by the open LBC scheme.

2.9.2 Upper boundary condition

In the Gal-Chen Sommerville coordinate system, the domain is terminated by a horizontal plane at $z = H$. This coincides with a plan of W points. The physical condition imposed at this level is that all turbulent vertical fluxes are zero.

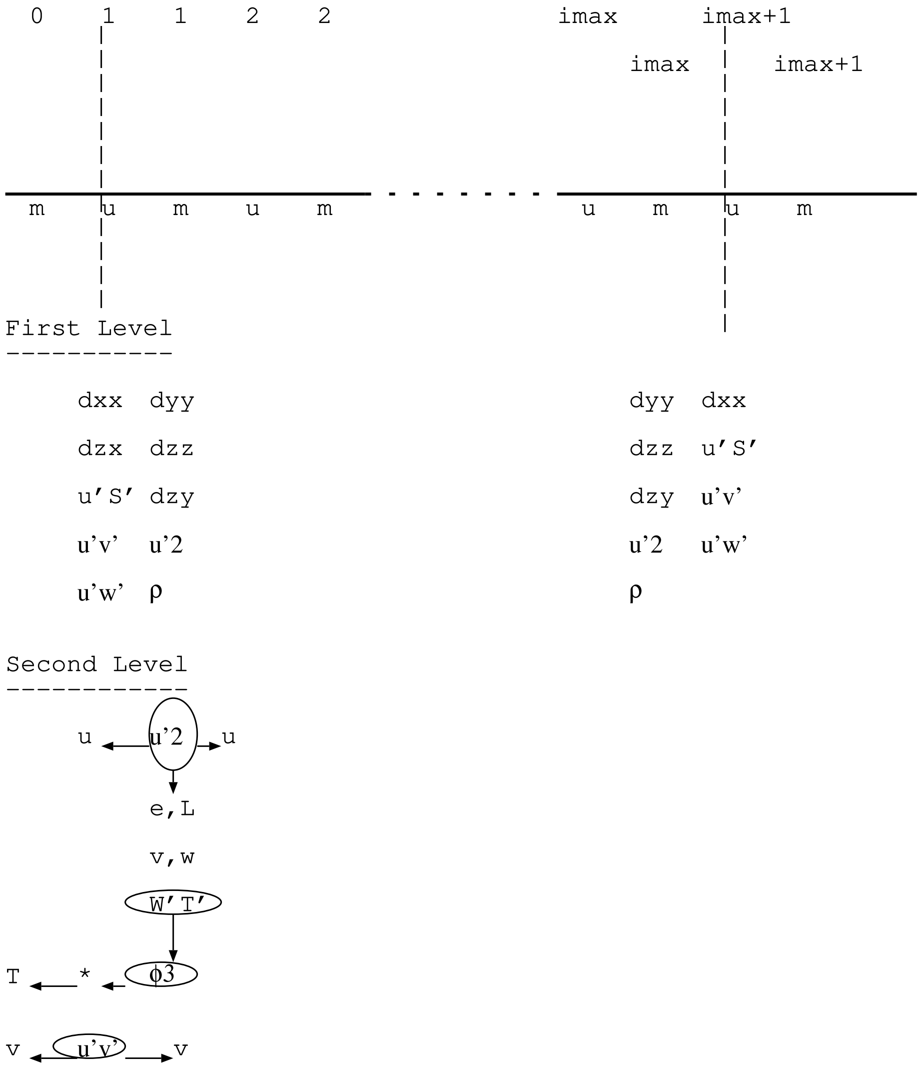

Figure 2.7: Open lateral boundary conditions.

Whenever vertical gradients of mean variables are needed at this height, they are computed by extrapolation of gradients immediately below. This procedure is assumed to have a negligible impact on the overall model results.

2.9.3 Surface boundary conditions

The physical forcing of turbulence at the surface is a major concern. We assume that the main information is contained in the value of the turbulent fluxes of heat, moisture and momentum, supplied by the soil-vegetation atmosphere transfer scheme (see Part II, Chapter 6). Depending on various options, these fluxes may be specified, or computed by bulk formulae.

One difficulty is to deal correctly with the terrain slope effect, in presence of steep orography. We assume that the soil vegetation atmosphere transfer scheme returns fluxes normal to the terrain. We then have to project these fluxes on to the Cartesian coordinates (Fig. 2.8).

If the flux ($\mathbf{\Phi}$) is normal to the surface, we can write it as $\mathbf{\Phi} = \Phi_n \boldsymbol{n}$. The projections over the

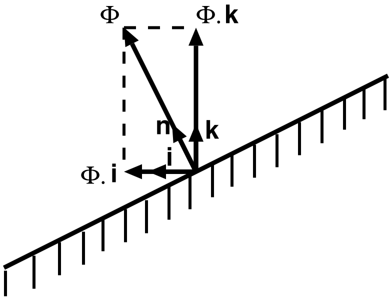

Figure 2.8: The Cartesian decomposition of the surface flux.

Cartesian coordinates are

$$\begin{aligned}\boldsymbol{\Phi i} &= \Phi_n \boldsymbol{n}\cdot\boldsymbol{i},\\ \boldsymbol{\Phi j} &= \Phi_n \boldsymbol{n}\cdot\boldsymbol{j},\\ \boldsymbol{\Phi k} &= \Phi_n \boldsymbol{n}\cdot\boldsymbol{k}.\end{aligned}\tag{2.93}$$

Referring to notations of Part I, Chapter 3, the contravariant vector basis normal to the surface is $\boldsymbol{e^3} = \|e^3\|\boldsymbol{n}$ (contravariant). Then,

$$e^3 = -\frac{d_{zx}}{d_{xx}d_{zz}}\boldsymbol{i} - \frac{d_{zy}}{d_{yy}d_{zz}}\boldsymbol{j} + \frac{1}{d_{zz}}\boldsymbol{k},\tag{2.94}$$

and

$$\|e^3\| = \frac{1}{d_{zz}}(1 + (\frac{d_{zx}}{d_{xx}})^2 + (\frac{d_{zy}}{d_{yy}})^2)^{1/2}.\tag{2.95}$$

To get the Cartesian components, we just compute the scalar products

$$\boldsymbol{n}\cdot\boldsymbol{i} = \frac{\boldsymbol{e^3}}{\|e^3\|}\cdot\boldsymbol{i} = \frac{1}{\|e^3\|}(-\frac{d_{zx}}{d_{xx}d_{zz}}),\tag{2.96}$$

$$\boldsymbol{\Phi}\cdot\boldsymbol{i} = \Phi_n\boldsymbol{n}\cdot\boldsymbol{i} = \Phi_n\,(-\frac{d_{zx}}{d_{xx}(1 + (\frac{d_{zx}}{d_{xx}})^2 + (\frac{d_{zy}}{d_{yy}})^2)^{1/2}}),\tag{2.97}$$

and for the other components

$$\begin{aligned}\boldsymbol{\Phi}\cdot\boldsymbol{j} &= \Phi_n\,(-\frac{d_{zy}}{d_{yy}(1 + (\frac{d_{zx}}{d_{xx}})^2 + (\frac{d_{zy}}{d_{yy}})^2)^{1/2}}),\\ \boldsymbol{\Phi}\cdot\boldsymbol{k} &= \Phi_n\,(-\frac{1}{(1 + (\frac{d_{zx}}{d_{xx}})^2 + (\frac{d_{zy}}{d_{yy}})^2)^{1/2}}).\end{aligned}\tag{2.98, 2.99}$$

The projection $\boldsymbol{\Phi}\cdot\boldsymbol{k}$ is then used as the vertical surface flux .

2.9.4 Extrapolation of gradients

Another point to stress is that many flux computations at the boundaries require the use of points outside the domain. This is for instance the case at the ground for sloping terrain. The expression of the flux , $\overline{u'\theta'}$ by the GX_M_U operator involves a vertical differencing of θ, with information below the ground. Whenever this problem arises, the approach taken has been to extrapolate the gradients in the adjacent points.

2.10 Semi-implicit time discretization

For high resolution, full 3D experiments (LES or CRM type), the explicit time stepping is not expected to place major restrictions on the time step compared to the advection scheme. This is no longer true when the model is run in "meso-scale" mode, with highly anisotropic grids. In this case the vertical diffusion terms severely restrict the time step.

We have therefore implemented a Crank-Nicholson time implicit scheme for the vertical diffusion terms. The degree of implicitness may be varied at will by the user, adjusting the parameter XIMPL. XIMPL=1 will result in the fully implicit scheme, XIMPL=0.5 is the semi-implicit scheme, and XIMPL=0. reverts to the fully explicit scheme.

We will now formulate the matrix inversion problem associated with this Crank-Nicholson scheme. s stands for any prognostic variable, and we use the notations $\alpha=$XIMPL and $\beta=$1-XIMPL. For short, we use the notation K for the vertical exchange coefficient (for instance, $K=\frac{2}{3}\frac{L}{C_s}e^{\frac{1}{2}}\phi_3$) for $s=\theta$). The evolution equation for s reads

$$\frac{\partial\tilde{\rho}s}{\partial t}=S^t+\alpha\frac{\partial}{\partial\tilde{z}}(\frac{\overline{\tilde{\rho}K^t}^z}{d_{zz}^2}\frac{\partial s}{\partial\tilde{z}}^{t+1})+\beta\frac{\partial}{\partial\tilde{z}}(\frac{\overline{\tilde{\rho}K^t}^z}{d_{zz}^2}\frac{\partial s}{\partial\tilde{z}}^{t-1}), \tag{2.100}$$

where S^t represents the other source terms.

This expression, discretised for a given level k (with i,j omitted for comfort) becomes

$$\begin{gathered}\frac{\tilde{\rho}s^{t+1}(k)-\tilde{\rho}s^{t-1}(k)}{2\Delta t}=S^t(k)+\\ \frac{\alpha}{\tilde{\rho}(k)}(\frac{\overline{\tilde{\rho}K^t(k+1)}^z}{d_{zz}^2(k+1)}(s^{t+1}(k+1)-s^{t+1}(k))-\frac{\overline{\tilde{\rho}K^t(k)}^z}{d_{zz}^2(k)}(s^{t+1}(k)-s^{t+1}(k-1)))\\ +\frac{\beta}{\tilde{\rho}(k)}(\frac{\overline{\tilde{\rho}K^t(k+1)}^z}{d_{zz}^2(k+1)}(s^{t-1}(k+1)-s^{t-1}(k))-\frac{\overline{\tilde{\rho}K^t(k)}^z}{d_{zz}^2(k)}(s^{t-1}(k)-s^{t-1}(k-1)))\end{gathered} \tag{2.101}$$

This gives the well known tri-diagonal matrix equation

$$s^{t+1}(k-1)(\alpha\frac{A(k)}{\tilde{\rho}(k)})+s^{t+1}(k)(1-\alpha\frac{A(k)}{\tilde{\rho}(k)}-\alpha\frac{C(k)}{\tilde{\rho}(k)})+s^{t+1}(k+1)(\alpha\frac{C(k)}{\tilde{\rho}(k)})=Y(k), \tag{2.102}$$

where

$$\begin{aligned}A(k)&=-2\Delta t\frac{\overline{\tilde{\rho}(k)K^t(k)}^z}{d_{zz}^2(k)}, &(2.103)\\ C(k)&=-2\Delta t\frac{\overline{\tilde{\rho}(k+1)K^t(k+1)}^z}{d_{zz}^2(k+1)}, &(2.104)\\ Y(k)&=2\Delta tS^t(k)+s^{t-1}(k-1)(-\beta\frac{A(k)}{\tilde{\rho}(k)})\\ &\quad+s^{t-1}(k)(1+\beta\frac{A(k)}{\tilde{\rho}(k)}+\beta\frac{C(k)}{\tilde{\rho}(k)})+s^{t-1}(k+1)(-\beta\frac{C(k)}{\tilde{\rho}(k)}). &(2.105)\end{aligned}$$

This matrix problem is solved by a specialized routine called TRIDIAG.

In practice, the source term S^t contains only the surface fluxes. It is therefore a "split" treatment. After solving for s^{t+1}, the equivalent tendency $\frac{\partial s}{\partial t}$ is recomputed, and added to the other sources of the variable s.

2.11 Turbulence Recycling Method

One of the main bottlenecks encountered when performing multiscale LES simulations on nested grids is to generate proper turbulence in the Atmospheric Boundary Layer (ABL). Indeed, a development fetch is needed within each domain to allow for the cascade of eddies of different scales in the inertial subrange to adapt to the new resolution (Munoz-Esparza et al (2014)). Realistic turbulent inflow conditions must be generated to reduce this fetch.

In Meso-NH, a recycling method adapted from the original proposition of Lund et al. (1998) is introduced: the prognostic variable fluctuations from a vertical plane parallel to the inflow boundary are calculated with respect to a moving temporal average and these fluctuations are added to the prognostic variable field at the inlet. First, it must be ensured that the turbulence is resolved down to MΔ in the father model, Δ being the horizontal grid size and M being ideally equal to 4 or 6, depending on the effective resolution of the father model (Skamarock (2004)). The effective resolution of a model is the minimum wavelength correctly seen by the model. In the son domain, the time window for the calculation of the moving temporal average (T_{recycl}) has to be selected sufficiently large for the fluid to be advected over a distance corresponding to about MΔ in the father model. Furthermore, to save computational time and memory, the variable average is calculated with a limited number of son domain timesteps (N) over T_{recycl}. N should be sufficiently high to reduce the statistical uncertainty of the calculated moving average and sufficiently low in terms of memory requirements, since the N values for each grid point in the recycling plane need to be kept in memory.

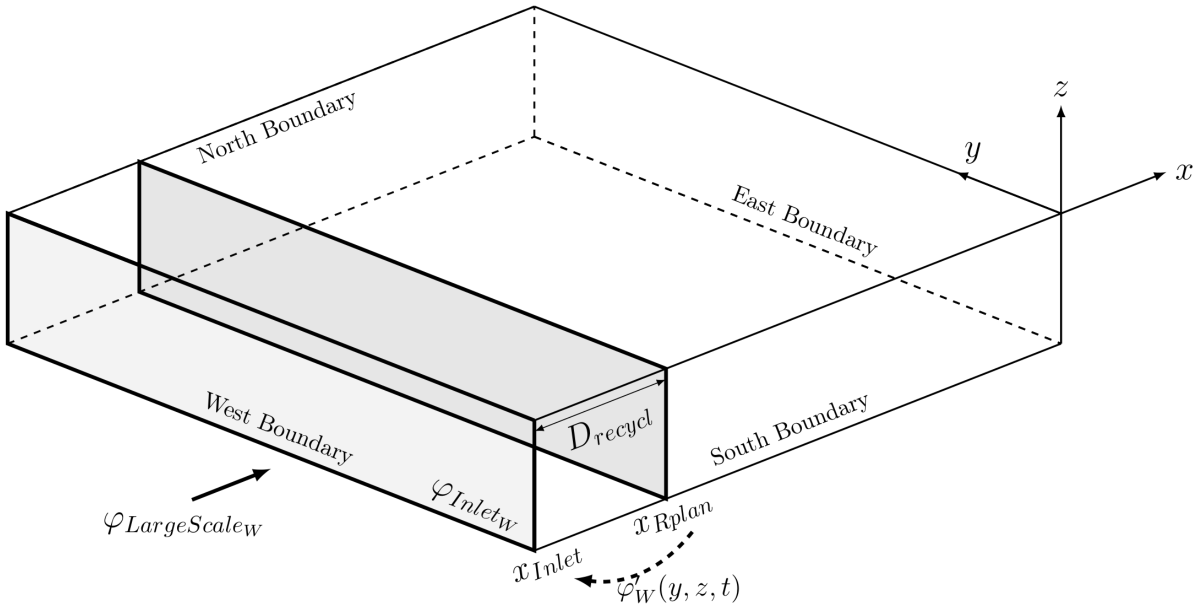

Figure 2.9: *Sketch of the turbulence recycling method used to generate turbulent inflow. For clarity, only the recycling of fluctuations at the West boundary is shown, but the same method applies on the four lateral sides.*

Figure 2.9 shows a domain where inflow boundary conditions may be imposed at each lateral side (North, East, South, West). For the sake of clarity, the recycling method is only shown for the West boundary but the same method applies on the four lateral sides, a wind vector that is not aligned with the grid axis will thus be recycled on two sides. Considering the prognostic variable at the West boundary (W) φ_W ($\varphi \in [u, v, w]$), the fluctuations φ'_W are calculated in the recycling plane being located at a distance $D_{recycle}$ from the inlet. The fluctuations calculation reads:

$$\varphi'_W(y,z,t) = \varphi_W(x_{Rplan}, y, z, t) - \overline{\varphi_W(x_{Rplan}, y, z)}, \tag{2.106}$$

where $\varphi_W(x_{Rplan}, y, z, t)$ is the instantaneous prognostic variable and $\overline{\varphi_W(x_{Rplan}, y, z)}$ the time average of the prognostic variable in one point of the recycling plane.
The value of $\varphi'_W(y,z,t)$ is added to the corresponding inflow prognostic variable, φ_{Inlet_W} :

$$\varphi_{Inlet_W}(y,z,t) = \varphi_{LargeScale_W}(y,z,t) + \varphi'_W(y,z,t)\beta\psi_W(y,z,t), \tag{2.107}$$

where $\varphi_{LargeScale_W}$ is the variable field imposed at the boundary, $\beta \in$ [0.1-0.3] a weighting coefficient preventing calculation divergence and $\psi_W(y,z,t)$ an inflow damping function calculated based on T_{recycl} and the Brunt-Väisälä period (T_{BV}):

$$\psi_w \rightarrow \begin{cases} 1 & ;\text{ if } T_{recycl} > 4T_{BV} \\ \dfrac{(T_{recycl} - 2T_{BV})}{(4T_{BV} - 2T_{BV})} & ;\text{ if } 2T_{BV} \leq T_{recycl} \leq 4T_{BV} \\ 0 & ;\text{ if } T_{recycl} < 2T_{BV} \end{cases} \tag{2.108}$$

ψ_W is calculated at the inlet, it is equal to 1 in neutral or near-neutral layers (e.g. in the boundary layer) and is linearly damped to 0 in stable layers. Its purpose is twofold: filtering the fluctuations due to gravity waves and preventing the imposed fluctuations to be affected by a potential increase in boundary-layer height between the recycling plane and the inlet.
Please note that even if the method has been built for grid-nested domains, it may also be applied to single domain configurations. Indeed, the variable field imposed at the boundary, $\varphi_{LargeScale_W}$, can result from any boundary condition type (father domain output or constant profile). However, in a single domain configuration, the efficiency of the method can not be assured. If the user is interested in using the recycling method for a single domain configuration only, she or he should adapt the recycling method. Some of the following ideas could be undertaken:

- Introduce a strong initial perturbation in NAM_PERT_PRE (more likely a temperature perturbation)
- Recycle the fluctuations on a very short period, at least in a first run.

If none of the previous tips are working, it is suggested to perform a two-domain simulation. Having a coarse-resolution father domain almost not increases the computational cost and ensures the efficiency of the recycling method.

Finally, please note that the turbulence recycling method has only been validated on idealized, cartesian, one-way nested and near-neutral cases.

2.12 References

Bister, M., and K. A. Emanuel, 1998: Dissipative heating and hurricane intensity. *Meteor. Atmos. Phys.*, **65**, 233-240.

Bougeault, P., and P. Lacarrère, 1989: Parameterization of orography-induced turbulence in a meso-beta scale model. *Mon. Wea. Rev.*, **117**, 1872-1890.

Cuxart, J., 1997: Planetary Boundary Layer Simulation: From LES to General Circulation Models, Ph.D. thesis, European thesis - Barcelone.

Cuxart, J., P. Bougeault, and J.-L. Redelsperger, 2000: A turbulence scheme allowing for mesoscale and large-eddy simulations. *Quart. J. Roy. Meteor. Soc.*, **126**, 1-30.

Duynkerke, P.G., 1988: Application of the E-ϵ turbulence closure model to the neutral and stable atmospheric boundary layer. *J. Atmos. Sci.*, **45**, 865-880.

Emanuel K. A. 1994, Atmospheric convection, Chp8: Theory of mixing in cumulus cloud, p215

Hanjalic, K., and B. E. Launder, 1972: A Reynolds stress model of turbulence and its application to thin shear flows. *J. Fluid Mech.*, **52**, 609-638.

Honnert, R., Masson, V., Lac, C., and Nagel, T. 2021: A Theoretical Analysis of Mixing Length for Atmospheric Models From Micro to Large Scales. *Front. Earth Sci*, **8**.

Klaassen, G. P., and T. L. Clark, 1985: Dynamics of the cloud environment interface and entrainment in small cumuli: Two-dimensional simulations in the absence of ambient shear. *J. Atmos. Sci.*, **42**, 2621-2642.

Lemarié, F., Samson, G., Redelsperger, J. L., Giordani, H., Brivoal, T., and G. Madec, 2021: A simplified atmospheric boundary layer model for an improved representation of air–sea interactions in eddying oceanic models: implementation and first evaluation in NEMO (4.0). *Geoscientific Model Development*, **14(1)**, 543-572.

Lund, Thomas S and Wu Xiohua and Squires, Kyle D, 1998: Generation of turbulent inflow data for spatially developing boundary layer simulations. *Journal of Computational Physics*, **140**, 233-258.

Muñoz-Esparza, D. and Kosović, B. and Mirocha, J. and van Beeck, J., Bridging the Transition from Mesoscale to Microscale Turbulence in Numerical Weather Prediction Models. *Boundary-Layer Meteorology*, **153**, 409-440.

Redelsperger, J.-L, and G. Sommeria, 1981: Méthode de représentation de la turbulence d'échelle inférieure à la maille pour un modèle tri-dimensionnel de convection nuageuse. *Boundary-Layer Meteor.*, **21(4)**, 509-530.

Rodier, Q., V. Masson, F. Couvreux and A. Paci, 2017: Evaluation of a Buoyancy and Shear Based Mixing Length for a Turbulence Scheme. *Frontiers in Earth Science*, **5**, 65.

Rodier Q, 2017. Paramétrisation de la turbulence atmosphérique dans la couche limite stable. PhD manuscrit. Université Toulouse 3 Paul Sabatier (UT3 Paul Sabatier).

Skamarock, William C, 2004: Evaluating mesoscale NWP models using kinetic energy spectra. *Monthly weather review*, **132**, 3019-3032.

Squire, P., 1958: The spatial variation of liquid water and droplet concentration in cumuli. *Tellus*, **10**, 372-380

Squire, P., 1958: Penetrative downdraughts in cumuli. *Tellus*, **10**, 381-389

Tomas, S., and V. Masson, 2006: A parameterization of third-order moments for the dry convective boundary layer. *Bound.-Layer. Meteor.*, **120**, 437-454.

Chapter 3

EDKF Shallow Convection Scheme

Contents

3.1 Introduction

In a dry or cloudy convective boundary layer (CBL), the evolution of a variable ϕ is strongly influenced by vertical turbulent transport. Therefore, a good estimation of the second-order moment $\overline{w'\phi'}$ is needed to determine the tendency of $\overline{\phi}$ (the mean value of ϕ) in the CBL.
Siebesma and Teixeira (2000) and Hourdin et al. (2002) developed a new parameterization that combines eddy diffusivity and mass flux approaches in a consistent way. Organized strong updrafts are parameterized by the mass flux part while the remaining turbulence is parameterized using K-theory. This parameterization, named EDMF (Eddy-Diffusivity / Mass Flux), has been developed to model cloudy shallow convection and dry convection in a unified way. In the EDMF framework, the turbulent flux of a conservative variable ϕ is defined as:

$$\overline{w'\phi'} = -K\frac{\partial\overline{\phi}}{\partial z} + \frac{M_u}{\rho}(\phi_u - \overline{\phi}), \tag{3.1}$$

where ρ is the density, K is the turbulent diffusivity, M_u is the convective mass flux $M_u = \rho a_u w_u$ (a_u is the updraft grid fraction area and w_u is the vertical velocity in the updraft), $\overline{\phi}$ is the mean value and ϕ_u is the updraft value of the variable ϕ.

In this formulation, it is assumed that the size of the updraft area is very small compared to the grid size ($a_u \ll 1$), so the environmental field values are taken as the mean field values. The effect of downdrafts is neglected as this parameterization is used only for shallow convection. The eddy-diffusivity term represents the remaining fluctuations due to the non-organized small-scale local turbulence.

Our parameterization contains an eddy-diffusivity term which is computed by the turbulence scheme of Cuxart et al. (2000) and a mass flux term computed by an updraft scheme which is described in the following section. Due to the fact that we use the Kain-Fritsch scheme to diagnose entrainment and detrainment in the cloudy portion, we decided to call the new scheme EDKF for Eddy-Diffusivity / Kain-Fritsch.

3.2 Description of the scheme

3.2.1 Updraft model

The updraft model is defined as a single entraining/detraining rising parcel as in Soares et al. (2004). One resulting updraft described by the mass flux is used to represent the effect of several plumes, and its characteristics are determined as a function of mixing between the updraft and its environment through entrainment E (the inward mass flux from the environment to the updraft) and detrainment D (the outward mass flux from the updraft to the environment). Moreover, the mass flux approximation assumes that the cloud ensemble is considered in steady state. The mass flux is defined as $M_u = \rho a_u w_u$, and its evolution is determined by a diagnostic equation of the mass continuity between the updraft and its surrounding environment (Fig. 3.1),

$$\frac{\partial M_u}{\partial z} = (E - D) \tag{3.2}$$

$$\text{or, } \frac{1}{M_u}\frac{\partial M_u}{\partial z} = (\epsilon - \delta) \tag{3.3}$$

where ϵ and δ are respectively the entrainment rate ($E = \epsilon M_u$) and the detrainment rate ($D = \delta M_u$).

The evolution of a conserved parcel characteristic ϕ_u during the ascent is defined as in Siebesma (1998):

$$\frac{\partial M_u \phi_u}{\partial z} = E\overline{\phi} - D\phi_u \tag{3.4}$$

using (3.3) and simplified as:

$$\frac{\partial \phi_u}{\partial z} = -\epsilon(\phi_u - \overline{\phi}) \tag{3.5}$$

where ϕ_u and $\overline{\phi}$ are respectively an updraft conserved variable and its mean value on the grid. This equation is used to determine the evolution of updraft conservative variables such as the liquid potential temperature θ_{lu} and the total mixing ratio r_{tu} during ascent.

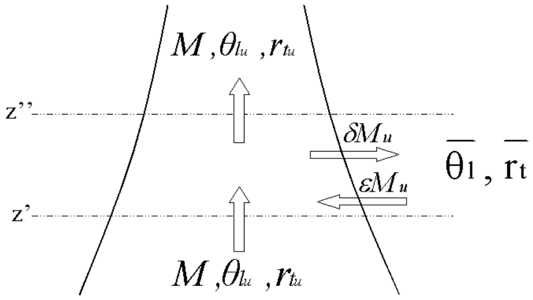

Figure 3.1: Variations of the updraft characteristics M_u, θ_{lu} and r_{tu} and dependent on the mixing with the environment dictated by the entrainment ϵM_u and the detrainment δM_u.

The vertical velocity (w_u) equation for the updraft is given by:

$$w_u \frac{\partial w_u}{\partial z} = B_u - \epsilon w_u^2 - P \tag{3.6}$$

where on the right-hand side (rhs), the first term is the buoyancy, the second term is the entrainment, and P represents the pressure term defined in, e.g. numerous studies (Simpson and Wiggert 1969; Siebesma et al. 2003; Soares et al. 2004) as a linear combination of the first two terms. Therefore, the equation is simplified as:

$$w_u \frac{\partial w_u}{\partial z} = aB_u - b\epsilon w_u^2 \tag{3.7}$$

where $a = 1$ and $b = 1$, defined respectively as a virtual mass coefficient and a drag coefficient (Simpson and Wiggert 1969). Numerical aspects are given in Appendix 3.4.2.

Following He et al. (2020), assuming the pressure term is proportional to buoyancy, with an additional advective and drag contribution, and considering the turbulent transport term to be negligible, we thus have:

$$(1-\alpha_a) w_u \frac{\partial w_u}{\partial z} = aB_u - b\epsilon w_u^2 - \frac{b'}{H} w_u^2 \tag{3.8}$$

where α_a is an advective coefficient, b' is a drag coefficient and H is characteristic drag length taken equal to $\sqrt{\alpha_u \Delta x \Delta y / \pi}$.

Using the definition of the mass flux, Soares et al. (2004) and Siebesma et al. (2007) were able to compute directly the mass flux in the dry portion of their updraft from the vertical velocity obtained from (3.8) and using a constant fraction area. At cloud base, they used a constant value of the cloud fractional area to compute the mass flux and to close the scheme.

Equation (3.8) is used to define the top of the updraft where w_u vanishes but also to diagnose the updraft fraction area, a_u, which is not a constant or a closure of the scheme as in Soares et al. (2004) and Siebesma et al. (2007).

Thanks to the independent computations of both mass flux M_u (3.3) and w_u (3.8), the updraft fraction area can vary vertically, and is defined as

$$a_u = \frac{M_u}{\rho w_u}. \tag{3.9}$$

The vertical variations of this last variable are important because a_u is used to diagnose the cloud fraction (see next section).

The mass flux approach is also used to realize a non-local mixing of momentum along the vertical in addition to the mixing yet realized by the turbulent scheme via the eddy-diffusivity approach. But, since the momentum is not conservative, the effect of pressure perturbations is added using a parameterization from Gregory et al. (1997). The evolution of the updraft horizontal wind component is defined as:

$$\frac{\partial u_u}{\partial z} = -\epsilon(u_u - \overline{u}) + C_u \frac{\partial \overline{u}}{\partial z}, \tag{3.10}$$

$$\frac{\partial v_u}{\partial z} = -\epsilon(v_u - \overline{v}) + C_v \frac{\partial \overline{v}}{\partial z}, \tag{3.11}$$

where $C_u = C_v = 0.5$, and u_u (v_u) represents the zonal (meridional) component of wind modified during the ascent in the updraft; $\overline{u}$ and $\overline{v}$ are zonal and meridional mean wind components respectively.

3.2.2 Lateral mass exchanges

The definition of entrainment and detrainment is the crucial issue in this type of parameterization. Various studies have used different definitions for various PBL regimes (e.g., Siebesma 1998; Neggers et al. 2002; De Rooy and Siebesma 2008).

We have chosen to define lateral mass exchanges from physical characteristics of the CBL. Arakawa (2004) explained that buoyancy is an important parameter in shallow convection. Moreover, the vertical velocity w_u is considered as a pertinent parameter in the description of mixing between dry updraft or the cloud and their environment in shallow convection. Neggers et al. (2002) defined the entrainment as inversely proportional to vertical velocity for shallow cumulus convection, and Cheinet (2003) also applies this formulation to dry plumes. This means that ϵ is not constant but decreases with higher vertical velocities. In other terms, an updraft with strong vertical velocity will be isolated from its environment.

In the dry portion of the CBL, ϵ and δ take into account physical characteristics of a buoyant ascending parcel. Equation (3.8) shows that buoyancy is linked to vertical velocity, ${w_u}^2$ being a vertical integral of the buoyancy. However, locally, both can be independent, for example in the non-buoyant part where negative buoyant air can still be ascending. Young (1988) explained that the correlation between buoyancy and w decreases in the upper part of the CBL, the buoyancy acting as a displacing force in the lower part of the CBL and as a restoring force in the upper part of the CBL. Thus, lateral mixing does not only depend on the vertical velocity as in Neggers et al. (2002) but must be locally defined as an equilibrium between w_u and buoyancy B_u. By dimensional analysis (Buckingham 1914), we obtain:

$$\epsilon_{dry}, \delta_{dry} \propto \frac{B_u}{w_u^2} \tag{3.12}$$

where $B_u = g(\theta_{v,u} - \overline{\theta_v})/\overline{\theta_v}$ is the buoyancy of the air parcels in the updraft.

Near the ground, a relative strong buoyancy and a weak vertical velocity allow strong entrainment to import many air parcels in the updraft, implying a positive proportionality coefficient for ϵ. Near the inversion, in the non-buoyant zone, much air is detrained implying a negative proportionality coefficient for δ. Since entrainment and detrainment rates cannot be negative, the entrainment rate is zero where the updraft is non-buoyant compared to its surrounding environment. Conditional sampling of detrainment in LES has shown that detrainment is not null in the mixed layer (see Fig. 9c of Pergaud et al. (2009)), so to keep a positive detrainment in the buoyant part of the updraft, a minimum detrainment is defined using a modified formulation from Lappen and Randall (2001): $\delta = (L_{up_{surf}} - z)^{-1}$ or $\delta = L_{up}(z)^{-1}$ with $L_{up_{surf}}$ computed at ground level, and $L_{up}(z)$ computed at level z inside the updraft; both options are available in Meso-NH.

Eventually, in the dry portion of the CBL, entrainment and detrainment are defined as:

$$\epsilon_{dry} = Max\left[0, C_\epsilon \frac{B_u}{w_u^2}\right], \tag{3.13}$$

$$\delta_{dry} = Max\left[\frac{1}{L_{up} - z}, C_\delta \frac{B_u}{w_u^2}\right], \tag{3.14}$$

where L_{up} is the Bougeault and Lacarrère (1989) (BL89) upward mixing length, C_δ and C_ϵ have been tuned to fit one-dimensional (1D) entrainment and detrainment to LES, $C_\delta = -10$ and $C_\epsilon = 0.55$. Numerical aspects are given in Appendix 3.4.3.

In the cloudy part, several descriptions of the exchanges exist.

We have chosen to define two different types of exchange differentiating the dry portion of the updraft from the moist one due to the fact that the environment of any updraft is strongly turbulent compared to the environment of a cloud. Taylor and Baker (1991) have emphasized the importance of buoyancy sorting in determining the cloud composition and in defining a continued lateral entrainment and detrainment. Zhao and Austin (2003) explained that a buoyancy sorting model can be used as a physically more realistic alternative to entraining plume models in shallow cumulus convection resolving notably the Warner paradox. In the parameterization presented here, if the lifting condensation level (LCL) is reached, lateral exchanges are computed using the parcel buoyancy sorting approach of Kain and Fritsch (1990) (KF90 in the following). Details are given in Kain and Fritsch (1990) and Bechtold et al. (2001) and you can see the chapter dealing with the Kain-Fritsch-Bechtold convection scheme. However, minor modifications have been put in the EDKF parameterization, the new parameterization uses a uniform distribution of the air parcels although, in the original formulation, the distribution was Gaussian; and, the entrainment cannot exceed the detrainment.

In the KF90 scheme, the rate at which environmental and updraft air enter the mixing zone is constant, leading to a constant $\epsilon_{wet} + \delta_{wet}$ quantity. Instead, we can activate a formulation based on Lappen and Randall (2001) in which $\epsilon_{wet} + \delta_{wet} \propto \frac{1}{2}\frac{L_{up}+L_{dn}}{L_{up}Ldn}$ where L_{up} and L_{dn} are respectively the upward and downward BL89 mixing lengths. In this case, the limitation of entrainement is suppressed.

The buoyancy sorting model requires calculating the critical fraction of updraft air to obtain zero buoyancy. In the case of KF90, this critical proportion is calculated by interpolation, but it can also be calculated analytically according to Rooy and Siebesma (2008). In Meso-NH, both options are available.

3.2.3 Scheme initialization and closure

Since the scheme is integrated upward from the surface (level z_{grd}), $M_u(z_{grd})$ is computed as a function of w_* as in Grant (2001) but at the surface, contrary to the closure at the cloud base defined by Grant (2001),

$$M_u(z_{grd}) = C_{M_0}\rho(\frac{g}{\theta_{vref}}\overline{w'\theta'_{vs}}L_{up})^{1/3} \tag{3.15}$$

where $\overline{w'\theta'_{v}}_{s}$ is the surface buoyancy flux, L_{up} is the BL89 upward mixing length corresponding to the distance that a parcel leaving the ground travel due to buoyancy. The value of $C_{M_0} = 0.065$ is based on LES results according to Pergaud et al. (2009). Note that, in the surface layer, this value is larger than the value $C_{M_0} = 0.03$ originally proposed by Grant (2001) at the LCL.
The rising parcel characteristics are determined at the ground using the formulation of Soares et al. (2004) in which an excess is added to the environmental values. For example, the updraft liquid potential temperature near the ground is:

$$\theta_{lu}(z_{grd}) = \overline{\theta_l}(z_{grd}) + \alpha \frac{\overline{w'\theta'_{l}}_{s}}{e^{1/2}(z_{grd})} \tag{3.16}$$

where the value of α is 0.3 as in Soares et al. (2004). Sensitivity tests in the range [0,1] indicate that results are independent of α. This excess is formulated as a function of the surface-layer variability according to Troen and Mahrt (1986) who demonstrated that the excess is well correlated with the ratio of the surface heat flux and the square root of turbulent kinetic energy. A similar equation is used for r_t.
At the surface, w_u is initialized from the turbulent kinetic energy e (provided by the turbulence scheme),

$${w_u}^2(z_{grd}) = \frac{2}{3} e(z_{grd}). \tag{3.17}$$

3.2.4 The subgrid condensation scheme

The updraft scheme represents the dynamical evolution of an air parcel during its ascent. Condensation can occur within the parcel. Therefore, a diagnostic sub-grid cloud based on the updraft characteristics is added. Although conservative variables are used, we can diagnose a sub-grid cloud mixing ratio $r_{np_{up}}$ and a cloud fraction CF. $r_{np_{up}}$ is computed from θ_l, r_t and pressure using a variation of all or nothing scheme since the updraft air parcels are considered completely cloudy. CF is defined proportional to the updraft fraction on the grid a_u:

$$CF = C_{cf} * a_u \tag{3.18}$$

where $C_{cf} = 2.5$. The horizontal size of the cloud is 2.5 times the size of the updraft. This parameter has been tuned to fit the 1D cloud fraction to LES results. This coefficient represents the difference between cloudy core fraction and cloud fraction.
The cloud mixing ratio can be approximated by the product between the cloud fraction previously computed and the updraft cloud mixing ratio computed from the updraft conservative variables (Bechtold and Cuijpers 1995):

$$\overline{r_c} = CF * r_{np_{up}} \tag{3.19}$$

In addition to this original cloud scheme, one can use a Guassian PDF centered on the updraft properties (θ_{lu} and $r_{np_{up}}$) using the saturation deficit (s) variable and a parametrised variance proportional to $(s_{up} - s)^2$. In this case, an extra variance proportional to $(s_{env} - s)^2$ is computed and can be used by the saturation adjustement. In these expressions, s_{up} and s_{env} are the saturation deficit in the updraft and in the environment respectively whereas s is the mean saturation deficit.
In our parameterization, r_np is not a prognostic variable. If the mass flux becomes null, the cloud disappears totally. Only a prognostic cloud scheme can evaporate a cloud over several timesteps. So passive clouds that are not maintained by a thermal are not taken into account in the parameterization. However, here, $\overline{r_np}$ represents only the contribution of the shallow convection clouds.

Others contributions for clouds can come from the subgrid turbulence scheme or from microphysics scheme (notably for resolved clouds). r_np is separated into liquid and ice phases in the same way as for mixed-phase saturation adjustment.

3.3 Initialisation of Mass-Flux scheme at hectometric scales

The triggering controls the activation of the mass-flux scheme at the surface while the closure controls its intensity. Often the boundary-layer mass-flux scheme triggers as soon as the surface sensible heat flux is positive while the intensity of the mass-flux at the ground is proportional to the convective velocity scale (see Pergaud et al.,2009).
Firstly, concerning the closure, Figure 3.2a shows the subgrid mass-flux normalized by the convective velocity scale as a function of the normalized resolution in the IHOP case at 1200 LT and the ARM case at 1400 LT in the middle of the boundary layer. The mass-flux normalized by the convective velocity scale in both the IHOP and ARM cases is dependent on the resolution normalized by the height of the thermals : it is constant at mesoscales and larger than in LES. Here the mass flux is computed in the middle of the CBL. It cannot be diagnosed directly at the ground where there is no really thermal formed yet and where the turbulent is more strongly dependent on the subgrid turbulence scheme. The normalized mass flux as a function of the normalized resolution has the same shape at all altitudes in the boundary layer (not shown). Therefore, here we propose to make the constant of proportionality between the mass-flux at the ground and the convective velocity scale (computed at ground level for the whole domain, $w*$) dependent on the resolution by this function :

$$\sigma(\frac{M_u}{w_*}) = tanh(C \times \sqrt(\Delta x \times \Delta y)/L_{up}) \tag{3.20}$$

In the magenta fit plotted in Fig. 3.2a, $C = 1.83$. We propose to use this function in the parametrization in order to make it scale-aware.
Moreover, the subgrid mass-flux variability is larger in the grey zone than in the LES and at mesoscales. This is visible in Fig. 3.2b which shows the standard deviation of the mass-flux normalized by the convective velocity scale ($\sigma(\frac{M_u}{w*})$) as a function of the normalized resolution in the IHOP case at 1200 LT and the ARM case at 1400 LT in the middle of the CBL. The large variability in the grey zone is also visible on the buoyancy and the entrainment (cf. Honnert et al.,2016) and it is consistent with Dorrestijn et al. (2013) which showed that the heat flux variability is larger in the grey zone. The fit of the data of Fig. 3.2b is:
Concequently, the closure of the mass-flux scheme of Pergaud et al. (2009) at hectometric scales depend on the model resolution following Eq. 4.6.

3.4 Appendix

3.4.1 Mass flux in the surface layer compared to w_*

The mass flux near the surface has been set proportional to the convective vertical velocity scale w_* as in Grant (2001). The coefficient of proportionality C_{M_0} in our scheme cannot have the same value than the one used by Grant (2001) due to the fact that Grant (2001) defines this relation at the LCL. So we used the CS defined in Pergaud et al. (2009) to obtain mass flux values in the surface layer for different convective cases at different dates (IHOP, ARM).

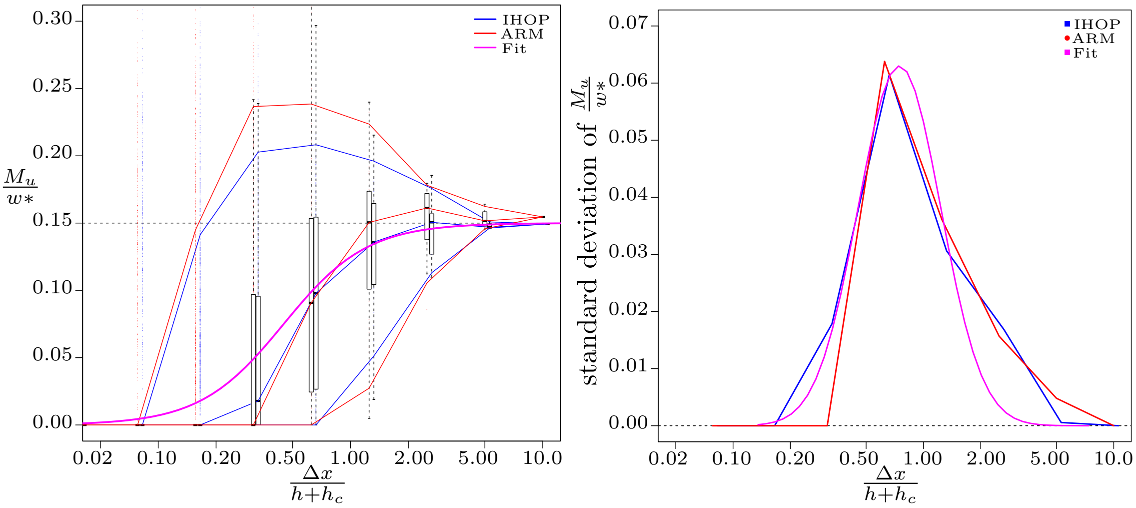

(a) Distribution (b) Dispersion

Figure 3.2: (a) Mass-flux of the subgrid thermals normalized by the convective velocity scale for grid cells ranging from 250 m to 8 km in the middle of the boundary layers of the ARM case at 1400 LT (blue points) and the IHOP case at 1200 LT (red points) as a function of $\Delta x/(h+h_c)$. Boxplots of the data (one per case) : the box shows 50% of the data and the line 99.3%. Median, quantile 5% and 95% in (red and blue) lines. A fit of the data (see text for more details) is in magenta. (b) Standard deviation of the same data in the same colors as in (a) as a function of the normalized horizontal resolution.

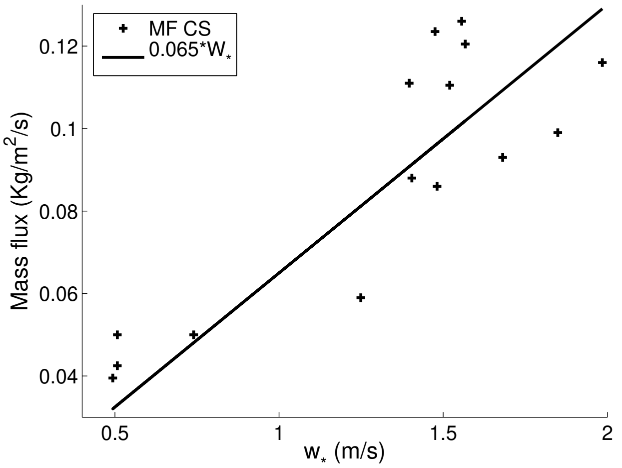

Figure 3.3: Mass flux in the surface layer computed using the Conditionnal Sampling defined in Pergaud et al. (2009) versus sub-cloud layer velocity scale w_*. Line shows $M = 0.065w_*$.

Figure 3.3 is a plot of the surface layer mass flux against sub-cloud layer velocity scale. The LES data suggest that $C_{M_0} = 0.065$.

3.4.2 Analytical solution for the vertical velocity w_u

Equation (3.8) presents the computation for vertical velocity in the updraft w_u. Combining the equation for entrainment (3.14), the w_u equation becomes :

$$\frac{\partial {w_u}^2}{\partial z} = 2aB_u - 2bC_\epsilon max(0, B_u) \tag{3.21}$$

C_{BUO} is defined equal to $2a$ if $B_u < 0$ (entrainment is zero) and to $2(a - bC_\epsilon)$ if $B_u > 0$. This equation is integrated over each layer. Figure 3.4 presents this integral. If z' is layer bottom, z'' is layer top and $\Delta z_D = z'' - z'$, ${w_u}^2$ is defined by:

$$\int_{\Delta z_D} \frac{\partial {w_u}^2}{\partial z} dz = \int_{\Delta z_D} C_{BUO} B_u dz \tag{3.22}$$

$${w_u}^2(z'') - {w_u}^2(z') = C_{BUO}\frac{g}{\theta_{ref}} \int_{\Delta z_D} \left[\theta_{v_{up}}(z) - \overline{\theta_v}(z)\right] dz \tag{3.23}$$

θ_{vup} is assumed constant between z' and z'', and the variations of $\overline{\theta_v}$ is supposed linear between z' and z".

$$\overline{\theta_v}(z) = \alpha_1 z + \overline{\theta_v}(z') \tag{3.24}$$

$$\theta_{v_{up}}(z) = \theta_{v_{up}}(z') \tag{3.25}$$

So the integral for w_u becomes

$${w_u}^2(z'') - {w_u}^2(z') = C_{BUO}\frac{g}{\theta_{ref}} \int_{\Delta z_D} \left[-\alpha_1 z - \overline{\theta_v}(z') + \theta_{v_{up}}(z')\right] dz \tag{3.26}$$

After computation, w_u at the level z'' computed from the level z' is :

$${w_u}^2(z'') = C_{BUO}\frac{g}{\theta_{ref}}\Delta z_D(\frac{-\alpha_1}{2}\Delta z_D - \overline{\theta_v}(z') + \theta_{v_{up}}(z')) + {w_u}^2(z') \tag{3.27}$$

3.4.3 Analytical integrated solution for entrainment and detrainment

The entrainment ϵ is defined by equation (3.14). This equation is integrated, as for w_u, on each vertical grid size for example between z' and z'' (see on Fig. 3.4):

$$\epsilon = \frac{C_\epsilon}{\Delta z_D} \int_{\Delta z_D} \frac{B}{{w_u}^2} dz \tag{3.28}$$

Using (3.27), ϵ becomes

$$\epsilon = \frac{C_\epsilon g}{\Delta z_D \theta_{ref}} \int_{\Delta z_D} \frac{\theta_{v_{up}}(z') - \alpha_1 z + \overline{\theta_v}(z')}{C_{BUO}\frac{g}{\theta_{ref}} z(-\alpha_1 z - \overline{\theta_v}(z') + \theta_{v_{up}}(z')) + {w_u}^2(z')} dz \tag{3.29}$$

$$\epsilon = \frac{C_\epsilon}{\Delta z_D C_{BUO}} \int_{\Delta z_D} \frac{-\alpha_1 z + \theta_{v_{up}}(z') + \overline{\theta_v}(z')}{\frac{-\alpha_1}{2} z^2 - \overline{\theta_v}(z') z + \theta_{v_{up}}(z') z) + \frac{\theta_{ref} {w_u}^2(z')}{g C_{BUO}}} dz. \tag{3.30}$$

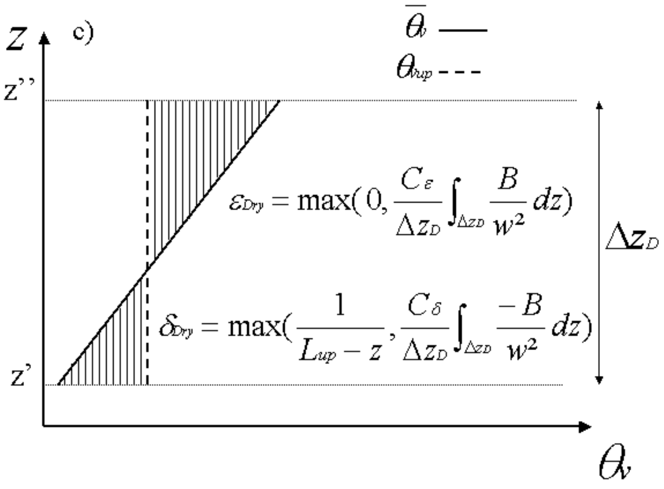

Figure 3.4: Parameterized entrainment and detrainment for dry layer

noting $X = \frac{-\alpha_1}{2}z^2 - \overline{\theta_v}(z')z + \theta_{v_{up}}(z')z) + \frac{\theta_{ref}{w_u}^2(z')}{gC_{BUO}}$:

$$dX = ((-\alpha_1)z + \theta_{v_{up}}(z') + \overline{\theta_v}(z'))dz \tag{3.31}$$

$$\epsilon = \frac{C_\epsilon}{C_{BUO}\Delta z_D}\int_{\Delta z_D}\frac{dX}{X} \tag{3.32}$$

$$\epsilon = \frac{C_\epsilon}{C_{BUO}\Delta z_D}[Ln(X)]_{\Delta z_D} \tag{3.33}$$

After computation, ϵ is defined as :

$$\epsilon = \frac{C_\epsilon}{C_{BUO}\Delta z_D}ln\left[1 + \frac{C_{BUO}\Delta z_D}{{w_u}^2(z')\theta_{ref}}(\frac{-\alpha_1}{2}\Delta z - \theta_{v_{up}}(z') + \overline{\theta_v}(z'))\right] \tag{3.34}$$

where α_1 is defined as previously. An identical solution can be found for δ taking the absolute value of the buoyancy.
A formulation of the transition between cloudy and dry regime is added to limit the sensitivity of the scheme to the change in the computation of entrainment and detrainment. If a liquid mixing ratio is detected at z” using an ”all or nothing” adjustment from updraft variables, the LCL height is determined assuming a linear increase of r_c with height. A weight for the KF90 lateral exchanges is defined proportional to the cloudy part occupying grid and integral dry entrainment and detrainment are computed only on the height of the dry part.

3.5 References

Arakawa, A., 2004: The Cumulus Parameterization Problem: Past, Present, and Future. *J. Clim.*, **17**, 2493–2525.

Bechtold, P., and J. W. M. Cuijpers, 1995: Cloud perturbations of temperature and humidity: A LES study. *Bound. Layer. Meteor.*, **76**, 377–386.

Bechtold, P., E. Bazile, P. Mascart and E. Richard, 2001: A Mass flux convection scheme for regional and global models. *Quart. J. Roy. Meteor. Soc.*, **127**, 869-886.

Bougeault, P, and P. Lacarrère, 1989: Parameterization of Orography-Induced Turbulence in a Mesobeta-Scale Model. *Mon. Wea. Rev.*, **117**, 1872–1890.

Buckingham, E., 1914: On physically similar systems: Illustrations of the use of dimensional equations. *Phys. Rev.*, **IV**, 345–376.

Cheinet, S., 2003: A multiple Mass-Flux Parameterization for the Surface-Generated Convection. Part1: Dry Plumes. *J. Atmos. Sci.*, **60**, 2313–2327.

Cuxart, J., P. Bougeault, and J.-L. Redelsperger, 2000: A turbulence scheme allowing for mesoscale and large-eddy simulations. *Quart. J. Roy. Meteor. Soc.*, **126,** 1–30.

De Rooy, W. C., and P. Siebesma, 2008: A simple parameterization for detrainment in shallow cumulus. *Mon. Wea. Rev.*, **136**, 560–576.

Dorrestijn J, Crommelin DT, Siebesma AP and Jonker HJJ, 2013: Stochastic convection parametrization estimated from high-resolution model data. 27:133–148 *Theor Comput Fluid Dyn*, **27**, 133–148.

Grant, A. L. M., 2001: Cloud-base fluxes in the cumulus-capped boundary layer. *Quart. J. Roy. Meteor. Soc.*, **127**, 407–421.

Gregory, D., R. Kershaw, and P. M. Inness, 1997: Parametrization of momentum transport by convection. II: Tests in single-column and general circulation models. *Quart. J. Roy. Meteor. Soc.*, **123**, 1153–1183.

He, J., Cohen, Y., Lopez-Gomez, I., Jaruga, A., and Schneider, T., 2020: An Improved Perturbation Pressure Closure for Eddy-Diffusivity Mass-Flux Schemes *https://doi.org/10.1002/essoar.10505084.1*.

Honnert, R., Couvreux, F., Masson, V. et David Lancz, 2016 : Sampling the Structure of Convective Turbulence and Implications for Grey-Zone Parametrizations *Bound. Layer. Meteor.*, **160**, 133.

Hourdin, F., F. Couvreux, and L. Menut, 2002: Parameterization of the Dry Convective Boundary Layer Based on a Mass Flux Representation of Thermals. *J. Atmos. Sci.*, **59**, 1105–1122.

Kain, J. S., and J. M. Fritsch, 1990: A one-dimensional entraining/detraining plume model and its application in convective parameterizations. *J. Atmos. Sci.*, **47**, 2784-2802.

Lappen, C. L., and D. A. Randall, 2001: Toward a Unified Parameterization of the Boundary Layer and Moist Convection. Part2 : Lateral Mass Exchanges and Subplume-Scale Fluxes. *J. Atmos. Sci.*, **58**, 2037–2051.

Neggers, R. A. J., P. Siebesma, and H. J. J. Jonker, 2002: A Multiparcel Model for Shallow Cumulus Convection. *J. Atmos. Sci.*, **59**, 1655–1668.

Pergaud, J., V. Masson, S. Malardel, and F. Couvreux, 2009: A Parameterization of Dry Thermals and Shallow Cumuli for Mesoscale Numerical Weather Prediction. *Bound. Layer. Meteor.*, **132**, 83–106.

W. C. de Rooy, W. C., Siebesma, A. P., 2008: A Simple Parameterization for Detrainment in Shallow Cumulus. *Monthly Weather Review*, **136**, 560–576.

Siebesma, P., 1998: Shallow Cumulus Convection. In *"Buoyant convection in geophysical flows"* (Eds. E.J. Plate et al), 441–486.

Siebesma, P., C. S. Bretherton, A. Brown, A. Chlond, J. Cuxart, P. G. Duynkerke, H. Jiang, M. Khairoutdinov, D. Lewellen, C. H. Moeng, E. Sanchez, B. Stevens, and D. E. Stevens, 2003:

A Large Eddy Simulation Intercomparaison Study of Shallow Cumulus Convection. *J. Atmos. Sci.*, **60**, 1201–1219.

Siebesma, P., P. M. M. Soares, and J. Teixeira, 2007: A combined Eddy-Diffusivity Mass-Flux approach for the convective boundary layer. *J. Atmos. Sci.*, **64**, 1230–1248.

Simpson J, and V. Wiggert, 1969: Models of precipitating cumulus towers. *Mon. Wea. Rev.*, **97**, 471–489.

Soares, P. M. M., P. M. A. Miranda, A. P. Siebesma, and J. Teixeira, 2004: An Eddy-Diffusivity/Mass-Flux parameterization for dry and shallow cumulus convection. *Quart. J. Roy. Meteor. Soc.*, **130**, 3055–3079.

Taylor, G. R., and M. B. Baker, 1991: Entrainment and Detrainment in cumulus clouds. *J. Atmos. Sci.*, **48**, 112–121.

Troen, I. B., and L. Mahrt, 1986: A simple model of the atmospheric boundary layer: Sensitivity to surface evaporation. *Bound. Layer. Meteor*, **37**, 129–148.

Young, G. S., 1988: Turbulence Structure of the convective Boundary Layer. Part II: Phoenix 78 Aircraft Observations of Thermals and their environment. *J. Atmos. Sci.*, **45**, 727–735.

Zhao, M., and P. H. Austin, 2003: Episodic Mixing and Buoyancy-Sorting Representations of Shallow Convection: A Diagnostic Study. *J. Atmos. Sci.*, **60**, 892–912.

Chapter 4

HRIO Shallow Convection Scheme

Contents

4.1 Introduction

The grey zone of turbulence is defined by Wyngaard (2004) as the scales on the order of the energy-containing turbulence scale. At these resolutions, the turbulence structures are neither entirely subgrid scale (as in global and mesoscale models) nor largely resolved (as in large-eddy simulations (LES)). Honnert et al. (2011) used LES coarse-graining to produce similarity functions linking the subgrid or resolved part of the turbulent fluxes and the horizontal resolution of the model out of the height of the thermals. They indicated that the grey zone exists from resolutions smaller than two times the boundary-layer height in convective boundary layers (CBL). Regional models are now approaching the sub-kilometic scales and Honnert et al. (2011) showed that neither unidirectional (1D) non-local mesoscale boundary-layer (BL) turbulence scheme nor isotropic (3D) LES schemes are appropriate at these scales. That is why the turbulence schemes have to be adapted to the grey zone of turbulence.

Boutle et al. (2014) blended a 3D-Smagorinsky with a 1D non-local BL scheme with the help of the similarity functions proposed by Honnert et al. (2011). Ito et al. (2015) extended the Mellor and Yamada scheme by modifiing the length scales using statistics obtained from LES coarse-graining. Shin and Hong (2015) quantified the local and non-local turbulence at scales in the grey zone to adjust the vertical profiles resulting from their non-local K-gradient scheme.

These adaptations stongly depend on the schemes which are currently used at mesoscale or LES. At Météo-France, the turbulence in the atmospheric BL is represented by an eddy-diffusivity/mass-flux parametrization (EDMF - Hourdin et al. (2002), Soares et al. (2004)). The updraughts are represented by the mass-flux scheme which starts at the ground (hereafter PM09 - Pergaud et al., 2009) and represents the shallow convection, while the rest of the turbulence is represented by a K-gradient scheme (hereafter CBR - Cuxart et al., 2000)). Both parts of this scheme are being modified to adapt Météo-France models to the grey zone of turbulence. In this article, modifications of PM09 are presented in the second section as well as preliminary results in the third section. As perspective, the ”true” CBR mixing lengths in the grey zone are presented.

4.2 Description of the scheme

As many mass-flux schemes, PM09 is based on several assumptions which are valid at large scales. It assumes in particular that the thermal surface is small, the resolved vertical velocity is zero, and the thermal field is quasi-stationnary.

Honnert at al. (2016) determined the characteristics of the non-local turbulence (BL thermals) in the grey zone by means of a conditional sampling. Figure 4.1 shows a 16-km long horizontal cross-section of an LES. The thermals (in white) and the part of the thermals which impact the subgrid mass-flux scheme at 1-km resolution (in black) have been determined by the conditional sampling of Honnert at al. (2016). The environment of the structures is in red. Figure 4.1 shows that at 16-km resolution, PM09's assumptions are valid : the thermal surface is small, the resolved vertical velocity is zero, as the grid-cell contains both the updraughts and the compensatory subsidence, and the thermal field is quasi-stationnary. However, in the grey-zone, they are not verified. Indeed, as seen on the 1-km zoom of Fig. 4.1, the thermal surface (in black) may be large, the resolved vertical velocity is not zero, as one thermal can fill the grid-cell, and the thermal field is probably not quasi-stationnary.

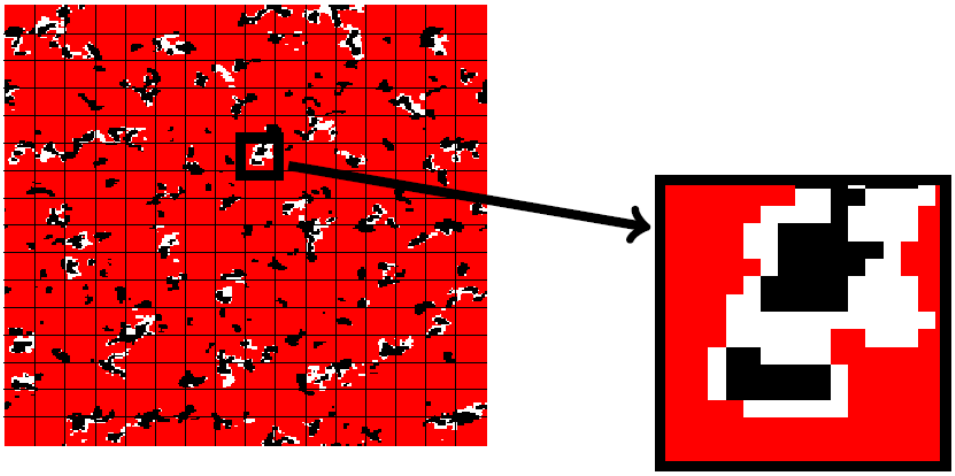

Figure 4.1: 16-km long horizontal cross-section of an LES (IHOP case , 1400 LT, 500-m altitude) and 1-km long zoom. The thermal fraction is in white, the core of the thermals (strong vertical velocity) is in black and the environment is in red. See Honnert et al. (2016)

However, mass-flux schemes can be developed without the three assumptions presented before. The initial schemes (PM09, Rio et al. 2009) describe the behaviour of parameters of one unique thermal in the mesh (the vertical velocity w_u, the mass-flux M_u, the total potential temperature θ_{lu}, the thermal surface area α, the buoyancy inside the thermal B_u and the pressure and the entrainment (ϵ)/ detrainment (δ) lateral closure). a_1 and b_1 are constant. Eq. (1-4) show the modifications (in red) of PM09. The non-negligible resolved vertical velocity ($\overline{w}^{\Delta x}$) is added in Eq. (1,3-4). The thermal surface is not negligible and appears at the denominator in Eq. (3-4). The surface triggering of the mass-flux ($M_{uz=0}$, Eq. (5)) depends on the resolution.

$$
\begin{aligned}
M_u &= \rho\alpha(w_u - \overline{w}^{\Delta x}) \tag{4.1}\\
\frac{1}{M_u}\frac{\partial M_u}{\partial z} &= \epsilon - \delta \tag{4.2}\\
\frac{\partial \theta_{lu}}{\partial z} &= -\frac{\epsilon}{1-\alpha}(\theta_{lu} - \overline{\theta_l}^{\Delta x}) \tag{4.3}\\
\frac{1}{2}\frac{\partial (w_u - \overline{w}^{\Delta x})^2)}{\partial z} &= a_1 B_u - b_1\frac{\epsilon}{1-\alpha}(w_u - \overline{w}^{\Delta x})^2 \tag{4.4}\\
& \tag{4.5}
\end{aligned}
$$

Then, the finer the resolution or the smaller the BL height, the smaller the subgrid turbulent flux. The scheme produces less subgrid turbulence. Consequently, resolved BL thermals are created.

4.3 Initialisation of Mass-Flux scheme

he triggering controls the activation of the mass-flux scheme at the surface while the closure controls its intensity. Often the boundary-layer mass-flux scheme triggers as soon as the surface sensible heat flux is positive while the intensity of the mass-flux at the ground is proportional to the convective velocity scale (see Pergaud et al.,2009).
Firstly, concerning the closure, Figure 3.2a shows the subgrid mass-flux normalized by the convective velocity scale as a function of the normalized resolution in the IHOP case at 1200 LT and the ARM case at 1400 LT in the middle of the boundary layer. The mass-flux normalized by the convective velocity scale in both the IHOP and ARM cases is dependent on the resolution normalized by the height of the thermals : it is constant at mesoscales and larger than in LES. Here the mass flux is computed in the middle of the CBL. It cannot be diagnosed directly at the ground where there is no really thermal formed yet and where the turbulent is more strongly dependent on the subgrid turbulence scheme. The normalized mass flux as a function of the normalized resolution has the same shape at all altitudes in the boundary layer (not shown). Therefore, here we propose to make the constant of proportionality between the mass-flux at the ground and the convective velocity scale (computed at ground level for the whole domain, $w*$) dependent on the resolution by this function :

$$\sigma(\frac{M_u}{w_*}) = tanh(C \times \sqrt(\Delta x \times \Delta y)/L_{up}) \tag{4.6}$$

In the magenta fit plotted in Fig. 3.2a, $C = 1.83$. We propose to use this function in the parametrization in order to make it scale-aware.
Moreover, the subgrid mass-flux variability is larger in the grey zone than in the LES and at mesoscales. This is visible in Fig. 3.2b which shows the standard deviation of the mass-flux normalized by the convective velocity scale ($\sigma(\frac{M_u}{w*})$) as a function of the normalized resolution in the IHOP case at 1200 LT and the ARM case at 1400 LT in the middle of the CBL. The large variability in the grey zone is also visible on the buoyancy and the entrainment (cf. Honnert et al., 2016) and it is consistent with Dorrestijn et al. (2013) which showed that the heat flux variability is larger in the grey zone. The fit of the data of Fig. 3.2b is:
Concequently, the closure of the mass-flux scheme of Pergaud et al. (2009) at hectometric scales depend on the model resolution following Eq. 4.6.

4.4 References

Boutle, I. A., Eyre, J. E. J., and Lock, A. P., 2014: Seamless stratocumulus simulation across the turbulent grey zone. *Mon. Wea. Rev.*, **42**, 1655–1668.

Cuxart, J., P. Bougeault, and J.-L. Redelsperger, 2000: A turbulence scheme allowing for mesoscale and large-eddy simulations. *Quart. J. Roy. Meteor. Soc.*, **126,** 1–30.

Dorrestijn J, Crommelin DT, Siebesma AP and Jonker HJJ, 2013: Stochastic convection parametrization estimated from high-resolution model data. 27:133–148 *Theor Comput Fluid Dyn*, **27**, 133–148.

Honnert, R., Masson, V., and Couvreux, F., 2011: A diagnostic for evaluating the representation of turbulence in atmospheric models at the kilometric scale. *J. Atmos. Sci.*, **68(12)**, 3112–3131.

Honnert, R., Couvreux, F., Masson, V., and David Lancz, 2016 : Sampling the Structure of Convective Turbulence and Implications for Grey-Zone Parametrizations *Bound. Layer. Meteor.*, **160**, 133.

Hourdin, F., F. Couvreux, and L. Menut, 2002: Parameterization of the Dry Convective Boundary Layer Based on a Mass Flux Representation of Thermals. *J. Atmos. Sci.*, **59**, 1105–1122.

Ito, J., Niino, H., Nakanishi, M., and Moeng, C. H., 2015: An extension of the Mellor–Yamada model to the terra incognita zone for dry convective mixed layers in the free convection regime. *Bound. Layer. Meteor.*, **157(1)**, 23–43.

Pergaud, J., V. Masson, S. Malardel, and F. Couvreux, 2009: A Parameterization of Dry Thermals and Shallow Cumuli for Mesoscale Numerical Weather Prediction. *Bound. Layer. Meteor.*, **132**, 83–106.

Rio, C., F. Hourdin, J. Y. Grandpeix, and J. P. Lafore, 2009: Shifting the diurnal cycle of parameterized deep convection over land. *Geophysical Research Letters.*, **36**, 7.

Shin, H., and Hong, S., 2013 : Analysis on resolved and parametrized vertical transports in the convective boundary layers at the gray-zone resolution. *J. Atmos. Sci.*, **70**, 3248–3261.

Soares, P. M. M., P. M. A. Miranda, A. P. Siebesma, and J. Teixeira, 2004: An Eddy-Diffusivity/Mass-Flux parameterization for dry and shallow cumulus convection. *Quart. J. Roy. Meteor. Soc.*, **130**, 3055–3079.

Wyngaard JC, 2004 : Toward numerical modelling in the 'Terra Incognita'. J Atmos Sci 61:1816–1826 *J. Atmos. Sci.*, **61**, 1816–1826.

Chapter 5

Convection Scheme

Contents

5.1 Introduction

It has been well recognized since the 1960s (e.g. Charney and Eliassen 1964; Manabe and Strickler 1964; Kuo 1965; Ooyama 1971; Yanai et al. 1973) that cumulus convection is one of the major processes that affects the dynamics and energetics of atmospheric circulation systems. Since then many cumulus parameterization schemes have been developed for numerical weather prediction (NWP) models and General Circulation Models (GCMs), to account for the subgrid-scale release of latent heat and mass transport associated with convective clouds. A non-exhaustive list of these schemes includes e.g. Arakawa and Schubert (1974), Anthes (1977), Kuo and Raymond (1980), Fritsch and Chappell (1980), Bougeault (1985), Betts and Miller (1986), Tiedtke (1989), Gregory and Rowntree (1990), Kain and Fritsch (1990), Emanuel (1991), Donner (1993), Grell (1993), Wang and Randall (1996), Sun and Haines (1996), and Hu (1997). The common point of all cumulus parameterizations is that they aim to diagnose the presence of larger-scale conditions that would support the development of convective activity and, under appropriate conditions, to introduce tendencies for temperature and moisture (and possibly momentum) that would be consistent with the effects of convective activity. In particular, most parameterizations are designed to drive the model atmosphere towards a convectively adjusted state when they activate. This adjusted state is either predefined (”adjustment” schemes) or is computed using a bulk or spectral cloud model and adjusting the atmosphere through mass exchange between the cloud and the environment (mass flux schemes).

Two necessary characteristics of any convective parameterization are i) a reasonable set of criteria to determine when convective adjustment should be initiated, and ii) reasonable procedures for determining the characteristics of a final convectively-adjusted state. In fully prognostic dynamic models, the efficacy of a convection parameterization is often measured by factors such as i) does it activate at the right time and place? ii) does it produce the right amount and areal coverage of precipitation? and iii) does it enhance the predictive skill of its host model? Of course, there are many ways of evaluating these measures, and the third criteria above, in particular, depends on the needs of the user. For example, from the practical point of view of a weather forecaster, a convection scheme used in a mesoscale model for a 1-2 day forecast provides valuable information if it has skill in predicting the initiation and evolution of convective events, especially if they involve severe convection. In addition, convective parameterization plays a critically important role in the accurate quantitative prediction of rainfall, especially heavy rain episodes, which present a major challenge for forecasters (Kuo et al. 1997; Fritsch et al. 1998). In contrast, for long-range GCM integrations a convective parameterization may be judged to be successful if it enhances the ability of the model to accurately represent the mean climate and variability of the tropical atmosphere. Because of these seemingly disparate expectations, cumulus parameterizations have been developed typically with a particular application in mind and may contain inherent biases toward that application.

It seems reasonable, however, to expect that, to the extent that the essential physics of convection can be represented in the crude framework of a parameterization in a manner that is compatible with the numerics of modeling systems, it might be possible to develop a parameterization that is useful over a broad range of scales and type of applications. Fundamentally, we believe that, beyond the detection of convective activity, a primary purpose of convective parameterization is to mitigate the effects of inappropriate scale-selection in a modeling system’s representation of deep convection. In particular, we propose that if a parameterization nudges towards a reasonable adjusted state, that its imposed time-scale of adjustment is reasonable, and that it activates in a timely manner, it can perform well in a variety of convective environments and model configurations. In this context a convection parameterization has been developped on the basis of existing frameworks, essentially the rather general framework proposed by Kain and Fritsch (1993). The parameterization is intended to provide an efficient representation of atmospheric shallow and deep convection for both mesoscale and global applications.

A detailed description of the scheme is provided below, however numerical applications in different 1D, mesoscale and global contexts are discussed in Bechtold et al. (2001) and Mallet et al. (1999). Further 1D evaluations of the scheme and intercomparisons with other models/schemes are presented in Xie et al. (2002) and Bechtold et al. (2000) in the context of the international program GCSS (GEWEX Cloud System Study). The corresponding computer code is also available as an optimized portable routine (both in Meso-NH and ECMWF/ARPEGE IFS code structure) in Fortran 90 on upon request from P. Bechtold (now at ECMWF).

5.2 Mass flux equations

Briefly, with the aid of the mass flux approximation the effect of a convective cloud population on its environment can be written (see e.g. Arakawa and Schubert (1974), Gregory and Miller (1989), Betts (1997) for various derivations)

$$\begin{aligned}
\left.\frac{\partial\overline{\Psi}}{\partial t}\right|_{\text{conv}} &= \frac{\partial(\overline{w'\Psi'})}{\partial z} \qquad (5.1)\\
&\approx \frac{1}{\overline{\rho}A}\frac{\partial}{\partial z}\left[M^u(\Psi^u-\overline{\Psi})+M^d(\Psi^d-\overline{\Psi})+\tilde{M}(\tilde{\Psi}-\overline{\Psi})\right]\\
&\approx \frac{1}{\overline{\rho}A}\frac{\partial}{\partial z}\left[M^u\Psi^u+M^d\Psi^d-(M^u+M^d)\overline{\Psi}\right], \qquad (5.2)
\end{aligned}$$

where Ψ is a conserved variable, $M = \overline{\rho}wA$ is the mass flux (kg s^{-1}), w the vertical velocity, and $A = A^u + A^d + \tilde{A}$ denotes the horizontal domain (grid size). Overbars denote ensemble mean (horizontal grid mean) values, tildes denote environmental values, up-and downdraft values are denoted by superscripts u and d, respectively. Furthermore, describing the mass exchange of the cloud ensemble with its environment by entrainment ϵ and detrainment δ, i.e.

$$\frac{\partial}{\partial z}(M^u\Psi^u) = \epsilon^u\overline{\Psi} - \delta^u\Psi^u; \qquad \frac{\partial}{\partial z}(M^d\Psi^d) = \epsilon^d\overline{\Psi} - \delta^d\Psi^d \qquad (5.3)$$

we obtain the final result

$$\left.\frac{\partial\overline{\Psi}}{\partial t}\right|_{\text{conv}} = \frac{1}{\overline{\rho}A}\left[\frac{\partial}{\partial z}([M^u+M^d]\overline{\Psi}) - [\epsilon^u+\epsilon^d]\overline{\Psi} + \delta^u\Psi^u + \delta^d\Psi^d\right]. \qquad (5.4)$$

It can be shown that this equation is also valid for non-conserved variables, i.e. temperature or water mixing ratios.

5.3 Cloud model

The ensemble average updraft and downdraft properties in (5.4) are determined with the aid of a one-dimensional cloud model that consists of a classical steady-state plume convective updraft, and a corresponding steady-state plume convective downdraft. The cloud model is designed to represent shallow and deep convective clouds that are characterized by their respective cloud radius.

5.3.1 Key cloud levels

First, it is useful to define the model cloud and a certain number of important levels in the cloud that will be needed in the following discussion. As illustrated in Fig. 5.1 the model cloud extends upward from the lifting condensation level (LCL) of an air parcel with departure level DPL

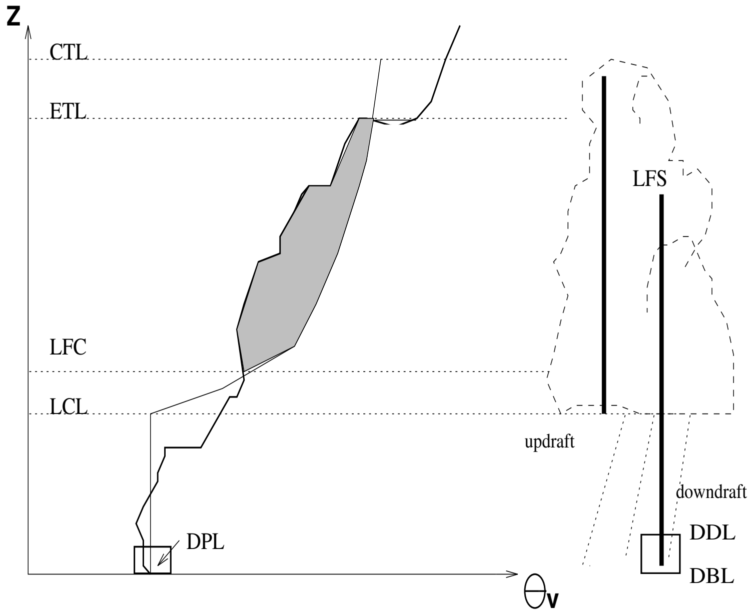

Figure 5.1: Environmental (thick solid line) and parcel sounding (thin solid line) of θ_v in a deep convective cloud. The convective available energy (CAPE) corresponds to the shaded area. The different key cloud levels are related to condensation and buoyancy. The updraft and downdraft regions are illustrated by the fat solid lines (the cloud is supposed to precipitate).

(DPL actually denotes a 60 hPa thick mixed layer) to the cloud top level (CTL). The level of free convection (LFC) is the level where the updraft becomes positively buoyant with respect to the environment, and the equilibrium temperature level (ETL) is the level where the buoyancy of the updraft redrops to zero. The convective available potential energy is defined as the positive area (from the LFC to the ETL) between the incloud virtual potential temperature sounding and the environmental sounding. The downdraft originates within the cloud at the level of free sink (LFS), and extends down to the downdraft base level (DBL). All downdraft mass is detrained over a fixed layer extending from DDL to DBL. Finally, note that the DPL and the DBL are of course not necessarily equal to the surface level, the present figure serving only as an example.
The following discussion of the different parts of the convection scheme is straightforward in the way that it closely follows the sequential structure of the scheme.

5.3.2 Trigger function

At present time, the physical processes initiating convection are not well understood. There is no general criterion that tells us when we should allow for convective overturning of the atmosphere; i.e. when we should allow a moist convective parcel to overcome the stable layer at cloud base and to have access to the CAPE that is stored aloft due to large scale forcing associated with e.g. midlatitude frontal systems, upper level jets or tropical waves. However, another important issue is the determination of the moist source layer for convection that will be lifted up and will finally determine the properties of the convective cloud (cloud top level, precipitation, etc.). It turns out that over the tropical ocean this initial moist layer corresponds to the 500-m deep boundary layer (Raymond 1995) and the most difficult problem is to locate the convection. However, in midlatitude convection, especially at night time, convection might root at upper atmospheric levels.

The numerical formalism is as follows. Starting from the ground level, we first construct an at least 60-hPa deep mixed layer with mean potential temperature $\overline{\theta}^{mix}$ and vapor mixing ratio $\overline{r}_v^{mix}$. Then this mixed air parcel is lifted without entrainment to its LCL. We directly determine the temperature at the LCL using an algorithm proposed by Davies-Jones (1983), and compute the pressure at the LCL as $P(\mathrm{LCL}) = P_{00}[T(\mathrm{LCL})/\theta^{mix}]^{C_{pd}/R_d}$, where P_{00} is the reference pressure. The air parcel is unstable with respect to moist convection if at the LCL

$$\overline{\theta}_v^{mix} - \overline{\theta}_v + \Delta T/\Pi \ > 0, \tag{5.5}$$

with θ_v the virtual potential temperature, and with the Exner function defined as $\Pi = (P/P_{00})^{R_d/C_{pd}}$. For shallow convection the temperature increment ΔT is simply set to 0.2 K. For deep convection ΔT is intended to crudely trigger/suppress convection as a function of grid-scale motion, where it is defined by $\Delta T = \pm c_w \ |\overline{w}|^{1/3}$, with c_w=6 (K m$^{-1/3}$ s$^{1/3}$). The sign of ΔT is equal to the sign of $\overline{w}$. As the large-scale vertical velocity varies quasi-linearly as a function of the grid size, it is normalized by $\overline{w}\sqrt{A}/\Delta x_{ref}$, with Δx_{ref} the 25-km reference grid space. Furthermore, we test if the air parcel is able to produce a sufficient cloud depth (at least 3 km for deep convection, and 500 m for shallow convection) by lifting the mixed layer parcel conserving the equivalent potential temperature $\theta_e(\overline{\theta}^{mix},\overline{r}_v^{mix})$, and searching for the intersection with the environmental saturated curve $\theta_{es}(\overline{T})$ (see e.g. Raymond 1995). If the air parcel is stable with respect to moist convection or if its probable cloud thickness is smaller than the specified value, the above procedure is repeated starting at the next higher 60-hPa mixed layer, and so on.

5.3.3 Updraft

Updrafts are assumed to originate at the DPL, entrain environmental air in the mixed layer, and then undergo undilute ascent up to the LCL. Starting from the LCL the thermodynamic characteristics of the updraft are computed assuming conservation (except from precipitation processes) of enthalpy or ”liquid water static energy” h_{il} and total water mixing ratio r_w

$$\begin{aligned} h_{il} &= C_{pm}T - L_v r_c - L_s r_i + (1 + r_w)gz \qquad (5.6)\\ r_w &= r_v + r_c + r_i. \qquad (5.7)\end{aligned}$$

where the specific heat of moist air is defined as $C_{pm} = C_{pd} + r_w C_{pv}$, g denotes the gravity constant, and r_v, r_c and r_i denote the maxing ratios of water vapor and non-precipitating cloud water/ice, respectively. A derivation of h_{il} is provided in the Appendix together with a definition of the various thermodynamic constants and functions used. The choice of h_{il} is motivated by the fact that it is linear, conserved in the presence of glaciation processes, and easily allows to switch on/off glaciation processes in the model.

The updraft computations are initiated at the LCL using $h_{il}^u = C_{pm}T(\mathrm{LCL}) + (1 + r_v^{mix})gz(\mathrm{LCL})$ and $r_w^u = r_v^{mix}$. The initial updraft mass flux is set to a unit value of $M^u(\mathrm{LCL}) = \overline{\rho}\, w_{\mathrm{LCL}}\, \pi R_0^2$, with a vertical velocity w_{LCL} of 1 m s^{-1} and an updraft radius R_0 of 1500 m for deep and 50 m for shallow convection - all the different parameter switches for deep and shallow convection are summarized in Table 5.1.

Hereafter we switch to the discretized equations on a vertical model grid k, with k increasing with height. The upstream operator is denoted by $\Delta\Psi = \Psi^{k+1} - \Psi^k$, layer mean values are denoted by the additional superscript m. If no superscript is indicated we simply mean the current model level k. Furthermore, it is convenient to denote the entrainment/detrainment rates ϵ and δ in mass

Table 5.1: Parameters and settings for deep and shallow convection

Parameter	**deep**	**shallow**
cloud radius (m)	1500	50
minimum cloud thickness (m)	3000	500
adjustment time (h)	$0.5 < \tau < 1$	3
ΔT (K) in ”trigger”	computed from $\overline{w}$	0.2
downdraft	yes	no
precipitation	yes	no

flux units kg s^{-1} instead of units mass flux per length as used in (5.2)-(5.4). In this notation the updraft mass flux as well as the updraft values of h_{il} and r_w change through mixing, detrainment and precipitation according to

$$\begin{aligned} \Delta M^u &= \epsilon^{um} - \delta^{um} && (5.8)\\ \Delta(M^u h_{il}^u) &= \epsilon^{um}\overline{h}_{il} - \delta^{um} h_{il}^u + M^{u(k+1)}(L_v \Delta r_r + L_s \Delta r_s) && (5.9)\\ \Delta(M^u r_w^u) &= \epsilon^{um}\overline{r}_w - \delta^{um} r_w^u - M^{u(k+1)}(\Delta r_r + \Delta r_s). && (5.10) \end{aligned}$$

The system (5.8)-(5.10) is solved together with a parameterization of microphysics and mixing that are described separately.

Microphysics and updraft velocity

The condensate mixing ratios r_c^u, r_i^u are deduced from h_{il}^u and r_w^u using a saturation adjustment, and allowing a gradual glaciation of the cloud in the temperature range between 268 and 248 K (see also Tao et al. 1989). The liquid and solid precipitation $\Delta r_r + \Delta r_s$ produced in each model layer is computed following Ogura and Cho (1973)

$$\Delta r_r + \Delta r_s = (r_c^{um} + r_i^{um})(1 - exp[-c_{pr}\Delta z / w^{um}]), \qquad (5.11)$$

where $c_{pr} = 0.02$ s^{-1} is a condensate to precipitation conversion factor. This formulation is essentially based on the fact that in high speed updrafts precipitation particles do not have time to form or are carried upward by the draft. The updraft vertical velocity w^u is evaluated with the aid of

$$\Delta((w^u)^2) = \frac{2g}{1+\gamma}\left[\frac{\theta_v^{um} - \overline{\theta}_v^m}{\overline{\theta}_v^m}\right]\Delta z - 2\frac{\epsilon^u}{M^u}(w^u)^2, \qquad (5.12)$$

where $\theta_v = \theta(1 + R_v/R_d\ r_v)/(1 + r_w)$, and $\gamma = 0.5$ is the virtual mass coefficient that approximately takes into account non-hydrostatic pressure perturbations (Kuo and Raymond 1980). The last term of the rhs of (5.12) accounts for zero environmental momentum. The vertical velocity is also used to compute the cloud top level CTL, which is defined as the level where $(w^u)^2$ becomes negative. Finally, the total precipitation flux produced by the updraft is simply given by

$$\mathrm{Pr} = \sum_{k=\mathrm{LCL}}^{k=\mathrm{CTL}} [\Delta r_r + \Delta r_s] M^u. \qquad (5.13)$$

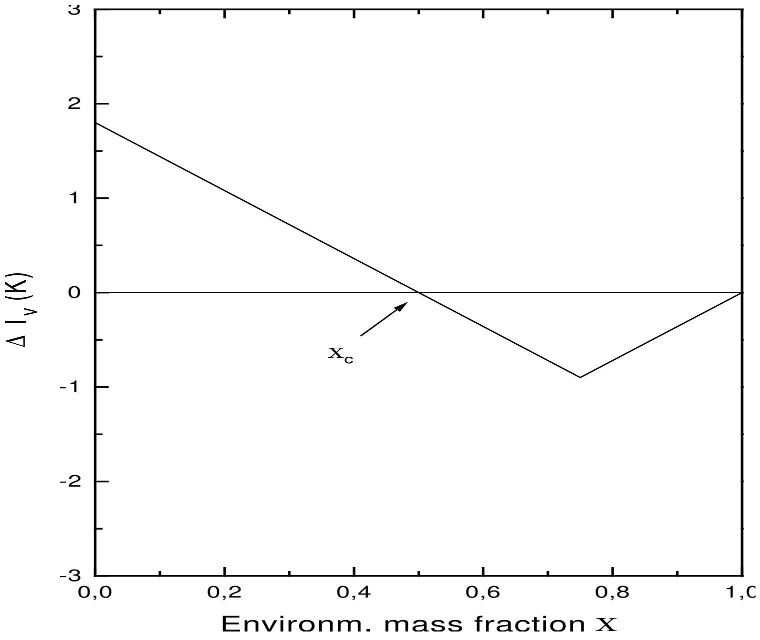

Figure 5.2: Plot of typical virtual temperature differences between updraft-environment mixtures and that of the environment as a function of the fraction of environmental mass in the mixtures.

Entrainment and detrainment

Unfortunately, the performance of a plume cloud model critically depends on the specification of updraft entrainment/detrainment rates which are functions of the cloud radius, and are generally assumed to be constant with height. We initially adopted the mixing formalism proposed by Kain and Fritsch (1990) where an ensemble of mixed parcels is generated, with positively buoyant parcels supposed to follow the cloudy updraft (entrain) and negatively buoyant parcels supposed to detrain. Denoting the fractional amount of environmental mass that just yields a neutrally buoyant mixture as χ_c, the net environmental entrainment rate and the updraft entrainment rate are given by

$$\begin{aligned} \epsilon^u &= \Delta M_t \int_0^{\chi_c} \chi \; f(\chi) d\chi && (5.14) \\ \delta^u &= \Delta M_t \int_{\chi_c}^1 (1-\chi) f(\chi) d\chi && (5.15) \\ \Delta M_t &= M^u c_{\rm etr} \Delta z / R_0, && (5.16) \end{aligned}$$

where ΔM_t with $c_{etr} = 0.2$ is the total rate at which mass enters the transition region between clear and cloudy air (Simpson 1983); $f(\chi)$ is a Gaussian type distribution satisfying $f(0) = f(1) = 0$ (Kain and Fritsch 1990).

The critical mixed fraction χ_c is solved for directly, knowing that the virtual temperature difference between updraft-environment mixtures and that of the unmixed environment varies linearly as a function of the environmental mass fraction χ (see Fig. 5.2). The zero crossing of this curve is evaluated from

$$\theta_v^{mix} - \overline{\theta}_v = 0 = \theta_v^u - \overline{\theta}_v - \frac{\theta_v^u - \theta_v^{mix}}{\chi} \chi_c \qquad (5.17)$$

so that χ_c is given by

$$\chi_c = \frac{\theta_v^u - \overline{\theta}_v}{\theta_v^u - \theta_v^{mix}}\chi; \quad \chi = 0.1; \quad 0 \leq \chi_c \leq 1; \tag{5.18}$$

we use a small value of 0.1 for χ which is supposed to be smaller than the critical value. θ_v^{mix} is determined as a function of h_{il}^{mix} and r_w^{mix}, where $h_{il}^{mix} = \chi\overline{h}_{il} + (1-\chi)h_{il}^u$; idem for r_w^{mix}. However, it turned out that in deep convective situations this mixing formulation often produced $\epsilon^u > \delta^u$ so that the convective mass flux always increased with height, and the upper-level mass flux was overestimated. Therefore, this mixing procedure was only retained for shallow convection. For deep convection we simply use vertically constant entrainment/detrainment rates with $\epsilon^u = \delta^u = 0.5\Delta M_t$.

Updraft flow summary

The updraft computations are an important part of the convection scheme as here we build up a characteristic precipitating cloud whose nominal mass flux is later modified by the closure assumption. The updraft computations can be summarized as follows:
1) Update CAPE for undilute ascent, i.e. assuming conservation of undilute θ_e at the LCL.
2) Estimate r_c^u and r_i^u at level $k+1$ setting $h_{il}^u(k+1) = h_{il}^u(k), r_w^u(k+1) = r_w^u(k)$, and applying a saturation adjustment procedure defined.
3) Compute $\theta_v^u(k+1)$ and square of vertical velocity using the just computed values of r_c^u and r_i^u in (5.12).
4) Compute precipitation produced in model layer using (5.11). Update total precipitation.
5) Update $r_c^u, r_i^u, h_{il}^u, r_w^u$ at level $k+1$ for precipitation.
6) Compute entrainment and detrainment rates at level $k+1$ using
7) Compute final values of updraft mass flux, h_{il}^u, r_w^u at level $k+1$ using (5.9)-(5.10).
8) Exit the updraft computations when the CTL is attained, i.e. when the updraft velocity becomes negative.
9) Adjust the updraft mass flux to reflect a linear decrease of the mass flux between the ETL and the CTL.

5.3.4 Downdraft

In contrast to the updraft computations where condensate production and glaciation processes are important and therefore h_{il} is a very convenient variable, the downdraft computations become simplified when using the equivalent potential temperature θ_e as it implicitly takes into account the evaporational cooling effect. The definition of θ_e is taken from Bolton (1980) and proved to be highly accurate

$$\theta_e = T(P_{00}/P)^{R_d/C_{pd}(1-0.28r_v)}\exp[(3374.6525/T - 2.5403)r_v(1+0.81r_v)]. \tag{5.19}$$

The downdraft is assumed to be driven by cooling through melting and evaporation of precipitation. It originates at the level of free sink (LFS), defined by the level of minimum environmental saturated θ_e between the LCL and the ETL. The initial values of the downdraft mass flux, θ_e and moisture at the LFS can be estimated as follows

$$M^d(LFS) = -(1 - \text{Pr}_{\text{eff}})M^u(LCL) \tag{5.20}$$

where the precipitation efficiency $\mathrm{Pr}_{\mathrm{eff}}$ is given as a function of wind shear and cloud base height (Zhang and Fritsch 1986). The initial humidity is obtained by mixing updraft and environmental air

$$r_w^d(\mathrm{LFS}) = \chi \overline{r}_w + (1-\chi) r_w^u; \quad \chi = (\theta_e^u - \overline{\theta}_{es})/(\theta_e^u - \overline{\theta}_e). \tag{5.21}$$

This definition of the mixed fraction gives a very smooth variation of χ, with a value that is close to χ_c defined in (5.18). According to (5.21) the value of θ_e^d at the LFS is set to its saturated environmental value corrected by melting effects, with the cooling due to melting estimated by $\Delta T_{\mathrm{melt}} = L_m/C_{ph}[r_w^u(\mathrm{LCL}) - r_w^u(\mathrm{CTL})]$. This method is motivated by the fact that the amount of downdraft mass flux is dependent on the total downdraft evaporation rate which is not known initially and is itself dependent on the magnitude of the melting effect. We know the amount of solid precipitation but we do not know the amount of ice that is evaporated in the downdraft.

The following equations are used to compute the downdraft properties starting from the LFS down to the downdraft base level (DBL) which is defined as the level where $\theta_e^d(\mathrm{LFS}) > \overline{\theta}_{\mathrm{es}}(\overline{\mathrm{T}})$.

$$\begin{aligned}
\epsilon^d &= -M^d(\mathrm{LFS}) c_{\mathrm{etr}} \Delta z / R_0; \quad k > \mathrm{DDL} && (5.22)\\
\delta^d &= 0; \qquad\qquad\qquad\qquad\quad k > \mathrm{DDL} && (5.23)\\
\Delta M^d &= \epsilon^d && (5.24)\\
\Delta(M^d \theta_e^d) &= \epsilon^d \overline{\theta}_e && (5.25)\\
\Delta(M^d r_w^d) &= \epsilon^d \overline{r}_w . && (5.26)
\end{aligned}$$

Note that M^d is negative but ϵ^d and δ^d are positive. All downdraft detrainment is assumed to occur over the 60 hPa deep layer DDL-DBL (Fig. 5.1). For the closure adjustment procedure we will need the values of h_{il}^d. As δ^d is zero everywhere apart from the detrainment layer, we only need to compute the values of h_{il}^d for this layer. It is computed from θ_e^d and r_w^d. The total downdraft evaporation rate is estimated using a specified value of 90% for the relative humidity. If the actual value of humidity in the downdraft in the detrainment layer is less than the specified value, water is evaporated to give the required value. If no water is evaporated, no downdraft is allowed and the downdraft mass flux is set to zero.

5.3.5 Closure

Finally, a closure assumption is needed to control the intensity of convection. Here we adopt a Fritsch Chappell type closure which is based on the assumption that all convective available potential energy (CAPE) in a grid element is removed within an adjustment period τ. For deep convection τ is set to the advective time period $\tau = \sqrt{A}/|\boldsymbol{v}|$, with $\boldsymbol{v}$ the mean horizontal wind vector between the LCL and the 500-hPa level, and is limited by 0.5 h $< \tau <$ 1 h. The upper limit roughly corresponds to one life cycle of a convective cloud. For shallow convection an adjustment time τ of 3 h is used. With the aid of the above presented cloud model we have already computed the initial guess updraft and downdraft mass fluxes and the corresponding entrainment/detrainment rates. Therefore, we are now able to compute the final convectively-adjusted environmental values (see also the main mass flux equations (5.4)) using a time integration over τ together with an iterative procedure

$$\overline{\Psi}^{(n+1)} = \overline{\Psi}^{(n)} + (\tau/m_t)\left[\begin{array}{l} - \quad \Delta(\tilde{M}^{(n)}\overline{\Psi}^{(n)}) - [\epsilon^{u(n)} + \epsilon^{d(n)}]\ \overline{\Psi}^{(n)} \\ + \quad \delta^{u(n)}\Psi^u + \delta^{d(n)}\Psi^d \end{array}\right] \tag{5.27}$$

$$\tilde{M} = \overline{\rho}\tilde{w}A; \quad \tilde{w} = \int (\partial\tilde{w}/\partial z) dz; \quad \left(\frac{\partial\tilde{w}}{\partial z}\right) = \frac{\epsilon^u + \epsilon^d - \delta^u - \delta^d}{m_t}, \tag{5.28}$$

where n denotes the iteration number, Ψ stands for either h_{il} or the various water species r_w, r_c, r_i. The total mass of the model layer is denoted by m_t, and $\tilde{M}$ is the compensating environmental mass flux. The esssential point of the present adjustment procedure is that only the environmental values $\Psi = h_{il}, r_w, r_c, r_i$ are updated and the mass fluxes are adjusted in the closure adjustment procedure, but no updraft or downdraft computations are repeated so that the updraft and downdraft values of the thermodynamic variables keep unchanged.
Now, computing the new environmental values of θ and r_v from $\overline{h}_{il}$ and $\overline{r}_w$ using (5.6)-(5.7), we can compute $\overline{\theta}_e$ and a new value of CAPE by using undilute parcel ascent

$$\mathrm{CAPE^{(n+1)}} \quad = \quad \int_{\mathrm{LCL}^{(n+1)}}^{\mathrm{ETL}} g \left[\frac{\overline{\theta}_e^{(n+1)}(\mathrm{DPL})}{\overline{\theta}_{es}^{(n+1)}} - 1 \right] dz, \tag{5.29}$$

where the new value LCL$^{(n+1)}$ is obtained from $\overline{\theta}_v^{(n+1)}$(DPL) by the same procedure as used in the trigger function. The use of the conserved variable $\overline{\theta}_e(DPL)$ instead of θ_v^u in (5.29) is motivated by the fact that this formulation allows to determine CAPE directly without executing additional updraft computations.
Then, at all model levels the updraft and downdraft mass fluxes as well as the entrainment/detrainment fluxes and the precipitation flux are multiplied by the adjustment factor

$$F_{adj}^{(n+1)} = F_{adj}^{(n)} \frac{\mathrm{CAPE}^{(0)}}{\mathrm{CAPE}^{(0)} - \mathrm{CAPE}^{(n+1)}}, \tag{5.30}$$

where $\mathrm{CAPE}^{(0)}$ is the initial value of CAPE. The above described procedure (5.27)-(5.30) is repeated until $\mathrm{CAPE}^{(n+1)} < 0.1\ \mathrm{CAPE}^{(0)}$. At the end of the adjustment procedure the final convective tendencies are simply evaluated as

$$\left.\frac{\partial\overline{\Psi}}{\partial t}\right|_{\mathrm{conv}} = (\overline{\Psi}^{(n)} - \overline{\Psi}^{(0)})/\tau, \tag{5.31}$$

where Ψ now stands for either θ, r_v, r_c, r_i.
A final remark concerns the conservation properties of the scheme, a point that is particularly important for long time or global applications. The scheme is designed to conserve mass and energy as can be verified numerically from the integral relationships

$$\int_0^{\mathrm{CTL}} \frac{(\epsilon^u + \epsilon^d - \delta^u - \delta^d)}{m_t} dz = 0 \tag{5.32}$$

$$\int_0^{\mathrm{CTL}} \left(\frac{\overline{\rho}}{\rho_l}\right) \frac{\partial \overline{r}_w}{\partial t}\bigg|_{\mathrm{conv}} dz = \frac{\mathrm{Pr}}{\rho_l A} \tag{5.33}$$

$$\int_0^{\mathrm{CTL}} \left(\frac{\overline{\rho}}{\rho_l}\right) \frac{\partial \overline{h}_{il}}{\partial t}\bigg|_{\mathrm{conv}} dz = L_v \frac{\mathrm{Pr}}{\rho_l A} \tag{5.34}$$

where ρ_l is the density of liquid water, and $\mathrm{Pr}\ \rho_l^{-1} A^{-1}$, is the adjusted surface precipitation flux in m s^{-1}.

5.4 Discussion

Our aim was to design a parameterization that incorporates the effects of the essential physics of moist convection while remaining as straightforward and numerically efficient as possible. In adhering to these guidelines, however, it is inevitable that numerous simplifications of real physical processes become necessary.

The limitations of a convective plume model to represent properties of a cloud ensemble are discussed in Warner (1970), Raymond and Blyth (1986), and Lin and Arakawa (1997). To limit these drawbacks, we also developed an ensemble version of the code, where the deep part can be called several times using different entrainment/detrainment rates (=different cloud radius), and different temperature/moisture perturbations for triggering. The resulting convective tendency is then the sum of the shallow part and the deep convective part (which is an average of the convective tendencies and mass fluxes of its individual ensemble members).

In the case of the present parameterization, an explicit dependence on grid-length is included in two places. First, grid-resolved vertical velocity, as it is used in the trigger function (see discussion related to (5)) is scaled as a linear function of grid length. Second, the convective time period is computed as the advective time period, based on the mean wind speed in the cloud layer and the model grid-length. This time period is constrained to be between 0.5 and 1 hour, however. In addition to these implicit sensitivities to horizontal resolution, certain physical processes have been neglected in the current parameterization. For example, convective transport of momentum is not yet included, but could be easily done using the scheme equations for passive tracers together with a pressure perturbation term (Kershaw and Gregory 1997) Also, we do not explicitly account for mesoscale transports that might give a substantial contribution to the mass flux at upper levels (Donner 1993; Betts 1997; Alexander and Cotton 1998), but the significance of this is largely unknown. This parameterization contains several parameters that are difficult to assess. However, extensive testing revealed minimal sensitivity to the values used for most of them, within a range of reasonable values. The most significant sensitivities appear in relation to specification of cloud radius (determining entrainment/detrainment), the precipitation efficiency (used to drive downdrafts), and to a lesser extent the adjustment time scale.

Finally, lets also mention a limitation that is related to the effects of convective downdrafts. In the atmosphere, convectively generated ”cold pools” often spread out over significant areas in the vicinity of thunderstorms, and the leading edge of this cold outflow can be a region of active generation of new convective cells. Since prognostic variables are represented as horizontally-averaged values in each layer within a grid-column, parameterization schemes introduce the effects of downdrafts as a mean cooling and drying of individual layers. When these stabilizing tendencies are introduced as a mean effect, parameterized convection may ”turn off” due to cooling and drying from parameterized downdrafts, whereas in reality only a portion of the total area represented by a grid element might experience intense downdraft cooling. Thus parameterization schemes may have a tendency to underpredict convective overturning at coarser resolutions. A possible solution for this problem would be to allow for partial coverage by downdraft outflow and appropriate subgrid-scale forcing associated with outflow propagation (Liang et al. 1998).

5.5 Appendix

5.5.1 Definition of latent and specific heats

The specific latent heats of vaporisation, sublimation and melting as a function of temperature are defined by

$$\begin{aligned} L_v(T) &= L_v(T_t) + (C_{pv} - C_l)(T - T_t) && (5.35)\\ L_s(T) &= L_s(T_t) + (C_{pv} - C_s)(T - T_t) && (5.36)\\ L_m(T) &= L_s(T) - L_v(T), && (5.37) \end{aligned}$$

with

$$T_t = 273.16; \quad L_v(T_t) = 2.5008 \times 10^6 \quad L_s(T_t) = 2.8345 \times 10^6, \qquad (5.38)$$

where T_t is given in K and where the specific heats for phase change are given in J kg^{-1}. The specific heat constants are defined as

$$C_{pv} = 4\ R_v; \quad C_l = 4.218 \times 10^3; \quad C_s = 2.106 \times 10^3, \qquad (5.39)$$

with R_v=461.525 J kg^{-1} K^{-1}. The gas constant and specific heat for dry air are defined as R_d=287.06 J kg^{-1} K^{-1} and $C_{pd} = 7/2R_d$.

5.5.2 Derivation of h_{il}

Following Dufour and van Mieghem (1975) an accurate and natural formulation of h_{il} can be derived from the enthalpy equation

$$C_{ph}dT - T(R_d + r_vR_v)d\ln P = d(L_vr_c + L_sr_i) - \left[r_c\frac{dL_v}{dT} + r_i\frac{dL_s}{dT}\right]dT, \qquad (5.40)$$

with $C_{ph} = C_{pd} + r_vC_{pv} + r_cC_l + r_iC_s$. Making use of the hydrostatic approximation and the relations (5.35)-(5.37), (5.40) can be integrated to obtain

$$h_{il} = C_{pm}T - L_vr_c - L_sr_i + (1 + r_w)gz, \qquad (5.41)$$

with $C_{pm} = C_{pd} + r_wC_{pv}$.

5.5.3 Definition of saturation mixing ratios

The saturation pressure for water vapor over liquid water and ice is derived from an integration of the Clausius-Clapeyron equation

$$e_{sl}(T) = exp\left[\alpha_l - \frac{\beta_l}{T} - \gamma_l \ln(T)\right] \tag{5.42}$$

$$e_{si}(T) = exp\left[\alpha_s - \frac{\beta_s}{T} - \gamma_s \ln(T)\right], \tag{5.43}$$

where

$$\alpha_l = \ln[e_s(T_t)] + \frac{\beta_l}{T_t} + \gamma_l \ln(T_t); \quad \beta_l = \frac{L_v(T_t)}{R_v} + \gamma_l T_t$$

$$\gamma_l = \frac{(C_l - C_{pv})}{R_v}, \tag{5.44}$$

and $e_s(T_t)$ =611.14 Pa. The corresponding coefficients for the saturation pressure over ice are obtained by simply replacing in (5.44) and (5.44) the index l (liquid) by the index s (solid) and by replacing L_v by L_s. Finally, the saturated water vapor mixing ratio is defined as $r_{vs}(T) = (m_v/m_d)(e_s(T)/P - e_s(T))$, with $m_v/m_d = R_d/R_v = 0.622$ the ratio of dry air to water vapor Mol mass.

5.5.4 Precipitation efficiency

Defining the windshear by

$$S = \frac{|\boldsymbol{v}(\mathrm{CTL}) - \boldsymbol{v}(\mathrm{LCL})|}{z(\mathrm{CTL}) - z(\mathrm{LCL})} \frac{|\boldsymbol{v}(\mathrm{CTL})| - |\boldsymbol{v}(\mathrm{LCL})|}{\big||\boldsymbol{v}(\mathrm{CTL})| - |\boldsymbol{v}(\mathrm{LCL})|\big|}, \tag{5.45}$$

with $\boldsymbol{v}$ the horizontal wind vector, the precipitation efficiency as a function of wind shear is expressed as

$$\mathrm{Pr}_{\mathrm{Sef}} = 1.591 - 0.639\, S + 0.0953\, S^2 - 0.00496\, S^3. \tag{5.46}$$

The precipitation efficiency as a function of cloud base height is given as

$$\begin{aligned} \mathrm{Pr}_{\mathrm{Zef}} = 0.967 \quad &- \quad 0.7 z_b + 1.62 \times 10^{-1} z_b^2 - 1.26 \times 10^{-2} z_b^3 \\ &+ \quad 4.27 \times 10^{-4} z_b^4 - 5.44 \times 10^{-6} z_b^5, \end{aligned} \tag{5.47}$$

with z_b the height difference between the LCL and the model surface level normalized by a cloud base height of 3280 m. Both $\mathrm{Pr}_{\mathrm{Sef}}$ and $\mathrm{Pr}_{\mathrm{Zef}}$ are limited to values between 0.4 and 0.92. Finally, the actual precipitation efficiency is given by $\mathrm{Pr}_{\mathrm{eff}} = 0.5(\mathrm{Pr}_{\mathrm{Sef}} + \mathrm{Pr}_{\mathrm{Zef}})$.

5.6 References

Alexander, G. D., and W. R. Cotton, 1998: The use of cloud resolving simulations of mesoscale convective systems to build a mesoscale parameterization scheme. *J. Atmos. Sci.*, **55**, 2137-2161.

Arakawa, A., and W. H. Schubert, 1974: Interaction of a cumulus cloud ensemble with the large-scale environment: Part I. *J. Atmos. Sci.*, **31**, 674-701.

Anthes, R. A., 1977: A cumulus parameterization scheme utilizing a one-dimensional cloud model. *Mon. Wea. Rev.*, **105**, 270-286.

Bechtold, P., E. Bazile, P. Mascart and E. Richard, 2001: A Mass flux convection scheme for regional and global models. *Quart. J. Roy. Meteor. Soc.*, **127**, 869-886.

Bechtold, P., J. L. Redelsperger, I. Beau, M. Blackburn, S. Brinkop, J. Y. Grandpeix, A. Grant, D. Gregory, F. Guichard, C. Hoff and E. Ioannidou, 2000: A GCSS model intercomparison for a tropical squall line observed during TOGA-COARE. II: Intercomparison of single-column models and a cloud-resolving model. *Quart. J. Roy. Meteor. Soc.*, **126**, 865-888.

Betts, A. K., and M. J. Miller, 1986: A new convective adjustment scheme. Part II: Single column tests using GATE wave, BOMEX, ATEX, and arctic air-mass data sets. *Quart. J. Roy. Meteor. Soc.*, **112**, 693-709.

———-, 1997: ‘The parameterization of deep convection’. In *”The physics and parameterization of moist atmospheric convection”* (Ed. R. K. Smith), *NATO ASI Series*, **505**, 255-279.

Bolton, D., 1980: The computation of equivalent potential temperature. *Mon. Wea. Rev.*, **108**, 1046-1053.

Bougeault, P., 1985: A simple parameterization of the large-scale effects of cumulus convection. *Mon. Wea. Rev.*, **113**, 2108-2121.

Bretherton, C. S., and P. K. Smolarkiewicz, 1989: Gravity waves, compensating subsidence and detrainment around cumulus clouds. *J. Atmos. Sci.*, **46**, 740-759.

Charney, J., and A. Eliassen, 1964: On the growth of the hurricane depression. *J. Atmos. Sci.,* **21,** 68-75.

Davies-Jones, R. P., 1983: An accurate theoretical approximation for adiabatic condensation temperature. *Mon. Wea. Rev.*, **111**, 1119-1121.

Donner, L. J., 1993: A cumulus parameterization including mass fluxes, vertical momentum dynamics, and mesoscale effects. *J. Atmos. Sci.*, **50**, 889-906.

————, C. J. Seman, and R. S. Hemler, 1999: Three dimensional cloud-system modeling of GATE convection. *J. Atmos. Sci.*, **56**, 1885-1912.

Dufour L., and J. van Mieghem, 1975: Thermodynamique de l’atmosphère. Institut Royal Météorologique de Belgique, 278 pp.

Emanuel, K. A., 1991: A scheme for representing cumulus convection in large-scale models. *J. Atmos. Sci.*, **48**, 2313-2335.

———-, 1997: The problem of convective moistening. In *”The physics and parameterization of moist atmospheric convection”* (Ed. R. K. Smith), *NATO ASI Series*, **505**, 447-462.

Fritsch, J. M., and C. F. Chappell, 1980: Numerical prediction of convectively driven mesoscale pressure systems. Part I: Convective parameterization. *J. Atmos. Sci.*, **37**, 1722-1733.

Fritsch, J. M., R. A. Houze, R. Adler, H. Bluestein, L. Bosart, J. Brown, F. Carr, C. Davies, R. H. Johnson, N. Junker, Y.-H. Kuo, S. Rutledge, J. Smith, Z. Toth, J. W. Wilson, E. Zipser, and D. Zrnic, 1998: Quantitative precipitation forecasting: Report of the eighth prospectus development team, U. S. weather research program. *Bull. Am. Meteorol. Soc.*, **79**, 285-299.

Gregory, D., and M. J. Miller, 1989: A numerical study of the parameterization of deep tropical convection. *Quart. J. Roy. Meteor. Soc.*, **115**, 1209-1241.

Gregory, D., and P. R. Rowntree, 1990: A mass-flux convection scheme with representation of cloud ensemble characteristics and stability dependent closure. *Mon. Wea. Rev.*, **118**, 1483-1506.

Grell, G. A., 1993: Prognostic evaluation of assumptions used by cumulus parameterizations. *Mon. Wea. Rev.*, **121**, 764-787.

Hu, Q., 1997: A cumulus parameterization based on a cloud model of intermittently rising thermals. *J. Atmos. Sci.*, **54**, 2292-2307.

Kain, J. S., and J. M. Fritsch, 1990: A one-dimensional entraining/detraining plume model and its application in convective parameterizations. *J. Atmos. Sci.*, **47**, 2784-2802.

———, and ———, 1993: Convective parameterization for mesoscale models: The Kain-Fritsch scheme. *Meteor. Monographs*, **46**, 165-170.

Kershaw, R., and D. Gregory, 1997: Parameterization of momentum transport by convection. Part I: Theory and cloud modelling results. *Quart. J. Roy. Meteor. Soc.*, **123**, 1133-1151.

Kuo, H. L., 1965: On formation and intensification of tropical cyclones through latent heat release by cumulus convection. *J. Atmos. Sci.*, **22**, 40-63.

———-, and W. H. Raymond, 1980: A quasi-one-dimensional cumulus cloud model and parameterization of cumulus heating and mixing effects. *Mon. Wea. Rev.*, **108**, 991-1009.

Kuo, Y.-H., J. F. Bresch, M.-D. Cheng, J. Kain, D. B. Parsons, W.-K. Tao and D.-L. Zhang, 1997: Summary of a mini workshop on cumulus parameterization for mesoscale models. *Bull. Am. Meteorol. Soc.*, **78**, 475-490.

Lin, C., and A. Arakawa, 1997: The macroscopic entrainment process of simulated cumulus ensemble. Part II: Testing the entraining-plume model *J. Atmos. Sci.*, **54**, 1027-1043.

Liang, Q., G. S. Young, and W. M. Frank, 1998: A convective wake parameterization scheme for use in general circulation models. *Mon. Wea. Rev.*, **126**, 456-469.

Mallet, I., J.-P. Cammas, P. Mascart and P. Bechtold, 1999: Effects of cloud diabatic heating on a FASTEX cyclone (IOP17) early development. *Quart. J. Roy. Meteor. Soc.*, **125**, 3415-3438.

Manabe, S., and R. Strickler, 1964: Thermal equilibrium of the atmopshere with a convective adjustment. *J. Atmos. Sci.*, **21**, 361-385.

Mapes, B. E., 1997: Equilibrium versus activation control of large-scale variations of tropical deep convection. In *”The physics and parameterization of moist atmospheric convection”* (Ed. R. K. Smith), *NATO ASI Series*, **505**, 321-358.

Moncrieff, M. W., D. Gregory, S. K. Krueger, J. L. Redelsperger, and W. K. Tao, 1997: GEWEX Cloud System Study (GCSS) working group 4: Precipitating convective cloud systems. *Bull. Am. Meteorol. Soc.*, **78**, 831-845.

Ogura, Y., and H.-R. Cho, 1973: Diagnostic determination of cumulus populations from large-scale variables. *J. Atmos. Sci.*, **30**, 1276-1286.

Ooyama, K., 1971: A theory on parameterization of cumulus convection. *J. Meteor. Soc. Japan*, **49**, 744-756.

Raymond, D. J., 1995: Regulation of moist convection over the West Pacific warm pool. *J. Atmos. Sci.*, **52**, 3945-3959.

———-, and A. M. Blyth, 1986: A stochastic mixing model for nonprecipitating clouds. *J. Atmos. Sci.*, **43**, 2708-2718.

Sun, W.-H., and P. A. Haines, 1996: Semi-prognostic tests of a new cumulus parameterization scheme for mesoscale modeling. *Tellus*, **48A**, 272-289.

Simpson, J., 1983: Cumulus clouds: interactions between laboratory experiments and observations as foundations for models. *Mesoscale Meteorology*, D. K. Lilly and T. Gal-Chen, Eds., Reidel, 399-412.

Slingo, J. M., M. Blackburn, A. K. Betts, R. Brugge, K. D. Hodges, B. J. Hoskins, M. J. Miller, L. Steenman-Clark, and J. Thuburn, 1994: Mean climate and transience in the tropics of the UGAMP GCM: Sensitivity to convective parameterization. *Q. J. R. Meteorol. Soc.*, **120**, 881-922.

Tao, W.-K., J. Simpson, and M. McCumber, 1989: An ice-water saturation adjustment. *Mon. Wea. Rev.*, **117**, 231-235.

Tiedtke, M., 1989: A comprehensive mass flux scheme for cumulus parameterization in large-scale models. *Mon. Wea. Rev.*, **117**, 1779-1800.

Wang, J., and D. A. Randall, 1996: A cumulus parameterization based on the generalized convective available potential energy. *J. Atmos. Sci.*, **53**, 716-727.

Warner, J., 1970: On steady-state one-dimensional models of cumulus convection. *J. Atmos. Sci.*, **27**, 1035-1040.

Xie, S.-C., K.-M. Xu, R. T. Cederwall, P. Bechtold, A. D. Del Genio, S. A. Klein, D. G. Cripe, S. J. Ghan, D. Gregory, S. F. Iacobellis, S. K. Krueger, U. Lohmann, J. C . Petch, D. A. Randall, L. D. Rotstayn, R. C. J. Somerville, Y. C. Sud, K. von Salzen, G. K. Walker, A. Wolf, J. J. Yio, G. J. Zhang and M. Zhang, 2002: Intercomparison and evaluation of cumulus parameterizations under summertime midlatitude continental conditions. *Q. J. R. Meteorol. Soc.*, **128**, 1095-1135.

Yanai, M., S. K. Esbensen, and J.-H. Chu, 1973: Determination of bulk properties of tropical cloud clusters from large-scale heat and moisture budgets. *J. Atmos. Sci.*, **30**, 611-627.

Zhang, D.-L., and J. M. Fritsch, 1986: Numerical simulation of the meso-β scale structure and evolution of the 1977 Johnstown flood. Part I: Model description and verification. *J. Atmos. Sci.*, **43**, 1913-1943.

Chapter 6

Microphysical Schemes for Warm Clouds

Contents

Three microphysical schemes for warm clouds are implemented into Meso-NH. The most simple scheme is the Kessler one, a one-moment scheme that prognoses mixing ratio of cloud and rain water. The two others are some two-moment schemes that predicts the mixing ratio and the concentrations of cloud and rain drops. The C2R2 scheme is the most general one while the KHKO scheme is designed for stratocumulus.

6.1 Kessler scheme

6.1.1 Equations

We note r_v, r_c, and r_r the water vapor, cloud water and rainwater mixing ratios, as defined in MESO-NH. For any constituent, r is the mass of the constituent divided by the reference mass of dry air.[1] The consevation equations for these quantities are written:

$$\frac{d}{dt}(\rho_{dref} r_v) = \rho_{dref}(P_{RE} - P_{CON}) \tag{6.1}$$

$$\frac{d}{dt}(\rho_{dref} r_c) = \rho_{dref}(-P_{RA} - P_{RC} + P_{CON}) \tag{6.2}$$

$$\frac{d}{dt}(\rho_{dref} r_r) = \rho_{dref}(P_{RA} + P_{RC} - P_{RE} + P_{RS}) \tag{6.3}$$

where P designates the sources and where the subscripts CON, RE, RA, RC and RS respectively refer to the following processes: evaporation/condensation, rain evaporation, accretion of cloud droplets by raindrops, conversion of cloud droplets into raindrops (autoconversion), and rain sedimentation. Condensation/evaporation is a very fast process, it cannot be computed explicitly and is obtained through an implicit saturation adjustment procedure, taking subgrid-scale processes into account (see Chapter on the sub-grid condensation schemes). All others terms are computed explicitly.

---

[1] Notice that $\rho_{dref} r = \rho_d \tilde{r}$ where $\tilde{r}$ is the usual mixing ratio i.e. the mass of the constituent divided by the mass of dry air.

6.1.2 Raindrops characteristics

Distribution

Raindrops are assumed to follow a Marshall-Palmer distribution. The number of raindrops whose diameter lies in the interval D and $D + dD$ is given by:

$$N(D)dD = N_0 \exp(-\lambda D)dD \tag{6.4}$$

Observations for different types of rain show a range of values for N_0 from $0.4\ 10^7$ to $3.5\ 10^7$ m^{-4}. $N_0 = 10^7$ m^{-4} is a value frequently used.
The λ parameter is obtained from

$$\rho_{dref} r_r = \int_0^\infty \frac{\pi}{6}\rho_{lw} D^3 N_0 \exp(-\lambda D)dD = \frac{\pi \rho_{lw} N_0}{\lambda^4}, \tag{6.5}$$

which leads to

$$\lambda = \Big(\frac{\pi \rho_{lw} N_0}{\rho_{dref} r_r}\Big)^{\frac{1}{4}}. \tag{6.6}$$

Fall velocity

The terminal fall velocity for a raindrop of diameter D is expressed as

$$V(D) = \big(\frac{\rho_{00}}{\rho_{dref}}\big)^\alpha a D^b, \tag{6.7}$$

with $\alpha = 0.4$, $a = 842$ m$^{0.2}$/s and $b = 0.8$, ρ_{00} being the air density at the reference pressure level P_{00}. This parameterization follows Liu and Orville (1969) and includes the effect of mean density variation as suggested by Foote and Du Toit (1969).
The rain terminal fall velocity is then given by

$$V_T \rho_{dref} r_r = \int_0^\infty \frac{\pi}{6}\rho_{lw} D^3 V(D) N(D) dD, \tag{6.8}$$

which leads to

$$V_T = \frac{a}{6}\big(\frac{\rho_{00}}{\rho_{dref}}\big)^\alpha \frac{\Gamma(b+4)}{\lambda^b}, \tag{6.9}$$

or

$$V_T = \frac{a}{6}\Gamma(b+4)\big(\frac{\rho_{00}}{\rho_{dref}}\big)^\alpha \big(\frac{\rho_{dref} r_r}{\pi \rho_{lw} N_0}\big)^{\frac{b}{4}}. \tag{6.10}$$

6.1.3 Explicit sources

Autoconversion

The sole rainwater initiation mechanism is the autoconversion process which is parameterized according to Kessler (1969). The Kessler rate relies on intuitive considerations: the autoconversion rate increases linearly with the cloud water content $(\rho_{dref} r_c)$ but cloud conversion does not occur below a threshold value q_{crit}.

$$P_{RC} = k\ \max(r_c - \frac{q_{crit}}{\rho_{dref}}, 0) \tag{6.11}$$

The parameters k and q_{crit} are usually set to 10^{-3} s^{-1} et 0.5 g/m^3.
In the code P_{RC} is written as:

$$P_{RC} = C1_{RC} Max(r_c - \frac{C2_{RC}}{\rho_{dref}}, 0) \tag{6.12}$$

with $C1_{RC} = k$ and $C2_{RC} = q_{crit}$.

Accretion

Once embryonic precipitation particles are formed, rainwater mixing ratio growth occurs primarily by accretion of cloud water in the form

$$P_{RA} = \int_0^\infty \frac{\pi}{4} D^2 V(D) E r_c N(D) dD, \tag{6.13}$$

where E is the collision efficiency (here taken equal to 1). After integration,

$$P_{RA} = \frac{\pi}{4} a N_0 (\frac{\rho_{00}}{\rho_{dref}})^\alpha r_c \frac{\Gamma(b+3)}{\lambda^{b+3}}. \tag{6.14}$$

After replacing λ,

$$P_{RA} = \frac{\pi}{4} a N_0 (\frac{\rho_{00}}{\rho_{dref}})^\alpha r_c \Gamma(b+3) \big(\frac{\rho_{dref} r_r}{\pi \rho_{lw} N_0}\big)^{\frac{b+3}{4}}. \tag{6.15}$$

In the code P_{RA} is written as:

$$P_{RA} = C_{RA} (\rho_{dref})^{C'_{RA} - \alpha} r_c (r_r)^{C'_{RA}} \tag{6.16}$$

with

$$C_{RA} = \frac{\pi}{4} a N_0 (\rho_{00})^\alpha \Gamma(b+3) \big(\frac{1}{\pi \rho_{lw} N_0}\big)^{\frac{b+3}{4}}$$

and

$$C'_{RA} = \frac{b+3}{4}$$

The accretion and autoconversion sources are limited by the amount of available cloud water. In the case where both processes are simultaneously operating, accretion is computed first.

Rain evaporation

According to Pruppacher and Klett (1978, p 420), the evaporation rate of a drop of diameter D is given by

$$D \frac{dD}{dt} = \frac{4 S \bar{f}}{\rho_{lw} A}, \tag{6.17}$$

where $\bar{f}$ is a ventilation factor and

$$S = \frac{r_{vs} - r_v}{r_{vs}}, \tag{6.18}$$

$$A = \frac{R_v T}{e_s(T) D_v} + \frac{L_v(T)}{k_a T} (\frac{L_v(T)}{R_v T} - 1) \tag{6.19}$$

$$\simeq \frac{R_v T}{e_s(T) D_v} + \frac{L_v(T)^2}{k_a R_v T^2}. \tag{6.20}$$

r_{vs} is the saturated vapor mixing ratio, D_v is the diffusivity of water vapor in air and k_a is the heat conductivity of air. For simplicity, D_v and k_a are taken constants: $D_v = 2.26\ 10^{-5}$ m^2/s and $k_a = 24.3\ 10^{-3}$ J/(msK).
e_s is the saturation vapor pressure and is computed according to

$$e_s(T) = \exp\big(\alpha_w - \frac{\beta_w}{T} - \gamma_w \ln(T)\big), \tag{6.21}$$

with

$$\begin{aligned} \alpha_w &= \ln(e_s(T_t)) + \frac{\beta_w}{T_t} - \gamma_w \ln(T_t), && (6.22)\\ \beta_w &= \frac{L_v(T_t)}{R_v} + \gamma_w T_t, && (6.23)\\ \gamma_w &= \frac{C_l - C_{pv}}{R_v}. && (6.24) \end{aligned}$$

L_v is the latent heat of vaporization and is computed according to

$$L_v(T) = L_v(T_t) + (C_{pv} - C_l)(T - T_t). \tag{6.25}$$

The ventilation factor $\bar{f}$ is given by

$$\bar{f} = 1 + F(Re)^{0.5}, \tag{6.26}$$

where Re is the Reynolds number which can be expressed as

$$Re = \frac{V(D)D}{\nu}, \tag{6.27}$$

ν being the air kinematic viscosity which is here assumed to be constant: $\nu = 0.15\ 10^{-4}$ kg/(ms).
F is a ventilation coefficient taken equal to 0.22.
After replacing (6.7) and (6.27) in (6.26), one gets

$$\bar{f} = 1 + F\big[\big(\frac{\rho_{00}}{\rho_{dref}}\big)^{\alpha}\frac{aD^{b+1}}{\nu}\big]^{0.5}. \tag{6.28}$$

The integration of (6.17) over the rain drop spectrum leads to the expression of the evaporation source

$$P_{RE} = \frac{1}{\rho_{dref}}\int_0^{+\infty}\frac{2\pi S\bar{f}}{A}DN(D)dD. \tag{6.29}$$

After replacing $\bar{f}$,

$$P_{RE} = \frac{2\pi S N_o}{A}\frac{1}{\rho_{dref}}\big[\frac{1}{\lambda^2} + F\big(\frac{\rho_{00}}{\rho_{dref}}\big)^{\alpha/2}\big(\frac{a}{\nu}\big)^{1/2}\frac{\Gamma(\frac{b+5}{2})}{\lambda^{\frac{b+5}{2}}}\big], \tag{6.30}$$

or

$$P_{RE} = \frac{2\pi S N_o}{A}\frac{1}{\rho_{dref}}\big[\big(\frac{\rho_{dref} r_r}{\pi\rho_{lw}N_o}\big)^{\frac{1}{2}} + F\big(\frac{\rho_{00}}{\rho_{dref}}\big)^{\alpha/2}\big(\frac{a}{\nu}\big)^{1/2}\Gamma\big(\frac{b+5}{2}\big)\big(\frac{\rho_{dref} r_r}{\pi\rho_{lw}N_o}\big)^{\frac{b+5}{8}}\big]. \tag{6.31}$$

In the code P_{RE} is written as

$$P_{RE} = \frac{S}{A}\big[C1_{RE}(\rho_{dref})^{-\frac{1}{2}}(r_r)^{\frac{1}{2}} + C2_{RE}(\rho_{dref})^{C'_{RE}-1-\alpha/2}(r_r)^{C'_{RE}}\big], \tag{6.32}$$

with

$$C1_{RE} = 2\pi N_o(\frac{1}{\pi\rho_{lw}N_o})^{\frac{1}{2}}$$

$$C2_{RE} = 2\pi N_o F\big(\rho_{00})^{\alpha/2}(\frac{a}{\nu})^{1/2}\Gamma(\frac{b+5}{2})\big(\frac{1}{\pi\rho_{lw}N_o})^{\frac{b+5}{8}}\big)$$

$$C'_{RE} = \frac{b+5}{8}$$

The rain evaporation source is limited by the amount of available rainwater.

Rain sedimentation

The sedimentation rate is given by

$$P_{RS} = \frac{1}{\rho_{dref}}\frac{\partial}{\partial z}\int_0^\infty N(D)V(D)\frac{\pi}{6}\rho_{lw}D^3V(D)N(D)dD \tag{6.33}$$

$$= \frac{1}{\rho_{dref}}\frac{\partial}{\partial z}(V_T\rho_{dref}r_r). \tag{6.34}$$

In the code, P_{RS} is written as

$$P_{RS} = \frac{1}{\rho_{dref}}\frac{\partial}{\partial z}\big[C_{RS}(\rho_{dref})^{C'_{RS}-\alpha}(r_r)^{C'_{RS}}\big], \tag{6.35}$$

with

$$C_{RS} = \frac{a}{6}\Gamma(b+4)(\rho_{00})^{\alpha}\big(\frac{1}{\pi\rho_{lw}N_0}\big)^{\frac{b}{4}},$$

$$C'_{RS} = \frac{4+b}{4}.$$

In order to maintain stability, the rain sedimentation source is computed with a time splitting technique and with an upstream differencing scheme. The small time step used for this computation is determined from the CFL stability criterion based on a maximum raindrop fall velocity V_{TRmax} of 7 m s^{-1}.

The sedimentation rate can be alternatively calculated using a Probability Density Function (PDF) -based approach. A general description of the method is done in Bouteloup et al. (2011). The sedimentation rate is given by

$$P_{RS} = \frac{1}{\rho_{dref}}\frac{\partial}{\partial z}F_r \tag{6.36}$$

where F_r is the sedimentation flux. The sedimentation flux is computed from the top to the bottom of the atmosphere following

$$F_r(j) = P_1\frac{\Delta z}{\Delta t}\rho_{dref}r_r + P_2F_r(j-1) \tag{6.37}$$

Δt is the time step and Δz the thickness of the layer. P_1 and P_2 are computed as in Bouteloup et al. (2011) in the case where the PDF of the fall speeds of the drops is a simple step function

$$P_1 = \min\left(1, \frac{V_{T1}\Delta t}{\Delta z}\right) \tag{6.38}$$

$$P_2 = \max\left(0, 1 - \frac{\Delta z}{V_{T2}\Delta t}\right) \tag{6.39}$$

V_{T1} and V_{T2} are the terminal velocities of the two groups of drops. The first one is computed using equation (6.10) and r_r of the level j. V_{T2} is computed with the same equation but using a mixing ratio representative of the incoming flux

$$r'_r = \frac{\Delta t}{\rho_{dref}\Delta z} F_r(j-1) \tag{6.40}$$

This method is unconditionally stable and avoids the use of a time splitting technique.

6.1.4 Implicit sources

Once the explicit sources are computed, the condensation/evaporation rate is obtained through a saturation adjustment procedure following Langlois (1973). If T^* and r_v^* are the temperature and vapor mixing ratio obtained after adding the explicit sources, we seek the zero-crossing of $F(T)$, defined as

$$F(T) = (T - T^*) + \frac{L_v(T)}{C_{ph}}(r_{vs}(T) - r_v^*). \tag{6.41}$$

To obtain a rapidly convergent algorithm, Langlois suggests to use a generalized Newton-Raphson procedure which employs the first and second derivatives of F:

$$T \simeq T^* - \frac{F(T^*)}{F'(T^*)}\left[1 + \frac{F(T^*)F''(T^*)}{2F'^2(T^*)}\right]. \tag{6.42}$$

The saturated vapor mixing ratio is given by

$$r_{vs}(T) = \frac{\epsilon e_s(T)}{p - e_s(T)}, \tag{6.43}$$

where $\epsilon = M_v/M_d$.
According to (6.21),

$$e'_s(T) = \left(\frac{\beta_w}{T^2} - \frac{\gamma_w}{T}\right)e_s(T) = A(T)e_s(T). \tag{6.44}$$

r'_{vs} is then given by

$$r'_{vs} = A(T)r_{vs}(T)\left(1 + \frac{r_{vs}(T)}{\epsilon}\right). \tag{6.45}$$

It follows:

$$T = T^* - \Delta_1\left(1 + \frac{1}{2}\Delta_1\Delta_2\right), \tag{6.46}$$

with

$$\Delta_1 = \frac{F(T^*)}{F'(T^*)} = \frac{L_v(T)}{C_{ph} + L_v(T) r'_{vs}(T^*)} \left[r_{vs}(T^*) - r_v^* \right], \tag{6.47}$$

$$\Delta_2 = \frac{F''(T^*)}{F'(T^*)} = \frac{L_v(T) r'_{vs}(T^*)}{C_{ph} + L_v(T) r'_{vs}(T^*)} \left[\frac{A'(T^*)}{A(T^*)} + A(T^*) + \frac{2 r_{vs}(T^*)}{\epsilon} \right], \tag{6.48}$$

and

$$A(T) = \frac{\beta_w}{T^2} - \frac{\gamma_w}{T}, \tag{6.49}$$

$$A'(T) = -\frac{2\beta_w}{T^3} + \frac{\gamma_w}{T^2}. \tag{6.50}$$

$$\tag{6.51}$$

In the above derivation, the variations of L_v with respect to T are ignored, being considered much smaller than the variations of r_{vs}. Langlois shows that with this procedure, iteration is unnecessary. The condensation/evaporation rate is then computed as:

$$P_{CON} = -\Delta_1 (1 + \frac{1}{2}\Delta_1 \Delta_2) \frac{C_{ph}}{L_v(T)} \frac{1}{2\Delta t} \tag{6.52}$$

In the case of evaporation (condensation), P_{CON} is limited by the amount of available cloud water (water vapor).

6.1.5 Global correction for negative values

The microphysical sink/sources are computed in such a way they never return negative values for r_v, r_c, or r_r. However, following the user's choice, the advection scheme can be not positive definite. It could be therefore necessary to remove all the negative mixing ratio values before applying the microphysical calculations. This is currently done inside the microphysical scheme, by a global filling algorithm based on a multiplicative method (Rood 1987). The negative values of the mixing ratio source distribution found are corrected (i.e set equal to zero). The total mass of the corrected distribution is calculated. Then the corrected distribution is mutiplied grid point by grid point by the ratio of the mass of the original distribution to the mass of the corrected distribution.

6.1.6 Practical implementation

The microphysical constants (N_o, a, b, α, $C1_{RC}$, $C2_{RC}$, C_{RA}, C'_{RA}, D_v, k_a, $C1_{RE}$, $C2_{RE}$, C'_{RE}, C_{RS}, C'_{RS} and V_{TRmax}) are set up in routine INI_CLOUD called during the initialization process. During the model run, the computations related to the resolved cloud and rain parameterization are monitored by the routine RESOLVED_CLOUD. When entering RESOLVED_CLOUD, the source array ψS of a variable ψ contains

$$\frac{\hat{\rho}\psi^{t-1}}{2\Delta t} + \sum_i S_i(\hat{\rho}\psi^t)$$

where S_i designate the previously computed tendencies (i.e. advection, numerical diffusion, turbulence, ...). ψS can be interpreted as a guess of $\hat{\rho}\psi^{t+1}/2\Delta t$. RESOLVED_CLOUD computes the microphysical tendencies and returns updated values of the source arrays affected by the explicit cloud and rain parameterization i.e. θS, $r_v S$, $r_c S$, and $r_r S$. The main steps of the scheme are the following

- The negative mixing ratios sources (r_vS, r_cS, and r_rS) are corrected according to the global filling algorithm described in the previous subsection.
- The θ, r_v, r_c, and r_r sources are divided by $\hat{\rho}$ to minimize computations in this section.
- Routine SLOW_TERMS is called and proceeds to the computation of the explicit sources:
  - Computes the rain sedimentation source P_{RS} and updates the rain source [$r_rS = r_rS + P_{RS}$].
  - Computes the accretion source P_{RA}, limits the accretion source by the amount of cloud water available at this stage [$P_{RA} = Min(P_{RA}, r_cS)$] and updates the cloud water and rainwater sources [$r_cS = r_cS - P_{RA}$ and $r_rS = r_rS + P_{RA}$].
  - Computes the autoconversion source P_{RC}, limits the autoconversion source by the amount of cloud water available at this stage [$P_{RC} = Min(P_{RC}, r_cS)$] and updates the cloud water and rainwater sources [$r_cS = r_cS - P_{RC}$ and $r_rS = r_rS + P_{RC}$].
  - Computes the rain evaporation source P_{RE}, limits the rain evaporation source by the amount of rainwater available at this stage [$P_{RE} = Min(P_{RE}, r_rS)$] and updates the water vapor, rainwater, and potential temperature sources [$r_vS = r_vS + P_{RE}$, $r_rS = r_rS - P_{RE}$ and $\theta S = \theta S - P_{RE}L_v/(\pi_{ref}C_{ph})$].
- Routine FAST_TERMS is called and performs the implicit saturation adjustment:
  - Computes the condensation/evaporation source P_{CON}, limits this source by the amount of cloud water (water vapor) available at this stage in the case of evaporation (condensation) [$P_{CON} = Min(P_{CON}, r_vS)$ or $P_{CON} = Min(P_{CON}, r_cS)$], and updates the water vapor, cloud water, and potential temperature sources [$r_vS = r_vS - P_{CON}$, $r_cS = r_cS + P_{CON}$ and $\theta S = \theta S + P_{CON}L_v/(\pi_{ref}C_{ph})$].
- The θ, r_v, r_c, and r_r sources are multiplied by $\hat{\rho}$ to go back to the original tendencies.

6.1.7 Available options and summary of the ajustable constants

According to the value of the CLOUD parameter given in namelist (see the Meso_NH user's guide), the one-moment microphysical scheme for warm clouds can be used in three different ways:

- CLOUD = 'NONE' : no microphysics, the water vapor (if present) is computed as a passive tracer,
- CLOUD = 'REVE' : only reversible processes are considered, no rain is generated (i.e the call to SLOW_TERM is by-passed),
- CLOUD = 'KESS' : the full scheme is operating.

Some others parameters might be reasonably modified by the user in routine INI_CLOUD. These are:
N_o the Marshall-Palmer distribution parameter,
a, b, and α the parameters used in the raindrop fall velocity expression,
$C1_{RC}$ and $C2_{RC}$, the autoconversion time constant and threshold,
V_{TRmax}, the maximum raindrop fall velocity used to ensure stability of the sedimentation computation.

6.2 The two-moment microphysical scheme for warm clouds

6.2.1 Purpose

This section describes the warm bulk microphysical scheme hereafter called C2R2 that predicts the concentration and the mixing ratio of both cloud droplets and rain drops. The salient feature of the scheme is the explicit incorporation of aerosol characteristics in the activation parameterization (a major sink in the big sized aerosol budget). The C2R2 scheme contains also a revised analysis of the coalescence terms that lead to a more reliable formation of the rain drops. The explicit evolution of the droplet concentration in C2R2 makes the scheme attractive for several topics such as the cloud chemistry and the radiative transfer. On the other side, the prognostic rain drop concentration provides a better description of the big precipitating drops which are a critical issue for an accurate modeling of either light drizzle or heavy showers.

The C2R2 scheme aims to extend the domain of applicability of crude bulk schemes like the Kessler scheme, for small cloud scale problems where generally expensive bin microphysical schemes are recommended. The scheme opens also an interesting field area by linking the cloud microphysical properties to the aerosol load in a rather simple way. The development of a similar two-moment approach to describe the microphysical evolution of cold clouds, is underway.

6.2.2 Introduction to the ”rain_C2R2” code

It is customary in bulk microphysical schemes to consider two modes around which liquid water is distributed thus providing a natural partition between cloud and rain water. These two modes are characterized by an equivalent mixing ratio (mass of condensate scaled by the mass of dry air) but by very different number concentrations from a few tens or hundreds per cubic centimeter for the cloud droplets down to a few units or tens per liter for the raindrops.

The present scheme assumes that each mode follows a generalized gamma distribution, so the droplet/drop size distributions are described by the normalized form:

$$n_i(D) = N_i \frac{\alpha_i}{\Gamma(\nu_i)} \lambda_i^{\alpha_i \nu_i} D^{\alpha_i \nu_i - 1} \exp\big(-(\lambda_i D)^{\alpha_i}\big) \tag{6.53}$$

where $\Gamma(x)$ is the gamma function (see Press *et al.* (1992) for the coding) and where the index $i \in [c, r]$ stands for cloud or rain, respectively. Our strategy is to predict only two of the most significant moments of (6.53) that possess a clear physical meaning, namely the zeroth N_i and third order moments $r_i = (1/\rho_a) \int_0^\infty (\pi/6) \rho_w D^3 n_i(D) dD$. As these two moments are determined from (6.53), the variable slope parameter λ_i can be deduced from

$$\lambda_i = \left(\frac{\pi}{6} \rho_w \frac{\Gamma(\nu_i + 3/\alpha_i)}{\Gamma(\nu_i)} \frac{N_i}{\rho_a r_i} \right)^{1/3} \tag{6.54}$$

whereas the remaining parameters α_i and ν_i that are mostly related to the spectral breadth of (6.53), are held fixed for the moment. Equation (6.54) is an application of a general formula to compute the p-moment of (6.53), that is

$$\int_0^\infty D^p n_i(D) dD = \frac{N_i}{\lambda_i^p} \frac{\Gamma(\nu_i + p/\alpha_i)}{\Gamma(\nu_i)} = N_i M_i(p). \tag{6.55}$$

6.2.3 The bulk microphysical scheme

System of equation

The continuity equations of the condensed phases, described in terms of concentration and mixing ratio, are written in symbolic form as follows:

$$\frac{\partial N_c}{\partial t} = \sum \frac{\partial N_c}{\partial t}\Big|_{NMT} + CVHENC - CCACCR - CCSCOC \qquad (7.93a)$$

$$\frac{\partial r_c}{\partial t} = \sum \frac{\partial r_c}{\partial t}\Big|_{NMT} + RVHENC + RVCONC - RCAUTR - RCACCR \qquad (7.93b)$$

$$\frac{\partial N_r}{\partial t} = \sum \frac{\partial N_r}{\partial t}\Big|_{NMT} + CCAUTR - CRSCOR - CSEDR \qquad (7.93c)$$

$$\frac{\partial r_r}{\partial t} = \sum \frac{\partial r_r}{\partial t}\Big|_{NMT} + RCAUTR + RCACCR - RREVAV - RSEDR \qquad (7.93d)$$

In addition to (7.93a-d), an equation of conservation for N_a, the number concentration of the activated Cloud Condensation Nuclei (CCN),

$$\frac{\partial N_a}{\partial t} = \sum \frac{\partial N_a}{\partial t}\Big|_{NMT} + CVHENC. \qquad (6.58)$$

is introduced to keep track of the CCN upon which cloud droplets have been already activated (see also the diagram of Fig. 6.1 which summarizes the scheme). The system is closed by expressing the conservation of the water vapor mixing ratio r_v and of the dry potential temperature θ:

$$\frac{\partial r_v}{\partial t} = \sum \frac{\partial r_v}{\partial t}\Big|_{NMT} + RREVAV - RVCONC - RVHENC \qquad (7.95a)$$

$$\frac{\partial \theta}{\partial t} = \sum \frac{\partial \theta}{\partial t}\Big|_{NMT} + \frac{L_v}{\Pi C_{ph}}\Big(RVCONC - RREVAV\Big) \qquad (7.95b)$$

In (7.93a)-(7.95b), the subscript $_{NMT}$ refers to Non-Microphysical Tendencies (advection, turbulence, numerics and other physical processes) while the meaning of the other symbols, given in Table 6.1, is detailed in the following section. A list of symbols is provided in the appendix and the coefficients appearing in the next formula are expressed in SI units unless specified.

CCN activation (CVHENC) and reversible condensation/evaporation of droplets (RVCONC)

The CCN activation and the condensation growth of cloud droplets are the dominant processes affecting distinctly the number concentration (N_c) and the mixing ratio (r_c) of cloud liquid water at the early stage of the cloud lifetime. These processes are difficult to model explicitly because they depend upon the maximum (CCN activation) and mean (condensation) local supersaturation values $s_{v,w}$ in contact with the CCN and the droplets. This quantity is not generally well captured in cloud models because its scale is highly variable and because the activation process results from an unstable thermodynamical equilibrium at short timescales in competition with the condensation growth that just tends to absorb any excess of supersaturation.
The parameterization of the CCN activation follows the diagnostic and integral approach of Twomey (1959) as improved by Cohard et al. (1998) where CCN activation spectra are expressed in the following functional form:

$$N_{CCN} = C s_{v,w}^k F(\mu, \frac{k}{2}, \frac{k}{2} + 1; -\beta s_{v,w}^2). \qquad (6.61)$$

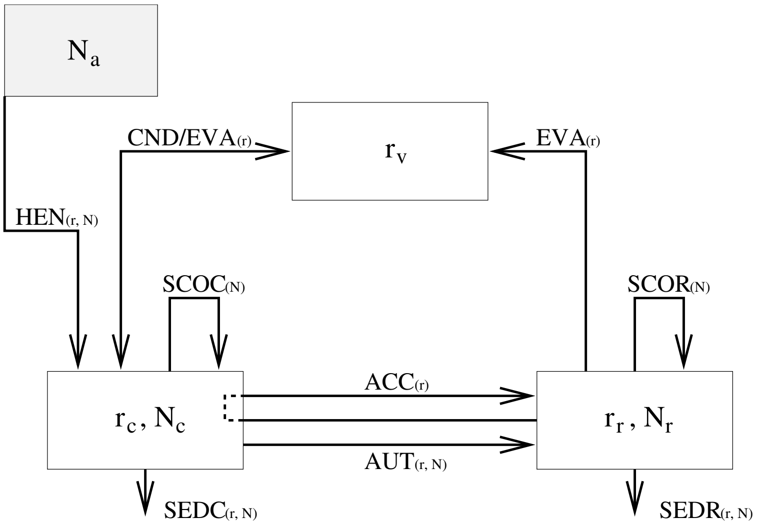

Figure 6.1: Warm microphysical processes included in the C2R2 scheme (see text for the acronyms and explanations).

$F(a, b, c; x)$ is the hypergeometric function. This form adheres more closely to observations of N_{CCN} at large $s_{v,w}$ (N_{CCN} is finite as $s_{v,w}$ goes to infinity) as compared to the traditional $Cs^k_{v,w}$ law. Furthermore Cohard et al. (2000c) show that it is possible to establish parametric relations between the four unknowns in (6.61) and characteristics of lognormal distributions of underlying aerosols with variable chemical composition and solubility. Thus the k, β and μ parameters of (6.61) can be expressed with the following formulas:

$$\frac{k}{k_0} = \left(\frac{\ln(\sigma)}{\ln(\sigma)_0}\right)^{\alpha^\sigma_k}, \tag{6.62a}$$

$$\frac{\beta}{\beta_0} = \left(\frac{\overline{r}}{\overline{r}_0}\right)^{\alpha^{\overline{r}}_\beta} \exp\left(\alpha^\sigma_\beta\left(\frac{\ln(\sigma)}{\ln(\sigma)_0} - 1\right)\right)\left(\frac{\epsilon_m}{\epsilon_{m0}}\right)^{\alpha^{\epsilon m}_\beta}\left(\frac{T}{T_0}\right)^{\alpha^T_\beta}, \tag{6.62b}$$

$$\frac{\mu}{\mu_0} = \left(\frac{\ln(\sigma)}{\ln(\sigma)_0}\right)^{\alpha^\sigma_\mu}. \tag{6.62c}$$

The values of the new coefficients in (6.62a-c) can be taken from Tables 2 and 3 of Cohard et al. (2000c). The remaining parameter C in (6.61) is deduced from the total CCN number concentration (N^{max}_{CCN}) using

$$\lim_{s_{v,w}\to+\infty} N_{CCN}(s_{v,w}) = N^{max}_{CCN} = \frac{C}{\beta^{k/2}} \frac{\Gamma(k/2+1)\Gamma(\mu - k/2)}{\Gamma(\mu)} \tag{6.64}$$

under the condition that k verifies $k < 2\mu$ which is always satisfied here.

Using (6.61) and following Twomey's method, Cohard et al. (1998) showed that an estimate of the maximum supersaturation $s_{v,w_{MAX}}$ is the root of

$$s^{k+2}_{v,w_{MAX}} F(\mu, \frac{k}{2}, \frac{k}{2} + \frac{3}{2}, -\beta s^2_{v,w_{MAX}}) = \frac{\rho_a(\psi_1 w)^{3/2}}{2kC\pi\rho_w\psi_2(G)^{3/2}B(\frac{k}{2}, \frac{3}{2})}. \tag{6.66}$$

Substituting values of $s_{v,w} = s_{v,w_{MAX}}$ into (6.61) provides an estimate of the potentially activable CCN number concentration, so the production rate of newly nucleated droplets is given by comparison with CCN that have been already activated. It is also worth to note that (6.61) and (6.66) can be easily generalized to a mixture of aerosols.

Table 6.1: Nomenclature of the microphysical processes involved in (7.93a-d).

Symbols	Mechanisms	Sinks	Sources	Processes
$RVHENC$	$r_v \Longrightarrow r_c$	r_v	r_c	nucleation (implicitly)
$CVHENC$	$N_n \Longrightarrow N_a$	N_n	N_a	
	$N_a \Longrightarrow N_c$	N_a	N_c	
$RVCONC$	$r_v \Longrightarrow r_c$	r_v	r_c	condensation & evaporation
	$r_v \Longleftarrow r_c$	r_c	r_v	
$RCAUTR$	$r_c + r_c \Longrightarrow r_r$	r_c	r_r	autoconversion
$CCAUTR$	$N_c + N_c \Longrightarrow N_r$	N_c	N_r	
$RCACCR$	$r_c + r_r \Longrightarrow r_r$	r_c	r_r	accretion
$CCACCR$	$N_c + N_c \Longrightarrow N_r$	N_c	N_r	
$RREVAV$	$r_r \Longrightarrow r_v$	r_r	r_v	evaporation
$CRSCOR$	$N_r + N_r \Longrightarrow N_r$	N_r	N_r	self-collection & break-up
$CCSCOC$	$N_c + N_c \Longrightarrow N_c$	N_c	N_c	
$RSEDR$	$r_r \Longrightarrow r_r$	r_r	r_r	sedimentation
$CSEDR$	$N_r \Longrightarrow N_r$	N_r	N_r	

The reversible condensation/evaporation process is treated implicitly as a result of a non-iterative vapor saturation adjustment (see Cohard and Pinty, 2000a). This treatment is well justified by observations that show that the interior of clouds is nearly in thermodynamical equilibrium ($s_{v,w} < 1\%$). The condensation rate is obtained after solving for T the equation of the first law of thermodynamics,

$$(T - T^*) + \frac{L_v(T)}{C_{ph}}(r_{vs}(T) - r_v^*) = 0 \tag{6.67}$$

where T^* and r_v^* are the temperature and vapor mixing ratio of an intermediate state after integrating all the other explicit processes. $r_{vs}(T)$ is the saturated water vapor mixing ratio, $L_v(T)$ the latent heat of vaporization and C_{ph} the heat capacity of cloudy air. The condensation rate is given by

$$RVCONC = max(-r_c, r_v^* - r_{vs}(T))/\delta t \tag{6.68}$$

Coalescence

A short analysis of the stochastic collection equation indicates that bulk microphysical schemes always need a parameterization for the autoconversion terms (formation of raindrops by droplet coalescence) while the other processes (including raindrop growth by accretion and self-collection) can be treated analytically using the collection kernels of Long (1974).

Autoconversion (RCAUTR and CCAUTR) The parameterization relies on the work of Berry and Reinhardt (1974) for the computation of the RCAUTR term. The parameterization is built on the observation that a characteristic water content L of small drops develops steadily over a characteristic timescale τ. These two positive quantities are expressed in the ranges 20 μm $\leq D_c \leq$

36 μm and $0 \leq \nu_c \leq 3$ by:

$$L = 2.7 \times 10^{-2} \rho_a r_c (\frac{1}{16} \times 10^{20} \sigma_c^3 D_c - 0.4) \quad (6.69\text{a})$$

$$\tau = 3.7 \frac{1}{\rho_a r_c} (0.5 \times 10^6 \sigma_c - 7.5)^{-1} \quad (6.69\text{b})$$

where the mean-volume drop diameter D_c and the standard deviation σ_c are computed using (6.55). Eqs(6.69a) and (6.69b) are combined to get:

$$RCAUTR = -\, max(\frac{L}{\tau}, 0.) \quad (6.71)$$

A suitable parameterization of the CCAUTR rate is more difficult to obtain because the original Berry and Reinhardt's parameterization tends to accumulate the freshly formed drops by autoconversion in the lowest part of the raindrop spectrum thus preventing the development of sizeable raindrops. This led Cohard and Pinty (2000a) to the conclusion that it is important to restrict the original Berry and Reinhardt formulation:

$$CCAUTR = -\, 3.5 \times 10^9 \; \frac{\rho_a L}{\tau} \quad (6.72)$$

to situations where $D_r < D_h$ where D_h is the "hump diameter" defined by Berry and Reinhardt (1974). For cases where $D_r > D_h$, it is assumed that the autoconversion of the cloud droplets does not modify the mean-volume diameter so (6.72) is replaced by:

$$CCAUTR = \frac{N_r}{r_r} RCAUTR \quad (6.73)$$

Accretion (RCACCR and CCACCR) and self-collections (CCSCOC and CRSCOR) The processes of accretion and self-collections associated to polynomial collection kernels, can be integrated analytically in bulk schemes as shown by Cohard and Pinty (2000a). The collection kernels of Long (1974), already used by Ziegler (1985), are considered in this study:

$$K(D_1, D_2) = \begin{cases} K_2(D_1^6 + D_2^6) & \text{if } D_1 \leq 100\mu\text{m}, \\ K_1(D_1^3 + D_2^3) & \text{if } D_1 > 100\mu\text{m}. \end{cases} \quad (6.74)$$

with $K_2 = 2.59 \times 10^{15}$ m^{-3}s^{-1} and $K_1 = 3.03 \times 10^3$ s^{-1}. As recommended by Berry and Reinhardt (1974), the accretion and the self-collection of raindrops are accounted for once $r_r > 1.2 \times L/\rho_a$. The cumbersome expressions of the different ACC and SCO terms have been obtained by Cohard and Pinty (2000a) for the raindrops:

If $D_r \geq 100\mu$m

$$\begin{aligned} CCACCR &= -K_1 N_c N_r \Big(\frac{\Gamma(\nu_c + 3/\alpha_c)}{\Gamma(\nu_c)\lambda_c^3} + \frac{\Gamma(\nu_r + 3/\alpha_r)}{\Gamma(\nu_r)\lambda_r^3} \Big) \\ RCACCR &= -\frac{\pi}{6} \frac{\rho_w}{\rho_a} K_1 \frac{N_c N_r}{\lambda_c^3} \Big(\frac{\Gamma(\nu_c + 6/\alpha_c)}{\Gamma(\nu_c)\lambda_c^3} + \frac{\Gamma(\nu_c + 3/\alpha_c)}{\Gamma(\nu_c)} \frac{\Gamma(\nu_r + 3/\alpha_r)}{\Gamma(\nu_r)\lambda_r^3} \Big) \quad (6.75) \\ CRSCOR &= -K_1 N_r^2 \frac{\Gamma(\nu_r + 3/\alpha_r)}{\Gamma(\nu_r)\lambda_r^3} \end{aligned}$$

$$\begin{aligned}
&\text{If } D_r < 100\mu\text{m}\\
&CCACCR = -K_2 N_c N_r \Big(\frac{\Gamma(\nu_c + 6/\alpha_c)}{\Gamma(\nu_c)\lambda_c^6} + \frac{\Gamma(\nu_r + 6/\alpha_r)}{\Gamma(\nu_r)\lambda_r^6} \Big)\\
&RCACCR = -\frac{\pi}{6}\frac{\rho_w}{\rho_a} K_2 \frac{N_c N_r}{\lambda_c^3} \Big(\frac{\Gamma(\nu_c + 9/\alpha_c)}{\Gamma(\nu_c)\lambda_c^6} + \frac{\Gamma(\nu_c + 3/\alpha_c)}{\Gamma(\nu_c)} \frac{\Gamma(\nu_r + 6/\alpha_r)}{\Gamma(\nu_r)\lambda_r^6} \Big)\\
&CRSCOR = -K_2 N_r^2 \frac{\Gamma(\nu_r + 6/\alpha_r)}{\Gamma(\nu_r)\lambda_r^6}
\end{aligned} \tag{6.76}$$

and for the cloud droplets

$$CCSCOC = -K_1 N_c^2 \frac{\Gamma(\nu_c + 3/\alpha_c)}{\Gamma(\nu_c)\lambda_c^3} \tag{6.77}$$

Break-up

Break-up is an efficient process acting on the concentration of the large drops (a key role to explain the high reflectivity core of the tropical rainband in the present case study).
Firstly, collisional break-up is introduced as in Verlinde and Cotton (1993), where a bulk collection efficiency $E_c < 1$ is used to damp the growth of the raindrops by self-collection. In the scheme, the preceeding $CRSCOR$ term is multiplied by the E_c factor with the following definition:

$$E_c = \begin{cases} 1 & \text{if } D_r < 600\mu\text{m},\\ \exp(-2.5\times 10^3(D_r - 6\times 10^{-4})) & \text{if } 600\mu\text{m} \le D_r < 2000\mu\text{m},\\ 0 & \text{if } D_r \ge 2000\mu\text{m}. \end{cases} \tag{6.78}$$

Values of the cutoff diameters in (6.78) have been subjected to a specific evaluation in Cohard and Pinty (2000b).
Secondly and as discussed by Cohard and Pinty (2000b), the inclusion of an additional drop size limiter (a substitute for a spontaneous break-up parameterization) is necessary to remove the giant drops that can be produced spuriously by an unaccurate differential transport of r_r and N_r (advection and sedimentation terms). The correction is applied whenever D_r is larger than 3000 μm so beyond the range of active collisional break-up (see Cohard and Pinty (2000b) for further details).

Evaporation (RREVAV)

The evaporation rate of a raindrop population, falling in an undersaturated environment ($s_{v,w} \ll 0$) is obtained after performing an analytical integration over the whole drop mass spectrum. The size evolution of a single evaporating drop of diameter D is given by

$$\frac{dD}{dt}\Big|_{EVA} = \frac{4 s_{v,w}\bar{f} G}{D} \tag{6.79}$$

where the ventilation factor $\bar{f}$, an empirical function of the Reynolds number $Re = VD/\nu_{cin}$ of the flow, is given by:

$$\bar{f} = 0.78 + F Re^{0.5} = 0.78 + 0.265 \Big[\Big(\frac{\rho_{00}}{\rho_a}\Big)^{0.4} \frac{cD^{d+1}}{\nu_{cin}} \Big]^{0.5} \tag{6.80}$$

after inserting (6.85). Integrating (6.79) with (6.80) and (6.53) leads to an analytical expression of the evaporation rate that is:

$$\begin{aligned} RREVAV &= \frac{1}{\rho_a}\int_0^{+\infty}\frac{\pi}{2}\rho_w D^2 \frac{dD}{dt}\Big|_{EVA} n_r(D)dD \\ &= \frac{2\pi s_{v,w} N_r G}{\lambda\Gamma(\lambda)}\frac{\rho_w}{\rho_a}\Big[0.78+0.265\Big(\frac{\rho_{00}}{\rho_a}\Big)^{0.2}\Big(\frac{c}{\nu_{cin}}\Big)^{0.5}\frac{\Gamma(\nu_r+(d+3)/2\alpha_r)}{\lambda_r^{(d+1)/2}}\Big]. \end{aligned} \tag{6.81}$$

Concentrations N_r are not affected by evaporation in the present scheme. However if the mean volume drop diameter becomes smaller than 82 μm (the hypothetical size separation between the droplet and drop modes) then all raindrops are converted into cloud droplets, i.e. $N_c = N_c + N_r; r_c = r_c + r_r$ and $N_r = r_r = 0$.

Sedimentation (RSEDR and CSEDR)

Due to the fact that the terminal velocity of drops depends on their size, the gravitational sedimentation of hydrometeors is selective if one considers the whole range of raindrop spectra. This leads to an efficient size sorting phenomenom which is important in the case of warm cumuli where some drops can be large enough to fall while smaller ones are delayed and maintained in updraft cores for further growth. This differential settling between drops is accounted for in two-moment schemes because both sedimentation fluxes of N_r and r_r are computed:

$$\begin{aligned} RSEDR &= \frac{1}{\rho_a}\frac{\partial}{\partial z}\int_0^{\infty}\frac{\pi}{6}\rho_w D^3 V(D) n_r(D)dD \\ &= \frac{1}{\rho_a}\frac{\partial}{\partial z}\Big[c\Big(\frac{\rho_{00}}{\rho_a}\Big)^{0.4}\rho_a r_r \frac{\Gamma(\nu_r+(d+3)/\alpha_r)}{\lambda_r^d\Gamma(\nu_r+3/\alpha_r)}\Big], \end{aligned} \tag{6.83}$$

$$CSEDR = \frac{\partial}{\partial z}\int_0^{\infty} V(D)n_r(D)dD = \frac{\partial}{\partial z}\Big[c\Big(\frac{\rho_{00}}{\rho_a}\Big)^{0.4} N_r \frac{\Gamma(\nu_r+d/\alpha_r)}{\lambda_r^d\Gamma(\nu_r)}\Big]. \tag{6.84}$$

In (6.83)-(6.84), a simple power law dependence in diameter including air density effect (Foote and Du Toit 1969) has been assumed:

$$V(D) = \Big(\frac{\rho_{00}}{\rho_a}\Big)^{0.4} cD^d, \tag{6.85}$$

Appendix: List of symbols

A	$= 4\sigma_{w/a}/R_v T\rho_w$
$B(a,b)$	beta function
c and d	parameters of the fall speed-diameter relationship for the water drops
C	activation spectrum coefficient
C_{vv}	heat capacity at constant volume of water vapor
C_{pd}, C_{pv} and C_w	heat capacity at constant pressure of dry air, water vapor and liquid water
C_{ph}	$= C_{pd} + r_v C_{pv} + (r_c + r_r)C_w$
D, D_1 and D_2	drop diameters

D_c, D_r	mean volume drop diameter for cloud droplet and raindrop distributions
D_v	diffusivity of water vapor in the air
e_v	water vapor pressure
e_{vs}	saturation vapor pressure over water
E_c	collection efficiency
$\bar{f}$	ventilation factor
F	ventilation coefficient
$F(a,b,c;x)$	hypergeometric function
$G(D,T,P)$	$= \frac{1}{\rho_w}\Big(\frac{R_vT}{e_{vs}(T)D_v} + \frac{L_v(T)}{k_aT}(\frac{L_v(T)}{R_vT} - 1)\Big)^{-1}$
k and k_0	activation spectrum coefficients
k_a	heat conductivity of air
$K(x,y)$ and $K(D_1,D_2)$	collection kernels
K_1 and K_2	Long's collection kernel coefficients
L	autoconversion water mass
L_v	latent heat of vaporization
n, n_c and n_r	total, cloud droplet and raindrop size distributions
N_0	intercept parameter of an exponential distribution law
N_c, N_r	cloud droplet and raindrop number concentration
N_n, N_a	condensation nuclei and activated CCN number concentration
N_{CCN}	total activable CCN number concentration
M_w	molar weight of water
$M_i(p)$	p_moment of the i_drop size distribution
P and P_{00}	pressure and reference pressure (1000 hPa)
$\overline{r}$	geometric mean radius of the CCN lognormal distribution
r_v, r_c and r_r	water vapor, cloud water and rain water mixing ratios
r_{vs}	saturated vapor mixing ratio
R_d and R_v	gas constant for dry air and water vapor
Re	Reynolds number
$s_{v,w}$	supersaturation ($= e_v/e_{vs} - 1$)
$s_{v,w_{MAX}}$	maximum supersaturation
t	time
T and T_{00}	temperature and reference temperature (273.16 K)
$V(D)$	drop fall speed of diameter D
w	updraft velocity
x and y	drop mass
z	height or vertical coordinate
$\alpha_{\{k,\beta,\mu\}}^{\{\overline{r},\ln(\sigma),\epsilon_m,T\}}$	adjusted parameters defining the CCN spectrum coefficients
α_c, α_r	dispersion parameter of the generalized gamma distribution law for the cloud droplets and the raindrops
β and β_0	activation spectrum coefficient
δt	time step
$\Gamma(a)$	complete gamma function
ϵ	$= R_v/R_d$
ϵ_m	aerosol soluble fraction
θ	potential temperature

λ_c, λ_r	slope parameter of the generalized gamma distribution law for the cloud droplets and the raindrops
μ and μ_0	activation spectrum coefficients
ν_c, ν_r	dispersion parameter of the generalized gamma distribution law for the cloud droplets and the raindrops
ν_{cin}	kinematic viscosity of air
Π	$=(P/P_{00})^{R_d/C_{pd}}$
ρ_a and ρ_w	air and liquid water densities
ρ_{00}	air density at $P = P_{00}$ and $T = T_{00}$
σ	geometric standard deviation of the CCN lognormal distribution
σ_c	standard deviation of cloud droplet distribution
$\sigma_{w/a}$	surface tension of water over the air
τ	timescale for autoconversion
$\psi_1(T,P)$	$= \dfrac{g}{TR_d}\Big(\dfrac{L_v}{c_pT} - 1\Big)$
$\psi_2(T,P)$	$= \Big(\dfrac{P}{\epsilon e_{vs}(T)} + \dfrac{\epsilon L_v^2}{R_dT^2c_p}\Big)$

6.3 The two-moment microphysical scheme for LES of stratocumulus

6.3.1 Introduction

The KHKO scheme is a 2-moment microphysical scheme specially designed for boundary layer clouds. These clouds are low precipitating warm clouds, and not sufficiently thick to produce heavy rain. The precipitating hydrometeors are drizzle only: their diameter are of the order of several dozens of micrometers. The conversion rates that impact drizzle formation and evolution are parameterized according to Khairoutdinov and Kogan (2000) (KK00) microphysical scheme. These processes are autoconversion, accretion, drizzle sedimentation and drizzle evaporation. Microphysical processes that impact cloud formation are parameterized as in the C2R2 scheme: cloud droplet condensation and evaporation follow Langlois (1973) and activation follows Cohard et al. (1998) (see the C2R2 scientific documentation). Moreover cloud droplet sedimentation is resolved by assuming a Stokes flow to calculate the cloud droplets terminal velocity and an analytical distribution to describe the cloud droplet spectra as in the C2R2 scheme. Microphysical prognostic variables are the same as in the C2R2 scheme: cloud droplet number concentration N_c and mixing ratio r_c, precipitating hydrometeors number concentration N_r and mixing ratio r_r, activated cloud condensation nuclei number concentration N_a.
The next section describes KK00 (the original scheme of Khairoutdinov and Kogan (2000)) and KHKO (the corresponding scheme implemented in Meso-NH) specificities and limits.

6.3.2 KK00 scheme specifities

The KK00 scheme is a 2-moment bulk microphysical scheme. All processes are parameterized only as a function of mixing ratios and number concentrations of each category (cloud droplet and drizzle). The methodology developed in KK00 consisted to assume firstly a power law relationship between conversion rate and the prognostic variables. Each power law introduces coefficients that have to be determined. These coefficients have been empirically adjusted by using about 100 000 hydrometeors spectra obtained from four 3-D LES simulations of stratocumulus clouds using an explicit (bin) microphysical model. For each of these spectra, autoconversion and accretion conversion rates are calculated by integrating the stochastic collection equation. Then the coefficients in the parameterized expressions are evaluated by regression analysis.

Figure 6.2a shows the range of cloud droplet mixing ratios and number concentrations of spectra used to evaluate conversion rates. These values are typical of values encountered in stratocumulus as shown in Fig 6.2b and Fig 6.2c that represent cloud droplet mixing ratios and number concentrations of spectra measured respectively during the ACE-1 and ACE-2 field experiments. The advantage of adjusting coefficients using spectra simulated with an explicit model is that these spectra are representative of boundary layer clouds realistic distributions.

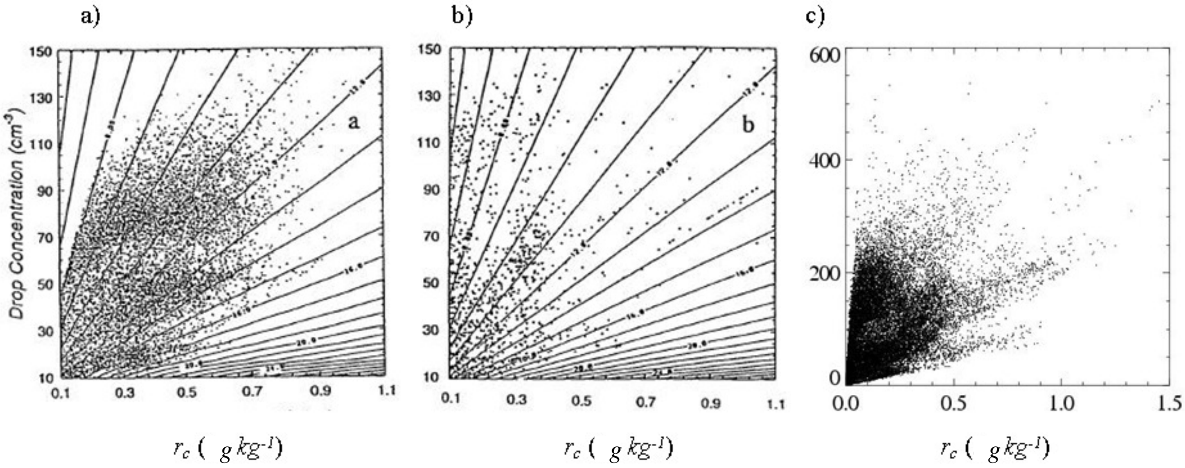

Figure 6.2: a) A scatterplot of the parameter space used to evaluate the coefficients of the KK00 microphysical processes parameterizations. Each data point represents the cloud droplet mixing ratio and the number concentration calculated from an individual hydrometeor size spectrum simulated by the explicit microphysical model. b) Similar to a) but for the spectra averaged over each aircraft flight leg in stratocumulus cloud during the first phase of ACE-1, (following Khairoutdinov et Kogan (2000)), c) Similar to a) but for the ensemble of spectra measured during ACE-2 field experiments (8 flights). Each spectra is averaged with a resolution of about 100 m horizontally. Note that different scales are used for this plot.

Note that a value for r_c of 1.1 g kg^{-1} (the maximum value in Fig. 6.2a) corresponds to an adiabatic cloud with a depth equal to about 550 m. This value can be calculated by assuming an adiabatic linear relationship between the mixing ratio at cloud top $r_c(H)$ and the cloud depth H with an adiabatic coefficient C_w equal to 2 10^{-6} kg m^{-4} : $r_c(H) = C_w H$. This scheme cannot be extended to deep convective clouds.

In the KK00 scheme, separation between cloud droplets and drizzle is defined at a diameter D_0 equal to 50 μm. This low value permits consideration of drizzle in the precipitating category.

Parameterizations are expressed as a function of local microphysical values. Thus the scheme is valid only for simulations where microphysical fields are explicitly resolved i.e. in the LES configuration. Resolution must not be more than 200 m horizontally and a few ten of meters vertically (a vertical resolution of 10 m in the cloud is recommended).

6.3.3 System of equations

For each prognostic variable, conservative equations in KHKO scheme are the following ones:

$$\frac{\partial N_a}{\partial t} = \sum \frac{\partial N_a}{\partial t}\Big|_{NMT} + \frac{\partial N_a}{\partial t}\Big|_{ACT} + \frac{\partial N_a}{\partial t}\Big|_{EVAPC} \tag{6.86a}$$

$$\frac{\partial N_c}{\partial t} = \sum \frac{\partial N_c}{\partial t}\Big|_{NMT} + \frac{\partial N_c}{\partial t}\Big|_{ACT} + \frac{\partial N_c}{\partial t}\Big|_{SEDC} + \frac{\partial N_c}{\partial t}\Big|_{AUTO} + \frac{\partial N_c}{\partial t}\Big|_{ACCR} + \frac{\partial N_c}{\partial t}\Big|_{EVAPC} \tag{6.86b}$$

$$\frac{\partial r_c}{\partial t} = \sum \frac{\partial r_c}{\partial t}\Big|_{NMT} + \frac{\partial r_c}{\partial t}\Big|_{ACT} + \frac{\partial r_c}{\partial t}\Big|_{SEDC} + \frac{\partial r_c}{\partial t}\Big|_{AUTO} + \frac{\partial r_c}{\partial t}\Big|_{ACCR} + \frac{\partial r_c}{\partial t}\Big|_{CONDC} + \frac{\partial r_c}{\partial t}\Big|_{EVAPC} \tag{6.86c}$$

$$\frac{\partial N_r}{\partial t} = \sum \frac{\partial N_r}{\partial t}\Big|_{NMT} + \frac{\partial N_r}{\partial t}\Big|_{SEDR} + \frac{\partial N_r}{\partial t}\Big|_{AUTO} + \frac{\partial N_r}{\partial t}\Big|_{ACCR} + \frac{\partial N_r}{\partial t}\Big|_{EVAPR} \tag{6.86d}$$

$$\frac{\partial r_r}{\partial t} = \sum \frac{\partial r_r}{\partial t}\Big|_{NMT} + \frac{\partial r_r}{\partial t}\Big|_{SEDR} + \frac{\partial r_r}{\partial t}\Big|_{AUTO} + \frac{\partial r_r}{\partial t}\Big|_{EVAPR} \tag{6.86e}$$

where the subscript NMT refers to Non-Microphysical Tendencies (advection, turbulence, numerics and other physical processes), ACT, $SEDC$, $SEDR$, $AUTO$, $ACCR$, $CONDC$, $EVAPC$, $EVAPR$ are the microphysical contributions, i.e. respectively, activation, cloud droplet sedimentation, drizzle sedimentation, autoconversion, accretion, cloud droplet condensation, cloud droplet evaporation and drizzle evaporation.

The KK00 scheme does not take into account the drizzle self-collection (on the contrary to C2R2 for raindrops): drizzle diameters are too low for this process to impact the drizzle number concentration N_r. Moreover in the KHKO scheme, water vapor condensation on precipitating hydrometeors is not taken into account (as in C2R2).

In order to close this system of equations the rhs terms are parameterized as a function of the prognostics variables. The next sections describe parameterizations of these processes except for cloud droplet condensation/evaporation and activation, that are identical to the C2R2 scheme. For a description of the latter the reader should refer to the C2R2 documentation.

6.3.4 Collection processes

Autoconversion Autoconversion is the process that initializes precipitating hydrometeor spectra. It depends on cloud droplet spectra characteristics. In the KK00 scheme it is assumed to depend on cloud droplets number concentration N_c and mixing ratio r_c. After regression analysis on bin model simulations, KK00 obtain the following parameterized expressions for the mixing ratios conversion rates by autoconversion:

$$\frac{\partial r_r}{\partial t}\Big|_{AUTO} = 1350.r_c^{2.47} N_c^{-1.79} \tag{6.88}$$

$$\frac{\partial r_c}{\partial t}\Big|_{AUTO} = -\frac{\partial r_r}{\partial t}\Big|_{AUTO} \tag{6.89}$$

The cloud droplet number concentration source term is evaluated by assuming that all collected cloud droplet diameters are equal to the mean volume diameter D_c:

$$\left.\frac{\partial N_c}{\partial t}\right|_{AUTO} = -\frac{\left.(\frac{\partial r_r}{\partial t})\right|_{AUTO}}{\frac{\pi\rho_w}{6\rho_a}D_c^3} \tag{6.90}$$

New drizzle drops are assumed to have the diameter D_0 equal to 50 μm. Thus the drizzle number concentration source term due to autoconversion is:

$$\left.\frac{\partial N_r}{\partial t}\right|_{AUTO} = \frac{\left.\frac{\partial r_r}{\partial t}\right|_{AUTO}}{\frac{\pi\rho_w}{6\rho_a}D_0^3} \tag{6.91}$$

Accretion

Accretion rate has to be expressed as a function of cloud droplets spectra and precipitating hydrometeors spectra because accretion represents an interaction between the two categories. KK00 assume that accretion rate depends only on cloud droplet and drizzle mixing ratios. After regression analysis the following expressions for mixing ratios conversion rates are obtained:

$$\left.\frac{\partial r_r}{\partial t}\right|_{ACCR} = 67(r_c r_r)^{1.15} \tag{6.92}$$

$$\left.\frac{\partial r_c}{\partial t}\right|_{ACCR} = -\left.\frac{\partial r_r}{\partial t}\right|_{ACCR} \tag{6.93}$$

Similar to autoconversion, cloud droplets number concentration accretion sink term is expressed as the following:

$$\left.\frac{\partial N_c}{\partial t}\right|_{ACCR} = -\frac{\left.\frac{\partial r_r}{\partial t}\right|_{ACCR}}{\frac{\pi\rho_w}{6\rho_a}D_c^3} \tag{6.94}$$

Cloud droplets collection by precipitating hydrometeors involves an increase of precipitating hydrometeors mass but not of their number. For that reason there is no accretion source term for the drizzle number concentration.

6.3.5 Break-up

Break-up is applied to achieve a numerical goal only. Drizzle drops are not large enough to take into account this process. However, at some grid point, the drizzle drops number concentration and mixing ratio have non-physical low values that can result in an inconsistency between these two values and thus overly large drizzle mean volume diameters. In order to avoid this divergence, break-up is applied to limit too low values of drizzle number concentration and keep consistency between the drizzle number concentration and mixing ratio. The same protection is done for the cloud droplets number concentration. The latter is corrected when necessary in order that the cloud droplets mean volume diameter do not exceed the limit diameter between cloud droplets and drizzle i.e. 50 μm.

6.3.6 Drizzle evaporation

Precipitating drops evaporation rate can be expressed as:

$$\frac{\partial r_r}{\partial t}\Big|_{EVAPR} = \frac{2\pi\rho_w}{\rho_a} G(T,P) s_{v,w} \int_0^\infty D n_r(D) dD \tag{6.95}$$

where $G(T,P)$ is a function of temperature and pressure, $n_r(D)$ is the drizzle density function and $s_{v,w}$ is the subsaturation ($s_{v,w} = e_v/e_{vs} - 1$). Note that drizzle drops have a sufficiently low diameter to ignore the ventilation factor. By introducing a coefficient C_{evap} equal to the ratio of the drizzle drop mean diameter to the drizzle drop mean volume diameter, it becomes:

$$\frac{\partial r_r}{\partial t}\Big|_{EVAPR} = 12 C_{evap} G(T,P) (\frac{\pi\rho_w}{6\rho_a})^{\frac{2}{3}} r_r^{\frac{1}{3}} N_r^{\frac{2}{3}} s_{v,w} \tag{6.96}$$

KK00 assume that C_{evap} is a constant parameter. Its value has been adjusted using the spectra derived from the bin model simulations. They propose: $C_{evap} = 0.86$. The uncertainty of this parameter is estimated on the order of $15 - 20\%$.
KK00 calculate the rate of change of drizzle number concentration as:

$$\frac{\partial N_r}{\partial t}\Big|_{EVAPR} = \frac{N_r}{r_r} \frac{\frac{\partial r_r}{\partial t}\Big|_{EVAPR}}{\frac{\pi\rho_w}{6\rho_a} D_r^3} \tag{6.97}$$

Water vapor condensation on drizzle is not taken into account in the model. In the presence of cloud droplets, the amount of water vapor condensed on drizzle is negligible. Because positive supersaturation is encountered in clouds only, it is consistent to neglect condensation on drizzle.

6.3.7 Sedimentation

Generalities

For the two categories of liquid water, number concentration and mixing ratio sedimentation rates can be expressed respectively as function of the number concentration sedimentation flux F_{N_i} (in m^{-2} s^{-1}) and the mixing ratio sedimentation flux F_{r_i} (in kg m^{-2} s^{-1}) with $i = [c, r]$.

$$\frac{\partial N_i}{\partial t}\Big|_{SED_i} = \frac{\partial F_{N_i}}{\partial z} \tag{6.98}$$

$$\frac{\partial r_i}{\partial t}\Big|_{SED_i} = \frac{1}{\rho_a}\frac{\partial F_{r_i}}{\partial z} \tag{6.99}$$

with : $F_{N_i} = V_{N_i} N_i$ and $F_{r_i} = V_{r_i} \rho_a r_i$,
and :

$$V_{N_i} = \frac{F_{N_i}}{N_i} = \frac{\int_0^\infty v(D) n_i(D) dD}{\int_0^\infty n_i(D) dD} \tag{6.100}$$

$$V_{r_i} = \frac{F_{r_i}}{\rho_a r_i} = \frac{\int_0^\infty \frac{\pi}{6}\rho_w D^3 v(D) n_i(D) dD}{\int_0^\infty \frac{\pi}{6}\rho_w D^3 n_i(D) dD} \tag{6.101}$$

V_{r_i} is an average weighted by the third momentum of the distribution. For a non-monodispersed distribution, the mean terminal velocity of the mixing ratio V_{r_i} is different and greater than the mean terminal velocity of the hydrometeors V_{N_i}, because the flux of the hydrometeor mixing ratio is driven by hydrometeors of larger diameter.

Drizzle sedimentation

KK00 propose parameterized expressions of the velocity of the drizzle number concentration and the velocity of the mixing ratio as a function of the drizzle distribution mean volume diameter D_r:

$$V_{N_r} = 0.0035 D_r - 0.1 \tag{6.102}$$

$$V_{r_r} = 0.006 D_r - 0.2 \tag{6.103}$$

The coefficients have been tuned against the spectra simulated with the explicit model.

Cloud droplets sedimentation

KHKO introduces cloud droplet sedimentation on the contrary to KK00 parameterization, because this process has an impact on cloud evolution by reducing entrainment at cloud top (Ackerman et al. 2004; Bretherton et al. 2007). As in the C2R2 scheme, it is parameterized by assuming a Stokes law to calculate the cloud droplets terminal velocity and by assuming an analytical distribution to represent cloud droplet spectra. The analytical distribution used is a generalized gamma law (cf. C2R2 documentation). This law can be expressed as a function of r_c and N_c and two free parameters α_c and ν_c.
After integration, the sedimentation fluxes for the cloud droplet number concentration and the mixing ratio respectively are the following:

$$F_{N_c} = k_1 N_c D_c^2 \frac{\Gamma(\nu_c + \frac{2}{\alpha_c})}{\Gamma(\nu_c + \frac{3}{\alpha_c})^{\frac{2}{3}}} \Gamma(\nu_c)^{-\frac{1}{3}} \tag{6.104}$$

$$F_{r_c} = k_2 N_c D_c^5 \frac{\Gamma(\nu_c + \frac{5}{\alpha_c})}{\Gamma(\nu_c + \frac{3}{\alpha_c})^{\frac{5}{3}}} \Gamma(\nu_c)^{\frac{2}{3}} \tag{6.105}$$

where $\Gamma(x)$ is the gamma function and $\alpha_c = 3$, $\nu_c = 2$. These values have been adjusted by comparison with measured cloud droplet spectra during ACE-2 field campaign (Geoffroy 2007).

Appendix: List of symbols

C_{evap}	ratio of the drizzle drop mean radius to the drizzle drop mean volume radius
D_0	separation between cloud droplets and drizzle (=50 μm)
D_c, D_r	mean volume drop diameter for cloud droplet and drizzle distributions
D_v	diffusivity of water vapor in the air
e_v	water vapor pressure
e_{vs}	saturation vapor pressure over water
F_{N_c}, F_{r_c}	cloud number concentration and mixing ratio sedimentation flux
F_{N_r}, F_{r_r}	drizzle number concentration and mixing ratio sedimentation flux
$G(T,P)$	$= = \frac{1}{\rho_w}(\frac{R_v T}{e_{vs}(T) D_v} + \frac{L_v(T)}{k_a T}(\frac{L_v(T)}{R_v T} - 1))^{-1}$
k_a	heat conductivity of air
L_v	latent heat of vaporisation

n, n_c and n_r	total, cloud droplet and drizzle size distributions
N_c, N_r	cloud droplet and drizzle number concentration
N_a	activated CCN number concentration
P	pressure
r_v, r_c and r_r	water vapor, cloud droplets and drizzle mixing ratios
r_{vs}	saturated water vapor mixing ratio
R_v	gaz constant for water vapor
$s_{v,w}$	supersaturation ($= e_v/e_{vs} - 1$)
T	temperature
$v(D)$	Hydrometeor of diameter D terminal velocity
V_{N_r}, V_{r_r}	drizzle number concentration and mixing ratio mean terminal velocity
α_c, ν_c	dispersion parameters of the generalized gamma distribution law for the cloud droplets distribution
ρ_a and ρ_w	air and liquid water densities
$\Gamma(a)$	complete gamma function

6.4 References

Berry, E. X., and R. L. Reinhardt, 1974: An analysis of cloud drop growth by collection: Part II. single initial distributions. *J. Atmos. Sci.*, **31**, 1825-1831.

Bouteloup, Y., Seity, Y. and E. Bazile, 2010. Description of the sedimentation scheme used operationally in all M´et´eo-France NWP models . *Tellus*, **63A**, 300-311.

Bretherton, C. S., P. N. Blossey, and J. Uchida, 2007: Cloud droplet sedimentation, entrainment efficiency, and subtropical stratocumulus albedo. *Geophys. Res. Lett.*, **34,** L03813

Cohard, J.-M., J.-P. Pinty, and C. Bedos, 1998: Extending Twomey's analytical estimate of nucleated cloud droplet concentrations from CCN spectra. *J. Atmos. Sci.*, **55,** 3348-3357.

Cohard, J.-M., and J.-P. Pinty, 2000a: A comprehensive two-moment warm microphysical bulk scheme. Part I: Description and selective tests. *Q. J. R. Meteorol. Soc.*, **126**, 1815-1842.

Cohard, J.-M., and J.-P. Pinty, 2000b: A comprehensive two-moment warm microphysical bulk scheme. Part I: 2D experiments with a non-hydrostatic model. *Q. J. R. Meteorol. Soc.*, **126**, 1843-1859.

Cohard, J.-M., J.-P. Pinty, and K. Suhre, 2000c: On the parameterization of activation spectra from CCN microphysical properties. *J. Geophys. Res.*, **105**, D9, 11753-11766.

Foote, G. B., and P. S. Du Toit, 1969: Terminal velocity of raindrops aloft. *J. Appl. Meteor.*, **8**, 249-253.

Geoffroy, O., 2007: Modelisation LES des precipitations dans les nuages de couche limite et parametrisation pour les GCM, Ph.D. thesis, Universite Paul Sabatier (Toulouse III).

Kessler, E., 1969: On the distribution and continuity of water sustance in atmospheric circulations. *Meteor. Monog.*, **10**, N° 32, 84pp.

Khairoudinov, M., and Y. Kogan, 2000: A new cloud physics parameterization in a large-eddy simulation model of marine stratocumulus. *Mon. Wea. Rev.*, **128,** 229-243.

Langlois, W.E., 1973: A rapidly convergent procedure for computing large-scale condensation in a dynamical weather model. *Tellus*, **25**, 86-87.

Long, A. B., 1974: Solutions to the droplet collection equation for polynomial kernels. *J. Atmos. Sci.*, **31**, 1040-1057.

Liu, J. Y, and H. D. Orville, 1969: Numerical modeling of precipitation and cloud shadow effects on mountain-induced cumuli. *J. Atmos. Sci.*, **26**, 1283-1298.

Press, W. H., S. A. Teukolsky, W. T. Vetterling, and B. P. Flannery, 1992: *Numerical Recipes in FORTRAN: The Art of Scientific Computing.* 2nd Ed. Cambridge University Press, 963 pp.

Pruppacher, H. R and J. D. Klett, 1978: Microphysics of clouds and precipitation. Reidel, 714pp

Rood, R. B., 1987: Numerical advection algorithms and their role in atmospheric transport and chemistry models. *Review of Geoph.*, **25**, 71-100.

Twomey, S., 1959: The nuclei of natural cloud formation. Part II: The supersaturation in natural clouds and the variation of cloud droplet concentration. *Geophys. Pure Appl.*, **43**, 243-249.

Verlinde, J, P. J. Flatau, and W. R. Cotton, 1990: Analytical solution to the collection growth equation: comparison with approximate methods and application to cloud microphysics parameterization schemes. *J. Atmos. Sci.*, **47**, 2871-2880.

Chapter 7

Microphysical Scheme for Atmospheric Ice

Contents

7.1 Introduction

7.1.1 Purpose of the parameterization

The importance of ice microphysics to radiation transfer, energy budget and precipitation formation in convective storms has been widely stressed until recently (Chen and Cotton 1988; Mc Cumber et al. 1991; Chin 1994; Caniaux et al. 1995; Krueger et al. 1995; Yang and Houze 1995). There are several features that differ between the liquid and the ice phase in clouds. First, the reversible transformation between the liquid and the ice is accompagnied by a significant latent heat release ($\sim 10\%$ of the latent heat of condensation/evaporation), which can contribute to a further growth of convective clouds aloft or cooling beneath by precipitating particles falling in an unsaturated environment. Second, the terminal fall speed of the solid hydrometeors is significantly reduced compared to that of the liquid drops of the same weight. A direct consequence of these different aerodynamical properties, is that a larger time scale for the life cycle of partially glaciated convective clouds can be expected due to a larger residence time of the solid hydrometeores and a modified spatial redistribution of precipitations as well. Finally due to their different habit, the light scattering properties of the ice crystals are different from those of the cloud droplets of equivalent size and thus must be specifically accounted for in a cloud radiative transfer scheme when the ice phase is present.

7.1.2 Representation of the ice categories

The most striking feature of the ice phase in clouds is the extreme diversity and complexity of the crystal habits (see Pruppacher and Klett 1978) which lead to some uncertainity in their morphological and aerodynamical properties. This is why a great amount of curve fitting relationships have been proposed in the past to relate a characteristic dimension of an ice crystal to its volume, mass and terminal fall speed. So in order to elucidate the impact of the ice phase in a mesoscale model such as **Meso-NH**, many practical arguments are in favor of unavoidable but necessary assumptions in the bulk representation of some selected ice categories.

Actual ice parameterizations retain 2 (Rutledge and Hobbs 1983; Cotton et al. 1982[1]), 3 (Lin et al. 1983; Rutledge and Hobbs 1984; Ziegler 1985) or 4 (Ferrier 1994) and even 5 (Walko et al. 1995) ice categories. In a recent evaluation of the impact of the number of ice categories, Mc Cumber et al. (1991) concluded that at least 3 different ice types are necessary to cover most of their precipitating case study but they draw attention on the fact that application and tuning of the scheme might be case specific. The common agreement about an ice phase microphysical scheme is that it must include the pristine or primary ice phase issuing from heterogeneous nucleation processes, the aggregates or snowflakes type corresponding to lightly rimed large ice crystals or dry assemblages and a third category of more or less heavily rimed crystals which are graupels, frozen drops or hail, depending of considerations on the density of the particles. A matter of discussion can be found regarding the last category of ice particles as a physical discrimination exists in the growth mode of low density (~ 0.4) rimed particles (assumed to be dry for the graupels) from that of the high density (~ 0.9) hailstones which grow in the wet mode. In the definition of the present scheme, the user can handle either 3 categories of ice for simplification or 4 categories that distinguish hail from graupel.

Another point of concern is related to the supplementary prognostic equations for the number concentration of ice crystal in each category. For instance Cotton et al. (1986) and others use a specific equation to predict the primary ice number concentration which is motivated by the representation of both the heterogeneous ice-nucleation processes (see for instance, the revised version of Meyers et al. (1992)) and the secondary production of ice crystals known as the Hallett-Mossop (HM) or rime-splitering mechanism (Hallett annd Mossop 1974). Furthermore, several authors (Ziegler 1985; Murakami 1990; Ferrier 1994; Meyeers et al. 1996) have included a number concentration equation for their precipitating ice particles in their scheme which is in contrast with other simplified approaches where the intercept parameter of the crystal distribution or the total number concentration is given. In the present scheme, a somewhat different solution have been adopted. For this first version of the scheme, neither the HM process nor the immersion freezing of cloud droplets will be considered at once thus giving the opportunity to simply diagnose[2] the primary ice total number in the manner described in Ferrier (1994)[3]. Secondly, rather than working with more or less fixed number concentrations of precipitating ice or developping prognostic equations where the shaping of the spectra by self-aggregation/break-up processes is difficult to control, we followed Caniaux (1993) who after compiling various published experimental observations, established that the total number concentration N can be simply related to the slope parameter λ of the

---

[1] This reference is purely historical as the CSU-RAMS ice microphysical scheme has been greatly improved by Cotton et al. (1986)

[2] Although there is no serious physical difficulty to consider a prognostic equation for the primary ice total number concentration, we shall consider this improvement in a future version of the code with a high priority.

[3] see his equation 4.33, which condenses the results of Meyers et al. (1992)

ice precipitating category as[4]:

$$N = C\lambda^x. \tag{7.1}$$

Taking $x = 0$ means that the total number concentration is held fixed while for $x = -1$, it is the intercept parameter ($N_0 \equiv C$) of a Marshall-Palmer distribution law ($n(D) = N_0\, e^{-\lambda D}$) which is assumed to be a constant. In fact, as we want to grossly reproduce the broadening of the spectra (a decrease of λ) by the self-aggregation processes (a reduction of N), it is imperative to have $x > 0$. In (7.1), both C and x depend on the ice category and must be specified from physical arguments. However, experimental evidence and a sensitivity study leads Caniaux (1993) to link C and x by the following relationship:

$$\log_{10} C = -3.55\, x + 3.89, \tag{7.2}$$

thus reducing the degree of freedom for the choice of C and x.

To summarize and as a first step toward a more advanced scheme, the following strategy is adopted:

- the scheme contains a prognostic equation for the primary ice mixing ratio r_i, the snowflakes mixing ratio r_s, and the rimed crystals mixing ratio r_g,
- the total number concentration of the primary ice N_i is diagnosed while the total number concentration of the snowflakes N_s and of the rimed crystals N_g follow (7.1),
- power law relationships are used to relate the mass to the diameter[5],

  $$m(D) = aD^b \tag{7.3}$$

  and the terminal speed velocity to the diameter

  $$v(D) = cD^d\, (\rho_{00}/\rho_{dref})^{0.4}, \tag{7.4}$$

  where the last factor is the Foote and Du Toit (1969) correction of the air density, ρ_{00} being the air density at the reference pressure level P_{00}.
- each category of ice particle is assumed to be distributed according to

  $$n(D) = N\, g(D), \tag{7.5}$$

  where $g(D)$ is a normalized distribution law to be chosen in Table 7.1.

  It can be noticed that according to Tripoli and al. (1988), the use of the generalized Gamma law allows the maximal flexibility without requiring much computation effort as for instance, $M(p)$, the p^{th} moment of the law is simply expressed as:

  $$M(p) = \int_0^\infty D^p g(D)\, dD = \frac{G(p)}{\lambda^p}, \tag{7.6}$$

  where

  $$G(p) = \frac{\Gamma(\nu + p/\alpha)}{\Gamma(\nu)}, \tag{7.7}$$

---

[4] The intercept parameter N_0 of a Marshall-Palmer law is used in the original formulation of Caniaux (1993), but we found more convenient to generalize the relationship in (7.1) to the total number concentration.

[5] The diameter D refers to the maximum ice particle dimension. From (7.3), it is easy to show that D_{sph}, the equivalent spherical diameter is $D_{sph} = (6/\pi\; a/\rho_{ice})^{1/3} D^{b/3}$ with ρ_{ice} being the density of the ice (taking $\rho_{ice} = \rho_w$ means that D_{sph} is the melted diameter).

Table 7.1: Analytical formulation of various normalized distribution laws (from Tripoli and al. 1988).

Name of the distribution law	Mathematical expression
generalized Gamma	$g(D) = \frac{\alpha}{\Gamma(\nu)} \lambda^{\alpha\nu} D^{\alpha\nu-1} \exp\big(-(\lambda D)^{\alpha}\big)$
Gamma ($\alpha = 1$)	$g(D) = \frac{\lambda^{\nu}}{\Gamma(\nu)} D^{\nu-1} \exp(-\lambda D)$
Marshall-Palmer ($\alpha = 1$ and $\nu = 1$)	$g(D) = \lambda \exp(-\lambda D)$
Weibull ($\nu = 1$)	$g(D) = \alpha \lambda^{\alpha} D^{\alpha-1} \exp\big(-(\lambda D)^{\alpha}\big)$
Rayleigh ($\alpha = 2$ and $\nu = 3/2$)	$g(D) = \frac{\lambda^{3}}{\sqrt{\pi}} D^{2} \exp\big(-(\lambda D)^{2}\big)$
Lognormal	$g(D) = \frac{1}{\sqrt{2\pi}\sigma D} \exp\big[-\big(\frac{\log(\lambda D)}{\sqrt{2}\sigma}\big)^{2}\big]$

for a generalized Gamma law or

$$G(p) = \exp\big(\frac{p^2\sigma^2}{2}\big), \tag{7.8}$$

in case of lognormal distribution.

- the ice content, $\rho_d r$, of any specy i, s or g is defined by:

$$\rho r = \int_0^{\infty} m(D)n(D)\,dD = aNM(b), \tag{7.9}$$

where (7.3), (7.5), and (7.6) have been used. The slope parameter λ is then easily computed by inserting (7.1) and (7.6) into (7.9) to give:

$$\lambda = \left(\frac{\rho_d r}{aCG(b)}\right)^{\frac{1}{x-b}}. \tag{7.10}$$

Corollarily, it can be seen from the above equation that $x < b$ to ensure an opposite sense of variation for ρr and λ (see Fig. 7.1) that is the presence of large ice particles (low λ) are associated with high mixing ratios r and probably low concentration $x > 0$ as shown above.

7.1.3 General characteristics of the ice crystals

Each ice category is characterized by a specific set of value for the parameters involved in (7.1) according to their relative size abundance and in (7.3; mass-diameter), (7.4; fall speed-diameter), (7.42; vapor growth capacity-diameter), and (7.43; ventilation factor-diameter) depending upon their habit and growth mode. Note that each ice crystal is potentially precipitating even if the terminal fall speed of the primary ice crystal is negligible compared to that of the aggregates and the rimed particles. Doing so ensures the long term dissipation of unactive cirrus clouds or thunderstorm anvils by the sublimation of crystals falling in the subsaturated layers underneath.
Cloud ice is assumed to be distributed by a low dispersion (high ν) generalized Gamma law corresponding to an exponential distribution of the volume of quasi-spherical crystals ($\alpha = 3$) (see,

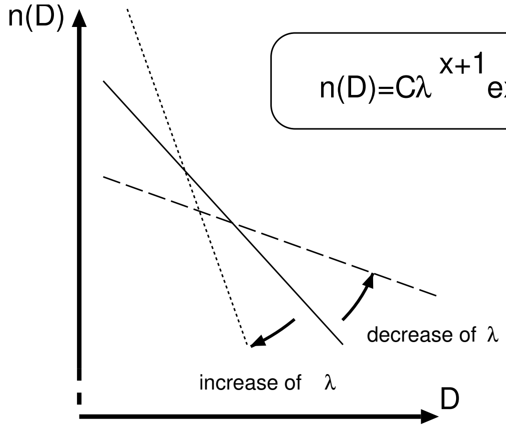

Figure 7.1: Modified Marshall-Palmer distribution $n(D)$ as a function of the slope parameter λ in log scale (from Caniaux 1993).

Ziegler 1985) while the precipitating particles follow the more classical exponential (or Marshall-Palmer) law.

In Table 7.2, the parameters of the r_s class describe the behavior of unrimed radiating assemblages of plates, side planes, bullets and columns or that of densely rimed radiating assemblages of dendrites. The parameters chosen for the r_g class correspond to those of lump graupels[6]. All the values of the a, b, c and d parameters are taken from Locatelli and Hobbs (1974) for the icy hydrometeors and from Starr and Cox (1985) and Heymsfield (1972) for the primary crystals (hexagonal plates)[7]. The ventilation coefficients ($\overline{f}_{0,1,2}$), based on Hall and Pruppacher (1977), are valid for spheres and for oblate spheroids as well. The $C - x$ values have been selected after the work of Passarelli (1978) and Mitchell (1988)[8] on the snowflake distribution theory and of Houze et al. (1979), but with a large uncertainty on the fact that the measured crystals could be graupels. It is important to stress that $x = 1$ is an acceptable value for snow because these particles are bidimensional particles ($b = 1.9$) with a variable density.

---

[6] For hailstones, $a = 470$ and $b = 3$ corresponding to spherical particles of density $\rho_{ice} = 900$ kg/m^3 together with $c = 207$ and $d = 0.64$ (Böhm 1989) and $C \sim 5\ 10^{-4}$ with $x \sim 2$ are recommended values from the analysis made by Cheng and English (1983).

[7] Starr and Cox (1985) provided several sets for a, b, c and d suitable for different crystal habits in cirrus clouds. They are recalled in the table below for completness.

Crystal habit	Columns	Bullet rosettes	Plates
a	$2.14\ 10^{-3}$	44	0.82
b	1.7	3.0	2.5
c	$2.1\ 10^{5}$	$4.3\ 10^{5}$	$8.0\ 10^{2}$
d	1.585	1.663	1.000

Note that the fall speed parameters are valid for the crystal size range of 0-200 μm and that c contains the air density correction ($\rho = 0.58$ kg/m^3 assumed at 40 kPa). The bullet rosettes with a quasi spherical shape ($b = 3$) impose to take $\mathcal{C}_{1_i}$ closer to 0.5 in such a case.

[8] Values for x close to 2 have been retrieved by recent radar and aircraft data analysis (see, Thomason et al. 1995 in 27th *Conf. on Radar Met.* but for spectrum tails due to large particles). However taking x too much close to 2 leads to some inconsistancies in computing λ from (7.10)

Table 7.2: Set of parameters used to characterize each ice category and the raindrops (Kessler scheme).

Parameters	r_i	r_s	r_g		r_r	r_c
α	3	1	1		1	3 on sea; 1 on land
ν	3	1	1		1	1 on sea; 3 on land
a	0.82	0.02	19.6		524	524
b	2.5	1.9	2.8		3	3
c	800	5.1	124		842	$3.2\ 10^7$
d	1.00	0.27	0.66		0.8	2
C		5	$5\ 10^5$		$8\ 10^6$	
x		1	-0.5		-1	
$\overline{f}_0$	1.00	0.86	0.86		1.00	
$\overline{f}_1$		0.28	0.28		0.26	
$\overline{f}_2$	0.14					
$\mathcal{C}_1$	$1/\pi$	$1/\pi$	0.5		0.5	

7.1.4 Nomenclature

The different rates at which microphysical processes involving one ice specy at least, have a symbolic name which is built according to the following rules:

- a first letter (R or C) to mean that the rate is relevant for a mixing Ratio or for a Concentration,
- a second letter (V, C, I, R, S or G) to identify the Sink specy,
- a group of three letters to shorten the name of the MICrophysical process,
- an optional letter to recall the name of the "Reactant" specy in case of three-component process,
- a last letter (I, R, S or G) to identify the Source specy.

7.1.5 Outlines of the microphysical scheme for mixed phase clouds

Warm processes

Cloud droplets nucleate and grow by condensation of water vapor or are forced to evaporate instantaneously according to the supply of water vapor by transport. Then autoconversion and accretion processes take place to form and accelerate the growth of the precipitable raindrops which evaporate when falling below the cloud base.

Table 7.3: List of the warm microphysical processes (not involving ice particles).

Symbol	Mechanism	Sink	Source	Process
$RVCNDC$	$r_v \Longrightarrow r_c$	r_v	r_c	condensation on cloud droplets
$RCAUTR$	$r_c + r_c \Longrightarrow r_r$	r_c	r_r	autoconversion of cloud droplets
$RCACCR$	$r_c + r_r \Longrightarrow r_r$	r_c	r_r	accretion of cloud droplets by raindrops
$RREVAV$	$r_r \Longrightarrow r_v$	r_r	r_v	evaporation(condensation)

Cold processes

Small ice crystals are initiated by two heterogeneous nucleation processes:

- deposition: formation of ice embryos in a supersaturated environment over ice,
- contact: freezing of supercooled droplet subsequent to the attraction of aerosol particles by Brownian motion or by phoretic diffusion (a function of temperature).

Also, when the temperature drops below -35°C, the homogeneous nucleation or droplet freezing takes place to deplete very rapidly the cloud droplets.
Ice crystals can grow by water vapor deposition or decay by sublimation depending on the level of saturation of the environment with respect to ice. Aggregates are formed by autoconversion process of pristine ice crystals while the primary source of graupel is either raindrop contact freezing or heavy riming of the snowflakes. When the air temperature is warmer than T_t, the small primary ice crystals are immediately converted into cloud water, the snowflakes are transfered into the graupel category at a rate proportional to their partial melting (Walko et al. 1995) and finally the graupels melt by shedding all the liquid water into raindrops.
The representation of ice crystal growth by collection processes (for instance by aggregation, riming or rain contact freezing) remains the most difficult and controversial task. As in many bulk parameterizations, the assumptions of continuous growth and the simple geometric sweep-out concept for the collection kernel K are retained. So the mutual gravitational interaction between species X and Y leads to a general definition of K,

$$K(D_x, D_y) = \frac{\pi}{4}(D_x + D_y)^2 |v_x(D_x) - v_y(D_y)| E_{xy}, \tag{7.11}$$

where E_{xy} is the collection efficiency (often, a poorly known quantity).
In the most general case, the collection process COL involving X and Y can lead to the formation of a third specy Z (simultaneous collection and conversion processes with sometimes further external conditions on the mixing ratios r_x and r_y), so the mixing ratio tendency of specy Y (a loss for Y) due to the mass collection of X is:

$$RYCOLXZ = \rho^{-1} \int_0^{\infty} \left\{ \int_0^{\infty} K(D_x, D_y)\, m_y(D_y) n_y(D_y) dD_y \right\} n_x(D_x) dD_x, \tag{7.12}$$

Table 7.4: List of the cold microphysical processes (involving ice particles).

Symbol	Mechanism	Sink	Source	Process
$RVHENI$	$r_v \Longrightarrow r_i$	r_v	r_i	heterogeneous nucleation
$RCHONI$	$r_c \Longrightarrow r_i$	r_c	r_i	homogeneous nucleation
$RRHONG$	$r_r \Longrightarrow r_g$	r_r	r_g	homogeneous nucleation
$RCBERI$	$r_c \Longrightarrow r_i$	r_c	r_i	Bergeron-Findeisen effect
$RVDEPI$	$r_v + r_i \Longrightarrow r_i$	r_v	r_i	deposition(sublimation)
$RVDEPS$	$r_v + r_s \Longrightarrow r_s$	r_v	r_s	deposition(sublimation)
$RVDEPG$	$r_v + r_g \Longrightarrow r_g$	r_v	r_g	deposition(sublimation)
$RIAUTS$	$r_i + r_i \Longrightarrow r_s$	r_i	r_s	autoconversion of pristine ice
$RIAGGS$	$r_i + r_s \Longrightarrow r_s$	r_i	r_s	aggregation of pristine ice
$RRCFRIG$	$r_i + r_r \Longrightarrow r_g$	r_r	r_g	raindrops contact freezing
$RICFRRG$	$r_i + r_r \Longrightarrow r_g$	r_i	r_g	raindrops contact freezing
$RCRIMSS$	$r_c + r_s \Longrightarrow r_s$	r_c	r_s	light riming of aggregates
$RCRIMSG$	$r_c + r_s \Longrightarrow r_g$	r_c	r_g	heavy riming of aggregates
$RSRIMCG$	$r_c + r_s \Longrightarrow r_g$	r_s	r_g	heavy riming of aggregates
$RRACCSS$	$r_r + r_s \Longrightarrow r_s$	r_r	r_s	accretion of rain and aggregates
$RRACCSG$	$r_r + r_s \Longrightarrow r_g$	r_r	r_g	accretion of rain and aggregates
$RSACCRG$	$r_r + r_s \Longrightarrow r_g$	r_s	r_g	accretion of rain and aggregates
$RCDRYG$	$r_c + r_g \Longrightarrow r_g$	r_c	r_g	dry growth of the graupels
$RIDRYG$	$r_i + r_g \Longrightarrow r_g$	r_i	r_g	dry growth of the graupels
$RRDRYG$	$r_r + r_g \Longrightarrow r_g$	r_r	r_g	dry growth of the graupels
$RSDRYG$	$r_s + r_g \Longrightarrow r_g$	r_s	r_g	dry growth of the graupels
$RCWETG$	$r_c + (r_g) \Longrightarrow r_r$	r_c	r_r & r_g	partial freezing & water shedding
$RRWETG$	$r_r + (r_g) \Longrightarrow r_g$	r_r	r_g	partial freezing & water shedding
$RIWETG$	$r_i + r_g \Longrightarrow r_g$	r_i	r_g	wet growth of the graupels
$RSWETG$	$r_s + r_g \Longrightarrow r_g$	r_s	r_g	wet growth of the graupels
$RIMLTC$	$r_i \Longrightarrow r_c$	r_i	r_c	melting
$RGMLTR$	$r_g \Longrightarrow r_r$	r_g	r_r	melting
$RSCVMG$	$r_s \Longrightarrow r_g$	r_s	r_g	conversion melting

conversely the mixing ratio tendency for X (a loss too but for X) is:

$$RXCOLYZ = \rho^{-1} \int_0^\infty \left\{ \int_0^\infty K(D_x, D_y)\, m_x(D_x) n_x(D_x) dD_x \right\} n_y(D_y) dD_y, \tag{7.13}$$

and the mixing ratio tendency of specy Z (a gain for Z) is simply $RXCOLYZ + RYCOLXZ$. When Z identifies to one of the initial specy X or Y, i. e. a two component process, a single mixing ratio collection rate needs to be computed as for instance Eq. (7.13) if $Z \equiv Y$ or Eq. (7.12) if $Z \equiv X$ as for instance

$$RYCOLX = \rho^{-1} \int_0^\infty \left\{ \int_0^\infty K(D_x, D_y)\, m_y(D_y) n_y(D_y) dD_y \right\} n_x(D_x) dD_x = -RXCOLY \tag{7.14}$$

is the mixing ratio rate of change of specy X due to the single collection of specy Y.
More complicated and as discussed by Farley et al. (1989) and Ferrier (1994), collection processes might be envisionned as both two and three component processes when threshold diameters are introduced for instance to convert specy Y into specy Z if and only if the diameter D_y of Y is larger than a required value D_y^{lim}. This means than only a fraction (generally the upper diameter one) of specy Y, collecting specy X, will be converted into specy Z and thus be removed from the Y category, while the remaining fraction of the former specy Y increases its mass as a binary collection process between X and Y. So, the growth of X from Y is now:

$$RYCOLXX = \rho^{-1} \int_0^\infty \left\{ \int_0^{D_y^{lim}} K(D_x, D_y)\, m_y(D_y) n_y(D_y) dD_y \right\} n_x(D_x) dD_x, \tag{7.15}$$

the growth of Z from both X and Y is:

$$\begin{aligned} RYCOLXZ &= RYCOLX - RYCOLXX \\ &= \rho^{-1} \int_0^\infty \left\{ \int_{D_y^{lim}}^\infty K(D_x, D_y)\, m_y(D_y) n_y(D_y) dD_y \right\} n_x(D_x) dD_x, \end{aligned} \tag{7.16}$$

while $RYCOLX$, the total loss of Y (leading to the growth of X in Eq. (7.15) and to the growth of Z in Eq. (7.16)), is given by Eq. (7.14).
Although, this approach has much more physical basis, it needs a (technically more complicated) partial integration over the dimensional spectrum of at least a specy to compute the mixing ratio tendencies.
In the present parameterization, any accreted material on the graupels cannot change the type of this crystal but the concurrent dry/wet growth regimes will compete in the manner described by Lin et al. (1983). So much of these collection processes will be described by integrals of type (7.14). Considering now the collection processes on aggregates, it is postulated that beyond a critical size of the initial aggregate, the riming of cloud droplets may modify so much the crystal characteristics that it is converted into a graupel. Furthermore, the collection of raindrops on aggregates is also very efficient to convert the upper part of the aggregate spectrum into graupels in the manner suggested by Ferrier (1994). So partial integrals of the form (7.15) need to be computed to represent the two latter collection processes.

7.2 Microphysical processes

7.2.1 Summary of the scheme

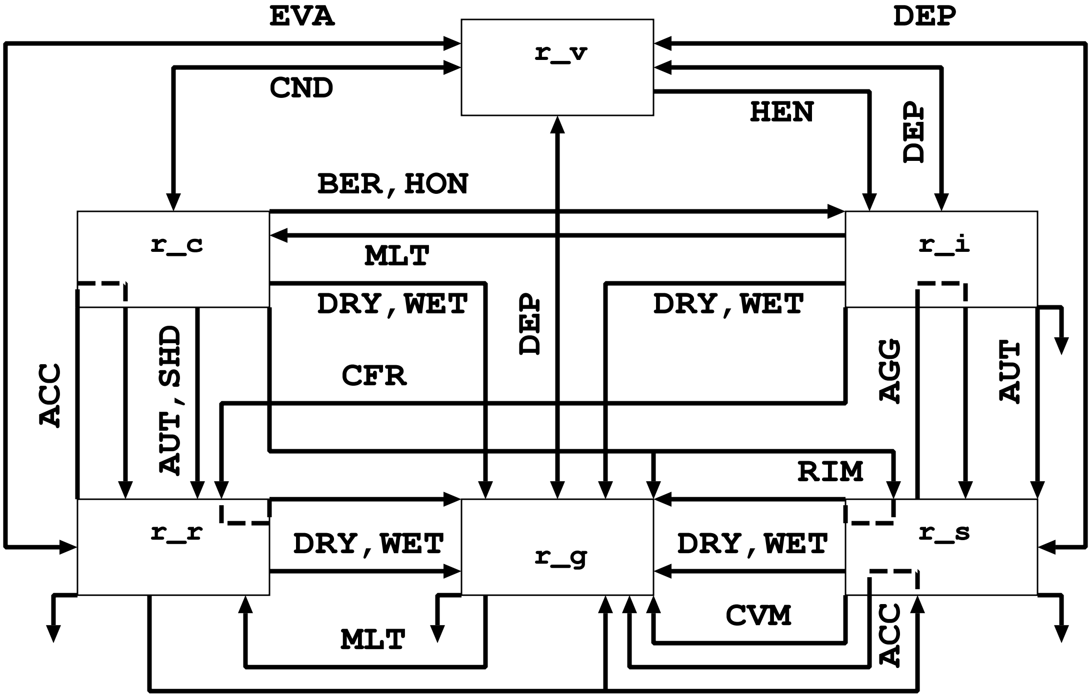

Figure 7.2: Diagram of the microphysical processes for mixed phase cloud in the present scheme.

7.2.2 Warm processes

The parameterization of these processes is borrowed from the widespread Kessler scheme described elsewhere. But the autoconversion process has been slightly generalised.

The original formulation

$$RCAUTR = k_{cr}\max(0, r_c - r_c^*) \tag{7.17}$$

with $k_{cr} = 10^{-3}$ s^{-1}, $r_c^* = q_c^*/\rho_{dref}$, and $q_c^* = 0.5\ 10^{-3}$ kg/m^3 has been first rewritten by Redelsperger and Sommeria (1986) by introducing a subgrid heterogeneity represented by a uniform PDF

$$RCAUTR = \begin{cases} 0, & \text{if } r_c + \sigma_{r_c} < r_c^* \\ k_{cr}(r_c - r_c^*), & \text{if } r_c - \sigma_{r_c} > r_c^* \\ k_{cr}\frac{(r_c+\sigma_{r_c}-r_c^*)^2}{4\sigma_{r_c}}, & \text{elsewhere} \end{cases} \tag{7.18}$$

Then it has been generalised for other PDF using

$$RCAUTR = k_{cr}CF_H\max(0, \frac{r_{c_H}}{CF_H} - r_c^*) \tag{7.19}$$

where CF_H and r_{c_H} are respecively the fraction and the content of the cloud part exceeding the autoconversion threshold. The Redelsperger and Sommeria (1986) formulation is found by setting

$$CF_H = \begin{cases} 0, & \text{if } r_c + \sigma_{r_c} < r_c^* \\ 1., & \text{if } r_c - \sigma_{r_c} > r_c^* \\ \frac{r_c + \sigma_{r_c} - r_c^*}{2\sigma_{r_c}}, & \text{elsewhere} \end{cases} \tag{7.20}$$

and

$$r_{c_H} = \begin{cases} 0, & \text{if } r_c + \sigma_{r_c} < r_c^* \\ r_c, & \text{if } r_c - \sigma_{r_c} > r_c^* \\ \frac{(r_c + \sigma_{r_c} - r_c^*)(r_c + \sigma_{r_c} + r_c^*)}{4\sigma_{r_c}}, & \text{elsewhere} \end{cases} \tag{7.21}$$

Besides, we can compute CF_H and r_{c_H} for an all-or-nothing scheme or for an in-cloud scheme or even during the vapor adjustement if it uses a PDF (i.e. the part of the PDF exceeding a threshold made of the sum between the saturation and the autoconversion thresholds) or from the shallow convection cloud scheme if based on a PDF.
For the other processes, their mathematical expression are only recalled here for completness.

$$RCACCR = \frac{\pi}{4} N_r r_c c_r M(d_r + 2) \left(\frac{\rho_{00}}{\rho_{dref}} \right)^{0.4} \tag{7.22}$$

and

$$RREVAV = \frac{4\pi}{\rho} \frac{(-SS_w)}{A_w(T,P)} N_r \mathcal{C}_{1r} \left[\overline{f}_{0r} M_r(1) + \overline{f}_{1r} c_r' M_r(\frac{d_r + 3}{2}) \right], \tag{7.23}$$

where $SS_w = r_v / r_{vs_w} - 1$ and

$$A_w(T,P) = \frac{L_v(T)^2}{k_a(T) R_v T^2} + \frac{R_v T}{D_v(T,P) e_{sw}(T)}.$$

$\mathcal{C}_{1r}$, f_{0_r} and f_{1_r} are taken from Table 7.2 and $c_r' = Sc_v^{1/3} (c_r \rho / \eta)^{1/2} (\rho_{00} / \rho_{dref})^{0.2}$ with $Sc_v \sim 0.635$ (see after (7.43)). Note that according to the nomenclature and sign convention: $RREVAV > 0$ in case of rain evaporation.
In order to reproduce the small drizzle of the fog necessary for its dissipation, the sedimentation of cloud droplets $RSEDC$ can be taken into account. The slope parameter for the cloud λ_c used for the mass sedimentation rate is defined by :

$$\lambda_c = \left[\frac{\pi}{6} \rho_w \frac{\Gamma(\nu_c + \frac{3}{\alpha_c})}{\Gamma(\nu_c)} \frac{N_c}{\rho_d r_c} \right]^{\frac{1}{3}}$$

α_c, ν_c and N_c are defined according to the fractions of sea and land surface cover of the grid mesh, with $N_{c_{sea}}$ =100 cm^{-3} and $N_{c_{land}}$ =300 cm^{-3}.

7.2.3 Heterogeneous nucleation

As in Ferrier (1994) and according to Meyers et al. (1992), the number concentration of primary ice crystals N_{NU} formed by heterogeneous nucleation is given by:

$$N_{NU} = \begin{cases} N_{NU1}, & T - T_t \geq -5\text{K}, \\ N_{NU2}, & T - T_t < -5\text{K} \end{cases} \tag{7.24}$$

Table 7.5: Set of parameters used to parameterize the nucleation processes (from Ferrier 1994).

N_{NU1_0}	N_{NU2_0}	α_1	β_1	α_2	β_2	m_{NU_0}
50 m^{-3}	1000 m^{-3}	4.5	0.6 K^{-1}	12.96	0.639	6.88 10^{-13} kg

where

$$N_{NU1} = N_{NU1_0}\,[(r_v - r_{vs_i})/(r_{vs_w} - r_{vs_i})]^{\alpha_1}\ exp(-\beta_1(T - T_t)), \tag{7.25}$$

$$N_{NU2} = N_{NU2_0}\,exp(\alpha_2 SS_i - \beta_2), \tag{7.26}$$

where $SS_i = r_v/r_{vs_i} - 1$ is the supersaturation ratio with respect to ice and r_{vs_w} is the saturated mixing ratio over supercooled water.

Assuming that $N_i = N_{NU}$ (because the secondary ice production is not yet considered) and for m_{NU_0}, the mass of a nucleated ice crystal, the mass nucleation rate $RVHENI$ equals to:

$$RVHENI = (\rho\Delta t)^{-1} m_{NU_0} Max(N_{NU} - N_i^{t-\Delta t}, 0). \tag{7.27}$$

The typical values of the unknown parameters are given in Table 7.5.

In (7.27), the previous ice crystal concentration $N_i^{t-\Delta t}$ is available because the diagnostic variable $N_i = N_{NU}$ is stored after an update by the mean of (7.24).

7.2.4 Homogeneous nucleation

When the temperature drops below $-35°$C, the spontaneous freezing of cloud droplets in absence of ice nuclei (the homogeneous nucleation) is an active process to convert any remaining small droplets into pristine crystals. This is an essential process in cirriform clouds so it needs to be modeled accurately in such cases.

The probability $\mathcal{P}$ of a water droplet of volume V to freeze in the interval of time $[t,\ t + \Delta t]$ is governed by the nucleation formula

$$\mathcal{P} = 1 - \exp\Big(-\int_t^{t+\Delta t} J_{HOM}(T)V\,dt\Big), \tag{7.28}$$

where V is the droplet volume and $J_{HOM}(T)$ the freezing rate, tabulated by Pruppacher (1995) and reported in Table 7.6[9],

The above set of data has been approximated by a fitting curve which is:

$$J_{HOM} = \exp(\alpha_3(T - T_t) - \beta_3), \tag{7.29}$$

with $\alpha_3 = -3.075\ \mathrm{K}^{-1}$ and $\beta_3 = 81.00356$.

Considering $J_{HOM}(T)$ and V as constant during the timestep Δt, (7.28) can be reduced to

$$\mathcal{P} \approx J_{HOM}(T)V\Delta t. \tag{7.30}$$

---

[9] Note that J_{HOM} goes to infinity as $T - T_t < -44$ K

Table 7.6: Values of $J_{HOM}(T)$ after Pruppacher (1995).

$T - T_t$ (K)	-35	-36	-37	-38	-39
J_{HOM} ($\mathrm{m}^{-3}\mathrm{s}^{-1}$)	$2\ 10^{11}$	$1\ 10^{13}$	$3\ 10^{14}$	$5\ 10^{15}$	$9\ 10^{16}$

$T - T_t$ (K)	-40	-41	-42	-43	-44
J_{HOM} ($\mathrm{m}^{-3}\mathrm{s}^{-1}$)	$1\ 10^{18}$	$2\ 10^{19}$	$1\ 10^{21}$	$5\ 10^{22}$	$2\ 10^{23}$

Integrating (7.30) over the cloud droplet spectrum and differentiating with respect to time and using (7.9) with an appropriate form for the cloud droplets, gives the final homogeneous nucleation rate

$$RCHONI = Min\Big\{\frac{r_c}{\Delta t}, \frac{\pi}{6} J_{HOM}(T)(\rho r_c)\frac{M_c(6)}{M_c(3)}\Big\}. \tag{7.31}$$

To compute the M_c ratio in (7.31), it is assumed that $\lambda_c = 1.1\ 10^5$ m^{-1} corresponding to a cloud droplet number concentration $N_c \sim 400\ 10^6$ m^{-3} and a mixing ratio $r_c \sim 10^{-3}$ kg/kg for $\rho \sim 1$ kg/m^3.

Because the scheme assumes that the ice crystal concentration is determined by the only heterogeneous nucleation parameterization, the diagnostic concentration of these pristine crystals is not modified by the present homogenous nucleation scheme. This is a source of error indeed because this concentration must be accounted for in computing the very slow speed of sedimentation of cirrus clouds in long lived simulations. The solution which has been adopted in the present scheme employs a specific ice crystal number concentration relationship to compute a sedimentation flux of these small crystals (see the subsection relative to the computation of $RSEDI$).

We assume also that the raindrops cannot survive to temperature colder than -35°C because they are spontaneously converted to graupels by homogenous freezing (nucleation)

$$RRHONG = \frac{r_r}{\Delta t} H(T_t - 35), \tag{7.32}$$

where $H(x)$ is the Heaviside distribution ($H(x) = 0$ if $x < 0$ and $H(x) = 1$ if $x \geq 0$)

7.2.5 Deposition (sublimation) of water vapor

The rate of mass growth or decay of a single aggregate or graupel particle by vapor deposition or sublimation can be written as:

$$\partial m/\partial t\ |_{DEP/SUB} = 4\pi S S_i \mathcal{C}\overline{f}/A_i(T,P), \tag{7.33}$$

where $\mathcal{C}$ is the capacity of the ice crystal, $\overline{f}$ is a ventilation factor and $A_i(T,P)$ is a thermodynamic function:

$$A_i(T,P) = \frac{L_s(T)^2}{k_a(T)R_v T^2} + \frac{R_v T}{D_v(T,P)e_{si}(T)}, \tag{7.34}$$

where e_{si} is the saturation vapor pressure over ice:

$$e_{si}(T) = exp\big(\alpha_i - \frac{\beta_i}{T} - \gamma_i \ln(T)\big), \tag{7.35}$$

with

$$\begin{aligned}
\alpha_i &= \ln(e_{si}(T_t)) + \frac{\beta_i}{T_t} - \gamma_i \ln(T_t) && (7.36)\\
\beta_i &= \frac{L_s(T_t)}{R_v} + \gamma_i T_t && (7.37)\\
\gamma_i &= \frac{C_i - C_{pv}}{R_v} && (7.38)
\end{aligned}$$

and L_s is the latent heat of sublimation:

$$L_s(T) = L_s(T_t) + (C_{pv} - C_i)(T - T_t). \tag{7.39}$$

The thermal conductivity of the air $k_a(T)$ and the diffusivity of water vapor in the air $D_v(T,P)$ are given by (see Pruppacher and Klett 1978, pp. 418 and 413):

$$\begin{aligned}
D_v(T,P) &= 0.2138\ 10^{-4}(T/T_t)^{1.94}(P_{00}/P), && (7.40)\\
k_a(T) &= 2.38\ 10^{-2} + 0.0071\ 10^{-2}(T - T_t). && (7.41)
\end{aligned}$$

In (7.33), $\mathcal{C}$ and $\overline{f}$ have the following expressions depending upon the crystal shape and size

$$\mathcal{C} = \mathcal{C}_1 D \tag{7.42}$$

$$\overline{f} = \overline{f}_0 + \overline{f}_1 \chi + \overline{f}_2 \chi^2 \tag{7.43}$$

where $\chi = Sc_v^{1/3} Re^{1/2}$ is a function of $Sc_v = \nu(T,P)/D_v(T,P)$, the Schmidt number for water vapor and of $Re = v(D)D\rho/\eta(T)$, the Reynolds number of the flow around a crystal of size D. The dynamic viscosity $\eta(T) = \rho(T,P)\nu(T,P)$ of the air of density $\rho(T,P)$ is given by (see Pruppacher and Klett 1978, p. 323):

$$\eta(T) = 1.718\ 10^{-5} + 0.0049\ 10^{-5}(T - T_t). \tag{7.44}$$

In the following, $Sc_v \approx 0.635$ with a very good approximation.
In 7.42, a cylindrical shape is assumed for the aggregates while the rimed particles are spherical (see Table 7.2). Furthermore, as the pristine ice category is assumed to contain small crystals only, in contrast to the aggregates and rimed particles which are rather large-size hydrometeors, the formulas of Hall and Pruppacher (1977) have been split for a simplified application to the $D < 70\mu$m range, relevant of the r_i specy (see below for the parameterization of the Bergeron-Findeisen effect), and for the $D > 70\mu$m range corresponding to the r_s and r_g categories (see Table 7.2).
Integration of (7.33) over the whole particle spectral range gives for $X(=j)$ being $S(=s)$ or $G(=g)$:

$$RVDEPX = \frac{4\pi}{\rho}\frac{SS_i}{A_i(T,P)} N_j \mathcal{C}_{1j}\left[\overline{f}_{0j} M_j(1) + \overline{f}_{1j} c'_j M_j(\frac{d_j+3}{2}) + \overline{f}_{2j} c'^2_j M_j(d_j+2)\right], \tag{7.45}$$

where $c'_j = Sc_v^{1/3}(c_j\rho/\eta)^{1/2}(\rho_{00}/\rho_{dref})^{0.2}$ and where the moments M_j of the ice category j can be expanded according to (7.6.)
Although the water vapor exchanges over the pristine ice crystals (and the cloud droplets) in the present scheme are treated implicitly by an adjustment process (see paragraph 7.3.4), an expression equivalent to the explicit rate $RVDEPX$ needs to be computed for the purpose of parameterizing the Bergeron-Findeisen effect described hereafter.

7.2.6 Bergeron-Findeisen effect

A mixed phase cloud is characterized by the simultaneous existence of cloud droplets and small ice crystals in equilibrium with the vapor saturation level over liquid water and ice water, respectively (Fig. 7.3). As the later is always lower that the former ($e_{si}(T) < e_{sw}(T)$), there is a systematic evaporation of the cloud droplets for deposition onto the ice crystals. This process is independent of the droplet and crystal growth or decay due to the supply or deficit of water vapor as for instance by vertical transport.

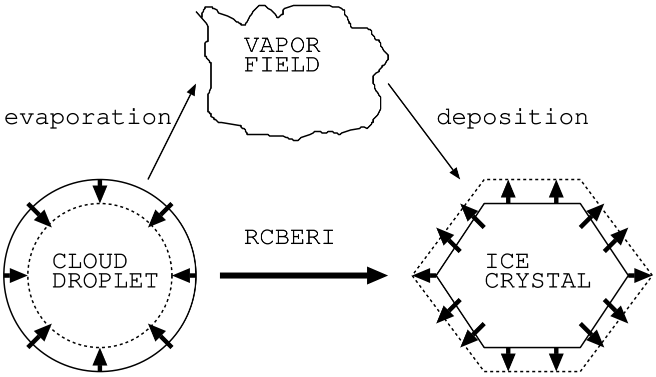

Figure 7.3: Illustration of the Bergeron-Findeisen effect and its parameterization.

In the present scheme, it is assumed that $RCBERI$, the resulting rate of mass transfer from the cloud droplets to the ice crystals, is determined by the rate of water vapor deposition onto the pristine ice crystals. This rate is assumed to be equal to the rate of evaporation of the cloud droplets so the process is neutral with respect to the water vapor reservoir but not for the heat budget as the corresponding heat of freezing is accounted to warm the environmental air. The expression of $RCBERI$ is a case application of (7.45) for the pristine ice that is:

$$RCBERI = \frac{4\pi}{\rho}\frac{SS_i}{A_i(T,P)}N_i\mathcal{C}_{1i}\left[\overline{f}_{0i}M_i(1) + \overline{f}_{2i}c_i'^2 M_i(d_i+2)\right], \tag{7.46}$$

where d_i, $\mathcal{C}_{1i}$, f_{0i} and f_{2i} are taken from Table 7.2 and $c_i' = Sc_v^{1/3}(c_i\rho/\eta)^{1/2}(\rho_{00}/\rho_{dref})^{0.2}$ with $Sc_v \sim 0.635$.

7.2.7 Autoconversion of primary ice crystal to form aggregates

This process is the only way to initiate aggregates in a cold cloud and generally two approaches are employed to describe it. In the first one (Cotton et al. 1986), the aggregation rate has some physical root as it is based upon the stochastic collection kernel (K_{PS}) of Passarelli and Srivastava (1978). In the second one (adopted in the present scheme because of its simplicity), a formula analogous to the cloud droplet autoconversion parameterization of Kessler is used with:

$$RIAUTS = k_{is}\, Max(0, r_i - r_i^*). \tag{7.47}$$

The inverse time constant k includes a temperature efficiency factor as in Lin et al. (1983) ($k_{is} = 10^{-3}\, e^{0.015(T-T_t)}$) while the critical ice mixing ratio r_i^* varies with temperature. This threshold, expressed as critical ice specific humidity q_i^*, was initially set equal to a fixed value of $0.5\ 10^{-3}$ kg/m^3, in the "realistic" range of $0.1\ 10^{-3}$ kg/m^3 to $1\ 10^{-3}$ kg/m^3 according to some suggestions of q_i^* ($\sim 1\ 10^{-3}$ kg/m^3 by Lin et al. (1983) or $\sim 0.7\ 10^{-3}$ kg/m^3 by Rutledge and Hobbs (1983)). The threshold was then reduced to the assigned value of $r_i^\star = 2 \times 10^{-5}$ kg kg^{-1} as deduced from an extended thick cloud regime over Atlantic (Chaboureau et al. 2002). Finally, in order to apply the formulation to several ice cloud types, Ryan (2000) parameterizes $r_i^\star$ as a function of the air temperature, T. This suggestion is now incorporated into the model setting as an adjustment for low temperature limits, which leads to:

$$r_i^\star = \min(2 \times 10^{-5}, 10^{0.06\times(T-273.16)-3.5}). \tag{7.48}$$

An improvement of the cirrus cover was shown by comparison with satellite observations (Chaboureau and Pinty 2006).
In the current implementation, the autonversion is written in such a way as to allow the use of a PDF (as for liquid autoconversion). It is possible to use a uniform PDF on the cloud or the distribution queue of the PDF used during saturation adjustment.

7.2.8 Contact freezing of raindrops to form graupels

The production of frozen drops due to collision between pristine ice crystals and raindrops is a typical three component collection process. As in other schemes, the effects of small ice crystal fall speeds on the collection kernel (7.11) can be legitimately ignored so (7.12) and (7.13) are easily integrated to give:

$$RRCFRIG = \frac{1}{\rho}\frac{\pi^2}{24}E_{ir}N_iN_r\rho_w c_r M(5+d_r)\left(\frac{\rho_{00}}{\rho_{dref}}\right)^{0.4}, \tag{7.49}$$

$$RICFRRG = \frac{\pi}{4}E_{ir}N_r r_i c_r M(2+d_r)\left(\frac{\rho_{00}}{\rho_{dref}}\right)^{0.4} \tag{7.50}$$

where (7.3)-(7.6) have been used. The terminal fall speed of the raindrops is assumed to follow (7.4) but for $c_r = 842$(m/s)$^{0.2}$ and for $d_r = 0.8$ (see Table 7.2) while $E_{ir} = 1$.

7.2.9 Collection growth of the aggregates

Aggregates grow by collecting small pristine crystals ($RIAGGS$) and by the partial riming of cloud droplets ($RCRIMSS$) and small raindrops ($RRACCSS$). In case of heavy riming by droplets or when the collected raindrops are large, the growth of the aggregates is followed by a conversion into the graupel category.

Collection of pristine crystals

Neglecting the relative size and fall speed of the pristine crystals compared to that of the aggregates and integrating over the dimensional spectrum of the aggregates give:

$$RIAGGS = \frac{\pi}{4}E_{is}N_s r_i c_s M(2+d_s)\left(\frac{\rho_{00}}{\rho_{dref}}\right)^{0.4}, \tag{7.51}$$

where (7.12) have been used with $D_x \sim 0$ in (7.11). The collection efficiency, estimated from Kajikawa and Heymsfield (1989) that is:

$$E_{is} = 0.25\, e^{0.05(T-T_t)}, \tag{7.52}$$

is consistent with the decrease of the sticking efficieny of the interacting solid crystals when the temperature is cooler than T_t.

Riming by cloud droplets

The approach of Farley et al. (1989) is used with the assumption that conversion of aggregates into graupels may occur for riming aggregates of size larger than $D_{cs}^{lim} = 7\text{mm}$[10] , thus the growth of aggregates by riming is reduced to:

$$RCRIMSS = \frac{\pi}{4} E_{cs} N_s r_c c_s M(2 + d_s; D_{cs}^{lim}) \left(\frac{\rho_{00}}{\rho_{dref}} \right)^{0.4}, \tag{7.53}$$

where $E_{cs} = 1$ and where $M(p; D^{lim})$ is the incomplete integration version of (7.6) which is evaluated numerically for computational efficiency, namely:

$$M(p; D^{lim}) = \int_0^{D^{lim}} D^p g(D)\, dD \sim \sum_0^{D^{lim}} D^p g(D) \Delta D. \tag{7.54}$$

Conversely, the graupel conversion rate consecutive to the heavy riming of the cloud droplets on the flakes is:

$$RCRIMSG = RCRIMS - RCRIMSS = \frac{\pi}{4} E_{cs} N_s r_c c_s M(2 + d_s) \left(\frac{\rho_{00}}{\rho_{dref}} \right)^{0.4} - RCRIMSS, \tag{7.55}$$

while the simultaneous rate of transfer of aggregate mixing ratio to the graupel category is simply estimated as the mass of aggregate larger than D_{cs}^{lim} that is readily available at each time step thus,

$$RSRIMCG = \frac{1}{\Delta t} N_s \int_{D_{cs}^{lim}}^{\infty} a_s D_s^{b_s} g(D_s)\, dDs = \frac{N_s}{\Delta t} a_s (M(b_s) - M(b_s; D_{cs}^{lim})). \tag{7.56}$$

Collection of raindrops

As for the riming of cloud droplets, it is postulated that the collection of small raindrops do not change the structure of an aggregate but larger colliding raindrops reshape it as a graupel. Furthermore as both raindrops and aggregates have significant fall speeds, it is not easy to solve the integrals of the form of (7.12) and (7.15) together with (7.11) and so the numerical technique suggested by Ferrier (1994) have been adopted. For instance, (7.14) with the full expansion of (7.11) is rewritten as:

$$RZCOLX = \frac{1}{\rho} \frac{\pi}{4} \left(\frac{\rho_{00}}{\rho_{dref}} \right)^{0.4} a_z N_x N_z \Lambda(\lambda_x, \lambda_z) \Delta v_{xz}(\lambda_x, \lambda_z), \tag{7.57}$$

where

$$\Delta v_{xz} = \Lambda(\lambda_x, \lambda_z)^{-1} \int_0^{\infty} \left\{ \int_0^{\infty} E_{xz} (D_x + D_z)^2 |c_x D_x^{d_x} - c_z D_z^{d_z}| D_z^{b_z} g_z(D_z)\, dD_z \right\} g_x(D_x)\, dD_x \tag{7.58}$$

and with the normalizing factor $\Lambda(\lambda_x, \lambda_z)$ obtained by removing E_{xz} and the absolute fall speed difference in (7.58) that leads to the formal expression:

$$\begin{aligned} \Lambda(\lambda_x, \lambda_z) &= \textstyle\int_0^{\infty} \left\{ \int_0^{\infty} (D_x + D_z)^2 D_z^{b_z} g_z(D_z)\, dD_z \right\} g_x(D_x)\, dD_x \\ &= M_x(2) M_z(b_z) + 2 M_x(1) M_z(1 + b_z) + M_z(2 + b_z). \end{aligned} \tag{7.59}$$

---

[10] The diameter D_{cs}^{lim} can be also estimated by considering the Macklin formula (see, Heymsfield and Pflaum 1985) which relates the rime density to the size of the collector particle

As Δv_{xz} is only a function of the time and space local values of λ_x and λ_z, a two-dimensionnal look-up table is created to contain numerical solutions of (7.58) for a series of logarithmically spaced couplet of λ_x and λ_z in the physically expected ranges $[\lambda_x^{min}, \lambda_x^{max}]$ and $[\lambda_z^{min}, \lambda_z^{max}]$, respectively. Then accurate estimates of Δv_{xz} can be obtained by bilinear interpolation with respect to the tabulated values of λ_x and λ_z.
For the specific case of raindrop-aggregate process, the growth of the aggregates $RRACCSS$ (at the expense of rain) by raindrop merging and freezing can be written:

$$RRACCSS = \frac{1}{\rho}\frac{\pi^2}{24}\rho_w \left(\frac{\rho_{00}}{\rho_{dref}}\right)^{0.4} N_s N_r \Lambda(\lambda_s, \lambda_r) \Delta v_{sr}(\lambda_s, \lambda_r), \tag{7.60}$$

with

$$\Delta v_{sr} = \Lambda(\lambda_s, \lambda_r)^{-1} \int_0^\infty \left\{ \int_0^{D_r^{lim}} E_{sr}(D_s + D_r)^2 |c_s D_s^{d_s} - c_r D_r^{d_r}| D_r^3 g_r(D_r)\, dD_r \right\} g_s(D_s)\, dD_s \tag{7.61}$$

and the conversion rate into the graupels becomes:

$$RRACCSG = RRACCS - RRACCSS \tag{7.62}$$

with $RRACCS$ computed as in (7.57). The threshold diameter D_r^{lim} beyond which aggregates collecting raindrops are considered as graupels, is defined as in Ferrier (1994) by computing the density ρ_{sr} of the newly formed aggregate-raindrop mixture from

$$\frac{\pi}{6}\rho_w D_r^3 + \frac{\pi}{6}\Big[\underbrace{a_s \frac{6}{\pi} D_s^{b_s - 3}}_{\rho_s}\Big] D_s^3 = \frac{\pi}{6}\rho_{sr} D_s^3. \tag{7.63}$$

The resulting particle is classified as graupel (of density ρ_g) if $\rho_{sr} > 0.5(\rho_g + \rho_s)$. Considering the graupels as quasi spheroids ($b_g \sim 3$ in Table 7.2), D_r^{lim} can be expressed as:

$$D_r^{lim} = \left[\frac{3}{\pi}\frac{(a_g - a_s D_s^{b_s - 3})}{\rho_w}\right]^{1/3} D_s. \tag{7.64}$$

In addition to (7.62), conversion of aggregates into graupels drain a fraction of aggregate mixing ratio onto the graupel category at a rate:

$$RSACCRG = \frac{1}{\rho}\frac{\pi}{4}\left(\frac{\rho_{00}}{\rho_{dref}}\right)^{0.4} N_s N_r a_s \Lambda(\lambda_r, \lambda_s) \Delta v_{rs}(\lambda_r, \lambda_s), \tag{7.65}$$

with

$$\Delta v_{rs} = \Lambda(\lambda_r, \lambda_s)^{-1} \int_0^\infty \left\{ \int_{D_r^{lim}}^\infty E_{sr}(D_s + D_r)^2 |c_s D_s^{d_s} - c_r D_r^{d_r}| g_r(D_r)\, dD_r \right\} D_s^{b_s} g_s(D_s)\, dD_s \tag{7.66}$$

7.2.10 Wet/dry growth of the graupels

Graupeln are very efficient collectors for condensed water so during their accretional growth, their surface temperature (T_s) is generally larger than the temperature of the environment because of the latent heat release by the liquid accreted material. At equilibrium this temperature excess is balanced by the convective heating of the ambiant air. Until the mean surface temperature of the graupels remains below T_t all the collected droplets and raindrops can freeze: this stage corresponds to the DRY growth mode. As soon as T_s reaches the value of T_t, a thin liquid film persists at the surface of the graupels and any excess of accreted liquid condensate is shed away: this second stage is the WET growth mode corresponding to the formation of hail.

Dry growth

The dry growth of the graupels by collection processes contains the sum of individual accretion processes that is:

$$RDRYG = RCDRYG + RRDRYG + RIDRYG + RSDRYG. \tag{7.67}$$

The expressions for $RCDRYG$ and for $RIDRYG$ are similar to that of $RIAGGS$ in Eq. (7.51), they read:

$$RCDRYG = \frac{\pi}{4} E_{cg} N_g r_c c_g M(2 + d_g) \left(\frac{\rho_{00}}{\rho_{dref}} \right)^{0.4}, \tag{7.68}$$

$$RIDRYG = \frac{\pi}{4} E_{ig} N_g r_i c_g M(2 + d_g) \left(\frac{\rho_{00}}{\rho_{dref}} \right)^{0.4}, \tag{7.69}$$

but with different efficiencies that is:

$$E_{cg} = 1 \qquad \text{and} \qquad E_{ig} = 0.01\ e^{0.1(T - T_t)} \tag{7.70}$$

as revised by Ferrier et al. (1995).[11]

The accretional growth of the graupels with large hydrometeors (aggregates and raindrops) is computed using the numerical technique of Ferrier (1994) which has been already applied for the aggregates collecting raindrops. However the present collection processes are simpler because the graupels are the final products regardless the type of collected particle; so one gets:

$$RSDRYG = \frac{1}{\rho} \frac{\pi}{4} \left(\frac{\rho_{00}}{\rho_{dref}} \right)^{0.4} N_g N_s a_s \Lambda(\lambda_g, \lambda_s) \Delta v_{gs}(\lambda_g, \lambda_s), \tag{7.71}$$

with

$$\Delta v_{gs} = \Lambda(\lambda_g, \lambda_s)^{-1} \int_0^\infty \left\{ \int_0^\infty E_{gs}(D_g + D_s)^2 |c_g D_g^{d_g} - c_s D_s^{d_s}| D_s^{b_s} g_s(D_s)\, dD_s \right\} g_g(D_g)\, dD_g \tag{7.72}$$

for graupels collecting flakes and

$$RRDRYG = \frac{1}{\rho} \frac{\pi^2}{24} \rho_w \left(\frac{\rho_{00}}{\rho_{dref}} \right)^{0.4} N_g N_r \Lambda(\lambda_g, \lambda_r) \Delta v_{gr}(\lambda_g, \lambda_r), \tag{7.73}$$

with

$$\Delta v_{gr} = \Lambda(\lambda_g, \lambda_r)^{-1} \int_0^\infty \left\{ \int_0^\infty E_{gr}(D_g + D_r)^2 |c_g D_g^{d_g} - c_r D_r^{d_r}| D_r^3 g_r(D_r)\, dD_r \right\} g_g(D_g)\, dD_g \tag{7.74}$$

for graupels collecting raindrops. The collision efficiencies are computed as in (7.70) with $E_{gr} = E_{cg}$ and $E_{gs} = E_{ig}$.

---

[11] The expression used to simulate the E_{ig} effect has a great importance to adjust the relative abundance of the snow/aggregate because giving a large value to E_{ig} tends to deplete rapidly this category of ice particles. Note that the solid-solid sticking coefficients are the poorest known quantities in cloud physics

Wet growth

The study of this mode growth has been made by Musil (1970) and reviewed by Nelson (1983). The heat balance equation of a graupel collecting liquid droplets/raindrops ($|_l$), solid pristine ice ($|_i$) and flakes ($|_s$) with $T_s = T_t$ can be written as:

$$\begin{aligned} &\tfrac{dm}{dt} \mid_l (L_m(T_t) - C_w(T_t - T)) - \left[\tfrac{dm}{dt} \mid_i + \tfrac{dm}{dt} \mid_s\right] C_i(T_t - T) \\ &= 4\pi \mathcal{C}_g \overline{f}_g \left[k_a(T)(T_t - T) + \frac{L_v D_v(T,P)}{R_v T}(e_{vs}(T_t) - e_v)\right]. \end{aligned} \tag{7.75}$$

As the mass increase of the individual graupel is

$$\frac{dm}{dt} \mid_g = \frac{dm}{dt} \mid_l + \frac{dm}{dt} \mid_i + \frac{dm}{dt} \mid_s, \tag{7.76}$$

the integration of (7.75) over the whole graupel spectrum using (7.1), (7.4), (7.5), (7.6), and (7.76), leads to an expression for the graupel wet growth ($RWETG$) which is:

$$\begin{aligned} RWETG = &\frac{4\pi \mathcal{C}_{1_g} N_g}{\rho(L_m(T_t) - C_w(T_t - T))}\left[k_a(T)(T_t - T) + \frac{L_v D_v(T,P)}{R_v T}(e_{vs}(T_t) - e_v)\right] \\ &\times \left[\overline{f}_{0g} M_g(1) + \overline{f}_{1g} c'_g M_g(\frac{d_g + 3}{2})\right] \\ &+ (RIWETG + RSWETG)\left[1 + \frac{C_i(T_t - T)}{(L_m(T_t) - C_w(T_t - T))}\right]. \end{aligned} \tag{7.77}$$

In the above expression, c'_g is defined in (7.45) and $RIWETG(RSWETG)$ is the graupel collection rate of pristine ice(aggregates) in the wet mode that is with $E_{ig}(E_{sg})$ in Eq. (7.70)(7.71) taken equal to unity in order to represent an enhanced sticking efficiency due to the wetting of the graupels.

Which growth mode?

To determine whether the dry (7.67) or the wet (7.77) growth mode is active, the two rates $RDRYG$ and $RWETG$ are compared and the lowest value is retained. For instance, if $RWETG > RDRYG$ means that enough water can freeze on the graupels and so the growth can operate in the dry regime. Conversely if $RDRYG > RWETG$, the growth is in the wet mode because potentially accreting water cannot freeze entirely as $RWETG$ represents the maximal freezing rate of the graupels.

Water shedding

In case of wet growth regime, any excess of liquid water at the surface of the graupels is removed (shed) and converted into raindrops. Although this process is active for large ice particles only (Rasmussen et al. 1984), it is assumed to occur even for small sized particles as the present parameterization does not contain any mixed phase category of ice. Lin et al. (1983) emphasized the role of the water shedding mechanism as a rapid transformation of cloud water into raindrops in the 0°C to -10°C region of clouds and they gave details how to handle this effect.
The key is to expand the wet growth rate $RWETG$ of (7.77) into the explicit form of (7.67), which is used to define the dry growth rate $RDRYG$, so:

$$RWETG = RRWETG + RCWETG + RIWETG + RSWETG. \tag{7.78}$$

Note that $RCWETG \equiv RCDRYG$ and that $RWETG - RIWETG - RSWETG$ is exactly the wet growth due to the liquid water collected so,

- if $RWETG - RIWETG - RSWETG > RCWETG$: there is no explicit water shedding as some raindrops can still be frozen on the surface of the graupels at the rate $RRWETG$ defined by Eq. (7.78) that is:

$$RRWETG = RWETG - RCWETG - RIWETG - RSWETG. \tag{7.79}$$

- if $RWETG - RIWETG - RSWETG < RCWETG$: even all the collected cloud droplets cannot freeze on the graupels and so are shed as raindrops at a rate $RRWETG$ defined in (7.79). In that case $RRWETG$, a negative quantity but a gain for the raindrops as it identifies to the rate of transfer of unfrozen cloud droplets into rain, is renamed as $RCSHDR$ with:

$$RCSHDR = -Min\Big\{0, RWETG - RCWETG - RIWETG - RSWETG\Big\}. \tag{7.80}$$

Finally (7.79) is recast as:

$$RRWETG = Max\Big\{0, RWETG - RCWETG - RIWETG - RSWETG\Big\}. \tag{7.81}$$

7.2.11 Melting of ice crystals

Pristine ice melting

When $T > T_t$, the small ice crystal cannot survive as they are supposed to melt instantaneously into cloud droplets at a rate:

$$RIMLTC = \frac{r_i}{\Delta t} H(T_t). \tag{7.82}$$

Melting of the graupels

In analogy with the wet growth mode of the graupels, the melting water formed at the surface of the graupels and the continuously collected water is shed away into raindrops. According to Mason (1956), the heat balance equation of a partially melting graupel is:

$$L_m(T_t)\frac{dm}{dt}\mid_g - \frac{dm}{dt}\mid_l C_w(T_t - T) = 4\pi \mathcal{C}_g \overline{f}_g \Big[k_a(T)(T_t - T) + \frac{L_v D_v(T,P)}{R_v T}(e_{vs}(T_t) - e_v)\Big]. \tag{7.83}$$

where $\frac{dm}{dt}\mid_g$ is the rate of change of the ice mass of a graupel and $\frac{dm}{dt}\mid_l$ the collected cloud droplets and raindrops (supposed to be at the same temperature T of the environment).
Integration of (7.83) over the whole dimensional spectrum of the graupels lead to an expression of the graupel melting rate,

$$\begin{aligned} RGMLTR = &-\frac{4\pi \mathcal{C}_{1_g} N_g}{\rho L_m(T_t)} \Big[k_a(T)(T_t - T) + \frac{L_v D_v(T,P)}{R_v T}(e_{vs}(T_t) - e_v)\Big] \\ &\times \big[\overline{f}_{0g} M_g(1) + \overline{f}_{1g} c'_g M_g(\frac{d_g + 3}{2})\big] \\ &-(RCWETG + RRWETG)\frac{C_w(T_t - T)}{L_m(T_t)}. \end{aligned} \tag{7.84}$$

Melting of the aggregates

The behavior of the snowflakes and aggregates is somewhat different from that of the graupels at the onset of melting. Tunnel experiments showed that during this stage, the structure of the aggregates collapse while the melting water is trapped in the gaps of the porous structure. Thus melting aggregates tend to densify and as a result get some ressemblance to the graupels in mixed phase. From a similar heat balance equation of (7.83), one can derive the melting rate of the aggregates which is:

$$\begin{aligned} RSMLT = -\frac{4\pi\mathcal{C}_{1_s}N_s}{\rho L_m(T_t)}\Big[k_a(T)(T_t-T)+\frac{L_vD_v(T,P)}{R_vT}(e_{vs}(T_t)-e_v)\Big] \\ \times\big[\overline{f}_{0s}M_s(1)+\overline{f}_{1s}c_s'M_s(\frac{d_s+3}{2})\big] \\ -(RCRIMSS+RRACCSS)\frac{C_w(T_t-T)}{L_m(T_t)}. \end{aligned} \tag{7.85}$$

Next, it is assumed that a given portion of aggregates is transfered into (melting) graupels at a rate $RSCVMG$ proportional to $RSMLT$. The former conversion rate represents the mixture of melted water and icy assemblages which is dense enough to be categorized as graupel

$$RSCVMG = \alpha_{S\to G}RSMLT. \tag{7.86}$$

In the present parameterization, $\alpha_{S\to G}$ has a value of 2 which means that an equal portion of solid ice and liquid water is required for the aggregates to build a graupel-like structure during their melting stage. It is worth to emphasize that in the spirit of the scheme, the ”melting-conversion” of the aggregates do not exchange heat with the environment, so the graupels must integrate the rate $RSCVMG$ prior the computation of their own melting rates $RGMLTR$.

7.2.12 Sedimentation rates

The present parameterization postulates that the pristine ice crystals have no significant fall speed however, in order to reproduce the slow erosion of cirrus sheets, an estimate of $RSEDI$ has been provided for that specific purpose. The sedimentation fluxes are computed by assuming that the crystals are shaped as columns with a concentration N_{Ci} given by Mc Farquhar and Heymsfield (1997) that is:

$$N_{Ci} = \frac{1}{4\pi\rho_i}\rho r_i(MAX\{0.05\ 10^6, -0.1532\ 10^6 - 0.021454\ 10^6 Log(\rho r_i)\})^3, \tag{7.87}$$

where $\rho_i = 900kg/m^3$ is the density of the ice. The sedimentation rate is thus given by

$$RSEDI = \frac{\partial}{\partial z}\Big[N_{Ci}a_ic_iM(b_i+d_i)\Big(\frac{\rho_{00}}{\rho_{dref}}\Big)^{0.4}\Big], \tag{7.88}$$

where $M(b_i+d_i) = G(b_i+d_i)(\rho r_i/a_iN_{Ci}G(b_i))^{\frac{b_i+d_i}{b_i}}$.
The ice mass sedimentation rates for precipitating particles $X = S$ or G are given by

$$\begin{aligned} RSEDX &= \frac{1}{\rho_{dref}}\frac{\partial}{\partial z}\Big[\int_0^\infty v(D_x)m(D_x)n(D_x)\,dD_x\Big] \\ &= \frac{1}{\rho_{dref}}\frac{\partial}{\partial z}\Big[N_xa_xc_xM(b_x+d_x)\Big(\frac{\rho_{00}}{\rho_{dref}}\Big)^{0.4}\Big] \\ &= \frac{1}{\rho_{dref}}\frac{\partial}{\partial z}\Big[C_xa_xc_xG(b_x+d_x)\Big(\frac{\rho_{dref}r_x}{a_xC_xG(b_x)}\Big)^{\frac{b+d-x}{b-x}}\Big(\frac{\rho_{00}}{\rho_{dref}}\Big)^{0.4}\Big], \end{aligned} \tag{7.89}$$

where (7.1), (7.6), and (7.10) have been used. As for the fallout of rain, the ice sedimentation terms are computed with a time splitting technique and with an upstream differencing scheme.

7.2.13 Extension to hail

The scheme described above is a three-ice category scheme where hailstones are implicitly mixed with less-dense graupel particles to form the broad class of heavily rimed particles. However hailstones may be of special interest in convective storms. Furthermore they have a specific growth rate which can be modeled in the manner of the ”wet growth” regime of the graupel particles. The physical basis is that hail particles are very efficient to collect particles so their growth rate is mostly limited by the capability of the collected drops to freeze out at the surface of the hailstones (heat budget equation). Therefore unfrozen drops are shed away and feed back the raindrop category of the condensate. The whole process corresponds to the RWETG growth rate expressed by Eq. (7.77). The drawback of the present method, which does not distinguish between graupel and hail particles is twofold: first, the relevant relationships (mass-size, fall speed-size, etc.) of the hail particles are not explicitly taken into account and second, the DRY/WET switch of the graupel growth mode is not size-segregated and affects the whole graupel spectrum while only the largest graupel particles are prone to grow in the wet mode. So in order to better represent the initiation of hail from the graupel reservoir and the microphysical evolution of these hydrometeors, a fourth category of ice is introduced. The extended microphysical scheme (Lascaux et al. 2006) is now referred to the ICE4 scheme.

Introduction to hail particles

All the variables relative to the ”hail” category are suffixed with an ”h”. For instance, the hail mixing ratio is r_h. The parameters used to characterize hail (here treated as ice spheres) are given in Table 7.7. The shape parameter ν is set to a high value of 8 in order to favor a narrow size distribution of the hailstones around the biggest sizes of the particles.

Table 7.7: Set of parameters used to characterize the hailstones.

Parameters	α	ν	a	b	c	d	C	x	$\overline{f}_0$	$\overline{f}_1$	$\overline{f}_2$	$\mathcal{C}_1$
r_h	1	8	470.	3.0	207.	0.64	4.E4	-1.0	0.86	0.28	0	0.5

Microphysical processes involving hail particles

The hail category originates from the graupel reservoir, which largest particles likely experience a wet growth mode. Once formed, hailstones exclusively grow in the wet growth mode too and do not go back to the graupel stage. Hailstones partially melt under the freezing level in the same way graupel particles do. There is no deposition/sublimation of the hailstones.

Formation from graupel particles

The formation rate of hail particles is derived from the **WET** and **DRY** growth modes of the graupel particles. The partial conversion of graupels into hailstones is then approximated by

$$\left.\frac{\partial r_h}{\partial t}\right|_{g\to h} = \left(\frac{\partial r_g}{\partial t}\right)^* \times \frac{\mathbf{DRY}}{\mathbf{DRY}+\mathbf{WET}} \tag{7.90}$$

where $\left(\partial r_g/\partial t\right)^*$ is the sum of the r_g tendencies before the conversion into hail. The corresponding sink on the r_g budget is $\partial r_g/\partial t\big|_{g\to h} = -\partial r_h/\partial t\big|_{g\to h}$. The above formulation allows for a progressive transition from graupel to hail. It is based on the simple idea that the more the graupel particles can grow in the **WET** mode (**DRY$\gg$WET** case), the more they are depleted and converted into hailstones. This macroscopic approach is in contrast with Ziegler (1985) who suggested a size distinction between graupel and hail which is based on a dry/wet growth threshold diameter to integrate by part over the graupel size distribution. We found that this technique is not easily applicable in a four-class microphysical scheme insofar the scheme is rendered increasingly complex (Ferrier 1994). The ratio introduced in Eq. (7.90) lies between 1 (full conversion into hail when **WET$\ll$DRY**) and 1/2 (no conversion into hail when **WET$\leq$ DRY**) so hail is produced only when $0<$**WET$\leq$DRY**.
The ratio expressed in Eq. (7.90) can be easily modified and adjusted to improve the transfer rate in accord with experimental data.

Growth of hail particles

Rigorously speaking, hailstones exclusively grow in the wet regime but these conditions are not strictly checked for the moment to simplify the coding. The consequence is that hail does not revert to the graupel category in the scheme. This situation will be improved in the future. The wet growth rate ($RWETH$) is analogous to (7.77), it writes:

$$\begin{aligned} RWETH = {} & \frac{4\pi \mathcal{C}_{1_h} N_h}{\rho(L_m(T_t) - C_w(T_t - T))}\left[k_a(T)(T_t - T) + \frac{L_v D_v(T,P)}{R_v T}(e_{vs}(T_t) - e_v)\right] \\ & \times \left[\overline{f}_{0h} M_h(1) + \overline{f}_{1h} c'_h M_h(\frac{d_h+3}{2})\right] \\ & + (RIWETH + RSWETH + RGWETH)\left[1 + \frac{C_i(T_t - T)}{(L_m(T_t) - C_w(T_t - T))}\right]. \end{aligned} \tag{7.91}$$

In the above expression, $RGWETH$ is the hail collection rate of graupel particles in the wet mode with $E_{gh} = 1$. $RIWETH$ and $RSWETH$ have a similar meaning to $RIWETG$ and $RSWETG$ in (7.77) but for hail. The $RSWETH$ and $RGWETH$ rates are tabulated and interpolated from lookup tables.

Melting of hail particles

We proceed the same way as for the graupel particles (in Eq. (7.84)).

$$\begin{aligned} RHMLTR = {} & -\frac{4\pi \mathcal{C}_{1_h} N_h}{\rho L_m(T_t)}\left[k_a(T)(T_t - T) + \frac{L_v D_v(T,P)}{R_v T}(e_{vs}(T_t) - e_v)\right] \\ & \times \left[\overline{f}_{0h} M_h(1) + \overline{f}_{1h} c'_h M_h(\frac{d_h+3}{2})\right] \\ & -(RCWETH + RRWETH)\frac{C_w(T_t - T)}{L_m(T_t)}. \end{aligned} \tag{7.92}$$

During the melting, hailstones can collect liquid water at $RCWETH$ and $RRWETH$ rates for the cloud droplets and raindrops, respectively. The collection rate $RRWETH$ is precomputed and interpolated from a lookup table.

Sedimentation of hail particles

The fallout of the hailstones is treated in the same way as rain, snow and graupel particles. The time splitting number is determined from the CFL stability criterium based on a maximum fall velocity of 40 m.s^{-1} instead of 10 m.s^{-1} without hail.

7.3 Integration of the equations of conservation

7.3.1 System of equation

The ice scheme predicts the evolution of the three specific ice categories r_i, r_s and r_g and also modifies the evolution of r_v and of the two other microphysical variables r_c and r_r. The system of equation for the ice variables differ considerably with respect to the temperature T and so two distinct systems of equation can be written.

- $T < T_t$

$$\begin{aligned}\frac{\partial r_i}{\partial t} &= \sum \frac{\partial r_i}{\partial t}\Big|_{DYN} + RSEDI + RVHENI + RCHONI + RCBERI + RVDEPI \\ &-RIAUTS - RICFRRG - RIAGGS - \delta_{DRY}RIDRYG - (1-\delta_{DRY})RIWETG,\end{aligned} \tag{7.93}$$

$$\begin{aligned}\frac{\partial r_s}{\partial t} &= \sum \frac{\partial r_s}{\partial t}\Big|_{DYN} + RSEDS + RVDEPS + RIAUTS + RIAGGS + RCRIMSS \\ &-RSRIMCG + RRACCSS - RSACCRG - \delta_{DRY}RSDRYG \\ &-(1-\delta_{DRY})RSWETG,\end{aligned} \tag{7.94}$$

$$\begin{aligned}\frac{\partial r_g}{\partial t} &= \sum \frac{\partial r_g}{\partial t}\Big|_{DYN} + RSEDG + RVDEPG + \underbrace{RICFRRG + RRCFRIG} \\ &+\underbrace{RCRIMSG + RSRIMCG} + \underbrace{RRACCSG + RSACCRG} \\ &+\delta_{DRY}(RCDRYG + RRDRYG + RIDRYG + RSDRYG) \\ &+(1-\delta_{DRY})(\underbrace{RRWETG + RCWETG + RIWETG + RSWETG}_{RWETG} - RCSHDR)\end{aligned} \tag{7.95}$$

where $\sum \frac{\partial r_x}{\partial t}\Big|_{DYN}$ includes the advection and the numerical and turbulent diffusions affecting the variable r_x. One recalls that $RCDRYG \equiv RCWETG$ and that $RRWETG + RCWETG + RIWETG + RSWETG = RWETG$ above. The other underbraced terms mark the conversion terms producing graupels namely, the contact freezing of the raindrops, the heavy riming of the aggregates by cloud droplets and by accretion of raindrops respectively. The switch δ_{DRY} tags the graupel growth mode so it is set to 1(0) in case of $DRY(WET)$ growth.

$$\begin{aligned}\frac{\partial r_v}{\partial t} &= \sum \frac{\partial r_v}{\partial t}\Big|_{DYN} + RREVAV - RVCNDC \\ &-RVHENI - RVDEPI - RVDEPS - RVDEPG\end{aligned} \tag{7.96}$$

$$\begin{aligned}\frac{\partial r_c}{\partial t} &= \sum \frac{\partial r_c}{\partial t}\Big|_{DYN} - RCAUTR - RCACCR \\ &-RCBERI - RCHONI - RCRIMSS - RCRIMSG \\ &-\delta_{DRY} RCDRYG - (1-\delta_{DRY}) RCWETG\end{aligned} \tag{7.97}$$

$$\begin{aligned}\sum \frac{\partial r_r}{\partial t} &= \frac{\partial r_r}{\partial t}\Big|_{DYN} + RSEDR + RCAUTR + RCACCR - RREVAV \\ &-RRCFRIG - RRACCSS - RRACCSG - \delta_{DRY} RRDRYG \\ &-(1-\delta_{DRY})(RRWETG - RCSHDR)\end{aligned} \tag{7.98}$$

$$\begin{aligned}\frac{\partial \theta}{\partial t} = \sum \frac{\partial \theta}{\partial t}\Big|_{DYN} &+ \frac{L_v}{\Pi_{ref} C_{ph}}\Big[RVCNDC - RREVAV\Big] \\ &+ \frac{L_f}{\Pi_{ref} C_{ph}}\Big[RCHONI + RCBERI + RRCFRIG + RCRIMSS \\ &+RCRIMSG + RRACCSS + RRACCSG + \delta_{DRY}(RCDRYG \\ &+RRDRYG) + (1-\delta_{DRY})(RCWETG + RRWETG - RCSHDR)\Big] \\ &+ \frac{L_s}{\Pi_{ref} C_{ph}}\Big[RVHENI + RVDEPI + RVDEPS + RVDEPG\Big]\end{aligned} \tag{7.99}$$

where the warm microphysical processes have been included.

- $T > T_t$

$$\frac{\partial r_i}{\partial t} = \sum \frac{\partial r_i}{\partial t}\Big|_{DYN} + RSEDI - RIMLTC, \tag{7.100}$$

$$\begin{aligned}\frac{\partial r_s}{\partial t} &= \sum \frac{\partial r_s}{\partial t}\Big|_{DYN} + RSEDS - RSCVMG \\ &+RCRIMSS + RRACCSS - RSRIMCG - RSACCRG - RSWETG,\end{aligned} \tag{7.101}$$

$$\begin{aligned}\frac{\partial r_g}{\partial t} &= \sum \frac{\partial r_g}{\partial t}\Big|_{DYN} + RSEDG - RGMLTR + RSCVMG \\ &+ \underbrace{RCRIMSG + RSRIMCG}_{} + \underbrace{RRACCSG + RSACCRG}_{} + RSWETG,\end{aligned} \tag{7.102}$$

$$\frac{\partial r_v}{\partial t} = \sum \frac{\partial r_v}{\partial t}\Big|_{DYN} - RVCNDC + RREVAV, \tag{7.103}$$

$$\begin{aligned}\frac{\partial r_c}{\partial t} &= \sum \frac{\partial r_c}{\partial t}\Big|_{DYN} + RVCNDC + RIMLTC \\ &-RCRIMSS - RCRIMSG - RCWETG,\end{aligned} \tag{7.104}$$

$$\begin{aligned}\frac{\partial r_r}{\partial t} &= \sum \frac{\partial r_r}{\partial t}\Big|_{DYN} RSEDR - RREVAV + RGMLTR \\ &-RRACCSS - RRACCSG + RCWETG,\end{aligned} \tag{7.105}$$

$$\begin{aligned}\frac{\partial \theta}{\partial t} = \sum \frac{\partial \theta}{\partial t}\Big|_{DYN} &+ \frac{L_v}{\Pi_{ref} C_{ph}}\Big[RVCNDC - RREVAV\Big] \\ &+ \frac{L_f}{\Pi_{ref} C_{ph}}\Big[RCRIMSS + RCRIMSG + RRACCSS + RRACCSG \\ &-RIMLTC - RGMLTR\Big].\end{aligned} \tag{7.106}$$

Note that $\delta_{DRY} = 0$ in warm clouds for the melting graupels and that the liquid water collected by the melting graupels is shed immediately so $RCWETG$ is a conversion rate of cloud droplets into raindrops in that case.

In the two above systems of equations, the condensation/evaporation term for r_c ($RVCNDC$) and the deposition/sublimation term for r_i ($RVDEPI$) are integrated implicitly during the final water vapor adjustment step (see below).

7.3.2 Positivity adjustments

As done for the variables used in the warm microphysics parameterization, it is necessary to check at first the positivity of the mixing ratios after the integration of the sole $\sum \left.\frac{\partial r_x}{\partial t}\right|_{DYN}$ terms in the preceeding systems of equation. Mixing ratios ending with negative values are corrected (reset to zero) and the global filling algorithm of Rood (1987) is applied to ensure the total mass conservation of each microphysical specy.

7.3.3 Ordering the integration of the microphysical sources

The time integration of the explicit rates in Eqs (7.93) up to (7.106) must be done carefully because some important processes are fueled by cloud ice or cloud droplets which contents are not necessary updated after the successive action of the numerous microphysical processes. As a result this may lead to situations where excessive depletion of a key specy by a single process has a dramatic effect on the long-term (chaotic) behavior of a cloud parcel. More practical arguments, such as the positiveness requirement of the final mixing ratios are also in favor of a strict control and update when adding up all the source terms (transport followed by a local growth/depletion) of the system of equations.

As shown by Lin et al. (1983) and Ziegler (1988) but for a different scheme and case study too, the highest rates in a mixed phase cloud are found for the accretion of cloud droplets and raindrops onto the snowflakes and the graupels (in the dry mode) and the freezing of the drops. Thus the source terms associated to these processes should be integrated at the end of the sequence and just before the late cloud ice and droplet transfers which anticipate the final water vapor-temperature adjustment.

In the present scheme, it is suggested to proceed as follow:

- first integrate the slow ”cold” processes: nucleations, vapor deposition/sublimation, aggregation and autoconversion
- then the ”warm” processes: accretion, autoconversion and rain evaporation
- then include the accretional growth of the aggregates, the contact freezing of the raindrops and the conversion-melting of the aggregates,
- then the accretional growth of the graupels and their melting
- then add the pristine ice melting and Bergeron-Findeisen transfer
- and finally integrate the sedimentation terms

Each process is computed with the prognostic variables (especially the mixing ratios) defined at the current time step but it is limited by the current state of the guess of the depleted prognostic variable before integration. This means that at the end of each step, the partially integrated mixing ratios of the decaying microphysical species are strictly checked for positivity so, in some circumstances, some specy may be available or not for the next process depending on the chosen order in the sequence of integration. It is clear that this systematic control makes the job easier at the end because no other algorithm for local compensation of negative value needs to be developped. But the drawback is that it introduces a dependency to the order of the processes.

A summary of the general algorithm for integrating the microphysical cold and warm processes is presented in Fig. 7.4.

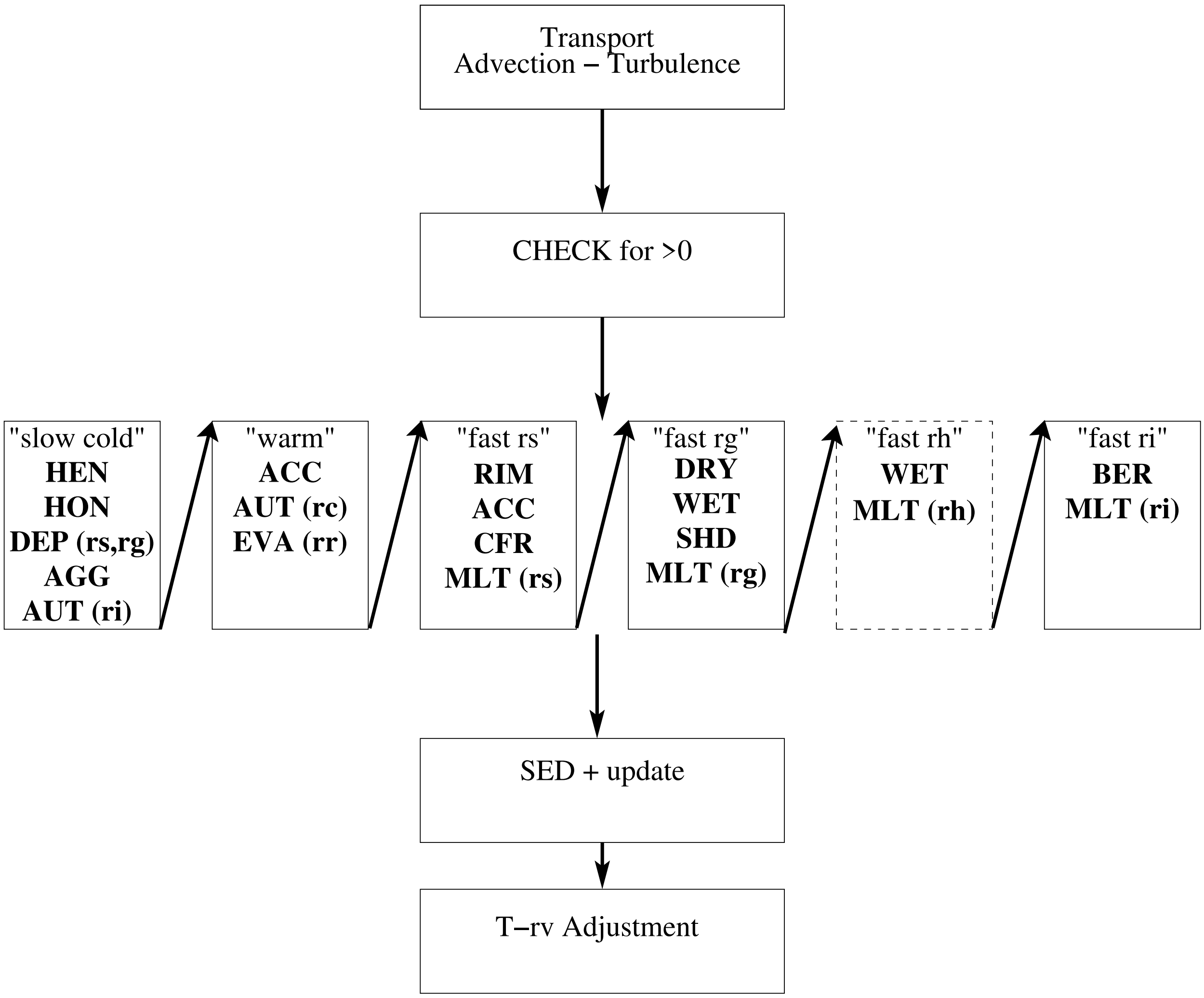

Figure 7.4: Algorithm of the step-by-step integration of the microphysical processes.

7.3.4 Water vapor adjustments

All the concurrent microphysical processes involving an exchange of heat and water vapor on the condensed particles are computed independently each other. In the warm microphysical scheme an implicit adjustment of the temperature, water vapor and cloud water fields is performed in order to introduce some consistency between θ and r_v with a strict saturation criterium in clouds leading to a subsequent passive adjustment of r_c. A by-product of this adjustment is the derivation of a condensation/evaporation rate ($RVCNDC$) of the cloud droplets. In mixed phase clouds the problem is far more complex because of the presence of cloud droplets and ice (so two species to re-adjust) and the difficulty of defining unambiguously a single level of saturation. The solution which has been chosen here is to perform an implicit adjustment as in Lord et al. (1984) or in Tao et al. (1989) because it seems superior to the explicit closure exposed in Ferrier (1994) where a simple saturation over ice is assumed leading to some controversial account of the Bergeron-Findeisen effect[12] and a single correction of r_i. In the present scheme the Bergeron-Findeisen conversion rate ($RCBERI$) is explicitly pre-integrated and so the traditional linear partition of

---

[12] Note that Krueger et al. (1995) emphasized the fact that the original adjustment introduced by Lord et al. (1984) cannot reproduce an implicit Bergeron-Findeisen transfer of mass

water vapor correction as a function of temperature can be subjected to some revision. Another advantage of using an implicit adjustment scheme in the spirit of that of Lord et al. (1984) is that it can revert to a classical adjustment scheme in case of warm cloud ($r_i = 0$) or fully glaciated cloud ($r_c = 0$).
The major assumptions used in the proposed saturation adjustment scheme are the following:

- the saturation vapor mixing ratio ($r_{vs_{iw}}$) inside a mixed phase cloud results from the barycentric formula introduced by Lord et al. (1984) that is:

$$r_{vs_{iw}} = \frac{r_c^* r_{vs_w}(T) + r_i^* r_{vs_i}(T)}{r_c^* + r_i^*} \tag{7.107}$$

- the super/sub-saturation adjustment over cloud ice/droplets is made isobarically and proportionnal to the explicitly estimated cloud water and cloud ice content, this gives:

  $$\Delta r_c = r_c - r_c^* = \Delta r_v CND \qquad \text{and} \qquad \Delta r_i = r_i - r_i^* = \Delta r_v DEP \tag{7.108}$$

  with

  $$\Delta r_v = r_v^* - r_v = r_v^* - r_{vs_{iw}} \tag{7.109}$$

  and with

  $$CND = \frac{r_c^*}{r_c^* + r_i^*} \qquad \text{and} \qquad DEP = \frac{r_i^*}{r_c^* + r_i^*}. \tag{7.110}$$

  So any deficit or excess of water vapor is compensated or absorbed by each cloudy condensed phase in proportion to their respective content and as a consequence, Δr_c and Δr_i have always the same sign. This way of doing seems raisonnable since once the Bergeron-Findeisen effect is accounted for, water vapor can be supplied or gathered by r_c and r_i in proportion to their actual amount[13] .

  However, the above adjustment formulation was found to produce to much ice at weakly negative temperature. As a consequence, since the Masdev 4.1 version, the CND and DEP terms are calculated following Tao et al. (1989) as:

  $$CND = \frac{T - T_{00}}{T_0 - T_{00}} \qquad \text{and} \qquad DEP = 1 - CND \tag{7.111}$$

  with $T_0 = 0$°C and $T_{00} = 40$°C.

The saturation adjustment then proceeds as for Tao et al. (1989) where a zero-crossing solution of

$$\begin{aligned} F(T) &= T - T^* - \frac{L_v(T)\Delta r_c + L_s(T)\Delta r_i}{C_{ph}} \\ &= T - T^* + \left(\frac{L_v(T)CND + L_s(T)DEP}{C_{ph}}\right)(r_{vs_{iw}}(T) - r_v^*) \end{aligned} \tag{7.112}$$

is sought using (7.107) to (7.110) and the non-iterative algorithm of Langlois (1973) already experienced for the warm microphysical adjustment is preferred to the first order solution of Tao et al. (1989). Of course, this adjustment is performed after integrating explicitly all the source terms in the θ and the r_v prognostic equations, the cloud condensation and ice deposition terms excepted.

---

[13] In the remaining text, the starred variables are the most recently updated (or ”guess”) variables

The procedure used for solving (7.112) is based upon the quasi-second order expansion of $F(T) = 0$, namely[14]

$$T \simeq T^* - \frac{F(T^*)}{F'(T^*)}\Big[1 + \frac{1}{2}\frac{F(T^*)}{F'(T^*)}\frac{F''(T^*)}{F'(T^*)}\Big] \tag{7.113}$$

where

$$\begin{aligned}
\Delta_1 &= \frac{F(T^*)}{F'(T^*)} &&= \frac{\big[L_v(T^*)CND + L_s(T^*)DEP\big]\big(r_c^* r_{vs_w}(T^*) + r_i^* r_{vs_i}(T^*) - (r_c^* + r_i^*)r_v^*\big)}{C_{ph}(r_c^* + r_i^*) + \big[L_v(T^*)CND + L_s(T^*)DEP\big]\big[r_c^* r'_{vs_w}(T^*) + r_i^* r'_{vs_i}(T^*)\big]},\\
\Delta_2 &= \frac{F''(T^*)}{F'(T^*)} &&= \frac{\big[L_v(T^*)CND + L_s(T^*)DEP\big]\big(r_c^* r''_{vs_w}(T^*) + r_i^* r''_{vs_i}(T^*)\big)}{C_{ph}(r_c^* + r_i^*) + \big[L_v(T^*)CND + L_s(T^*)DEP\big]\big[r_c^* r'_{vs_w}(T^*) + r_i^* r'_{vs_i}(T^*)\big]},
\end{aligned} \tag{7.114}$$

and where

$$\begin{aligned}
r'_{vs_w}(T^*) &= A_w(T^*) r_{vs_w}(T^*)\Big[1 + \frac{r_{vs_w}(T^*)}{\epsilon}\Big],\\
r'_{vs_i}(T^*) &= A_i(T^*) r_{vs_i}(T^*)\Big[1 + \frac{r_{vs_i}(T^*)}{\epsilon}\Big],\\
r''_{vs_w}(T^*) &= r'_{vs_w}(T^*)\Big[\frac{A'_w(T^*)}{A_w(T^*)} + A_w(T^*)\big(1 + 2\frac{r_{vs_w}(T^*)}{\epsilon}\big)\Big],\\
r''_{vs_i}(T^*) &= r'_{vs_i}(T^*)\Big[\frac{A'_i(T^*)}{A_i(T^*)} + A_i(T^*)\big(1 + 2\frac{r_{vs_i}(T^*)}{\epsilon}\big)\Big]
\end{aligned} \tag{7.115}$$

with $\epsilon = M_v/M_d$ and

$$\begin{aligned}
A_w(T) &= \frac{\beta_w}{T^2} - \frac{\gamma_w}{T} \qquad \text{and} \qquad & A'_w(T) &= -\frac{2\beta_w}{T^3} + \frac{\gamma_w}{T^2}\\
A_i(T) &= \frac{\beta_i}{T^2} - \frac{\gamma_i}{T} \qquad \text{and} \qquad & A'_i(T) &= -\frac{2\beta_i}{T^3} + \frac{\gamma_i}{T^2}.
\end{aligned} \tag{7.116}$$

Finally the rates $RVDEPI$ and $RVCNDC$ in the r_c and r_i equations, are estimated by:

$$\begin{aligned}
RVDEPI &= \frac{(r_v^* - r_{vs_{iw}})DEP}{2\Delta t} &&= \frac{C_{ph}}{L_v(T^*)CND + L_s(T^*)DEP}\Big[-\Delta_1(1 + \frac{1}{2}\Delta_1\Delta_2)\Big]\frac{DEP}{2\Delta t}\\
RVCNDC &= \frac{(r_v^* - r_{vs_{iw}})CND}{2\Delta t} &&= \frac{C_{ph}}{L_v(T^*)CND + L_s(T^*)DEP}\Big[-\Delta_1(1 + \frac{1}{2}\Delta_1\Delta_2)\Big]\frac{CND}{2\Delta t}.
\end{aligned} \tag{7.117}$$

7.4 References

Böhm, H. P., 1989: A general equation for the terminal fall speed of solid hydrometeors. *J. Atmos. Sci.*, **46**, 2419-2427.

Caniaux, G., 1993: Paramétrisation de la glace dans un modèle non-hydrostatique de nuage: Application à une ligne de grain tropicale. Thèse de Doctorat de l'Université Paul-Sabatier, 257 pp.

Chaboureau, J.-P., J.-P. Cammas, P. J. Mascart, J.-P. Pinty, and J.-P. Lafore, 2002: Mesoscale model cloud scheme assessment using satellite observations. *J. Geophys. Res.*, **107(D16)**, 4301, doi:10.1029/2001JD000714.

---

[14] The slow variations of $L_v(T)$ and of $L_s(T)$ with the temperature are neglected but not those of $r_{vs_w}(T)$ and of $r_{vs_i}(T)$.

Chaboureau, J.-P. and J.-P. Pinty, 2006: Evaluation of a cirrus parameterization with Meteosat Second Generation. *Geophys. Res. Let.*, **33**, L03815, doi:10.1029/2005GL024725.

Cheng, L., and M. English, 1983: A relationship between hailstone concentration and size. *J. Atmos. Sci.*, **40**, 204-213.

Chin, H.-N. S., 1994: The impact of the ice phase and radiation on a midlatitude squall line system. *J. Atmos. Sci.*, **51**, 3320-3343.

Cotton, W. R., G. J. Tripoli, R. M. Rauber and E. A. Mulvihill, 1986: Numerical simulations of the effects of varying ice crystal nucleation rates and aggregation processes on orographic snowfall. *J. Climate Appl. Meteor.*, **25**, 1658-1680.

Farley, R. D., P. A. Price, H. D. Orville and J. H. Hirsch, 1989: On the numerical simulation of graupel/hail initiation via the riming of snow in bulk water microphysical cloud models. *J. Appl. Meteor.*, **28**, 1128-1131.

Ferrier, B. S., 1994: A double-moment multiple phase four-class bulk ice scheme. Part I: description. *J. Atmos. Sci.*, **51**, 249-280.

Ferrier, B. S., W.-K. Tao and J. Simpson, 1995: A double-moment multiple phase four-class bulk ice scheme. Part II: simulations of convective storms in different large-scale environments and comparison with other bulk parameterizations. *J. Atmos. Sci.*, **52**, 1001-1033.

Foote, G. B., and P. S. Du Toit, 1969: Terminal velocity of raindrops aloft. *J. Appl. Meteor.*, **8**, 249-253.

Hall, W. D., and H. R. Pruppacher, 1977: The survival of ice particles falling from cirrus clouds in subsaturated air. *J. Atmos. Sci.*, **33**, 1995-2006.

Hallett, J., and S. C. Mossop, 1974: Production of secondary ice particles during the riming process. *Nature*, **249**, 26-28.

Heymsfield, A. J., 1972: Ice crystals terminal velocities. *J. Atmos. Sci.*, **29**, 1348-1356.

Heymsfield, A. J. and J. C. Pflaum, 1985: A quantitative assessment of the accuracy of techniques for calculating graupel growth. *J. Atmos. Sci.*, **42**, 2264-2274.

Houze, R. A. Jr., P. V. Hobbs, P. H. Herzegh and D. B. Parsons, 1979: Size distributions of precipitation particles in frontal clouds. *J. Atmos. Sci.*, **36**, 156-162.

Kajikawa, M., and A. J. Heymsfield, 1989: Aggregation of ice crystals in cirrus. description *J. Atmos. Sci.*, **46**, 3108-3121.

Langlois, W. E., 1973: A rapidly convergent procedure for computing large-scale condensation in a dynamical weather model. *Tellus*, **25**, 86-87.

Krueger, S. K., Q. Fu, K. N. Liou, and H.-N. S. Chin, 1995: Improvements of an ice-phase microphysics parameterization for use in numerical simulations of tropical convection. *J. Appl. Meteor.*, **34**, 281-287.

Lascaux, F., E. Richard, and J.-P. Pinty, 2006: Numerical simulations of three MAP IOPs and the associated microphysical processes. *Quart. J. Roy. Meteor. Soc.*, **132**, 1907-1926.

Lin, Y.-L., R. D. Farley, and H. D. Orville, 1983: Bulk parameterization of snow field in a cloud model. *J. Climate Appl. Meteor.*, **22**, 1065-1092.

Locatelli, J. D., and P. V. Hobbs, 1974: Fall speeds and masses of solid precipitation particles. *J. Geophys. Res.*, **79D**, 2185-2197.

Lord, S. J., H. E. Willoughby, and J. M. Piotrowicz, 1984: Role of a parameterized ice-phase microphysics in an axisymmetric non-hydrostatic tropical cyclone model. *J. Atmos. Sci.*, **41**, 2836-2848.

Nelson, S. P., 1983: The influence of storm flow structureon hail growth. *J. Atmos. Sci.*, **40**, 1965-1983.

Mc Cumber, M., W.-K. Tao, J. Simpson, R. Penc, and S. T. Soong, 1991: Comparaison of ice-phase microphysical parameterization schemes using numerical simulations of tropical convection. *J. Appl. Meteor.*, **30**, 985-1004.

Mc Farquhar, G. M., A. J. Heymsfield, 1997: Parameterization of tropical cirrus ice crystal size distributions and implications for radiative transfer: Results from CEPEX *J. Atmos. Sci.*, **54**, 2187-2200.

Masson, B. J., 1956: On the melting of hailstones. *Quart. J. R. Met. Soc.*, **82**, 209-216.

Meyers, M. P., P. J. DeMott, and W. R. Cotton, 1992: New primary ice-nucleation parameterizations in an explicit cloud model. *J. Appl. Meteor.*, **31**, 708-721.

Meyers, M. P., R. L. Walko, J. Y. Harrington and W. R. Cotton, 1996: New RAMS cloud microphysics parameterization. Part II: The two-moment scheme. *Atmos. Res.* **45**, 3-39.

Murakami, M., 1990: Numerical modeling of dynamical and microphysical evolution of an isolated convective cloud -the 19 July 1981 CCOPE cloud. *J. Meteor. Soc. Japan*, **68**, 107-128.

Musil, D. J., 1970: Computer modeling of hailstone growth in feeder clouds. *J. Atmos. Sci.*, **27**, 474-482.

Passarelli, R. E., Jr., 1978: An approximate analytical model of the vapor deposition and aggregation growth of snow. *J. Atmos. Sci.*, **35**, 118-124.

Pruppacher, H. R., and J. D. Klett, 1978: *Microphysics of Clouds and Precipitation.* Reidel,714 pp.

Rutledge, S. A. and P. V. Hobbs, 1983: The mesoscale and microscale structure and organization of clouds and precipitation in midlatitude cyclones. Part VIII: A model for the ”Seeder-Feeder” process in warm-frontal rainbands. *J. Atmos. Sci.*, **40**, 1185-1206.

Rutledge, S. A. and P. V. Hobbs, 1984: The mesoscale and microscale structure and organization of clouds and precipitation in midlatitude cyclones. Part XII: A diagnostic modeling study of precipitation development in narrow cold-frontal rainbands. *J. Atmos. Sci.*, **41**, 2949-2972.

Ryan, B. F., 2000: A bulk parameterization of the ice particle size distribution and the optical properties in ice clouds, *J. Atmos. Sci.*, **57**, 1436-1451.

Starr, D. O'C. and S. K. Cox, 1985: Cirrus clouds. Part I: A cirrus cloud model. *J. Atmos. Sci.*, **42**, 2663-2681.

Sue Chen, and W. R. Cotton, 1988: The sensitivity of a simulated extratropical mesoscale convective system to longwave radiation and ice-phase microphysics. *J. Atmos. Sci.*, **45**, 3897-3910.

Tao, W.-K., J. Simpson, and M. Mc Cumber, 1989: An ice-water saturation adjustment. *Mon. Wea. Rev.*, **117**, 231-235.

Tripoli, G. J., P. J. Flatau, and W. R. Cotton, 1988: Generalized microphysics scheme for use in mesoscale cloud model. *Preprints 10*th *International Cloud Physics Conference*. Bad-Homburg. FRG August, 1988, 109-111.

Walko, R. L., W. R. Cotton, M. P. Meyers, and J. Y. Harrington, 1995: New RAMS cloud microphysics parameterization. Part I: The single-moment scheme. *Atm. Res.*, **38**, 29-62.

Yang M.-J. and R. A. Houze, 1995: Sensitivity of squall-line rear inflow to ice microphysics and environmental humidity. *Mon. Wea. Rev.*, **123**, 3175-3193.

Ziegler, C. L., 1985: Retrieval of thermal and microphysical variables in observed convective storms. Part I: Model development and preliminary testing. *J. Atmos. Sci.*, **42**, 1487-1509.

Ziegler, C. L., 1988: Retrieval of thermal and microphysical variables in observed convective storms. Part II: Sensitivity of cloud processes to variation of the microphysical parameterization. *J. Atmos. Sci.*, **45**, 1072-1090.

Chapter 8

The 2-moment mixed-phase microphysical scheme LIMA

Contents

8.1 General considerations

This chapter describes the LIMA (Liquid Ice Multiple Aerosols) quasi two-moment microphysical scheme. In short, LIMA relies on the prognostic evolution of an aerosol population, and the careful description of the nucleating properties that enable cloud droplets and pristine ice crystals to form from aerosols (Vié et al. 2016).

8.1.1 Thermodynamics basics

Latent heat

$$L_v(T) = L_v(273.15) + (c_{pv} - c_{pw})(T - 273.15) \tag{8.1}$$

$$L_s(T) = L_s(273.15) + (c_{pv} - c_{pi})(T - 273.15) \tag{8.2}$$

Saturation vapor pressure

Liquid water saturation:

$$e_{sw}(T) = \exp(\alpha_w - \frac{\beta_w}{T} - \gamma_w \ln(T)) \tag{8.3}$$

with

$$\alpha_w = \ln(e_{sw}(273.15)) + \frac{\beta_w}{273.15} + \gamma_w \ln(273.15) \tag{8.4}$$

$$\beta_w = \frac{L_v(273.15)}{R_v} + \gamma_w\, 273.15 \tag{8.5}$$

$$\gamma_w = \frac{c_{pw} - c_{pv}}{R_v} \tag{8.6}$$

Ice saturation:

$$e_{si}(T) = \exp(\alpha_i - \frac{\beta_i}{T} - \gamma_i \ln(T)) \tag{8.7}$$

with

$$\alpha_i = \ln(e_{si}(273.15)) + \frac{\beta_i}{273.15} + \gamma_i \ln(273.15) \tag{8.8}$$

$$\beta_i = \frac{L_s(273.15)}{R_v} + \gamma_i\, 273.15 \tag{8.9}$$

$$\gamma_i = \frac{c_{pi} - c_{pv}}{R_v} \tag{8.10}$$

Saturation mixing ratio

For a perfect gas, $PV = nRT$, so $m = PVM/RT$. The water vapor mass mixing ratio is the ratio of water vapor mass by dry air mass. Writing e the water vapor partial pressure, and $P - e$ the dry air partial pressure, we have:

$$r_v = \frac{m_v}{m_d} = \frac{e}{P - e}\frac{M_v}{M_d} \tag{8.11}$$

So we can express the saturation water vapor mixing ratio with respect to liquid water:

$$r_{sw}(T) = \frac{M_v e_{sw}(T)}{M_d(P - e_{sw}(T))} \tag{8.12}$$

Similarly for ice saturation:

$$r_{si}(T) = \frac{M_v e_{si}(T)}{M_d(P - e_{si}(T))} \tag{8.13}$$

8.1.2 Representation of aerosols

The number concentration N is expressed in kg^{-1}. Aerosols are represented in LIMA by a superposition of an unlimited number of aerosol modes. Each mode and has its own activation properties, and can therefore be used as CCN to create cloud droplets, IFN to nucleate ice crystals, or as “coated IFN”. This last type of aerosols acts as IFN coated with hydrophilic material. They have the ability to first form cloud droplets as standard CCN, and then have the ability to freeze these droplets by immersion nucleation when they are lifted to negative temperature regions.
All aerosol modes have a lognormal particle size distribution.
Each CCN mode has its own activation properties (currently to be chosen between two sets of parameters, for maritime or continental aerosols) and size distribution parameters (mean diameter and spectral width).
Four types of IFN are distinguished in the nucleation parameterization by Phillips et al. (2008) which was included in LIMA: small dust particles, large dust particles, black carbon, and organics. In LIMA, each IFN mode is composed of a given (fixed during the model initialization) fraction of each IFN type.

Free and activated areosols
For CCN modes, two prognostic variables are used to track the aerosols, N^{free} for the free aerosols and N^{acti} for the aerosols in cloud droplets. We therefore retrieve the complete population by summing $N = N^{free} + N^{acti}$.
Similarly for IFN, we track both N^{free} the number of free IFN and N^{nucl} the number of IFN in ice crystals.
For “coated IFN”, three prognostic variables are necessary: N^{free} to track the number of free aerosols, N^{acti} for the aerosols in cloud droplets and N^{nucl} for the aerosols in ice crystals.

Size distribution
Each aerosol mode m follows a lognormal particle size distribution with $r_m = D_m/2$ and σ_m:

$$n_m(D)\mathrm{d}D = N_m \frac{1}{\sqrt{2\pi}\ D\ ln(\sigma_m)} e^{-\left(\frac{ln(D/D_m)}{\sqrt{2}ln(\sigma_m)}\right)^2} \mathrm{d}D \tag{8.14}$$

with $n_m(D)$ (resp. N_m) the number concentration (kg^{-1} m^{-1}, resp. kg^{-1}) for aerosols with a diameter between D et $D + \mathrm{d}D$ (resp. total number concentration).

Moments of the size distribution
The p order moment $M(p)$ of the size distribution is:

$$M(p) = D_m^p \exp\left(\frac{p^2 ln(\sigma_m)^2}{2}\right) \tag{8.15}$$

8.1.3 Representation of hydrometeors

Hydrometeors are classified in 6 different species as in the ICE4 scheme: cloud droplets, rain drops, pristine ice crystals, snow/aggregates, graupel, and hail. A 2-moment representation was adopted in LIMA for cloud droplets, rain drops and pristine ice crystals. Thus, for these three hydrometeor species, two prognostic variables are used: the mass mixing ratio r (kg kg^{-1}) and the number concentration N (kg^{-1}). For precipitating ice species (snow/aggregates, graupel, hail), the

1-moment representation from ICE4 was kept, and the only prognostic variable is the mass mixing ratio r.

Size distribution

The size distribution of all hydrometeors in LIMA follows a generalized gamma law:

$$n(D)\mathrm{d}D = N\frac{\alpha}{\Gamma(\nu)}(\lambda D)^{\alpha\nu}D^{-1}e^{-(\lambda D)^{\alpha}}\mathrm{d}D \tag{8.16}$$

with $n(D)$ (resp. N) the number concentration (kg^{-1} m^{-1}, resp. kg^{-1}) for particles with a diameter between D et $D + \mathrm{d}D$ (resp. total number concentration).
Values for parameters α et ν are usually (they can be chosen in the EXSEG1 namelist at runtime, e.g. XALPHAR et XNUR, those indicated in Table 8.1. λ depends on the local mass mixing ratio and number concentration.
When $\alpha = 1$ and $\nu = 1$, the size distribution becomes:

$$n(D)\mathrm{d}D = N\lambda e^{-\lambda D}\mathrm{d}D \tag{8.17}$$

Moments of the size distribution

The p order moment $M(p)$ of the size distribution is:

$$M(p) = \frac{1}{\lambda^p}\frac{\Gamma(\nu + p/\alpha)}{\Gamma(\nu)} \tag{8.18}$$

The mean diameter and variance are:

$$\bar{D} = \frac{1}{\lambda}\frac{\Gamma(\nu + 1/\alpha)}{\Gamma(\nu)} \tag{8.19}$$

$$\sigma^2 = \frac{1}{\lambda^2}\left(\frac{\Gamma(\nu + 2/\alpha)}{\Gamma(\nu)} - \left(\frac{\Gamma(\nu + 1/\alpha)}{\Gamma(\nu)}\right)^2\right) \tag{8.20}$$

However, for cloud droplets and rain drops (assumed spherical), the mean volume diameter and its associated variance are more often used:

$$\bar{D} = M(3)^{\frac{1}{3}} = \frac{1}{\lambda}\left(\frac{\Gamma(\nu + 3/\alpha)}{\Gamma(\nu)}\right)^{\frac{1}{3}} \tag{8.21}$$

$$\sigma^2 = \frac{1}{\lambda^2}\left(\frac{\Gamma(\nu + 6/\alpha)}{\Gamma(\nu)} - \left(\frac{\Gamma(\nu + 3/\alpha)}{\Gamma(\nu)}\right)^2\right)^{\frac{1}{3}} \tag{8.22}$$

Diagnostic number concentrations for snow/aggregates, graupel and hail

A 1-moment representation of snow, graupel and hail was chosen in LIMA. The number concentrations are estimated using the parameterized relationship

$$N = \frac{C\lambda^x}{\rho_d} \tag{8.23}$$

where C and x are linked, as in the ICE3 scheme, by $\log_{10}(C) = -3.55x + 3.89$ (Caniaux 1993), and their values can be found in Table 8.1.

Relationships between r, N, D_m and λ
Combining the particle size distribution and the mass-diameter relationship, we get:

$$r = \int_D m(D)n(D)\mathrm{d}D \tag{8.24}$$

$$r = aN\int_D D^b \frac{\alpha}{\Gamma(\nu)}(\lambda D)^{\alpha\nu}D^{-1}e^{-(\lambda D)^\alpha}\mathrm{d}D \tag{8.25}$$

$$r = aNM(b) \tag{8.26}$$

$$r = aN\frac{1}{\lambda^b}\frac{\Gamma(\nu+b/\alpha)}{\Gamma(\nu)} \tag{8.27}$$

Therefore, we can determine λ:

$$\lambda = \left(a\frac{N}{r}\frac{\Gamma(\nu+b/\alpha)}{\Gamma(\nu)}\right)^{\frac{1}{b}} \quad \text{for } 2-\text{moment species} \tag{8.28}$$

$$\lambda = \left(a\frac{C}{\rho_d r}\frac{\Gamma(\nu+b/\alpha)}{\Gamma(\nu)}\right)^{\frac{1}{b-x}} \quad \text{for } 1-\text{moment species} \tag{8.29}$$

For spherical droplets and drops ($b = 3$), we get the mean volume diameter D_m and λ as:

$$\bar{D} = \left(\frac{r}{aN}\right)^{\frac{1}{3}} \tag{8.30}$$

$$\lambda = \left(a\frac{N}{r}\frac{\Gamma(\nu+3/\alpha)}{\Gamma(\nu)}\right)^{\frac{1}{3}} \tag{8.31}$$

where the equation for λ can be simplified if $\alpha = 1$ and $\nu = 1$:

$$\lambda = \left(a\frac{N}{r}\Gamma(4)\right)^{\frac{1}{3}} \tag{8.32}$$

The Γ function

$$\Gamma(x) = \int_0^\infty t^{x-1}e^{-t}\mathrm{d}t \tag{8.33}$$

$$\Gamma(x+1) = x\Gamma(x) \tag{8.34}$$

$$\Gamma(n+1) = n! \quad (n \in \mathbb{N}) \tag{8.35}$$

$$\Gamma(1/2) = \sqrt{\pi} \tag{8.36}$$

$$\Gamma(1) = 1 \tag{8.37}$$

Mass-diameter relationship

For all hydrometeors, the mass-diameter relationship takes the form $m(D) = aD^b$. Values for a et b are found in Table 8.1. For icy hydrometeors, they account for the shape and density of ice particles. For cloud droplets and rain drops (assumed spherical), they are equivalent to:

$$m(D) = \frac{4}{3}\pi\left(\frac{D}{2}\right)^3\rho_w \tag{8.38}$$

Terminal fall speed

For all hydrometeors, the terminal fall speed also depends on the diameter through the following equation, where values for c et d are again found in Table 8.1:

$$v(D) = \left(\frac{\rho_0}{\rho_d}\right)^{0.4} cD^d \tag{8.39}$$

The air density correction term comes from Foote and Du Toit (1969) and is based on the air density ρ_0 = 1.2041 kg m^{-3} at P = 1013.25 hPa and T = 293.15 K.
Values for c and d come from:

- Pruppacher and Klett (1997, Eq. (10-138)) for cloud droplets, with P = 1013.25 hPa and T = 293.15 K.
- Liu and Orville (1969, Eq. (2.22)) for rain drops. They fitted data from the Smithsonian Meteorological Tables (List 1958) valid at P = 1013.25 hPa and T = 293.15 K.
- Starr and Cox (1985, Table B.2, for sizes between 0 and 200 μm), who modified relationships from Heymsfield (1972), valid at 400 hPa. The value for c is corrected to use D in m, and multiplied by $(0.58/\rho_0)^{0.4}$ (assuming that the air density at 400 hPa is 0.58 kg m^{-3}) so that the previous equation can be used.
- Locatelli and Hobbs (1974) for snow (their parameters for aggregates of densely rimed radiating assemblages of dendrites) and graupel (their second set of values for lump graupel), converted for D in m. They do not specify the air pressure or temperature. Considering their experimental set-up, we assume P = 900 hPa (altitudes between 750 and 1500 m) and T = 273.15 K, and therefore multiply c by $(1.15/\rho_0)^{0.4}$.
- Böhm (1989) for hail, valid at ρ_d = 1.1 kg m^{-3}. The value of c was changed to use D in m and adapt to the previous equation again.

8.2 CCN activation to form cloud droplets

CCN activation in LIMA follows the parameterization from the C2R2 scheme, and was extended to treat the competition between several CCN modes. It is based on the same method to determine first a diagnostic maximum supersaturation (which depends mostly on the aerosol population, the vertical lifting and the cooling rate). The number of activated CCN in each mode is then computed using the activation spectrum of each mode.

8.2.1 Activation spectrum

For each hydrophilic aerosol mode (considered chemically homogeneous), the activation spectrum is parameterized after Cohard et al. (1998) as a function of the supersaturation S_w (with $S_w = 0.01$ for a 1% supersaturation):

$$N_m^{CCN} = C_m S_w^{k_m} F(\mu_m, \frac{k_m}{2}, \frac{k_m}{2} + 1, -\beta_m S_w^2) \tag{8.40}$$

Table 8.1: Set of parameters used to characterize each hydrometeor category

	r_c	r_r	r_i			r_s	r_g	r_h
			plates	columns	rosettes			
α	3	1	3			1	1	1
ν	1	2	3			1	1	8
a	$\rho_w\pi/6$	$\rho_w\pi/6$	0.82	$2.14\ 10^{-3}$	44	0.02	19.6	470
b	3	3	2.5	1.7	3	1.9	2.8	3
c	$2.98\ 10^7$	842	747	$1.96\ 10^5$	$4\ 10^5$	5	122	201
d	2	0.8	1	1.585	1.663	0.27	0.66	0.64
C	-	-	-			5	$5\ 10^5$	$4\ 10^4$
x	-	-	-			1	-0.5	-1
$\bar{f}_0$	1	0.78	1			0.86	0.86	0.86
$\bar{f}_1$	0	0.308	0			0.28	0.28	0.28
$\bar{f}_2$	0.108	0	0.14			0	0	0
C_1	0.5	0.5	$1/\pi$	0.8	0.5	$1/\pi$	0.5	0.5

where C_m, k_m, μ_m and β_m depend on the aerosol population, and F is the hypergeometric function (Gradshteyn and Ryzhik 1965)[1]. Some properties of this activation spectrum are presented in the appendices of Cohard et al. (2000), such as:

$$\lim_{S_w \to \infty} N_m^{CCN} = \frac{C_m}{\beta_m^{k_m/2}} \frac{\Gamma(k_m/2+1)\Gamma(\mu_m - k_m/2)}{\Gamma(\mu_m)} \quad ; \quad k_m < 2\mu_m \tag{8.41}$$

$$\frac{\partial N_m^{CCN}}{\partial S_w} = k_m C_m S_w^{k_m-1}(1+\beta_m S_w^2)^{-\mu_m} \tag{8.42}$$

k_m, β_m and μ_m parameters are determined following Cohard et al. (2000):

$$\frac{k_m}{k_0} = \left(\frac{ln(\sigma_m)}{ln(\sigma_0)}\right)^{\alpha_k^\sigma} \tag{8.43}$$

$$\frac{\beta_m}{\beta_0} = \left(\frac{r_m}{r_0}\right)^{\alpha_\beta^r} exp\left\{\alpha_\beta^\sigma\left[\frac{ln(\sigma_m)}{ln(\sigma_0)} - 1\right]\right\}\left(\frac{\epsilon_m}{\epsilon_0}\right)^{\alpha_\beta^{\epsilon m}}\left(\frac{T_m}{T_0}\right)^{\alpha_\beta^T} \tag{8.44}$$

$$\frac{\mu_m}{\mu_0} = \left(\frac{ln(\sigma_m)}{ln(\sigma_0)}\right)^{\alpha_\mu^\sigma} \tag{8.45}$$

where r_m and σ_m are the parameters defining the aerosol particle size distribution. Reference values k_0, β_0, μ_0, r_0, σ_0, T_0 and ϵ_{m0} are given in Tables 1 and 2 from Cohard et al. (2000) for marine and continental aerosols. Cohard et al. (2000) also explain how to compute the $\alpha_\bullet^\bullet$ parameters.
C_m can then be determined using Eq. (8.41) considering that all available aerosols are activated when the supersaturation tends to infinity.

Implementation in LIMA

In *init_aerosol_properties.f90*, parameters k_m, β_m and μ_m are computed for each CCN mode, in the

---

[1] Note that in Cohard et al. (1998) $S_{\%} = 100 S_w$ is used instead of S_w. Values for β_m and C_m are therefore adapted in LIMA: $\beta_m = 100^2 \beta_m$ and $C_m = 100^{k_m} C_m$

variables XKHEN_MULTI, XMUHEN_MULTI and XBETAHEN_MULTI (when the HINI_CCN variable is set to AER). Since the number concentration of aerosols is a prognostic variable, C_m cannot be computed during the initialization. However, the variable XLIMIT_FACTOR is computed and C_m at each grid point and time step will simply be derived as $C_m = N_m/\mathrm{XLIMIT\_FACTOR}$.

8.2.2 Diagnostic maximum supersaturation

This parameterization is adapted from Cohard et al. (1998). The evolution of S is described by Eq. (8.46), where the three terms represent the effects of (1) the vertical lifting, (2) the cloud droplets growth by vapor condensation, and (3) the cooling rate. This equation is derived from Pruppacher and Klett (1997, their Eqs. (13)-(29)), using the assumption $1+S_w \approx 1$, and is therefore valid only at, or close to, saturation.

$$\frac{\mathrm{d}S}{\mathrm{d}t} = \underbrace{\psi_1 \omega}_{(1)} - \underbrace{\psi_2 \frac{\mathrm{d}q_c}{\mathrm{d}t}}_{(2)} + \underbrace{\psi_3 \frac{\mathrm{d}T}{\mathrm{d}t}}_{(3)} \tag{8.46}$$

where ψ_1, ψ_2 and ψ_3 are thermodynamical functions depending on T and P (Cohard et al. 1998):

$$\psi_1(T,P) = \frac{g}{TR_d}\left(\frac{M_v L_v}{M_d c_{pd} T} - 1\right) \tag{8.47}$$

$$\psi_2(T,P) = \frac{M_d P}{M_v e_{sw}(T)} + \frac{M_v L_v^2}{M_d R_d T^2 c_{pd}} = \frac{M_d P}{M_v e_{sw}(T)} + \frac{L_v^2}{T^2 c_{pd} R_v} \tag{8.48}$$

$$\psi_3(T,P) = -\frac{M_v L_v}{M_d R_d T^2} \tag{8.49}$$

The following resolving method is similar to the solution from Pruppacher and Klett (1997) and Cohard et al. (1998), who did not account for the cooling rate [Eq. (8.46), term 3].
Following Pruppacher and Klett (1997, their Eqs. (13)-(34)), the cloud droplet growth at a supersaturation S_w follows:

$$\frac{\mathrm{d}m}{\mathrm{d}t} = 2\pi\rho_w \left(\frac{2}{\rho_w} A_w^{-1}\right)^{3/2} S_w \left[\int_\tau^t S_w(t')\mathrm{d}t'\right]^{1/2} \tag{8.50}$$

where τ is the time at which the considered droplet was activated, and A_w a thermodynamical function:

$$A_w = \frac{R_v T}{D_v e_{sw}(T)} + \frac{L_v}{k_a T}\left(\frac{L_v}{R_v T} - 1\right) \simeq \frac{R_v T}{D_v e_{sw}(T)} + \frac{L_v^2}{k_a R_v T^2} \tag{8.51}$$

Writing $n_m^{CCN}(S_w)\mathrm{d}S_w$ the number of activated droplets for one CCN mode m, and for a supersaturation between S_w and $S_w + \mathrm{d}S_w$, we have:

$$\int_0^{S_w} n_m^{CCN}(S')\mathrm{d}S' = N_m^{CCN}(S_w) = C_m S_w^{k_m} F(\mu_m, \frac{k_m}{2}, \frac{k_m}{2}+1, -\beta_m S_w^2) \tag{8.52}$$

and then

$$n_m^{CCN}(S_w) = k_m C_m S_w^{k_m-1}(1+\beta_m S_w^2)^{-\mu_m} \tag{8.53}$$

When several CCN modes are present, we get:

$$n^{CCN}(S_w) = \sum_{m\ modes} k_m C_m S_w^{k_m-1}(1+\beta_m S_w^2)^{-\mu_m} \tag{8.54}$$

Integrating over all the cloud droplets, the cloud water mass mixing ratio change is:

$$\frac{\mathrm{d}q_c}{\mathrm{d}t} = 2\pi\frac{\rho_w}{\rho_d}\left(\frac{2}{\rho_w}A_w^{-1}\right)^{3/2} S_w \int_0^{S_w} n^{CCN}(S')\left[\int_{\tau(S')}^{t} S_w(t')\mathrm{d}t'\right]^{1/2}\mathrm{d}S' \tag{8.55}$$

This equation cannot be solved analytically, but the temporal integral of supersaturation admits a lower bound, which helps us determine an upper bound S_{max} for the supersaturation. Twomey proposed (Pruppacher and Klett 1997, their Eqs. (13)-(37)) the following lower bound:

$$\int_{\tau(S')}^{t} S_w(t')\mathrm{d}t' > \frac{S_w^2 - S'^2}{2(\psi_1\omega)} \tag{8.56}$$

which becomes, when accounting for the cooling rate:

$$\int_{\tau(S')}^{t} S_w(t')\mathrm{d}t' > \frac{S_w^2 - S'^2}{2(\psi_1\omega + \psi_3\mathrm{d}T/\mathrm{d}t)} \tag{8.57}$$

Thus:

$$\frac{\mathrm{d}r_c}{\mathrm{d}t} > \frac{2\pi\rho_w\left(\frac{2}{\rho_w}A_w^{-1}\right)^{3/2} S_w}{\rho_d\left[2(\psi_1\omega+\psi_3\mathrm{d}T/\mathrm{d}t)\right]^{1/2}}\sum_{m\ modes}\left[k_m C_m \underbrace{\int_0^{S_w} S'^{k_m-1}(1+\beta_m S'^2)^{-\mu_m}(S_w^2-S'^2)^{1/2}\mathrm{d}S'}_{I}\right] \tag{8.58}$$

Using the variable change $x = (S'/S)^2$, Cohard et al. (1998) get:

$$I = \frac{S_w^{k_m+1}}{2}\underbrace{B\left(\frac{k_m}{2},\frac{3}{2}\right)}_{B_m}\underbrace{F\left(\mu_m,\frac{k_m}{2},\frac{k_m+3}{2},-\beta_m S_w^2\right)}_{F_{3/2,m,S_w}} \tag{8.59}$$

and

$$\frac{\mathrm{d}r_c}{\mathrm{d}t} > \frac{2\pi\rho_w\rho_w^{-3/2}A_w^{-3/2}}{\rho_d\,(\psi_1\omega+\psi_3\mathrm{d}T/\mathrm{d}t)^{1/2}}\sum_{m\ modes}\left[C_m k_m S_w^{k_m+2}B_m F_{3/2,m,S_w}\right] \tag{8.60}$$

For the maximum supersaturation, we have $\mathrm{d}S/\mathrm{d}t = 0$. Using Eqs. (8.46) and (8.60) gives:

$$\sum_{m\ modes}\left[C_m k_m S_w^{k_m+2}B_m F_{3/2,m,S_w}\right] < \frac{\rho_d\,(\psi_1\omega+\psi_3\mathrm{d}T/\mathrm{d}t)^{3/2}}{2\pi\rho_w\rho_w^{-3/2}A_w^{-3/2}\psi_2} \tag{8.61}$$

The diagnostic maximum supersaturation S_{max} is the supersaturation for which the equality is reached, all other factors being determined by the aerosol population and atmospheric conditions.

Implementation in LIMA
As presented in the previous section, k_m, β_m and μ_m, as well as the XLIMIT_FACTOR parameter necessary to compute C_m, are initialized for each CCN mode in *init_aerosol_properties.f90*.

In ini_lima_warm.f90:

- For each aerosol mode, the function $F\left(\mu_m, \frac{k_m}{2}, \frac{k_m+3}{2}, -\beta_m S_w^2\right)$ of supersaturation S_w, used in Eq. (8.61), is tabulated between two values ZSMIN et ZSMAX, with a logarithmic scale in S_w, in the XHYPF32 variable.
- For each aerosol mode, the function $F\left(\mu_m, \frac{k_m}{2}, \frac{k_m}{2}+1, -\beta_m S_w^2\right)$ of supersaturation S_w, used in Eq. (8.40), is tabulated between the same two values ZSMIN et ZSMAX, with the same logarithmic scale in S_w, in the XHYPF12 variable.
- Functions ψ_1 and ψ_3 of T are also tabulated, for T from -40°C to +40°C, in the XPSI1 and XPSI3 variables.
- Eventually, the XAHENG= $(2\pi\rho_w\rho_w^{-3/2}A_w^{-3/2})^{-1}$ function is also tabulated on the same temperature domain.

Eq. (8.61) is solved in *lima_warm_nucl.f90*:

- C_m for each CCN mode with $C_m = N_m/XLIMIT\_FACTOR$ (PTSTEP and ZRHODREF account for the unit change from N_m to get C_m in m^{-3}). C_m is computed from the total aerosol population $N_m^{free} + N_m^{acti}$.
- ψ_2 is computed in ZZW1.
- Using a linear interpolation from the tabulated functions XPSI1, XPSI3 and XAHENG, we get ZZW3= $\frac{\rho_d}{\rho_w}\frac{(\psi_1\omega+\psi_3 \mathrm{d}T/\mathrm{d}t)^{3/2}}{2\pi\rho_w\rho_w^{-3/2}A_w^{-3/2}\psi_2}$
- Functions FUNCSMAX and SINGL_FUNCSMAX compute the difference of the two terms in Eq. (8.61).
- The maximum supersaturation S_{max} is then determined by looking for a zero of this function for a supersaturation between ZS1 and ZS2 (ZS1 and ZS2 are chosen within the ZSMIN to ZSMAX range used to tabulate XHYPF32= $F_{3/2,m,S_w}$) using the Ridder algorithm (Press et al. 1992).

8.2.3 Number of activated cloud droplets

According to the Köhler theory, for a given maximum supersaturation S_{max}, aerosols activated are exactly those with a critical supersaturation lower than S_{max}. Thus, to determine the number of aerosols really activated at time t, we first compute the number of activable aerosols for S_{max} and the total aerosol population $N_m^{free} + N_m^{acti}$, using Eq. (8.40). The number of aerosols really activated is then the difference between the number of activable aerosols and the number of aerosols previously activated during the simulation N_m^{acti}:

$$\Delta N_m^{acti}(t) = Max(0, N_m^{CCN}(S_{max}) - N_m^{acti}(t - \Delta t)) \quad (8.62)$$

$$N_m^{free}(t) = N^{free}(t - \Delta t) - \Delta N_m^{acti}(t) \quad (8.63)$$

$$N_m^{acti}(t) = N^{acti}(t - \Delta t) + \Delta N_m^{acti}(t) \quad (8.64)$$

Implementation in LIMA

Computations are also led in *lima_warm_nucl.f90.* ZTMP is the number of activable aerosols for each mode (using the tabulated function XHYPF12). The N_m^{free} and N_m^{acti} number concenterations for each mode are the updated.

A final test restrains the activation to regions where the total number of activable cloud droplets is higher than 25 cm^{-3}.

8.3 Pristine ice nucleation

Three ways to initiate pristine ice are parameterized in LIMA. The homogeneous nucleation of rain drops, cloud droplets and CCN is active only at very cold temperatures, below -35°C. Two parameterizations of the heterogeneous nucleation are available. The first one is based upon Meyers et al. (1992) and depends only on the atmospheric conditions. The second follows the empirical parameterization by Phillips et al. (2008), and explicitly predicts the number of ice crystals formed from the nucleation of a prognostic IFN population.

The third way to create ice crystals in LIMA is the secondary production of ice by the Hallet-Mossop process when aggregates or graupel freeze cloud droplets. It is presented in the mixed phase collection processes presentation.

8.3.1 Homogeneous ice nucleation

Computations are carried in lima_cold_hom_nucl.f90.

Rain drops homogeneous freezing

All raindrops are instantly transformed into graupel when they reach temperatures below -35°C.

Cloud droplets homogeneous freezing

The cloud droplet homogeneous freezing rate J (number of ice embryos formed per cubic cm of water per second, cm^{-3} s^{-1}) is taken from Eadie (1971), and was since used in many studies (e.g. Heymsfield and Miloshevich 1993; DeMott et al. 1994; Milbrandt and Yau 2005):

$$\ln_{10}(J) = \alpha_1 + \alpha_2 T + \alpha_3 T^2 + \alpha_4 T^3 + \alpha_5 T^4 \quad (8.65)$$

$$J = \exp\left[\alpha_1 \ln(10) + \alpha_2 \ln(10)\, T + \alpha_3 \ln(10)\, T^2 + \alpha_4 \ln(10)\, T^3 + \alpha_5 \ln(10)\, T^4\right] \quad (8.66)$$

with

$$\alpha_1 = -606.3952 \tag{8.67}$$
$$\alpha_2 = -52.6611 \tag{8.68}$$
$$\alpha_3 = -1.7439 \tag{8.69}$$
$$\alpha_4 = -0.0265 \tag{8.70}$$
$$\alpha_5 = -1.536\ 10^{-4} \tag{8.71}$$
$$\tag{8.72}$$

The probability for a raindrop of volume V not to freeze in a time Δt is given by:

$$P = \exp[-J\ V\ \Delta t] \tag{8.73}$$

Computations if $\alpha_c = 3$
In this case the number of droplets that are not frozen can be derived:

$$N_c(t+\Delta t) = \int_0^\infty \exp[-J\ \frac{\pi}{6}D^3\ \Delta t]n(D)dD \tag{8.74}$$
$$= \int_0^\infty e^{-J\ \frac{\pi}{6}D^{\alpha_c}\ \Delta t}N_c\frac{\alpha_c}{\Gamma(\nu_c)}\lambda_c^{\alpha_c\nu_c}D^{\alpha_c\nu_c-1}e^{-(\lambda_c D)^{\alpha_c}}dD \quad \text{using } \alpha_c = 3 \tag{8.75}$$
$$= \int_0^\infty N_c\frac{\alpha_c}{\Gamma(\nu_c)}\lambda_c^{\alpha_c\nu_c}D^{\alpha_c\nu_c-1}e^{-D^{\alpha_c}(\lambda_c^{\alpha_c}+J\Delta t\pi/6)}dD \tag{8.76}$$
$$= \int_0^\infty X^{-\alpha_c\nu_c}\lambda_c^{\alpha_c\nu_c}\quad N_c\frac{\alpha_c}{\Gamma(\nu_c)}X^{\alpha_c\nu_c}D^{\alpha_c\nu_c-1}e^{-D^{\alpha_c}X^{\alpha_c}}dD \quad \text{with } X = \left(\lambda_c^{\alpha_c}+\frac{J\Delta t\pi}{6}\right)^{1/\alpha_c} \tag{8.77}$$
$$= X^{-\alpha_c\nu_c}\lambda_c^{\alpha_c\nu_c}N_c \tag{8.78}$$
$$= \left(\frac{\lambda_c^{\alpha_c}}{\lambda_c^{\alpha_c}+\frac{J\Delta t\pi}{6}}\right)^{\nu_c}N_c \tag{8.79}$$
$$= \left(\frac{1}{1+\frac{1}{\lambda_c}\frac{J\Delta t\pi}{6}}\right)^{\nu_c}N_c \tag{8.80}$$

Similarly, for the mass of droplets that are not frozen, we get:

$$r_c(t+\Delta t) = \left(\frac{1}{1+\frac{1}{\lambda_c}\frac{J\Delta t\pi}{6}}\right)^{\nu_c}N_c a\frac{1}{\lambda_c^3}\frac{\Gamma(\nu_c+3/\alpha_c)}{\Gamma(\nu_c)} \tag{8.81}$$
$$= \left(\frac{1}{1+\frac{1}{\lambda_c}\frac{J\Delta t\pi}{6}}\right)^{\nu_c}r_c \tag{8.82}$$

Computation if $\alpha_c \neq 3$
In this case, an approximation is necessary, either by carrying the computations for the mean-volume diameter only, such as in Milbrandt and Yau (2005), or by taking $1-\exp(-JV_c\Delta t) \approx JV_c\Delta t$ as in the ICE3 scheme. This case is not coded yet.

CCN homogeneous freezing

The homogeneous freezing of CCN particles follows Kärcher and Lohmann (2002). Equations (12)-(28) from Pruppacher and Klett (1997) become, with our notations, using the supersaturation $S_i = r_v/r_{si}$ [2] and without the approximation $p - e = p$:

$$\frac{\mathrm{d}S_i}{\mathrm{d}t} = \frac{p}{\epsilon e_{sat,i}}\frac{\mathrm{d}r_v}{\mathrm{d}t} - S_i\left(\frac{L_s\epsilon}{R_dT^2}\frac{\mathrm{d}T}{\mathrm{d}t} + \frac{g}{R_dT}w\right) \tag{8.83}$$

Using Eq. (12-26) and (12-29) from Pruppacher and Klett (1997) with $\mu = 0$ (entrainment effects are neglected):

$$\frac{\mathrm{d}S_i}{\mathrm{d}t} = \left(\frac{L_s\epsilon g}{R_dT^2c_{pd}} - \frac{g}{R_dT}\right)S_iw - \left(\frac{p}{\epsilon e_{sat,i}} + \frac{\epsilon L_s^2}{R_dT^2c_{pd}}S_i\right)\frac{\mathrm{d}r_i}{\mathrm{d}t} \tag{8.84}$$

Replacing $\epsilon = M_v/M_d$ and using the M_d, M_v, R, R_d, R_v relationships, this equation takes the same form as Eq. (1) from Kärcher and Lohmann (2002). They use R_i (the number of water molecules deposited at the surface of ice crystals per unit of time and air volume, m^{-3} s^{-1}), where we use the ice mass mixing ratio r_i instead ($\mathrm{d}r_i/\mathrm{d}t = R_im_w/\rho_d$), and therefore multiply a_2 and a_3 by ρ_d/m_w:

$$\frac{\mathrm{d}S_i}{\mathrm{d}t} = a_1S_iw - (a_2 + a_3S_i)\frac{\mathrm{d}r_i}{\mathrm{d}t} \tag{8.85}$$

$$a_1 = \frac{M_vL_sg}{Rc_{pd}T^2} - \frac{M_dg}{RT} \tag{8.86}$$

$$a_2 = \frac{p}{\epsilon e_{sat,i}} \approx r_{si}^{-1} \tag{8.87}$$

$$a_3 = \frac{L_s^2}{R_vc_{pd}T^2} \tag{8.88}$$

Homogeneous freezing occurs when the supersaturation exceeds a critical value, depending on temperature, which they fitted with the following equation:

$$S_{cr} = 2.583 - \frac{T}{207.83} \tag{8.89}$$

The characteristic time of homogeneous nucleation is:

$$\tau = c(T)\left(\left|\frac{\partial\ln(J)}{\partial T}\right|\right)_{S_i=S_{cr}}\frac{\mathrm{d}T}{\mathrm{d}t} \tag{8.90}$$

where Kärcher and Lohmann (2002) obtained the following fits:

$$c(T) = \max[100, 100(22.6 * 0.1T)] \tag{8.91}$$

$$\left.\frac{\partial\ln(J)}{\partial T}\right|_{S_i=S_{cr}} = 4.37 - 0.03T \tag{8.92}$$

To compute the solution of homogeneous freezing, we need to evaluate the ratio $b_2/2\pi b_1$ where b_1 and b_2 are defined in their Eq. (7), for the peak supersaturation supposed to be $S_i^{max} = S_{cr}$. Using

---

[2] Pruppacher and Klett (1997) use $s_{v,w} = r_v/r_{si} - 1$.

$m_w n_{sat}/\rho_d = r_{v,sat}$ (n_{sat} is in m^{-3}) and $D_v(T,P) = 0.211(T/T_0)^{1.94}(P_0/P)$ (Eq. (13-3) from Pruppacher and Klett 1997, with D_v expressed in cm^2 s^{-1}):

$$\frac{b_2}{2\pi b_1} = \frac{\rho_i}{\rho_d\, 2\pi\, 0.211\, 10^{-4}\, (P_0/P)(T/T_0)^{1.94}\, r_{si}(S_{cr}-1)} \tag{8.93}$$

We use Eq. (11a) from Kärcher and Lohmann (2002) to compute the number of frozen CCN (N_i, kg^{-1}), dividing their right side by ρ_d because their n_i is expressed in m^{-3}, and multiplying by ρ_d/m_w to convert our a_2 and a_3 parameters:

$$N_i = \frac{1}{\rho_d}\frac{m_w}{\rho_i}\left(\frac{b_2}{2\pi b_1}\right)^{3/2}\frac{a_1}{(a_2+a_3\,S_{cr})(m_w/\rho_d)}\frac{w}{\sqrt{\tau}} \tag{8.94}$$

$$= \frac{1}{\rho_i}\left(\frac{b_2}{2\pi b_1}\right)^{3/2}\frac{a_1}{a_2+a_3\,S_{cr}}\frac{w}{\sqrt{\tau}} \tag{8.95}$$

Eventually, we determine the ice mass mixing ratio formed following their Eq. (11c), with the same transformations as for the previous one:

$$r_i = \frac{1}{\rho_d}\frac{\pi}{6}m_w\frac{a_1}{(a_2+a_3\,S_{cr})(m_w/\rho_d)}w\tau \tag{8.96}$$

$$= \frac{\pi}{6}\frac{a_1}{a_2+a_3\,S_{cr}}w\tau \tag{8.97}$$

$$= \frac{\pi}{6}N_i\,\rho_i\left(\frac{b_2}{2\pi b_1}\right)^{-3/2}\tau^{3/2} \tag{8.98}$$

Remarks on this parameterization

- As stated by Kärcher and Lohmann (2002), this parameterization does not explicitely depend on the number of available aerosols, and the resulting number of ice particles formed is simply limited to the maximum number of available CCN.
- We assume in LIMA that only the fast growth case occurs (see their paragraph 27, p 5).
- They stated (paragraph 28, p 5) that T_{cr} (the temperature at which the critical supersaturation S_{cr} is reached) should be used in the computations. In LIMA, computations are currently carried with T.

Implementation in LIMA

The following computations are carried once:

$$\text{ZZY} = S_{cr} \tag{8.99}$$

$$\text{ZPSI1} = a_1\,S_{cr} \tag{8.100}$$

$$\text{ZPSI2} = a_2 + a_3\,S_{cr} \tag{8.101}$$

$$\text{ZTAU} = \tau \qquad (\text{using } \mathrm{d}T/\mathrm{d}t = \text{ZTHS }(P/P_{00})^{R_d/c_{pd}}) \tag{8.102}$$

$$\text{ZBFACT} = \frac{b_2}{2\pi b_1} \quad (\text{using } S_i/r_v = r_{v,sat}^{-1}) \tag{8.103}$$

$$\text{ZZX} = \frac{1}{\Delta t}N_i \quad \text{limited between 0 and ZNFS} \tag{8.104}$$

$$\text{ZZW} = \frac{1}{\Delta t}r_i \quad \text{limited to ZRVS} \tag{8.105}$$

CCN homogeneous freezing is supposed to act equally on each CCN mode, and the number of frozen CCN is depleted from each mode in proportion of the initial number of available CCN in each mode.

8.3.2 Heterogeneous pristine ice nucleation following Meyers et al. (1992)

The ice nucleation parameterization by Meyers et al. (1992) links the number concentration of ice crystals to the supersaturation only.

Heterogeneous nucleation by deposition

Using data from continuous flow chambers, Meyers et al. (1992, Eq. (2.4)) expressed the number of ice forming nuclei as a function of the supersaturation with respect to ice (using the decimal form of S_i, so that $S_i = 0.01$ for a 1% supersaturation):

$$N_{IN}(S_i)[L^{-1}] = \exp[12.96\ 10^{-2}\ 100\ S_i - 0.639] \tag{8.106}$$

This parameterization is easily implemented in LIMA.
First, some variables are initialized in *ini_lima_cold_mixed.f90*:

- XNUC_DEP $=$ 1000 XFACTNUC_DEP ZFACT_NUCL, where the 1000 factor is used to convert from the previous formula to concentrations in m^{-3}, XFACTNUC_DEP (default value 1) can be changed in namelist to modulate the ice nucleation process, and $ZFACT\_NUCL = 1$.

Then, in *lima_meyers.f90*, ZZY is computed where $T < 5$°C and $S_i > 0$. The decimal formulation of S_i is used in LIMA ($S_i = 0.01$ for a 1% supersaturation), and the number concentrations are in kg^{-1}, so the pristine ice number concentration tendency is:

$$\mathrm{ZZY}[\mathrm{kg}^{-1}\mathrm{s}^{-1}] = \frac{\mathrm{XNUC\_DEP}}{\rho_d \Delta t} \exp[12.96\ 10^{-2}\ 100\ S_i - 0.639] \tag{8.107}$$

To compute the mass mixing ratio created by this process, we first need to determine the number of ice crystals actually nucleated at this time step by subtracting the number of already nucleated ice crystals. The mass mixing ratio tendency is then deduced assuming that an ice embryo has a mass of XMNU0 $= 6.88\ 10^{-13}$ kg.

Heterogeneous nucleation by contact

Meyers et al. (1992, Eq. (2.6)) also expressed the number of ice crystals nucleated by contact freezing of cloud droplets as a function of temperature:

$$N_{IN}(T)[\mathrm{L}^{-1}] = \exp[-2.80 - 0.262(T - T_0)] \tag{8.108}$$

This number is computed in the same way as the nucleation by deposition in LIMA, and the number concentration of crystals is limited by the number of available cloud droplets.
To compute the mass mixing ratio created by this process, we first need to determine the number of ice crystals actually nucleated at this time step by subtracting the number of already nucleated ice crystals. The mass mixing ratio tendency is then deduced assuming that the cloud droplets mass is evenly distributed among cloud droplets, so:

$$ZZW = r_{i,contact} = \frac{r_c}{N_c} N_{i,contact} \tag{8.109}$$

8.3.3 IFN nucleation following the parameterization by Phillips et al. (2008)

Instead of the parameterization by Meyers et al. (1992), which does not link the pristine ice number concentration to the available aerosols, the parameterization proposed by Phillips et al. (2008, 2013) can be used in LIMA. This implementation is described in Berthet (2010); Vié et al. (2016).

Reference activity spectrum

Based on observations of ice nucleation in the continuous flow diffusion chamber (CFDC), Phillips et al. (2008) proposed a parameterization of the ice nucleation reference activity spectrum, taking the same form as the one proposed by Meyers et al. (1992), but distinguishing three temperature regimes. Note that, as specified by Phillips et al. (2008), S_i is artificially prevented from exceeding water saturation in the computation of $N_{i,ref}$. For temperatures colder than -35°C, they got [their Eq. (2)]:

$$N_{i,ref}(T,S_i) = \frac{1000}{\rho_{CFDC}}\,\gamma\,(\exp[12.96(S_i-0.1)])^{0.3} \tag{8.110}$$

For temperatures warmer than -25°C, they got ([Their Eq. (3)]:

$$N_{i,ref}(T,S_i) = 0.058707\,\frac{1000}{\rho_{CFDC}}\,\gamma\,\exp[12.96\,S_i-0.639] \tag{8.111}$$

The reference activity spectrum for temperatures between -25°C and -35°C is a bit more complicated and involves intermediate computations [their Eqs. (4)-(7) and appendix A]:

$$N_{max}(T,S_i) = \frac{1000}{\rho_{CFDC}}\,\gamma\,(\exp[12.96(S_i^w-0.1)])^{0.3} \qquad \text{for T between -30°C and -35°C} \tag{8.112}$$

$$N_{max}(T,S_i) = 0.058707\,\frac{1000}{\rho_{CFDC}}\,\gamma\,\exp[12.96\,S_i^w-0.639] \qquad \text{for T between -25°C and -30°C} \tag{8.113}$$

$$\hat{n}(T,S_i) = \min\left(0.058707\,\frac{1000}{\rho_{CFDC}}\,\gamma\,\exp[12.96\,S_i-0.639]\ ;\ n_{max}(T,S_i)\right) \tag{8.114}$$

$$\tilde{n}(T,S_i) = \min\left(\frac{1000}{\rho_{CFDC}}\,\gamma\,(\exp[12.96(S_i-0.1)])^{0.3}\ ;\ n_{max}(T,S_i)\right) \tag{8.115}$$

$$\bar{n}(T,S_i) = \hat{n}(T,S_i)\left(\frac{\tilde{n}(T,S_i)}{\hat{n}(T,S_i)}\right)^{\delta_1^0(T,-35,-25)} \tag{8.116}$$

$$N_{i,ref}(T,S_i) = \min\left(\bar{n}(T,S_i)\ ;\ N_{max}(T,S_i)\right) \tag{8.117}$$

Integration of the number of activable IFN

The reference activity spectrum is used to predict the fraction of each IFN species X which can be nucleated into ice crystals for given thermodynamical conditions, as (Eq. (9) from Phillips et al. 2008):

$$N_X^{IFN} = \int_{0.1\ 10^{-6}}^{\infty}\left[1-\exp(-\mu_X(D,S_i,T))\right]\frac{\mathrm{d}N_X}{\mathrm{d}D}\mathrm{d}D \tag{8.118}$$

where the integration starts at 0.1 μm because we assume that smaller aerosols cannot form ice crystals.

The expression for μ_X, and the parameters necessary to compute it, are found in Phillips et al. (2008, Eqs. (10)-(12) and Table 1). Writing

$$A(S_i,T) = H_X(S_i,T)\xi(T)\frac{\alpha_X N_{i,ref}(T,S_i)}{\Omega_{X,1,*}} \tag{8.119}$$

we have

$$\mu_X(D,S_i,T) = A(S_i,T)\frac{\mathrm{d}\Omega_X}{\mathrm{d}N_X} \tag{8.120}$$

$$\approx A(S_i,T)\pi D^2 \tag{8.121}$$

Two methods are used to perform the integration, depending on the temperature.

For temperatures warmer than -35°C

For temperatures warmer than -35°C, we assume that the number of ice crystals formed remains small, therefore $\mu_x << 1$ and we can write:

$$N_X^{IFN} \approx \int_{0.1\ 10^{-6}}^{\infty} \mu_X(D,S_i,T)\frac{\mathrm{d}N_X}{\mathrm{d}D}\mathrm{d}D \tag{8.122}$$

$$\approx \int_{0.1\ 10^{-6}}^{\infty} \mu_X(D,S_i,T)n_X(D)\mathrm{d}D \tag{8.123}$$

$$\approx A(S_i,T)\pi N_X \int_{0.1\ 10^{-6}}^{\infty} D^2 n_X(D)\mathrm{d}D \tag{8.124}$$

We need to compute the integral in the previous equation:

$$\int_{0.1\ 10^{-6}}^{\infty} D^2 n_X(D)\mathrm{d}D = \int_{0.1\ 10^{-6}}^{\infty} \frac{D^2}{\sqrt{2\pi}\ D\ \ln(\sigma_X)} e^{-\left(\frac{\ln(D/D_X)}{\sqrt{2}\ln(\sigma_X)}\right)^2}\mathrm{d}D \tag{8.125}$$

We proceed to the variable change:

$$x = \frac{\ln(D/D_X)}{\sqrt{2}\ln(\sigma_X)}$$

$$D = D_X e^{x\sqrt{2}\ln(\sigma_X)}$$

$$\mathrm{d}D = \sqrt{2}\ln(\sigma_X) D_X e^{x\sqrt{2}\ln(\sigma_X)}\mathrm{d}x$$

which gives:

$$\int_{0.1\ 10^{-6}}^{\infty} D^2 n_X(D)\mathrm{d}D = \int_{B}^{\infty} \frac{D_X^2}{\sqrt{\pi}} e^{2\sqrt{2}x\ln(\sigma_X)-x^2}\mathrm{d}x \quad \text{with} \quad B = \frac{\ln(0.1\ 10^{-6}/D_X)}{\sqrt{2}\ln(\sigma_X)} \tag{8.126}$$

$$= \frac{D_X^2}{\sqrt{\pi}} e^{2\ln(\sigma_X)^2} \int_{B}^{\infty} e^{-(x-\sqrt{2}\ln(\sigma_X))^2}\mathrm{d}x \tag{8.127}$$

We proceed to a second variable change:

$$u = x - \sqrt{2}\ln(\sigma_X)$$

$$x = u - \sqrt{2}\ln(\sigma_X)$$

$$\mathrm{d}x = \mathrm{d}u$$

Which gives, using $\int_{-\infty}^{\infty} \exp(-x^2)\mathrm{d}x = \sqrt{\pi}$ and the definition of the error function $\mathrm{erf}(x) = \frac{2}{\sqrt{\pi}} \int_0^x e^{-t^2}\mathrm{d}t$:

$$\int_{0.1\ 10^{-6}}^{\infty} D^2 n_X(D)\mathrm{d}D = \frac{D_X^2}{\sqrt{\pi}} e^{2\ln(\sigma_X)^2} \int_{B-\sqrt{2}\ln(\sigma_X)}^{\infty} e^{-u^2}\mathrm{d}u \tag{8.128}$$

$$= \frac{D_X^2}{2} e^{2\ln(\sigma_X)^2} \Big[1 - \mathrm{erf}(B - \sqrt{2}\ln(\sigma_X))\Big] \tag{8.129}$$

and eventually (with $\mathrm{erf}(-x) = -\mathrm{erf}(x)$)

$$N_X^{IFN} \approx A(S_i, T)\pi N_X \int_{0.1\ 10^{-6}}^{\infty} D^2 n_X(D)\mathrm{d}D \tag{8.130}$$

$$\approx A(S_i, T)\pi N_X \frac{D_X^2}{2} e^{2\ \ln(\sigma_X)^2} \Big[1 + \mathrm{erf}(\sqrt{2}\ln(\sigma_X) - B)\Big] \tag{8.131}$$

For temperatures colder than -35°C

For temperatures colder than -35°C, we resort to another integration method.

$$N_X^{IFN} = \int_0^{\infty} \big[1 - \exp(-A(S_i, T)\pi D^2)\big] n_X(D)\mathrm{d}D - \int_0^{0.1\ 10^{-6}} \big[1 - \exp(-A(S_i, T)\pi D^2)\big] n_X(D)\mathrm{d}D \tag{8.132}$$

$$= T1 - T2 \tag{8.133}$$

To integrate $T1$, we develop the expression for $n_X(D)$ and use the same variable change as for the integration for temperatures warmer than -35°C:

$$T1 = N_X \Bigg[1 - \frac{1}{\sqrt{\pi}} \int_{-\infty}^{\infty} e^{-x^2} \exp\big[-A(S_i, T)\pi D_X^2 e^{2\sqrt{2}\ln(\sigma_X)x}\big]\mathrm{d}x\Bigg] \tag{8.134}$$

We use the Gauss-Hermitte quadrature to compute $T1$:

$$\int_{-\infty}^{\infty} e^{-x^2} f(x)\mathrm{d}x \approx \sum_i w_i f(x_i) \tag{8.135}$$

To integrate $T2$, we assume that the approximation $\exp(x) = 1 + x + O(x^2)$ is acceptable in the range of diameters from 0 to 0.1μm, so that we can perform the same integration as for temperatures warmer than -35°C, and get

$$T2 = N_X A(S_i, T)\pi \frac{D_X^2}{2} e^{2\ln(\sigma_X)^2} \Big[1 - \mathrm{erf}(\sqrt{2}\ln(\sigma_X) - B)\Big] \tag{8.136}$$

Update of the ice and aerosols number concentrations

The singular hypothesis allows to treat the IFN nucleation in the same fashion as the CCN activation. Therefore, the number concentration of nucleated IFN at a given timestep is obtained by subtracting the number of IFN already activated from the number of activable IFN.

Implementation in LIMA

Four different IFN particle types are considered in LIMA, following Phillips et al. (2008) (small dust, large dust, black carbon, organics) or Phillips et al. (2013) (small dust, large dust, black carbon, biogenics), therefore most variables are vectors of four values, corresponding to each IFN type considered.
The choice between the two versions of this sheme is made in namelist by setting the NPHILLIPS variable to 8 or 13.
Some variables are initialized in *ini_lima_cold_mixed.f90*:
Computations begin in *lima_phillips.f90*:

$$\mathrm{ZSI} = S_i \tag{8.137}$$
$$\mathrm{ZZY} = e_{sw} \tag{8.138}$$
$$\mathrm{ZSW} = S_w \tag{8.139}$$
$$\mathrm{ZSI\_W} = S_i^w \tag{8.140}$$
$$\mathrm{ZSI0} = S_{i,0}^X \quad \text{from Phillips et al. (2008, Table 1)} \tag{8.141}$$

Then, *lima_phillips_ref_spectrum.f90* returns the reference activity spectrum presented above in the ZZY variable.
Then, for each IFN species, *lima_phillips_integ.f90* computes the fraction of aerosols that can be nucleated into ice crystals, using the integration method presented in the appendix of Vié et al. (2016):

$$\mathrm{XB} = B = \frac{\ln(0.1\;10^{-6}/D_X)}{\sqrt{2}\ln(\sigma_X)} \tag{8.142}$$
$$\mathrm{ZFACTOR} = f_C \qquad \text{Eq. (12) from Phillips et al. (2008)} \tag{8.143}$$
$$\mathrm{ZSUBSAT} = H_X(S_i,T) \qquad \text{Eq. (11) from Phillips et al. (2008)} \tag{8.144}$$
$$\mathrm{ZEMBRYO} = A = H_X(S_i,T)\xi(T)\frac{\alpha_X N_{i,ref}(T,S_i)}{\Omega_{X,1}} \quad \text{Eq. (10) from Phillips et al. (2008)} \tag{8.145}$$
$$\tag{8.146}$$

and outputs for each IFN species the fraction of activable IFN $\mathrm{Z\_FRAC\_ACT}(X) = N_X^{IFN}/N_X$, computed as detailed above depending on the temperature. To compute the value of $\mathrm{erf}(x)$, we use the incomplete gamma function:

$$\Gamma_{inc}(a,x) = \frac{1}{\Gamma(a)}\int_0^x t^{a-1}e^{-t}\mathrm{d}t$$
$$\Gamma_{inc}(\frac{1}{2},x^2) = \mathrm{erf}(x) \quad \text{for } x > 0$$

Back in *lima_phillips.f90*, we compute, for each IFN mode (which is composed of a mix of the four IFN chemical types for which the fraction of activable particles were computed previously), the number of activable IFN, and get the number of really activated IFN by subtracting the number of already activated aerosols.
As for the parameterization by Meyers et al. (1992), to get the mass mixing ratio of pristine ice crystals formed, we assume that a single new ice crystal has a mass of $\mathrm{XMNU0} = 6.88\;10^{-13}$ kg.

Immersion freezing of cloud droplets by coated IFN

Coated IFN in LIMA are a special kind of hydrophilic aerosols. They are treated as acting first as CCN, and produce tagged cloud droplets which are the reservoir for ice nucleation by immersion freezing. Practically, the same parameterization as for insoluble IFN is used, but the integration is performed using $N_{acti} + N_{nucl}$, the number of coated IFN that were used to produce cloud droplets or ice crystals. To perform this integration, we assume a lognormal size distribution with constant parameters (D_X, σ_X), and a pure chemical composition, that are not necessarilly those of the initial aerosols.

8.3.4 Ice crystal shapes

Each ice crystal shape is associated with different values of the parameters a, b, c and d, and of the capacitance, allowing different fall speeds and vapour deposition growth rates depending on the shape selected. In reality, however, different shapes coexist within the same cloud. So, to compensate for the lack of diversity of ice crystal shapes in the model, we introduced the possibility of representing several ice crystal shapes simultaneously. The two primary columnar and plate-like ice crystal shapes are considered along with droxtal and bullet-rosette shapes.

Particular attention was paid to microphysical coupling (LIMA; Vié et al. 2016; Taufour et al. 2024) – radiation (ecRad; Hogan and Bozzo 2018) using (i) information from the microphysical scheme (effective radius and crystal shape) rather than empirical values or values from parameterizations in the radiation scheme, and (ii) consistent assumptions in both schemes. For a given crystal shape, the relationships between mass, velocity, area, and diameter are generally based on empirical estimates in microphysical schemes, and derive from theoretical considerations of ideally shaped crystals in radiative transfer schemes. Given that calculating the optical properties of ice crystal shapes is complex, our original approach is to rely on the high-resolution dimensional and spectral database of the optical properties of nine ice crystal shapes developed by Yang et al. (2013). Thus, the crystal shape characteristics from the Yang et al. database are implemented in LIMA. For each shape, interpolation tables are generated from the Yang et al. database and are used in ecRad to calculate the optical properties from the effective radius and ice content of each shape in each cloud cell.

Specifically, four new prognostic variables representing the concentration in number of each crystal form are introduced into Meso-NH. Each crystal shape is associated with mass-diameter and velocity-diameter relationships, as well as a capacitance. The primary production of ice crystals allows the primary forms of ice crystals to be formed. The concentration of each crystal shape then evolves through the various microphysical processes already present in LIMA. Crystals with primary forms can change shape if the temperature conditions no longer correspond to the nominal growth conditions (Chen and Lamb 1994).

8.4 Warm-phase collection/coalescence processes and rain initiation

Cloud droplets and rain drops evolution by coalescence processes is described by the equation:

$$\frac{\partial n(x,t)}{\partial t} = \frac{1}{2}\int_0^x K(y,x-y)n(y,t)n(x-y,t)dy - n(x,t)\int_0^\infty K(x,y)n(y,t)dy \tag{8.147}$$

where $n(x,t)$ is the number concentration of drops with a volume x (m^{-3}), and $K(x,y)$ (m^3 s^{-1}) is the "collection kernel" of a drop with volume x by a drop with volume y, and includes the stochastic aspect of collection. The first term of the coalescence equation represents the creation of drops with a volume x from two drops with volumes y and $x-y$. The second term represents the loss of volume x drops by coalescence with a drop of volume y, to form a drop with volume $x+y$.

The coalescence equation treats the droplets and drops populations as a whole. However, following Cohard and Pinty (2000a), assuming that there is little overlap between the cloud droplets (mostly with a diameter $D_c < 82$ μm) and rain drops (mostly with a diameter $D_r > 82$ μm)), we can split this equation into distinct processes:

- The auto-collection of cloud droplets
- The auto-collection of rain drops
- The accretion of cloud droplets by rain drops

When only cloud droplets are present (before rain is initiated), the auto-collection of cloud droplets is the only active process, and it is necessary to treat separately the autoconversion of cloud droplets into rain drops to represent the formation of the first small rain drops (from 90 to 200 μm). The autoconversion parameterization follows Berry and Reinhardt (1974). This parameterization includes all the coalescence processes during the initial evolution of the cloud droplets population into a bimodal population with both cloud droplets and rain drops. The coalescence parameterization presented hereafter is therefore only activated after rain has been created with a mixing ratio r_r at least equal to $1.2L$ (Sect. 8.4.1), or when the mean volume diameter of rain is larger than r_H from Berry and Reinhardt (1974) (Sect. 8.4.1). In *lima_warm_coal.f90*, the GENABLE_ACCR_SCBU variable is used to check where coalescence processes are activated:

```
GENABLE_ACCR_SCBU(:) =
           ZRRT(:)>1.2*ZZW2(:)/ZRHODREF(:)
           .OR.
           ZZW4(:)>=MAX(XACCR2,XACCR3/(XACCR4/ZLBDC(:)-XACCR5))
```

where ZZW2= L (kg m^{-3}), ZZW4= $\bar{D}_r$ the mean volume diameter of rain drops, XACCR2= 5 μm, and XACCR3/(XACCR4/ZLBDC(:)-XACCR5)= D_h corresponds to r_H from Berry and Reinhardt (1974).

"Collection kernels" in LIMA

In LIMA, the "collection kernels" from Long (1974) are used:

$$K(x,y) = \begin{cases} K_2(x^2+y^2) & \text{if } D_r \leq 100\ \mu\text{m} \\ K_1(x+y) & \text{if } D_r > 100\ \mu\text{m} \end{cases} \tag{8.148}$$

with $K_2 = 9.44\ 10^9$ cm^{-3} s^{-1} and $K_1 = 5.78\ 10^3$ s^{-1}, x and y the drops volumes in cm^3, and with K in cm^3 s^{-1}. In LIMA, pfor drops with diameters D_1 and D_2 (m), and with K in m^3 s^{-1}, we get:

$$K(D_1, D_2) = \begin{cases} K_2(D_1^6 + D_2^6) & \text{if } D_1 \leq 100\ \mu\text{m} \\ K_1(D_1^3 + D_2^3) & \text{if } D_1 > 100\ \mu\text{m} \end{cases} \tag{8.149}$$

with $K_2 = 2.59\ 10^{15}$ m^{-3} s^{-1} and $K_1 = 3.03\ 10^3$ s^{-1}.

8.4.1 Autoconversion of cloud droplets in rain drops

The autoconversion of cloud droplets into raindrops is parameterized after Berry and Reinhardt (1974) and Cohard and Pinty (2000a) (see also Gilmore and Straka 2008). Berry and Reinhardt (1974) simulated the evolution by collection of a unimodal population of cloud droplets into a bimodal distribution of cloud droplets and raindrops. They repeated this study for different initial distribution spreads and mean radii and proposed simple expressions to compute the rain formation rate. Using their notations, a raindrop mixing ratio L_2' develops in a time T_2 (note that there is a mistake in their Eq. (16) for T_2, which is correctly expressed in their Fig. 8). By converting their expressions into LIMA units, the autoconversion rate is obtained as L/τ, where L (kg m^{-3}) and τ (s) depend on the mean-volume droplet diameter $\bar{D}_\text{c}$ (m), the corresponding standard deviation σ_c (m), and the cloud droplet mixing ratio r_c (kg kg^{-1}). The 10^{20} and 10^6 factors, and the presence of ρ_d, account for unit conversion. The $1/16$ and 0.5 factors account for the change between particle radius in Berry and Reinhardt (1974) and diameter in LIMA.

$$L = 2.7\ 10^{-2} \left(\frac{1}{16} 10^{20} \sigma_\text{c}^3 \bar{D}_\text{c} - 0.4 \right) \rho_d r_\text{c} \tag{8.150}$$

$$\tau = 3.7 \left(0.5 \times 10^6 \sigma_\text{c} - 7.5\right)^{-1} \frac{1}{\rho_d\, r_\text{c}} \tag{8.151}$$

As explained in Cohard and Pinty (2000a), the raindrop number concentration production rate proposed by Berry and Reinhardt (1974) is kept only for the initial formation of small raindrops. In LIMA, when the raindrop mean-volume radius exceeds the hump radius defined by Berry and Reinhardt (1974), it is assumed that the autoconversion does not modify the mean-volume diameter, and therefore the raindrop number concentration production rate (kg^{-1} s^{-1}) is reduced to $N_\text{r}/r_\text{r} \times L/\tau$.

Implementation in LIMA
The computation of $\bar{D}_\text{c}$ and σ_c is presented in sect. 8.1.3. In *lima_warm_coal.f90*:

$$\text{ZZW2} = L \tag{8.152}$$

$$\text{ZZW3} = \frac{L}{\tau} \frac{1}{\rho_d} \tag{8.153}$$

Division by ρ_d in ZZW3 accounts for units change, because L is in kg m^{-3} instead of kg kg^{-1}. Thus ZZW3 is the mass mixing ratio of cloud droplets transformed into raindrops. Then:

$$\text{ZZW1} = \min\left(\frac{1}{80\mu\text{m}}; \frac{1}{D_\text{h}}; \frac{1}{\bar{D}_\text{r}} \right) \tag{8.154}$$

Where D_{h} (m) corresponds to r_{H} (cm) from Berry and Reinhardt (1974) (there is a mistake in their Eq. (20) for r_{H}, which is correctly expressed in their Fig. 8):

$$D_{\mathrm{h}} = 1.26\ 10^{-3}\left(0.5 \times 10^{6}\sigma_{\mathrm{c}} - 3.5\right)^{-1} \tag{8.155}$$

The diameter computed by ZZW1 is then used with the mass mixing ratio ZZW3 to predict the number of rain drops formed.

8.4.2 Accretion

When the accretion of cloud droplets by rain drops is considered indenpendantly from the auto-collection processes, and we want to determine the mass and number of cloud droplets collected by this process, only the second term from the equation collection is used.
The choice of $K(D_1, D_2)$ is based on the rain drops mean volume diameter ($\bar{D}_r$ = ZZW4 in *lima_warm_coal.f90*). The equations governing the evolution of r_c, r_r and N_c are presented in Cohard and Pinty (2000a). The number of cloud droplets captured (-CCACCR) for $D_r > 100$ μm is presented here as an example, where M_r and M_c are the moments of the rain drops and cloud droplets size distributions, and ρ_d arises from the units conversion (kg^{-1} to m^{-3}):

$$\begin{aligned}
-CCACCR &= \int_0^\infty \left.\frac{\partial n_c(D_2)}{\partial t}\right|_{ACC} dD_2 && (8.156)\\
&= \rho_d \int_0^\infty n_c(D_2)\left(\int_0^\infty K(D_1, D_2) n_r(D_1) dD_1\right) dD_2 && (8.157)\\
&= \rho_d \int_0^\infty n_c(D_2)\left(\int_0^\infty \left(K_1 D_1^3 n_r(D_1) + K_1 D_2^3 n_r(D_1)\right) dD_1\right) dD_2 && (8.158)\\
&= \rho_d K_1 \int_0^\infty \left(n_c(D_2)\left(N_r M_r(3) + D_2^3 N_r\right)\right) dD_2 && (8.159)\\
&= \rho_d K_1 N_r N_c \left(M_r(3) + M_c(3)\right) && (8.160)\\
&= \rho_d K_1 N_r N_c \left(\frac{1}{\lambda_r^3}\frac{\Gamma(\nu_r + 3/\alpha_r)}{\Gamma(\nu_r)} + \frac{1}{\lambda_c^3}\frac{\Gamma(\nu_c + 3/\alpha_c)}{\Gamma(\nu_c)}\right) && (8.161)
\end{aligned}$$

We get the mass of collected cloud droplets similarly:

$$\begin{aligned}
-RCACCR &= \int_0^\infty \frac{\pi}{6} D_2^3 \rho_w \left.\frac{\partial n_c(D_2)}{\partial t}\right|_{ACC} dD_2 && (8.162)\\
&= \frac{\pi}{6}\rho_w \rho_d \int_0^\infty D_2^3\, n_c(D_2)\left(\int_0^\infty K(D_1, D_2) n_r(D_1) dD_1\right) dD_2 && (8.163)\\
&= \frac{\pi}{6}\rho_w \rho_d K_1 N_c N_r \left(\frac{1}{\lambda_c^6}\frac{\Gamma(\nu_c + 6/\alpha_c)}{\Gamma(\nu_c)} + \frac{1}{\lambda_c^3}\frac{\Gamma(\nu_c + 3/\alpha_c)}{\Gamma(\nu_c)}\frac{1}{\lambda_r^3}\frac{\Gamma(\nu_r + 3/\alpha_r)}{\Gamma(\nu_r)}\right) && (8.164)
\end{aligned}$$

And for $D_r \leq 100\ \mu m$:

$$-CCACCR = \rho_d K_2 N_r N_c \left(\frac{1}{\lambda_r^6}\frac{\Gamma(\nu_r + 6/\alpha_r)}{\Gamma(\nu_r)} + \frac{1}{\lambda_c^6}\frac{\Gamma(\nu_c + 6/\alpha_c)}{\Gamma(\nu_c)}\right) \tag{8.165}$$

$$-RCACCR = \frac{\pi}{6}\rho_w \rho_d K_2 N_c N_r \left(\frac{1}{\lambda_c^9}\frac{\Gamma(\nu_c + 9/\alpha_c)}{\Gamma(\nu_c)} + \frac{1}{\lambda_c^3}\frac{\Gamma(\nu_c + 3/\alpha_c)}{\Gamma(\nu_c)}\frac{1}{\lambda_r^6}\frac{\Gamma(\nu_r + 6/\alpha_r)}{\Gamma(\nu_r)}\right) \tag{8.166}$$

8.4.3 Auto-collections in LIMA

In LIMA, the onset of rain by cloud droplets coalescence is parameterized by the autoconversion. The cloud droplets auto-collection is therefore supposed to produce only cloud droplets. It is also clear that the rain drops auto-collection has no impact on the cloud droplets. In both cases, the hydrometeors mass is conserved, so the RCSCOC and RRSCOR term are zero (see the demonstration in appendix A of Cohard and Pinty 2000a). The coalescence equation thus becomes (appendix A of Cohard and Pinty 2000a):

$$-CCSCOC = \frac{1}{2}\int_0^\infty n(x,t)\left(\int_0^\infty K(y,x)n(y,t)dy\right)dx \tag{8.167}$$

Auto-collection of cloud droplets

The diameter of cloud droplets is always smaller than 82 μm, so we always use $K(x,y) = K_2(x^2 + y^2)$. As for the accretion above, the evolution of the cloud droplets number concentration by auto-collection is:

$$-CCSCOC = \rho_d K_2 N_c^2 \frac{1}{\lambda_c^6}\frac{\Gamma(\nu_c + 6/\alpha_c)}{\Gamma(\nu_c)} \tag{8.168}$$

Auto-collection of rain drops

For rain drops, we have one equation if $D_r \leq 100$ μm:

$$-CRSCOR = \rho_d K_2 N_r^2 \frac{1}{\lambda_r^6}\frac{\Gamma(\nu_r + 6/\alpha_r)}{\Gamma(\nu_r)} \tag{8.169}$$

and one if $D_r > 100$ μm:

$$-CRSCOR = \rho_d K_1 N_r^2 \frac{1}{\lambda_r^3}\frac{\Gamma(\nu_r + 3/\alpha_r)}{\Gamma(\nu_r)} \tag{8.170}$$

8.4.4 Rain drops break-up

Collisional break-up of rain drops

The “collisional breakup” is an important process impacting the large rain drops number concentration. It is implemented in LIMA through the definition of an auto-collection efficiency E_c (as introduced by Ziegler 1985; Verlinde et al. 1990), which limits the growth of large rain drops by this process. E_c in LIMA is inspired by Verlinde and Cotton (1993, their Eq. (4.22))

$$E_c = \begin{cases} 1 & \text{if } \bar{D}_r < 600\ \mu\text{m} \\ \exp\left(-2.5\ 10^3(\bar{D}_r - 6\ 10^{-4})\right) & \text{if } 600\ \mu\text{m} \leq \bar{D}_r < 2000\ \mu\text{m} \\ 0 & \text{if } \bar{D}_r \geq 2000\ \mu\text{m} \end{cases} \tag{8.171}$$

“Spontaneous break-up” of rain in LIMA

A “spontaneous break-up” process, independant from the rain drops collisions, is introduced to limit the rain drop size. As explained by Cohard and Pinty (2000b), this mechanism is necessary to prevent the creation of unrealistically huge rain drops which can reslut from the differential

evolution of the mass mixing ratio r_r (kg kg^{-1}) and the number concentration N_r (# kg^{-1}) (e.g. by transport and sedimentation processes).
The "spontaneous break-up" is parameterized as a function of the mean volume diameter $\bar{D}_r$. When $\bar{D}_r$ is larger than 5000 μm, N_r is corrected to bring $\bar{D}_r$ back to the maximum value $D_{max} = 5000$ μm:

$$N_{r,new} = N_{r,old} \left(\frac{\bar{D}_r}{D_{max}} \right)^3 \tag{8.172}$$

When $\bar{D}_r$ is between 3000 and 5000 μm, N_r is corrected to bring $\bar{D}_r$ back to a value computed as follows, and limited to the maximum value of 5000 μm:

$$\left(\frac{D_{old}}{D_{new}} \right)^3 = 1 + \left(\left(\frac{5\ 10^{-3}}{4\ 10^{-3}} \right)^3 - 1 \right) \left(\frac{D_{old} - 3\ 10^{-3}}{5\ 10^{-3} - 3\ 10^{-3}} \right)^2 \tag{8.173}$$

8.5 Water vapor exchanges

8.5.1 Growth of a liquid / ice particle by vapor condensation / deposition

The parameterization of condensation / evaporation and deposition / sublimation processes in LIMA is based upon the equations governing the growth of a single water drop or ice crystal as presented in Pruppacher and Klett (1997). Their Eq. (13-28) expresses the rate of change of the radius of a stationary liquid drop. Neglecting the small curvature and solute terms (that is setting $y = 0$), and adding a ventilation factor $\bar{f}$ to account for the movement of the liquid drop in the air [their Eq. (13-53)], we get (using the particle diameter D instead of the radius):

$$D \frac{\mathrm{d}D}{\mathrm{d}t} = 4 S_w \overline{f} \rho_w^{-1} A_w^{-1} \tag{8.174}$$

where $S_w = \frac{r_v}{r_{sw}} - 1$ is the supersaturation over liquid water, ρ_w the density of liquid water, and A_w a thermodynamical function:

$$A_w = \frac{R_v T}{e_{sw} D_v} + \frac{L_v}{k_a T} \left(\frac{L_v}{R_v T} - 1 \right) \tag{8.175}$$

$$\approx \frac{R_v T}{e_{sw} D_v} + \frac{L_v^2}{k_a R_v T^2} \tag{8.176}$$

We have a similar equation for ice particles:

$$D \frac{\mathrm{d}D}{\mathrm{d}t} = 4 S_i \overline{f} \rho_i^{-1} A_i^{-1} \tag{8.177}$$

with

$$A_i = \frac{R_v T}{e_{si} D_v} + \frac{L_s}{k_a T} \left(\frac{L_s}{R_v T} - 1 \right) \tag{8.178}$$

$$\approx \frac{R_v T}{e_{si} D_v} + \frac{L_s^2}{k_a R_v T^2} \tag{8.179}$$

These equations can also be expressed as the rate of change of a drop / crystal mass:

$$\frac{\mathrm{d}m}{\mathrm{d}t} = 4\pi \, \frac{1}{2} \, D \, S_w \, A_w^{-1} \, \bar{f} \tag{8.180}$$

for liquid drops, and as follows for ice particles [their Eqs. (13-75), (13-76), (13-91)]:

$$\frac{\mathrm{d}m}{\mathrm{d}t} = 4\pi\, C_1\, D\, S_i\, A_i^{-1}\, \bar{f} \tag{8.181}$$

In the previous equations, we use the following approximations for the diffusivity of water vapor in air D_v and the heat conductivity of air k_a:

$$D_v[\mathrm{m}^2\ \mathrm{s}^{-1}] = 0.211\ 10^{-4} \left(\frac{T}{T_0}\right)^{1.94} \frac{P_0}{P} \quad \text{(Pruppacher and Klett 1997, their Eq. (13-3))} \tag{8.182}$$

$$k_a[\mathrm{kg\ m\ s}^{-3}\ \mathrm{K}^{-1}] = 2.38\ 10^{-2} + 0.071\ 10^{-3}(T - T_0) \quad \text{(Pruppacher and Klett 1997, their Eq. (13-18a))} \tag{8.183}$$

$$\tag{8.184}$$

And the ventilation coefficient $\bar{f}$ is parameterized as a function of $\chi = N_{Sc,v}^{1/3} N_{Re}^{1/2}$, where $N_{Sc,v} \approx 0.63$ is the Schmidt number for water vapor and N_{Re} the Reynolds number of the flow around a particle of diameter D:

$$\bar{f} \approx \bar{f}_0 + \bar{f}_1\chi + \bar{f}_2\chi^2 \tag{8.185}$$

with

$$N_{Re} = \frac{v(D)D}{\nu(T)} = \frac{v(D)D\rho_d}{\eta(T)} \tag{8.186}$$

where $\nu(T)$ is the kinematic viscosity of air, and $\eta(T) = \rho_d\nu(T)$ the dynamic viscosity of air can be approximated by (Pruppacher and Klett 1997, their Eq. (10-141), converting with $1\ poise = 0.1$ Pa s):

$$\eta(T)[Pa\ s] = 1.718\ 10^{-5} + 0.0049\ 10^{-5}(T - T_0) \tag{8.187}$$

They propose various sets of values for $\bar{f}_0$, $\bar{f}_1$ and $\bar{f}_2$ depending on the particle type (liquid/ice) and size [their Eqs. (13-60), (13-61), (13-88) and (13-89)]:

$$\left.\begin{array}{l}\bar{f}_0 = 1\\ \bar{f}_1 = 0\\ \bar{f}_2 = 0.108\end{array}\right\} \text{for the condensation of vapor on cloud droplets} \tag{8.188}$$

$$\left.\begin{array}{l}\bar{f}_0 = 0.78\\ \bar{f}_1 = 0.308\\ \bar{f}_2 = 0\end{array}\right\} \text{for the evaporation of rain drops} \tag{8.189}$$

$$\left.\begin{array}{l}\bar{f}_0 = 1\\ \bar{f}_1 = 0\\ \bar{f}_2 = 0.14\end{array}\right\} \begin{array}{l}\text{for the deposition of vapor on ice crystals}\\ \text{and the Bergeron-Findeisen process}\end{array} \tag{8.190}$$

$$\left.\begin{array}{l}\bar{f}_0 = 0.86\\ \bar{f}_1 = 0.28\\ \bar{f}_2 = 0\end{array}\right\} \begin{array}{l}\text{for the deposition of vapor on snow, graupel and hail}\\ \text{and the growth of ice crystals into snow}\end{array} \tag{8.191}$$

$$\tag{8.192}$$

Writing

$$c' = N_{Sc,v}^{1/3} \left(\frac{\rho_0}{\rho_d}\right)^{0.2} \left(\frac{c\rho_d}{\eta}\right)^{1/2} \tag{8.193}$$

and using the terminal fall speed-diameter relationship, we get the mass mixing ratio rate of change for a given hydrometeor type from the integration of Eqs. (8.180) and (8.181) (note that $c'/\sqrt{c}$ does not depend on the hydrometeor):

$$
\begin{aligned}
\frac{\mathrm{d}r}{\mathrm{d}t} &= \int_0^\infty \frac{\mathrm{d}m}{\mathrm{d}t}(D)n(D)\mathrm{d}D && (8.194)\\
&= \int_0^\infty 4\pi\, C_1\, D\, S_i\, A_i^{-1}\left(\bar{f}_0 + \bar{f}_1 N_{Sc,v}^{1/3}\left(\frac{v(D)D\rho_d}{\eta}\right)^{1/2} + \bar{f}_2 N_{Sc,v}^{2/3}\frac{v(D)D\rho_d}{\eta}\right)n(D)\mathrm{d}D && (8.195)\\
&= 4\pi\, C_1\, S_i\, A_i^{-1}\int_0^\infty \left(\bar{f}_0 D + \bar{f}_1 c' D^{1+\frac{d+1}{2}} + \bar{f}_2 c'^2 D^{1+d+1}\right)n(D)\mathrm{d}D && (8.196)\\
&= N\, 4\pi\, C_1\, S_i\, A_i^{-1}\left(\bar{f}_0 M(1) + \bar{f}_1 c' M(\frac{d+3}{2}) + \bar{f}_2 c'^2 M(d+2)\right) && (8.197)
\end{aligned}
$$

where $M(p)$ is the p-order moment of the particle size distribution, and the same equation for liquid drops.

8.5.2 Rain evaporation

We get the change in mass from Eq. (8.174) and:

$$
\frac{\mathrm{d}m}{\mathrm{d}t} = \frac{\pi}{6}\rho_w 3D^2\frac{\mathrm{d}D}{\mathrm{d}t} \qquad (8.198)
$$

The mass evolution of the rain drops population is therefore:

$$
\begin{aligned}
RREVAV &= \int_0^\infty \frac{\pi}{6}\rho_w 3D^2\frac{\mathrm{d}D}{\mathrm{d}t}n(D)dD && (8.199)\\
&= \frac{\pi}{2}\rho_w\int_0^\infty D^2\frac{4S_w\bar{f}\rho_w^{-1}A_w^{-1}}{D}n(D)dD && (8.200)\\
&= 2\pi\rho_w S_w\rho_w^{-1}A_w^{-1}\int_0^\infty D\bar{f}n(D)dD && (8.201)\\
&= 2\pi\rho_w S_w\rho_w^{-1}A_w^{-1}\int_0^\infty \left(\bar{f}_0 D + \bar{f}_1 D\left(\frac{\rho_0}{\rho_a}\right)^{0.2}\left(\frac{c}{\nu_{cin}}\right)^{0.5}D^{\frac{d+1}{2}}\right)n(D)dD && (8.202)\\
&= 2\pi\rho_w S_w\rho_w^{-1}A_w^{-1}N_r\left(\bar{f}_0\frac{1}{\lambda}\frac{\Gamma(\nu+1/\alpha)}{\Gamma(\nu)} + \bar{f}_1\left(\frac{\rho_0}{\rho_a}\right)^{0.2}\left(\frac{c}{\nu_{cin}}\right)^{0.5}\frac{1}{\lambda^{\frac{d+3}{2}}}\frac{\Gamma(\nu+(d+3)/2\alpha)}{\Gamma(\nu)}\right) && (8.203)\\
& && (8.204)
\end{aligned}
$$

In *lima_warm_evap.f90*, computations are led from the mass mixing ratio r_r instead of the number concentration N_r, using:

$$
N_r = \frac{r\lambda^3}{a}\frac{\Gamma(\nu)}{\Gamma(\nu+3/\alpha)} \qquad (8.205)
$$

with $a = \rho_w \pi/6$, which gives:

$$RREVAV = 12 S_w \rho_w^{-1} A_w^{-1} r_r \frac{\Gamma(\nu)}{\Gamma(\nu+3/\alpha)} \left(\bar{f}_0 \lambda^2 \frac{\Gamma(\nu+1/\alpha)}{\Gamma(\nu)} + \bar{f}_1 \left(\frac{\rho_0}{\rho_a}\right)^{0.2} \left(\frac{c}{\nu_{cin}}\right)^{0.5} \lambda^{3-\frac{d+3}{2}} \frac{\Gamma(\nu+(d+3)/2\alpha)}{\Gamma(\nu)} \right) \tag{8.206}$$

The evaporation of rain drops does not impact their number concentration, except in the case when the mean volume diameter $\bar{D}_r$ becomes lower than 82 μm, and then all the rain is transformed into cloud droplets.

8.5.3 Deposition of water vapor on ice

In LIMA, the following processes are represented:

- Deposition of vapor on snow / sublimation of snow
- Deposition of vapor on graupel / sublimation of graupel
- Conversion of pristine ice into snow
- Conversion of snow into pristine ice
- Bergeron-Findeisen process

The depostion of vapor on ice crystals is treated during the adjustment step. The deposition of vapour on hail is currently neglected.
For 2-moment species (only pristine ice crystals currently), the deposition of water vapour (or the sublimation) does not affect the number concentration, except in the special cases of ice crystals growing into snowflakes (this process is described hereafter) and removing of crystals by sublimation.

Deposition on snow

In *ini_lima_cold_mixed.f90*, the following variables are initialized:

$$\mathrm{XSCFAC} = N_{sc,v}^{1/3} \rho_0^{0.2} \tag{8.207}$$

$$\mathrm{X0DEPS} = 4\pi\, C\, C_1\, \bar{f}_0 \frac{\Gamma(\nu+1/\alpha)}{\Gamma(\nu)} \tag{8.208}$$

$$\mathrm{XEX0DEPS} = x - 1 \tag{8.209}$$

$$\mathrm{X1DEPS} = 4\pi\, C\, C_1\, \bar{f}_1 \sqrt{c} \frac{\Gamma(\nu+(d+3)/2\alpha)}{\Gamma(\nu)} \tag{8.210}$$

$$\mathrm{XEX1DEPS} = x - \frac{d+3}{2} \tag{8.211}$$

(8.212)

In *lima_cold_slow_processes.f90*, the following computations are conducted:

$$\mathrm{ZSSI} = S_i \tag{8.213}$$

$$\mathrm{ZKA} = k_a \tag{8.214}$$

$$\mathrm{ZDV} = D_v \tag{8.215}$$

$$\mathrm{ZAI} = A_i \tag{8.216}$$

$$\mathrm{ZCJ} = c'/\sqrt{c} \tag{8.217}$$

$$\mathrm{ZZW} = \dot{r}_s = \frac{1}{\rho_d}\frac{\mathrm{ZSSI}}{\mathrm{ZAI}}[\mathrm{X0DEPS}\ \lambda^{\mathrm{XEX0DEPS}} + \mathrm{X1DEPS}\ \mathrm{ZCJ}\ \lambda^{\mathrm{XEX1DEPS}}] \tag{8.218}$$

$$= \frac{1}{\rho_d} S_i\ A_i^{-1}\left[4\pi C C_1 \bar{f}_0 \frac{\Gamma(\nu+1/\alpha)}{\Gamma(\nu)}\lambda^{x-1} + 4\pi C C_1 \bar{f}_1 \frac{c'}{\sqrt{c}}\sqrt{c}\frac{\Gamma(\nu+(d+3)/2\alpha)}{\Gamma(\nu)}\lambda^{x-\frac{d+3}{2}}\right] \tag{8.219}$$

$$= \frac{C\lambda^x}{\rho_d}\ 4\pi C_1\ S_i\ A_i^{-1}\left[\bar{f}_0 M(1) + \bar{f}_1 c' M(\frac{d+3}{2})\right] \tag{8.220}$$

which corresponds to Eq. (8.197) (for snow, $\bar{f}_2 = 0$). The next line computes

$$\min(r_v, \dot{r}_s)\ (0.5 + 0.5\ \mathrm{sign}(\dot{r}_s)) - \min(r_s, |\dot{r}_s|)\ (0.5 - 0.5\ \mathrm{sign}(\dot{r}_s)) \tag{8.221}$$

This limits the deposition rate $\dot{r}_s$ to the available water vapour source r_v when deposition occurs ($\dot{r}_s > 0$), and the sublimation rate to the available snow source r_s when sublimation occurs ($\dot{r}_s < 0$).

Deposition on graupel

The deposition of vapor on graupel is similar to the deposition on snow.

8.5.4 Ice → snow conversion

Knowing both N_i (kg^{-1}) and r_i (kg kg^{-1}), the pristine ice to snow conversion by deposition of water vapor can be refined, following the parameterization proposed by Harrington et al. (1995). The implementation of this process in LIMA is based on Eqs. (19) and (20) from Harrington et al. (1995), describing the evolution of ice crystals number concentration and mass mixing ratio (expressed in m^{-3} and kg m^{-3}):

$$N_{i->s} = \left.\frac{dD}{dt}\right|_{D=D_b} n(D_b) \tag{8.222}$$

and

$$\dot{r}_s = \frac{1}{\rho_d} m(D_b) \left.\frac{dD}{dt}\right|_{D=D_b} n(D_b)\ +\ \frac{1}{\rho_d}\int_{D_b}^{\infty}\frac{dm}{dt} n(D) dD \tag{8.223}$$

Equation (8.223) [their Eq. (20)] accounts for both the conversion into snow of pristine ice crystals growing over a threshold diameter D_b (first term), and the depositional growth of crystals already larger than D_b (second term). In LIMA, the deposition of vapor on ice crystals is treated during the adjustment step, and deposition on snow is handled separately, so the second term is ignored, which leads to the simplified equation system (removing ρ_d because units in LIMA for N_i and r_i are kg^{-1} and kg kg^{-1}):

$$N_{i->s} = \left.\frac{dD}{dt}\right|_{D=D_b} n(D_b) \tag{8.224}$$

$$\dot{r}_s = m(D_b)\left.\frac{dD}{dt}\right|_{D=D_b} n(D_b) \tag{8.225}$$

In LIMA, the threshold diameter is fixed at $D_b = 125\ \mu$m.
Using the mass-diameter relationship $m = aD^b$, we have:

$$\frac{dD}{dt} = \frac{dD}{dm}\frac{dm}{dt} = \frac{1}{\alpha\beta D^{\beta-1}}\frac{dm}{dt} \tag{8.226}$$

Using Eq. (8.181) $\mathrm{d}m/\mathrm{d}t$, we get:

$$N_{i->s} = \frac{1}{\alpha\beta D_b^{\beta-1}} 4\pi\ C_1\ S_i\ A_i^{-1}\ (\bar{f}_0 D_b + \bar{f}_1 c' D_b^{1+\frac{d+1}{2}}) n(D_b) \tag{8.227}$$

$$= \frac{4\pi}{\alpha\beta}\ C_1\ S_i\ A_i^{-1}\ (\bar{f}_0 D_b^{2-\beta} + \bar{f}_1 c' D_b^{1+\frac{d+1}{2}+1-\beta}) n(D_b) \tag{8.228}$$

$$\dot{r}_s = m(D_b) N_{i->s} \tag{8.229}$$

$$= \frac{4\pi}{\beta}\ C_1\ S_i\ A_i^{-1}\ (\bar{f}_0 D_b^2 + \bar{f}_1 c' D_b^{1+\frac{d+1}{2}+1}) n(D_b) \tag{8.230}$$

with

$$n(D_b) = N_i \frac{\alpha_i}{\Gamma(\nu_i)} (\lambda_i D_b)^{\alpha_i \nu_i} D_b^{-1} e^{-(\lambda_i D_b)^{\alpha_i}} \tag{8.231}$$

Implementation in LIMA
In *ini_lima_cold_mixed.f90*, the following variables are initialized:

$$\mathrm{XSCFAC} = N_{sc,v}^{1/3} \rho_0^{0.2} \tag{8.232}$$

$$\mathrm{XDICNVS\_LIM} = D_b = 125\ \mu m \tag{8.233}$$

$$\mathrm{XC0DEPIS} = \frac{4\pi}{\alpha\beta}\ C_1\ \bar{f}_0\ \frac{\alpha_i}{\Gamma(\nu_i)}\ D_b^{1-\beta} \tag{8.234}$$

$$\mathrm{XC1DEPIS} = \frac{4\pi}{\alpha\beta}\ C_1\ \bar{f}_1\ \sqrt{c}\ \frac{\alpha_i}{\Gamma(\nu_i)}\ D_b^{1-\beta+\frac{d+1}{2}} \tag{8.235}$$

$$\mathrm{XR0DEPIS} = \mathrm{XC0DEPIS}\ \alpha D_b^{\beta} \tag{8.236}$$

$$= \frac{4\pi}{\beta}\ C_1\ \bar{f}_0\ \frac{\alpha_i}{\Gamma(\nu_i)}\ D_b \tag{8.237}$$

$$\mathrm{XR1DEPIS} = \mathrm{XC1DEPIS}\ \alpha D_b^{\beta} \tag{8.238}$$

$$= \frac{4\pi}{\beta}\ C_1\ \bar{f}_1\ \sqrt{c}\ \frac{\alpha_i}{\Gamma(\nu_i)}\ D_b^{1+\frac{d+1}{2}} \tag{8.239}$$

$$\tag{8.240}$$

In *lima_cold_slow_processes.f90*, the following computations are conducted:

$$\mathrm{ZSSI} = S_i \tag{8.241}$$

$$\mathrm{ZKA} = k_a \tag{8.242}$$

$$\mathrm{ZDV} = D_v \tag{8.243}$$

$$\mathrm{ZAI} = A_i \tag{8.244}$$

$$\mathrm{ZCJ} = c'/\sqrt{c} \tag{8.245}$$

$$\mathrm{ZZX} = S_i \; A_i^{-1} \; N_i (\lambda_i D_b)^{\alpha_i \nu_i} e^{-(\lambda_i D_b)^{\alpha_i}} \tag{8.246}$$

$$= S_i \; A_i^{-1} \; n(D_b) \; \frac{\Gamma(\nu_i)}{\alpha_i} D_b \tag{8.247}$$

$$\mathrm{ZZW} = \dot{r}_s = \mathrm{ZZX} \; [\mathrm{XR0DEPIS} + \mathrm{XR1DEPIS} * \mathrm{ZCJ}] \tag{8.248}$$

$$= S_i \; A_i^{-1} n(D_b) \frac{\Gamma(\nu_i)}{\alpha_i} D_b \left[\frac{4\pi}{\beta} C_1 \frac{\alpha_i}{\Gamma(\nu_i)} (\bar{f}_0 \; D_b + \bar{f}_1 \sqrt{c} D_b^{1+\frac{d+1}{2}} \frac{c'}{\sqrt{c}}) \right] \tag{8.249}$$

$$= \frac{4\pi}{\beta} \; C_1 \; S_i \; A_i^{-1} (\bar{f}_0 \; D_b^2 + \bar{f}_1 c' D_b^{2+\frac{d+1}{2}}) n(D_b) \tag{8.250}$$

Which corresponds to Eq. (8.230). Computations for $N_{i->s}$ are similar.

8.5.5 Snow → ice conversion

When the air is undersaturated with respect to ice, the same computations are led to determine the mass of snow converted into ice by sublimation, based on the same threshold diameter $D_b = 125 \; \mu$m.

8.5.6 Bergeron-Findeisen process

Since the vapor saturation pressure over ice is always lower than that over liquid water ($e_{si} < e_{sw}$), there is a systematic evaporation of cloud droplets and deposition on the ice crystals. The present parameterization assumes that the mass transfer rate is determined by the vapor deposition rate on ice crystals, and that it is equivalent to the droplet evaporation rate, so that the process is neutral for the ambient water vapor. The computation is therefore based on Eq. (8.197).

In *ini_lima_cold_mixed.f90*, the following variables are initialized:

$$\mathrm{XSCFAC} = N_{sc,v}^{1/3} \rho_0^{0.2} \tag{8.251}$$

$$\mathrm{X0DEPI} = 4\pi \; C_1 \; \bar{f}_0 \; \frac{\Gamma(\nu + 1/\alpha)}{\Gamma(\nu)} \tag{8.252}$$

$$\mathrm{X2DEPI} = 4\pi \; C_1 \; \bar{f}_2 \; c \; \frac{\Gamma(\nu + (d+2)/\alpha)}{\Gamma(\nu)} \tag{8.253}$$

$$\tag{8.254}$$

In *lima_mixed_slow_processes.f90*, the following computations are conducted:

$$\mathrm{ZZW} = S_i \tag{8.255}$$

$$\mathrm{ZAI} = A_i \quad \text{(in the routine arguments)} \tag{8.256}$$

$$\mathrm{ZCJ} = c'/\sqrt{c} \quad \text{(in the routine arguments)} \tag{8.257}$$

$$\mathrm{ZZW} = \dot{r}_i = \frac{\mathrm{ZZW}}{\mathrm{ZAI}}\mathrm{ZCIT}\left[\mathrm{X0DEPI}\,\frac{1}{\lambda} + \mathrm{X2DEPI}\;\mathrm{ZCJ}^2\,\frac{1}{\lambda^{d+2}}\right] \tag{8.258}$$

$$= N_i 4\pi C_1 S_i\, A_i^{-1}\left[\bar{f}_0 M(1) + \bar{f}_2 c'^2 M(d+2)\right] \tag{8.259}$$

which corresponds to Eq. (8.197) (for pristine ice, $\bar{f}_1 = 0$).

8.5.7 Adjustment

The adjustment step updates the mass mixing ratios of pristine ice crystals and cloud droplets accounting for deposition/condensation or sublimation/evaporation depending on the saturation. LIMA does not allow supersaturations with respect to liquid water, but the saturatio with respect to ice can evolve freely depending on the explicit deposition of water vapour on ice crystals. Three cases are distinguished in LIMA:

- When only cloud droplets are present, an immediate adjustment to saturation with respect to liquid water is performed.
- When only ice crystals are present, the deposition rate is explicitely predicted if $S_i > 0$, and an implicit immediate adjustment to saturation is performed if $S_i < 0$.
- When both cloud droplets and ice crystals are present, we first perform an adjustment to liquid water saturation for cloud droplets, and then compute explicit mass transfer rates following the parameterization of Reisin et al. (1996, Section 2b4 and appendix B).

In contrast with all the other processes, which computations are based on the concentrations and mixing ratios from the previous timestep, the adjustment, performed at the end of the timestep integration, uses the concentration and mixing ratios rates obtained after adding all the microphysical processes sources. We will keep the same notations (e.g. r_v, T) for convenience.

Where $r_c > 0$ and $r_i = 0$

The implicit adjustment follows Langlois (1973), to reach saturated conditions with respect to liquid water, thereby changing the temperature as well due to evaporation/condensation. So we are looking for the temperature T' for which we have $F(T') = 0$ where F is the following function relating the temperature change to the water vapor mass mixing ratio change:

$$F(x) = (x - T) + \frac{L_v(x)}{c_{ph}}(r_{sw}(x) - r_v) \tag{8.260}$$

To find the zero of F, Langlois (1973) showed that the Newton-Raphson method can be used and no iterations are necessary, therefore:

$$T' = T - \frac{F(T)}{F'(T)}[1 + \frac{F(T)F''(T)}{2\,F'(T)^2}] \tag{8.261}$$

$$= T - \Delta_1\left(1 + \frac{1}{2}\Delta_1\Delta_2\right) \quad \text{with } \Delta_1 = \frac{F(T)}{F'(T)} \text{ et } \Delta 2 = \frac{F''(T)}{F'(T)} \tag{8.262}$$

The expressions for $r_{sw}(x)$ and $e_{sw}(x)$ are found in the therodynamics documentation, so we have:

$$e'_{sw}(x) = A(x)e_{sw}(x) \quad \text{with } A(x) = \frac{\beta_w}{x^2} - \frac{\gamma_w}{x} \tag{8.263}$$

$$r'_{sw}(x) = A(x)r_{sw}(x)(1 + \frac{M_d r_{sw}(x)}{M_v}) \tag{8.264}$$

Assuming that the variations of L_v are much smaller than those of r_{sw}, we get:

$$F'(x) = 1 + \frac{L_v(x)}{c_{ph}}r'_{sw}(x) \tag{8.265}$$

$$F''(x) = \frac{L_v(x)}{c_{ph}}r'_{sw}(x)\left[A(x) + \frac{A'(x)}{A(x)} + \frac{2M_d A(x) r_{sw}(x)}{M_v}\right] \tag{8.266}$$

$$A'(x) = -\frac{2\beta_w}{x^3} + \frac{\gamma_w}{x^2} \tag{8.267}$$

and then

$$\Delta_1 = \frac{L_v(T)}{c_{ph}}\frac{(r_{sw}(T) - r_v)}{1 + \frac{L_v(T)}{c_{ph}}r'_{sw}(T)} \tag{8.268}$$

$$\Delta_2 = \frac{L_v(T)}{c_{ph}}\frac{r'_{sw}(T)}{1 + \frac{L_v(T)}{c_{ph}}r'_{sw}(T)}\left[A(x) + \frac{A'(x)}{A(x)} + \frac{2M_d A(x) r_{sw}(x)}{M_v}\right] \tag{8.269}$$

Eventually, the mixing ratio of condensed water vapor is deduced from the temperature difference $T - T'$ and transformed to a tendency by dividing by Δt:

$$r_{v,cnd} = (T - T')\frac{c_{ph}}{L_v(T)}\frac{1}{\Delta t} \tag{8.270}$$

Implementation in LIMA
In *lima_adjust.f90*:

$$\mathrm{ZLVFACT} = \frac{L_v(T)}{c_{ph}} \tag{8.271}$$

$$\mathrm{ZZW} = e_{sw}(T) \tag{8.272}$$

$$\mathrm{ZRVSATW} = r_{sw}(T) \tag{8.273}$$

$$\mathrm{ZRVSATW\_PRIME} = r'_{sw}(T) \tag{8.274}$$

$$\mathrm{ZAWW} = 1 + \frac{L_v(T)}{c_{ph}} r'_{sw}(T) \tag{8.275}$$

$$\mathrm{ZDELT2} = \frac{L_v(T)}{c_{ph}} \frac{r'_{sw}(T)}{1+\frac{L_v(T)}{c_{ph}} r'_{sw}(T)} \frac{1}{T} \left[\frac{-2\beta_w + \gamma_w T}{\beta_w - \gamma_w T} + \left(\frac{\beta_w}{T} - \gamma_w\right)\left(1 + \frac{2M_d r_{sw}(T)}{M_v}\right)\right] \tag{8.276}$$

$$= \Delta_2 \tag{8.277}$$

$$\mathrm{ZDELT1} = \Delta_1 \quad \text{(with } r_v = \text{ZRVS * ZDT to convert a tendency into a mixing ratio)} \tag{8.278}$$

$$\mathrm{ZCND} = \Delta_1 \left(1 + \frac{1}{2}\Delta_1\Delta_2\right) \frac{c_{ph}}{L_v(T)} \frac{1}{\Delta t} \tag{8.279}$$

Where $r_c > 0$ and $r_i > 0$

The rate of change of r_i and r_c is given by Eq. (8.197), where S_i, A_i, $c' = N_{Sc,v}^{1/3} \left(\frac{\rho_0}{\rho_d}\right)^{0.2} \left(\frac{c\rho_d}{\eta}\right)^{1/2}$ and the moments of the ice crystals size distribution all depend on time t.
The adjustment procedure is based on the treatment of simultaneous deposition/condensation of water vapour on ice/droplets by Reisin et al. (1996). For a Δt timestep, instead of assuming a constant deposition/condensation rate, we compute the new mass mixing ratio by integrating the previous equation:

$$r_i(t+\Delta t) - r_i(t) = \int_t^{t+\Delta t} \frac{\mathrm{d}r_i}{\mathrm{d}t}(u)\mathrm{d}u \tag{8.280}$$

As in Reisin et al. (1996), we use in the following $\Delta S_i = r_{si} S_i$, and assume that everything else varies slowly with time (therefore assuming that r_{si} has only small variations with time, but not small enough to be neglected in their Eq. (B5), Appendix B). Using also $\bar{f}_1 = 0$ (for both ice crystals and cloud droplets):

$$r_i(t+\Delta t) - r_i(t) = N_i\, 4\pi\, C_1\, A_i^{-1} r_{si}^{-1} \left(\bar{f}_0 M(1) + \bar{f}_2 c'^2 M(d+2)\right) \int_t^{t+\Delta t} \Delta S_i(u)\mathrm{d}u \tag{8.281}$$

$$\frac{r_i(t+\Delta t) - r_i(t)}{\Delta t} = N_i\, 4\pi\, C_1\, A_i^{-1} r_{si}^{-1} \left(\bar{f}_0 M(1) + \bar{f}_2 c'^2 M(d+2)\right) \frac{1}{\Delta t} \int_t^{t+\Delta t} \Delta S_i(u)\mathrm{d}u \tag{8.282}$$

The expressions for the integrals of ΔS_i and its counterpart ΔS_w are adapted from Reisin et al. (1996) to our configuration (using our representation based on particle diameter instead of particle mass), so that their parameters A, B, P and R become:

$$A^{\bullet}_{w} = 1 + \frac{L_v}{c_{ph}}\frac{\mathrm{d}r_{sw}}{\mathrm{d}T} \tag{8.283}$$

$$A^{\bullet}_{i} = 1 + \frac{L_v}{c_{ph}}\frac{\mathrm{d}r_{si}}{\mathrm{d}T} \tag{8.284}$$

$$B^{\bullet}_{w} = 1 + \frac{L_s}{c_{ph}}\frac{\mathrm{d}r_{sw}}{\mathrm{d}T} \tag{8.285}$$

$$B^{\bullet}_{i} = 1 + \frac{L_s}{c_{ph}}\frac{\mathrm{d}r_{si}}{\mathrm{d}T} \tag{8.286}$$

$$R_w = A^{\bullet}_{w}\, N_c\, 4\pi\, C_{1c}\, A_w^{-1} r_{sw}^{-1} \left(\bar{f}_{0c} M_c(1) + \bar{f}_{2c} c'^2 M_c(d_c+2)\right) \tag{8.287}$$

$$R_i = B^{\bullet}_{i}\, N_i\, 4\pi\, C_{1i}\, A_i^{-1} r_{si}^{-1} \left(\bar{f}_{0i} M_i(1) + \bar{f}_{2i} c'^2 M_i(d_i+2)\right) \tag{8.288}$$

$$P_w = A^{\bullet}_{i}\, N_c\, 4\pi\, C_{1c}\, A_w^{-1} r_{sw}^{-1} \left(\bar{f}_{0c} M_c(1) + \bar{f}_{2c} c'^2 M_c(d_c+2)\right) \tag{8.289}$$

$$P_i = B^{\bullet}_{w}\, N_i\, 4\pi\, C_{1i}\, A_i^{-1} r_{si}^{-1} \left(\bar{f}_{0i} M_i(1) + \bar{f}_{2i} c'^2 M_i(d_i+2)\right) \tag{8.290}$$

So that we can eventually use Eqs. (32) and (33) from Reisin et al. (1996):

$$\frac{1}{\Delta t}\int_t^{t+\Delta t} \Delta S_w(u)\mathrm{d}u = \Delta S_w - \frac{R_w \Delta S_w + P_i \Delta S_i}{R_w + R_i}\left[1 - \frac{1 - e^{-(R_w+R_i)\Delta t}}{(R_w+R_i)\Delta t}\right] \tag{8.291}$$

$$\frac{1}{\Delta t}\int_t^{t+\Delta t} \Delta S_i(u)\mathrm{d}u = \Delta S_i - \frac{P_w \Delta S_w + R_i \Delta S_i}{R_w + R_i}\left[1 - \frac{1 - e^{-(R_w+R_i)\Delta t}}{(R_w+R_i)\Delta t}\right] \tag{8.292}$$

Implementation in LIMA

All computations are led in the order presented below in *lima_adjust.f90*.

First, computations are performed to bring the water vapor back to saturation with respect to liquid water, assuming that both cloud droplets and ice crystals contribute to this adjustment. That is, the absolute values of the rates of change $\dot{r}_i$ and $\dot{r}_i$ are computed, from which the respective contribution of ice and cloud water is deduced. The equilibrium is sought using the same method as in the case when $r_c > 0$ and $r_i = 0$, and the mass of water vapor exchanged is distributed to or taken from each species according to their respective contribution. Note that during this stage, both cloud droplets and ice crystals are evaporated if $S_w < 0$, and both grow by deposition if $S_w > 0$, no matter what S_i is.

$$\mathrm{ZLVFACT} = \frac{L_v(T)}{c_{ph}} \tag{8.293}$$

$$\mathrm{ZLSFACT} = \frac{L_s(T)}{c_{ph}} \tag{8.294}$$

$$\mathrm{ZKA} = k_a \tag{8.295}$$

$$\mathrm{ZDV} = D_v \tag{8.296}$$

$$\mathrm{ZCJ} = c'/\sqrt{c} \tag{8.297}$$

$$\mathrm{ZZW} = e_{sw}(T) \tag{8.298}$$

$$\mathrm{ZRVSATW} = r_{sw}(T) \tag{8.299}$$

$$\mathrm{ZRVSATW\_PRIME} = r'_{sw}(T) \tag{8.300}$$

$$\mathrm{ZDELTW} = |r_v - r_{sw}(T)| = |\Delta S_w| \tag{8.301}$$

$$\mathrm{ZAW} = A_w \tag{8.302}$$

$$\mathrm{ZZW} = e_{si}(T) \tag{8.303}$$

$$\mathrm{ZRVSATI} = r_{si}(T) \tag{8.304}$$

$$\mathrm{ZRVSATI\_PRIME} = r'_{si}(T) \tag{8.305}$$

$$\mathrm{ZDELTI} = |r_v - r_{si}(T)| = |\Delta S_i| \tag{8.306}$$

$$\mathrm{ZAI} = A_i \tag{8.307}$$

$$\mathrm{ZZW} = \lambda_c \tag{8.308}$$

$$\mathrm{ZITW} = \frac{1}{\mathrm{ZRVSATW\ ZAW}}\mathrm{ZCCT}\left[\mathrm{X0CNDC}\ \frac{1}{\lambda} + \mathrm{X2CNDC\ ZCJ}^2\ \frac{1}{\lambda^{d+2}}\right] \tag{8.309}$$

$$= \frac{R_w}{A_w^\bullet} = \frac{P_w}{A_i^\bullet} = \frac{\dot{r}_c}{\Delta S_w} \tag{8.310}$$

$$\mathrm{ZZW} = \lambda_i \tag{8.311}$$

$$\mathrm{ZITI} = \frac{1}{\mathrm{ZRVSATI\ ZAI}}\mathrm{ZCIT}\left[\mathrm{X0DEPI}\ \frac{1}{\lambda} + \mathrm{X2DEPI\ ZCJ}^2\ \frac{1}{\lambda^{d+2}}\right] \tag{8.312}$$

$$= \frac{R_i}{B_i^\bullet} = \frac{P_i}{B_w^\bullet} = \frac{\dot{r}_i}{\Delta S_i} \tag{8.313}$$

$$\mathrm{ZAII} = \mathrm{ZITI\ ZDELTI} = |\dot{r}_i| \tag{8.314}$$

$$\mathrm{ZFACT} = \frac{L_v|\dot{r}_c| + L_s|\dot{r}_i|}{c_{ph}(|\dot{r}_c| + |\dot{r}_i|)} = \frac{\hat{L}}{c_{ph}} \tag{8.315}$$

$$\mathrm{ZAWW} = 1 + r'_{sw}\frac{\hat{L}}{c_{ph}} \tag{8.316}$$

$$\mathrm{ZDELT2} = \frac{\hat{L}}{c_{ph}}\frac{r'_{sw}}{1 + \frac{\hat{L}}{c_{ph}}r'_{sw}}\frac{1}{T}\left[\frac{-2\beta_w + \gamma_w T}{\beta_w - \gamma_w T} + \left(\frac{\beta_w}{T} - \gamma_w\right)\left(1 + \frac{2M_d r_{sw}}{M_v}\right)\right] \tag{8.317}$$

$$= \Delta_2 \quad \text{(see the case when } r_c > 0 \text{ and } r_i = 0) \tag{8.318}$$

$$\mathrm{ZDELT1} = \frac{\hat{L}}{c_{ph}}\frac{(r_{sw} - r_v)}{1 + \frac{\hat{L}}{c_{ph}}r'_{sw}} \tag{8.319}$$

$$= \Delta_1 \quad \text{(see the case when } r_c > 0 \text{ and } r_i = 0) \tag{8.320}$$

$$\mathrm{ZZW} = -\Delta_1\left(1 + \frac{1}{2}\Delta_1\Delta_2\right)\frac{c_{ph}}{\hat{L}}\frac{1}{\Delta t} \tag{8.321}$$

$$\mathrm{ZCND} = \mathrm{ZZW}\frac{|\dot{r}_c|}{|\dot{r}_c| + |\dot{r}_i|} \tag{8.322}$$

$$\mathrm{ZDEP} = \mathrm{ZZW}\frac{|\dot{r}_i|}{|\dot{r}_c| + |\dot{r}_i|} \tag{8.323}$$

At this point, all sources (ZRVS, ZRCS, ZRIS, ZTHS) are updated to start the adjustment using Reisin et al. (1996) from atmospheric conditions exactly at liquid water saturation, and the computations resume by first performing an implicit adjustment at ice saturation only where conditions are undersaturated with respect to ice (inside the WHERE(ZRVS(:)∗ZDT<ZRVSATI(:)) loop). Then begins the real adjustment procedure:

$$\mathrm{ZZT} = T \tag{8.324}$$

$$\mathrm{ZLVFACT} = \frac{L_v(T)}{c_{ph}} \tag{8.325}$$

$$\mathrm{ZLSFACT} = \frac{L_s(T)}{c_{ph}} \tag{8.326}$$

$$\mathrm{ZKA} = k_a \tag{8.327}$$

$$\mathrm{ZDV} = D_v \tag{8.328}$$

$$\mathrm{ZCJ} = c'/\sqrt{c} \tag{8.329}$$

$$\mathrm{ZZW} = e_{sw}(T) \tag{8.330}$$

$$\mathrm{ZRVSATW} = r_{sw}(T) \tag{8.331}$$

$$\mathrm{ZRVSATW\_PRIME} = r'_{sw}(T) \tag{8.332}$$

$$\mathrm{ZDELTW} = r_v - r_{sw}(T) = \Delta S_w \tag{8.333}$$

$$\mathrm{ZAW} = A_w \tag{8.334}$$

$$\mathrm{ZZW} = e_{si}(T) \tag{8.335}$$

$$\mathrm{ZRVSATI} = r_{si}(T) \tag{8.336}$$

$$\mathrm{ZRVSATI\_PRIME} = r'_{si}(T) \tag{8.337}$$

$$\mathrm{ZDELTI} = r_v - r_{si}(T) = \Delta S_i \tag{8.338}$$

$$\mathrm{ZAI} = A_i \tag{8.339}$$

$$\mathrm{ZZW} = \lambda_c \tag{8.340}$$

$$\mathrm{ZITW} = \frac{1}{\mathrm{ZRVSATW\ ZAW}}\mathrm{ZCCT}\left[\mathrm{X0CNDC}\ \frac{1}{\lambda} + \mathrm{X2CNDC\ ZCJ}^2\ \frac{1}{\lambda^{d+2}}\right] \tag{8.341}$$

$$= \frac{R_w}{A_w^\bullet} = \frac{P_w}{A_i^\bullet} = \frac{\dot{r}_c}{\Delta S_w} \tag{8.342}$$

$$\mathrm{ZZW} = \lambda_i \tag{8.343}$$

$$\mathrm{ZITI} = \frac{1}{\mathrm{ZRVSATI\ ZAI}}\mathrm{ZCIT}\left[\mathrm{X0DEPI}\ \frac{1}{\lambda} + \mathrm{X2DEPI\ ZCJ}^2\ \frac{1}{\lambda^{d+2}}\right] \tag{8.344}$$

$$= \frac{R_i}{B_i^\bullet} = \frac{P_i}{B_w^\bullet} = \frac{\dot{r}_i}{\Delta S_i} \tag{8.345}$$

Then, parameters A and B adapted from Reisin et al. (1996) are computed, so that we can get P and R by $\mathrm{ZAWW}*\mathrm{ZITW} = R_w$, $\mathrm{ZAIW}*\mathrm{ZITW} = P_w$, $\mathrm{ZAWI}*\mathrm{ZITI} = P_i$ and $\mathrm{ZAII}*\mathrm{ZITI} = R_i$:

$$\mathrm{ZAWW} = A_w^\bullet \tag{8.346}$$

$$\mathrm{ZAIW} = A_i^\bullet \tag{8.347}$$

$$\text{ZAWI} = B_w^\bullet \tag{8.348}$$
$$\text{ZAII} = B_i^\bullet \tag{8.349}$$

To perform the intergration:

$$\text{ZZW} = R_w + R_i \tag{8.350}$$
$$\text{ZFACT} = \frac{1}{R_w + R_i}\left[1 - \frac{1 - e^{-(R_w+R_i)\Delta t}}{(R_w + R_i)\Delta t}\right] \tag{8.351}$$
$$\text{ZCND} = \text{ZITW}[\Delta S_w - (R_w \Delta S_w + P_i \Delta S_i)\ \text{ZFACT}] \tag{8.352}$$
$$= \frac{r_c(t + \Delta t) - r_c(t)}{\Delta t} \tag{8.353}$$
$$\text{ZDEP} = \text{ZITI}[\Delta S_i - (P_w \Delta S_w + R_i \Delta S_i)\ \text{ZFACT}] \tag{8.354}$$
$$= \frac{r_i(t + \Delta t) - r_i(t)}{\Delta t} \tag{8.355}$$

where ZCND and ZDEP are computed following Eqs. (8.282) and (8.292) for r_i, and the similar relations for r_c. At this point, all sources (ZRVS, ZRCS, ZRIS, ZTHS) are updated. One last step in the adjustment procedure performs an adjustment to ice saturation in regions where conditions are undersaturated with respect to ice.

Where $r_c = 0$ and $r_i > 0$

Using the same equations as for the previous case ($r_c > 0$ and $r_i > 0$) but using the special condition $r_c = 0$, we get the following equation for r_i (from Eqs. (8.282) and (8.292)):

$$\frac{r_i(t + \Delta t) - r_i(t)}{\Delta t} = N_i\, 4\pi\, C_1\, A_i^{-1} r_{si}^{-1} \left(\bar{f}_0 M(1) + \bar{f}_2 c'^2 M(d + 2)\right) \frac{1}{\Delta t} \int_t^{t+\Delta t} \Delta S_i(u)\mathrm{d}u \tag{8.356}$$

$$\frac{1}{\Delta t} \int_t^{t+\Delta t} \Delta S_i(u)\mathrm{d}u = \Delta S_i - \frac{R_i \Delta S_i}{R_i}\left[1 - \frac{1 - e^{-R_i \Delta t}}{R_i \Delta t}\right] \tag{8.357}$$
$$= \Delta S_i \frac{1 - e^{-R_i \Delta t}}{R_i \Delta t} \tag{8.358}$$

Implementation in LIMA
In *lima_adjust.f90*:

$$\begin{aligned}
\text{ZLSFACT} &= \frac{L_s(T)}{c_{ph}} && (8.359)\\
\text{ZKA} &= k_a && (8.360)\\
\text{ZDV} &= D_v && (8.361)\\
\text{ZCJ} &= c'/\sqrt{c} && (8.362)\\
\text{ZZW} &= e_{si}(T) && (8.363)\\
\text{ZRVSATI} &= r_{si}(T) && (8.364)\\
\text{ZRVSATI\_PRIME} &= r'_{si}(T) && (8.365)\\
\text{ZDELTI} &= r_v - r_{si}(T) && (8.366)\\
\text{ZAI} &= A_i && (8.367)\\
\text{ZZW} &= \lambda_i && (8.368)\\
\text{ZITI} &= \frac{1}{\text{ZRVSATI ZAI}}\text{ZCIT}\left[\text{X0DEPI}\,\frac{1}{\lambda} + \text{X2DEPI ZCJ}^2\,\frac{1}{\lambda^{d+2}}\right] && (8.369)\\
\text{ZAII} &= 1 + \frac{L_s(T)}{c_{ph}} r'_{si}(T) && (8.370)\\
\text{ZZW} &= R_i\,\Delta t && (8.371)\\
\text{ZDEP} &= \text{ZITI}\,\Delta S_i\,\frac{1 - e^{-R_i \Delta t}}{R_i \Delta t} && (8.372)\\
&= \frac{r_i(t+\Delta t) - r_i(t)}{\Delta t} && (8.373)
\end{aligned}$$

At this point, all sources (ZRVS, ZRIS, ZTHS) are updated. This explicit adjustment is followed by an implicit sublimation of ice crystals to reach ice saturation where conditions are undersaturated with respect to ice.

8.6 Mixed-phase collection processes

These processes are parameterized as in ICE3, specific LIMA documentation not written yet.

8.7 Sedimentation

8.7.1 2-moment sedimentation

The vertical discretization in Meso-NH has mass points between the flux points, so $r(k)$ and $N(k)$ represent the mass mixing ratio and the number concentration in the grid cell between k and $k+1$. The grid cell height is $z(k+1) - z(k)$.
The splitted sedimentation uses a shorter time step t_{split} so that hydrometeors cannot fall through more than one grid cell at a time.
Let's consider the grid cell between levels k and $k+1$, and write $V(D)$, $m(D)$ and $n(k, D)$ the terminal fall speed (m s^{-1}), mass mixing ratio (kg) and number concentration (kg^{-1}) of hydrometeors

with a diameter D at level k. With i and j the grid cell dimensions along x and y, hydrometeors with a diameter D sedimenting from the grid cell k to the grid cell $k-1$ are those contained in a volume $(i, j, V(D)t_{split})$. Thus, the mass and number sedimentation for these hydrometeors is:

$$n_{sedim}(k,D) = i\;j\;V(D)t_{split}\;n(k,D)\rho_d(k) \tag{8.374}$$

$$m_{sedim}(k,D) = i\;j\;V(D)t_{split}\;n(k,D)\rho_d(k)\;m(D) \tag{8.375}$$

Then, for all hydrometeors:

$$n_{sedim}(k) = \int_D i\;j\;V(D)t_{split}\;n(k,D)\rho_d(k) \tag{8.376}$$

$$m_{sedim}(k) = \int_D i\;j\;V(D)t_{split}\;n(k,D)\rho_d(k)\;m(D) \tag{8.377}$$

The number (no units) and mass (kg) evolution at level k is:

$$n_{ap}(k) = n_{av}(k) - n_{sedim}(k) + n_{sedim}(k+1) \tag{8.378}$$

$$m_{ap}(k) = m_{av}(k) - m_{sedim}(k) + m_{sedim}(k+1) \tag{8.379}$$

$n_{ap}(k)$ and $m_{ap}(k)$ are related to the prognostic variables $N_{ap}(k)$ (kg^{-1}) and $r_{ap}(k)$ ($kg.kg^{-1}$):

$$n_{ap}(k) = N_{ap}(k)\;i\;j\;(z(k+1)-z(k))\;\rho_d(k) \tag{8.380}$$

$$m_{ap}(k) = r_{ap}(k)\;i\;j\;(z(k+1)-z(k))\;\rho_d(k) \tag{8.381}$$

Substituting these expressions and Eqs. (8.376) and (8.377) in Eqs. (8.378) and (8.379), and writing $h(k) = z(k+1) - z(k)$, we get:

$$\begin{aligned} N_{ap}(k)h(k)\rho_d(k) = N_{av}(k)h(k)\rho_d(k) - \int_D V(D)t_{split}n(k,D)\rho_d(k) \\ + \int_D V(D)t_{split}n(k+1,D)\rho_d(k+1) \end{aligned} \tag{8.382}$$

$$\begin{aligned} r_{ap}(k)h(k)\rho_d(k) = r_{av}(k)h(k)\rho_d(k) - \int_D V(D)t_{split}n(k,D)\rho_d(k)m(D) \\ + \int_D V(D)t_{split}n(k+1,D)\rho_d(k+1)m(D) \end{aligned} \tag{8.383}$$

Then

$$N_{ap}(k) = N_{av}(k) + \frac{tsplit}{h(k)}\left(-\int_D V(D)n(k,D) + \frac{\rho_d(k+1)}{\rho_d(k)}\int_D V(D)n(k+1,D)\right) \tag{8.384}$$

$$r_{ap}(k) = r_{av}(k) + \frac{tsplit}{h(k)}\left(-\int_D V(D)n(k,D)m(D) + \frac{\rho_d(k+1)}{\rho_d(k)}\int_D V(D)n(k+1,D)m(D)\right) \tag{8.385}$$

The hydrometeors size distribution follows a generalized gamma law, which parameters α and ν are fixed. λ depends on N et r, and therefore also depends on k. Using the expressions for $V(D)$, $m(D)$, r, N and λ found in the description of LIMA hydrometeors, we derive:

$$\int_D V(D)\;n(k,D) = c\left(\frac{\rho_{00}}{\rho_d(k)}\right)^{0.4}\frac{N(k)}{\lambda(k)^d}\frac{\Gamma(\nu+d/\alpha)}{\Gamma(\nu)} \tag{8.386}$$

and

$$\int_D V(D)\,n(k,D)\,m(D) = a\,\left(\frac{\rho_{00}}{\rho_d(k)}\right)^{0.4} c\,\frac{N(k)}{\lambda(k)^{d+b}}\,\frac{\Gamma(\nu+(d+b)/\alpha)}{\Gamma(\nu)} \tag{8.387}$$

$$= c\left(\frac{\rho_{00}}{\rho_d(k)}\right)^{0.4}\frac{1}{\lambda(k)^d}\,a\frac{N(k)}{\lambda(k)^b}\frac{\Gamma(\nu+b/\alpha)}{\Gamma(\nu)}\frac{\Gamma(\nu+(d+b)/\alpha)}{\Gamma(\nu+b/\alpha)} \tag{8.388}$$

$$= c\left(\frac{\rho_{00}}{\rho_d(k)}\right)^{0.4}\frac{1}{\lambda(k)^d}\frac{\Gamma(\nu+(d+b)/\alpha)}{\Gamma(\nu+b/\alpha)}\,r(k) \tag{8.389}$$

Terminal fall speed of cloud droplets correction

Following Pruppacher and Klett (1997, Chapter 10.3.6, Eq. (10-139)), the terminal fall speed of small cloud droplets must be corrected by a factor first introduced by Cunningham (1910):

$$V(D) = (1+1.26\frac{\lambda_a}{D/2})V(D) \tag{8.390}$$

where

$$\lambda_a = \lambda_{a,0}\frac{p_0}{p}\frac{T}{T_0} \tag{8.391}$$

with $\lambda_{a,0} = 6.6\ 10^{-8}$ cm, $p_0 = 1013.25$ mb and $T_0 = 293.15$ K. In LIMA, this corrective factor is computed using the mean cloud droplet diameter:

$$D_{c,m} = \frac{1}{\lambda_c}\frac{\Gamma(\nu_c+1/\alpha_c)}{\Gamma(\nu_c)} \tag{8.392}$$

Implementation dans LIMA

In *ini_lima_warm.f90*, the following variables are initialized:

$$\mathrm{XFSEDRC} = c\,\frac{\Gamma(\nu+(d+b)/\alpha)}{\Gamma(\nu+b/\alpha)}\,\rho_{00}^{0.4} \tag{8.393}$$

$$\mathrm{XFSEDCC} = c\,\frac{\Gamma(\nu+d/\alpha)}{\Gamma(\nu)}\,\rho_{00}^{0.4} \tag{8.394}$$

In *lima_warm_sedim.f90*:

$$\mathrm{ZRAY}(k) = D_{c,m} = \frac{1}{2}\frac{1}{\lambda_c}\frac{\Gamma(\nu_c+1/\alpha_c)}{\Gamma(\nu_c)} \tag{8.395}$$

$$\mathrm{ZCC}(k) = (1+1.26\frac{\lambda_a}{D_{c,m}/2})\quad \text{Cunningham correction factor (cloud droplets only)} \tag{8.396}$$

$$\mathrm{ZW}(k) = \frac{t_{split}}{z(k+1)-z(k)} \tag{8.397}$$

$$\mathrm{ZLBD}\bullet(k) = \lambda = \left(a\,\frac{N(k)}{r(k)}\frac{\Gamma(\nu+b/\alpha)}{\Gamma(\nu)}\right)^{1/b} \tag{8.398}$$

$$\mathrm{ZWSEDR}(k) = c\left(\frac{\rho_{00}}{\rho_d(k)}\right)^{0.4}\frac{1}{\lambda(k)^d}\frac{\Gamma(\nu+(d+b)/\alpha)}{\Gamma(\nu+b/\alpha)}\,r(k)\,\rho_d(k) \tag{8.399}$$

$$\mathrm{ZWSEDC}(k) = c\left(\frac{\rho_{00}}{\rho_d(k)}\right)^{0.4}\frac{1}{\lambda(k)^d}\frac{\Gamma(\nu+d/\alpha)}{\Gamma(\nu)}\,N(k)\,\rho_d(k) \tag{8.400}$$

allow to update the number concentrations and mass mixing ratios using Eqs. (8.384) et (8.385).

8.7.2 1-moment sedimentation

For 1-moment species (snow, graupel, hail), using the equations for r, N, and λ (see the description of hydrometeors), Eq. (8.389) becomes:

$$\int_D V(D)\, n(k,D)\, m(D) = c\left(\frac{\rho_{00}}{\rho_d(k)}\right)^{0.4} \frac{1}{\lambda(k)^d}\frac{\Gamma(\nu+(d+b)/\alpha)}{\Gamma(\nu+b/\alpha)}\, r(k) \tag{8.401}$$

$$= c\left(\frac{\rho_{00}}{\rho_d(k)}\right)^{0.4} \frac{1}{\lambda(k)^d}\frac{\Gamma(\nu+(d+b)/\alpha)}{\Gamma(\nu+b/\alpha)} a\frac{C\lambda(k)^x}{\rho_d(k)}\frac{1}{\lambda(k)^b}\frac{\Gamma(\nu+b/\alpha)}{\Gamma(\nu)} \tag{8.402}$$

$$= ca\frac{C}{\rho_d(k)}\left(\frac{\rho_{00}}{\rho_d(k)}\right)^{0.4}\frac{\Gamma(\nu+(d+b)/\alpha)}{\Gamma(\nu)}\lambda(k)^{x-b-d} \tag{8.403}$$

$$= ca\frac{C}{\rho_d(k)}\left(\frac{\rho_{00}}{\rho_d(k)}\right)^{0.4}\frac{\Gamma(\nu+(d+b)/\alpha)}{\Gamma(\nu)}\left(a\frac{C}{\rho_d(k)r(k)}\frac{\Gamma(\nu+b/\alpha)}{\Gamma(\nu)}\right)^{\frac{x-b-d}{b-x}} \tag{8.404}$$

Implementation in LIMA
In *ini_lima_cold_mixed.f90*, the following variables are initialized:

$$\text{XEXSED}\bullet = \frac{b+d-x}{b-x} \tag{8.405}$$

$$\text{XFSED}\bullet = caC\rho_{00}^{0.4}\frac{\Gamma(\nu+(d+b)/\alpha)}{\Gamma(\nu)}\left(aC\frac{\Gamma(\nu+b/\alpha)}{\Gamma(\nu)}\right)^{\frac{x-b-d}{b-x}} \tag{8.406}$$

In *lima_cold_sedimentation.f90*:

$$\text{ZW}(k) = \frac{t_{split}}{z(k+1)-z(k)} \tag{8.407}$$

$$\text{ZWSEDR}(k) = \frac{1}{\rho_d(k)}\text{XFSED}\bullet\left(\frac{1}{\rho_d(k)r(k)}\right)^{\frac{x-b-d}{b-x}}\left(\frac{1}{\rho_d(k)}\right)^{0.4}\rho_d(k) \tag{8.408}$$

$$= ca\frac{C}{\rho_d(k)}\left(\frac{\rho_{00}}{\rho_d(k)}\right)^{0.4}\frac{\Gamma(\nu+(d+b)/\alpha)}{\Gamma(\nu)}\left(a\frac{C}{\rho_d(k)r(k)}\frac{\Gamma(\nu+b/\alpha)}{\Gamma(\nu)}\right)^{\frac{x-b-d}{b-x}}\rho_d(k) \tag{8.409}$$

allow to update the mass mixing ratios using Eqs. (8.385) and (8.404).

8.8 List of symbols

A_i	m s kg^{-1}	Thermodynamical function, deposition/sublimation
A_w	m s kg^{-1}	Thermodynamical function, condensation/evaporation
a	kg m^{-b}	Parameter for the mass-diameter relationship
B	-	Beta function
b	-	Parameter for the mass-diameter relationship
C	m^{x-3}	Parameter for the $N = C\lambda^x$ relationship

C	m	Impact of the ice crystal shape on deposition of vapor
C_1	-	Parameter for the relationship ($C = C_1 D$)
C_i	J kg^{-1} K^{-1}	Ice crystal heat capacity
C_m	kg^{-1}	Aerosol mode m parameter for the activation spectrum
c	m^{1-d} s^{-1}	Parameter for the fall-speed-diameter relationship
c_{pd}	J kg^{-1} K^{-1}	Heat capacity of dry air at constant pressure
c_{ph}	J kg^{-1} K^{-1}	$= c_{pd} + r_v c_{pv} + (r_c + r_r) c_{pw}$
c_{pi}	J kg^{-1} K^{-1}	Heat capacity of ice at constant pressure
c_{pv}	J kg^{-1} K^{-1}	Heat capacity of water vapor at constant pressure
c_{pw}	J kg^{-1} K^{-1}	Heat capacity of liquid water at constant pressure
D	m	Diameter
$\bar{D}$	m	Mean volume diameter
$D_{lim,is}$	m	Limit diameter for snow $\leftrightarrow$ ice conversion
D_m	m	Aerosol mode m size distribution modal diameter
D_v	m^2 s^{-1}	Diffusivity of water vapor in the air
D_X	m	IFN type X size distribution modal diameter
d	-	Parameter for the fall-speed-diameter relationship
e_{sw}	Pa	Saturation vapor pressure over water
e_{si}	Pa	Saturation vapor pressure over ice
F	-	Hypergeometric function (for CCN activation spectrum)
$\bar{f}$	-	Ventilation factor (deposition/condensation/sublimation/evaporation)
$\bar{f}_0,\ \bar{f}_1,\ \bar{f}_2$	-	(to compute the ventilation factor)
G	m^2 s^{-1}	Thermodynamical function (CCN activation, rain evaporation)
g	m s^{-2}	Gravitational acceleration
K	m^3 s^{-1}	Collection Kernel (droplets and drops coalescence)
K_1	s^{-1}	(To compute K)
K_2	m^{-3} s^{-1}	(To compute K)
k_0		Aerosol reference parameter for the activation spectrum
k_a	kg m s^{-3} K^{-1}	Heat conductivity of air
k_B	m^2 kg s^{-2} K^{-1}	Boltzmann's constant
k_m		Aerosol mode m parameter for the activation spectrum
L_s	J kg^{-1}	Latent heat of sublimation
L_v	J kg^{-1}	Latent heat of vaporization
$M(p)$	-	p-order moment of the particle size distribution
M_d	kg mol-1	Molar mass of dry air
M_v	kg mol-1	Molar mass of water vapor
m	kg	Mass
N_A	mol^{-1}	Avogadro's number
N_c	kg^{-1}	Number concentration of cloud droplets
N_i	k^{-1}	Number concentration of pristine ice crystals
$N_{i \to s}$	kg^{-1}	Number concentration of pristine ice crystals transformed into snow
N_m	kg^{-1}	Total number concentration of aerosols (mode m)
N_m^{acti}	kg^{-1}	Number concentration of already activated aerosols (CCN) (mode m)
N_m^{free}	kg^{-1}	Number concentration of free aerosols (mode m)
N_m^{nucl}	kg^{-1}	Number conc. of already nucleated aerosols (IFN or coated IFN) (mode m)
N_m^{CCN}	kg^{-1}	Number concentration of activable CCN for aerosol mode m
N_X^{IFN}	kg^{-1}	Number concentration of activable IFN for aerosol type X

N_r	kg^{-1}	Number concentration of rain drops
N_{Re}	-	Reynolds number
$N_{Sc,v}$	-	Schmidt number for water vapor
$n_i(D)$	kg^{-1} m^{-1}	Number conc. of pristine ice crystals with $D < diameter < D + \mathrm{d}D$
$n_m(D)$	kg^{-1} m^{-1}	Number conc. of aerosols (mode m) with $D < diameter < D + \mathrm{d}D$
$n_m^{CCN}(S)$	kg^{-1}	Number conc. of activable CCN (mode m) for a supersaturation S
$n^{CCN}(S)$	k^{-1}	Total number conc. of activable CCN for a supersaturation S
P	Pa	Pressure
R	J mol^{-1} K^{-1}	Gas constant ($= N_A k_B$)
R_d	J kg^{-1} K^{-1}	Specific gas constant for dry air ($= R/M_d$)
R_v	J kg^{-1} K^{-1}	Specific gas constant for water vapor ($= R/M_v$)
r	m	Radius
r_0	m	Aerosol reference radius for the activation spectrum
r_c	kg kg^{-1}	Cloud droplets mixing ratio
r_g	kg kg^{-1}	Graupel mixing ratio
r_h	kg kg^{-1}	Hail mixing ratio
r_i	kg kg^{-1}	Ice crystals mixing ratio
r_m	m	Aerosol mode m size distribution modal radius
r_r	kg kg^{-1}	Rain mixing ratio
r_s	kg kg^{-1}	Snow mixing ratio
r_{sw}	kg kg^{-1}	Saturation vapor mixing ratio over water
r_{si}	kg kg^{-1}	Saturation vapor mixing ratio over ice
r_v	kg kg^{-1}	Water vapor mixing ratio
S_w	-	Supersaturation over liquid water ($S = 0.01$ for a 1% supersaturation)
$S_{\%}$	-	S_w in percentage ($S_{\%} = 1$ for a 1% supersaturation)
S_i	-	Supersaturation over ice ($S_i = 0.01$ for a 1% supersaturation)
S_i^w	-	Supersaturation over ice at water saturation ($S_i = 0.01$ for a 1% supersat.)
S_w^{max}	-	Diagnosed maximum supersaturation ($S_{max} = 0.01$ for a 1% supersat.)
T	K	Temperature
T_0	K	Aerosol reference activation T (for the activation spectrum)
T_m	K	Aerosol mode m expected activation T (for the activation spectrum)
t	s	Time
v	m s^{-1}	Hydrometeor terminal fall speed
w	m s^{-1}	Vertical wind speed
x	-	Parameter for the $N = C\lambda^x$ relationship
$\alpha_{\bullet}^{\bullet}$		Parameters to compute the aerosol activation spectrum
α	-	Parameter for the hydrometeors size distributions
β_0		Aerosol reference parameter for the activation spectrum
β_m		Aerosol mode m parameter for the activation spectrum
Γ	-	Gamma function
$\Delta N_m^{acti}(t)$	kg^{-1}	Number conc. aerosols activated at t (CCN) (mode m)
$\Delta N_m^{nucl}(t)$	kg^{-1}	Number conc. aerosols nucleated at t (IFN or coated IFN) (mode m)
ϵ_0		Aerosol reference solubility (for the activation spectrum)
ϵ_m		Aerosol mode m solubility (for the activation spectrum)
η	Pa s	Dynamic viscosity of air
λ	m^{-1}	Parameter for the hydrometeors size distributions
μ_0		Aerosol reference parameter for the activation spectrum

μ_m		Aerosol mode m parameter for the activation spectrum
ν	-	Parameter for the hydrometeors size distributions
ρ_d	kg m^{-3}	Air density
ρ_i	kg m^{-3}	Ice density
ρ_w	kg m^{-3}	Liquid water density
σ_0	-	Aerosol reference size distribution modal width
σ	m^2	Variance of the particle size distribution
σ_m	-	Aerosol mode m size distribution modal width
σ_X	-	IFN type X size distribution modal width
ψ_1	m^{-1}	Thermodynamical function for the evolution of S
ψ_2	-	Thermodynamical function for the evolution of S
ψ_3	K^{-1}	Thermodynamical function for the evolution of S
ω	m s^{-1}	Vertical velocity

Unit conversion
J = kg m^2 s^{-2}
Pa = kg m^{-1} s^{-2}
N = kg m s^{-2}

8.9 References

Berry, E. X. and R. L. Reinhardt, 1974: An analysis of cloud drop growth by collection Part II. Single initial distributions. *Journal of the Atmospheric Sciences*, **31 (7)**, 1825–1831.

Berthet, S., 2010: Développement d'un nouveau schéma de physique des nuages dans le modèle de méso-échelle MesoNH pour l'étude des interactions aérosol-nuage. Ph.D. thesis, UT3 Paul Sabatier.

Böhm, H. P., 1989: A general equation for the terminal fall speed of solid hydrometeors. *Journal of the Atmospheric Sciences*, **46 (15)**, 2419–2427, doi:10.1175/1520-0469(1989)046⟨2419:ageftt⟩2.0.co;2.

Caniaux, G., 1993: Paramétrisation de la glace dans un modèle non-hydrostatique de nuage : Application à une ligne de grain tropicale. Ph.D. thesis, Université Paul Sabatier.

Chen, J.-P. and D. Lamb, 1994: The theoretical basis for the parameterization of ice crystal habits: Growth by vapor deposition. **51 (9)**, 1206 – 1222, doi:10.1175/1520-0469(1994)051⟨1206:TTBFTP⟩2.0.CO;2, URL `https://journals.ametsoc.org/view/journals/atsc/51/9/1520-0469_1994_051_1206_ttbftp_2_0_co_2.xml`.

Cohard, J.-M. and J.-P. Pinty, 2000a: A comprehensive two-moment warm microphysical bulk scheme. I: Description and tests. *Quarterly Journal of the Royal Meteorological Society*, **126 (566)**, 1815–1842.

Cohard, J.-M. and J.-P. Pinty, 2000b: A comprehensive two-moment warm microphysical bulk scheme. II: 2D experiments with a non-hydrostatic model. *Quarterly Journal of the Royal Meteorological Society*, **126 (566)**, 1843–1859.

Cohard, J.-M., J.-P. Pinty, and C. Bedos, 1998: Extending Twomey's analytical estimate of nucleated cloud droplet concentrations from CCN spectra. *Journal of the atmospheric sciences*, **55 (22)**, 3348–3357.

Cohard, J.-M., J.-P. Pinty, and K. Suhre, 2000: On the parameterization of activation spectra from cloud condensation nuclei microphysical properties. *Journal of Geophysical Research: Atmospheres (1984–2012)*, **105 (D9)**, 11 753–11 766.

Cunningham, E., 1910: On the velocity of steady fall of spherical particles through fluid medium. *Proceedings of the Royal Society A: Mathematical, Physical and Engineering Sciences*, **83 (563)**, 357–365, doi:10.1098/rspa.1910.0024.

DeMott, P. J., M. P. Meyers, and W. R. Cotton, 1994: Parameterization and impact of ice initiation processes relevant to numerical model simulations of cirrus clouds. *Journal of the Atmospheric Sciences*, **51 (1)**, 77–90, doi:10.1175/1520-0469(1994)051⟨0077:paioii⟩2.0.co;2.

Eadie, W. J., 1971: A molecular theory of the homogeneous nucleation of ice from supercooled water. Ph.D. thesis, University of Chicago, Cloud Physics Lab.

Foote, G. B. and P. S. Du Toit, 1969: Terminal velocity of raindrops aloft. *Journal of Applied Meteorology*, **8 (2)**, 249–253, doi:10.1175/1520-0450(1969)008⟨0249:tvora⟩2.0.co;2.

Fouquart, Y. and B. Bonnel, 1980: Computations of solar heating of the earth's atmosphere- a new parameterization. *Beitraege zur Physik der Atmosphaere*, **53**, 35–62.

Gilmore, M. S. and J. M. Straka, 2008: The Berry and Reinhardt autoconversion parameterization: A digest. *Journal of Applied Meteorology and Climatology*, **47 (2)**, 375–396.

Gradshteyn, I. S. and I. M. Ryzhik, 1965: *Table of Integrals, Series and Products*. Academic Press.

Harrington, J. Y., M. P. Meyers, R. L. Walko, and W. R. Cotton, 1995: Parameterization of ice crystal conversion processes due to vapor deposition for mesoscale models using double-moment basis functions. part i: Basic formulation and parcel model results. *J. Atmos. Sci.*, **52 (23)**, 4344–4366, doi:10.1175/1520-0469(1995)052⟨4344:POICCP⟩2.0.CO;2.

Heymsfield, A., 1972: Ice crystal terminal velocities. *Journal of the Atmospheric Sciences*, **29 (7)**, 1348–1357, doi:10.1175/1520-0469(1972)029⟨1348:ictv⟩2.0.co;2.

Heymsfield, A. J. and L. M. Miloshevich, 1993: Homogeneous ice nucleation and supercooled liquid water in orographic wave clouds. *Journal of the Atmospheric Sciences*, **50 (15)**, 2335–2353, doi:10.1175/1520-0469(1993)050⟨2335:hinasl⟩2.0.co;2.

Hogan, R. J. and A. Bozzo, 2018: A flexible and efficient radiation scheme for the ecmwf model. *J. Adv. Model. Earth Sy.*, **10 (8)**, 1990–2008, doi:10.1029/2018MS001364, URL `https://agupubs.onlinelibrary.wiley.com/doi/abs/10.1029/2018MS001364`.

Kärcher, B. and U. Lohmann, 2002: A parameterization of cirrus cloud formation: Homogeneous freezing of supercooled aerosols. *Journal of Geophysical Research: Atmospheres*, **107 (D2)**.

Langlois, W. E., 1973: A rapidly convergent procedure for computing large-scale condensation in a dynamical weather model. *Tellus*, **25 (1)**, 86–87, doi:10.1111/j.2153-3490.1973.tb01598.x.

List, R. J., 1958: *Smithsonian Meteorological Tables*. Smithsonian Institution.

Liu, J. Y. and H. D. Orville, 1969: Numerical modeling of precipitation and cloud shadow effects on mountain-induced cumuli. *Journal of the Atmospheric Sciences*, **26 (6)**, 1283–1298, doi: 10.1175/1520-0469(1969)026⟨1283:nmopac⟩2.0.co;2.

Locatelli, J. D. and P. V. Hobbs, 1974: Fall speeds and masses of solid precipitation particles. *Journal of Geophysical Research*, **79 (15)**, 2185–2197, doi:10.1029/jc079i015p02185.

Long, A. B., 1974: Solutions to the droplet collection equation for polynomial kernels. *Journal of the Atmospheric Sciences*, **31 (4)**, 1040–1052.

Meyers, M. P., P. J. DeMott, and W. R. Cotton, 1992: New primary ice-nucleation parameterizations in an explicit cloud model. *Journal of Applied Meteorology*, **31 (7)**, 708–721.

Milbrandt, J. and M. Yau, 2005: A multimoment bulk microphysics parameterization. Part II: A proposed three-moment closure and scheme description. *Journal of the atmospheric sciences*, **62 (9)**, 3065–3081.

Phillips, V. T., P. J. DeMott, and C. Andronache, 2008: An empirical parameterization of heterogeneous ice nucleation for multiple chemical species of aerosol. *Journal of the Atmospheric Sciences*, **65 (9)**, 2757–2783.

Phillips, V. T., P. J. Demott, C. Andronache, K. A. Pratt, K. A. Prather, R. Subramanian, and C. Twohy, 2013: Improvements to an empirical parameterization of heterogeneous ice nucleation and its comparison with observations. *Journal of the Atmospheric Sciences*, **70 (2)**, 378–409.

Press, W. H., S. A. Teukolsky, W. T. Vetterling, and B. P. Flannery, 1992: *Numerical Recipes in FORTRAN: The art of scientific computing, 963 pp*. Cambridge Univ. Press, New York.

Pruppacher, H. R. and J. D. Klett, 1997: *Microphysics of clouds and precipitation*. Kluwer Academic Publishers (Dordrecht and Boston).

Reisin, T., Z. Levin, and S. Tzivion, 1996: Rain production in convective clouds as simulated in an axisymmetric model with detailed microphysics. Part I: Description of the model. *Journal of the atmospheric sciences*, **53 (3)**, 497–519.

Starr, D. O. and S. K. Cox, 1985: Cirrus Clouds. Part I: A Cirrus Cloud Model. *Journal of the Atmospheric Sciences*, **42 (23)**, 2663–2681, doi:10.1175/1520-0469(1985)042⟨2663:ccpiac⟩2.0.co;2.

Taufour, M., J.-P. Pinty, C. Barthe, B. Vié, and C. Wang, 2024: LIMA (v2.0): A full two-moment cloud microphysical scheme for the mesoscale non-hydrostatic model Meso-NH v5-6. *Geosci. Model Dev.*, **17 (23)**, 8773–8798, doi:10.5194/gmd-17-8773-2024, URL `https://gmd.copernicus.org/articles/17/8773/2024/`.

Verlinde, J. and W. R. Cotton, 1993: Fitting microphysical observations of nonsteady convective clouds to a numerical model: An application of the adjoint technique of data assimilation to a kinematic model. *Monthly Weather Review*, **121 (10)**, 2776–2793, doi:10.1175/1520-0493(1993)121⟨2776:fmoonc⟩2.0.co;2.

Verlinde, J., P. J. Flatau, and W. R. Cotton, 1990: Analytical solutions to the collection growth equation: Comparison with approximate methods and application to cloud microphysics parameterization schemes. *Journal of the Atmospheric Sciences*, **47 (24)**, 2871–2880, doi:10.1175/1520-0469(1990)047⟨2871:asttcg⟩2.0.co;2.

Vié, B., J.-P. Pinty, S. Berthet, and M. Leriche, 2016: LIMA (v1.0): A quasi two-moment microphysical scheme driven by a multimodal population of cloud condensation and ice freezing nuclei. *Geosci. Model Dev.*, **9 (2)**, 567–586, doi:10.5194/gmd-9-567-2016.

Yang, P., L. Bi, B. A. Baum, K.-N. Liou, G. W. Kattawar, M. I. Mishchenko, and B. Cole, 2013: Spectrally consistent scattering, absorption, and polarization properties of atmospheric ice crystals at wavelengths from 0.2 to 100 μm. *J. Atmos. Sci.*, **70 (1)**, 330 – 347, doi:10.1175/JAS-D-12-039.1, URL `https://journals.ametsoc.org/view/journals/atsc/70/1/jas-d-12-039.1.xml`.

Ziegler, C. L., 1985: Retrieval of thermal and microphysical variables in observed convective storms. part 1: Model development and preliminary testing. *Journal of the Atmospheric Sciences*, **42 (14)**, 1487–1509, doi:10.1175/1520-0469(1985)042⟨1487:rotamv⟩2.0.co;2.

Chapter 9

Sub-Grid Condensation Schemes

Contents

9.1 Sub-Grid Condensation Scheme for warm-phase clouds

9.1.1 Introduction

Sommeria and Deardorff (1977) have first suggested that taking into account sub-grid condensation in the turbulence parameterization would improve the physical behaviour of a model: The numerical shocks between cloudy and non cloudy grid cells are attenuated, and the vertical turbulent flux of virtual potential temperature can then be positive in partially cloudy layers.
The turbulence scheme of Meso-NH has been described in the previous chapter in the hypothesis of a cloudless atmosphere. Here we explain how the sub-grid clouds are represented. This presentation assumes that the reader knows the gross characteristics of the turbulence scheme. The principle of the sub-grid cloud scheme is to use *conservative forms* of the prognostic variables describing the entropy and the total non-precipitating water content. This was first proposed by Betts (1973). As a consequence, there are only minor modifications to the general turbulence computations.

9.1.2 Definition of conservative variables

The difficulty of treating the source terms for the mixing ratios r_* due to such processes as evaporation/condensation, accretion of cloud droplets by raindrops, etc. , can be considerably reduced by using quasi-conservative variables. Let us consider the equations for r_v, r_c, and r_r:

$$\begin{aligned}\frac{d(\rho_{dref} r_v)}{dt} &= \rho_{dref}(S_{RE} - S_{CON}), && (9.1)\\ \frac{d(\rho_{dref} r_c)}{dt} &= \rho_{dref}(-S_{RA} - S_{RC} + S_{CON}), && (9.2)\\ \frac{d(\rho_{dref} r_r)}{dt} &= \rho_{dref}(S_{RA} + S_{RC} - S_{RE} + S_{RS}), && (9.3)\end{aligned}$$

where the S_* represent the source terms, with subscripts CON, RE, RA, RC, RS corresponding respectively to evaporation/condensation, rain evaporation, accretion of cloud droplets by raindrops, conversion of cloud droplets into raindrops, and rain sedimentation. If one defines a new variable

$$r_{np} = r_v + r_c, \tag{9.4}$$

the equation of evolution of r_{np} will read

$$\frac{d(\rho_{dref} r_{np})}{dt} = \rho_{dref}(S_{RE} - S_{RA} - S_{RC}). \tag{9.5}$$

Note that the standard Meso-NH notations compell to use the subscript np (for *non precipitating*) instead of w, since r_w is already defined as the sum of all species r_*. r_{np} is the sum of the mixing ratios of water species which *accompany air movements*, as opposed to r_r, whose evolution equation involves rain sedimentation, thus an independent fall velocity, assumed to be much larger than the air velocity. *For the time beeing, we consider that the turbulent fluctuations of rain are negligible, and the turbulence scheme will only take into account the vapour vapor and the cloud liquid water.* The right-hand side of Eq. (9.5) involving only source terms that have slow characteristic time scales, r_{np} can be considered as quasi-conservative. In the future, the inclusion of ice (r_i), snow (r_s), or graupels (r_g) in Meso-NH may require careful attention to the definition of a suitable, quasi-conservative mixing ratio.

Similarly, we may define

$$\theta_l = \theta - \frac{L_v}{C_{ph}} {\Pi_{ref}}^{-1} r_c, \tag{9.6}$$

where L_v is the latent heat of vaporization of water, C_{ph} is the specific heat at constant pressure for moist air ($C_{ph} = C_{pd} + r_v C_{pv} + (r_c + r_r) C_l + (r_i + r_s + r_g + r_h) C_i$), and $\Pi_{ref}^{-1} = \left(\frac{\theta}{T}\right)_{ref}$. θ_l is a quasi-conservative potential temperature, except for the same source terms that remain in the equation of evolution of r_{np}, as can be seen if we come back to the equation of evolution of θ in the absence of moist correction, solid species of water, and diabatic effects due to radiation and diffusion: starting from the usual expressions

$$\begin{aligned}\frac{d(\rho_{dref}\theta)}{dt} &= \frac{L_v}{C_{ph}} \Pi_{ref}^{-1} \underbrace{\rho_{dref}(-S_{RE} + S_{CON})}_{=-\frac{d(\rho_{dref} r_v)}{dt}}, && (9.7)\\ \frac{d(\rho_{dref} r_c)}{dt} &= \rho_{dref}(-S_{RA} - S_{RC} + S_{CON}), && (9.8)\end{aligned}$$

we deduce

$$\frac{d(\rho_{dref}\theta_l)}{dt} = \frac{L_v}{C_{ph}} \Pi_{ref}^{-1} \rho_{dref}(S_{RA} + S_{RC} - S_{RE}). \tag{9.9}$$

This shows that except for the slow microphysical terms, the new variables are approximately as well conserved as θ and r_v in the absence of condensation. We take advantage of this to apply the turbulence scheme described in the previous chapter to θ_l and r_{np}, with a single modification linked to the expression of the buoyancy.

The course of computations is therefore the following:

- enter the turbulence scheme with the usual prognostic variables
- compute conservative variables
- compute turbulent fluxes of conservative variable formally as in the cloudless case (except for the expression of the buoyancy flux $\overline{u_i'\theta_v'}$)
- diagnose turbulent fluxes in non-conservative variables from their conservative counterparts
- come back to non-conservative variables
- come back to the main model

9.1.3 Retrieval of cloud water mixing ratio

As shown by Sommeria and Deardorff (1977), the mean value of r_c can be diagnosed from the grid scale values of θ_l and r_{np}, and their variances, which are supplied by the general turbulence scheme. This diagnosis relies on a simple statistical theory based on the shape of the sub-grid scale fluctuations histogram.

We first note that whenever cloud is present, the mixing ratio is equal to the saturation mixing ratio $r_{vs}(\theta, p)$. This can be expressed using θ_l and a first-order Taylor expansion as

$$r_v = r_{vs}\,(\theta, p) \approx r_{vs}(\theta_l) + (\frac{\partial r_{vs}}{\partial \theta})_{\theta_l}(\theta - \theta_l). \tag{9.10}$$

Here, the variations of r_{vs} with pressure have been neglected, because $|\frac{\partial r_{vs}}{\partial \theta}\Delta\theta| \gg |\frac{\partial r_{vs}}{\partial p}\Delta p|$. In the following, we will use the notation $J = \left(\frac{\partial r_{vs}}{\partial \theta}\right)_{\theta_l}$. Using the Clausius-Clapeyron relation, we have $J = \frac{r_{vs}(T_l)L_v}{R_v T_l \theta_l}$. Thus, we get

$$r_c = r_{np} - r_v = r_{np} - r_{vs}(\theta_l) - J(\theta - \theta_l). \tag{9.11}$$

Since by definition, $\theta - \theta_l = \frac{L_v}{C_{ph}}\Pi_{ref}^{-1} r_c$, this gives

$$r_c = r_{np} - r_{vs}(\theta_l) - J\frac{L_v}{C_{ph}}\Pi_{ref}^{-1} r_c, \tag{9.12}$$

$$r_c = \frac{r_{np} - r_{vs}(\theta_l)}{1 + M}, \tag{9.13}$$

where $M = J\frac{L_v}{C_{ph}}\Pi_{ref}^{-1}$.

On the other hand, in the unsaturated case, $r_c = 0$, thus a general expression is

$$r_c = \text{Max}\left(0, \frac{r_{np} - r_{vs}(\theta_l)}{1 + M}\right). \tag{9.14}$$

The mean cloud water mixing ratio in the grid cell is then obtained by averaging Eq. (9.14). For historical reasons, we use the notation

$$s = \frac{r_{np} - r_{vs}(\theta_l)}{2(1 + M)}. \tag{9.15}$$

s may be seen as a turbulent quantity that controls local saturation within the grid. Whenever $s \geq 0$, there is saturation. Then, $s = \overline{s} + s'$, and saturation may be defined as $s' \geq -\overline{s}$.
Note that the standard deviation σ_s of s may be easily computed, since to first order approximation,

$$s' = \frac{r'_{np} - J\theta'_l}{2(1 + M)}, \tag{9.16}$$

leading to

$$\sigma_s = \frac{\left(\overline{r'^2_{np}} + J^2\overline{\theta'^2_l} - 2J\overline{r'_{np}\theta'_l}\right)^{\frac{1}{2}}}{2(1 + M)}. \tag{9.17}$$

To compute the statistical average of r_c within the grid, it is useful to introduce the centered, normalized variable $t = s'/\sigma_s$, and its probability distribution $G(t)dt$. In terms of t, saturation is present whenever $t \geq -\overline{s}/\sigma_s$. We will therefore define the quantity

$$Q_1 = \frac{\overline{r_{np}} - r_{vs}(\overline{\theta_l})}{2(1 + M)\sigma_s}. \tag{9.18}$$

The fraction of the grid cell occupied by clouds is then

$$N = \int_{-Q_1}^{+\infty} G(t)dt, \tag{9.19}$$

and the mean cloud water content is

$$\frac{\overline{r_c}}{2\sigma_s} = \int_{-Q_1}^{+\infty} (Q_1 + t)G(t)dt. \tag{9.20}$$

The problem is therefore solved.
Note that in the case of elongated grids with $\Delta x, \Delta y \gg \Delta z$, it will be useful to assimilate the cloud fraction N to the cloud *cover*, in the usual meteorological sense. For isotropic grid, the cloud fraction is more of a three dimensional nature.

9.1.4 Flux of liquid water

We also need to compute the fluxes $\overline{u_i' r_c'}$, where u_i can be any of the three components of the velocity u_1, u_2, or u_3. Indeed, these fluxes will be used to compute the buoyancy fluxes $\overline{u_i' \theta_v'}$ (appearing in the TKE prognostic equation), and to retrieve the fluxes of non-conservative variables, once the fluxes of conservative variables are known.
With the same notations as in the previous section, according to Bougeault (1981, 1982), we have

$$\frac{\overline{s' r_c'}}{2{\sigma_s}^2} = \int_{-Q_1}^{+\infty} t(Q_1 + t)G(t)dt\ . \tag{9.21}$$

We assume that this second-order correlation can be used as a generic model for the $\overline{u_i' r_c'}$ correlations. However, Bechtold et al. (1993) have shown this to underestimate the real correlation in cases of low cloud fraction. We therefore introduce an empirical coefficient λ_i to obtain more realistic results:

$$\frac{\overline{u_i' r_c'}}{\overline{u_i' s'}} = \lambda_i \frac{\overline{s' r_c'}}{\sigma_s^2}. \tag{9.22}$$

Once the turbulent fluxes of cloud liquid water are known, going back to turbulent fluxes in non-conservative variables is straightforward, because they are linear combinations of turbulent fluxes in conservative variables. From Eqs. (9.4) and (9.6), we obtain readily

$$\overline{u_i' \theta'} = \overline{u_i' \theta_l'} + \frac{L_v}{C_{ph}} {\Pi_{ref}}^{-1} \overline{u_i' r_c'}, \tag{9.23}$$

$$\overline{u_i' r_v'} = \overline{u_i' {r'}_{np}} - \overline{u_i' r_c'}. \tag{9.24}$$

9.1.5 Closure of the scheme

The closure relies on adequate choices for G and λ_i. In their original paper, Sommeria and Deardorff proposed to use by simplicity a gaussian distribution for G. However, Bougeault (1981, 1982) showed that this would underestimate the cloud fraction in most cases, because actual distributions are skewed. He proposed several solutions, the most general being the Gamma probability density. The importance of using skewed distributions has been confirmed by later work (Cuijpers and Bechtold 1995).

Using this theory, N, $\frac{\overline{r_c}}{2\sigma_s}$, and $\frac{\overline{s'r'_c}}{2\sigma_s{}^2}$ are then computed from Eqs. (9.19), (9.20), and (9.21) and expressed as:

$$N = F_0(Q_1, A_s), \tag{9.25}$$
$$\frac{\overline{r_c}}{2\sigma_s} = F_1(Q_1, A_s), \tag{9.26}$$
$$\frac{\overline{s'r'_c}}{2\sigma_s^2} = F_2(Q_1, A_s). \tag{9.27}$$

Q_1 has been defined above, and A_s is the skewness of the distribution of t, that requires parametrization. The detailed expressions of F_0, F_1, and F_2 may be found in Bougeault (1982).
As far as the coefficients λ_i are concerned, they are unfortunately not well known when $i = 1$ or $i = 2$. By simplicity, we will assume $\lambda_1 = \lambda_2 = 1$. For $i = 3$, the study of Cuijpers and Bechtold (1995) shows that its value can range from 1 when G is a gaussian function, to 3 when Q_1 is of the order of -2, and up to 50 when Q_1 is as low as -4. However, in the later case, these values of Q_1 are sparse and the dispersion of the numerical value of λ_3 obtained after LES 3D simulations for different conditions of saturation is high, which makes difficult the fitting of any curve for λ_3.

The current choice of parameters in Meso-NH is the following:

1. For 1D or quasi-1D mode,

    - $Q_1 \geq 0$: $A_s = 0$ and $\lambda_3 = 1$,
    - $Q_1 < -2$: $A_s = 2$ and $\lambda_3 = 3$,
    - $-2 \leq Q_1 < 0$: $A_s = -Q_1$ and $\lambda_3 = 1 - Q_1$.

    The values of A_s for the first two cases correspond respectively to a gaussian function and a skewed exponential function. The latter case is only a linear interpolation of the two previous ones. In any of the three previous cases, $\lambda_1 = \lambda_2 \equiv 1$.

2. For the LES mode,

    - $A_s \equiv 0$ and $\lambda_1 = \lambda_2 = \lambda_3 \equiv 1$ in all cases.

The expression of the fluxes of cloud water is finally obtained from Eqs. (9.16), (9.22), and (9.27), as

$$\overline{u'_i r'_c} = A_{moist}\overline{u'_i r'_{np}} + A_\theta \overline{u'_i \theta'_l}, \tag{9.28}$$

with

$$A_{moist} = \frac{\lambda_i F_2(Q_1, A_s)}{1 + M}, \tag{9.29}$$
$$A_\theta = -J\frac{\lambda_i F_2(Q_1, A_s)}{1 + M}. \tag{9.30}$$

9.1.6 Buoyancy flux

As mentionned above, the only modification in the turbulence scheme in presence of saturation is the expression of the virtual potential temperature. Cloud water increase the density of the parcel, but the latent heat produced by condensation has an opposite effect. In general cloudy parcels are therefore more buoyant than clear air parcels. Using the conservative variables, this is expressed as

$$\begin{aligned}
\theta_v &= \theta(1+\delta\frac{r_v}{1+r_w}-\frac{r_c}{1+r_w}-\frac{r_w-r_v-r_c}{1+r_w}) \\
&= \left(\theta_l+\frac{L_v}{C_{ph}}{\Pi_{ref}}^{-1}r_c\right)\left(1+\delta\frac{r_{np}}{1+r_w}-(1+\delta)\frac{r_c}{1+r_w}-\frac{r_w-r_{np}}{1+r_w}\right). \qquad (9.31)
\end{aligned}$$

The fluctuations of θ are then given by

$$\begin{aligned}
\theta_v' &\approx \delta\frac{\overline{\theta}}{1+\overline{r_w}}r_{np}' \\
&+ \left(\frac{L_v}{C_{ph}}{\Pi_{ref}}^{-1}\left(1+\delta\frac{\overline{r_{np}}}{1+\overline{r_w}}-(1+\delta)\frac{\overline{r_c}}{1+\overline{r_w}}-\frac{\overline{r_w}-\overline{r_{np}}}{1+\overline{r_w}}\right)-(1+\delta)\frac{\overline{\theta}}{1+\overline{r_w}}\right){r_c}' \\
&+ \left(1+\delta\frac{\overline{r_{np}}}{1+\overline{r_w}}-(1+\delta)\frac{\overline{r_c}}{1+\overline{r_w}}-\frac{\overline{r_w}-\overline{r_{np}}}{1+\overline{r_w}}\right)\theta_l', \qquad (9.32)
\end{aligned}$$

where $\delta=\frac{R_v}{R_d}-1$. This shows that the expression of $\overline{u_i'\theta_v'}$ will include a $\overline{u_i'{r_c}'}$ term.

It is convenient to define the following coefficients:

$$\begin{aligned}
A &= 1+\delta\frac{\overline{r_{np}}}{1+\overline{r_w}}-(1+\delta)\frac{\overline{r_c}}{1+\overline{r_w}}-\frac{\overline{r_w}-\overline{r_{np}}}{1+\overline{r_w}}, \qquad (9.33)\\
B &= \delta\frac{\overline{\theta}}{1+\overline{r_w}}, \qquad (9.34)\\
C &= \frac{L_v}{C_{ph}}{\Pi_{ref}}^{-1}\left(1+\delta\frac{\overline{r_{np}}}{1+\overline{r_w}}-(1+\delta)\frac{\overline{r_c}}{1+\overline{r_w}}-\frac{\overline{r_w}-\overline{r_{np}}}{1+\overline{r_w}}\right)-(1+\delta)\frac{\overline{\theta}}{1+\overline{r_w}} \\
&= \frac{L_v}{C_{ph}}{\Pi_{ref}}^{-1}A-\frac{1+\delta}{\delta}B. \qquad (9.35)
\end{aligned}$$

With these notations, the buoyancy flux $\overline{u_i'\theta_v'}$ can be written

$$\overline{u_i'\theta_v'}=A\overline{u_i'\theta_l'}+B\overline{u_i'r_{np}'}+C\overline{u_i'r_c'}\,. \qquad (9.36)$$

A more compact expression may be obtained by use of eq. (9.28):

$$\overline{u_i'\theta_v'}=E_\theta\overline{u_i'\theta_l'}+E_{moist}\overline{u_i'r_{np}'}\,, \qquad (9.37)$$

where $E_\theta=A+CA_\theta$ and $E_{moist}=B+CA_{moist}$.

9.1.7 Modification to the mixing length

There are three different ways of computing the mixing length in Meso-NH.

- For the LES mode, the mixing length is usually set equal to $(d_{xx}d_{yy}d_{zz})^{1/3}$. In this case, no change is necessary to account for SGC.
- In the case of a K-ϵ turbulence scheme, condensation processes will be taken into account implicitely in the length scale when working in conservative variables.
- Finally, when the Bougeault-Lacarrère scheme is adopted, one has to use the potential temperature $\theta_v = \theta \left(\frac{1+\delta r_v}{1+r_w} \right)$ to obtain the level, either upward or downward, where all the TKE has been transformed into potential energy due to buoyancy, yielding:

  $$-\,\overline{e}(z) = \int_{z}^{z+l_{up}} \beta(\overline{\theta_{vp}}(z') - \overline{\theta_{ve}}(z'))dz' = \int_{z-l_{down}}^{z} \beta(\overline{\theta_{ve}}(z') - \overline{\theta_{vp}}(z'))dz' \ ,$$

  where the subscripts e and p refer respectively to the environment and to the particle which has left its initial height.

If the transformation is adiabatic, when a particle leaves its initial height, then:

$$\overline{\theta_{vp}}(z') = \overline{\theta}_p(z') \left(\frac{1+\delta\overline{r_{vp}}(z')}{1+\overline{r_{wp}}(z')} \right) \ , \tag{9.38}$$

$$\overline{\theta_{ve}}(z') = \overline{\theta}_e(z') \left(\frac{1+\delta\overline{r_{np}}_e(z')}{1+\overline{r_{we}}(z')} \right) \ , \tag{9.39}$$

where $\overline{\theta}_p(z')$, $\overline{r_{vp}}(z')$, and $\overline{r_{wp}}(z')$ account for the change of phase of water when the particle is lifted from height z.

9.1.8 Spatial Discretization

The discretization in space follows from the general turbulence scheme. The cloud fraction, the cloud mixing ratio, the conservative variables and the variances are all located at mass points. The application of the theory is therefore straightforward.

On the other hand, the fluxes are located at u_i points. Thus, application of Eq. (9.28) requires an average of A_r and A_θ in the direction i. This reads:

$$\overline{u_i' r_c'} = \overline{A_r}^{x_i}\, \overline{u_i' r_{np}'} + \overline{A_\theta}^{x_i}\, \overline{u_i' \theta_l'}. \tag{9.40}$$

9.1.9 Practical implementation

As this method is providing a diagnostic estimate of the cloud water mixing ratio, it substitutes to the condensation adjustment procedure. This could be done in the turbulence scheme very conveniently. However, the general code organization would become very complicated, and different wether the SGC is used or not. Therefore, we decided not to mix the turbulence scheme and the condensation adjustment in one routine and to adhere to the usual order of call of the routines inside one model time step, where the condensation adjustment is the last routine called before the end of the time step.

The code organization follows from these considerations. It is understood that the objective of the time step is to compute values at $t+1$.

1. The input variables to the turbulence scheme are the usual prognostic variables at t and $t-1$, their sources, and the value of $\lambda_3 \overline{s'r'_c}/2\sigma_s^2 \equiv \lambda_3 F_2(Q_1, A_s)$, saved from the previous time step.

2. In routine TURB, the conservative variables and their sources are computed from the input variables, through Eqs. (9.4) and (9.6).

3. The computation of turbulent fluxes follows as described in the previous chapter. However, when the buoyancy flux is needed, the formulation of the E_θ and E_{moist} coefficients uses eq. (9.37) instead of the formulation given in the previous chapter. Note that the two formulations coincides in the total absence of cloud. This computation is based on the value of $\lambda_3 \overline{s'r'_c}/2\sigma_s^2$.

4. The fluxes of cloud water $\overline{u'_i r'_c}$ are diagnosed through Eq. (9.28). This uses also Eq. (9.29). Note that only $\lambda_3 F_2$ is transmitted to the routine to save ressources. This trick is possible because in the present version of the scheme, λ_1 and λ_2 are not used in the 1DIM case, and equal to λ_3 in the 3DIM case.

5. The divergence of $\overline{u'_i r'_c}$ is used to evaluate the source of r_c due to the turbulent exchanges, at the exclusion of the condensation/evaporation process.

6. The value of σ_s^t is computed, and is an output of the turbulence scheme.

7. At the end of the TURB routine, we get back to the usual form of the temperature, the water mixing ratio, and their sources. Note that the cloud water mixing ratio r_c is not modified during the turbulence computation, but its source now includes the effect of turbulent transport, as do the sources of the potential temperature and water vapor.

8. At the end of the model time step, routine FAST_TERMS receives as input the non-adjusted value of the prognostic variables at time $t+1$. We shall call these θ^*, r_v^*, and r_c^*. It also receives σ_s^t.

9. FAST_TERMS computes the final value of the conservative variables by applying Eqs. (9.4) and (9.6) to θ^*, r_v^*, and r_c^*. This does not involve any approximation, since the conservative variables are conserved by definition in the saturation adjustment.

10. It computes Q_1 by applying Eq. (9.48) with the final values of the conservative variables, and σ_s^t. This step thus assimilates σ_s^t to σ_s^{t+1}. This is done in order to save computer ressources. The alternative would be to carry a large number of additionnal variables, or to redo part of the turbulence computation. This is a price to pay for clarity and efficiency of the code.

11. The adjusted value r_c^{**} is obtained from Eq. (9.26), again assimilating σ_s^t to σ_s^{t+1}. At the same time, $\lambda_3 \overline{s'r'_c}/2\sigma_s^2$ is computed and saved for the next time step.

12. Finally, the adjusted value of the non-conservative, prognostic variables at time $t+1$ are obtained through

$$\overline{r_c}^{t+\Delta t} = \overline{r_c}^{**} \tag{9.41}$$

$$\overline{\theta}^{t+\Delta t} - \overline{\theta}^{*} = \frac{L_v}{C_{ph}} {\Pi_{ref}}^{-1} \left(\overline{r_c}^{**} - \overline{r_c}^{*}\right) \tag{9.42}$$

$$\overline{r_v}^{t+\Delta t} - \overline{r_v}^{*} = -\left(\overline{r_c}^{**} - \overline{r_c}^{*}\right) \tag{9.43}$$

9.2 Sub-Grid condensation scheme for ice-phase and convective clouds

9.2.1 Introduction

The application of a statistical sub-grid condensation scheme to deep convective tropospheric clouds and to upper tropospheric stratiform clouds requires a couple of extensions to the warm-phase scheme presented in the previous chapter. These extensions include i) the representation of ice phase and mixed-phase clouds ii) a definition of statistical cloud relations that approximately hold for all types of tropospheric clouds, and iii) a proper definition of sub-grid variance including a convective contribution. These specific developments are described below and closely follow the Méso-nh Cloud Resolving Model (CRM) study by Chaboureau and Bechtold (2002). However, all issues concerning the coupling of the sub-grid condensation scheme with the Méso-nh prognostic thermodynamic framework (section ”practical implementation”) as described in the previous chapter keep unchanged.

9.2.2 Thermodynamic framework

The properties of a moist adiabatically ascending air parcel are conveniently expressed assuming conservation (in the absence of precipitation) of enthalpy or ”liquid water static energy” h_l and total water mixing ratio r_w

$$\begin{aligned} h_l &= C_{pm}T - L_v r_c - L_s r_i + (1+r_w)gz && (9.44)\\ r_w &= r_v + r_c + r_i, && (9.45)\end{aligned}$$

where the specific heat of moist air is defined as $C_{pm} = C_{pd} + r_w C_{pv}$, L_v and L_s are the specific latent heats of vaporization and sublimation, g denotes the gravitational acceleration, z is height, and r_v, r_c and r_i denote the mixing ratios of water vapor and non-precipitating cloud water/ice, respectively. We further define a ”liquid” temperature as

$$\begin{aligned} T_l &= T - L_v/C_{pm}\, r_c - L_s/C_{pm}\, r_i \\ &= (h_l - (1+r_w)gz)/C_{pm}, && (9.46)\end{aligned}$$

and combine the moisture and temperature effects to one single variable $s = ar_w - bT_l$ (see e.g. Mellor 1977) with

$$\begin{aligned} a = (1 + Lr_{sl}/C_{pm})^{-1}, \qquad b = a\; r_{sl}, \\ r_{sl} = \partial r_{sat}/\partial T(T = T_l) = Lr_{sat}(T_l)/(R_v T_l^2). && (9.47)\end{aligned}$$

Here L and r_{sat} are the latent heat and water vapor saturation mixing ratio that inside a given glaciation interval $T_0 > T > T_1$ are linearly interpolated as a function of temperature between their respective values for liquid water and ice, i.e. $L = (1-\chi)L_v + \chi L_s$, $r_{sat} = (1-\chi)r_{satw} + \chi r_{sati}$ (r_{satw} and r_{sati} are the saturation mixing ratios over water and ice, respectively) with two options for parameterising χ: either based on temperature with $\chi = (T_0 - T)/(T_0 - T_1)$ and adjustable T_0 and T_1 (by default T_0 =273.16 K, and T_1=253 K), or keeping χ constant during condensation (χ then evolves according to the mycrophysical processes).

Finally, with the above definitions Q_1 is expressed as the saturation deficit of the ensemble or grid average (denoted by overbars) normalized by σ_s, the variance of s, with primes denoting deviations from the ensemble (grid) mean

$$
\begin{aligned}
Q_1 &= \overline{a}\,(\overline{r}_w - r_{sat}(\overline{T}_l))/\sigma_s, \\
\sigma_s &= (\overline{a}^2\,\overline{r_w'^2} - 2\overline{a}\overline{b}\;\overline{r_w'T_l'} + \overline{b}^2\,\overline{T_l'^2})^{1/2}.
\end{aligned} \tag{9.48}
$$

9.2.3 Fractional cloudiness and cloud condensate

As shown in Chaboureau and Bechtold (2002) using CRM data, the cloud fraction N and the grid-mean condensate mixing ratio $r_l = r_c + r_i$ of tropospheric clouds can be represented by the following relations that have been earlier established for boundary-layer clouds

$$N = \max\{0, \min[1, 0.5 + 0.36\arctan(1.55Q_1)]\} \tag{9.49}$$

$$
\begin{aligned}
\tfrac{\overline{r}_l}{\sigma_s} &= e^{(1.2Q_1-1)}, && Q_1 < 0. \\
\tfrac{\overline{r}_l}{\sigma_s} &= e^{-1} + 0.66Q_1 + 0.086Q_1^2 && 0 \le Q_1 \le 2 \\
\tfrac{\overline{r}_l}{\sigma_s} &= Q_1 && Q_1 > 2.
\end{aligned} \tag{9.50}
$$

The respective mixing ratios for cloud water and cloud ice are then retrieved using $r_c = (1-\chi)\,r_l$, and $r_i = \chi\,r_l$.
Alternatively, a Gaussian PDF can be used to compute the cloud content and fraction.
In addition, the shallow convection scheme can provide (depending on the option activated) a cloud contribution in the form of a content and a fraction to be added to these values.

9.2.4 Parameterization of σ_s

The practical application of the cloud relations [Eqs. (9.49) and (9.50)] in meteorological models requires the knowledge of the second-order moment σ_s. This quantity is provided by the Méso-nh turbulence scheme and used as that in the warm-phase sub-grid condensation scheme.
However, it turned out that this formulation is not yet well adapted to deep and upper tropsopheric clouds as it generally has zero value above the boundary-layer. Here, a simple parameterization is suggested representing the total variance of s as a sum of a turbulent, a convective and a critical humidity-like contribution

$$\sigma_s^2 = \sigma_{sturb}^2 + \sigma_{sconv}^2 + \sigma_{q_{sat}} \tag{9.51}$$

Turbulent contribution

The turbulent contribution is either the value computed by the turbulence scheme (possible option in the computer code) or (present default option) expressed as

$$\sigma_s = c_\sigma\, l \left[\overline{a}^2\left(\frac{\partial\overline{r}_w}{\partial z}\right)^2 - 2\overline{a}\overline{b}\,C_{pm}^{-1}\frac{\partial\overline{h}_l}{\partial z}\frac{\partial\overline{r}_w}{\partial z} + \overline{b}^2\,C_{pm}^{-2}\left(\frac{\partial\overline{h}_l}{\partial z}\right)^2\right]^{1/2}, \tag{9.52}$$

where $C_{pm}^{-1}\,\partial h_l/\partial z = \partial T_l/\partial z\ + g/C_{pm}(1+r_w)$, l is a constant length-scale of value $l_0 = 600$ m (for $z > l_0$; $l = z$ for $z <= l_0$), and c_σ is a constant of value 0.2 (Cuxart et al. 2000).

Convective contribution

Using the top-hat approximation, the variance and the flux of a quantity s can be expressed as (see e.g. Lappen and Randall 2001)

$$\overline{s'^2} = N\,(1-N)(s^c - s^e)^2, \tag{9.53}$$

where N is the cloud fraction, and where c and e denote cloud and environmental values, respectively. However, as noted by the authors and Siebesma (personal communication) the top-hat approximation reasonably represents the convective fluxes but not the variances, and is also sensible to the decomposition chosen, i.e. cloud/environment or updraft/downdraft. Therefore, instead of Eq. (9.53) we seek a simple expression as a function of the convective mass flux (a quantity that is readily available from the mass flux convection parameterization):

$$\sigma_s^{conv} = \overline{s'^2}^{1/2} \approx \frac{\overline{w's'}}{w^*} \approx M\,\frac{(s^c - s^e)}{w^*\rho^*} \tag{9.54}$$

where $M = \overline{\rho}\,N\,w$ is the convective mass flux (kg s^{-1} m^{-2}), w^* a convective scale velocity and ρ^* a tropospheric density scale. Finally, Eq. (9.54) is further simplified to

$$\sigma_s^{conv} \approx M\,\frac{(s^c - s^e)}{w^*\rho^*} \approx \alpha\;M\,f(z/z^*) \tag{9.55}$$

where a vertical scaling function f has been introduced. It turns out that σ_s is mainly determined (especially in the tropics and the upper troposphere) by the moisture variance. For simplicity the scaling function is set to $f = a^{-1}$ so that it is proportional to the saturation mixing ratio.
Finally, the value of the proportionality coefficient α can be obtained by minimizing the function $(\sigma_s^2 - \sigma_{sturb}^2 - \sigma_{sconv}^2)^2$, where σ_s^2 are the values derived from convective data sets and where σ_{sturb} and σ_{sconv} are replaced by Eqs. (9.52) and (9.55), respectively. A value $\alpha = 3 \times 10^{-3}$ is obtained using the cloud mass flux from the CRM.

Critical humidity-like contribution

The critical humidity-like contribution is described in de Rooy et al. (2010), an extract of which is reproduced below:

> The production of variance is coupled to the activity of the turbulence and the convection scheme [...]. However, this does not mean that in the absence of turbulent or convective activity the variance is zero. In nature other possible sources for variance are e.g. gravity waves, meso-scale circulations or large-scale advection. For situations without convective or turbulent activity, models therefore prescribe a small minimum value for the variance. However, in practice this minimum value can be too low sometimes leading to large areas with too little cloud fraction. To address this problem Geert Lenderink and Pier Siebesma came up with the idea of an extra variance term proportional to the saturation specific humidity. In principle this extra term adds characteristics of an old-fashioned relative humidity scheme to a statistical cloud scheme (personal communication Pier Siebesma). In a relative humidity (RH) scheme cloud cover starts at a certain critical relative humidity value (RHc) and then increases linearly with increasing RH.

Formally the above mentioned correspondence between the extra variance term proportional to q_{sat} and a RH-scheme can be written as follows:

$$Q = \frac{q_t - q_{sat}}{\sigma_s} \tag{9.56}$$

$$NN = f(Q) \tag{9.57}$$

Assume $\sigma_s = \alpha q_{sat} \Rightarrow Q = \frac{q_t - q_{sat}}{\alpha q_{sat}} = \alpha^{-1} RH - \alpha^{-1}$

Where Q is the normalized distance to saturation curve, σ_s is the standard deviation of s, NN is the cloud fraction, and α is a constant. Note that in the text we use the word ‘variance’ instead of ‘standard deviation’ (being the root of the variance). Now suppose that significant cloud cover starts at $Q = -2$, then $RH_c = 1 - 2\alpha$. Here we assume that $\alpha = 0.02$ which corresponds to $RH_c = 96\%$. Normally some turbulence will be present near the surface but at the same time q_{sat} is relatively large in the lower part of the atmosphere, therefore the extra "q_{sat}" variance contribution is multiplied by a function of height which reduces the influence in the lower troposphere (note that also RH-schemes are height-dependent). Details of this function are not discussed here.

9.3 Treatment of mixed-phase clouds

9.3.1 Definition of new conservative variables

The standard Meso-NH sub-grid condensation scheme computes the turbulent fluxes in a moist atmosphere assuming a reversible condensation/evaporation process for non-precipitating cloud droplets. The inclusion of the ice phase leads to a generalization of the scheme to mixed-phase clouds. This is done using new quasi-conservative variables. First, the total *non precipitating* mixing ratio is redefined by

$$r_{np} = r_v + r_c + r_i, \tag{9.58}$$

where the additional term r_i is the non-precipitating pristine ice mixing ratio. Second, the ice-liquid potential temperature, θ_{il}, is substituted for θ_l which is only applicable to warm clouds

$$\theta_{il} = \theta - \frac{L_v}{C_{ph}} {\Pi_{ref}}^{-1} r_c - \frac{L_s}{C_{ph}} {\Pi_{ref}}^{-1} r_i, \tag{9.59}$$

where L_s is the latent heat of sublimation of ice and with the usual definition of C_{ph}. Note that r_{np} and θ_{il} still revert to r_v and θ in a cloudless atmosphere so the moist turbulence scheme can be employed with only slight modifications to account for the presence of the ice phase.

9.3.2 Some weighted thermodynamical functions

In most of the cases, a simple weighting function $f_{ice} = \dfrac{r_i}{r_c + r_i}$ is sufficient to update some ancillary thermodynamical functions from their "warm cloud" definition. For instance the mixed-phase saturation mixing ratio is defined by the barycentric formula $r_{vs}(T) = (1 - f_{ice}) r^l_{vs}(T) + f_{ice} r^i_{vs}(T)$ with $r^l_{vs}(T)$ and $r^i_{vs}(T)$ being the saturation mixing ratios over water and ice, respectively. Consequently, the function $J = \left(\dfrac{\partial r^l_{vs}}{\partial \theta}\right)_{\theta_{il}}$ which is introduced in the warm cloud case ($J \equiv J_l$)

becomes

$$J \equiv J_{il} = (1 - f_{ice})J_l + f_{ice}J_i, \tag{9.60}$$

where $J_i = \dfrac{r^i_{vs}(T_{il})L_s}{R_v T_{il}\theta_{il}}$. The same approximation is made for the function M, for the stability functions ϕ_i and ψ_i, and hence for the resulting A_{moist} and A_θ functions. We recall that the assumption of saturation mixing ratio is always made when a cloud is present (although this may not be accurate in the case of cold ice clouds where a significant degree of supersaturation over ice can be found), so:

$$r_c + r_i = \frac{r_{np} - r_{vs}(\theta_l)}{1 + M}, \tag{9.61}$$

with a new definition of M which can be derived analytically as $M \equiv M_{il} = J_{il}\dfrac{L_v(1 - f_{ice}) + L_s f_{ice})}{C_{ph}}\Pi^{-1}_{ref}$.

9.3.3 Ice and liquid fluxes

Then we need to compute the divergence of the turbulent fluxes $\overline{u'_i r'_c}$ and $\overline{u'_i r'_i}$, where u_i can be any of the three components of the velocity. This is done using the same theory developed in the pure warm cloud case but with $r'_{(c+i)} = r'_c + r'_i$

$$\frac{\overline{s' r'_{(c+i)}}}{2{\sigma_s}^2} = \int_{-Q_1}^{+\infty} t(Q_1 + t)G(t)dt\ , \tag{9.62}$$

and with an actualized definition of $s' = \dfrac{r'_{np} - J\theta'_{il}}{2(1 + M)}$ which now incorporates both r'_c and r'_i fluctuations. Q_1 still has its usual meaning. Similar characteristics of the probability distribution $G(t)dt$ are implicitly assumed for liquid and mixed-phase clouds. The current implementation uses the same F_2 function (Bougeault, 1982) used in the warm case, or uses the Gaussian relation in case the Gaussian PDF is used for condensates. The simplest way to partition the liquid and ice turbulent fluxes of condensed material is to consider the following closure

$$\overline{u'_i r'_{(c+i)}} = \lambda_i \frac{\overline{u'_i s'}\ .\ \overline{s' r'_{(c+i)}}}{\sigma^2_s} = \overline{u'_i r'_c} + \overline{u'_i r'_i} \tag{9.63}$$

with $\overline{u'_i r'_c} = (1 - f_{ice})\overline{u'_i r'_{(c+i)}}$ and with $\overline{u'_i r'_i} = f_{ice}\overline{u'_i r'_{(c+i)}}$.

9.3.4 Buoyancy flux

The last point of concern is the computation of the buoyancy term in presence of ice in the TKE equation. The expression of θ_v in Eq. (9.31) is slightly modified when switching from θ_l to θ_{il} and when using the new expression for r_{np}

$$\begin{aligned}
\theta_v &= \theta(1 + \delta\frac{r_v}{1 + r_w} - \frac{r_c + r_i}{1 + r_w} - \frac{r_w - r_v - r_c - r_i}{1 + r_w}) \\
&= \left(\theta_{il} + \frac{L_v}{C_{ph}}{\Pi_{ref}}^{-1} r_c + \frac{L_s}{C_{ph}}{\Pi_{ref}}^{-1} r_i\right) \\
&\times \left(1 + \delta\frac{r_{np}}{1 + r_w} - (1 + \delta)\frac{r_c + r_i}{1 + r_w} - \frac{r_w - r_{np}}{1 + r_w}\right),
\end{aligned} \tag{9.64}$$

where again $\delta = \dfrac{R_v}{R_d} - 1$. The fluctuations of θ_v now depend on both r_c and r_i

$$
\begin{aligned}
\theta'_v \;\approx\; & \delta \frac{\overline{\theta}}{1+\overline{r_w}} r'_{np} \\
+ \; & \left(\frac{L_v}{C_{ph}} \Pi_{ref}{}^{-1} \left(1 + \delta \frac{\overline{r_{np}}}{1+\overline{r_w}} - (1+\delta)\frac{\overline{r_c}+\overline{r_i}}{1+\overline{r_w}} - \frac{\overline{r_w}-\overline{r_{np}}}{1+\overline{r_w}} \right) - (1+\delta)\frac{\overline{\theta}}{1+\overline{r_w}} \right) r'_c \\
+ \; & \left(\frac{L_s}{C_{ph}} \Pi_{ref}{}^{-1} \left(1 + \delta \frac{\overline{r_{np}}}{1+\overline{r_w}} - (1+\delta)\frac{\overline{r_c}+\overline{r_i}}{1+\overline{r_w}} - \frac{\overline{r_w}-\overline{r_{np}}}{1+\overline{r_w}} \right) - (1+\delta)\frac{\overline{\theta}}{1+\overline{r_w}} \right) r'_i \\
+ \; & \left(1 + \delta \frac{\overline{r_{np}}}{1+\overline{r_w}} - (1+\delta)\frac{\overline{r_c}+\overline{r_i}}{1+\overline{r_w}} - \frac{\overline{r_w}-\overline{r_{np}}}{1+\overline{r_w}} \right) \theta'_{il}, \qquad (9.65)
\end{aligned}
$$

After recasting the above expression as $\theta'_v = A^{il}\theta'_{il} + Br'_{np} + C^l r'_c + C^i r'_i$ (see Eq.(9.37)), a good approximation of $\overline{u'_i\theta'_v}$ is deduced

$$\overline{u'_i\theta'_v} \approx E_\theta \overline{u'_i\theta'_{il}} + E_{moist}\overline{u'_i r'_{np}}, \qquad (9.66)$$

where the updated factors $E_\theta = A + CA_\theta$ and $E_{moist} = B + CA_{moist}$ are a function of $A \equiv A^{il}$ (including $\overline{r_i}$) and of $C = (1 - f_{ice})C^l + f_{ice}C^i$.

9.4 Mixing length

No modification is brought for the moment.

9.5 Fractional nebulosity of mixed-phase clouds

Although all ingredients of the ”warm cloud” scheme are available and are directly applicable to mixed-phase clouds, the partial cloudiness N has not yet been tested in this case. Note that N is already coupled to the radiative transfer scheme.

9.6 References

Bechtold, P., J.-P. Pinty and P. Mascart, 1993: The use of partial cloudiness in a warm-rain parameterization: a subgrid-scale precipitation scheme, *Mon. Wea. Rev.*, **121**, 3301-3311.

Betts, A. K., 1973: on precipitating cumulus convection and its parameterization, *Quart. J. Roy. Meteorol. Soc.*, **99**, 178-196.

Bougeault, P. 1981: Modeling the trade-wind cumulus boundary layer. Part I: testing the ensemble cloud relations against numerical data, *J. Atmos. Sci.*, **38**, 2414-2428, 1981.

Bougeault, P., 1982: Cloud-ensemble relations based on the gamma probability distribution for the higher-order models of the planetary boundary layer, *J. Atmos. Sci.*, **39**, 2691-2700.

Bougeault, P., and P. Lacarrère, 1989: Parameterization of orography-induced turbulence in a meso-beta scale model, *Mon. Wea. Rev.*, **117**, 1872-1890.

Chaboureau J.-P., and P. Bechtold, 2002: A simple cloud parameterization derived from cloud resolving model data: Diagnostic and prognostic applications. *J. Atmos. Sci.*, **59**, 2362-2372.

Chaboureau J.-P., and P. Bechtold, 2005: Statistical representation of clouds in a regional model and the impact on the diurnal cycle of convection during Tropical Convection, Cirrus and Nitrogen Oxides (TROCCINOX). *J. Geophys. Res.*, **110**, D17103, doi:10.1029/2004JD005645.

Cuxart, J., P. Bougeault, and J.-L. Redelsperger, 2000: A turbulence scheme allowing for mesoscale and large-eddy simulations. *Quart. J. Roy. Meteor. Soc.*, **126,** 1–30.

Cuijpers, J. W. M. and P. Bechtold, 1995: A Simple Parameterization of Cloud Water Related Variables for Use in Boundary Layer Models, *J. Atmos. Sci.*, **52**, 2486-2490.

Lappen, C.-L., and D. A. Randall, 2001: Toward a unified parameterization of the boundary layer and moist convection. Part I: A new type of mass-flux model. *J. Atmos. Sci.,* **58,** 2021-2036.

Mellor, G. L., 1977: The Gaussian cloud model relations. *J. Atmos. Sci.,* **34,** 356-358.

Sommeria, G. and J. W. Deardorff, 1977: Subgrid scale condensation in models for non precipitating clouds, *J. Atmos. Sci.*, **34**, 344-355.

de Rooy, Wim and de Bruijn, Cisco and Tijm, Sander and Neggers, Roel and Siebesma, Pier and Barkmeijer, Jan, 2010: Experiences with Harmonie at KNMI, *HIRLAM Newsletter*, **56,** 19-29.

Chapter 10

Electrical Scheme

Contents

As in a storm most of the electric charges are carried out by the hydrometeors, there are strong links between the electrical state and the cloud microphysics. Consequently the present electrification scheme is highly related to the ICE3/ICE4 scheme described in Chapter 6 of this book ”Microphysical Scheme for Atmospheric Ice”.

10.1 Cloud electrification

10.1.1 Electrical variables

Electric charges are carried by hydrometeors (cloud water, rain, pristine ice, snow, graupel and hail) and ions, so they are submitted to the dynamical and microphysical processes. Consequently, it is necessary to have a prognostic equation for the charge density (q_x, in C kg^{-1}) of each hydrometeor category:

$$\frac{\partial}{\partial t}(\rho_{dref} q_x) + \nabla \cdot (\rho_{dref} q_x \boldsymbol{U}) = \rho_{dref}(S_x^q + T_x^q) \tag{10.1}$$

where $\boldsymbol{U}$ is the 3D air velocity. The source terms S_x^q include the turbulence diffusion, the charging mechanism rates, the charge sedimentation by gravity and the charge neutralization by lightning flashes. T_x^q is the transfer rates due to the microphysical evolution of the particles (see Section 10.2). We assume the individual charge density follows a power law relationship depending on the particle diameter D_x:

$$q_x(D_x) = e_x D^{f_x} \tag{10.2}$$

The values of the coefficients f_x are those found by Beard and Ochs (1986). They are given in Table 10.1.

Parameters	r_i	r_s	r_g	r_h	r_c	r_r
f	0.5	1.3	2.0	2.0	0.5	1.3

Table 10.1: Beard and Ochs (1986) coefficients.

e_x can be calculated using:

$$e_x = \frac{q_x}{N_x M(f_x)} \tag{10.3}$$

The charge density of each microphysical species q_x is a prognostic variable obtained by integrating the individual charge density over the hydrometeor x number concentration:

$$q_x = \int_0^{+\infty} q_x(D_x) n_x(D_x) dD_x = e_x N_x M_x(f_x) \tag{10.4}$$

The total charge density is the sum of the individual charge density:

$$q_{tot} = q_v + q_c + q_r + q_i + q_s + q_g + q_h \tag{10.5}$$

10.1.2 Non-inductive charging mechanism

Even if the physical explanations are still unclear, laboratory studies (Takahashi 1978; Jayaratne et al. 1983; Saunders et al. 1991; Avila et al. 1995; Saunders and Peck 1998, among others) show indeed that the non-inductive (NI) charging mechanism after rebounding collisions between small unrimed and big rimed ice particles is likely the dominant process for charge separation that must be considered at first. Four different parameterizations of the non-inductive mechanism are available in Meso-NH. They result from the published works of Takahashi (1978), Gardiner et al. (1985), Saunders et al. (1991), Saunders and Peck (1998), Tsenova and Mitzeva (2009) and Tsenova and Mitzeva (2011). For each colliding event, the polarity and quantity of separated charge are given as a function of the temperature and the liquid water content or riming rate. This concerns only three types of collision: pristine ice-snow, pristine ice-graupel and snow-graupel. Hail is not efficient to generate electric charges in Meso-NH because these particles are supposedly wrapped by a film of water (Saunders and Brooks 1992). The analytical expressions of the charging rates relies heavily on the microphysical scheme:

$$\frac{\partial q_{xy}}{\partial t} = \int_0^{+\infty} \int_0^{+\infty} \frac{\pi}{4} \delta q (1 - E_{xy})(D_x + D_y)^2 |V_x - V_y| n_x(D_x) n_y(D_y) dD_x dD_y \tag{10.6}$$

with D_x and D_y the diameter for species x and y, respectively. $|V_x - V_y|$ is the relative fall speed, n_x and n_y are the number concentrations of species x and y, respectively, and E_{xy} is the collection efficiency. The collection efficiency depends on the temperature and follows Kajikawa and Heymsfield (1989) for ice-snow and snow-graupel collisions, and Mansell et al. (2005) for ice-graupel collisions. Differents parameterizations of this mechanism are coded in Meso-NH.

Helsdon and Farley (1987) parameterization

It is the simplest parameterization of the non-inductive mechanism. It only takes into account the dependence of the charge exchanged with the temperature and the type of colliding hydrometeors.

The temperature charge reversal (TCR) is constant and fixed to -10°C. During a pristine ice-graupel collision, the charge δq_{NI}^{H} gained by the larger particle is:

$$\delta q_{NI}^{H} = \begin{cases} 2 \times 10^{-15} C & \text{if } T > TCR \\ -2 \times 10^{-15} C & \text{if } T \leq TCR \end{cases} \tag{10.7}$$

For snow-graupel collisions, the charge exchanged is:

$$\delta q_{NI}^{H} = \begin{cases} 2 \times 10^{-13} C & \text{if } T > TCR \\ -2 \times 10^{-13} C & \text{if } T \leq TCR \end{cases} \tag{10.8}$$

And for pristine ice-snow collisions:

$$\delta q_{NI}^{H} = \begin{cases} 2 \times 10^{-14} C & \text{if } T > TCR \\ -2 \times 10^{-14} C & \text{if } T \leq TCR \end{cases} \tag{10.9}$$

Takahashi (1978) parameterization

Laboratory studies of Takahashi (1978) are multiplied by a factor that depends on temperature, liquid water content, particles size and terminal velocity (Takahashi 1984). The sign and the amplitude of the charge exchanged are given by:

$$\delta q_{NI}^{T} = f_T(T, LWC) \mathrm{Min} \left[10, 5 \left(\frac{\mathrm{D_{i,s}}}{\mathrm{D_0}} \right)^2 \frac{|\mathrm{v_g} - \mathrm{v_{i,s}}|}{\mathrm{v_0}} \right] \tag{10.10}$$

where $f_T(T, LWC)$ results from an interpolation of the Takahashi's look-up table (Wojcik 1994; Mansell 2000). It gives the charge exchanged in function of the temperature and the liquid water content (Figure 10.1). $D_{i,s}$ is the diameter of the smaller particle (pristine ice or snow), v_g and $v_{i,s}$ are the terminal velocity of graupel and of the smaller particle, respectively. D_0 and v_0 are set to 10^{-4} m and 8 m s^{-1}, respectively.

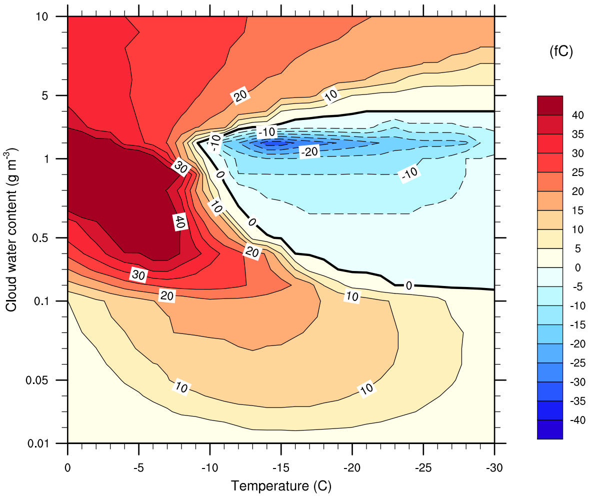

Figure 10.1: Plot of charge transfer as a function of the temperature and the liquid water content (adapted from Takahashi (1978)).

Gardiner et al. (1985) parameterization

This parameterization uses the works of Jayaratne et al. (1983). The charge transfered to the graupel when it collides with an ice particle or with an aggregate is given by:

$$\delta q_{NI}^{G} = k_q D_i^m (\Delta v_{gi})^n (LWC - LWC_{crit}) f(\Delta T) \tag{10.11}$$

where k_q is equal to 73, and m and n are fixed to 4 and 3, respectively. LWC_{crit} is the critical liquid water content that is fixed to 0.1 g m^{-3}. $D_{i,s}$ is the ice crystal diameter and Δv_{gi} is the relative impact velocity. $f(\Delta T)$ is :

$$f(\Delta T) = a\Delta T^3 + b\Delta T^2 + c\Delta T + d \tag{10.12}$$

a = -1.7 $\times 10^{-5}$, b = -0.003, c = -0.05 and d = 0.13 if δq is in fC. ΔT = T - 273.15 if $T < 273.15$ K. This function becomes zero for a temperature equal to -21°C. However, to allow the temperature of charge reversal to vary, Ziegler et al. (1991) changed ΔT into τ with $\tau = (-21/T_r)(T - 273.15)$.

Saunders et al. (1991) parameterization

It is based on laboratory experiments covering a large range of values for temperature, liquid water content and particles sizes and terminal velocities. The expression of the charge exchanged is similar to the one of Gardiner et al. (1985):

$$\delta q_{NI}^{S91} = B D_i^m (\Delta v_{gi})^n \delta Q \tag{10.13}$$

The values of the constants m, n and B are given in Table 10.2.

Crystal size (μ m)	Situation	B	m	n
d < 155	+	4.92×10^{13}	3.76	2.5
155 < d ≤ 452	+	4.04×10^{6}	1.90	2.5
d > 452	+	52.80	0.44	2.5
d ≤ 253	-	5.24×10^{8}	2.54	2.8
d > 253	-	24.00	0.50	2.8

Table 10.2: Values of constants B, m and n used in the equation of the charge transfer (Saunders et al. 1991).

An equation describing the charge exchanged in function of the temperature and the effective liquid water content (EW, in g m^{-3}) corresponds to each region of the graph $\delta Q(T, EW)$ (Figure 10.2). EW is the effective liquid water content. It is equal to the liquid water content times the drop collision efficiency. EW is used instead of LWC because the charge transfer mechanism is dependant on the rate of capture of the droplets rather than the liquid water content in the cloud. The critical liquid water content, CEW, is defined as :

$$CEW = -0.49 - 6.64 \times 10^{-2} T \tag{10.14}$$

where T is given in °C.

The equations describing each region of the graph are given in Table 10.3. In region S1, there is no

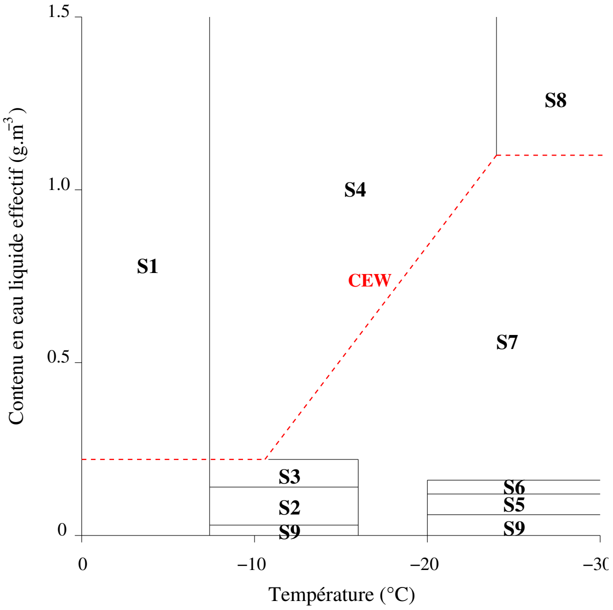

Figure 10.2: Graphical representation of the regions of charge transfer as a function of temperature and effective liquid water content (Helsdon et al. (2001) adapted from Saunders et al. (1991)).

laboratory results for temperature higher than -7.35°C. So, the values of δQ at -7.35°C are linearly interpolated until 0°C. At T = 0°C, the charge tranfer is null. This interpolation concerns regions S1, S2, S3 and S9 :

$$\begin{aligned} \delta Q_{S1} &= (-2.75 \times EW - 0.007) \times T \\ \delta Q_{S3} &= (-57.06 \times EW + 12.60) \times T \\ \delta Q_{S2} &= (42.78 \times EW - 1.08) \times T \\ \delta Q_{S9} &= 0 \end{aligned} \tag{10.15}$$

Saunders and Peck (1998) parameterization

Brooks et al. (1997) reexamined the results of Saunders et al. (1991) laboratory experiments, but transformed the effective liquid water content (EW) into the rime accretion rate (RAR, in g m^{-2} s^{-1}):

$$RAR = EW \times V$$

with V the relative velocity of the two particles (x and y) experiencing collision. In Meso-NH, the rime accretion rate is defined by:

$$RAR = \rho_{air} \times r_c \times E_{cg} \times |V_{xmean} - V_{ymean}| \text{ with } V_{mean} = \frac{\int_0^{+\infty} V(D)m(D)n(D)dD}{\int_0^{+\infty} m(D)n(D)dD} \tag{10.16}$$

E_{cg} represents the collection efficiency of cloud droplets by graupel, and V_{mean} is the mean fall speed of the considered particle. The charge exchanged (in fC) during an elastic collision between two ice particles is the same as in the parameterization of Saunders et al. (1991):

$$\delta q_{NI}^{SP98} = BD^m (\Delta v)^n \delta Q \tag{10.17}$$

D is the diameter of the smallest particle (m), Δv is the relative fall speed (m s^{-1}). The m, n and B coefficients are the same as for Saunders et al. (1991) (see Table 10.2). The critical rime accretion

Equation number	Charge transfer equation
S1	values linearly interpolated
S2	$\delta Q = -314.40 \times EW + 7.92$
S3	$\delta Q = 419.40 \times EW - 92.64$
S4	$\delta Q = 20.22 \times EW + 1.36 \times T + 10.05$
S5	$\delta Q = 2041.76 \times EW - 128.70$
S6	$\delta Q = -2900.22 \times EW + 462.91$
S7	$\delta Q = 3.02 - 31.76 \times EW + 26.53 \times EW^2$
S8	$\delta Q = 20.22 \times EW - 22.26$
S9	$\delta Q = 0.0$

Table 10.3: Charge transfer equations from Saunders et al. (1991).

rate (RAR_{crit}, in g m^{-2} s^{-1}) is the RAR above which the biggest particle charges positively and below which it charges negatively:

$$RAR_{crit} = a + bT + cT^2 + dT^3 + eT^4 + fT^5 + gT^6 \tag{10.18}$$

$a = 1.0$, $b = 7.9262 \times 10^{-2}$, $c = 4.4847 \times 10^{-2}$, $d = 7.4754 \times 10^{-3}$, $e = 5.4686 \times 10^{-4}$, $f = 1.6737 \times 10^{-5}$ et $g = 1.7613 \times 10^{-7}$.

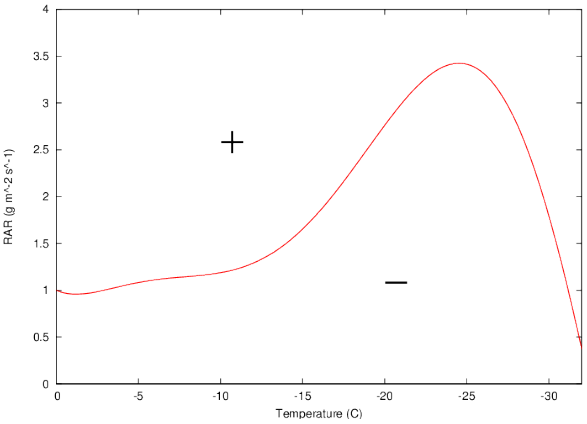

Figure 10.3: Plot of the critical rime accretion rate curve (red line) used in the Saunders and Peck (1998) noninductive ice-ice parameterization. Graupel charges positively at rime accretion rates above the curve and negatively below.

The charge transfered per collision (δQ, in fC) depends on the temperature and the rime accretion rate. Since the original equations of Saunders and Peck (1998) are only valid for temperatures between -8°C and -23°C, the parameterization of Saunders and Peck (1998) is adapted, partially following Mansell et al. (2005).
For $RAR < RAR_{crit}$, Equation (20) of Mansell et al. (2005) is used to extend the application of the charge separation regime to RAR between 0.1 and 0.3 g m^{-2} s^{-1}.

$$\delta Q = 3.9(RAR_{crit} - 0.1) \times \left(4 \left[\frac{RAR - (RAR_{crit} + 0.1)/2}{RAR_{crit} - 0.1} \right]^2 - 1 \right) \tag{10.19}$$

For $RAR > RAR_{crit}$, the original formula of Saunders and Peck (1998) is kept. Outside the temperature range of -8°C to -23°C where the original Saunders and Peck (1998) scheme is strictly valid, the charging rate is linearly decreased to zero at 0(-40)°C from the computed value at -8(-23)°C, as suggested by Mansell et al. (2005). Then for $RAR > RAR_{crit}$ and $T < -8$°C:

$$\delta Q = 6.74RAR - 1.36(-T) + 10.05 \tag{10.20}$$

while for $RAR > RAR_{crit}$ and $T > -8$°C:

$$\delta Q = -(6.74RAR - 0.83) \times \frac{(T - T_t)}{8} \tag{10.21}$$

Charging is set to 0 for $RAR < 0.1$ g m^{-2} s^{-1}.

Brooks et al. (1997) parameterization

This parameterization uses the original parameterization of non-inductive charging proposed in Brooks et al. (1997), where the separated charge in Saunders et al. (1991) is calculated by means the rime accretion rate RAR. The critical liquid water content, $CRAR$, is defined as :

$$CRAR = -1.47 - 0.2 \times T \tag{10.22}$$

The equations of Brooks et al. (1997) describing each region of the graph are given in Table 10.4.

Equation number	Charge transfer equation
S1	values linearly interpolated
S2	$\delta Q = -104.8 \times RAR + 7.92$
S3	$\delta Q = 139.8 \times RAR - 92.64$
S4	$\delta Q = 6.74 \times RAR + 1.36 \times T + 10.05$
S5	$\delta Q = 680.6 \times RAR - 128.70$
S6	$\delta Q = -966.73 \times RAR + 462.91$
S7	$\delta Q = 3.02 - 10.59 \times RAR + 10.59 \times RAR^2$
S8	$\delta Q = 6.74 \times RAR - 22.26$
S9	$\delta Q = 0.0$

Table 10.4: Charge transfer equations from Brooks et al. (1997).

The values of δQ at -7.35°C are linearly interpolated until 0°C. At T = 0°C, the charge transfer is null. This interpolation concerns regions S1, S2, S3 and S9:

$$\begin{array}{lcl} \delta Q_{S1} & = & (-0.9 \times RAR - 0.007) \times T \\ \delta Q_{S3} & = & (-19.02 \times RAR + 12.60) \times T \\ \delta Q_{S2} & = & (14.26 \times RAR - 1.08) \times T \\ \delta Q_{S9} & = & 0 \end{array} \tag{10.23}$$

Tsenova and Mitzeva (2009) parameterization of Takahashi (1978) laboratory results

This parameterization uses the work of Tsenova and Mitzeva (2009) where empirical equations for sign and magnitude of separated charge obtained by Takahashi (1978) are proposed. The sign and amplitude of the charge exchanged are expressed according to Saunders et al. (1991):

$$\delta q_{NI}^{T09} = BD_i^m (\Delta v_{gi})^n \delta Q \tag{10.24}$$

Crystal size (μ m)	Situation	B	m	n
d < 155	+	6.1×10^{12}	3.76	2.5
155 < d $\leq$ 452	+	5×10^{5}	1.90	2.5
d > 452	+	6.5	0.44	2.5
d $\leq$ 253	-	4.3×10^{7}	2.54	2.8
d > 253	-	2	0.50	2.8

Table 10.5: Values of constants B, m and n proposed by Tsenova and Mitzeva (2009) to be used in the equation of the charge transfer obtained in Takahashi (1978).

The values of the constants m, n and B are given in Table 10.5.
(1) For $T >$ -10°C:

- at $EW <= 1.6$ g m^{-3}:

$$\begin{aligned}
\delta Q &= 146.981 \times EW - 116.37 \times EW^2 + 29.762 \times EW^3 \\
&\quad -0.03 \times T^3 \times EW - 2.581 \times T - 0.0209 \times T^3 \times EW^3 \\
&\quad +0.356 \times T^3 \times EW^2 + 0.15 \times T^2 + 2.918 \times T \times EW^3 \\
&\quad -4.215 \times T \times EW - 8.5059
\end{aligned} \tag{10.25}$$

- at $EW > 1.6$ g m^{-3}:

$$\begin{aligned}
\delta Q &= 4.179 \times T - 0.0045 \times T^2 \times EW^2 + 0.916 \times EW^2 \\
&\quad -1.333 \times T \times EW - 7.465 \times EW + 0.109 \times T \times EW^2 \\
&\quad +0.0006 \times T^2 \times EW^3 - 0.035 \times EW^3 + 50.845
\end{aligned} \tag{10.26}$$

(2) For $T <=$ -10°C:

- at $EW <= 0.4$ g m^{-3}:

$$\begin{aligned}
\delta Q &= -3.35 \times T + 95.9 \times T \times EW^2 + 511.83 \times EW \\
&+ 17.45 \times T^2 \times EW^3 - 0.0007 \times T^3 + 20.57 \times T \times EW \\
&\quad +0.165 \times T^2 \times EW + 0.495 \times T^3 \times EW^3 - 0.098 \times T^3 \times EW^2 \\
&\quad +67.46 \times T \times EW^3 - 0.107 \times T^2 - 24.5715
\end{aligned} \tag{10.27}$$

- at 0.4 g m^{-3} $< EW <=$ 3.2 g m^{-3}:

$$\begin{aligned}
\delta Q &= -1.567 \times T \times EW + 0.248 \times T \times EW^3 + 0.01 \times T^3 \\
&\quad +19.2 \times T + 0.805 \times T^2 + 5.97 \times EW^3 - 83.39 \times EW \\
&\quad +15.36 \times EW^2 + 167.93
\end{aligned} \tag{10.28}$$

- at $EW > 3.2$ g m^{-3}:

$$\delta Q = 4.213 \times T - 0.831 \times T \times EW + 0.067 \times T \times EW^2 + 0.004 \times T^2 \times EW + 40.964 \tag{10.29}$$

Tsenova and Mitzeva (2011) parameterization of Takahashi (1978) laboratory results

This parameterization uses the work of Tsenova and Mitzeva (2011) where empirical equations for sign and magnitude of separated charge obtained by Takahashi (1978) using the rime accretion rate (RAR) are proposed.
(1) For $T >$ -10°C:

- at $RAR <=$ 12.8 g m^{-2} s^{-1}:

$$\begin{aligned}\delta Q &= 18.37\times RAR - 1.82\times RAR^2 - 0.06\times RAR^3\\ &-0.004\times T^3\times RAR - 2.581\times T + 0.0004\times T^3\times RAR^3\\ &+0.006\times T^3\times RAR^2 + 0.15\times T^2 + 0.006\times T\times RAR^3\\ &-0.53\times T\times RAR - 8.5059 \qquad (10.30)\end{aligned}$$

- at $RAR >$ 12.8 g m^{-2} s^{-1}:

$$\begin{aligned}\delta Q &= 4.179\times T - 0.00007\times T^2\times RAR^2 + 0.01\times RAR^2\\ &-0.17\times T\times RAR - 0.93\times RAR + 0.002\times T\times RAR^2\\ &+0.000001\times T^2\times RAR^3 - 0.00007\times RAR^3 + 50.845 \qquad (10.31)\end{aligned}$$

(2) For $T <=$ -10°C:

- at $RAR <=$ 3.2 g m^{-2} s^{-1}:

$$\begin{aligned}\delta Q &= -3.35\times T + 1.5\times T\times RAR^2 + 63.98\times RAR\\ &+0.03\times T^2\times RAR^3 - 0.0007\times T^3 + 2.57\times T\times RAR\\ &+0.02\times T^2\times RAR + 0.001\times T^3\times RAR^3 - 0.002\times T^3\times RAR^2\\ &+0.13\times T\times RAR^3 - 0.107\times T^2 - 24.5715 \qquad (10.32)\end{aligned}$$

- at 3.2 g m^{-2} s^{-1} $< RAR <=$ 25.6 g m^{-2} s^{-1}:

$$\begin{aligned}\delta Q &= -0.2\times T\times RAR + 0.0005\times T\times RAR^3 + 0.01\times T^3\\ &+19.2\times T + 0.805\times T^2 + 0.01\times RAR^3 - 10.42\times RAR\\ &+0.24\times RAR^2 + 167.93 \qquad (10.33)\end{aligned}$$

- at $RAR >$ 25.6 g m^{-2} s^{-1}:

$$\delta Q = 4.213\times T - 0.1\times T\times RAR + 0.001\times T\times RAR^2 + 0.0005\times T^2\times RAR + 40.964 \qquad (10.34)$$

Limitations of the charge exchanged per collision As in Mansell et al. (2005), the charge exchanged per rebounding collision δq is limited to prevent unreasonable charging rate. Based on Keith and Saunders (1990), it is assumed that the charging rate of the pristine ice crystal with $D_{max} \sim 100\ \mu$m is the most limiting one, that is 30(10) fC per collision with graupel(aggregate) particles. We take a larger value (100 fC) for the graupel-snow collisions because it corresponds roughly to an average of the saturation levels when the particle sizes reach $\sim$ 1 mm (see Keith and Saunders (1990) or Fig. 3.13 in MacGorman and Rust (1998)). This limitation is introduced in the computation of the bulk charging rates which result from an integration over the size spectrum of the ice particles.

10.1.3 Inductive mechanism

Laboratory studies conducted by Aufdermaur and Johnson (1972) have shown that in the presence of an electric field stronger than a few kV m^{-1} collisions between particles would lead to significant charge exchange. Drop-drop inductive charging is not considered because most of the time the two colliding particles end up with a single bigger drop. Concerning ice-ice inductive charging, the short duration and small size of the contact zone and the low ice electrical conductivity do not allow for a substantial charge exchange when ice particles collide (Illingworth and Caranti 1985). Therefore only bouncing collisions between graupel and droplets are likely needed to be taken into account. Even if the rate of rebounding collisions is low compared to the rate of sticking collisions, the amount of charge separated is important. The inductive charging rate parameterization follows the expression given by Ziegler et al. (1991):

$$\frac{\partial \rho_g(D_g)}{\partial t} = \frac{\pi}{4} E_{cg} E_r D_g^2 V(D_g) N_c \alpha \left[\frac{\pi^3}{2} D_c^2 \epsilon E_z \cos(\theta) - \frac{\pi^2}{6} \rho_g(D_g) \frac{D_c^2}{D_g^2} \right] \tag{10.35}$$

where E_{cg} is the graupel-droplets collision efficiency, E_r the rebound probability, and E_z the vertical component of the electric field. ϵ is the permittivity of air. ρ_g is the graupel charge density, D_c the cloud droplets diameter, and D_g the graupel diameter. V is the fall speed of graupel, and N_c is the number concentration of cloud droplets. The second term of the expression accounts for a preexisting charge polarity of the graupel. Assuming that grazing collisions are the most efficient ones, α is the fraction of droplets experiencing grazing trajectories, and $\cos(\theta)$ is the mean cosine collision angle. E_r, α and $\cos(\theta)$ are set to 0.1, 0.07 and 0.2, respectively, as suggested by Ziegler et al. (1991).

10.2 Charge transfers associated to mass transfers

Once charges are separated by the non-inductive process, they can be exchanged between the different hydrometeor categories during the microphysical processes.

Similarly to the microphysical scheme, the rate of charge exchanged during mass transfer follows:

$$QYCOLXZ = \int_0^{+\infty} \left\{ \int_0^{+\infty} K(D_x, D_y) q_y n_y(D_y) dD_y \right\} n_x(D_x) dD_x \tag{10.36}$$

The kernel K can be written:

$$K(D_x, D_y) = \frac{\pi}{4} (D_x + D_y)^2 |v_x(D_x) - v_y(D_y)| E_{xy} \tag{10.37}$$

E_{xy} is the collection efficiency.

10.2.1 Sedimentation

For precipitating particles (rain, snow, graupel and hail, then X = R, S, G and H), the sedimentation rate of charge density follows:

$$QSEDX = \frac{\partial}{\partial z} \left[\left(\frac{\rho_{00}}{\rho_{dref}} \right)^{0.4} c_x e_x C_x G(d_x + f_x) \lambda^{x-(d_x+f_x)} \right] \tag{10.38}$$

For pristine ice:

$$QSEDI = \frac{\partial}{\partial z} \left[\left(\frac{\rho_{00}}{\rho_{dref}} \right)^{0.4} c_i e_i N_i G(d_i + f_i) \left(\frac{\rho_{dref} r_i}{a_i N_i G(b_i)} \right)^{\frac{d_x+f_x}{b_x}} \right] \tag{10.39}$$

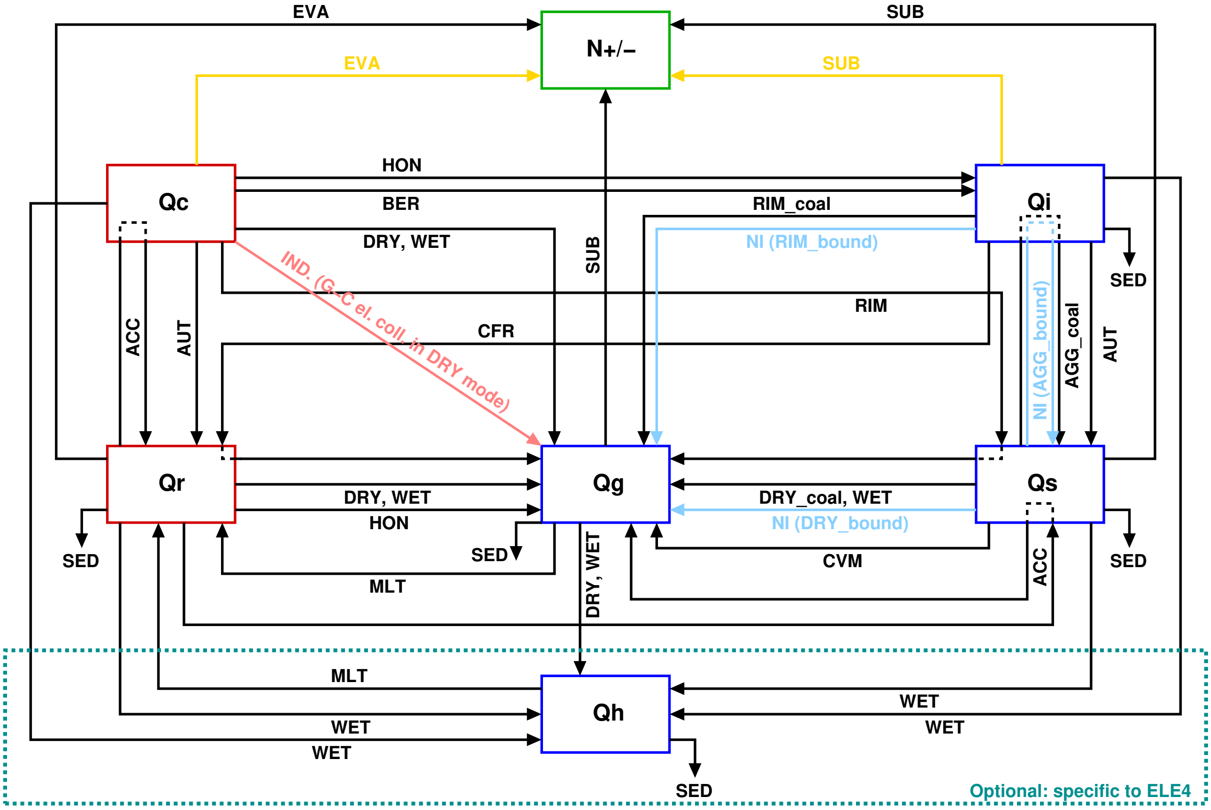

Figure 10.4: Diagram of the electric charge transfers. Black, light blue and pink lines represent charge transfers associated to mass transfers, to the non-inductive mechanisms, and to the inductive mechanism, respectively. The yellow lines show the electric charge transfers treated as an ajustement in ice_adjust_elec.f90. Ion attachment to hydrometeors is not represented in this diagram.

10.2.2 Warm processes

Autoconversion

$$QCAUTR = q_c \frac{RCAUTR}{r_c} \tag{10.40}$$

Accretion

$$QCACCR = q_c \frac{RCACCR}{r_c} \tag{10.41}$$

Evaporation and condensation of rain

$$QREVAV = q_r \frac{RREVAV}{r_r} \tag{10.42}$$

The charge released during rain evaporation is transfered to the ions categories following:

$$n_+ = n_+ + QREVAV/e \quad \text{if} \quad QREVAV > 0 \tag{10.43}$$

$$n_- = n_- - QREVAV/e \quad \text{if} \quad QREVAV < 0 \tag{10.44}$$

10.2.3 Ice nucleation

Heterogeneous nucleation It is considered there is no charge exchanged during this mass transfer.

Homogeneous nucleation For temperatures colder than -35°C, cloud droplets spontaneously freeze and are transfered to the ice crystals category. If $P \approx J_{HOM}(T)V\Delta t$ is the probability for a cloud droplet with volume V to freeze during Δt, the charge exchanged during this process can be computed in the same manner as for the microphysical process:

$$\begin{aligned} QCHONI &= \int_0^{+\infty} q_c P M_c(D_c) dD_c \\ &= \frac{\pi}{6} J_{HOM} \rho r_c \frac{e_c}{a_c} \frac{G(f_c+3)}{G(b_c)} \lambda^{b_c-(f_c+3)} \end{aligned} \tag{10.45}$$

a$_c$ is the proportionality factor in the mass-diameter relation ($a_c = 1000 \times \frac{\pi}{6}$). Moments are computed using: λ_c = 1.1 × 10^5 m^{-3}, α_c = 3 and ν_c = 1.

Homogeneous nucleation For temperatures lower than -35°C, raindrops freeze spontaneously.

$$\begin{aligned} QRHONG &= q_r H(T_t - 35) \\ &= q_r \frac{RRHONG}{r_r} \end{aligned} \tag{10.46}$$

10.2.4 Bergeron-Findeisen effect

$$QCBERI = q_c \frac{RCBERI}{r_c} \tag{10.47}$$

However, the charge exchanged during this process is too high. Then QCBERI is reduced to 1% of its value.

10.2.5 Water vapor deposition on snow and graupel

$$QSSUBV = q_s \frac{RSSUBV}{r_s} \tag{10.48}$$

$$QGSUBV = q_g \frac{RGSUBV}{r_g} \tag{10.49}$$

RSSUBV and RGSUBV are the negative part of the mass transfer rate during vapor deposition. The charge released during the graupel/snow ($x = G/S$) sublimation is transfered to the ions categories following:

$$n_+ = n_+ + \frac{QxSUBV}{e} \text{ if } QxSUBV > 0 \tag{10.50}$$

$$n_- = n_- - \frac{QxSUBV}{e} \text{ if } QxSUBV < 0 \tag{10.51}$$

10.2.6 Autoconversion of pristine ice and formation of snow

$$QIAUTS = q_i \frac{RIAUTS}{r_i} \tag{10.52}$$

10.2.7 Contact freezing of rain and formation of graupel

This is a 3-species mechanism. The collision between ice crystal and raindrop produces frozen drops. If the pristine ice fall speed can be neglected compared to the raindrop fall speed, then the charge lost by raindrops is:

$$\begin{aligned} QRCFRIG &= \int_0^{+\infty} \left[\int_0^{+\infty} K(D_r, D_i) n_r(D_r) q_r(D_r) dD_r \right] n_i(D_i) dD_i \\ &= \frac{\pi}{4} C_r N_i c_r e_r \left(\frac{\rho_{00}}{\rho_{dref}} \right)^{0.4} G_r(d_r + f_r + 2) \lambda_r^{x_r - (d_r + f_r + 2)} \end{aligned} \tag{10.53}$$

And the charge lost by pristine ice is:

$$\begin{aligned} QICFRRG &= \int_0^{+\infty} \left[\int_0^{+\infty} K(D_r, D_i) n_i(D_i) q_i(D_i) dD_i \right] n_r(D_r) dD_r \\ &= q_i \frac{\pi}{4} C_r \lambda_r^{x_r} c_r \left(\frac{\rho_{00}}{\rho_{dref}} \right)^{0.4} G_r(d_r + 2) \lambda_r^{d_r + 2} \\ &= q_i \frac{RICFRRG}{r_i} \end{aligned} \tag{10.54}$$

10.2.8 Aggregation of pristine ice on snow

$$QIAGGS = QIAGGS_{bound} + QIAGGS_{coal} \tag{10.55}$$

Case with coalescence

$$QIAGGS_{coal} = \int_0^{+\infty} \left\{ \int_0^{+\infty} \frac{\pi}{4} (D_i + D_s)^2 |v_i(D_i) - v_s(D_s)| E_{is} q_i n_i(D_i) dD_i \right\} n_s(D_s) dD_s$$

The ice-snow collection efficiency takes the form: $E_{is} = 0.25 \exp[0.005(T - T_t)]$. The pristine ice diameter (fall speed) can be neglected compared to the snow diameter (fall speed):

$$\begin{aligned} QIAGGS_{coal} &= \int_0^{+\infty} \left\{ \int_0^{+\infty} \frac{\pi}{4} D_s^2 v_s(D_s) E_{is} q_i n_i(D_i) dD_i \right\} n_s(D_s) dD_s \\ &= q_i \frac{RIAGGS}{r_i} \end{aligned} \tag{10.56}$$

Case with elastic collision If ice crystals and snow particles experience elastic collisions, this is considered as part of the non-inductive mechanism. The same approximations about diameter and fall speed as in the case with coalescence can be done.

$$\begin{aligned} QIAGGS_{boun} &= \int_0^{+\infty} \left\{ \int_0^{+\infty} \frac{\pi}{4} (D_i + D_s)^2 |v_i(D_i) - v_s(D_s)| (1 - E_{is}) q_i n_i(D_i) dD_i \right\} n_s(D_s) dD_s \\ &= \frac{\pi}{4} (1 - E_{is}) c_s \left(\frac{\rho_{00}}{\rho_{dref}} \right)^{0.4} \int_0^{+\infty} D_s^{(2+d_s)} \left[\int_0^{+\infty} q_i n_i(D_i) dD_i \right] n_s(D_s) dD_s \end{aligned} \tag{10.57}$$

Different parameterizations are available for this process.

1. **Helsdon and Farley (1987)**

   For a snow-ice collision, $\delta q_{is} = 2.10^{-15}$C, then:

$$\begin{aligned} QIAGGS_{boun} &= \frac{\pi}{4}(1-E_{is})c_s\left(\frac{\rho_{00}}{\rho_{dref}}\right)^{0.4}\delta q_{is}N_i\int_0^{+\infty}D_s^{(2+d_s)}n_s(D_s)dD_s \\ &= \frac{1-E_{is}}{E_{is}}RIAGGS\frac{\delta q_{is}}{r_i}N_i \end{aligned} \tag{10.58}$$

2. **Takahashi (1978)**

$$\begin{aligned} QIAGGS_{boun} &= \frac{\pi}{4}(1-E_{is})c_s\left(\frac{\rho_{00}}{\rho_{dref}}\right)^{0.4}\int_0^{+\infty}D_s^{(2+d_s)}\left[\int_0^{+\infty}f(T,LWC)\times\right. \\ &\left.\mathrm{Min}\left(10,5\left(\frac{D_i}{D_0}\right)^2\frac{|v_s-v_i|}{v_0}\right)n_i(D_i)dD_i\right]n_s(D_s)dD_s \end{aligned}$$

   It is assumed that $v_i \ll v_s$:

$$\begin{aligned} QIAGGS_{boun} &= \frac{\pi}{4}(1-E_{is})c_s\left(\frac{\rho_{00}}{\rho_{dref}}\right)^{0.4}f(T,LWC)\int_0^{+\infty}D_s^{(2+d_s)}\left[\int_0^{+\infty}\times\right. \\ &\left.\mathrm{Min}\left(10,5\left(\frac{D_i}{D_0}\right)^2\frac{|v_s-v_i|}{v_0}\right)N_i g(D_i)dD_i\right]n_s(D_s)dD_s \\ &= \frac{\pi}{4}(1-E_{is})\left(\frac{\rho_{00}}{\rho_{dref}}\right)^{0.4}c_sN_iN_sf(T,LWC)\times \\ &\mathrm{Min}\left[10G_s(2+d_s)\lambda_s^{-(2+d_s)},\frac{5c_s}{D_0^2v_0}\left(\frac{\rho_{00}}{\rho_{dref}}\right)^{0.4}G_i(2)\lambda_i^{-2}G_s(2+2d_s)\lambda^{-(2+2d_s)}\right] \end{aligned} \tag{10.59}$$

3. **Gardiner et al. (1985)**

$$\begin{aligned} QIAGGS_{boun} &= \frac{\pi}{4}(1-E_{is})c_s\left(\frac{\rho_{00}}{\rho_{dref}}\right)^{0.4}\int_0^{+\infty}D_s^{(2+d_s)} \\ &\left[\int_0^{+\infty}73D_i^4(v_s-v_i)^3\delta Lf(\tau)n_i(D_i)dD_i\right]n_s(D_s)dD_s \end{aligned}$$

   Since $v_i \ll v_s$:

$$QIAGGS_{boun} = \frac{\pi}{4}(1-E_{is})\left(\frac{\rho_{00}}{\rho_{dref}}\right)^{4\times0.4}c_s^4N_iC_sG_i(4)\lambda_i^{-4}G_s(2+4d_s)\lambda_s^{x_s-(2+4d_s)}73\delta Lf(\tau)\times10^{15} \tag{10.60}$$

4. **SAUNDERS ET AL. (1991), SAUNDERS ET PECK (1998), BROOKS ET AL. (1997), TSENOVA AND MITZEVA (2009, 2011)**

$$\begin{aligned} QIAGGS_{boun} &= \frac{\pi}{4}(1-E_{is})c_s\left(\frac{\rho_{00}}{\rho_{dref}}\right)^{0.4}\int_0^{+\infty} D_s^{(2+d_s)} \\ &\left[\int_0^{+\infty} BD_i^a|v_s-v_i|^b\delta QN_ig(D_i)dD_i\right] n_s(D_s)dD_s \end{aligned}$$

$v_i \ll v_s$ and q only depends on temperature and liquid water content:

$$\begin{aligned} QIAGGS_{boun} &= \frac{\pi}{4}(1-E_{is})\left(\frac{\rho_{00}}{\rho_{dref}}\right)^{0.4(1+b_s)} c_s^{1+b_s}N_iC_sG_i(a_i)\lambda_i^{a_i} \\ &G_s(2+(1+b_s)d_s)\lambda_s^{x_s-2-(1+b_s)d_s}B\delta Q \end{aligned} \tag{10.61}$$

10.2.9 Riming of aggregates

During the riming of aggregates, cloud droplets lose charge at rate:

$$\begin{aligned} QCRIMS &= \int_0^{+\infty}\left[\int_0^{+\infty}\frac{\pi}{4}(D_s+D_c)^2|v_s-v_c|E_{cs}q_cn_c(D_c)dD_c\right]n_s(D_s)dD_s \\ &= q_c\frac{RCRIMS}{r_c} \end{aligned} \tag{10.62}$$

We assume: $v_i \ll v_s$, $D_i \ll D_s$, and E_{cs} = 1. It is also hypothesized that conversion of aggregates into graupels may occur for riming aggregates of size larger than D_{cs}^{lim} = 7 mm (Farley et al. 1989). Thus the charge gained by aggregates during their growth by riming takes the form:

$$\begin{aligned} QCRIMSS &= \int_0^{D_s^{lim}}\left[\int_0^{+\infty}\frac{\pi}{4}(D_s+D_c)^2|v_s-v_c|E_{cs}q_cn_c(D_c)dD_c\right]n_s(D_s)dD_s \\ &= \frac{\pi}{4}\left(\frac{\rho_{00}}{\rho_{dref}}\right)^{0.4}c_sC_s\lambda^{x_s}q_cM(S+d_s;D_s^{lim}) \\ &= q_c\frac{RCRIMSS}{r_c} \end{aligned} \tag{10.63}$$

If $D_s > D_{cs}^{lim}$:

$$\begin{aligned} QCRIMSG &= \int_0^{+\infty}\left[\int_{D_s^{lim}}^{+\infty}\frac{\pi}{4}(D_s+D_c)^2|v_s-v_c|E_{cs}q_cn_c(D_c)dD_c\right]n_s(D_s)dD_s \\ &= QCRIMS - QCRIMSS \\ &= \frac{q_c}{r_c}(RCRIMS - RCRIMSS) \end{aligned} \tag{10.64}$$

10.2.10 Accretion of rain and aggregates

As for the riming of cloud droplets, it is postulated that the collection of small raindrops do not change the structure of an aggregate but larger colliding raindrops reshape it as a graupel. The rate of charge exchanged during the collection of raindrops by snow has the form:

$$QRACCS = \int_0^{+\infty}\left[\int_0^{+\infty}\frac{\pi}{4}(D_s+D_r)^2|v_r-v_s|E_{rs}q_rn_r(D_r)dD_r\right]n_s(D_s)dD_s$$

It is assumed that E_{rs} = 1. Furthermore, as both raindrops and aggregates have significant fall speeds, it is not easy to solve the integrals. They are tabulated in function of λ_r et λ_s.

$$\begin{aligned} QRACCS &= \int_0^{+\infty}\left[\int_0^{+\infty} E_{rs}\frac{\pi}{4}\left(\frac{\rho_{00}}{\rho_{dref}}\right)^{0.4}(D_r+D_s)^2|c_rD_r^{d_r}-c_sD_s^{d_s}|q_rN_rg(D_r)dD_r\right]\times \\ &\quad N_sg(D_s)dD_s \end{aligned}$$

We define:

$$\begin{aligned} \Delta vq_{rs}(\lambda_s,\lambda_r) &= \Lambda q(\lambda_s,\lambda_r)^{-1}\int_0^{+\infty}\left[\int_0^{+\infty} E_{rs}(D_r+D_s)^2|c_rD_r^{d_r}-c_sD_s^{d_s}|D_r^{f_r}g(D_r,\lambda_r)dD_r\right]\times \\ &\quad g(D_s,\lambda_s)dD_s \end{aligned}$$

with:

$$\begin{aligned} \Lambda q(\lambda_s,\lambda_r) &= \int_0^{+\infty}\left[\int_0^{+\infty}(D_r+D_s)^2D_r^{f_r}g(D_r,\lambda_r)dD_r\right]g(D_s,\lambda_s)dD_s \\ &= M_r(2+f_r)+M_s(2)M(f_r)+2M_s(1)M_r(1+f_r) \\ &= G_r(2+f_r)\lambda_r^{-(2+f_r)}+G_s(2)G(f_r)\lambda_s^{-2}\lambda_r^{-f_r} \\ &\quad +2G_s(1)G_r(1+f_r)\lambda_s^{-1}\lambda_r^{-(1+f_r)} \end{aligned} \tag{10.65}$$

Since $q_r(D_r)=e_rD_r^{f_r}$:

$$QRACCS=\frac{\pi}{4}\left(\frac{\rho_{00}}{\rho_{dref}}\right)^{0.4}N_rN_se_r\Delta vq_{rs}(\lambda_s,\lambda_r)\Lambda q(\lambda_s,\lambda_r) \tag{10.66}$$

<u>If $D_r<D_r^{lim}$</u>, the structure of the aggregates is not changed:

$$\begin{aligned} QRACCSS &= \int_0^{+\infty}\left[\int_0^{D_r^{lim}}\frac{\pi}{4}(D_r+D_s)^2|v_r-v_s|E_{rs}q_r(D_r)n_r(D_r)dD_r\right]n_s(D_s)dD_s \\ &= \frac{\pi}{4}\left(\frac{\rho_{00}}{\rho_{dref}}\right)^{0.4}N_sN_re_r\Lambda q(\lambda_s,\lambda_r)\Delta vq_{rss}(\lambda_s,\lambda_r) \end{aligned} \tag{10.67}$$

with :

$$\begin{aligned} \Delta vq_{rss}(\lambda_s,\lambda_r) &= \Lambda q(\lambda_s,\lambda_r)^{-1}\int_0^{+\infty}\left[\int_0^{D_r^{lim}} E_{rs}(D_r+D_s)^2|c_rD_r^{d_r}-c_sD_s^{d_s}|D_r^{f_r}g(D_r,\lambda_r)dD_r\right]\times \\ &\quad g(D_s,\lambda_s)dD_s \end{aligned} \tag{10.68}$$

<u>If $D_r>D_r^{lim}$</u>, the structure of the aggregates is turned into graupel. The rate of charge transfered from rain to graupel is:

$$QRACCSG=QRACCS-QRACCSS \tag{10.69}$$

Since $q_x(D_x)=e_xD_x^{f_x}$, $n_x(D_x)=N_xg(D_x)=C_x\lambda^{x_x}g(D_x)$ and $v_x(D_x)=\left(\frac{\rho_{00}}{\rho_{dref}}\right)^{0.4}c_xD_x^{d_x}$, with x = r or s, the charge lost by aggregates follows:

$$\begin{aligned} QSACCRG &= \int_{D_r^{lim}}^{+\infty}\left[\int_0^{+\infty}\frac{\pi}{4}E_{rs}(D_r+D_s)^2|v_r(D_r)-v_s(D_s)|q_s(D_s)n_s(D_s)dD_s\right]n_r(D_r)dD_r \\ &= \frac{\pi}{4}\left(\frac{\rho_{00}}{\rho_{dref}}\right)^{0.4}N_sN_re_s\Lambda q(\lambda_s,\lambda_r)\Delta vq_{rs}(\lambda_s,\lambda_r) \end{aligned} \tag{10.70}$$

with:

$$\begin{aligned}\Delta vq_{rss}(\lambda_s,\lambda_r) \;&=\; \Lambda q(\lambda_s,\lambda_r)^{-1}\int_{D_r^{lim}}^{+\infty}\left[\int_0^{+\infty} E_{rs}(D_r+D_s)^2|c_rD_r^{d_r}-c_sD_s^{d_s}|D_s^{f_s}g(D_s,\lambda_s)dD_s\right]\times \\ & \quad g(D_r,\lambda_r)dD_r\end{aligned}\tag{10.71}$$

$$\begin{aligned}\Lambda q(\lambda_s,\lambda_r) \;&=\; \int_0^{+\infty}\left[\int_0^{+\infty}(D_r+D_s)^2D_s^{f_s}g(D_s,\lambda_s)dD_s\right]g(D_r,\lambda_r)dD_r \\ &=\; M_s(2+f_s)+M_r(2)M(f_s)+2M_r(1)M_s(1+f_s) \\ &=\; G_s(2+f_s)\lambda_s^{-(2+f_s)}+G_r(2)G(f_s)\lambda_r^{-2}\lambda_s^{-f_s} \\ & \quad +2G_r(1)G_s(1+f_s)\lambda_r^{-1}\lambda_s^{-(1+f_s)}\end{aligned}\tag{10.72}$$

10.2.11 Dry growth of graupel

The charge grained by graupel during their dry growth by collection processes contains the sum of charge gained by graupel during the individual accretion processes that is:

$$QDRYG = QCDRYG + QRDRYG + QIDRYG + QSDRYG \tag{10.73}$$

Dry growth of graupel by collection of cloud droplets

$$\begin{aligned}QCDRYG \;&=\; \int_0^{+\infty}\left[\int_0^{+\infty}K(D_c,D_g)q_c(D_c)n_c(D_c)dD_c\right]n_g(D_g)dD_g \\ &=\; q_c\frac{RCDRYG}{r_c}\end{aligned}\tag{10.74}$$

Dry growth of graupel by collection of raindrops

$$QRDRYG = \int_0^{+\infty}\left[\int_0^{+\infty}\frac{\pi}{4}E_{rg}(D_g+D_r)^2|v_g(D_g)-v_r(D_r)|q_r(D_r)n_r(D_r)dD_r\right]n_g(D_g)dD_g$$

We define $\Delta vq_{rg}(\lambda_g,\lambda_r)$ as:

$$\begin{aligned}\Delta vq_{rg}(\lambda_g,\lambda_r) \;&=\; \Lambda q(\lambda_g,\lambda_r)^{-1}\int_0^{+\infty}\left[\int_0^{+\infty} E_{rg}(D_g+D_r)^2|c_gD_g^{d_g}-c_rD_r^{d_r}|D_r^{f_r}g(D_r,\lambda_r)dD_r\right]\times \\ & \quad g(D_g,\lambda_g)dD_g\end{aligned}\tag{10.75}$$

with:

$$\begin{aligned}\Lambda q(\lambda_g,\lambda_r) \;&=\; \int_0^{+\infty}\left[\int_0^{+\infty}(D_g+D_r)^2D_r^{f_r}g(D_r,\lambda_r)dD_r\right]g(D_g,\lambda_g)dD_g \\ &=\; G_r(2+f_r)\lambda_s^{-(2+f_r)}+2G_r(1+f_r)\lambda_r^{-(1+f_r)}G_g(1)\lambda_g^{-1} \\ & \quad +G_r(f_r)\lambda_r^{-f_r}G_g(2)\lambda_g^{-2}\end{aligned}\tag{10.76}$$

Thus, we obtain:

$$QRDRYG = \frac{\pi}{4}\left(\frac{\rho_{00}}{\rho_{dref}}\right)^{0.4}C_r\lambda_r^{x_r}C_g\lambda_g^{x_g}e_r\Lambda q(\lambda_g,\lambda_r)\Delta vq_{rg}(\lambda_g,\lambda_r)\tag{10.77}$$

Dry growth of graupel by collection of pristine ice

$$QIDRYG = QIDRYG_{coal} + QIDRYG_{boun} \tag{10.78}$$

$QIDRYG_{coal}$ corresponds to the process for which there is collection of pristine ice by graupel, whereas for QIDRYG$_{boun}$ the collection process is not effective.

In the case with coalescence, it is hypothesized that $v_i \ll v_g$:

$$\begin{aligned} QIDRYG_{coal} &= \int_0^{+\infty} \left[\int_0^{+\infty} K(D_i, D_i) q_i(D_i) n_i(D_i) dD_i \right] n_g(D_g) dD_g \\ &= q_i \frac{RIDRYG}{r_i} \end{aligned} \tag{10.79}$$

In the case with elastic collision, we can also assume that $v_i \ll v_g$:

$$\begin{aligned} QIDRYG_{boun} &= \int_0^{+\infty} \left[\int_0^{+\infty} \frac{(1-E_{ig})}{E_{ig}} K(D_i, D_g) \delta q_{ig} n_i(D_i) dD_i \right] n_g(D_g) dD_g \\ &= \int_0^{+\infty} \left[\int_0^{+\infty} \frac{\pi}{4} (1-E_{ig}) (D_i + D_g)^2 |v_g(D_g) - v_i(D_i)| \delta q_{ig} n_i(D_i) dD_i \right] n_g(D_g) dD_g \\ &\simeq \frac{\pi}{4} (1-E_{ig}) c_g N_i N_g \left(\frac{\rho_{00}}{\rho_{dref}} \right)^{0.4} \int_0^{+\infty} D_g^{(2+d_g)} \left[\int_0^{+\infty} \delta q_{ig} g(D_i) dD_i \right] g(D_g) dD_g \end{aligned} \tag{10.80}$$

The solution of this equation depends on the form of δq_{ig} for which different parameterizations exist.

1. **HELSDON ET FARLEY (1987)**

   $\delta q_{ig} = \pm 2 \times 10^{-15}$. The sign depends on the ambient temperature. If the temperature is lower than the temperature charge reversal (TCR), the biggest particle gains a negative charge. The opposite happens if the temperature is higher than the TCR: a positive charge is transfered to the largest particle. Then:

   $$QIDRYG_boun = \frac{(1-E_{ig})}{E_{ig}} N_i \delta q_{ig}(T) \frac{RIDRYG}{r_i} \tag{10.81}$$

2. **TAKAHASHI (1978)**

   δq_{ig} depends on the ice crystal size, on the relative fall speed of the two particles, on the temperature and the liquid water content. Since $v_i \ll v_g$ and $v_g = c_g D_g^{d_g} (\rho_{00}/\rho_{dref})^{0.4}$:

$$\begin{aligned} QIDRYG_{boun} &= \frac{\pi}{4} (1-E_{ig}) c_g N_i N_g \left(\frac{\rho_{00}}{\rho_{dref}} \right)^{0.4} f(T, LWC) \times \\ & \int_0^{+\infty} D_g^{(2+d_g)} \left[\int_0^{+\infty} \mathrm{Min} \left(10, 5 \left(\frac{D_i}{D_0} \right)^2 \frac{v_g}{v_0} \right) g(D_i) dD_i \right] g(D_g) dD_g \\ &= \frac{\pi}{4} (1-E_{ig}) c_g N_i C_g \left(\frac{\rho_{00}}{\rho_{dref}} \right)^{0.4} \lambda_g^{x_g} f(T, LWC) \times \\ & \mathrm{Min} \left[10 G(2+d_g) \lambda_g^{-(2+d_g)}, \frac{5}{D_0^2 v_0} c_g \left(\frac{\rho_{00}}{\rho_{dref}} \right)^{0.4} G_i(2) \lambda_i^{-2} G_g(2+2d_g) \lambda_g^{-(2+2d_g)} \right] \end{aligned} \tag{10.82}$$

3. **Gardiner et al. (1985)**

   In the same way:

$$\begin{aligned}QIDRYG_{boun} &= \frac{\pi}{4}(1-E_{ig})c_gN_iN_g\left(\frac{\rho_{00}}{\rho_{dref}}\right)^{0.4}73(LWC-LWC_c)f(\tau)10^{15}\times\\ &\int_0^{+\infty}D_g^{(2+d_g)}v_g^3\left[\int_0^{+\infty}D_i^4g(D_i)dD_i\right]g(D_g)dD_g\\ &= \frac{\pi}{4}(1-E_{ig})c_g^4N_iC_g\left(\frac{\rho_{00}}{\rho_{dref}}\right)^{4\times0.4}73(LWC-LWC_c)f(\tau)10^{15}\times\\ &G_i(4)\lambda_i^{-4}G_g(2+4d_g)\lambda_g^{x_g-(2+4d_g)} \qquad (10.83)\end{aligned}$$

4. **Saunders et al. (1991), Saunders et Peck (1998), Brooks et al. (1997), Tsenova and Mitzeva (2009, 2011)**

   δq_{ig} is replaced by the equation given by Saunders et al. (1991), and assuming $v_g \gg v_i$:

$$\begin{aligned}QIDRYG_{boun} &= \frac{\pi}{4}(1-E_{ig})c_g^{(1+b_g)}N_iC_g\left(\frac{\rho_{00}}{\rho_{dref}}\right)^{0.4(1+n)}\\ &G_i(m)\lambda_i^{-m}G_g(2+(1+n)d_g)\lambda_g^{x_g-(2+(1+n)d_g)}B\delta Q \qquad (10.84)\end{aligned}$$

Dry growth of graupel by collection of snow

$$QSDRYG = QSDRYG_{coal} + QSDRYG_{boun} \qquad (10.85)$$

We first consider the case with coalescence:

$$QSDRYG_{coal} = \int_0^{+\infty}\left[\int_0^{+\infty}\frac{\pi}{4}E_{sg}(D_g+D_s)^2|v_g(D_g)-v_s(D_s)|q_s(D_s)n_s(D_s)dD_s\right]n_g(D_g)dD_g$$

We define $\Delta vq_{sg}(\lambda_g,\lambda_s)$ as:

$$\begin{aligned}\Delta vq_{sg}(\lambda_g,\lambda_s) &= \Lambda q(\lambda_g,\lambda_s)^{-1}\int_0^{+\infty}\left[\int_0^{+\infty}E_{sg}(D_g+D_s)^2|c_gD_g^{d_g}-c_sD_s^{d_s}|D_s^{f_s}g(D_s,\lambda_s)dD_s\right]\times\\ &g(D_g,\lambda_g)dD_g \qquad (10.86)\end{aligned}$$

with:

$$\begin{aligned}\Lambda q(\lambda_g,\lambda_s) &= \int_0^{+\infty}\left[\int_0^{+\infty}(D_g+D_s)^2D_s^{f_s}g(D_s,\lambda_s)dD_s\right]g(D_g,\lambda_g)dD_g\\ &= G_s(2+f_s)\lambda_s^{-(2+f_s)}+2G_s(1+f_s)\lambda_s^{-(1+f_s)}G_g(1)\lambda_g^{-1}\\ &+G_s(f_s)\lambda_s^{-f_s}G_g(2)\lambda_g^{-2} \qquad (10.87)\end{aligned}$$

Thus, we obtain:

$$QSDRYG_{coal} = \frac{\pi}{4}\left(\frac{\rho_{00}}{\rho_{dref}}\right)^{0.4}C_s\lambda_s^{x_s}C_g\lambda_g^{x_g}e_s\Lambda q(\lambda_g,\lambda_s)\Delta vq_{sg}(\lambda_g,\lambda_s) \qquad (10.88)$$

If there is an elastic collision between graupel and snow, the equation is treated the same way as the other non-inductive processes. However, the common simplifications on the fall speed cannot be considered herein:

$$QSDRYG_{boun} = \int_0^{+\infty} \left[\int_0^{+\infty} (1 - E_{sg})(D_g + D_s)^2 |v_g(D_g) - v_s(D_s)| \delta q_{sg} n_s(D_s) dD_s \right] n_g(D_g) dD_g \tag{10.89}$$

1. **HELSDON AND FARLEY (1987)**

   $\delta q_{sg} = \pm 2 \times 10^{-13}$ C. The sign of the charge exchanged between the two particles depends on the ambient temperature. If $T > TCR$, the graupel gains a positive charge, while if $T < TCR$, the graupel gains a negative charge.

   $$QSDRYG_{boun} = \frac{\pi}{4}(1 - E_{sg}) \left(\frac{\rho_{00}}{\rho_{dref}} \right)^{0.4} \delta q_{sg} C_s \lambda_s^{x_s} C_g \lambda_g^{x_g} \Lambda q1_{sg}(\lambda_g, \lambda_s) \Delta vq1_{sg}(\lambda_g, \lambda_s) \tag{10.90}$$

   with:

   $$\begin{aligned}
   \Delta vq1_{sg}(\lambda_g, \lambda_s) &= \Lambda q1_{sg}(\lambda_g, \lambda_s)^{-1} \int_0^{+\infty} \left[\int_0^{+\infty} (D_g + D_s)^2 |c_g D_g^{d_g} - c_s D_s^{d_s}| g(D_s, \lambda_s) dD_s \right] \times \\
   &\quad g(D_g, \lambda_g) && (10.91) \\
   \Lambda q1_{sg}(\lambda_g, \lambda_s) &= \int_0^{+\infty} \left[\int_0^{+\infty} (D_g + D_s)^2 g(D_s, \lambda_s) dD_s \right] g(D_g, \lambda_g) \\
   &= G_s(2)\lambda_s^{-2} + 2G_s(1)\lambda_s^{-1} G_g(1)\lambda_g^{-1} + G_g(2)\lambda_g^{-2} && (10.92)
   \end{aligned}$$

2. **TAKAHASHI (1978)**

   If we substitute δq_{sg} (Eq. 10.10) in $QSDRYG_{boun}$, we must define the following functions:

   $$\begin{aligned}
   \Delta vqtaka1_{sg}(\lambda_g, \lambda_s) &= |c_g M_g(d_g) M_s(2) - c_s M_s(2 + d_s)| && (10.93) \\
   \Delta vqtaka2_{sg}(\lambda_g, \lambda_s) &= |c_g M_g(2 + d_g) - c_s M_g(2) M_s(d_s)| && (10.94) \\
   \Delta vqtaka3_{sg}(\lambda_g, \lambda_s) &= |2c_g M_g(1 + d_g) M_s(1) - 2c_s M_g(1) M_s(1 + d_s)| && (10.95) \\
   \Delta vqtaka4_{sg}(\lambda_g, \lambda_s) &= \Lambda qtaka4_{sg}(\lambda_g, \lambda_s)^{-1} && (10.96) \\
   &\quad \int_0^{+\infty} \left[\int_0^{+\infty} (D_g + D_s)^2 |c_g D_g^{d_g} - c_s D_s^{d_s}|^2 D_s^2 g(D_s, \lambda_s) dD_s \right] g(D_g, \lambda_g) \\
   \Lambda qtaka4_{sg}(\lambda_g, \lambda_s) &= M_s(4) + 2M_s(3) M_g(1) + M_g(2) M_s(2) && (10.97) \\
   & && (10.98)
   \end{aligned}$$

   with:

   $$M_x(p) = \frac{G_x(p)}{\lambda_x^p} \tag{10.99}$$

   Then:

   $$\begin{aligned}
   QSDRYG_{boun} &= \frac{\pi}{4}(1 - E_{sg}) \left(\frac{\rho_{00}}{\rho_{dref}} \right)^{0.4} C_s \lambda_s^{x_s} C_g \lambda_g^{x_g} f(T, LWC) \\
   &\quad \mathrm{Min}\,(10 \times (\mathrm{\Delta vqtaka1_{sg}(\lambda_g, \lambda_s)} + \mathrm{\Delta vqtaka2_{sg}(\lambda_g, \lambda_s)} + \mathrm{\Delta vqtaka3_{sg}(\lambda_g, \lambda_s)}), \\
   &\quad \left. \left(\frac{\rho_{00}}{\rho_{dref}} \right)^{0.4} \frac{5}{D_0^2 v_0} \Delta vqtaka4_{sg}(\lambda_g, \lambda_s) \Lambda qtaka4_{sg}(\lambda_g, \lambda_s) \right) && (10.100)
   \end{aligned}$$

3. **GARDINER ET AL. (1985)**

   δq_{sg} is replaced by Gardiner's equation (Eq. 10.11). Then:

$$\begin{aligned} QSDRYG_{boun} &= \frac{\pi}{4}(1-E_{sg})\left(\frac{\rho_{00}}{\rho_{dref}}\right)^{4\times0.4} C_s\lambda_s^{x_s}C_g\lambda_g^{x_g}73.10^{15}\delta Lf(\tau) \\ &\quad \Delta vq2_{sg}(\lambda_g,\lambda_s)\Lambda q2_{sg}(\lambda_g,\lambda_s) \end{aligned} \tag{10.101}$$

   with:

$$\begin{aligned} \Delta vq2_{sg}(\lambda_g,\lambda_s) &= \Lambda q2_{sg}(\lambda_g,\lambda_s)^{-1}\times \qquad (10.102) \\ &\int_0^{+\infty}\left[\int_0^{+\infty}(D_g+D_s)^2|c_gD_g^{d_g}-c_sD_s^{d_s}|^4D_s^4g(D_s,\lambda_s)dD_s\right]q(D_g,\lambda_g)dD_g \\ \Lambda q2_{sg}(\lambda_g,\lambda_s) &= \int_0^{+\infty}\left[\int_0^{+\infty}(D_g+D_s)^2D_s^4g(D_s,\lambda_s)dD_s\right]q(D_g,\lambda_g)dD_g \\ &= M_s(6)+2M_s(5)M_g(1)+M_g(2)M_s(4) \qquad (10.103) \end{aligned}$$

4. **SAUNDERS ET AL. (1991), SAUNDERS ET PECK (1998), BROOKS ET AL. (1997), TSENOVA AND MITZEVA (2009, 2011)**

   We proceed the same way as for the other non-inductive processes:

$$QSDRYG_{boun}=\frac{\pi}{4}(1-E_{sg})\left(\frac{\rho_{00}}{\rho_{dref}}\right)^{0.4\times(1+n)} C_s\lambda_s^{x_s}C_g\lambda_g^{x_g}\Delta vq3_{sg}(\lambda_g,\lambda_s)\Lambda q3_{sg}(\lambda_g,\lambda_s)B\delta Q \tag{10.104}$$

$$\begin{aligned} \Delta vq3_{sg}(\lambda_g,\lambda_s) &= \Lambda q3_{sg}(\lambda_g,\lambda_s)^{-1}\times \\ &\int_0^{+\infty}\left[\int_0^{+\infty}(D_g+D_s)^2|c_gD_g^{d_g}-c_sD_s^{d_s}|^{1+n}D_s^mg(D_s,\lambda_s)dD_s\right]\times \\ &q(D_g,\lambda_g)dD_g \qquad (10.105) \\ \Lambda q3_{sg}(\lambda_g,\lambda_s) &= \int_0^{+\infty}\left[\int_0^{+\infty}(D_g+D_s)^2D_s^mg(D_s,\lambda_s)dD_s\right]q(D_g,\lambda_g)dD_g \\ &= M_s(2+m)+2M_s(1+m)M_g(1)+M_g(2)M_s(m) \qquad (10.106) \end{aligned}$$

   Two cases are distinguished: when graupel charges positively and when it charges negatively. Indeed, the value of m depends on the charge transfered to the biggest particle. Then, when $\Delta vq3_{sg}(\lambda_g,\lambda_s)$ is computed, regions with graupel charging positively and negatively must be treated separately.

10.2.12 Wet growth of graupel

$$QWETG=QCWETG+QRWETG+QIWETG+QSWETG+QGWETG \tag{10.107}$$

$$\begin{aligned}
QCWETG &= q_c \frac{RCDRYG}{r_c} && (10.108)\\
QIWETG &= q_i \frac{RIWETG}{r_i} && (10.109)\\
QSWETG &= q_s \frac{RSWETG}{r_s} && (10.110)\\
QRWETG &= \frac{q_r}{r_r}(RWETG - RIWETG - RSWETG - RCDRYG) && (10.111)
\end{aligned}$$

10.2.13 Melting of ice crystals

$$QIMLTC = \frac{q_i}{\Delta t} H(T_t) \tag{10.112}$$

$$QGMLTR = q_g \frac{RGMLTR}{r_g} \tag{10.113}$$

$$QSCVMG = q_s \frac{RSCVMG}{r_s} \tag{10.114}$$

10.2.14 Extension to hail

Formation from graupel particles

$$\left.\frac{\partial q_h}{\partial t}\right|_{g\to h} = \left(\frac{\partial q_g}{\partial t}\right)^{*} \times \frac{DRY}{DRY + WET} \tag{10.115}$$

where $(\partial q_g/\partial t)^*$ is the sum of the q_g tendencies before the conversion to hail. Hail is produced only when $0 < WET \leq DRY$.

Growth of hail particles

$$QWETH = QCWETH + QRWETG + QIWETH + QSWETH + QGWETH \tag{10.116}$$

Melting of hail particles

$$QHMLTR = q_h \frac{RHMLTR}{r_h} \tag{10.117}$$

10.3 Small ions parameterization

The budget equations for the positive and for the negative small ion concentrations are:

$$\frac{\partial n_\pm}{\partial t} = -\nabla \cdot (n_\pm \overrightarrow{V} \pm n_\pm \mu_\pm \overrightarrow{E} - K \nabla n_\pm) + G - \alpha n_+ n_- - S_{att}^\pm + S_{evap}^\pm + S_{light}^\pm + S_{pd}^\pm \tag{10.118}$$

where S_{att}, S_{evap}, S_{light}, and S_{pd} are ion source/sink terms from ion attachment to hydrometeors (sink), release of charge as ions produced by hydrometeors that evaporate completely (source), ion production by a lightning flash and by point discharge at the surface of the earth, respectively.

The three terms in parentheses are the ion advection by the flow, the drift motion and the turbulent diffusion terms, respectively.
It is assumed that the ions carry an elementary charge ($e = 1.6022 \times 10^{-19}$ C). The ions are responsible for all the space charge density in fair weather (FW) conditions in the absence of cloud electrification process. This property is used to initialize $n_\pm$ and to evaluate the cosmic ray source G which is assumed be stationary and isotropic.
The initial values of $n_\pm = n_\pm^{FW}$ are deduced from Gauss'law and assuming a constant air-earth conduction current density $J_c^{FW} = -2.7 \times 10^{-12}$ Am^{-2}:

$$\frac{\mathrm{d}E^{FW}}{\mathrm{d}z} = \frac{e}{\epsilon}(n_+^{FW} - n_-^{FW}) \tag{10.119}$$

$$J_c^{FW} = e(\mu_+ n_+^{FW} - \mu_- n_-^{FW}) \tag{10.120}$$

Here $E^{FW} = E_0[b_1 \exp(-a_1 z) + b_2 \exp(-a_2 z) + b_3 \exp(-a_3 z)]$ with $E_0 = -80$ Vm^{-1}, $a_{1,2,3} = \{4.5 \times 10^{-3}, 3.8 \times 10^{-4}, 10^{-4}\}$ m^{-1} and $b_{1,2,3} = \{0.5, 0.65, 0.1\}$. The ion mobility writes $\mu_\pm = c_\pm \exp(\beta z)$ with $c_{+,-} = \{1.4 \times 10^{-4}, 1.9 \times 10^{-4}\}$ and with $\beta = 1.4 \times 10^{-4}$ m^{-1}. This leads to the FW small ion concentrations:

$$n_+^{FW} = \left[\frac{J^{FW}}{E^{FW}} + \epsilon\mu_- \left(\frac{\mathrm{d}E^{FW}}{\mathrm{d}z}\right)\right] \times \frac{1}{e(\mu_+ + \mu_-)} \tag{10.121}$$

$$n_-^{FW} = n_+^{FW} - \frac{\epsilon}{e}\left(\frac{\mathrm{d}E^{FW}}{\mathrm{d}z}\right) \tag{10.122}$$

The background cosmic ray ion source is deduced from the equilibrium between G, the ion recombination ($\alpha n_+ n_-$ term of Eq. 10.118) and the drift transport term in FW conditions:

$$G = \pm\frac{\mathrm{d}(n_\pm^{FW}\mu_\pm E^{FW})}{\mathrm{d}z} + \alpha n_+^{FW} n_-^{FW} \tag{10.123}$$

After algebrical manipulations, a analytical expression of G is obtained:

$$G(z) = \frac{\mu_+\mu_-\epsilon}{e(\mu_+ + \mu_-)}[\beta E^{FW}\frac{\mathrm{d}E^{FW}}{\mathrm{d}z} + \left(\frac{\mathrm{d}E^{FW}}{\mathrm{d}z}\right)^2 + E^{FW}\frac{\mathrm{d}^2E^{FW}}{\mathrm{d}z^2}] + \alpha n_+^{FW} n_-^{FW}$$

10.3.1 Ion recombination

The Thomson ion recombination coefficient is taken from Helsdon et al. (2002):

$$\alpha = \alpha_0 \left(\frac{T_0}{T}\right)^{3/2} f(x) \tag{10.124}$$

where $\alpha_0 = 1.95 \times 10^{-12}$ m^{3}s^{-1}, $T_0 = 273$ K, and $f(x)$ is given by

$$f(x) = 1 - \frac{4}{x^4}\left[1 - (x+1)^2 \exp(-x)\right]^2, \text{with} \quad x = 2.43\left(\frac{T_0}{T}\right)^2\left(\frac{P}{P_0}\right) \tag{10.125}$$

where P is the pressure and $P_0 = 1013$ hPa. In the atmosphere, α varies between 1.8×10^{-12} m^{3}s^{-1} at ground level and 0.9×10^{-12} m^{3}s^{-1} in the stratosphere.

10.3.2 Ion attachment

Ion attachment to hydrometeors is a combination of free ion diffusion to the surface of the particles (Brownian capture of ions including electrical attraction due to ion motion driven by the electric field produced by the collector particle, S_{diff}) and electrical conduction (capture by ion motion driven by the ambient electric field, S_{cond}). Chiu (1978) postulated that both effects could be treated independently and added together:

$$S_{att} = S_{diff} + S_{cond} \tag{10.126}$$

Diffusion

After careful derivations detailed in Chap. 18 of Pruppacher and Klett (1996) and according to Helsdon (1980) and Helsdon et al. (2002), the "diffusion" contribution writes:

$$S^{\pm}_{diff} = \sum_j 4\pi D_{\pm} n_{\pm} \int_0^{\infty} \frac{D}{2} \left[\frac{\pm X_j(D)}{\exp(\pm X_j(D)) - 1} \right] \times \left[1 + \left(\frac{DV_j(D)}{4\pi D_{\pm}} \right)^{1/2} \right] n_j(D) dD \tag{10.127}$$

where D, $V_j(D)$ and $n_j(D)$ are the size, the terminal fall speed and number concentration (m^{-3}) of the j^{th} hydrometeor category, respectively. $D_{\pm}$ is a diffusion coefficient, it is related to the ion mobility according $D_{\pm} = \mu_{\pm} k_B T/e$. $X_j(D)$ is a scaled electrical charge defined by:

$$X_j(D) = \frac{Q_j(D)}{Q_D}, \tag{10.128}$$

where $Q_j(D)$ is the charge of individual particle of the j^{th} hydrometeor category of size D, and $Q_D = 4\pi\epsilon(D/2)k_B T/e$ is the magnitude of charge on the hydrometeor for which the electrical potential and thermal energies of an ion are balanced at the surface. $k_B = 1.3805 \times 10^{-23}$ J K^{-1} is the Boltzmann constant, and T is the ambient air temperature (in K). The first bracketed term acts to limit the diffusion of an ion of one sign to a hydrometeor charged with the same polarity, while enhancing the diffusion of an ion of opposite charge (HL). The last bracketed term is the hydrometeor ventilation effect on ion capture at its terminal fallspeed.
Integration of Eq. 10.127 is performed with some approximations after computing the size distribution weighted averages $\overline{X_j(D)}$ and $\overline{DV_j(D)}$. The final expression for $S^{\pm}_{diff}$ is:

$$S^{\pm}_{diff} \sim \sum_j 4\pi D_{\pm} n_{\pm} N_j \frac{M_j(1)}{2} \left[\frac{\pm\overline{X_j(D)}}{\exp(\pm\overline{X_j(D)}) - 1} \right] \times \left[1 + \left(\frac{\overline{DV_j(D)}}{4\pi D_{\pm}} \right)^{1/2} \right] \tag{10.129}$$

Conduction

According to Chiu (1978), the rate of attachment due to ion motion driven by an electric field, depends on the charge of the targeted hydrometeor but also on the magnitude and direction of the mean ion drift velocity ($\mu_{\pm}\overrightarrow{E}$) with respect to the hydrometeor fall speed. When the charge of the hydrometeor reaches a charge limit, the electric field cannot polarize any part of the hydrometeor's surface, so only ions of opposite polarity to the charge of the hydrometeor can be collected. For a particle of size D, this charge limit is defined as:

$$Q_A = 3\pi\epsilon|\overrightarrow{E}|D^2 \tag{10.130}$$

and the attachment due to conduction is expressed according the following conditions:

1. $Q_j \geq Q_A$: the particle charge is fully positive

$$S^+_{cond} = 0 \tag{10.131}$$

$$S^-_{cond} = \sum_j (N_j \mu_- n_- Q_j/\epsilon) \tag{10.132}$$

2. $Q_j \leq -Q_A$: the particle charge is fully negative

$$S^+_{cond} = -\sum_j (N_j \mu_+ n_+ Q_j/\epsilon) \tag{10.133}$$

$$S^-_{cond} = 0 \tag{10.134}$$

3. $-Q_A < Q_j < Q_A$: the attachment depends on whether the electric field and terminal fall speed are in the same or opposite directions, and on the sign of the hydrometeor charge

   - if $\overrightarrow{E} \parallel \overrightarrow{V_T}$ then

$$S^+_{cond} = \begin{cases} 0, & 0 < Q_j < Q_A, \quad |V_{jT}| > \mu_+|E| \\ \sum_j(-N_j\mu_+n_+Q_j/\epsilon), & -Q_A < Q_j < 0, \quad |V_{jT}| > \mu_+|E| \\ \sum_j N_j\mu_+n_+|E|3\pi(D/2)^2(1-Q_j/Q_A)^2, & |V_{jT}| < \mu_+|E| \end{cases}$$

$$S^-_{cond} = \sum_j N_j\mu_-n_-|E|3\pi(D/2)^2(1+Q_j/Q_A)^2$$

   - if $\overrightarrow{E} \parallel -\overrightarrow{V_T}$ then

$$S^+_{cond} = \sum_j N_j\mu_+n_+|E|3\pi(D/2)^2(1-Q_j/Q_A)^2$$

$$S^-_{cond} = \begin{cases} 0, & -Q_A < Q_j < 0, \quad |V_{jT}| > \mu_-|E| \\ \sum_j(N_j\mu_-n_-Q_j/\epsilon), & 0 < Q_j < Q_A, \quad |V_{jT}| > \mu_-|E| \\ \sum_j N_j\mu_-n_-|E-3\pi(D/2)^2(1+Q_j/Q_A)^2, & |V_{jT}| < \mu_-|E| \end{cases}$$

10.3.3 Emission or point discharge

When the vertical component of the electric field $E(z=0)$ exceeds a given threshold E_0, a point ion discharge (corona) current (J_{pd}, in A m^{-2}) is produced according to

$$J_{pd} = CE(z=0)(|E(z=0)| - E_0)^2$$

where C = 2 × 10^{-20} A m V^{-3}, and E_0 = 5000 V m^{-1}. $E(z=0)$ is the vertical component of the electric field at the surface. The corresponding ion concentration rate is given by

$$S^+_{pd} = \frac{J_{pd}}{e\Delta z} \quad \text{if} \quad \mathrm{J_{pd}} > 0 \tag{10.135}$$

$$S^-_{pd} = \frac{-J_{pd}}{e\Delta z} \quad \text{otherwise} \tag{10.136}$$

where Δz is the vertical thickness of the grid at ground level. Note that because the ion charge concentration (negative for negative ions) is considered in the flash routine, the minus sign should be ignored in this case.

10.4 Electric field computation

The electric field $\overrightarrow{E}$ is solution of a Gauss equation forced by the total volume charge density (ρ_{tot}):

$$\nabla \cdot \overrightarrow{E} = \frac{\rho_{tot}}{\epsilon} \tag{10.137}$$

with ϵ the dielectric constant of air. The electric potential V is defined as:

$$\overrightarrow{E} = -\overrightarrow{\nabla} V \tag{10.138}$$

In order to stick to the elliptic pressure solver of Meso-NH, it is better to define a pseudo electric potential V':

$$\overrightarrow{\nabla} V' = \frac{\overrightarrow{E}}{\tilde{\rho}} \tag{10.139}$$

with $\tilde{\rho} = \rho_{dref} J$, J is the Jacobian of the transformation, and $\tilde{\rho}$ represents the mass of dry air contained in a grid mesh. Then the Gauss equation expressed in V' becomes:

$$GDIV(\tilde{\rho}\overrightarrow{\nabla} V') = \frac{\rho_{tot}}{\epsilon} \tag{10.140}$$

where $GDIV$ is the generalized divergence operator in a curvilinear non-orthogonal coordinates system. This equation is similar to the one used to compute the pressure in Meso-NH. Consequently, the standard algorithm of the elliptic ”pressure” solver of Meso-NH can be employed to compute the pseudo-potential V' and to derive $\overrightarrow{E}$ but after modifications. The original solver is using Neuman boundary conditions on the six faces of the computation domain. In contrast, the computation of V' needs to introduce a Dirichlet boundary condition $V' = 0$ on the Earth surface and a non-homogeneous Neuman boundary condition $\partial V'/\partial z = E^{FW}/\tilde{\rho}$ at the model top. So in order to avoid the duplication of common routines of the ”pressure” solver, the computation of V' has been adapted accordingly.
The generic tridiagonal system to solve $F\tilde{V'}_{mn}(k) = \tilde{Y}_{mn}(k)$ (see section ”The Pressure Problem”) can be written as:

$$a(k)\tilde{V'}_{mn}(k-1) + b(k)\tilde{V'}_{mn}(k) + c(k)\tilde{V'}_{mn}(k+1) = \tilde{\rho_{tot}}_{mn}(k)/\epsilon$$

where $\tilde{V'}_{mn}(k)$ and $\tilde{\rho_{tot}}_{mn}(k)$ are the x, y Fourier coefficients of V' and ρ_{tot} at model level k, respectively. The $a(k)$, $b(k)$ and $c(k)$ coefficients have the same definition of those introduced in section ”The Pressure Problem”, except at the two boundaries.
At the model top ($k = kmax + 1 + jpvext$): the Neuman condition

$$\tilde{\rho}\frac{\partial V'}{\partial z} = E^{FW} \quad \text{or} \quad \tilde{\rho}\frac{\partial \tilde{V'}_{mn}}{\partial z} = \tilde{E}^{FW} \tag{10.141}$$

imposes that $\overrightarrow{E}$ recovers its fair weather value E^{FW}. This condition is discretized as

$$\left[\frac{<\tilde{\rho}>_{x,y}(kmax + jpvext) + <\tilde{\rho}>_{x,y}(kmax + 1 + jpvext)}{2\,\Delta z(kmax + 1 + jpvext)}\right] \times \tag{10.142}$$

$$(V'(kmax + 1 + jpvext) - V'(kmax + jpvext)) = E^{FW}(kmax + 1 + jpvext) \tag{10.143}$$

and leads to:

$$\begin{aligned}
a(kmax+1+jpvext) &= \frac{<\tilde{\rho}>_{x,y}(kmax+jpvext)+<\tilde{\rho}>_{x,y}(kmax+1+jpvext)}{2\,\Delta z(kmax+1+jpvext)^2} \\
b(kmax+1+jpvext) &= -\frac{<\tilde{\rho}>_{x,y}(kmax+jpvext)+<\tilde{\rho}>_{x,y}(kmax+1+jpvext)}{2\,\Delta z(kmax+1+jpvext)^2}
\end{aligned}$$

while at the corresponding level, the rhs of the tridiagonal system includes now:

$$Y(kmax+1+jpvext) = \frac{E^{FW}(kmax+1+jpvext)}{\Delta z(kmax+1+jpvext)} + \rho_{tot}/\epsilon \tag{10.144}$$

At the Earth surface ($k = 1 + jpvext$): the Dirichlet condition simply writes

$$V' = 0 \quad \text{or} \quad \tilde{V'}_{mn} = 0 \tag{10.145}$$

to assume that the Earth surface is a perfect conductor so the electric field is strictly vertical when approaching the Earth surface. This equation is discretized as

$$V'(jpvext) = -V'(jpvext+1) \tag{10.146}$$

where the Earth surface is defined on the staggered ”flux” grid because it is a surface where $w = 0$. Then the degenerate generic tridiagonal system to solve becomes:

$$\begin{aligned}
b'(1+jpvext) &= b(1+jpvext) - \frac{<\tilde{\rho}>_{x,y}(jpvext)+<\tilde{\rho}>_{x,y}(1+jpvext)}{2\,\Delta z(1+jpvext)^2} \\
c(1+jpvext) &= -\frac{<\tilde{\rho}>_{x,y}(jpvext)+<\tilde{\rho}>_{x,y}(1+jpvext)}{2\,\Delta z(1+jpvext)^2}
\end{aligned}$$

where $b'(1 + jpvext)$ is the modified diagonal coefficient in place of $b(1 + jpvext)$ in the original system.
In order to keep the same dimension of the tridiagonal system of the ”pressure” equation to solve, we impose $b(jpvext) = 1$, $c(jpvext) = a(1 + jpvext) = 0$ to neutralize the unnecessary computations made at level $k = jpvext$.

10.5 Lightning flashes

The objective of the lightning flash scheme is to reproduce the morphological characteristics of the lightning flashes as in Barthe and Pinty (2007a), but for electrified storms growing over large grids and complex terrain. This is achieved by simplifying the original algorithm to get a parallel code as explained below.
Because the nature of most of the calculations involves only a local knowledge of the global 3D fields (with storage on distributed memory), each processor can easily work independently on its side. In our case however, building the filamentary structure of a lightning flash path is leading ineluctably to frequent communications between processors which must be optimized.
In the following, the variables suffixed by $\_ll$ refer to global variables with a single updated value available to all processors. It is hypothesized that the domain is divided into N_{proc} subdomains, with N_{proc} being the number of working processors.

10.5.1 Electrified cells identification

An iterative algorithm is first developed to identify all the electrified cells in the domain of simulation. In the following, a cell is termed ”electrified” if conditions to trigger and to propagate a flash inside it are fulfilled.

The electric field module is first multiplied by a factor to get free of the height effect. It is noted E_0 and corresponds to the electric field module reduced to the ground level. The peak value of E_0, E_{max}, is sought in each subdomain. Then, the global value of the maximum electric field $E_{max}\_ll = \max(E_{max})$ is determined and the processor number (IP_{cell}) where $E_{max}\_ll = E_{max}$ is identified. If E_{max}_ll is higher than 200 kV m^{-1}, the electric field threshold for flash triggering at the ground level, a first electrified cell is detected. The maximum electric field is a natural marker of lightning-triggering cells since a flash is triggered only if $E_{max} >$ 200 kV m^{-1}. The point where $E_{max}\_ll >$ 200 kV m^{-1} is hereafter called the cell center. The local coordinates of the cell center and IP_{cell} are then broadcast to all processors.

The next step explores the vertical and horizontal extensions of the selected cell. The domain volume is scanned from the bottom to the top. The cell center is projected onto the horizontal plane of the running level and contiguous grid points are tagged if they meet the following conditions:

- $r_{tot} > 1 \times 10^{-5}$ kg kg^{-1} to restrict a flash propagation to a single cloud,
- at least one hydrometeor category has $|\tilde{q}_x| > \tilde{q}_{cell}$ where $\tilde{q}_{cell}$ is a given threshold to isolate individual storm cells. $\tilde{q}_x$ is the volume charge density (C m^{-3}) for species x.

The process is repeated along the horizontal until no more grid points can be added to the cell volume. Updates in the halo zones (in a parallel architecture, a ”halo” zone contains the overlapping grid-points which are exchanged with the neighbor processors) are necessary because electrified cells may span over several neighboring subdomains. Then the algorithm loops to analyse the electric field out of the electrified cell to find out if another disjuncted electrified cell exists in the whole domain.

10.5.2 Flash triggering

The local electric field condition which initiates a flash, follows MacGorman et al. (2001) and Barthe and Pinty (2007a). The triggering electric field, E_{trig} decreases with altitude as observed by Marshall et al. (1995):

$$E_{trig} = \pm 167 \times 1.208 \exp\left(\frac{-z}{8.4}\right) \tag{10.147}$$

where z is the altitude (km) and E_{trig} is given in kV m^{-1}. To account crudely for grid scale uncertainty, a flash is triggered where the electric field exceeds a slightly smaller value than E_{trig} (such as $k \times E_{trig}$, with $k = 0.9$). If more than one grid point per convective cell meets the condition $E > 0.9 \times E_{trig}$, then the triggering point is chosen at random.

The processor IP_{trig} containing this point is identified. The value of the triggering electric field, the coordinates of the flash origin and the sign of the vertical component of the electric field at this point are broadcast from IP_{trig} to all processors. This procedure is repeated for each cell. Then, if several cells exist in the domain several flashes can be treated simultaneously since there is a mask that discriminate the different cells in the domain.

Once the characteristics (center and extension) of all electrified cells are available, the lightning flash stage follows. The treatment of the flashes is broken down into two parts with a ”leader” phase that precedes a phase that generates the branches.

10.5.3 Bidirectional leader

The approach follows Helsdon et al. (1992) that relies on the bidirectional leader theory of Kasemir (1960). Kasemir assumes that the flash leader propagates bi-directionally from the triggering point, in the parallel and anti-parallel directions of the ambient electric field. The propagation is stopped once the electric field drops below a threshold value. As previously done by Helsdon et al. (1992), Barthe and Pinty (2007a) simplified this concept since they used the ambient electric field to control the leader propagation instead of the total electric field. They acknowledged that it was a shortcoming, but argued that computing the local electric field at the tip of each segment added to the leader was computationally expensive. In the present scheme, a new simplification is considered, still for sake of reducing the computational cost. The bidirectional leader is allowed to propagate along the vertical axis only and not slantwise along $\boldsymbol{E}$ as in the previous scheme, to avoid communication between the processors each time a new segment is added at the tip of the leader. The two branches of the leader propagate until the ambient vertical electric field (E_z) at the tips of the last segments falls below $\sim$ 15 kV m^{-1} or when the sign of the vertical component of the electric field reverses.

As in other studies (MacGorman et al. 2001; Mansell et al. 2002; Barthe et al. 2005; Mansell et al. 2005, 2010), a flash is categorized as "cloud-to-ground" (CG) when the lower end of the leader reaches the bottom of the cell which altitude is below 2 km above ground level (AGL). CG flashes are artificially prolonged to the ground.

Only processor IP_{cell} is in charge of the bidirectional leader. The coordinates of the leader channel and the flash type are broadcast to all processors.

10.5.4 Horizontal extension of the flash

VHF mapping systems have highlighted the extensive horizontal structure of lightning flashes in two distinct layers (Shao and Krehbiel 1996; Rison et al. 1999; Thomas et al. 2001; Wiens et al. 2005; Bruning et al. 2007), with a single vertical channel connecting the two layers. Therefore, in this context, the new lightning flash scheme must reproduce this feature but in an economical way, since a physically consistent representation of the discharges is too expensive and would be technically impraticable on powerful massively parallel computers.

According to VHF observations, a positively and a negatively charged region must be delineated (propagation is not allowed in a third region in case of a tripole structure of charges). The positively and negatively charged regions where the flash can propagate are explored separately. From the positive part of the leader, the region with negative total charge density where the positive branches can propagate is explored. First, a 3D mask $\mathrm{M}(:,:,:)$ is initialized with value equal to 1 where grid points are reached by the positive leader. Then the neighboring grid points matching the following conditions are selected as part of the negative charge pocket:

- the grid point belongs to the electrified cell of the leader
- the total charge density must be negative
- $|\tilde{q}_{tot}| > \tilde{q}_{cell}$

The fields in the halo zones are updated to allow a continuous extension of the pocket of negative charge to nearby subdomains. This step is resumed until no more point can be added. The positive charge pocket is build the same way around the negative leader, leading to two regions of opposite charge embedded in the electrified cell contour.

10.5.5 Distribution of the branches

Williams et al. (1985) initiated discharges through plastic slabs with regions of stronger and weaker negative charge density. They observed that the discharges tend to propagate toward regions of high charge density, which underlined the importance of the charge density in discharge propagation. Niemeyer et al. (1984) showed that a stochastic dielectric breakdown model naturally leads to a fractal structure of the discharge. Tsonis and Elsner (1987) analyzed a set of lightning pictures and deduced an average fractal dimension of the lightning projection. The dielectric breakdown model has been widely used in the past to simulate different types of lightning discharges (Wiesmann and Zeller 1986; Wiesmann 1988; Petrov and Petrova 1993; Sañudo et al. 1995; Kawasaki and Matsuura 2000, among others). However, none of these studies simulated lightning discharges in a real storm context. Mansell et al. (2002) first introduced the dielectric breakdown concept to simulate the lightning flashes in a cloud model. Then Barthe and Pinty (2007b) developed a probabilistic branching algorithm adapted from the dielectric breakdown concept to mimic the horizontal extension of the flash toward regions of high charge density. The present scheme keeps the idea of charge density criterion to build a 3D branched discharge (Williams et al. 1985) and to monitor the fractal nature of the flash (Niemeyer et al. 1984) as previously highlighted.

The electrified cell domain is divided into concentric spheres with radius r centered on the triggering point. The global number of branches N_ll at a distance r from the triggering point is assumed to follow a fractal law (Niemeyer et al. 1984):

$$N\_ll(i) = \frac{L_\chi}{L_{mean}} i^{\chi-1} \tag{10.148}$$

with L_{mean}, the mean mesh size (m), L_χ, a characteristic length scale (m), and χ, the fractal dimension ($2 < \chi < 3$ according to Petrov and Petrova (1993)). The running integer i, computed as $i = NINT(r/L_{mean})$, varies from $i_{min} = 0$ to i_{max} where i_{max} corresponds to the maximum distance where branching is possible, i.e. for gridpoints belonging to mask $\mathbf{M}$. $NINT$ is a function returning the nearest integer of a real number.

So a local array $\mathbf{A}$ that contains all the nearest integer distances i between the triggering point and each grid point passing mask $\mathbf{M}(:,:,:) = 1$ is filled in each subdomain. The minimum (i_{min}) and maximum (i_{max}) distances are checked so that the next steps are iterated for $i_{min} \leq i \leq i_{max}$.

On each processor, the number of grid points belonging to mask $\mathbf{M}$ and located at distance i ($N_{poss}(i)$) is computed and summed over all processors to get the global number of possible locations $N_{poss}\_ll(i)$. Then $N_{poss}\_ll(i)$ is compared to $N\_ll(i)$ of Eq. 10.148:

- if $N_{poss}\_ll(i) \leq N\_ll(i)$: all the possible grid points at distance i from the triggering point are selected,
- if $N_{poss}\_ll(i) > N\_ll(i)$: too much grid points are found so a subset must be selected at random.

In order to randomize properly the selection of the grid points which are dispersed on several subdomains, two 1D working arrays $\mathbf{V}(:)$ and $\mathbf{V}'(:)$ of size $N_{poss}\_ll(i)$ are allocated to each subdomain. Each processor packs the 3D array $\mathbf{A}$ into a 1D array $\mathbf{V}$ under a running mask control defined by $\mathbf{A}(:,:,:) = i$. $\mathbf{V}'$ is initially set to 0.

The number of grid points, $N_{poss}(i)$, at a given distance i is gathered by each processor and the result is broadcast to all processors. Consequently, each of the IP_{flash} processor knows the proportion of grid points which is granted in its physical subdomain since the total lightning flash path should contain at most $N\_ll(i)$ grid points. A random integer n is then taken in the interval 0 and $N_{poss}\_ll(i)$. The grid point number $\mathbf{V}(n)$ is extracted and element $\mathbf{V}'(\mathbf{V}(n))$ is turned to 1. This step is repeated until $N\_ll(i)$ points are chosen. Finally, the elements of V' are scattered (equivalent to an unpack operation) in a 3D array $\mathbf{S}(:,:,:)$ under the same mask condition $\mathbf{A}(:,:,:) = i$. As a result, the sparse array $\mathbf{S}(:,:,:)$ obtained at the last iteration $i = i_{max}$, marks the full path of the lightning flash. The branches coordinates are then broadcast to all processors.

See Barthe et al. (2012) for an illustration of lightning development in this scheme.

10.5.6 Neutralization

The total charge in excess of $\tilde{q}_{neut}$ along the lightning channel is neutralized in the lightning flash.

$$\begin{cases} \delta q(i,j,k) = \frac{q(i,j,k)}{|q(i,j,k)|} \times (|q(i,j,k)| - q_{neut}) & \text{if } |q(i,j,k)| > q_{neut} \\ \delta q(i,j,k) = 0 & \text{otherwise} \end{cases} \tag{10.149}$$

It is distributed to the ions of opposite sign at each grid point of the flash.
For intra-cloud flashes, a charge correction δq_{neut} is applied to all grid points of the flash to ensure the total charge neutrality (MacGorman et al. 2001) before the redistribution of net charge at grid points.

$$\delta q_{neut} = \sum_{i,j,k} \delta q(i,j,k) \times \frac{1}{N} \tag{10.150}$$

N is the number of flash segments. Then the charge distributed to the ions of opposite sign becomes:

$$\frac{dq(i,j,k)}{dt} = \delta q(i,j,k) - \delta q_{neut} \tag{10.151}$$

For cloud-to-ground discharges, the charge neutrality constraint does not apply.
Then the attachment process redistributes the charge on hydrometeors. Once the charge is neutralized, the electric field is updated. If at least one new triggering point is found in the domain, the procedure is repeated. Thus, in a single time step, each cell can generate several flashes.

10.6 References

Aufdermaur, A. N. and D. A. Johnson, 1972: Charge separation due to riming in an electric field. *Quart. J. Roy. Meteor. Soc.*, **98**, 369–382.

Avila, E. E., G. G. A. Varela, and G. M. Caranti, 1995: Temperature dependance of static charging in ice growing by riming. *J. Atmos. Sci.*, **52**, 4515–4520.

Barthe, C., M. Chong, J.-P. Pinty, C. Bovalo, and J. Escobar, 2012: Cells v1.0: updated and parallelized version of an electrical scheme to simulate multiple electrified clouds and flashes over large domains. *Geosci. Model Dev.*, **5 (1)**, 167–184, doi:10.5194/gmd-5-167-2012.

Barthe, C., G. Molinié, and J.-P. Pinty, 2005: Description and first results of an explicit electrical scheme in a 3D cloud resolving model. *Atmos. Res.*, **76**, 95–113.

Barthe, C. and J.-P. Pinty, 2007a: Simulation of a supercellular storm using a three-dimensional mesoscale model with an explicit lightning flash scheme. *J. Geophys. Res.*, **112 (D06210)**, doi: 10.1029/2006JD007484.

Barthe, C. and J.-P. Pinty, 2007b: Simulation of electrified storms with comparison of the charge structure and lightning efficiency. *J. Geophys. Res.*, **112 (D19204)**, doi:10.1029/2006JD008241.

Beard, K. K. and H. T. Ochs, 1986: *The Earth's Electrical Environment*. Studies in Geophysics, Nat. Academic Press, Washington, D.C., 114-130 pp.

Brooks, I. M., C. P. R. Saunders, R. P. Mitzeva, and S. L. Peck, 1997: The effect on thunderstorm charging of the rate of rime accretion by graupel. *Atmos. Res.*, **43**, 277–295.

Bruning, E. C., W. D. Rust, T. J. Schuur, D. R. MacGorman, P. R. Krehbiel, and W. Rison, 2007: Electrical and polarimetric radar observations of a multicell storm in TELEX. *Mon. Wea. Rev.*, **135**, 2525–2544.

Chiu, C.-S., 1978: Numerical study of cloud electrification in a axisymmetric, time-dependant cloud model. *J. Geophys. Res.*, **83**, 5025–5049.

Farley, R. D., P. A. Price, H. D. Orville, and J. H. Hirsch, 1989: On the numerical simulation of graupel/hail initiation via the riming of snow in bulk water microphysical cloud models. *J. Appl. Meteor.*, **28**, 1128–1131.

Gardiner, B. A., D. Lamb, R. Pitter, J. Hallett, and C. Saunders, 1985: Measurements of initial potential gradient and particle charge in a Montana summer thunderstorm. *J. Geophys. Res.*, **90**, 6079–6086.

Helsdon, J. H., 1980: Chaff seeding effects in a dynamical-electrical cloud model. *J. Appl. Meteor.*, **19**, 1101–1125.

Helsdon, J. H., S. Gattaleeradapan, R. D. Farley, and C. C. Waits, 2002: An examination of the convective charging hypothesis : Charge structure, electric fields, and Maxwell currents. *J. Geophys. Res.*, **107 (D22)**, 4630, doi:10.1029/2001JD001495.

Helsdon, J. H., W. A. Wojcik, and R. D. Farley, 2001: An examination of thunderstorm-charging mechanism using a two-dimensional storm electrification model. *J. Geophys. Res.*, **106 (D1)**, 1165–1192, doi:10.1029/2000JD900532.

Helsdon, J. H., G. Wu, and R. D. Farley, 1992: An intracloud lightning parameterization scheme for a storm electrification model. *J. Geophys. Res.*, **97**, 5865–5884.

Illingworth, A. J. and J. M. Caranti, 1985: Ice conductivity restraints on the inductive theory of thunderstorm electrification. *J. Geophys. Res.*, **90 (D4)**, 6033–6039.

Jayaratne, R., C. P. R. Saunders, and J. Hallet, 1983: Laboratory studies of the charging of soft hail during ice crystal interactions. *Quart. J. Roy. Meteor. Soc.*, **103**, 609–630.

Kajikawa, M. and A. J. Heymsfield, 1989: Aggregation of ice crystals in cirrus. *J. Atmos. Sci.*, **46 (20)**, 3108–3121.

Kasemir, H. W., 1960: A contribution to the electrostatic theory of a lightning discharge. *J. Geophys. Res.*, **65**, 1873–1878.

Kawasaki, Z. and K. Matsuura, 2000: Does a lightning channel show a fractal ? *Applied Energy*, **67**, 147–158.

Keith, W. D. and C. P. R. Saunders, 1990: Further laboratory studies of the charging of graupel during ice crystal interactions. *Atmos. Res.*, **25**, 4345–4464.

MacGorman, D. R. and W. D. Rust, 1998: *The electrical nature of storms*. Oxford Univ. Press, 422 pp. pp.

MacGorman, D. R., J. M. Straka, and C. L. Ziegler, 2001: A lightning parameterization for numerical cloud model. *J. Appl. Meteor.*, **40**, 459–478.

Mansell, E., D. R. MacGorman, C. L. Ziegler, and J. M. Straka, 2005: Charge structure and lightning sensitivity in a simulated multicell thunderstorm. *J. Geophys. Res.*, **110**, doi:10.1029/2004JD005 287.

Mansell, E. R., 2000: Electrification and lightning in simulated supercell and non-supercell thunderstorms. Ph.D. thesis, Univ. Oklahoma, 211 pp. pp.

Mansell, E. R., D. MacGorman, C. L. Ziegler, and J. M. Straka, 2002: Simulated three-dimensional branched lightning in a numerical thunderstorm model. *J. Geophys. Res.*, **107**, doi:10.1029/2000JD000 244.

Mansell, E. R., C. L. Ziegler, and E. C. Bruning, 2010: Simulated electrification of a small thunderstorm with two-moment bulk microphysics. *J. Atmos. Sci.*, **67**, 171–194, doi:10.1175/2009JAS2965.1.

Marshall, T. C., M. P. MacCarthy, and W. D. Rust, 1995: Electric field magnitudes and lightning initiation in thunderstorms. *J. Geophys. Res.*, **100**, 7097–7103.

Niemeyer, L., L. Pietronero, and H. J. Wiesmann, 1984: Fractal dimension of dielectric breakdown. *Phys. Rev. Let.*, **52 (12)**, 1033–1036.

Petrov, N. I. and G. N. Petrova, 1993: Physical mechanisms for intracloud lightning discharges. *Technical Physics*, **44**, 472–475.

Pruppacher, H. and J. Klett, 1996: *Microphysics of Clouds and Precipitation*. Atmospheric and Oceanographic Sciences Library, Kluwer Academic Publishers.

Rison, W., R. J. Thomas, P. R. Krehbiel, T. Hamlin, and J. Harlin, 1999: A GPS-based three-dimensional lightning mapping system : initial observations in Central New-Mexico. *Geophys. Res. Lett.*, **26**, 3573–3576.

Sañudo, J., J. B. Gómez, F. C. no, and A. F. Pacheco, 1995: Fractal dimension of lightning discharge. *Nonlinear Processes in Geophysics*, **2**, 101–106.

Saunders, C. P. R. and I. Brooks, 1992: The effects of high liquid water content on thunderstorm charging. *J. Geophys. Res.*, **97 (D13)**, 14 671–14 676.

Saunders, C. P. R., W. D. Keith, and R. P. Mitzeva, 1991: The effect of liquid water on thunderstorm charging. *J. Geophys. Res.*, **96**, 11 007–11 017.

Saunders, C. P. R. and S. L. Peck, 1998: Laboratory studies of the influence of the rime accretion rate on charge transfer during crystal/graupel collisions. *J. Geophys. Res.*, **103**, 13 949–13 956.

Shao, X. M. and P. R. Krehbiel, 1996: The spatial and temporal development of intracloud lightning. *J. Geophys. Res.*, **101**, 26 641–26 668.

Takahashi, T., 1978: Riming electrification as a charge generation mechanism in thunderstorms. *J. Atmos. Sci.*, **35**, 1536–1548.

Takahashi, T., 1984: Thunderstorm electrification - A numerical study. *J. Atmos. Sci.*, **41**, 2541–2558.

Thomas, R. J., P. R. Krehbiel, W. Rison, T. Hamlin, J. Harlin, and D. Shown, 2001: Observations of VHF source powers radiated by lightning. *Geophys. Res. Lett.*, **28**, 143–146.

Tsenova, B. and R. Mitzeva, 2009: New parameterization of non-inductive charge transfer based on previous laboratory experiments. *Atmos. Res.*, **91**, 79–85.

Tsenova, B. and R. Mitzeva, 2011: Comparative modelling study of the effect of parameterizations based on rime accretion rate and on effective water content on simulated charge density in thunderstorms. *IDOJARAS*, **115 (4)**, 247–263.

Tsonis, A. A. and J. B. Elsner, 1987: Fractal characterization and simulation of lightning. *Beitr. Phys. Atmos.*, **60**, 187–192.

Wiens, K. C., S. A. Rutledge, and S. A. Tessendorf, 2005: The 29 June 2000 supercell observed during STEPS. Part II: Lightning and charge structure. *J. Atmos. Sci.*, **62**, 4151–4177.

Wiesmann, H. J., 1988: *Realistic models of dielectric breakdown, Fractals physical origin and properties*, 243–257. Plenum, New York.

Wiesmann, H. J. and H. R. Zeller, 1986: A fractal model of dielectric breakdown and prebreakdown in solid dielectrics. *J. Appl. Phys.*, **60**, 1770–1773.

Williams, E. R., C. M. Cooke, and K. A. Wright, 1985: Electrical discharge propagation in and around space charge clouds. *J. Geophys. Res.*, **90**, 6054–6070.

Wojcik, W. A., 1994: An examination of thunderstorm charging mechanisms using the IAS 2D storm electrification model. M.S. thesis, So. Dakota Schl. Mines Technol., Rapid City, SD.

Ziegler, C. L., D. R. MacGorman, J. E. Dye, and P. S. Ray, 1991: A model evaluation of noninductive graupel-ice charging in the early electrification of a mountain thunderstorm. *J. Geophys. Res.*, **96**, 12,833–12,855.

Chapter 11

Wind turbine parameterizations

Contents

11.1 Introduction

Several wind turbine parameterizations have been introduced in Meso-NH with the aim of studying the interactions between wind farms and local meteorology. The wind turbines are taken into account using actuator methods (or body forces). For more details about the wind turbines parameterizations introduced in Meso-NH, see Joulin (2019). For a general review of wind turbines and wind farm flows, see Porté-Agel et al. (2020).

11.2 Non-Rotating Actuator Disk (ADNR)

11.2.1 Overview

The *Non-Rotating Actuator Disk* (ADNR) is a pioneer theory proposed by Rankine (1865) and Froude (1889). It allows to obtain interesting results about propellers. Nowadays, it has been generalized for wind turbine study.

The ADNR consists in applying a thrust force over the disk drawn by the blades. This aerodynamic force acts against the wind to disturb the flow. The evaluation of the thrust force is based on a 1D momentum theory : only an axial force is considered. The Non-Rotating Actuator Disk model can be seen as a simplified Actuator Disk with Rotation, which has been initially coupled by Sorensen and Myken (1992) to a CFD code.

The first simulations coupled to a LES have been done by Jimenez et al. (2007), Jimenez et al. (2008), and Wu and Porté-Agel (2011). It has been used to study wind farms as showed by Wu and Porté-Agel (2015) or Shamsoddin and Porté-Agel (2017), or impact on local meteorology such as in Calaf et al. (2010) or Calaf et al. (2011).

11.2.2 Theory

Hypotheses

The flow is assumed to be stationary and irrotational, and the fluid incompressible. Besides, as the wind turbine is simplified to a porous disk drawn by the blades, it is assumed that the wind turbine has an infinite number of blades, that the thrust is uniformly distributed over the disk, and that the wake rotation can be neglected. See (Joulin 2019) for discussions.

Stream-tube

By extracting the kinetic energy from the wind, the wind turbine produces a velocity deficit downstream, generating the so-called “wake”. It is possible to consider a stream-tube around the rotor disk of the wind turbine, as illustrated in Fig. 11.1. As the fluid is considered incompressible, the mass flow rate is conserved. Then, the cross-sectional area of the stream-tube must expand downstream to balance the velocity deficit.

A vertical cut of the stream-tube is given in Figure 11.2. One can write U the axial velocity, p the pressure and A the cross-sectional area. The indices $_\infty$, $_d$ and $_W$ indicate respectively the upstream, disk and downstream positions. The exponents $^+$ and $^-$ indicate the infinitesimal upstream and downstream sides of the disc. The thrust force F_T writes:

$$F_T = A_d(p_d^+ - p_d^-). \tag{11.1}$$

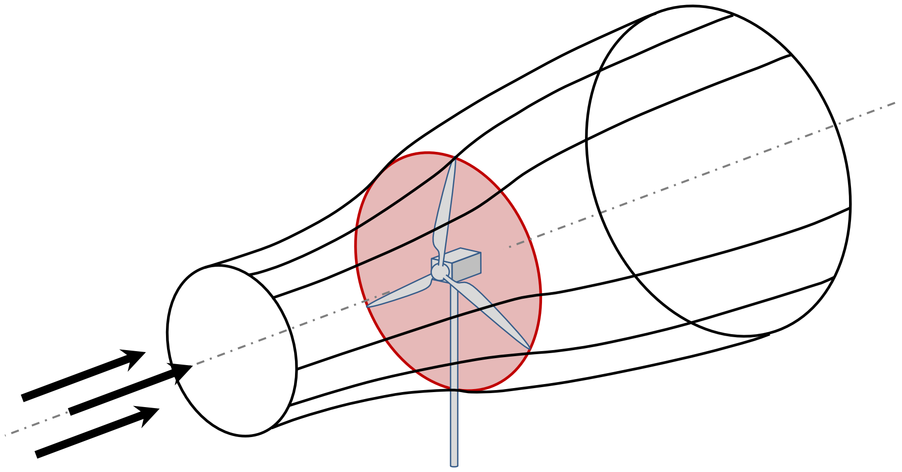

Figure 11.1: Stream-tube around the rotor disk of a wind turbine. Joulin (2019) adapted from Burton et al. (2001)

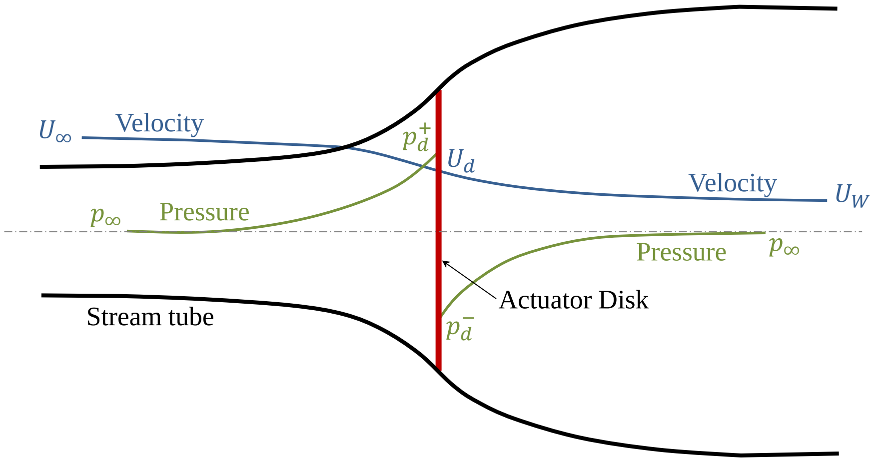

Figure 11.2: Vertical cut of the stream-tube around the rotor disk of a wind turbine and its variables. Joulin (2019) adapted from Burton et al. (2001)

It is possible to apply the Bernoulli's theorem to the upstream part, and to the downstream one, separately. It gives:

$$\begin{cases} p_\infty + \frac{1}{2}\rho U_\infty^2 = p_d^+ + \frac{1}{2}\rho U_d^2 \\ p_d^- + \frac{1}{2}\rho U_d^2 = p_\infty + +\frac{1}{2}\rho U_W^2, \end{cases} \tag{11.2}$$

where ρ is the air density. Using (11.2) in (11.1), the thrust force becomes:

$$\boxed{F_T = \frac{1}{2}\rho A_d (U_\infty^2 - U_W^2)}. \tag{11.3}$$

This first expression gives the thrust force by knowing the upstream velocity: $F_T = f(U_\infty)$. In practice, it is impossible to define a proper U_∞. Then, an expression with the velocity at the disk position: $F_T = f(U_d)$ has to be found. It is the aim of the next paragraphs.

Momentum theory

The axial induction factor a describes the percentage of velocity deficit:

$$U_d = U_\infty(1-a). \tag{11.4}$$

By applying the moment theory, the thrust force F_T can be expressed at the position of the disc (see Joulin (2019) for more details) as:

$$\boxed{F_T = \frac{1}{2}\rho A_d U_d^2 \frac{4a}{1-a}.} \tag{11.5}$$

The thrust coefficient C_{T_∞} is the rate between the thrust force and the dynamic force of the wind. One can note that it is defined with the upstream velocity U_∞. It can be expressed using the axial induction factor a:

$$C_{T_\infty} = \frac{F_T}{\frac{1}{2}\rho A_d U_\infty^2} = 4a(1-a). \tag{11.6}$$

Final expression of thrust force

The thrust coefficient C_{T_∞} is a well-known data (tabulated data $C_{T_\infty} = f(U_\infty)$ given by the constructor). Then, by using (11.6), one can write a as:

$$a = \frac{1}{2}(1-\sqrt{1-C_{T_\infty}}). \tag{11.7}$$

Then, one can define C_{T_d}:

$$C_{T_d} = \frac{4a}{1-a}, \tag{11.8}$$

to finally obtain a suitable expression for the thrust coefficient, using U_d only:

$$\boxed{F_T = \frac{1}{2}\rho A_d U_d^2 C_{T_d}}. \tag{11.9}$$

11.2.3 Numerical implementation

In Meso-NH, the ADNR is discretised according to the mesh, as illustrated in Fig. 11.3.

The first step of the coupling algorithm is to find the cells where the infinitesimal thrust forces will be applied. It is done by checking if the cell is located into the rotor disk. Then, the wind speed of the cell U_d is extracted, after it has been evaluated at mass point (C-type of Arakawa). It is possible to use the closest value of the wind, or to interpolate it from the 8-neighborhood cells. Finally, the discrete thrust force is calculated by using (11.9) as follows:

$$\boxed{dF_T = \frac{1}{2}\rho \Delta y \Delta z U_d^2 C_{T_d}}, \tag{11.10}$$

where $\Delta y \Delta z$ is the vertical area of the cell. This force will act against the wind field, as shown in Figure 11.4. This is why, in the end, the force $dF_{T_{WT\rightarrow WIND}} = -dF_T$ is added to the global momentum budget of Meso-NH. Please note that the equation is only valid for a thrust force applied along the x-axis: the ANDR only operates when the disk is normal to the x-axis, facing upstream.

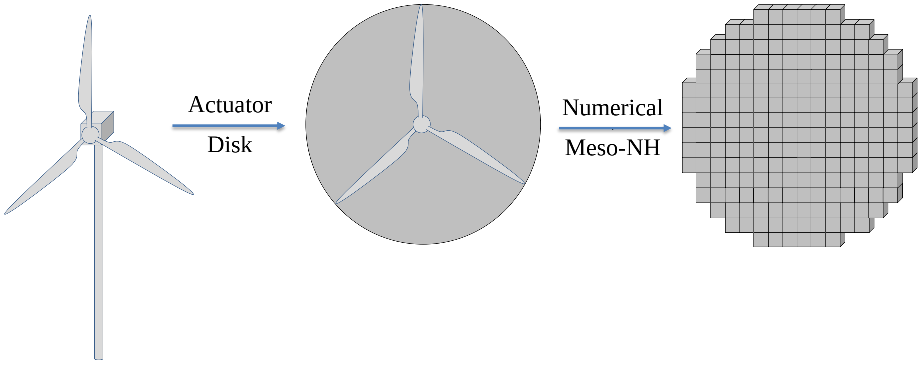

Figure 11.3: Discretization of the ADNR Joulin (2019).

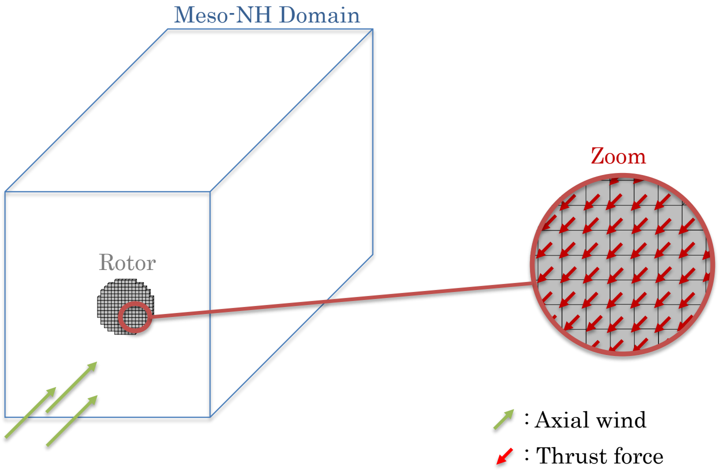

Figure 11.4: Applying discrete thrust forces in Meso-NH Joulin (2019).

11.2.4 Additional implementations

1D Linear smearing

To avoid numerical instabilities, it is possible to apply a linear smearing to the force field. It is done by using the C-type cells of Arakawa. To smear the forces linearly, one can apply successively:

$$dF_{x_i^m} = \frac{dF_{x_i^f} + dF_{x_{i+1}^f}}{2}, \tag{11.11}$$

and then,

$$dF_{x_i^f} = \frac{dF_{x_i^m} + dF_{x_{i+1}^m}}{2}, \tag{11.12}$$

where x_i^m and x_i^f are respectively the mass point and the flux point of the i^{th} cell of x-axis. An illustration is given in Figure 11.5. This method is less expensive numerically than the usual convolution product, and seems to provide similar results. See Joulin (2019) for discussions.

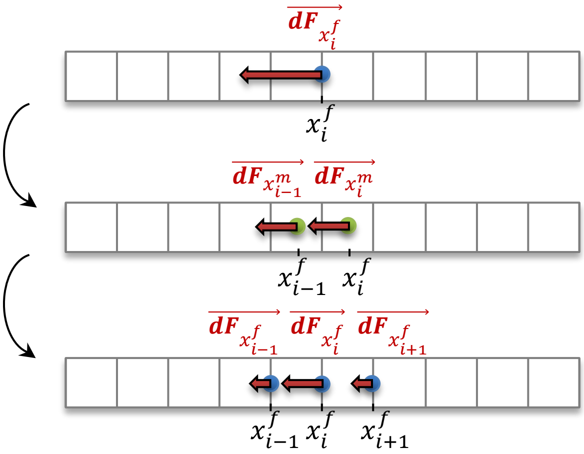

Figure 11.5: Scheme of an 1D linear smearing of the force field Joulin (2019).

3D linear smearing

It is possible to use a 3D linear smearing based on the 1D Linear distribution, by applying the same method on y-axis and z-axis successively.

11.3 Rotating Actuator Disk (ADR)

11.3.1 Overview

In the Actuator Disk model developed by Rankine (1865) and Froude (1889), rotor rotation and tangential forces are neglected. The Rotating Actuator Disk (ADR) model addresses these effects by incorporating the Blade Element (BE) theory developed by Glauert (1935). This theory involves dividing the blade into multiple sections and studying the flow over each section (Figure 11.6). It is used to assess the forces acting on a blade based on the lift and drag forces generated at each section of the blade.

Based on the principle of 'body forces', the ADR method does not explicitly represent the geometry of the blades. Once again, the rotor effect is considered through equivalent volume forces. With the ADR, not only is the thrust force of the turbine on the wind modeled, but also the rotor torque, which is not considered in the ADNR model. The concept involves considering an average effect of the blades on the surface they sweep during their rotations. In this methodology, the ADR is discretized in a cylindrical coordinate system, with a certain number of azimuthal elements (segmented by $\Delta\theta$) and radial elements (segmented by dr), as shown in Figure 11.7. At each time step and at a specific radial location r, each azimuthal position carries the effects of the blades, weighted by the ratio of the surface element to the total annular surface at the given r.

To enhance the representation of wind wakes, Sorensen and Myken (1992) introduced the rotation of the Actuator Disk model in their CFD code. Their work demonstrates that this addition provides fundamental insights into wake characteristics (Sorensen and Kock (1995); Sorensen et al. (1998)). Subsequent studies by Madsen (1997) and Mikkelsen (2003) focused on wind turbines with precones or misalignment to the wind direction.
Later on, the ADR wind turbine model was coupled with Large Eddy Simulation (LES) by the EPFL team (Porté-Agel et al. (2011); Wu and Porté-Agel (2011, 2015); Porté-Agel et al. (2014)).

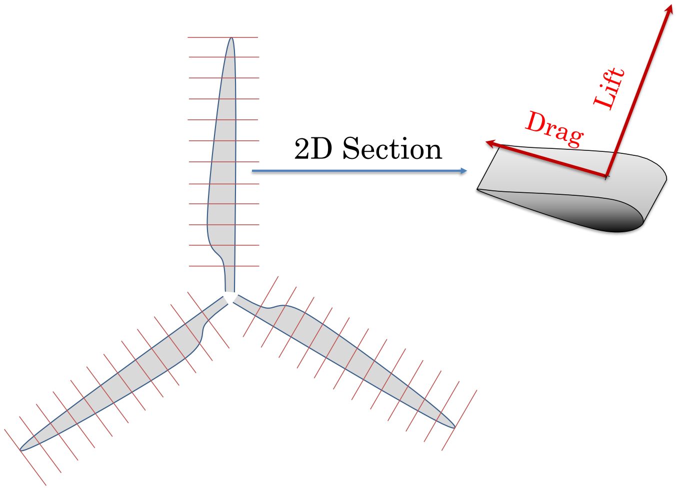

Figure 11.6: Schematic representation of Blade Element theory Joulin (2019).

This coupling enables a simple yet effective representation of the wind turbine while leveraging the detailed turbulence representation provided by LES. This approach allowed the study of wake evolution and its impacts on the atmospheric boundary layer.
Subsequently, ADR was coupled with WRF LES, a U.S. atmospheric code, to initiate the study of real wind farms (Aitken and Lundquist (2014); Aitken et al. (2014); Mirocha et al. (2014, 2015); Marjanovic (2015)). These studies aimed to analyze wind farm layout and wake evolution, with the ultimate goal of optimizing wind resource exploitation, potentially through control and command strategies.

11.3.2 Theory

Hypotheses

The model is based on a number of assumptions:

- Incompressible flow,
- 2D flow along the airfoils,
- No aerodynamic interaction between each blade element (which excludes any radial flow),
- As the wind turbine is simplified to a porous disk, an infinite number of blades is considered.

Applying blade element theory

Determination of U_{rel} and α: Thanks to the kinematic definition and to the rotation matrices (detailed in 11.5), the determination of the relative wind U_{rel} is almost direct. Indeed, the kinematic relations (see 11.5) enable to know the velocity of translation U^{ij}_{trans}. Considering the j^{th} radial elements of the i^{th} annular section in a surrounding volume of air with a velocity U^{ij}_{wind}, the relative

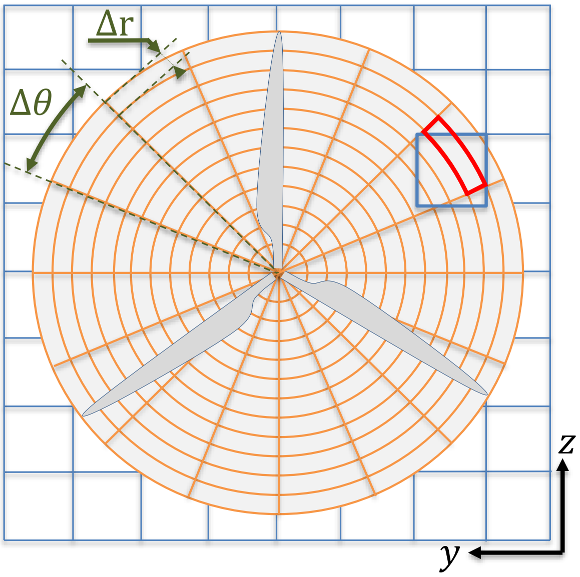

Figure 11.7: Overview of ADR mesh Joulin (2019).

velocity writes:

$$\boxed{\overrightarrow{U^{ij}_{rel}}|_{R^{AELT_j}_{CYL_i}} = \mathcal{M}_{R^{AELT_j}_{CYL_i} \to R_{GLO}} \times \overrightarrow{U^{ij}_{wind}|_{R_{G_{ij}}}} - \overrightarrow{U^{ij}_{trans}}|_{R^{AELT_j}_{CYL_i}}}. \tag{11.13}$$

And the angle of attack α can be evaluated thanks to:

$$\boxed{\alpha = tan^{-1}\left(\frac{\overrightarrow{U^{ij}_{rel}}|_{R^{AELT_j}_{CYL_i}} \cdot \overrightarrow{x}}{\overrightarrow{U^{ij}_{rel}}|_{R^{AELT_j}_{CYL_i}} \cdot \overrightarrow{y}}\right)}. \tag{11.14}$$

Aerodynamic forces: By knowing U_{rel} and α, the blade element theory can be applied. The aerodynamic forces can be expressed in the aerodynamic frame as:

$$\begin{cases} dF_L = \dfrac{1}{2}\rho S U_{rel}^2 C_L(\alpha), \\ \\ dF_D = \dfrac{1}{2}\rho S U_{rel}^2 C_D(\alpha). \end{cases} \tag{11.15}$$

where the lift C_L and drag C_D coefficients are known according to the angle of attack α and the Reynolds number Re. The lifting surface S, evaluated with the airfoil chord c and the radial width dr ($S = cdr$).

This elementary force represents the force from a section of one blade (not from an annular element). Applying this force throughout the infinite number of blades would be incorrect. To ensure momentum conservation, the loads need to be distributed evenly over the discretized disc. This is achieved using the ratio between the number of blades N_{blades} and the number of azimuthal elements $2\pi/\Delta\theta$. Introducing a new surface S' defined as:

$$S' = SN_{blades}\frac{\Delta\theta}{2\pi}, \tag{11.16}$$

One can obtain:

$$\boxed{\begin{cases} df_L = \dfrac{1}{2}\rho S' U_{rel}^2 C_L, \\ \\ df_D = \dfrac{1}{2}\rho S' U_{rel}^2 C_D. \end{cases}} \tag{11.17}$$

By applying a rotation angle α, the forces can be expressed in $R_{CYL_i}^{AELT_j}$, and then in the global frame by using $\mathcal{M}_{R_{GLO}\rightarrow R_{CYL_i}^{AELT_j}}$ (see 11.5).

11.3.3 Numerical implementation

The first step of the Rotating Actuator Disc is to compute the kinematics of the wind turbine. The kinematic algorithm computes, at each time step, the new positions and velocities of all elements. Knowing the position of an annular blade element, the local wind speed can be extracted. To do so, the wind speed is computed at mass point. Then, it is possible to use the closest value (from the blade element) of the wind, or to interpolate it from the 8-neighborhood cells. Afterwards, the relative velocity is computed using (11.13), and the angle of attack α with (11.14). The aerodynamic coefficients C_L and C_D are then computed by knowing α, from a spline-cubic interpolation of the tabulated input data. Finally, the aerodynamic forces are computed in the aerodynamic frame using (11.17):

$$\boxed{\begin{cases} df_L = \dfrac{1}{2}\rho S' U_{rel}^2 C_L(\alpha), \\ \\ df_D = \dfrac{1}{2}\rho S' U_{rel}^2 C_D(\alpha). \end{cases}} \tag{11.18}$$

A last change of frame enables the projection of these forces to the global momentum budget of Meso-NH. One can note that, for the moment, only the effects of the blades are computed: the nacelle and the tower are neglected.

Note: Special attention must be given to the number of radial (NNB_RADELT) and azimuthal (NNB_AZIELT) elements depending on the mesh used in Meso-NH. To avoid gaps in the mesh and ensure a proper distribution of efforts, it is recommended to have:

$$NNB\_RADELT > \frac{2R}{\min(\Delta x, \Delta y, \Delta z)} \tag{11.19}$$

and

$$NNB\_AZIELT > \pi/\sin^{-1}\left(\frac{\min(\Delta x, \Delta y, \Delta z)}{2R}\right) \tag{11.20}$$

where R is the radius of the rotor, and $\min(\Delta x, \Delta y, \Delta z)$ is the smallest dimension of the Meso-NH mesh at the rotor level.

11.3.4 Additional implementations

1D linear smearing

It is possible to use the 1D linear smearing mentionned in 11.2.4.

3D linear smearing

It is possible to use the 3D linear smearing mentionned in 11.2.4.

3D Gaussian kernel smearing

In the literature, it is quite common to smear the forces by applying a convolution of each body force with a 3D Gaussian kernel η_ϵ (Sorensen and Shen 2002):

$$\eta_\epsilon(r) = \frac{\exp\left[-(r/\epsilon)^2\right]}{\epsilon^3 \pi^{3/2}} \tag{11.21}$$

where ϵ is the kernel size and r is the distance between the body force and the considered mesh point. The function η_ϵ is normalised so its integral is equal to 1 and thus the total body force applied to the system is not modified.
The smeared body forces are applied only if $r < \sqrt{\epsilon \cdot \log(1000)}$. This allows to reduce consequently the cost of this method (though it is still less efficient than the linear smearing methods) while recovering 99.9% of the total forces (from the SOWFA code commentaries).
The recommended kernel size is twice the size of the mesh (Troldborg 2009), but this value can be changed by the user with the variable XKERNEL_SIZE. Indeed, this value is debated in the literature (Meyer Forsting et al. 2019; Jha et al. 2014)

Tip loss correction

As an infinite number of blades is considered in this Actuator method, the induction of each blade is not well reproduced, and the tip vortices are not properly modeled. To overcome this issue, Glauert (1935) developed the so-called tip loss correction. It introduces a factor F to take into account the wake-induced losses:

$$F = \frac{2}{\pi} \arccos(e^{-f}) \tag{11.22}$$

where f can be expressed using the radius of the tip r_{tip} and the flow angle φ:

$$f = \frac{N_{pales}}{2} \frac{r_{tip} - r}{r sin(\varphi)} \tag{11.23}$$

Then, the factor is introduced as follows:

$$\left\{ \begin{aligned} dF_L &= \frac{1}{2} C_L \rho S' U_{rel}^2 F, \\ dF_D &= \frac{1}{2} C_D \rho S' U_{rel}^2 F. \end{aligned} \right. \tag{11.24}$$

11.4 Actuator Line Method (ALM)

11.4.1 Overview

The previous model, the ADR, can be seen as the average of the blade motion over one or several rotations. It gives the tendency of the wake, but it cannot represent its instantaneous particularities. To overcome this problem, it is possible to use lines to model the blades, instead of a disk: it is the *Actuator Line Method* (ALM). The method has been generalized by Sorensen and Shen (2002). Each blade applies a force on the fluid, as shown in Figure 11.8. In order to find the position of the blades and their velocity, it is necessary to take into account their kinematic motion. Then, the blade element theory allows to determine the aerodynamic forces to apply.

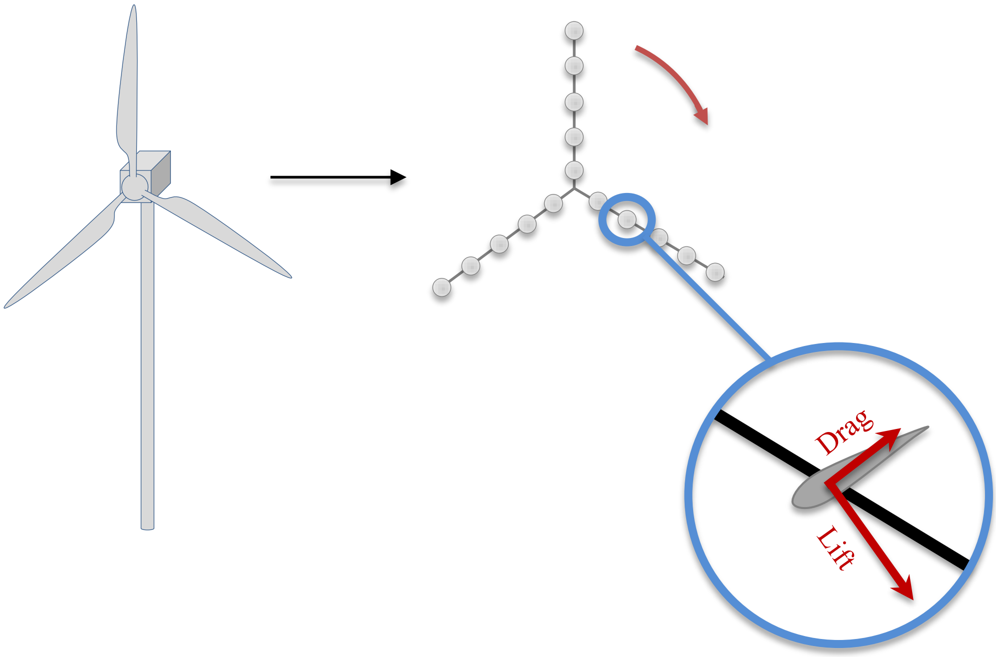

Figure 11.8: Overview of the Actuator Line Method Joulin (2019).

The first coupling between the Actuator Line Method and a CFD code has been introduced by Mikkelsen (2003). It allows to reproduce the helical shape of the unsteady wake and to capture tip and root vortices (Ivanell et al. (2007a), Ivanell et al. (2007b)) giving a better description of the wake downstream the wind turbines (Ivanell (2009), Troldborg (2009)).

For these reasons, the ALM has been introduced in several LES frameworks (Porté-Agel et al. (2011) or Tabib et al. (2017)). Interactions between wind turbines and atmospheric boundary layer have been studied (Lu and Porté-Agel (2011), Lu and Porté-Agel (2015)). It has also been coupled with WRF-LES (Marjanovic (2015) and Marjanovic et al. (2017)) for wind farm studies, or in SOWFA, based on OpenFOAM Churchfield et al. (2012). The coupling with Meso-NH has been introduced by Joulin et al. (2020).

11.4.2 Theory

Hypotheses

The model is based on a number of assumptions:

- Incompressible flow,
- 2D flow along the airfoils,
- No aerodynamic interaction between each blade element (which excludes any radial flow).

Applying blade element theory

Determination of U_{rel} and α: Thanks to the kinematic definition and to the rotation matrices (detailed in 11.5), the determination of the relative wind U_{rel} is almost direct. Indeed, the kinematic relations enable to know the velocity of translation U^{ij}_{trans}. Considering the j^{th} radial elements of the i^{th} blade located in a surrounding volume of air with a velocity U^{ij}_{wind}, the relative velocity writes:

$$\boxed{\overrightarrow{U^{ij}_{rel}}\big|_{R^{AELT_j}_{BLA_i}} = \mathcal{M}_{R^{AELT_j}_{BLA_i} \rightarrow R_{GLO}} \times \overrightarrow{U^{ij}_{wind}}\big|_{R_{GLO}} - \overrightarrow{U^{ij}_{trans}}\big|_{R^{AELT_j}_{BLA_i}}}. \tag{11.25}$$

And the angle of attack α can be evaluated thanks to:

$$\boxed{\alpha = tan^{-1}\left(\frac{-\overrightarrow{U^{ij}_{rel}}\big|_{R^{AELT_j}_{BLA_i}} \cdot \overrightarrow{z}}{\overrightarrow{U^{ij}_{rel}}\big|_{R^{AELT_j}_{BLA_i}} \cdot \overrightarrow{y}}\right)}. \tag{11.26}$$

Aerodynamic forces: By knowing U_{rel} and α, the blade element theory can be applied. The aerodynamic forces can be expressed in the aerodynamic frame as:

$$\boxed{\begin{cases} dF_L = \dfrac{1}{2}\rho S U_{rel}^2 C_L(\alpha), \\[2ex] dF_D = \dfrac{1}{2}\rho S U_{rel}^2 C_D(\alpha). \end{cases}} \tag{11.27}$$

where the lift C_L and drag C_D coefficients are known according to the angle of attack α and the Reynolds number Re. The lifting surface S, evaluated with the airfoil chord c and the radial width dr ($S = cdr$). By applying a rotation angle α, the forces can be expressed in $R^{AELT_j}_{BLA_i}$, and then in the global frame by using $\mathcal{M}_{R_{GLO}} \rightarrow R^{AELT_j}_{BLA_i}$ (see 11.5).

11.4.3 Numerical implementation

The first step of the Actuator Line Method algorithm is to compute the kinematics of the wind turbine, detailed in 11.5. The kinematic algorithm computes, at each time step, the new positions and velocities of all elements. Knowing the position of a blade element, the local wind speed can be extracted. To do so, the wind speed is computed at mass point. Then, it is possible to use the closest value (from the blade element) of the wind, or to interpolate it from the 8-neighborhood cells. Afterwards, the relative velocity is computed using (11.25), and the angle of attack α with (11.26). The aerodynamic coefficients C_L and C_D are then computed by knowing α, from a spline-cubic interpolation of the tabulated input data. Finally, the aerodynamic forces are computed in the aerodynamic frame using (11.27):

$$\boxed{\begin{cases} dF_L = \frac{1}{2}\rho c \Delta r U_{rel}^2 C_L(Re,\alpha), \\ \\ dF_D = \frac{1}{2}\rho c \Delta r U_{rel}^2 C_D(Re,\alpha). \end{cases}} \tag{11.28}$$

A last change of frame enables the projection of these forces to the global momentum budget of Meso-NH. One can note that, for the moment, only the effects of the blades are computed: the nacelle and the tower are neglected.
Note: Special attention must be paid to the number of radial (NNB_BLAELT) elements depending on the mesh used in Meso-NH. To avoid gaps in the mesh and ensure a proper distribution of efforts, it is recommended to have:

$$NNB\_RADELT > \frac{2R}{\min(\Delta x, \Delta y, \Delta z)} \tag{11.29}$$

where R is the radius of the rotor, and $\min(\Delta x, \Delta y, \Delta z)$ is the smallest dimension of the Meso-NH mesh at the rotor level.

11.4.4 Additional implementations

1D linear smearing

It is possible to use the 1D linear smearing mentionned in 11.2.4.

3D linear smearing

It is possible to use the 3D linear smearing mentionned in 11.2.4.

3D Gaussian kernel smearing

It is possible to use the 3D gaussian smearing mentionned in 11.3.4.

Tip loss correction

An over-estimation of loads is commonly predicted by the Actuator Line Method. It appears when the mollification (smearing) or the resolution are not adequate to generate tip vortices and so tip losses. To overcome this issue, the community usually applies the tip loss correction of Glauert (1935), explained in 11.3.4. It allows a better prediction of the loads (Mikkelsen (2003) or Shen et al. (2005)).

One can note that in the ALM, the number of blades is finite and this correction should not be used. Some specific corrections could be implemented, as shown by Breton et al. (2008). Besides, a better distribution of forces is also possible as proposed by Churchfield et al. (2017). As Meso-NH is a meteorological tool, the resolution might be too large compared to the guidelines recommanded for the ALM Jha et al. (2014). Then, the tip loss correction is applied by default in Meso-NH (LTIPLOSSG = .TRUE.).

Time-splitting method

In order to save computational cost, a time-splitting method has been introduced Joulin et al. (2020). This method is also called Actuator Sector Method Storey et al. (2015). If this technique allows for computational time savings, it should be used with caution, as the results may be degraded (see Joulin (2019); Jézéquel (2022)). The Courant-Friedrichs-Lewy (CFL) criterion of Meso-NH imposes a time step Δt_{MNH}. The criterion writes:

$$n_{CFL} = c\frac{\Delta t_{MNH}}{min(\Delta x, \Delta y, \Delta z)}, \tag{11.30}$$

where c is the flow velocity, and Δx, Δy, Δz the cell sizes. In Meso-NH, $n_{CFL} < 3$ is imposed according to the scheme used.

Nevertheless, the ALM often requires a shorter time step in order to ensure that a blade element point will not skip a mesh cell during this time step. The criterion for the Actuator Line Method time step Δt_{ALM} can thus be expressed as:

$$\Delta t_{ALM} \leqslant \frac{min(\Delta x, \Delta y, \Delta z)}{\Omega r_{tip}}, \tag{11.31}$$

where Ω is the angular velocity of the wind turbine, and r_{tip} the tip radius of the blade.

Because Meso-NH does not need such a short time step, a Δt_{MNH} respecting the CFL criterion is preserved. On the other side, the ALM algorithm is called N_{split} times over this duration in order to respect the ALM time step criterion (eq. (11.31)) and to reduce by $N_{split} - 1$ the number of iterations from the LES solver.

The method is illustrated in Figure 11.9. The red lines indicate blade positions at t_i and t_{i+1}. The red dots indicate blade elements. The black crosses on the left Figure show the cells missing the blade passage. On the right, the time-splitting method enables to get the history of the blade motion (green lines and dots) to compute to aerodynamic forces.
One can note that during a Meso-NH time step, the wind field is frozen. In the end, for each blade element point, the applied force is the aerodynamic force evaluated by the ALM divided by N_{split} to respect the momentum budget over Δt_{MNH}.

11.5 Kinematic

Note: For now, the management of kinematic motions is only available for ADR and ALM models (not for ADNR).

11.5.1 Kinematic classes

The wind turbine can be divided into different kinematic classes, illustrated in 11.10 .
As shown in Figure 11.11 and 11.12, each class is associated with specific frames:

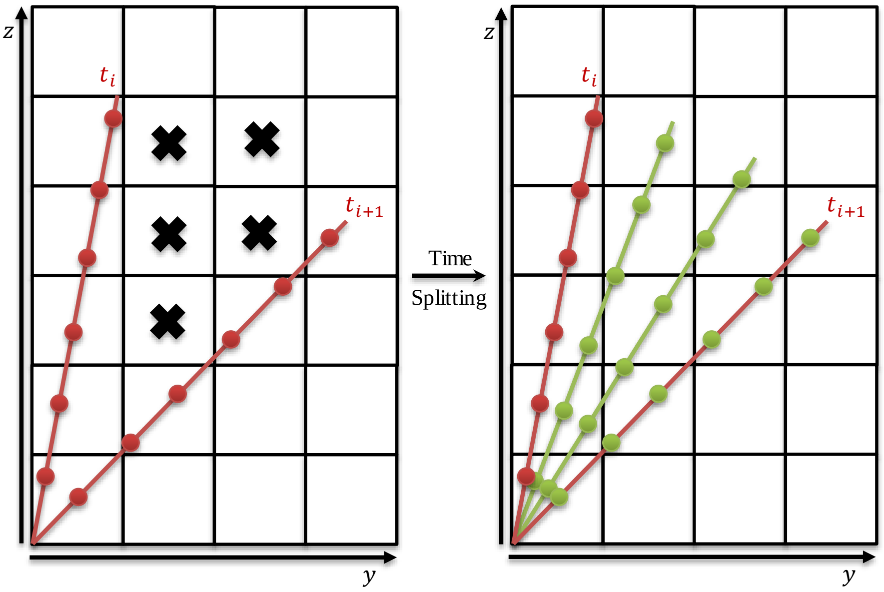

Figure 11.9: Illustration of time-splitting method, for $N_{split} = 3$. Joulin (2019)

- The domain associated with the R_{GLO} frame.
- The floater (if LFLOAT_EOL = .TRUE.), associated with the R^*_{FLO} frames (detailed in 11.5.3).
- The tower associated with the R^*_{TOW} frames.
- The nacelle associated with the R^*_{NAC} frames.
- The hub associated with the R^*_{HUB} frames.
- In the case of the ADR model: the cylindrical mesh associated with the R^*_{CYL} frames.
- In the case of the ALM model: the blade mesh associated with the R^*_{BLA} frames.

To facilitate frame management and kinematic construction, three types of frames are considered in the code:

- R^{ROOT}_*: An intermediate frame to simplify the construction of the following frame.
- R^{BASE}_*: A frame considered as the origin of the kinematic chain.
- R^{AELT}_*: A frame related to Actuator Elements.

Examples:

- R^{ROOT}_{HUB} (not shown) facilitates the placement of R^{BASE}_{HUB} relative to the nacelle by providing an intermediate reference frame, which avoids the complexity of directly handling the non-commutativity of Cardan angles.
- R^{ROOT}_{FLO} (see Figure 11.13) serves as a fixed reference frame, providing a basis for positioning R^{BASE}_{FLO}. The frame R^{BASE}_{FLO} captures the floater's motion relative to R^{ROOT}_{FLO}, enabling the representation of floating dynamics.

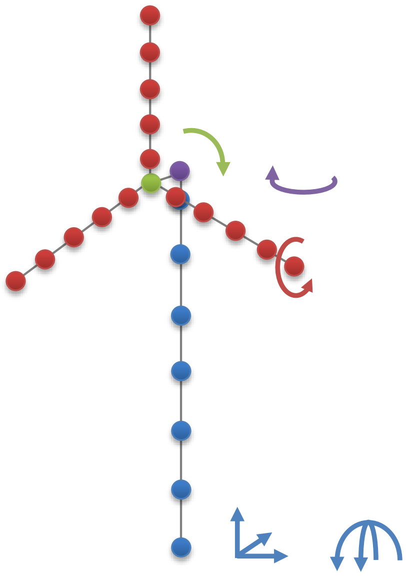

Figure 11.10: Illustration of the discretised kinematic classes. Each color is a different class, and each arrow indicates a possible motion. Joulin (2019)

- If activated, the aerodynamic computations of the drag of the tower are performed in $R_{TOW}^{AELT_k}$, which is constructed from R_{TOW}^{BASE}.

The transformation matrices $\mathcal{M}_{R_\clubsuit \to R_\spadesuit}$ are calculated at each time step to transform between frames using the `EOL_COMPUTE_TFRM` subroutine, detailed in the next subsection.

11.5.2 Description of the EOL_COMPUTE_TFRM Subroutine

The subroutine `EOL_COMPUTE_TFRM` is designed to recursively update the kinematic characteristics of the frames associated with different kinematic classes, as defined earlier. This update is performed frame by frame, where each frame is updated based on its anchor frame in a hierarchical manner.

In this context, the frame currently being updated is referred to as the Current Frame (CF), and the Anchor Frame (AF) represents the preceding frame in the hierarchy to which CF is attached. For example, CF might correspond to the nacelle base frame (R_{NAC}^{BASE}), while AF would correspond to the tower base frame (R_{TOW}^{BASE}) to which the nacelle is anchored. The subroutine integrates the relative motion between CF and AF while ensuring consistency within the global reference frame (GF).

This recursive process allows the kinematic properties, such as position, orientation, and velocity, to propagate accurately across the entire system, maintaining coherence between all interconnected frames.

The algorithm begins by determining whether CF is moving relative to AF and GF. If no relative motion is detected, the update is skipped to optimize computation. Otherwise, the subroutine proceeds with three primary steps:

First, the spatial position of CF is updated. The origin of CF in AF is calculated using an implicit Euler scheme:

$$\mathbf{O}_{CF}|_{AF} \leftarrow \mathbf{O}_{CF}|_{AF} + \mathbf{V}_{CF}|_{AF} \cdot \Delta t,$$

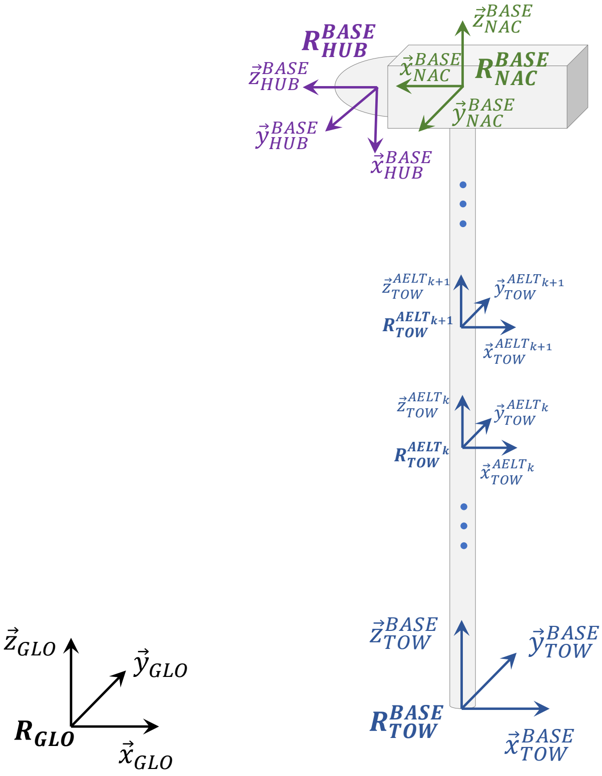

Figure 11.11: Illustration of the frames for the wind turbine.

where $\mathbf{O}_{CF}|_{AF}$ is the origin of CF relative to AF, $\mathbf{V}_{CF}|_{AF}$ is the relative translational velocity, and Δt is the time step. This origin is then transformed into GF:

$$\mathbf{O}_{CF}|_{GF} = \mathbf{O}_{AF}|_{GF} + \mathcal{M}_{R_{AF}\to R_{GF}} \cdot \mathbf{O}_{CF}|_{AF},$$

where $\mathbf{O}_{AF}|_{GF}$ is the origin of AF in GF, and $\mathcal{M}_{R_{AF}\to R_{GF}}$ is the transformation matrix from AF to GF.

Second, the angular orientation of CF is updated. The relative angular displacement in AF is computed using:

$$\boldsymbol{\theta}_{CF}|_{AF} \leftarrow \boldsymbol{\theta}_{CF}|_{AF} + \boldsymbol{\omega}_{CF}|_{AF} \cdot \Delta t,$$

where $\boldsymbol{\omega}_{CF}|_{AF}$ is the relative angular velocity. The rotation matrix $\mathcal{M}_{R_{CF}\to R_{AF}}$ is derived from the updated angles and combined with $\mathcal{M}_{R_{AF}\to R_{GF}}$ to yield:

$$\mathcal{M}_{R_{CF}\to R_{GF}} = \mathcal{M}_{R_{AF}\to R_{GF}} \cdot \mathcal{M}_{R_{CF}\to R_{AF}}.$$

Finally, the kinematic velocities in GF are updated. The angular velocity is given by:

$$\boldsymbol{\omega}_{CF}|_{GF} = \boldsymbol{\omega}_{AF}|_{GF} + \mathcal{M}_{R_{CF}\to R_{GF}} \cdot \boldsymbol{\omega}_{CF}|_{AF},$$

where $\boldsymbol{\omega}_{AF}|_{GF}$ is the angular velocity of AF in GF. The translational velocity accounts for both linear motion and rotational coupling:

$$\mathbf{V}_{CF}|_{GF} = \mathbf{V}_{AF}|_{GF} + \boldsymbol{\omega}_{AF}|_{GF} \times \mathbf{O}_{CF}|_{GF} + \mathcal{M}_{R_{AF}\to R_{GF}} \cdot \mathbf{V}_{CF}|_{AF},$$

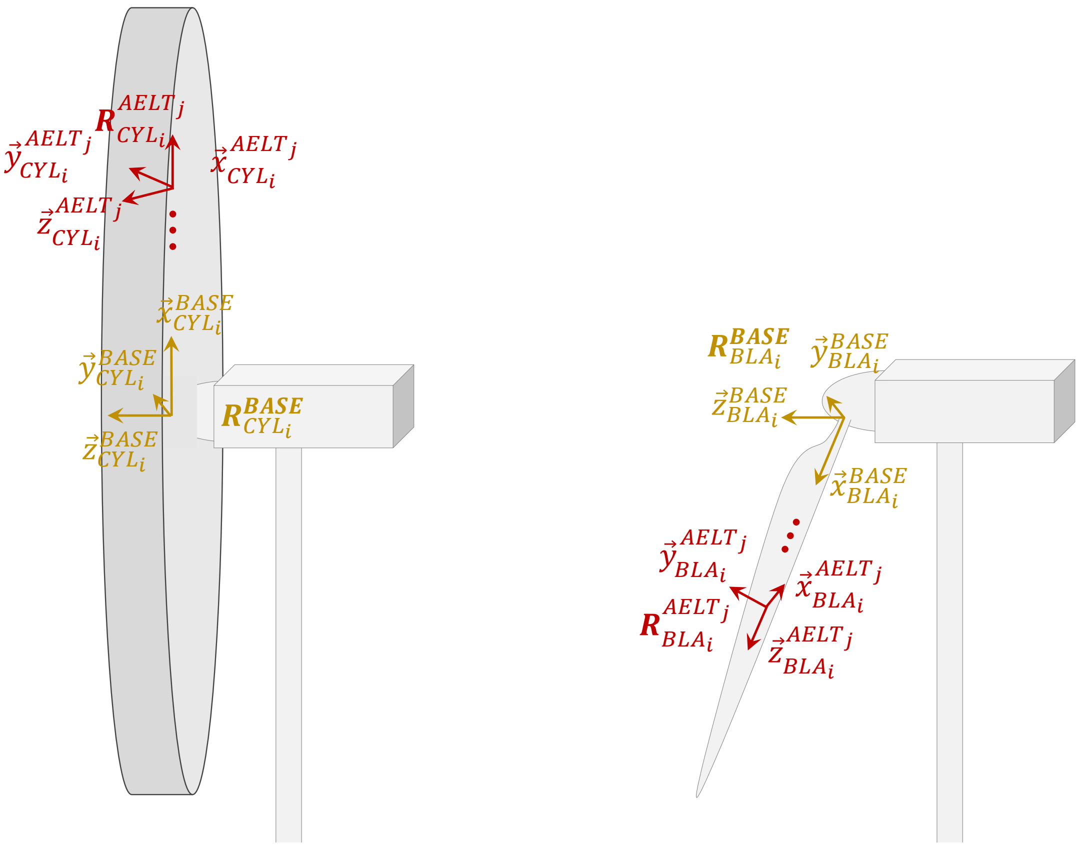

Figure 11.12: Illustration of the frames for the ALM and ADR.

where $\mathbf{O}_{CF}|_{GF}$ represents the vector from the origin of AF to CF in GF.
By combining these computations, the subroutine ensures that the kinematic state of CF is consistently updated in GF while respecting relative motions and transformations.

11.5.3 Floating Motion

Floating motions of the wind turbine can be simulated by imposing harmonic movements along all six Degrees of Freedom (DoF): surge (longitudinal translation), sway (lateral translation), heave (vertical translation), roll (rotation about the longitudinal axis), pitch (rotation about the lateral axis), and yaw (rotation about the vertical axis). These motions can be combined to create more complex oscillatory behaviors. In this context, the motion of the frame R^{BASE}_{FLO}, which anchors the base of the tower R^{BASE}_{TOW}, is modeled as a relative movement with respect to R^{ROOT}_{FLO}.
A harmonic motion is described by its mean value x_0, amplitude A, frequency f, and phase ϕ. The displacement $x(t)$ of the motion as a function of time t is given by the equation:

$$x(t) = x_0 + A \cdot \sin(2\pi f t + \phi).$$

The figure 11.13 illustrates the key frames used to model the floater's motion. The frame R^{ROOT}_{FLO} serves as a fixed reference position for the floater, while the frame R^{BASE}_{FLO} captures the floating motion relative to R^{ROOT}_{FLO}, driving the turbine's movement.

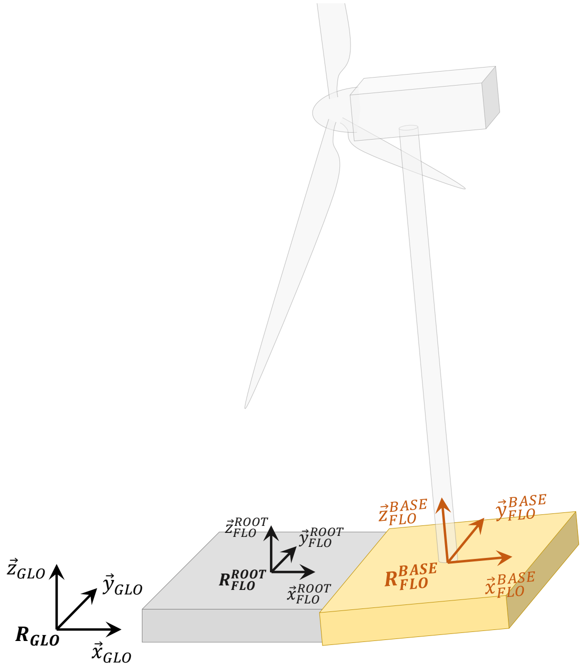

Figure 11.13: Illustration of the frames for the floatting system.

11.6 Additional features

11.6.1 Operating State Controller

The wind turbine's energy harvesting efficiency has an optimum point, which depends on the rotational velociy. Moreover, the structural reliability of the turbine also depends on its operating point. Control of the turbine's operating condition is therefore crucial. The aerodynamic forces acting on the blades generate a torque which drives the rotor through the drive train. The torque generated by the fluid flow on the rotor depends on its rotational speed, and this relationship is bidirectional. By adjusting the rotor's rotational speed, the desired torque can be achieved. Alternatively, modifying the force applied to the rotor by changing the blade pitch angle also affects rotational speed to start the turbine or to protect the structure. Consequently, the two critical operating parameters that require precise control in a wind turbine are the rotor's rotational velocity (Ω) and the blade pitch angle (γ).

An initial rotational velocity and blade pitch angle are prescribed in the CSV file *data_farm.csv* by the user. By default, these values remain constant throughout the simulation. However, this simplification does not reflect real wind turbine behavior, where both parameters must be adapted dynamically to optimize energy capture while ensuring structural reliability. In practice, the rotational velocity Ω is progressively increased with rising wind speed to maintain an optimal tip-speed ratio (TSR), defined as the ratio of the blade tip speed to the wind speed. Maintaining an optimal TSR is essential for maximizing aerodynamic efficiency, as it ensures that the blades interact with the wind at an angle that maximizes energy extraction. Once the turbine reaches its rated power, Ω is held constant, and the blade pitch angle γ is adjusted to regulate power output and protect the structure. This control strategy is particularly significant when wind conditions are uncertain, such as in time-dependent inflow scenarios or when a turbine operates within the wake of another. Fig. 11.14 illustrates an example of the operating states (Ω,γ) of an NREL 5MW wind turbine, along with the resulting power output and thrust, for various wind speeds. The real control laws are typically protected by business confidentiality, and are thus not accessible for most researchers. Consequently, the community has developed open-source control laws to mimic the actual behaviour of wind turbines. Three versions have been added to Meso-NH (by increasing complexity): look-up table, JONKM and ROSCO.

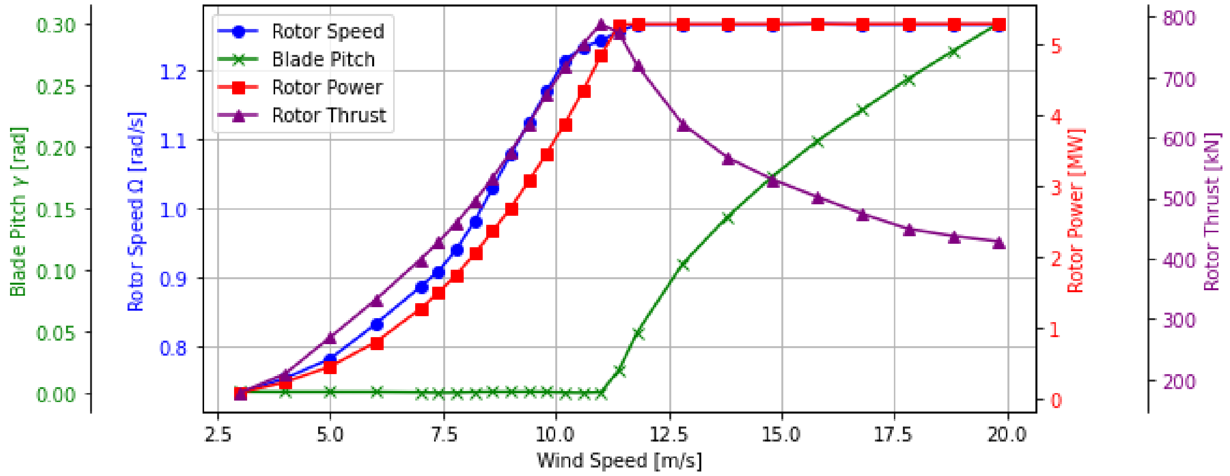

Figure 11.14: Operating points for the NREL 5MW turbine, replotted from (Jonkman 2007) data.

Look-up table

This is the most straight-forward implementation. If the value of Ω and γ are known as a function of upstream velocities u_∞ (i.e. the blue and green points of Fig. 11.14), then one can simply interpolate linearly these two variables on the measured u_∞ upstream the turbine. The user has to write the table of known values for u_∞, Ω and γ (taking care of the units) in the CSV file data_control.csv. Note however the following remarks:

- In reality, this is not how controllers work. Real-life controllers are based on a mechanical equilibrium between the shaft and the rotor to maintain optimal performance (see the following sections).
- Therefore, the sampling of the upstream velocity is arbitrary, because it has no equivalent in real life. In Meso-NH the following choices were made:
  - The velocity is the norm of the wind speed: $\sqrt{U^2+V^2+W^2}$.
  - This velocity is averaged in time over a user-defined time period $\Delta\tau$.
  - The velocity is averaged over a virtual disk upstream the rotor S, whose distance from the turbine and radius are also user-defined.

If the time-averaging is denoted with an overbar and the spatial averaging with brackets, it gives:

$$u_\infty = \left\langle \overline{\sqrt{U^2+V^2+W^2}}^{\Delta\tau} \right\rangle_S \tag{11.32}$$

- It is important to note that u_∞ and thus the operating conditions of the turbine are dependent on S and $\Delta\tau$. Since these parameters are arbitrary, it induces uncertainty in the results. In particular, there is the tricky question of the distance between S and the rotor when operating in wake conditions. If too small, it will include the induction of the rotor (which should not be included when using look-up tables), but if too big, it will underestimate the actual velocity encountered by the turbine because wakes dissipate with distance.
- Finally, one must note that with this method, Ω and γ are instantly changed every $\Delta\tau$. This may introduce unrealistic change of performance if $\Delta\tau$ is too large. On the other hand, the inertia of a real-time system damps the small turbulent variations in the upstream flow, and thus $\Delta\tau$ should not be too small either.

JONKM model

The Jonkman baseline model for the NREL 5MW turbine, hereafter named JONKM, aims to answer the above-mentioned issues and to provide the turbine a more realistic behaviour. In reality, one cannot directly control the rotational velocity, but it is possible to act on the generator's torque. The torque and velocity of the generator are linked to those of the rotor with the gearbox ratio, but the inertia of the structure causes a delay in the transmission of changes between the rotor's variables and those of the generator. This is the phenomenon that the JONKM controller, thoroughly described in section 3.1 of Jonkman (2007), tries to mimic. In Meso-NH, the implementation is divided in four steps:

1) Compute a low-pass-filtered rotational velocity:

$$\Omega_f(t_i) = (1-\alpha)\Omega(t_i) + \alpha\Omega_f(t_{i-1}) \tag{11.33}$$

with $\alpha = e^{-2\pi\Delta t f_s}$ where Δt is the simulation's time step and f_s the filter frequency.

2) Compute the command for the generator torque $\mathcal{T}_c$ depending on the "5-region law" (Fig. 11.15). The idea is to decompose the power curve (Fig. 11.14) into three parts:

    - In region 1, when the generator speed is low, no torque is demanded (and thus no power is produced). This is the starting procedure, typically below cut-in wind speed.
    - In region 2, the generator torque is commanded to be proportional to the square of the generator velocity. This is the region where power increases with wind speed.
    - In region 3, the generator torque is kept constant to its rated value and the pitch control takes over. This is the region of constant power (called rated or nominal power).

    Then, two additional regions ($1^{1/2}$ and $2^{1/2}$) are added between region 1 and 2 and regions 2 and 3 where the generator torque is linearly interpolated between the two regions, to ensure continuity.

3) A Proportional-Integral-Derivative (PID) law is applied for the pitch. The error $\Delta\Omega$ between the current filtered velocity Ω_f and the rated velocity is computed, as well as its derivative and integral. Then the command pitch is given by:

$$\gamma_c = K_1(\gamma)\left(K_p * \Delta\Omega + K_i * \int \Delta\Omega + K_d * \frac{\partial}{\partial t}\Delta\Omega\right) \tag{11.34}$$

where K_1, K_p, K_i and K_d are the global, proportional, integral and derivative gains. Finally, the blade pitch is imposed as γ_c, taking into account the maximum and minimum pitch values pre-defined by the control law. Note that K_1 depends on the current value of γ and must be recomputed at each time step. Otherwise the other gains are constant and given by the control law. In the JONKM controller, $K_d = 0$, so it is actually a PI controller.

4) The rotational velocity Ω is updated by integrating numerically the following equation, derived from the drivetrain's equation of motion:

$$\frac{\partial \Omega}{\partial t} = \frac{\eta_{gb} \mathcal{T}_{rotor} - N_{gb} \mathcal{T}_c}{I_{dt}} \tag{11.35}$$

where η_{gb} is the gearbox efficiency, $\mathcal{T}_{rotor}$ is the current rotor torque (given by the actuator method), N_{gb} is the gearbox ratio, $\mathcal{T}_c$ is the torque command (given by the controller) and I_{dt} is the drivetrain inertia.

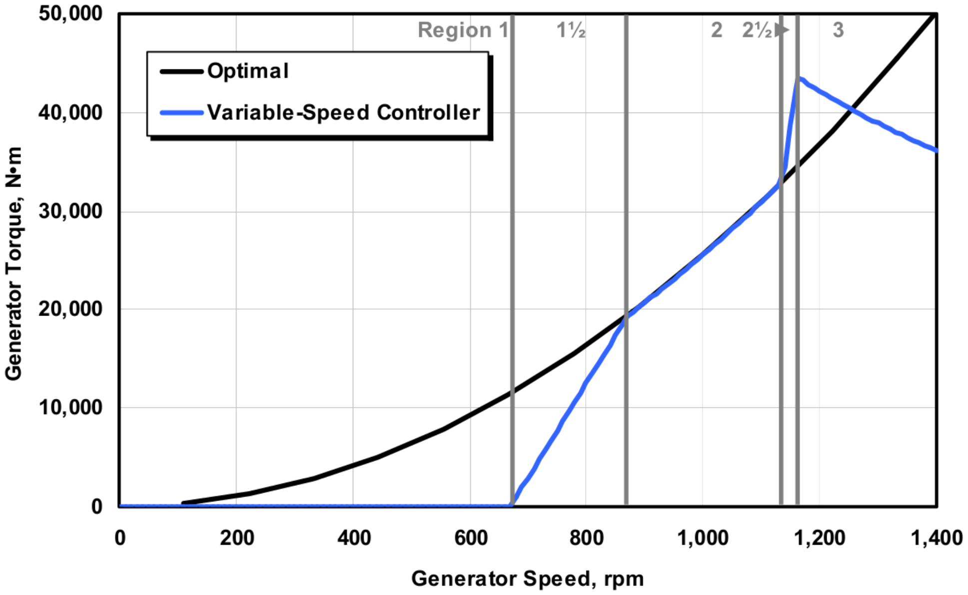

Figure 11.15: The 5-regions of the JONKM controller, figure copied from (Jonkman 2007).

Even though this model is much more realistic than the look-up table method, and less prone to error due to arbitrary variables, it requires much more knowledge on the turbine and the control law (which is also turbine-dependent). The user must indeed write the following 17 variables in the data_control file, some of which can be tricky to get:

- Filter frequency
- Drive train inertia
- Gearbox ratio and efficiency
- Ω for the cut-in, beginning and end of region 2, and its rated value.
- Cut-in and rated generator torque

- Maximum and minimum pitch values
- Constant of proportionality between $\mathcal{T}_c$ and Ω in region 2
- Constant for computation of K_1
- Proportional, integral and derivative gains.

ROSCO model

The Reference Open-Source Controller (ROSCO) (Abbas et al. 2022) has been developed as a modular reference wind turbine controller that aligns with industry standards and performs similarly to existing reference controllers. The current implementation of ROSCO is an adaptation of the original code, incorporating Control Mode 1, which utilizes a $K\Omega^2$ relationship with PI (Proportional-Integral) transitions. In this controller, Region 1.5 is not simply a linear interpolation between Region 1 and Region 2, as described in the **JONKM model**. Instead, a PI controller modifies the generator torque to maintain a defined minimum rotational velocity, while the blades are pitched to their minimum allowable angle. Similarly, in Region 2.5, when the wind speed is near the rated value, both pitch and torque are controlled by a PI controller. The control of the rotational velocity relies on the regulation of the generator torque. A simplified model of the drivetrain dynamics, based on the equation of motion, is used to establish the relationship between generator torque and rotational velocity. The control of the blade pitch relies on a PI controller to modify the aerodynamic characteristics, thereby influencing the torque and rotor behavior. The original ROSCO employs a set point smoother to handle the coupling between torque control and pitch control, particularly in the transition between below-rated and above-rated wind speeds. This mechanism ensures smooth operation and prevents conflicts between the two control systems. The set point smoother feature has not been implemented in the current version. Initial testing of the controller in both single wind turbine and wake configurations has shown satisfactory stability and performance for our specific use cases. While not exhaustive, these tests indicate that the current implementation meets our immediate operational needs without the additional complexity of a set point smoother. Fig. 11.16 illustrates the control region differences between the operating points of the NREL 5MW and IEA 15MW wind turbines. Notably, the IEA 15MW turbine enforces a minimum the rotational velocity for structural reasons, a feature not accounted for in the **JONKM model**. However, the **ROSCO model** is capable of handling the control behavior of both turbines. The implementation, similar to the **JONKM model**, is as follows:

1) Compute a second-order low-pass filter for the rotational velocity Ω and aerodynamic torque $\mathcal{T}_{rotor}$.

   The first step in the control of the rotational velocity is to filter the signals. This filtering process serves to clean the signal by removing high-frequency. The resulting smoother signal ensures better stability of the control system, leading to more precise and reliable turbine operation. A second-order low-pass filter is chosen for this purpose due to its effectiveness in attenuating high-frequency components while preserving the lower frequency content that is relevant for control. The second-order low-pass filter can be expressed as the following difference equation:

$$y(k) = \frac{1}{A_2}\left(B_2 \cdot x(k) + B_1 \cdot x(k-1) + B_0 \cdot x(k-2) - A_1 \cdot y(k-1) - A_0 \cdot y(k-2)\right) \tag{11.36}$$

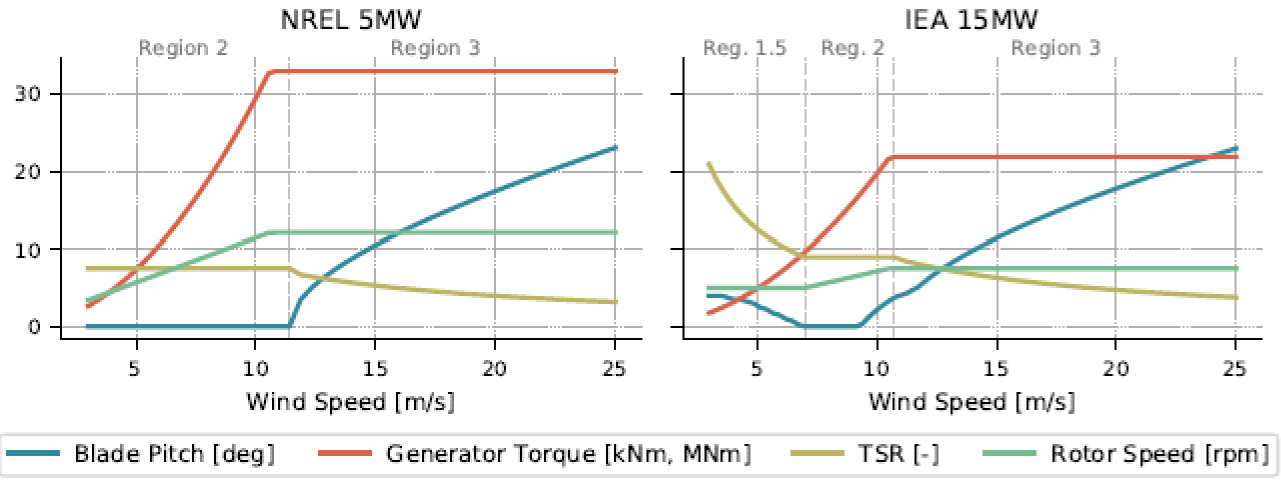

Figure 11.16: Steady-state operating points for the NREL 5-MW and IEA 15-MW turbines with ROSCO, highlighting control region differences. The IEA 15-MW turbine exhibits a nonzero blade pitch in region 1.5, and across regions 2, and 3 due to pitch-saturation. Generator torque is in kNm for NREL 5-MW and MNm for IEA 15-MW. Figure is copied from (Abbas et al. 2022).

Where:

- $y(k)$ is the output at time step k,
- $x(k)$ is the input signal at time step k,
- $y(k-1)$ and $y(k-2)$ are the previous two output values,
- $x(k-1)$ and $x(k-2)$ are the previous two input values,
- $A_0, A_1, A_2, B_0, B_1, B_2$ are the filter coefficients.

The filter coefficients $A_0, A_1, A_2, B_0, B_1, B_2$ are calculated as follows:

$$\begin{aligned}
A_2 &= \Delta t^2 f_{\text{LPF}}^2 + 4 + 4\zeta f_{\text{LPF}} \Delta t \\
A_1 &= 2\Delta t^2 f_{\text{LPF}}^2 - 8 \\
A_0 &= \Delta t^2 f_{\text{LPF}}^2 + 4 - 4\zeta f_{\text{LPF}} \Delta t \\
B_2 &= \Delta t^2 f_{\text{LPF}}^2 \\
B_1 &= 2\Delta t^2 f_{\text{LPF}}^2 \\
B_0 &= \Delta t^2 f_{\text{LPF}}^2
\end{aligned} \tag{11.37}$$

where:

- Δt is the time step,
- f_{LPF} is the cutoff frequency of the low-pass filter,
- ζ is the damping factor.

2) Compute the generator torque command $\mathcal{T}_c$ for power production target.

The generator torque command depend on the control region as follows:

- region 1: no torque is demanded,
- region 1.5: command torque is computed with the below rated PI Controller,
- region 2: command torque is computed using the empirical relationship for torque $\mathcal{T}_c = K\Omega^2$
- region 2.5: command torque is computed with the above rated PI Controller,
- region 3: command torque is computed as constant power output $\mathcal{T}_c = P_{rated}/\Omega$

The generator torque command is saturated between minimal and maximal allowable values.

3) Compute the rotational velocity Ω according to the generator torque command $\mathcal{T}_c$.

   As mentioned in the **JONKM model**, the rotational velocity Ω of the wind turbine drivetrain can be determined using the equation of motion 11.35, which provides a simplified representation of the system's dynamics. The equation is solved using a straightforward Euler time integration scheme.

4) Compute the blade pitch angle γ according to the rotational velocity Ω.

   A PI controller is used, where proportional and integral gain coefficients are derived from a polynomial fit of the gain-scheduling table in the DISCON.IN file. This file is part of the ROSCO framework integrated within the main ROSCO repository: `https://github.com/NREL/ROSCO`. The PI controller then calculates the blade pitch command based on the error between the current rotational velocity and the rated rotational velocity.

   The blade pitch command is saturated between minimal and maximal allowable values.

11.6.2 Tower and nacelle

The tower and nacelle drag forces can be added in Meso-NH. This is a very simple implementation based on the work of Stevens et al. (2018). The drag forces are implemented similarly to the actuator forces for blades, except that they are assumed to be simple cylinder (oriented vertically for the tower and horizontally for the nacelle). The total forces read:

$$F_{nacelle} = \rho \frac{1}{2} C'_{nacelle} u^2 \frac{\pi}{4} D^2_{nacelle} \tag{11.38}$$

$$F_{tower} = \rho \frac{1}{2} C'_{tower} u^2 \frac{\pi}{4} D^2_{tower} z_h \tag{11.39}$$

where $C'_{nacelle} = 4$ and $C'_{tower} = 0.68$, ρ is the density, D the diameter of the nacelle and tower, respectively, and z_h the hub height. To distribute the forces, the nacelle is assumed to be a disk thick of 1 mesh point, but whose surface can span on several mesh points. In such case, every mesh point is given an equal proportion of $F_{nacelle}$. The tower is assumed to span on only one cell horizontally, and each cell between the ground and the hub height receives a drag force equal to F_{tower}/n_h where n_h is the number of cell between the ground and the hub height.

11.6.3 Wind turbine passive scalar variables

This implementation allows emitting a virtual passive scalar variable for any wind turbine simulated (each turbine has its own passive scalar). When activated, it creates a virtual disk defined by the user similarly as described in the velocity look-up table (first paragraph of Sect. 11.6.1) that will be the source of the tracer.

The value of the source of each passive scalar variable is imposed to 1 at each time step. Note that it is further multiplied by $PTSTEP/PRHODJ$, so one may not retrieve 1 as the value at the disk. Afterwards, it is advected with the chosen numerical scheme as any other passive scalar variable.

This implementation has been thought as a way to track the wakes of each wind turbine independently. Note that this method has not been validated in a report or a publication so far (only used in Jézéquel et al. (2024)), so consider it to be experimental at this stage. In the namelist and code, it is called 'tracers', but keep in mind that this is a passive scalar advection, and not a Lagrangian variable.

11.7 References

Abbas, N. J., D. S. Zalkind, L. Pao, and A. Wright, 2022: A reference open-source controller for fixed and floating offshore wind turbines. *Wind Energy Science*, **7 (1)**, 53–73.

Aitken, M. L., B. Kosović, J. D. Mirocha, and J. K. Lundquist, 2014: Large eddy simulation of wind turbine wake dynamics in the stable boundary layer using the weather research and forecasting model. *Journal of Renewable and Sustainable Energy*, **6 (3)**, 033 137.

Aitken, M. L. and J. K. Lundquist, 2014: Utility-scale wind turbine wake characterization using nacelle-based long-range scanning lidar. *Journal of Atmospheric and Oceanic Technology*, **31 (7)**, 1529–1539.

Breton, S.-P., F. N. Coton, and G. Moe, 2008: A study on rotational effects and different stall delay models using a prescribed wake vortex scheme and nrel phase vi experiment data. *Wind Energy: An International Journal for Progress and Applications in Wind Power Conversion Technology*, **11 (5)**, 459–482.

Burton, T., D. Sharpe, N. Jenkins, and E. Bossanyi, 2001: *Wind energy handbook*. John Wiley & Sons.

Calaf, M., C. Meneveau, and J. Meyers, 2010: Large eddy simulation study of fully developed wind-turbine array boundary layers. *Physics of fluids*, **22 (1)**, 015 110.

Calaf, M., M. B. Parlange, and C. Meneveau, 2011: Large eddy simulation study of scalar transport in fully developed wind-turbine array boundary layers. *Physics of Fluids*, **23 (12)**, 126 603.

Churchfield, M., S. Lee, P. Moriarty, L. Martinez, S. Leonardi, G. Vijayakumar, and J. Brasseur, 2012: A large-eddy simulation of wind-plant aerodynamics. *50th AIAA Aerospace Sciences Meeting including the New Horizons Forum and Aerospace Exposition*, 537.

Churchfield, M. J., S. J. Schreck, L. A. Martinez, C. Meneveau, and P. R. Spalart, 2017: An advanced actuator line method for wind energy applications and beyond. *35th Wind Energy Symposium*, 1998.

Froude, R. E., 1889: On the part played in propulsion by differences of fluid pressure. *Trans. Inst. Naval Architects*, **30**, 390.

Glauert, H., 1935: Airplane propellers. *Aerodynamic theory*, Springer, 169–360.

Ivanell, S., J. N. Sorensen, and D. Henningson, 2007a: Numerical computations of wind turbine wakes. *Wind Energy*, Springer, 259–263.

Ivanell, S., J. N. Sorensen, R. Mikkelsen, and D. Henningson, 2007b: Numerical analysis of the tip and root vortex position in the wake of a wind turbine. *Journal of Physics: Conference Series*, **75 (1)**, 012–035.

Ivanell, S. S. A., 2009: Numerical computations of wind turbine wakes. Ph.D. thesis, KTH, Mechanics, Linné Flow Center, FLOW, xx, 77 pp., qC 20100720.

Jézéquel, E., F. Blondel, and V. Masson, 2024: Breakdown of the velocity and turbulence in the wake of a wind turbine – part 2: Analytical modelling. *Wind Energy Science*, **9 (1)**, 119–139, doi:10.5194/wes-9-119-2024.

Jézéquel, E. J., 2022: Simulations of wind turbine wakes in realistic atmospheric conditions: from large eddy simulations to analytical models. Ph.D. thesis, Institut National Polytechnique de Toulouse-INPT.

Jha, P. K., M. J. Churchfield, P. J. Moriarty, and S. Schmitz, 2014: Guidelines for volume force distributions within actuator line modeling of wind turbines on large-eddy simulation-type grids. *Journal of Solar Energy Engineering*, **136 (3)**.

Jimenez, A., A. Crespo, E. Migoya, and J. García, 2007: Advances in large-eddy simulation of a wind turbine wake. *Journal of Physics: Conference Series*, **75 (1)**, 012–041.

Jimenez, A., A. Crespo, E. Migoya, and J. García, 2008: Large-eddy simulation of spectral coherence in a wind turbine wake. *Environmental Research Letters*, **3 (1)**, 015 004.

Jonkman, J. M., 2007: *Dynamics Modeling and Loads Analysis of an Offshore Floating Wind Turbine*. doi:10.2172/921803.

Joulin, P.-A., 2019: Modélisation à fine échelle des interactions entre parcs éoliens et météorologie locale. Ph.D. thesis, SDU2E - INPT.

Joulin, P.-A., M. L. Mayol, V. Masson, F. Blondel, Q. Rodier, M. Cathelain, and C. Lac, 2020: The actuator line method in the meteorological les model meso-nh to analyze the horns rev 1 wind farm photo case. *Frontiers in Earth Science*, **7**, 350, doi:10.3389/feart.2019.00350.

Lu, H. and F. Porté-Agel, 2011: Large-eddy simulation of a very large wind farm in a stable atmospheric boundary layer. *Physics of Fluids*, **23 (6)**, 065 101.

Lu, H. and F. Porté-Agel, 2015: On the impact of wind farms on a convective atmospheric boundary layer. *Boundary-layer meteorology*, **157 (1)**, 81–96.

Madsen, H. A., 1997: A cfd analysis of the actuator disc flow compared with momentum theory results. *10th IEA meeting on aerodynamics*, Technical University of Denmark. Department of Fluid Mechanics, 109–124.

Marjanovic, N., 2015: *Simulation of the Atmospheric Boundary Layer for Wind Energy Applications*. University of California, Berkeley.

Marjanovic, N., J. D. Mirocha, B. Kosović, J. K. Lundquist, and F. K. Chow, 2017: Implementation of a generalized actuator line model for wind turbine parameterization in the weather research and forecasting model. *Journal of Renewable and Sustainable Energy*, **9 (6)**, 063 308, doi:10.1063/1.4989443.

Meyer Forsting, A. R., G. R. Pirrung, and N. Ramos-García, 2019: A vortex-based tip/smearing correction for the actuator line. *Wind Energy Science*, **4 (2)**, 369–383.

Mikkelsen, R., 2003: Actuator disc methods applied to wind turbines. technical university of denmark. Ph.D. thesis, PhD Thesis.

Mirocha, J., B. Kosovic, M. Aitken, and J. Lundquist, 2014: Implementation of a generalized actuator disk wind turbine model into the weather research and forecasting model for large-eddy simulation applications. *Journal of Renewable and Sustainable Energy*, **6 (1)**, 013 104.

Mirocha, J. D., D. A. Rajewski, N. Marjanovic, J. K. Lundquist, B. Kosović, C. Draxl, and M. J. Churchfield, 2015: Investigating wind turbine impacts on near-wake flow using profiling lidar data and large-eddy simulations with an actuator disk model. *Journal of Renewable and Sustainable Energy*, **7 (4)**, 043 143.

Porté-Agel, F., M. Bastankhah, and S. Shamsoddin, 2020: Wind-turbine and wind-farm flows: a review. *Boundary-Layer Meteorology*, **174 (1)**, 1–59.

Porté-Agel, F., H. Lu, and Y.-T. Wu, 2014: Interaction between large wind farms and the atmospheric boundary layer. *Procedia Iutam*, **10**, 307–318.

Porté-Agel, F., Y.-T. Wu, H. Lu, and R. J. Conzemius, 2011: Large-eddy simulation of atmospheric boundary layer flow through wind turbines and wind farms. *Journal of Wind Engineering and Industrial Aerodynamics*, **99 (4)**, 154–168.

Rankine, W., 1865: On the mechanical principles of the action of propellers. *Trans. Inst. Naval Architects*, **6**, 13–39.

Shamsoddin, S. and F. Porté-Agel, 2017: Large-eddy simulation of atmospheric boundary-layer flow through a wind farm sited on topography. *Boundary-Layer Meteorology*, **163 (1)**, 1–17.

Shen, W. Z., J. N. Sorensen, and R. Mikkelsen, 2005: Tip loss correction for actuator/navier–stokes computations. *Journal of Solar Energy Engineering*, **127 (2)**, 209–213.

Sorensen, J., W. Shen, and X. Munduate, 1998: Analysis of wake states by a full-field actuator disc model. *Wind Energy*, **1 (2)**, 73–88.

Sorensen, J. N. and C. W. Kock, 1995: A model for unsteady rotor aerodynamics. *Journal of wind engineering and industrial aerodynamics*, **58 (3)**, 259–275.

Sorensen, J. N. and A. Myken, 1992: Unsteady actuator disc model for horizontal axis wind turbines. *Journal of Wind Engineering and Industrial Aerodynamics*, **39 (1-3)**, 139–149.

Sorensen, J. N. and W. Z. Shen, 2002: Numerical modeling of wind turbine wakes. *Journal of fluids engineering*, **124 (2)**, 393–399.

Stevens, R. J., L. A. Martínez-Tossas, and C. Meneveau, 2018: Comparison of wind farm large eddy simulations using actuator disk and actuator line models with wind tunnel experiments. *Renewable Energy*, **116**, 470–478, doi:10.1016/j.renene.2017.08.072.

Storey, R. C., S. E. Norris, and J. E. Cater, 2015: An actuator sector method for efficient transient wind turbine simulation. *Wind Energy*, **18 (4)**, 699–711, doi:10.1002/we.1722.

Tabib, M., M. S. Siddiqui, E. Fonn, A. Rasheed, and T. Kvamsdal, 2017: Near wake region of an industrial scale wind turbine: comparing les-alm with les-smi simulations using data mining (pod). *Journal of Physics: Conference Series*, **854 (1)**, 012–044.

Troldborg, N., 2009: Actuator line modeling of wind turbine wakes. Ph.D. thesis, DTU.

Wu, Y.-T. and F. Porté-Agel, 2011: Large-eddy simulation of wind-turbine wakes: evaluation of turbine parametrisations. *Boundary-layer meteorology*, **138 (3)**, 345–366.

Wu, Y.-T. and F. Porté-Agel, 2015: Modeling turbine wakes and power losses within a wind farm using les: An application to the horns rev offshore wind farm. *Renewable Energy*, **75**, 945–955.

Chapter 12

Blaze fire model

Contents

12.1 Introduction

The fire's existence is represented in the atmospheric model by the latent and sensible heat fluxes at the surface, and the impact of the atmosphere on the fire's behavior is represented in the fire model by the surface wind in MÉSONH-BLAZE. The role of the BLAZE model can be summarized as follows :

- identify the position of the fire front at a time t,
- communicate with MÉSONH to retrieve surface wind data at time t,
- compute the normal rate of spread of the fire front $\mathcal{R}$ at this time t as a function of meteorological and environmental factors,
- to make the fire front move on the terrain surface up to the time $t + \Delta t$,
- calculate the latent and sensible heat fluxes induced by the fire between the instants t and $t + \Delta t$,
- communicate with MÉSONH to provide heat flux data for the period $[t, t + \Delta t]$,
- operate in a massively parallel environment by using the parallelization tools of MÉSONH.

The Blaze fire model features the following components: *i)* an Eulerian two-dimensional front-tracking model that relies on a level-set (LS) method and uses a description of the local rate of spread based on Balbi's formulation (Balbi et al. 2009); and *ii)* a flux parametrization that estimates the spatial distribution and intensity of the surface latent and sensible heat fluxes. If Blaze is embedded in an atmospheric model, these heat fluxes act as surface boundary conditions to solve the atmospheric flow perturbed by the fire.
The interested reader is strongly advised to read the thesis of Aurélien COSTES and the original paper of Blaze in addition to this technical note (Costes et al. 2021).

12.2 Level-set method for fire spread

12.2.1 Fire mesh

The LS method is used to propagate the time-evolving fireline on a two-dimensional horizontal plane (x, y). The two-dimensional fire grid is defined with respect to the resolution of the atmospheric data. Since the fireline propagation is a subgrid-scale process with respect to the atmosphere, the atmospheric mesh is divided into Γ_x cells in the x-direction and Γ_y cells in the y-direction to form the fire mesh in Blaze. A distinction is therefore made between the atmospheric surface mesh, referred to as "atmospheric mesh", of resolution $(\Delta x, \Delta y)$, and the fire mesh of resolution $(\Delta x_f, \Delta y_f)$ with $\Delta x_f = \Delta x/\Gamma_x$ and $\Delta y_f = \Delta y/\Gamma_y$.

From a technical point of view, it means that the fire mesh is a 2D array of size $(\Gamma_x N_x, \Gamma_y N_y)$ where N_x and N_y represent the size of the atmospheric mesh in x and y directions respectively. However, this 2D grid size is not supported by the parallelization paradigm of MÉSONH, which needs a 2D array of size (N_x, N_y). Therefore, every fire-related array which is generally of size $(\Gamma_x N_x, \Gamma_y N_y)$ shall be stored as a 3D array of size $(N_x, N_y, \Gamma_x \Gamma_y)$. The 3D format arrays are not very convenient for gradient operators. Fire-related fields are stored in this 3D format in output files which is not very convenient for post-processing. Two functions are then defined to switch from one representation to another.

The first uses 3D representation indexes (i, j, k) to compute 2D representation indexes (l, m). It defines temporary variables a and b.

$$\begin{aligned} b &= (k-1) \div \Gamma_x + 1 \\ a &= k - (b-1)\Gamma_x \\ l &= (i-1)\Gamma_x + a \qquad (12.1) \\ m &= (j-1)\Gamma_y + b \qquad (12.2) \end{aligned}$$

where ÷ is the euclidian division.

The second one uses 2D representation indexes (l, m) to compute 3D representation indexes (i, j, k). It defines temporary variables a and b.

$$\begin{aligned} a &= l - (i-1)\Gamma_x \\ b &= m - (j-1)\Gamma_y \\ i &= \left\lceil \frac{l}{\Gamma_x} \right\rceil \qquad (12.3) \\ j &= \left\lceil \frac{m}{\Gamma_y} \right\rceil \qquad (12.4) \\ k &= (b-1)\Gamma_x + a \qquad (12.5) \end{aligned}$$

These functions are commonly used in the code in three steps: *i)* switch a fire-related array from 3D to 2D representation, *ii)* use an operator (gradient, for example) on the 2D array, *iii)* switch the result of the operator from 2D to 3D representation.
For post-processing purposes, the two functions are available in the Pyrolib package.

12.2.2 Governing equation

In Blaze, the LS function $\phi \equiv \phi(x, y, t)$ is not a signed distance but rather a bounded function $0 \leqslant \phi \leqslant 1$, where the contour line $\phi = 0.5$ is identified as the fire front; $\phi > 0.5$ represents burnt vegetation, and $\phi < 0.5$ represents unburnt vegetation at a given time t. The LS field is transported at the rate of spread $\mathcal{R}$ and satisfies the following Hamilton-Jacobi equation:

$$\frac{\partial \phi}{\partial t} = \mathcal{R}\left(|\nabla\phi| + \epsilon_\phi \widetilde{\Delta}\phi\right) \qquad (12.6)$$

where $\nabla\phi = \left(\frac{\partial\phi}{\partial x}, \frac{\partial\phi}{\partial y}\right)$ is the LS gradient, $\widetilde{\Delta}\phi = \left(\Delta x_f \frac{\partial^2\phi}{\partial x^2} + \Delta y_f \frac{\partial^2\phi}{\partial y^2}\right)$ is the fire-mesh-size-proportional Laplacian, $\epsilon_\phi\widetilde{\Delta}\phi$ is the artificial viscosity term to ensure numerical stability, and $\mathcal{R}$ represents the speed projected onto the normal direction $\underline{n}$ to the fireline, $\underline{n} = -\nabla\phi/|\nabla\phi|$. $\mathcal{R}$ is evaluated using Balbi's rate-of-spread parameterization (Santoni et al. 2011). Numerical tests have shown that $\epsilon_\phi = 0.1$ gives satisfactory results.

In BLAZE, the Hamilton-Jacobi equation (Equation 12.6) is solved numerically using a third-order Runge-Kutta scheme in time and a third-order WENO (*Weighted Essentially Non-Oscillatory*) scheme in space (RK3-WENO3). A first-order WENO method and the same RK schemes available in MÉSONH can also be used.

Due to the potential heterogeneity of the fuel parameters that may affect the stability of the numerical schemes, an artificial viscosity is added to the ROS computation (in addition to the one added to the level-set ϕ function) as follows:

1. At each point on the fire grid, a temporary rate of spread, denoted $\mathcal{R}^*$, is calculated from Balbi's analytical formulation.

2. The modified Laplacian operator is computed on the temporary field, $widetilde\Delta\mathcal{R}^*$, subject to local variations due to heterogeneities in the input parameters :

$$\mathcal{R} = \mathcal{R}^* + \varepsilon_{\mathcal{R}}\widetilde{\Delta}\mathcal{R}^*, \tag{12.7}$$

   where $\varepsilon_{\mathcal{R}}$ is the viscosity coefficient on the rate of spread which is set by default to 0.1. This value was considered reasonable in view of numerical tests not shown here.

3. This smoothing operation is repeated a second time in order to obtain a satisfactory result on the rate of spread $\mathcal{R}$, that is:

$$\mathcal{R} = \mathcal{R}^* + \varepsilon_{\mathcal{R}}\widetilde{\Delta}\mathcal{R}^* + \varepsilon_{\mathcal{R}}\widetilde{\Delta}\left(\mathcal{R}^* + \varepsilon_{\mathcal{R}}\widetilde{\Delta}\mathcal{R}^*\right). \tag{12.8}$$

12.2.3 Wind interpolation

In order to compute the rate of spread on the fire mesh, we need to interpolate the wind speed from the atmospheric mesh to the fire mesh. We need to compute U_0 defined by:

$$U_0 = \underline{U} \cdot \underline{n}, \tag{12.9}$$

where $\underline{U}$ is the wind vector at the fire front, and $\underline{n}$ is the fire front normal vector. As $\underline{n}$ is a 3D vector, every wind component needs to be interpolated.

Vertical interpolation

For now, there is no vertical wind interpolation in BLAZE. The horizontal wind (u, v) is taken at the first vertical level (excluding the halo). The vertical wind is linearly interpolated at the same level between the ground and the first vertical level (excluding the halo). The lack of independence between the mesh and the interpolation method is a real problem for the model. This development should be one of the priorities of the community.

Horizontal interpolation

The simplest horizontal interpolation method is to distribute the wind from one atmospheric cell to all the fire cells included in it, which is equivalent to considering a uniform wind in an atmospheric cell. This method is used when LINTERPWIND is set to False. It can lead to discontinuities in the rate of spread and is not recommended.

When LINTERPWIND is set to True, a 2D interpolation of the wind (u, v, w) is applied.
The first step in this method is to linearly interpolate each wind component at the corners of the considered atmospheric mesh, represented by the white circles in Figure 12.1. For example, for the bottom right point of the considered atmospheric mesh, the intermediate wind is computed as follows :

$$\underline{u}_1 = (u_1, v_1) = \frac{1}{2}(u_{ij} + u_{ij-1}, v_{ij} + v_{i-1j}). \tag{12.10}$$

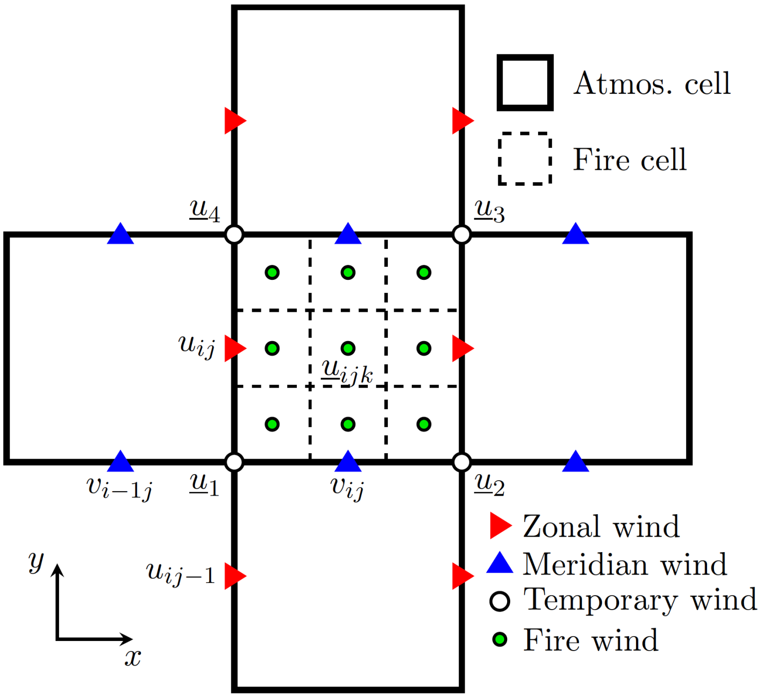

Figure 12.1: Horizontal interpolation of wind from the atmospheric grid to the fire grid.

The second step consists in bilinearly interpolating the wind $\underline{u}_{ijk}$ at each fire cell indexed with $k \in [1, \Gamma_x\Gamma_y]$ and contained in the considered atmospheric mesh, labeled by the indexes (i, j) from the values $\underline{u}_1$, $\underline{u}_2$, $\underline{u}_3$, and $\underline{u}_4$:

$$\underline{u}_{ijk} = \frac{1}{(\Gamma_x + 1)(\Gamma_y + 1)} \Big[m(l\underline{u}_3 + (\Gamma_x + 1 - l)\underline{u}_4) + (\Gamma_y + 1 - m)(l\underline{u}_2 + (\Gamma_x + 1 - l)\underline{u}_1) \Big], \quad (12.11)$$

with

$$m = (k - 1) \div \Gamma_x + 1, \quad (12.12)$$

$$l = k - (m - 1)\Gamma_x, \quad (12.13)$$

where $\div$ is the Euclidean division.

Time-based smoothing

For very rapidly varying wind intensity, the temporal signal given to the rate-of-spread parameterization can be smoothed by using a moving average method. The recursive Exponential Weighted Averaging Method is used in BLAZE. The interest quantity s_n given to BLAZE is computed from the previous time step s_{n-1} and the interpolated wind computed by MÉSONH u_n as:

$$s_n = s_{n-1} + \beta(u_n - s_{n-1}), \quad (12.14)$$

where $\beta \in [0, 1]$ is a control parameter. The value of β is computed by:

$$\beta = \frac{2}{1 + \left\lceil \frac{\tau}{\Delta t} \right\rceil}, \quad (12.15)$$

where τ [s] is the averaging time (the same time constant one would find in a simple averaging method), and Δt is the MÉSONH time step.
The time-based smoothing can be activated by LWINDFILTER=.TRUE.. The filter's time constant τ is set by XEWAMTAU (default value: 20s).

12.2.4 Slope impact on the rate of spread

Section 12.2.2 described the governing equation for the level-set method on a flat and uniform cartesian grid. However, the terrain is not always flat and the rate of spread parameterization needs to take into account the slope.

vector space definition

Let's consider here four vector bases. The orthonormal reference base of the atmospheric model $(\underline{e}_x, \underline{e}_y, \underline{e}_z)$. It contains, for example, the wind $\underline{U}$. There is also the contravariant basis $(\underline{\hat{e}}_x, \underline{\hat{e}}_y, \underline{\hat{e}}_z)$ which corresponds to the deformed basis of the atmospheric mesh.

Then, we find the basis of the flame plane $(\underline{n}, \underline{p}, \underline{q})$ with $\underline{n}$ the normal to the front parallel to the surface, $\underline{p}$ the normal to the surface and $\underline{q}$ the vector product of the two previous vectors.

Let us project this basis on the horizontal surface, which constitutes the basis for the level set $(\underline{\tilde{n}}, \underline{\tilde{p}}, \underline{\tilde{q}})$. These vectors are determined by $\underline{\tilde{n}} \cdot \underline{n} = \cos\alpha$, where α is the slope in the propagation direction. In this case, $\underline{\tilde{p}} = \underline{e}_z$ and $\underline{\tilde{q}} = \underline{q}$. This basis corresponds to the rotation of angle $-\alpha$ according to the vector $\underline{q}$ of the basis $(\underline{n}, \underline{p}, \underline{q})$.

Vector composition

The purpose is to implement the effect of slope on the rate of spread $\mathcal{R}$ of the Balbi model. As a reminder, the ROS is affected by the wind and the slope in a single expression depending on the value of the *tilt angle* of the flame γ. This angle corresponds to the composition of the mid-flame wind vector $\underline{U}_0$ and the vertical velocity vector in the flame $\underline{v}_f$:

$$\underline{V} = \underline{U}_0 + \underline{v}_f. \tag{12.16}$$

The γ angle is then defined as

$$\tan\gamma = \frac{\underline{V} \cdot \underline{n}}{\underline{V} \cdot \underline{p}}. \tag{12.17}$$

The wind vector is, by definition, collinear to the front normal

$$\underline{U}_0 = U_0 \underline{n}. \tag{12.18}$$

The vertical velocity in the flame is, by definition, collinear with the vertical direction

$$\underline{v}_f = v_f \underline{e}_z. \tag{12.19}$$

In (Santoni et al. 2011), the vertical velocity along the surface normal v_0 is known as a function of the other model parameters. Moreover, Santoni et al. (2011) shows that

$$v_f = \frac{v_0}{\cos\alpha}. \tag{12.20}$$

Decomposing $\underline{e}_z$ in the flame plane basis and using the previous relation, one gets

$$\underline{V} = (U_0 + v_0 \tan\alpha)\underline{n} + v_0\underline{p}. \tag{12.21}$$

Therefore, it is possible to write

$$\tan\gamma = \tan\alpha + \frac{U_0}{v_0}. \tag{12.22}$$

Computation of the base spaces

It is necessary to compute a few basis vectors to determine γ. In particular, the level set propagation is done on an imaginary horizontal plane of basis $(\underline{e}_x, \underline{e}_y)$. From $\underline{\nabla}\phi$, we can determine $\underline{\tilde{n}}$. It is then necessary to calculate α, $\underline{n}$, and U_0.

The slope is a two-dimensional vector that can be expressed in several bases. A natural basis, already used in many models, consists of two angles α_s and α_a, representing the angle of the steepest slope and the direction of the face with respect to the North, respectively. The second option is to use a projection of the slope vector on an orthonormal basis, typically $(\underline{e}_x, \underline{e}_y)$.

For MÉSONH-BLAZE, the slope can be determined by two methods:

- through a height map on the atmospheric grid, $z(x, y)$, or the fire grid, $z(x_f, y_f)$,
- or a map of angles α_s and α_a on the fire grid.

The two representations are strictly equivalent, but the numerical use of angles requires the use of many trigonometric and non-linear functions which has a significant numerical cost. Whenever possible, it is better to work with vector projection, which only requires scalar products (*i.e.* a product of vectors component by component, which is easily vectorized by the machine).
We, therefore, set up a calculation strategy based on the height map and the components of the orographic gradient.

Computation of the orographic gradient The expression of the components of the orographic gradient $\underline{\nabla}z$, noted $\underline{h}$ at the center of the atmospheric cell (i, j) is given by:

$$\begin{aligned}
\underline{\nabla}z \cdot \underline{e}_x = h^{x,a}_{i,j} &= \frac{z_{i+1,j-1} - z_{i-1,j-1} + 2(z_{i+1,j} - z_{i-1,j}) + z_{i+1,j+1} - z_{i-1,j+1}}{8\Delta x}, \\
\underline{\nabla}z \cdot \underline{e}_y = h^{y,a}_{i,j} &= \frac{z_{i-1,j+1} - z_{i-1,j-1} + 2(z_{i,j+1} - z_{i,j-1}) + z_{i+1,j+1} - z_{i+1,j-1}}{8\Delta y}.
\end{aligned} \tag{12.23}$$

As for the interpolation of the wind, we interpolate at the corners of the atmospheric mesh, noted $\llcorner$. There are thus $(N_x + 1, N_y + 1)$ interpolated slopes. For the x component, it is defined by:

$$h^{x,a\llcorner}_{i,j} = \frac{h^{x,a}_{i,j} + h^{x,a}_{i-1,j} + h^{x,a}_{i,j+1} + h^{x,a}_{i+1,j+1}}{4}. \tag{12.24}$$

Same on the y component.
Finally, we interpolate the orographic gradient components on the fire grid with the same approach as for the wind components.

Computation of the front normal on the surface plane For a particular fire cell, the components of the orographic gradient allow determining two director vectors of the plane forming the mean surface of the fire cell.

$$\underline{s}_1 = (1, 0, h_x), \tag{12.25}$$

$$\underline{s}_2 = (0, 1, h_y). \tag{12.26}$$

The normal vector $\underline{n}$ lies in this plane and has for projection on the horizontal plane the vector $\underline{\tilde{n}}$ whose components are known as

$$\underline{\tilde{n}} = \frac{1}{\|\underline{\nabla}\phi\|}(\underline{\nabla}_x\phi, \underline{\nabla}_y\phi, 0). \tag{12.27}$$

$\underline{n}$ is, therefore, a linear combination of the two director vectors

$$\underline{n} = a\underline{s}_1 + b\underline{s}_2. \tag{12.28}$$

However, $\underline{n}$ shares its components on x and y with $\underline{\tilde{n}}$, which can be written

$$\begin{cases} n_x = a = \tilde{n}_x \\ n_y = b = \tilde{n}_y \\ n_z = ah_x + bh_y \end{cases} \tag{12.29}$$

This allows us to write that the angle of the slope in the direction of propagation α respects

$$\tan\alpha = \frac{\tilde{n}_x h_x + \tilde{n}_y h_y}{\sqrt{\tilde{n}_x^2 + \tilde{n}_y^2}}. \tag{12.30}$$

However, $\underline{\tilde{n}}$ is a unit vector which implies that its norm is 1. Therefore we get

$$\tan\alpha = \tilde{n}_x h_x + \tilde{n}_y h_y. \tag{12.31}$$

This is equivalent to calculating $\underline{\tilde{n}} \cdot \underline{h}$ in the horizontal plane. . This scalar product can be used to directly calculate the slope term in the equation (12.22). With this definition, $\underline{n}$ is not a unit vector. This property will be advantageous when projecting the wind. We then normalize the vector $\underline{n}$. The norm is denoted by $\mathcal{N}$.

$$\mathcal{N}^2 = 1 + \tilde{n}_x^2 h_x^2 + \tilde{n}_y^2 h_y^2. \tag{12.32}$$

We finally change the definition of the normalized $\underline{n}$ vector:

$$\begin{cases} n_x = \frac{\tilde{n}_x}{\mathcal{N}}, \\ n_y = \frac{\tilde{n}_y}{\mathcal{N}}, \\ n_z = \frac{\tilde{n}_x h_x + \tilde{n}_y h_y}{\mathcal{N}}. \end{cases} \tag{12.33}$$

Rate of spread projection on the horizontal plane

We compute $\mathcal{R}$ according to the front normal on the surface plane

$$\underline{\mathcal{R}} = \mathcal{R}\underline{n}. \tag{12.34}$$

We want to compute the projection of $\underline{\mathcal{R}}$ on $\underline{\tilde{n}}$.

$$\widetilde{\mathcal{R}} = \mathcal{R}\underline{n} \cdot \underline{\tilde{n}} = \mathcal{R}\cos\alpha \tag{12.35}$$

Numerically, we already know the value of $\tan\alpha$ but not the value of the angle. To compute this projection, it is necessary to compute $\cos(\mathrm{arctan}(\tan\alpha))$ which costs on average 3 times more than using the expression $\cos\alpha = 1/\sqrt{1+\tan^2\alpha}$. To optimize this calculation, we have

$$\widetilde{\mathcal{R}} = \mathcal{R}\frac{1}{\sqrt{1+\tan^2\alpha}}. \tag{12.36}$$

12.3 Heat fluxes parameterizations

In BLAZE, sensible and latent heat fluxes computation is based on energy reservoir. Each fire cell constitutes a sensible and latent energy reservoir called Available Sensible Energy (ASE) and Available Water Content (AWC), respectively, based on fuel properties. Then, the heat flux parameterization is the temporal description of how fast this reservoir is emptying. These parameterizations for sensible and latent heat fluxes are noted $\psi_h(t, t^a(\underline{x}))$ and $\psi_w(t, t^a(\underline{x}))$, respectively. They are functions of time and arrival time t^a at the position $\underline{x}$. To improve the spatial description of heat flux, these functions are moderated by the subgrid surface that is currently burning in the fire cell $\mathcal{S}(\underline{x}, t)$. Then, the surface fluxes are given by:

$$\Psi_h(\underline{x}, t) = \psi_h(t, t^a(\underline{x}))\mathcal{S}(\underline{x}, t), \tag{12.37}$$

$$\Psi_w(\underline{x}, t) = \psi_w(t, t^a(\underline{x}))\mathcal{S}(\underline{x}, t). \tag{12.38}$$

Ψ_h $[\mathrm{W\,m^{-2}}]$ is the sensible heat flux, and Ψ_w $[\mathrm{kg\,s^{-1}\,m^{-2}}]$ is the water vapor flux.

The complete description of the current flux models and the EFFR method are given in (Costes et al. 2021).

The paper will give the method used to compute surface heat flux. However, these surface fluxes are distributed over several vertical level in MÉSONH as volume source terms. For sensible and latent heat fluxes, these source terms are written, respectively as:

$$\frac{\partial \rho_{dref}\theta}{\partial t} = Q_h + \frac{\mathcal{F}_h}{C_{ph}}, \tag{12.39}$$

$$\frac{\partial \rho_{dref} r_v}{\partial t} = Q_w + \mathcal{F}_w. \tag{12.40}$$

Q_h represents all the others processes in the MÉSONH energy balance equation (advection, humidity correction, phase change, etc.), $\mathcal{F}_h$ $[\mathrm{W\,m^{-3}}]$ is the volume source term from BLAZE, and C_{ph} is the specific heat of moist air. Q_w represents all the others processes in the MÉSONH water vapor conservation equation, and $\mathcal{F}_w$ $[\mathrm{kg\,s^{-1}\,m^{-3}}]$ is the source term from BLAZE.

The surface terms computed by BLAZE are distributed by an exponential law. For the sensible heat flux, this distribution is written as:

$$\mathcal{F}_h(z) = \mathcal{F}_h^0 \exp\left(-\frac{z}{z_f}\right), \tag{12.41}$$

where $\mathcal{F}_h(z)$ is the volume source term, $\mathcal{F}_h^0$ is the value at the surface, and z_f is a characteristic height used as a parameter (XFLUXZEXT in the namelist). To determine $\mathcal{F}_h^0$, we add a constraint on the integral of the volume source term:

$$\int_0^{z_{\max}} \mathcal{F}_h(z)\,\mathrm{d}z = \Psi_h. \tag{12.42}$$

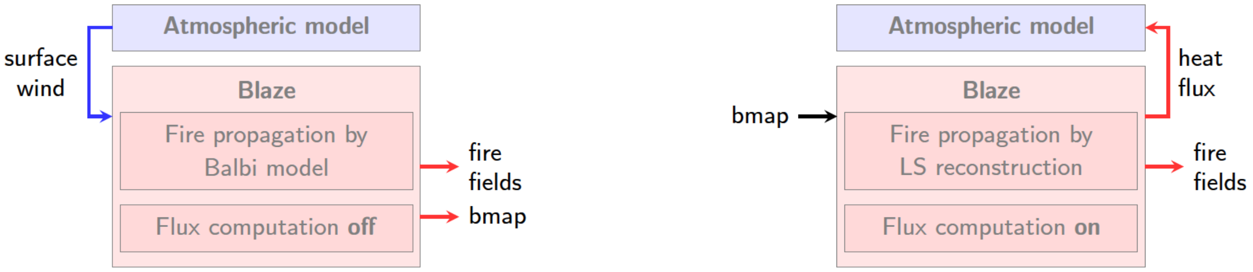

(a) Atmosphere-to-fire (A2F) mode (b) Fire-to-atmosphere (F2A) mode

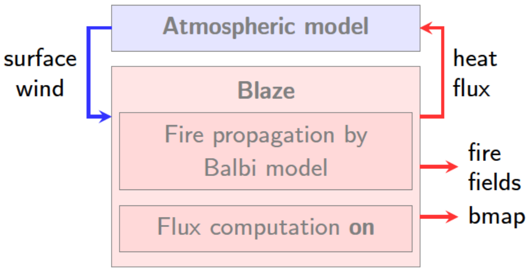

(c) Two-way coupled (2WC) mode

Figure 12.2: Two-way coupled (2WC) mode

The parameter $z_{\max}$ is the maximum injection height (XFLUXZMAX in the namelist). Numerically, the discretized volume source term $\mathcal{F}_k$ is the mean value of $\mathcal{F}_h(z)$ in the considered cell, noted k. It is computed as:

$$\mathcal{F}_k = \begin{cases} \frac{psi_h}{\Delta z_k} \frac{\exp\left(-\frac{z_{k-1/2}}{z_f}\right) - \exp\left(-\frac{\min\left(z_{k+1/2}, z_{\max}\right)}{z_f}\right)}{1 - \exp\left(-\frac{z_{\max}}{z_f}\right)} & \text{if } z_{k-1/2} < z_{\max}, \\ 0 & \text{else}. \end{cases} \tag{12.43}$$

Flux vertical levels are noted with semi-integer indexes, and mass vertical levels are noted with integer indices $z_k = \frac{z_{z-1/2} + z_{k+1/2}}{2}$. Then the vertical cell size is $\Delta z = z_{z+1/2} - z_{z-1/2}$.

12.4 Coupling modes

This section presents the three coupling modes between BLAZE and MÉSONH. For each mode, the coupling variables are exchanged at each atmospheric time step.

12.4.1 Forced atmosphere-to-fire mode (forced mode)

In the forced (A2F) mode (Fig. 12.2a), the fire spread is affected by the atmospheric flow, but the wind conditions are not disturbed by the fire. Blaze requires the wind conditions near the surface from an atmospheric model to compute Balbi's rate of fire spread, but no heat flux computation is needed. As output, Blaze provides the burning map and the fire-related fields (LS function ϕ, rate of spread $\mathcal{R}$, wind contribution to the rate of spread $(\mathcal{R} - \mathcal{R}_0)$, ASE and AWC).

12.4.2 Forced fire-to-atmosphere mode (fire replay mode)

To perform numerical convergence tests or investigate the atmospheric response to fire energy release, running simulations from a predetermined fire is of primary interest. This fire replay (F2A) mode (Fig. 12.2b) takes as input an existing burning map (obtained from simulation or observation) and computes latent and sensible heat fluxes to be injected into the atmospheric model. The fire spread model component is not used. Instead, a temporal reconstruction of the LS function ϕ is performed from information contained in the burning map. This is done through a sigmoid function of parameter λ:

$$\phi(x, y, t) = \frac{1}{1 + e^{-\lambda(t - t^a(x,y))}} \tag{12.44}$$

where the stiffness parameter λ [s^{-1}] corresponds to the numerical spread of the LS function that would be obtained by integrating Eq. (12.6) using RK3-WENO3 numerical schemes. Several Blaze simulations run on a simplified test case have shown that λ is given by the following law with respect to Δx_f:

$$\lambda(\Delta x_f) = 2.136\, e^{-0.211(\Delta x_f + 8.613)} + 0.064 \tag{12.45}$$

for $1 \leqslant \Delta x_f \leqslant 25$ [m]. This reconstruction leads to the maximum error between reconstructed LS and original LS lower than 9% for the coarsest mesh and lower than 0.5% for the most refined mesh. Most importantly, the sigmoid formulation (Eq. 12.44) guarantees by definition the exact same fire front position represented by the contour line $\phi = 0.5$. The injected heat fluxes are thereby well reproduced in the F2A simulations compared to the original simulations carried out in two-way coupled mode for varying fire mesh resolution Δx_f.

12.4.3 Two-way coupled mode

The 2WC (Fig. 12.2c) accounts for the two-way interactions between the fire model and the atmospheric model, meaning that surface winds simulated by the atmosphere model are used as input to the fire spread model component and that the fire feedback onto the atmosphere is imposed through the surface latent and sensible heat flux model component in Blaze.

12.5 Pyrolib: pre/post-processing python package for Blaze

Pyrolib is an open-source python package built for MÉSONH/BLAZE. It is freely available on Github and can be installed via Pypi.
The use of Pyrolib is particularly recommended for the preparation of FuelMap and the post-processing of the netcdf output files. An example of a script to generate a FuelMap.nc file is given in the package examples (simplecase.py). The CLI *pyrolib-post* is particularly recommended for post-processing tasks. See Pyrolib documentation for more information.

12.6 References

Balbi, J. H., F. Morandini, X. Silvani, J. B. Filippi, and F. Rinieri, 2009: A physical model for wildland fires. *Combustion and Flame*, **156 (12)**, 2217–2230, doi:10.1016/j.combustflame.2009.07.010.

Costes, A., M. C. Rochoux, C. Lac, and V. Masson, 2021: Subgrid-scale fire front reconstruction for ensemble coupled atmosphere-fire simulations of the fireflux i experiment. *Fire Safety Journal*, **126**, 103 475.

Santoni, P.-A., J.-B. Filippi, J.-H. Balbi, and F. Bosseur, 2011: Wildland fire behaviour case studies and fuel models for landscape-scale fire modeling. *Journal of Combustion*, **2011**, ID613 424, doi:10.1155/2011/613424.